Zeolite Synthesis

Mario L. Occelli, EDITOR
Unocal Corporation

Harry E. Robson, EDITOR
Louisiana State University

Developed from a symposium sponsored
by the Division of Colloid and Surface Chemistry
at the 196th National Meeting
of the American Chemical Society,
Los Angeles, California,
September 25–30, 1988

American Chemical Society, Washington, DC 1989

ACS Symposium Series

M. Joan Comstock, *Series Editor*

1989 ACS Books Advisory Board

Foreword

The ACS SYMPOSIUM SERIES was founded in 1974 to provide a medium for publishing symposia quickly in book form. The format of the Series parallels that of the continuing ADVANCES IN CHEMISTRY SERIES except that, in order to save time, the papers are not typeset but are reproduced as they are submitted by the authors in camera-ready form. Papers are reviewed under the supervision of the Editors with the assistance of the Series Advisory Board and are selected to maintain the integrity of the symposia; however, verbatim reproductions of previously published papers are not accepted. Both reviews and reports of research are acceptable, because symposia may embrace both types of presentation.

Preface

THE FIRST ZEOLITE, STILBITE, WAS DISCOVERED IN 1756 by Baron Cronstedt, a Swedish mineralogist. He named these types of minerals *zeolites* from the Greek words *zeo* (boil) and *lithos* (stone), because when gently heated, the stones evolved water vapor. Because of the multiplicity of properties possessed by natural zeolites, it is not surprising that extensive attempts at their synthesis began so long ago. In fact, efforts to achieve the hydrothermal synthesis of analogs of natural zeolites date back to 1845, although the elevated temperatures and pressures employed and the lack of proper identification techniques precluded a high degree of success for more than a century. The bulk of successful work began in the 1940s when X-ray diffraction provided easy product identification and R. M. Barrer developed the gel synthesis. This approach was based on starting with very reactive components in closed systems and employing temperature and crystallization conditions that were more typical of the synthesis of organic compounds than of mineral formation. *Zeolite Synthesis*, and the symposium on which it is based, is a review of the progress that, to date, has been made toward understanding the various aspects of this field on a molecular level.

By 1959, under the leadership of R. M. Milton, the Linde Division of Union Carbide had successfully synthesized nearly all the commercially important zeolites. The first chapter of this volume is a personal account by Milton of how Union Carbide pioneered the synthetic molecular sieve zeolite business. In the synthesis area, results have indeed been impressive. Of the 35 now-recognized naturally occurring zeolites, 24 have been duplicated in the laboratory. In the process, more than 200 new synthetic phases have been discovered, including VPI–5, ZSM–5, and ALPO, a new family of molecular sieves. Today, ZSM–5 is considered to be one of the most important catalytic materials to be found since the cracking properties of faujasite were established in the early 1960s by Plank and Rosinsky. Aluminophosphates, such as ALPO, SAPO, and MEAPO, equip the chemist with an almost endless supply of crystalline molecular sieves with unique composition and structural characteristics. Synthesis of VPI–5, the first 18-membered ring molecular sieve, suggests that many more new and technologically important molecular sieves (some of which exist already as models) await to be synthesized.

Until fairly recently, zeolite synthesis has been mainly an empirical science in which a large number of experiments were used to systematically change synthesis parameters in the hope of obtaining new phases and crystal composition. Good luck and the execution of the right "mistakes" were thought by many to be essential to the synthesis and discovery of new zeolites. This Edisonian approach to zeolite synthesis is now being gradually replaced by methods based on the use of new characterization techniques that will provide a better understanding of gel chemistry, zeolite nucleation, crystal growth, crystallization kinetics, and structure-directing phenomena.
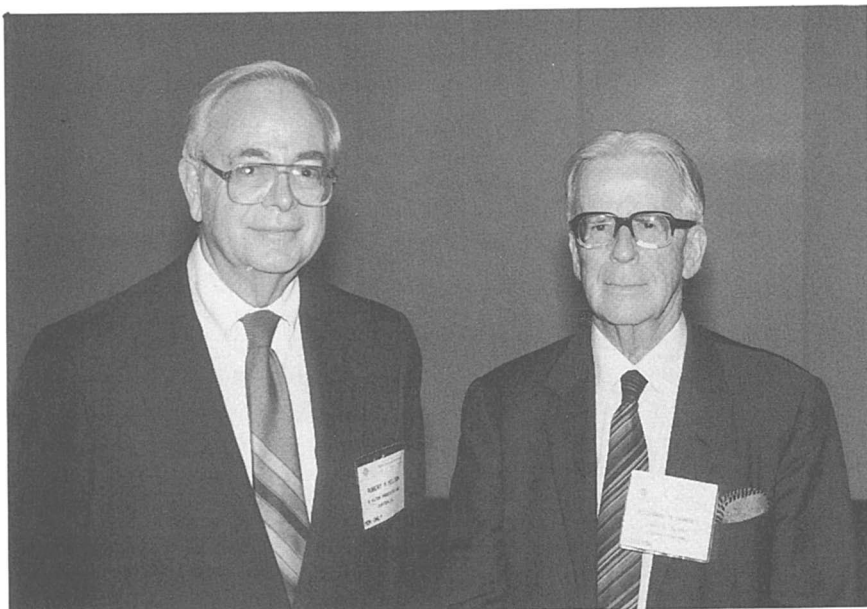
The two founders of zeolite synthesis technology, R. M. Barrer (right) and R. M. Milton (left), September 22, 1988, Los Angeles, CA (photo by Mario L. Occelli).

We would also like to thank D. E. W. Vaughan, E. M. Flanigen, T. Inui, D. Bibby, and G. Volyocsik for helping to chair the symposium, and to express our gratitude to the many colleagues who acted as technical referees. Mario L. Occelli is particularly grateful to Unocal for permission to participate in and complete this project, and to G. Smith for her invaluable secretarial help.

Finally, we would like to thank the authors of *Zeolite Synthesis* for the time and effort they gave to presenting their research at the symposium and preparing the manuscripts for this book.

MARIO L. OCCELLI
Unocal Corporation
Science and Technology Division
Brea, CA 92621

HARRY E. ROBSON
Department of Chemistry
Louisiana State University
Baton Rouge, LA 70803

February 16, 1989

Chapter 1

Molecular Sieve Science and Technology

A Historical Perspective

Robert M. Milton[1]

5991 Set-N-Sun Place, Jupiter, FL 33458

Union Carbide pioneered the synthetic molecular sieve zeolite business, initiating research in 1948, entering the market in 1954, and turning a profit on an annual basis beginning in 1960 with an up-front cost of a little over $7 million. Based on this effort, Union Carbide dominated the field of synthetic molecular sieves for many years. This state-of-the-art volume on zeolite synthesis represents a giant step from 1949, when I first began hydrothermal synthesis studies on zeolites at Union Carbide. Although this chapter is not intended to provide a thorough, historical perspective, it should give readers a view of the atmosphere and the people contributing to the initial development of the field of zeolite synthesis.

The work leading to Union Carbide's success began in 1948 after I had been at Linde's Tonawanda Research Laboratory for nearly two years. Management asked me to investigate physical adsorption as a potentially useful methodology in the purification and separation of air. At that time the only group working actively in zeolites was R. M. Barrer's group abroad. This introduction represents a condensed history of Union Carbide's work on molecular sieve zeolites from discovery to commercial success.

New Zeolite Synthesis Methodology

In the fall of 1948, I was measuring the adsorption characteristics of numerous commercial adsorbents and of the natural zeolite, chabazite. Several uses for silica gel in air separation plants were identified. But the more we learned about chabazite, the more intrigued I became by its potential as a commercial adsorbent as well as its possible use in air purification and separation. I envisioned, as others had before me [1-5], major new separation processes based on a series of different pore size zeolites. The stumbling blocks were that (1) chabazite was the only known zeolite with seemingly practical adsorption

characteristics, (2) large deposits of the mineral had never been found, and (3) although many had tried, no one had succeeded in synthesizing chabazite [6]. I requested and received permission for a limited exploratory zeolite synthesis program in mid 1949.

We started hydrothermal syntheses in September 1949, using relatively insoluble forms of silica and alumina in mildly alkaline solutions (pH 8-11) containing calcium, magnesium, and sodium cations at temperatures of 200°-300°C. Reaction periods varied from a few days to a week. In some experiments there was no reaction; in others we made analcime or small pore mordenite. These had been made by others under similar conditions and neither was considered a commercially useful adsorbent [7, 8].

Our first change in synthesis procedures was to repeat some of the earlier experiments while applying a hydrostatic pressure of about 2,000 psig. This additional pressure had no apparent effect on zeolite crystallization.

By October 1949, I started experimenting with crystallization at 100°C, reasoning that the higher water content zeolites with larger pore volumes and, presumably, larger pore sizes, would be more likely to crystallize at temperatures lower than 200°-300°C. In nature the anhydrous aluminosilicates were formed at relatively high temperatures, and the hydrous ones were believed to have been formed later as the earth's surface cooled. Not surprisingly, when we first tried low temperature synthesis with relatively insoluble silica and alumina in mildly alkaline solutions, there was no reaction in reasonable time periods.

This was solved by using soluble forms of silica and alumina under highly alkaline conditions. We dissolved sodium aluminate in water, or dissolved alumina trihydrate in hot sodium hydroxide solutions and then mixed the aluminate solution with sodium silicate solutions. On mixing a gel usually formed. The gel was stirred thoroughly and placed in metal or glass containers, which were sealed and immersed in a 100°C water bath. The results were dramatic. Within a few hours, hydrated solid species usually settled out of the mother liquor and in most cases these were crystalline zeolites. The relative amounts of sodium oxide, alumina, silica, and water in the initial gel were key variables in determining what materials were formed. Temperature, gel stirring, and gel aging were also important variables.

Following crystallization, the solid was separated from the mother liquor by filtration, washed with distilled water, and air dried in an oven at 100°C to remove loosely bound water. Samples of the dried powder were sent routinely to the x-ray laboratory. The fact that we could obtain a strip chart recording of the x-ray powder pattern within 30 minutes was an important factor in the pace of our work. Adsorption evaluations were facilitated by use of multiple, quartz spring, McBain-Bakr balances connected in parallel. As many as 16 adsorbent samples could be evaluated simultaneously.

By year end 1949 we had developed not only a new and widely applicable method for synthesizing zeolites but had discovered the A zeolite, the B zeolite later shown to be gismondite, the C zeolite later identified as basic sodalite, and a crystalline impurity named X [9-10].

I first identified the X zeolite by its x-ray peaks as an impurity in the B zeolite in 1949 at about a 20% concentration. We next saw it in February 1950 at about a 50% concentration with the B zeolite when N. R. Mumbach brought in the x-ray pattern from his first attempt to scale up the synthesis of B. By mid 1950, I had discovered how to routinely make pure zeolite X [11]. Chabazite was synthesized in late 1950, and by mid 1951 I had made three new

zeolites in the potassium-aluminosilicate system [12-14]. Adsorption properties of A and X had been determined including the discovery that the pore size could be reduced or enlarged by appropriate ion exchange with potassium, calcium, or magnesium ions. Both A and X had proven stable at 500°C. [15,16]. By mid 1953 we had made a total of 20 crystalline zeolites, including erionite, gmelinite, and 14 with no know natural counterparts [15].

Crystal Structure

In mid 1951 two young scientists joined the laboratory staff, Drs. T. B. Reed, a crystallographer, and D. W. Breck, an inorganic chemist. Reed had hoped to work with me on molecular sieves. In the applicant interview, I had challenged him to determine the detailed structures of the A and X zeolites from powder x-ray data, pore size and volume information, and ion exchange properties. He was assigned, however, to a different project in another group.

Dr. Breck was assigned to my molecular sieve group. He quickly appreciated the value of knowing the crystal structures of A and X if we were to fully understand their unique properties. Early in 1952 Reed and Breck decided to work together on the A and X structures. Progress was slow. Their studies were conducted frequently during lunch hour and in the evenings, since Reed had another full time assignment and Breck was busy with continuing zeolite synthesis and characterization studies.

By March 1954 they achieved their final structure for the A zeolite, verifying it shortly thereafter with single crystal x-ray data on a 30 micron A crystal that Breck and Nancy A. Acara had recently grown [17]. By mid 1954, they also completed the structures of X and faujasite [18], with help from single crystal x-ray data on faujasite. This was completed two to six years before these structures were described by others [19-21]. Interestingly, a manuscript by Breck et al. on the synthesis, structure, and properties of X was rejected by the *Journal of Physical Chemistry* in 1958 on the basis of insufficient reader interest.

These were remarkable accomplishments considering the size of the unit cells and the complexity of the structures. I remember posing the problem to Dr. Linus Pauling when he visited our laboraory in the mid fifties. Some 25 years earlier he had published on the structure of the zeolite natrolite and several feldspathoids [22]. He assured me that it was a waste of time to even try to determine the detailed structure of zeolites from powder x-ray data.

X, Y, Faujasite

In August 1952 Breck located the powder x-ray data for mineral faujasite and realized that it was very similar to that of the X zeolite. We obtained about 50 mg. of faujasite and studied it carefully. The x-ray pattern was indeed very similar to that of X. The adsorption capacity was somewhat lower but similar. The silica/alumina ratio was 4.7 compared to 2.5 for X. The cations in faujasite were calcium, magnesium, and barium, not sodium as in X. It was clear that X and faujasite were isostructural but with different compositions. Further similarities and differences could not be studied at that time due to the limited supply of faujasite.

In mid 1954 Breck proposed that it should be possible to synthesize the X structure with silica/alumina ratios as high as 4.7, found in faujasite, and possibly higher. He further hypothesized that the higher ratio materials, with lower aluminum and exchangeable cation content, would be more stable to acid attack

and to heat in the presence of water vapor than the 2.5 ratio X. If true, this could be a valuable property as X had limited stability to the high temperature burn-off of carbon deposits necessary in regeneration of petroleum cracking catalysts and to acid containing gases such as cracker gases.

N. A. Acara, Breck's synthesis assistant, collected samples of X made over the past few years and sent some of them in for chemical analysis. Heretofore most lots of X had never been analyzed. Those that had, always gave silica/alumina ratios very close to 2.5 with none higher than about 2.7. This analysis of old lots of X showed some lots with ratios as high as 2.83 and 2.92. With this background, Breck and Acara soon learned how to routinely synthesize X with ratios between 3.0 and 4.0. Later analyses of additional old lots of X showed ratios of 3.05, 3.47, and 3.48. We had made high silica X before but had not recognized it.

Beginning in 1956, E. M. Flanigen learned how to make X with silica/alumina ratios between 4.0 and 5.7. Now with a full range of ratios from 2.5 to 5.7, we were able to study systematically the variation in properties with alumina content. Breck's original hypothesis proved to be correct. The high silica forms were more stable to acid attack and to high temperatures in the presence of water vapor than the low silica forms [23].

Since X had been defined in our patent applications as having silica/alumina ratios between 2.0 and 3.0, and because there was a significant change in properties at a ratio of 3.0, the isostructural zeolites with ratios above 3.0 and up to 6.0 were named and patented as zeolite Y. The Y zeolite was not introduced into the market place until we had time to file appropriate patents and evaluate it as a catalyst [24].

Patents

Scientists do not usually get deeply involved in the intricacies of patent coverage, but it was essential in the case of the A and X zeolites because they involved concepts and science totally new to Union Carbide patent lawyers. During 1952 and 1953 I spent probably 20% of my time on patent matters.

The first lawyer assigned to molecular sieves planned to base protection on the process of manufacture. Since we could not possibly cover all practical methods of making A and X, we asked for composition of matter coverage, with process claims only to protect our actual manufacturing methods, and broad use claims covering as many applications as possible, so as to minimize the possibility of restrictive use claims by others.

Carbide's patent department had reservations because in their experience, composition of matter claims had to be drawn very narrowly to be valid and as such were frequently easy to circumvent. We convinced them that the unique properties that make A and X useful are singular results of their specific chemical composition and the arrangement of atoms in the crystal lattice of the zeolites. To our knowledge, the use of powder x-ray data as a finger print to uniquely identify a specific crystal structure was a new concept in patent protection.

When the first drafts of the patent applications came back from our patent department for checking, it was clear that major changes were needed. After several unsuccessful attempts to revise the original drafts, I had to rewrite both applications. At about that time a young patent lawyer, J. B. Browning, replaced the original attorney. He was quick to comprehend the significance of

the project, approved the basic strategy, made several important suggestions to clarify the disclosure and simplify the claims, and the applications were filed on December 24, 1953.

Both applications were rejected a number of times primarily based on the examiner's inability to understand the differences between our new A and X zeolites and prior art in non-crystalline zeolites used in water softeners and their unfamiliarity with compositions of matter identified by x-ray patterns. Finally Dr. Breck and I, armed with crystal models, models of variously sized adsorbate molecules, x-ray patterns, and comparative data on water softening zeolites, visited the examiner and his assistants in Washington.

With these props we were able to explain molecular sieve adsorption, relate it to the crystal structures of A and X, and relate those to the x-ray patterns. The examiners understood, and after they removed the use claims for separate continuation-in-part filing, they issued the patents on April 14, 1959 [9,11].

Catalysis

In September 1951, I authored an Idea Memorandum arguing that both the A and X zeolites should make good catalysts or catalyst supports, specifically mentioning hydrocarbon cracking, abnormally strong adsorption forces, molecular size selectivity, and the possibility of atomically dispersed metals on the internal surfaces. In March 1952, I discussed these ideas in a paper at a Union Carbide catalyst conference and later at our Bakelite Division laboratory.

First results came from the Bakelite Division in 1953. They were catalytically cracking ditolyethane to make methyl styrene. They found that magnesium/hydrogen exchanged A and calcium/hydrogen exchanged A were both more active and more selective catalysts than the best commercial silica-alumina cracking catalysts. The pure sodium A form was inactive and the pure hydrogen exchanged form was unstable. Ditolyethane is too large a molecule to enter the A zeolite pore structure.

In February and March of 1954, Breck and I prepared hydrogen exchanged X with greater than 60% of the sodium cations replaced, both by direct exchange with acid and by exchange with ammonium ions followed by heating to drive off ammonia. Both forms of hydrogen X were tested in cracking of n-tetradecane and isopropylbenzene. Both forms were extremely active catalysts producing primarily C_6 - C_7 hydrocarbons from n-tetradecane and benzene and propylene from isopropylbenzene. This was the first discovery of the unique hydrocarbon cracking activity of the X structure, providing at least 60% of the sodium cations are removed from the lattice.

A patent application [25] was filed on March 13, 1956 on the catalytic cracking of hydrocarbons with hydrogen X in the names of Milton and Breck. This application, too, was rejected by the examiner because he could not understand wherein our crystalline zeolite X was different from the amorphous, water softening zeolites of the prior art. This objection should have been easily overcome as it was in the basic A and X cases. For some unknown and still unexplained reason, however, this application was abandoned by our patent department on June 30, 1959.

By mid 1954 Dr. Breck and I had developed methods for dispersing metals on the inner surfaces of the A, X, and Y zeolites and had initiated catalytic studies with them [26-27]. Dr. C. R. Castor and S. W. Bukata were added to this effort; during 1954-1955 they carried out exploratory studies with platinum, other

metals, and select metal oxides dispersed on the X and Y zeolites. Very active hydrocarbon hydrogenation and dehydrogenation catalysts were made, tested, and patented [28-31]. These catalytic studies were not continued at Linde as Research management decided to emphasize other zeolite programs.

With this hiatus in catalytic research on zeolites at Carbide, we began encouraging outside groups to evaluate A and X as catalysts. In an invited paper on molecular sieves at the Gordon Research Conference on Separations in 1955, I concluded my presentation with an explanation of why I thought the A and X zeolites would show unusual catalytic effects-- highly polar surfaces, unusually high heats of adsorption, molecular size selective availability of the internal surfaces, and the ease of dispersal of metal atoms on the internal surfaces. Dr. P.B. Weisz and another Mobil Oil scientist attending the conference questioned me at length after the paper. I made similar presentations in 1955 and 1956 at Esso Research and Engineering, Mobil Oil, Union Oil, Standard of California, and Shell Development laboratories.

In 1956 I organized a new in-house catalytic research group in Linde's Development Department, reporting to Dr. T. L. Thomas. Dr. J. E. Boyle joined in June 1956 and P. E. Pickert, in early 1957. Dr. J. A. Rabo was brought in as group leader in June 1957. The charter we gave Dr. Rabo was to develop zeolite based catalysts for use in major petroleum refining operations such as catalytic cracking, isomerization, reforming, and hydrocracking. Our confidence was based on the earlier results with exchanged A and with hydrogen and decationized X, the availability of the more stable Y zeolite, and the promising initial studies with platinum on X and Y.

When Dr. J. Rabo arrived, the group was studying reforming with platinum impregnated X zeolite. He broadened the program to include cracking and isomerization, shifted emphasis from X to Y, replaced sodium ions in the lattice with ammonium and polyvalent cations, and worked with unimpregnated as well as impregnated Y zeolite. By mid 1958 we had developed a unique zeolite catalyst for the dealkylation of alkyl aromatics to produce benzene. By early 1959 we had developed and completed laboratory testing of a superior pentane and hexane isomerization catalyst based on a decationized, 0.5 wt.% platinum loaded Y zeolite. By December 30, 1959 we had filed a patent application on hydrocarbon conversion processes and catalyst using polyvalent exchanged Y with greater than 40% removal of sodium cations from the lattice. This patent issued on February 22, 1966 was the first one to cover the Y based catalysts now used world wide in the cracking of gas oils [32].

Simultaneously scientists at Esso Research and Engineering and Mobil Oil were working with X based catalysts [33-35]. Mobil Oil introduced the first zeolite based catalysts for cracking gas oils in 1962 using rare earth exchanged X in a silica-alumina matrix. This replaced the older silica-alumina catalysts. When we made Y available, the Y based catalysts largely replaced the X based catalysts in this application.

In mid 1959 a significant decision was made, with the sales manager and me dissenting, not to enter the finished catalyst business at that time with our new isomerization catalyst, and to concentrate instead on the adsorbent portion of the molecular sieve business. Accordingly, a major reduction was made in the level of our catalytic studies with zeolites shortly thereafter.

Commercialization

Early in 1950, only a few months after the discovery of A and B, an application group and a process group were set up to develop uses, scale up synthesis, and agglomerate the powder into useful forms. By mid 1951 all signs were positive [Milton, R.M., Linde Technical, B-148, 2/7/51, unpublished], and the level of activity was raised. In June 1953 we issued a project status report recommending test marketing [Burdick, J.N., Milton, R.M., Peters, P.E., Linde Technical Memorandum, B-173, 6/9/53, unpublished]. In the spring of 1954, test marketing was initiated with molecular sieve types 4A, 5A, and 13X. Research management, R. A.Jones, and I made most of the customer visits, usually accompanied by a member of the regular Linde sales department. Interest was very high and by fall of that year, Linde announced it was entering the business of manufacturing and selling molecular sieve zeolites.

At this time prime responsibility for the project was shifted from the Research Department to the Development Department under W.B. Nicholson. E.R. Behnke was given responsibility for molecular sieve sales, and I was made Manager of the Tonawanda Development Laboratory, responsible for molecular sieve applications, and in time, process development and manufacturing.

Major expansions in both development and sales groups occurred in the period 1955-1958. A sales force was staffed with specially trained engineers working full time on molecular sieves. Laboratory engineers and chemists studied specific applications and developed the technology to optimize the design of adsorption systems. Moving bed systems were evaluated jointly with Union Oil. Catalysis research was reactivated. Latent catalyst systems were developed for curing rubber and plastics with active accelerators adsorbed on the molecular sieves.

Synthesis, filtering, drying, ion exchange, and activation processes were successfully scaled up. Pellet forming procedures were perfected and bead forming techniques developed. A pilot plant and modest scale production facility were built and operated at Tonawanda.

In a cooperative effort, Linde Research and Union Carbide Nuclear Co. prospected for and located deposits of natural zeolites in Western United States. No deposits of A, X, Y, or faujasite were found. Numerous and extensive deposits of other useful zeolites were located (chabazite, erionite, mordenite, clinoptilolite), claimed and at a later date some were mined and sold for special uses. We learned how to dealuminate zeolites while maintaining crystal structure, opening the pore and increasing the silica/alumina from 10 to about 20 in mordenite. Procedures for synthesizing A, X, and Y from clays were discovered.

In early 1958 responsibility for the molecular sieve project was shifted to Linde's New Product Department where it was to be treated as an independent business, no longer a development project. I was made Assistant Manager of New Products and was responsible for the molecular sieve business. E.R. Behnke became Sales Manager, and R.W. Pressing became Manager of Development and Production; both reported to me.

In February 1959 I was transferred back to research as Director of Linde's Tonawanda Research Laboratory, including its molecular sieve research group. Mr. Behnke took over as General Manager of the Molecular Sieve Department with Mr. R.A. Jones as Sales Manager and Dr. T.L. Thomas as Director of Technology. Mr. Langerhans became Manager of the Mobile Plant when it was opened.

Major Contributors

Many people have contributed to the success of the molecular sieve project at Union Carbide over the years. I would like to mention the following whose contributions were very important during this initial period, through approximately 1959.

- Dr L.I. Dana, Linde Vice President, hired me and put me to work on air separation. He and Dr. J.M. Gaines, Director of Research, asked me to work on physical adsorption and strongly supported the molecular sieve project at all times. Dr. Dana made the decision to test market and set the initial prices.

- Dr W.G. Eversole was my supervisor from 1946 to 1953. Besides being a fine scientist, he was inspiring, imaginative, fully supportive, and a valuable consultant.

- W.B. Nicholson was responsible for the decision to enter the molecular sieve business, for selling top management on the heavy expenditures needed to launch the new business, and for guiding the project through its most difficult period.

- E.R. Behnke developed the initial sales strategy, built the sales force, was put in charge of the molecular sieve business when I returned to research, and shepherded the business until it was secure and profitable.

- Dr. T.L. Thomas participated in the earliest research on adsorption/desorption kinetics, air separation, pressure swing adsorption systems, liquid phase separations, and ion exchange applications. He directed many of the application studies between 1955 and 1959.

- R.L. Mays was the technical expert on drying of gases and liquids, recovery of olefins, and regeneration of molecular sieve beds, and a key supervisor in application technology.

- R.A. Jones initiated application studies in 1950, was coinventor of the first major application of molecular sieves [36], led our entire application engineering group prior to going into field sales, and later became Sales Manager.

- R.L. Langerhans was my assistant during the initial discovery period (1948-1950), the first person to work with the clay bonding of zeolite powders, and assisted in siting and design of the Mobile plant and was its first plant manager.

- Dr. D.W. Breck was the discoverer of the Y zeolite, a co-discoverer of the unique catalytic cracking activity of the X zeolite, and with Dr. T.B. Reed worked out the crystal structures of A and X. He was certainly one of the world's outstanding zeolite scientists.

- Dr. E.M. Flanigen is a world expert on zeolite synthesis. In the early years she was first to synthesize high silica Y with silica/alumina rations above 4.0, first to remove aluminum from zeolite lattices without loss of structure, and was responsible for identification and evaluation of the myriad of samples from Union Carbide's investigation of sedimentary zeolite deposits in Western United States. Additionally, I would like to acknowledge her assistance in

preparation of this paper, particularly for reviewing old data books to check the accuracy of my memory.

- Dr. J.A. Rabo led our catalyst research group from 1957 to 1961 and played a key role in the discovery of the catalyticly active ingredient used world wide in the catalytic cracking of gas oils to produce gasoline.

- When we started selling molecular sieves, little was known about heat and mass transfer in fixed bed adsorption/desorption. Design was an art. G.J. Griesmer, J.J. Collins, F.W.Leavitt, W.F. Avery, and K. Kiyonaga made it a science, a unit process we understand and can optimize. Griesmer led much of this activity and was primarily responsible for Union Carbide's Iso Sieve process for separating normal from iso paraffins [37].

- E.H. Westerland and G.L. Ribaud conducted and/or supervised most of our very successful process and manufacturing development studies including development of our pellet forming technology.

- W. Drost was my synthesis assistant from 1950 to 1952 and later developed our methods for making hard, attrition-resistant molecular sieve beads.

- R. E. Cuddeback led the design team for the Union Carbide Mobile Plant for manufacture of molecular sieve products.

Literature Cited

1. Lamb, A. B. U.S. Patent 1 813 174, 1931.
2. Lamb, A. B.; Woodhouse, J. C. *J. Am. Chem. Soc.* 1936, 58. 2637.
3. Barrer, R. M. U.S. Patent 2 306 610, 1943.
4. Barrer, R. M. *J. Soc. Chem. Ind.* 1945, 64, 130.
5. Barrer, R. M. British Patent 574 911, 1946.
6. Barrer, R. M. *Discuss. Faraday Soc.* 1949, 5, 326.
7. Straub, F. G. *Ind. Eng. Chem.* 1936, 28, 113.
8. Barrer, R. M. *J. Chem. Soc.* 1948, 2158.
9. Milton, R. M. U.S. Patent 2 882 243, 1959.
10. Milton, R. M. U.S. Patent 3 008 803, 1961.
11. Milton, R. M. U.S. Patent 2 882 244, 1959.
12. Milton, R. M. U.S. Patent 2 996 358, 1961.
13. Milton, R. M. U.S. Patent 3 010 789, 1961.
14. Milton, R. M. U.S. Patent 3 012 853, 1961.
15. Breck, D. W.; Eversole, W. G.; Milton, R. M. *J. Am. Chem. Soc.* 1956, 78, 2338.
16. Breck, D. W.; Eversole, W. G.; Milton, R. M.; Reed, T. B.; Thomas, T.L. *J. Am. Chem. Soc.* 1956, 78, 5963.
17. Reed, T. B.; Breck, D. W. *J. Am. Chem. Soc.* 1956, 78, 5972.
18. Breck, D. W.; Flanigen, E. M.; Milton, R. M.; Reed, T. B. *Abstracts 134th Natl. Meeting, Am. Chem. Soc.* Chicago, Sept. 1958.
19. Bergerhoff, G.; Koyama, H.; Nowacki, W. *Experienta* 1956, 12, 418.
20. Bergerhoff, G.; Baur, W. H.; Nowacki, W. *Neues Jahrb. Mineral,* Monatsh 1958, 9, 193.
21. Broussand, L.; Shoemaker. D. P. *J. Am. Chem. Soc.* 1960, 82, 1041.
22. Pauling, L. *Proc. Nat. Acad. Sci.* 1930, 16, 453.
23. Breck, D. W.; Flanigen, E. M. *Molecular Sieves, Soc. Chem. Ind.,* London, 1968, 47.

24. Breck, D. W.   U.S. Patent 3 130 007, 1964.
25. Milton, R. M.; Breck, D. W.   U. S. Patent Application, Ser. No.   571,129, 1956.
26. Breck, D. W.; Milton, R. M.   U. S. Patents 3 013 982, 3 013 983, 3 013 985, 1961.
27. Milton, R. M.   U.S. Patents 3 200 083, 1965, 3 236 903, 1966.
28. Milton, R. M.; Castor, C. R.   U.S. Patent 3 013 987, 1961.
29. Breck, D. W.; Castor, C. R.; Milton, R. M.   U.S. Patent 3 013 990, 1961.
30. Bukata, S. W.; Castor, C. R.; Milton, R. M.   U.S. Patents 3 013 988, 1961, 3 236 910, 1966.
31. Breck, D. W.; Bukata, S. W.   U.S. Patent 3 200 082, 1966.
32. Rabo, J. A.; Pickert, P. E.; Boyle, J. E.   U.S. Patent 3 236 762, 1966.
33. Kimberlin, C. N. Jr.; G1adrow, E. M.   U.S. Patent 2 971 903, 1961.
34. Plank, C. J.; Rosinski, E. J.; Hawthorne, W. P.   *Ind. Enq Chem., Prod. Res. Dev.* 1964, 3, 165.
35. Weisz, P. B.; Frilette, V. J.   *J. Phys. Chem.* 1960, 64, 382.
36. Jones, R. A.; Milton, R. M.   U.S. Patent 2 810 454, 1957.
37. Griesmer, G. J.; Avery, W. F.; Lee, M. N. Y.   *Hydc. Proc. Petr.*   Ref. 1965, 44 [6], 147.

RECEIVED December 22, 1988

Chapter 2

Zeolites: Their Nucleation and Growth

R. M. Barrer

Chemistry Department, Imperial College, London SW7 2AZ, England

Zeolite synthesis proceeds via nucleation, which
is a consequence of local fluctuations, small in
extent but considerable in degree of departure
from the mean for the solution, followed by spon-
taneous growth of nuclei exceeding a critical size.
A physico-chemical basis for the critical size
requirement has been described. There is evidence
that chemical events rather than diffusion can
govern subsequent linear growth of zeolite crystals.
To succeed in synthesis it is essential during
growth to stabilise the open structure by inclusion
of quest molecules. This requirement has a thermo-
dynamic origin which has been developed and applied
to formation of zeolites, porosils and AlPO's.
The explanation of some experimentally observed
features of zeolite synthesis follows from the
treatment. A distinction is made between zeolitic
stabilisers and nucleation templates.

As the potentialities of micropores in crystals rather slowly
became realised there developed an area of synthetic chemistry
which has yielded a remarkable variety of microporous structures.
Most are 3-dimensional 4-connected nets, of which the numbers
envisaged vastly exceed the numbers prepared experimentally.
Accordingly the search for chemical pathways to new porous crystals
proceeds apace, both for its scientific interest and its possible
industrial rewards.
    This account will emphasise several physico-chemical aspects of
synthesis which help in understanding the "green fingers" approach
of much current research on the formation of porous crystals.

Aluminate and Silicate Solutions

In the high pH range needed for zeolite synthesis aluminate solutions
are relatively simple in that the anions present are almost exclus-
ively $Al(OH)_4^-$. On the other hand in silicate solutions around room

temperature various anions co-exist according to the ratio of base to silica, the nature of the base, and the concentration.

There has, on the other hand, been little study of silicate solutions in the temperature range most important for zeolite synthesis (up to ~250°C). However Knight et al (1) made an interesting observation on tetramethylammonium silicate solutions 1 M in Si and with Si/N = 1/2. The room temperature equilibrium was perturbed by ~30 s heating to 100°C, quenching in liquid nitrogen and warming to room temperature. For the first few minutes the NMR spectrum then showed predominantly monomeric silicate anions with small amounts of dimer and trimer. Trigonal prism anions next began to appear followed after several hours by cubic anions. The latter increased steadily in relative amount until after 16 days equilibrium was established. The experiment shows slow equilibration at room temperature, rapid perturbation of this equilibrium at 100°C, and a primarily monomeric anionic constitution at 100°C. This experiment should be extended to other systems since it may have general implications for molecular mechanisms of nucleation. This would be especially true of the clear aluminosilicate solutions referred to below.

Reaction Mixtures

The usual result of mixing aluminate and silicate solutions is the formation of a gel, which may later separate into a clear supernatant liquid and a gel. One may ask whether nucleation is homogeneous (in solution) or heterogeneous (in gel). A partial answer may be provided if it can be demonstrated that zeolites can grow from clear solutions. Guth et al (2) and Ueda et al (3,4) have shown how such solutions can be prepared.

From clear Na- aluminosilicate solutions Ueda et al have crystallised analcime, sodalite hydrate, mordenite, faujasite (Na-Y), zeolite S (gmelinite type) and zeolite P (gismondine type), so that homogeneous nucleation is at least possible. Where gel is present crystals nucleated homogeneously would, as growing crystals, become enmeshed with gel so that homogeneous and heterogeneous nucleation are difficult to differentiate in gel-containing media.

Whether nucleation is homogeneous, heterogeneous or both there is strong evidence that in subsequent crystal growth the gel, if present, progressively dissolves and that the dissolved material then feeds the growing crystals. This also applies in successive transformations such as (4):

$$\text{solution} \rightarrow \text{Na-Y} \rightarrow \text{Na-S} \rightarrow \text{Na-P},$$
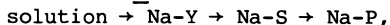
because each crop of crystals in the succession has its own size range and morphology rather than being a pseudomorph of its parent, as would be the case in an internal solid state transformation.

Zeolite Crystallisation from clear Solutions

The clear aluminosilicate solutions from which Ueda et al (4) studied crystallisation of zeolites Y, S and P were based on the composition range $10Na_2O.(0.35-0.55)Al_2O_3.(22-28)SiO_2.(250-300)H_2O$. Figure 1 shows the region in which gel and solution co-existed (cross-hatched), the region of clear solution, and the formation fields of the three zeolites from the clear solution.
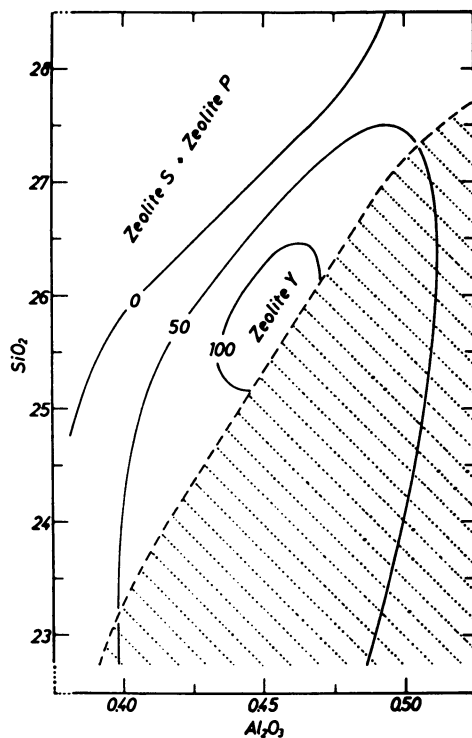
Figure 1. Crystallisation fields of zeolites Y, S and P at 100°C from clear aluminosilicate solutions. In the cross-hatched area gel and solution co-exist. (Reproduced with permission from Ref. 4. Copyright 1984 Butterworths.)

For crystallisation of Y the optimum composition of solution was $10Na_2O.0.45Al_2O_3.26SiO_2.270H_2O$. Faujasite (zeolite Y) appeared after ~12 hours, and the crystals were of rather constant composition, having, over all the experiments, ratios SiO_2/Al_2O_3 between 5.1 and 5.6. Because these ratios are so much greater in the parent solutions the Al has been selectively removed from solution and its concentration therein drops much faster than those of Na and Si. When SiO_2/Al_2O_3 in solution had in this way risen from 58 to 73 zeolite S began to appear and the yield of Y to decrease. When SiO_2/Al_2O_3 had reached about 102 zeolite P started to form and the yield of S began to decline.

Also, if the solutions had an initial SiO_2/Al_2O_3 ratio of 73, S formed but no Y, while if this initial ratio was 102, P formed but no S. This behaviour suggests caution in interpreting all crystallisation sequences as examples of Ostwald's rule of successive transformations. The rule states that in a crystallisation sequence the new phases replace each other in the order of a step by step descent of a ladder of increasing thermodynamic stability. An example in a hydrothermal system is (5):

Amorphous SiO_2 → cristobalite → keatite → quartz.
The optimum check of Ostwald's rule would, as in the above sequence, involve parent gel and successive phases all of the same composition. This condition is not met in many crystallisation sequences.

Nucleation and Crystal Growth

Studies of Raman (2) and NMR (6) spectra of solutions of aluminates and silicates, and of their mixtures under conditions yielding clear aluminosilicate solutions, agree in showing at least partial suppression of the $Al(OH)_4^-$ ion when silicate anions are present, supporting the view that aluminosilicate anions form around room temperature. It is then possible to visualise how such anions could form more complex units and germ nuclei. An example is shown in Figure 2 in which 4-ring anions yield the cubic unit found in the zeolite A framework, or the double crankshaft chain found in felspars or in phillipsite-harmotome zeolites (7).

While actual chemical events involved in nucleation and crystal growth are not known a phenomenological treatment (8) gives some insight. Willard Gibbs (9) considered processes of phase separation of two extreme kinds. In the first, fluctuations in concentration occur which are minute in volume but large in extent of departure from the mean (the case of binodal phase separation). In the second the volume of the fluctuation is large but the deviation from the mean for the solution is minute (responsible for spinodal phase separation). In nucleation of zeolites one is conerned only with fluctuations of the first kind.

One may enquire what factors oppose the immediate appearance of viable nuclei growing spontaneously. Whether in gel or solution a positive interfacial free energy term Δg_σ arises which is increasingly important relative to other free energy terms the larger the surface to volume ratio. In a restraining matrix the germ, through misfit, may also produce a positive strain free energy, Δg_s. Both these terms greatly reduce the probability of a germ nucleus becoming viable. The net free energy of formation of a germ
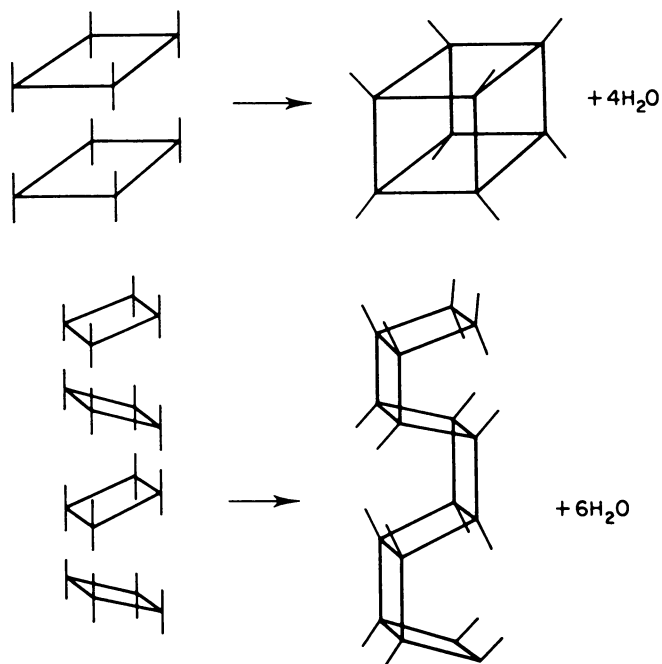
$+4H_2O$

$+6H_2O$

Figure 2.   Formation from 4-ring anions of cubic units found in
            zeolite A and double crankshaft chains found in felspars
            and phillipsite-harmotome zeolites. (Reproduced with
            permission from Ref. 7. Copyright 1982 Academic Press.)

consisting of j structural units of a particular kind is therefore

$$\Delta g_j = \frac{\Delta G}{N_A} j \quad + \quad \Delta g_\sigma + \quad \Delta g_s \tag{1}$$

where ΔG is the free energy of formation of a mole of bulk crystal, i.e. the amount of crystal containing an Avogadro number, N_A, of the structural units. ΔG is negative in sign. Δg_σ is proportional to the interfacial area, and so to $j^{2/3}$, while Δg_s is proportional to j. Thus, with $A = -\Delta G/N_A$, one has

$$\Delta g_j = -Aj + Bj^{2/3} + Cj \tag{2}$$

where A, B and C are positive coefficients. For small j, where the surface to volume ratio is very large, the positive term $Bj^{2/3}$ can be dominant. In solution or gel we expect C to be zero or small, i.e. $A > C$. As j increases the negative term $-(A-C)j$ will grow more rapidly than $Bj^{2/3}$. Accordingly, when Δg_j is plotted against j the curve initially has a positive slope and Δg_j is positive, but at some value of j this curve passes through a maximum and thereafter decreases, as shown in Figure 3 (<u>8</u>). At the maximum $d\Delta g_j/dj = 0$ and so from Equation 2 the values of j and of Δg_j at the maximum are

$$j_m = \frac{8B^3}{27(A-C)^3} \quad ; \quad \Delta g_{jm} = j_m \frac{(A-C)}{2} \tag{3}$$

Any nucleus in which j exceeds j_m will <u>add</u> more lattice-forming units with a decrease in free energy and therefore tends to grow spontaneously; but any germ nucleus in which j is less than j_m will <u>lose</u> lattice-forming units with a decrease in free energy, and will therefore tend to disappear. Even so, fluctuations ensure that some germs eventually reach and cross the saddle point in Figure 2 and then grow spontaneously.

As the total surface area of growing crystals increases, and vastly exceeds the total area of germ nuclei, crystals will dominate more and more strongly over fresh nuclei in consuming the lattice-forming units available. Accordingly the nucleation rate should build to a maximum early in the curve of yield against time, but will thereafter, through the competition with crystals for chemical nutrients, tend to decay towards zero. This behaviour was found by Zdhanov and Samuelevich (<u>10</u>) from an analysis of the linear growth rates of individual crystals of Na-X and the size distribution of the final crop of crystals.

Also, as the total area of growing crystals increases so does the rate at which chemical nutrients are consumed. The slope of the curve of yield against time therefore increases. Later, as the supply of nutrients becomes more and more exhausted, the slope of the curve decreases to zero. As a result curves of yield vs. time are sigmoid in contour, as illustrated in Figure 4 (<u>11</u>).

Two results of practical interest follow from the above reasoning. Firstly, the smaller the number of viable nuclei the larger will be the average crystallite size in the final crop of crystals. Secondly,
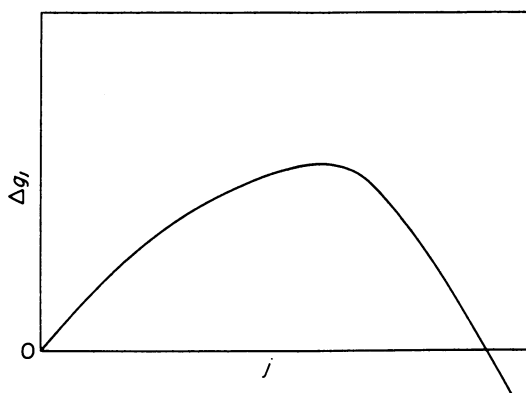
Figure 3.   The form of the curve of Δg_j plotted against j.
(Reproduced with permission from Ref. 8.   Copyright 1982
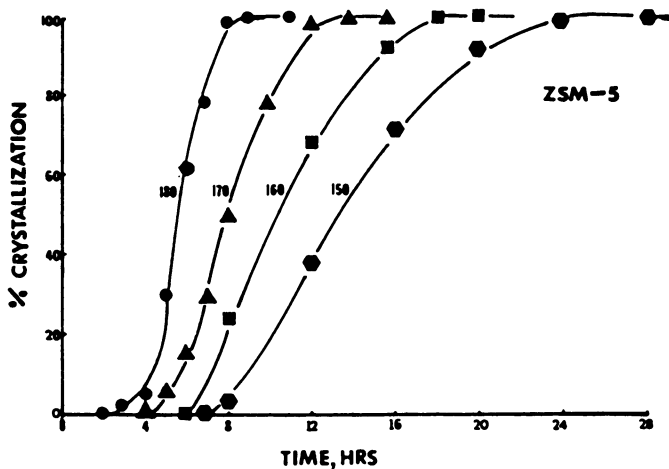Academic Press.)

Figure 4.   The typical sigmoid form of curves of yield of zeolite
plotted against time.   The illustration is for ZSM-5
(Silicalite 1).   ● 150°C; ■ 160°C; ▲ 170°C; ● 180°C
(Reproduced with permission from Ref. 11.   Copyright 1984
Butterworths.)

the extent of overlap of the curve of nucleation rate against time
with the curve of yield of crystals against time will determine the
size distribution in the final crop. If fresh nucleation is very
rapidly suppressed by crystal growth, crystal size will tend to be
more uniform because the viable nuclei will all have been growing as
crystals for a similar length of time. Conversely, if fresh
nucleation extends well into the period of crystal growth, then
crystals in the final crop will have grown over different lengths of
time and the final size distribution will be broad.

Low temperature limits for zeolite crystallisation are set only
by increasing slowness of nucleation and crystal growth. In this
connection activation free energies for each of the succession of
steps leading to a viable nucleus, and for subsequent crystal growth
are the decisive factors. Creswell et al (12) measured reaction
rates between silicate anions in aqueous alkaline solutions of
potassium silicate and reported an activation free energy of
~93 kJ mol^{-1} for dimerisation of orthosilicate anions, but nothing can
be said of the free energies of activation for the steps involved in
nucleating a zeolite. Measurements of linear growth rates on seed
crystals of zeolite X (13) gave the energies of activation in
Table I. These energies show that crystal growth is controlled by
a chemical process because E is too large for control by diffusion.

**TABLE I.   Activation Energy, E, in kJ mol^{-1} for Growth Rates on
          Crystals of Faujasite (Na-X)(13)**

Batch Composition	Si/Al in Product	E
$NaAlO_2.2.1(Na_{1.06}H_{2.94}SiO_4).400H_2O$	1.53	49.4
$NaAlO_2.3.0(Na_{0.92}H_{3.08}SiO_4).400H_2O$	1.78	51.5
$NaAlO_2.5.0(Na_{0.78}H_{3.22}SiO_4).400H_2O$	2.20	59.0
$NaAlO_2.7.5(Na_{0.73}H_{3.27}SiO_4).400H_2O$	2.54	65.3

Mineralisers

Water and hydroxyl ion are the classic mineralisers in hydrothermal
synthesis, firstly because aqueous alkali dissolves amphoteric
oxides and so promotes mobility and mixing of molecular and ionic
species as a pre-requisite for reaction. A second vital role is that
of molecular water which (see below) stabilises aluminous zeolites
by filling channels and cavities. This role can be shared or taken
over by organic molecules (e.g. in porosils, silica-rich zeolites or
AlPO's), and by salts (e.g. in scapolites, sodalite and cancrinite).

Stabilising Porous Crystals: Host-Guest Solutions

The zeolite, porosil or AlPO is the "host" and the zeolitic component
the "guest". The host-guest complex is a solution, amenable at
equilibrium to solution thermodynamics (14,15), and the host-guest
relationship thereby described is one of the most important in the
chemistry of porous crystals because, without the zeolitic guest,

microporous crystals could not be synthesised. The guest is required only during synthesis and is thereafter removed before the porous crystals are put to use.

For porosils the natural choice of the gram molecule (or mole) in host-guest solutions is SiO_2, and for comparability among all porosils and zeolites the mole will therefore be taken as $M_x Al_x Si_{(1-x)} O_2$ where $0 < x < 0.5$ and M is an equivalent of cations. For AlPO's the natural choice of mole is $AlPO_4$. For a two component solution at constant temperature the Gibbs-Duhem equation is

$$n_H d\mu_H + n_G d\mu_G = VdP \tag{4}$$

where n_H and n_G denote numbers of moles of host and quest in the solid solution of volume V at total pressure P. μ_H and μ_G are the respective chemical potentials of host and guest in the solution. Equation 4 can be re-arranged, with $d\mu_G = RTd\ln a$, and integrated to give

$$\Delta\mu_H = \mu_H - \mu_H^o = V_H P - RT\nu \int_0^a \frac{\theta}{a} da \tag{5}$$

The activity, a, of the guest is zero when the host is guest-free and has chemical potential μ_H^o. $\Delta\mu_H$ is thus the change in chemical potential of the host due to the inclusion of the guest. θ is the fractional saturation of the host by the guest, $\nu = n_G^{sat}/n_H$ and n_G^{sat} is the number of moles of guest at saturation of the host, so that $n_G^{sat}\theta = n_G$. $V_H = V/n_H$ is the molar volume of the host because the rigid host framework renders V_H virtually independent of n_G. The total pressure, P, is often the vapour pressure, p, of the guest, and the activity, a, can sometimes be replaced by the relative vapour pressure, x, of the guest, so that

$$\Delta\mu_H = V_H P - RT\nu \int_0^x (\theta/x) dx \tag{6}$$

This integral can be evaluated graphically from the sorption isotherm of the guest plotted as θ/x against x. From Equation 6, $\Delta\mu_H$ is seen to consist of two parts: a positive term $\Delta\mu_1 = V_H P$; and a negative term $\Delta\mu_2 = -RT\nu \int_0^x (\theta/x) dx$. These two parts will be evaluated in turn.

Table II gives values of V_H and of $V_H P$ at 100°C where P = 1 atm. V_H is based upon the number of Si + Al atoms per 1000 $\mathring{A}^3$ of zeolite (16). At 100°C for water $\Delta\mu_1 = V_H P$ is insignificant for all zeolites. However, in a closed system above 100°C, P=p for water rises rapidly. The smallest and largest molecular volumes are those of bikitaite and faujasite respectively, and in Table III values of $V_H P$ are therefore given for these two zeolites up to 365°C neglecting any small change in V_H with temperature. $V_H P$ for all other zeolites lies between the values for these two. Accordingly in the temperature range most relevant for zeolite synthesis, $\Delta\mu_1$, if water is the guest, will not be large. However, if,by using an inert piston fluid, one moves into the kilobar pressure range the term $V_H P$ will have a major effect on $\Delta\mu_1$.

TABLE II.   Molar Volumes, V_H, of Zeolites and $V_H P$ at one Atm
(100°C for Water as Guest)

Zeolite	V_H $cm^3 mol^{-1}$	$V_H P$ $J mol^{-1}$	Zeolite	V_H $cm^3 mol^{-1}$	$V_H P$ $J mol^{-1}$
Bikitaite	29.8	3.03	Merlinoite	37.6	3.82
Li-ABW	31.7	3.21	Phillipsite	38.1	3.88
Analcime	32.4	3.28	Erionite	38.6	3.92
Ferrierite	34.0	3.45	Offretite	38.9	3.94
Dachiardite	34.8	3.53	Paulingite	38.9	3.94
Mordenite	35.0	3.55	Chabazite	41.3	4.18
Sodalite			Gmelinite	41.3	4.18
Hydrate	35.0	3.55	RHO	42.1	4.29
Heulandite	35.4	3.59	LTA	46.7	4.73
LTL	36.7	3.72	Faujasite	47.4	4.83
Mazzite	37.4	3.79			

We consider now the term $\Delta\mu_2$. Table IV gives values of ν in Equation 6 for a variety of hydrophilic zeolites, according to the unit cell compositions given by Meier and Olson (16). To proceed further a simple model of the host-guest solution will be employed.

A Model for Host-Guest Solutions

Intracrystalline sorption is normally of Type 1 in Brunauer's class-ification (17) and isotherm contours therefore resemble those according to Langmuir's isotherm equation. This can describe actual isotherms well enough (18) to be of value in predicting, through Equations 5 or 6, some features of zeolite chemistry.

The maximum value of the relative pressure, x, is unity and this value will be closely approached for the aqueous phase where the guest is water. Then for Langmuir's isotherm

$$\Theta = Kx/(1 + Kx) \tag{7}$$

Isotherm contours in Figure 5 show how large K must be to give rect-angular isotherms like those usually observed for water in zeolites and also show some values of Θ at $x = 1$. With Equation 7, Equation 6 integrates to

$$\Delta\mu_H = \Delta\mu_1 + \Delta\mu_2 = V_H p + RT\nu\ln(1-\Theta)$$

$$= V_H p - RT\nu\ln(1+Kx) \tag{8}$$

The negative term, $\Delta\mu_2$, becomes increasingly so the larger the value of K, and hence the nearer the value of Θ at $x = 1$ is to unity and the more rectangular the isotherm.

TABLE III. $V_H p$ for Faujasite and Bikitaite in Water* at Different Temperatures

T°C	p/atm	$V_H p/\text{J mol}^{-1}$	
		Faujasite	Bikitaite
110	1.413	6.82	4.29
120	1.959	9.46	5.95
130	2.665	12.87	8.08
140	3.565	17.22	10.82
150	4.695	22.67	14.25
160	6.100	29.94	18.50
170	7.811	37.71	23.71
180	9.888	47.69	29.98
190	12.378	59.76	35.57
200	15.334	74.0	46.54
210	18.81	90.8	57.1
220	22.88	110.5	64.4
230	27.59	133.2	83.8
240	33.01	159.8	99.5
250	39.22	189.4	119.0
260	46.28	223.5	140.4
270	54.28	262.0	164.7
280	63.29	305.5	192.1
290	73.41	352.5	222.8
300	84.72	409.1	257.1
310	97.32	469.9	295.4
320	111.32	537.5	337.9
365	195.50	726.5	456.7
–	1,000	4,828	3,033
–	5,000	24,140	15,165

* Vapour pressures of water from NBS/NRC Steam Tables. Hemisphere Publishing Co., 1984. Converted from bars to atm.

TABLE IV.   Moles of Water per Mole of Zeolite (ν)

| ν	Examples	ν	Examples
0.33	Analcime, bikitaite	0.72$_2$	EAB
0.40	Natrolite	0.75	Erionite, merlinoite, phillipsite
0.50	Li-ABW, dachiardite ferrierite, mordenite, yugawaralite	0.77	Mazzite, offretite
		0.80	Edingtonite
		0.91	RHO
0.58$_3$	LTL	0.92	Levynite
0.60	Thomsonite	1.00	Gismondine, gmelinite
0.62$_5$	Brewsterite	1.04	Paulingite
0.66	Epistilbite, heulandite laumontite, sodalite hydrate	1.11	Chabazite
		1.12$_5$	LTA
		1.25	Faujasite
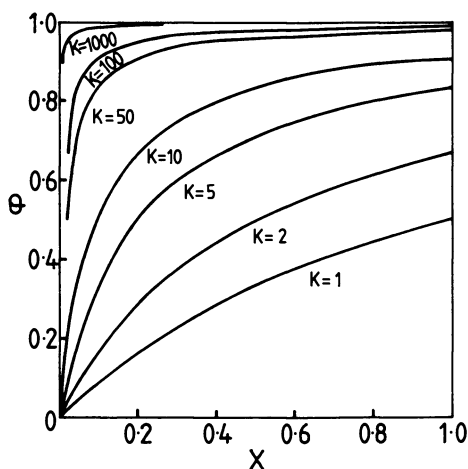
Figure 5.   Isotherms of Θ = Kx/(1 + Kx), showing Θ at x = 1 and the changes in curvature with increasing values of K.

Table V gives values of $-\Delta\mu_2/RT\nu$ for different values of K or of Θ at x = 1, according to Equation 8. For large K, $\Delta\mu_2$ dominates this equation and the zeolite is therefore much stabilised relative to its guest-free state. Thus for faujasite at 100°C, $\Delta\mu_1$ = $V_H p$ = 0.005 kJ mol^{-1} (Table II) and ν = 1.25 (Table IV). The final two columns in Table V give $\Delta\mu_2$ at 100°C for different K when ν = 1.25

TABLE V. $\Delta\mu_2$ in kJ mol^{-1} at x = 1 for different Values of K using the Langmuir Model

K	Θ at x = 1	$-\Delta\mu_2/RT\nu$	$-\Delta\mu_2$ at 100°C	
			ν = 1.25	ν = 0.33
1	0.500	0.6932	2.687	0.717
2	0.66	1.0986	4.259	1.136
3	0.750	1.3863	5.374	1.433
5	0.833	1.7918	6.946	1.853
10	0.90909	2.3979	9.295	2.479
15	0.93750	2.7726	10.75	2.867
25	0.96154	3.2581	12.63	3.368
50	0.98039	3.9318	15.24	4.064
100	0.99010	4.6151	17.89	4.771
500	0.99800	6.2166	24.10	6.427
1000	0.99900	6.9088	26.78	7.141

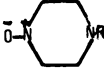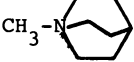and 0.33, and so for the extremes among the values of ν for zeolites (Table IV).
    One may conclude from Figure 5 and Tables IV and V that:-
(i) Because as zeolites become richer and richer in silica they are known to become less hydrophilic and eventually hydrophobic, water will increasingly lose its effectiveness as a stabiliser because as K declines so does $-\Delta\mu_2$.

(ii) For silica-rich zeolites, porosils and AlPO's water must therefore in part or wholly be replaced by other guest molecules which are more strongly sorbed giving more rectangular isotherms than water. These are usually multiatomic organic molecules. They often contain a basic group to improve their solubility in water and help maintain a high pH.

(iii) The stabilising role is a general one exercised by any guest molecules able to enter the porous crystal or be incorporated during its growth. This applies equally to permanent gases at pressures high enough to give significant uptakes. Thus crystallisation of the porosil melanophlogite was effected for the first time at 170°C under a pressure of 150 bar of CH_4 (19). Table VI gives some of the guest molecules used to aid formation of ZSM-5 (20) and serves to illustrate the generality of the effect.

TABLE VI. Some Guest Molecules used to aid Synthesis of ZSM-5 (20)

NPr_4OH	$NH_3 + C_2H_5OH$	Triethylenetetramine
NEt_4OH	Glycerine	Diethylenetriamine
NPr_3	$n\text{-}C_3H_7NH_2$	
$NH_2C_2H_4NH_2$	$(n\text{-}C_4H_9)_2NH$	
$OHC_2H_4NH_2$	$NH_2(CH_2)_3NH_2$	Hexanediol
$OHC_3H_6NH_2$		Propylamine

CH_3-N⟨⟩

$C(CH_2OH)_4$
Dipropylenetriamine

C_2H_5OH

The Effect of Temperature upon Host Stabilisation

Temperature influences the vapour pressure, p, and hence changes $\Delta\mu_1 = V_Hp$ as already considered (Table III). For the Langmuir model $\Delta\mu_2 = -RT\nu\ln(1 + Kx)$ is also dependent upon temperature. The effect is readily evaluated assuming that ν is independent of T and that

$$K = K_o \exp(-\Delta H/RT) \tag{9}$$

where K_o is a constant and ΔH is the heat of wetting of the water-free zeolite by liquid water (x = 1).

Relevant heats of wetting for several zeolites in different cationic forms fell in the range -6.8 to -3.2 kcal mol^{-1} of liquid water (21). Calculations of $\Delta\mu_H = \Delta\mu_1 + \Delta\mu_2$ are here made for $\Delta H = -6.0$, -4.0 and -2.0 kcal mol^{-1} (i.e. -25.1, -16.7 and 8.37 kJ mol^{-1}) taking K at 100°C to be 100, and also 10. The results in Table VII show that $\Delta\mu_H$ becomes less negative as temperature increases. For a given K the change in $\Delta\mu_H$ is larger the greater the heat of wetting. The calculations lead one to expect that:

(i)   As T increases zeolites will tend to be replaced at equilibrium by denser phases, because, in the relation $\Delta\mu_H = (\mu_H - \mu_H^o)$, μ_H of the zeolite stabilised by water may no longer be less at high T than the μ for dense phases (felspars, non-porous felspathoids, silicates or oxides).   Conversely, as T is lowered so that $\Delta\mu_H$ becomes increasingly negative, zeolites will increasingly replace dense phases ($\mu_H < \mu$).

(ii) The more porous the host the greater one expects its chemical potential, μ_H^o when guest-free, to become. The crystallisation of the most porous zeolites will therefore require unusually big negative values of $\Delta\mu_H$ to compensate for the large μ_H^o. $\Delta\mu_H$ is seen in Table VII to become more negative the lower the temperature so that the most porous crystals which need the greatest stabilisation should form best towards the low end of the temperature range for zeolite formation.

TABLE VII.   Influence of Temperature, for $\nu = 1.25$ and 0.33, upon $\Delta\mu_H/kJ\ mol^{-1}$ of Zeolite

ΔH kJ mol^{-1} liquid H_2O	T°C	K	$-\Delta\mu_H$ for: $\nu = 1.25$	$\nu = 0.33$
−25.10	27	717	20.5	5.47
	100	100	17.9	4.77
	177	25.0	15.2	4.04
	300	5.93	11.1	2.82
	365	3.47	9.21	2.19
−16.74	27	371.9	18.5	4.93
	100	100	17.9	4.77
	177	39.71	17.3	4.60
	300	15.20	16.2	4.17
	365	10.63	15.6	3.89
−16.74	27	37.19	11.4	3.04
	100	10.00	9.30	2.48
	177	3.97	7.46	1.96
	300	1.52	5.10	1.21
	365	1.06	4.08	0.83
−8.37	27	19.29	9.38	2.50
	100	10.00	9.30	2.48
	177	6.30	9.26	2.45
	300	3.90	9.06	2.27
	365	3.26	8.88	2.10

The five conclusions regarding zeolite synthesis given in this and the previous section are derived largely via the Gibbs-Duhem equation and are in general accord with practical experience.   The physico-chemical interpretation of so much observed behaviour is of considerable interest.

Stabilisation by Organic Guest-Molecules

Because many of the organic molecules which have served as guests
have molecular volumes substantially larger than water their values
of ν are less than that of water. Values of ν and some structural
information are given in Table VIII for several porosils and AlPO's.

TABLE VIII.   Values of ν for some Porosils and AlPO's

Compound	Polyhedra	Polyhedra per u.c	ν	Examples of Guest
Silicalite I	Channels	-	1/24	Pr_4NOH
Silica-ZSM-22	Channels	-	1/24	Et_2NH
Silica-sodalite	$4^6 6^8$	2	1/6	Glycol
(12 SiO_2 per u.c)				
Melanophlogite	5^{12}	2	1/23+	CH_4
(46 SiO_2 per u.c)	$5^{12}6^2$	6	3/23	CO_2, N_2, CH_3NH_2
Dodecasil 3C	5^{12}	16	2/17+	CH_4
(136 SiO_2 per u.c)	$5^{12}6^4$	8	1/17	Piperidine
Dodecasil 1H	5^{12}	3	3/34+	CH_4
(34 SiO_2 per u.c)	$4^3 5^6 6^3$	2	2/34+	CH_4
	$5^{12}6^8$	1	1/34	Adamantylamine
AlPO-12	-	-	1/3	$NH_2CH_2CH_2NH_2$
AlPO-20	$4^6 6^8$	2	1/3	$NH_2CH_2CH_2NH_2$
(6 $AlPO_4$ per u.c)				

For polyhedra, notation such as 5^{12} denotes a dodecahedron with
twelve pentagonal faces, and so on. With $\nu = 1/24$, $T = 170°C$ and
$\theta = 0.99$ $\Delta\mu_2$ is -0.706 kJ mol^{-1} of SiO_2 (cf.Silicalite and silica-
ZSM-22). Any additional uptake of zeolite water will further
stabilise Silicalite or ZSM-5. Indeed ZSM-5 can be made with water
as the only stabiliser. For the two AlPO's of Table VIII, in which
the mole is taken as $AlPO_4$, the negative values of $-\Delta\mu_2$ would be
8-fold larger than for Silicalite.
      When more than one cavity type occurs there is a term for each
type:

$$\Delta\mu_2 = - RT\nu_1 \int_0^a \frac{\theta_1}{a} da \ - RT\nu_2 \int_0^a \frac{\theta_2}{a} da \ ... \qquad (11)$$

When sorption in each cavity can be represented by Langmuir's
isotherm with the same or a different guest in each cavity,
Equation 11 becomes:

$$\Delta\mu_2 = RT\nu_1 \ln(1-\theta_1) + RT\nu_2 \ln(1-\theta_2) + \ldots \tag{12}$$

In the case of dodecasil 3C crystallised at 170°C, with CH_4 in the 5^{12} cavities and piperidine in the $5^{12}6^4$ cavities, and when the pressure of CH_4 gives $\theta_1 = 0.99$ and θ_2 for piperidine is also 0.99, one finds that $\Delta\mu_2 = -2.99$ kJ mol^{-1}.

Concluding Remarks

A specific cation, organic or inorganic, often appears to favour the nucleation of a particular zeolite. It has been suggested that the cation then functions as a template for nucleating a particular kind of zeolite. It is also likely that solid surfaces can function in a similar way, for example in the multiple nucleation often occurring at growing zeolite surfaces which gives polycrystalline particles. I wish here only to suggest that there can be a clear difference between specific template-based nucleation and the relatively non-specific stabilising role of guest molecules which can be diverse in type and shape, as seen in Table VI. Perhaps the distinction can be drawn best with water molecules in mind, which fill and stabilise so many different zeolite structures during synthesis. Water can hardly be a universal template for zeolites of any structure but is a near universal stabiliser. Its role is closer to that of a catalyst, defined classically as a substance that promotes a reaction (in this case by stabilising the product) but which can be recovered unchanged from the product.

Finally, as regards the pre-nucleation and nucleation stages it could be of interest to augment other modes of investigation by light scattering experiments to examine heterogeneities of composition, using clear aluminosilicate solutions like those prepared by Guth et al (2) and by Ueda et al (3,4). Conditions should be such as ultimately lead to zeolite precipitation and one would seek to follow the development of germ nuclei.

Literature Cited

1. Knight, C.T.G., Kirkpatrick, R.J., Oldfield, E. J.Chem.Soc.Chem. Comm. 1986, 66.
2. Guth, J.L., Caullet, P., Wey, R. Bull. Soc. Chim. Fr. 1980, 3-4, 121.
3. Ueda, S., Koizumi, M. Amer. Mineralog. 1979, 64, 23.
4. Ueda, S., Kageyama, N., Koizumi, M. In Proc. 6th International Zeolite Conference, Olson, D.H., Bisio, A. Eds. Butterworth, 1984, p.905.
5. Carr, R.M., Fyfe, W.S. Amer. Mineralog. 1958, 43, 908.
6. Barrer, R.M. Hydrothermal Chemistry of Zeolites. Academic: London, 1982, pp.113-117.
7. Barrer, R.M., Chemistry in Britain, 1966, 380 and Ref. 6, p.127.
8. Barrer, R.M. Hydrothermal Chemistry of Zeolites, Academic: London, 1982, pp.133-7.
9. Gibbs, J.W. Collected Works, Yale Univ. Press, 1948, Vol. 1, pp.105-115.

10. Zdhanov, S.P., Samuelwich, N.N. In Proc. 5th International Conference on Zeolites; Rees, L.V.C., Ed., Heyden: London, 1980, p.75.
11. Hou, L.Y., Sand, L.B. In Proc. 6th International Zeolite Conference; Olson, D.H., Bisio, A. Ads. Butterworths, 1984, p.887.
12. Creswell, C.J., Harris, R.K., Jageland, Per T. J. Chem. Soc. Chem. Comm., 1984, 1261.
13. Kacirek, H., Lechert, H. J. Phys. Chem. 1976, 80, 1291.
14. Barrer, R.M. J. Phys. Chem. Solids., 1960, 16, 84.
15. Barrer, R.M. In Studies in Surface Science and Catalysis 24, Zeolites: Synthesis, Structure, Technology and Application Drzaj, B., Hocevar, S., Pejovnik, S. Eds. Elsevier, 1984, p.1.
16. Meier, W.M., Olson, D.H. Atlas of Zeolite Structural Types; Structure Commission of the I.Z.A., 1978.
17. Brunauer, S. The Adsorption of Gases and Vapours. Oxford University Press, 1944, p. 150.
18. Barrer, R.M. Zeolites and Clay Minerals as Sorbents and Molecular Sieves. Academic: London 1978, Chap. 3.
19. Gies, H., Gerke, H., Liebeau, F. Neues Jb. Miner. Mh, 1982, H3, 119.
20. Lok, B.M., Cannan, T.R., Messina, C.A. Zeolites, 1983, 3, 282.
21. Barrer, R.M., Cram, P.J. In Molecular Sieve Zeolites II Advances in Chemistry Series 102, Am. Chem. Soc.: Washington D.C. 1971, p. 105.

Chapter 3

Precursors in Zeolite Synthesis

A Critical Review

J. J. Keijsper and M. F. M. Post

Koninklijke/Shell-Laboratorium, Amsterdam (Shell Research BV), Badhuisweg 3, 1031 CM Amsterdam, Netherlands

Double n-ring (DnR) silicates have been proposed as possible precursor species in zeolite synthesis since, for example, the formation of ZSM-5 can be easily envisaged starting from D5R silicates only. In this contribution we have critically examined this hypothesis. The observed composition and dynamics of various silicate solutions, which conform to the data for silicalite forming mixtures, are in line with such a possible precursor role but do not give a definite proof. In a number of instances, however, rates of nucleation towards ZSM-5 fail to show a correlation with the concentration of D5R silicates present in the starting mixtures. Moreover, the apparent random distribution of defect sites in zeolite ZSM-5, the number of which increases with the Si/Al ratio, does not support a precursor role for D5R silicates during crystallization. Therefore, we conclude that the D5R silicate condensation mechanism is not generally operative in the synthesis of MFI structures.

Although the use of organics in zeolite synthesis has had, and is still having, an enormous impact on the formation of Si-rich forms of already known structures and on the formation of novel materials, the precise role of the organics is still a matter of extensive debate. Often only their templating or structure-directing role is emphasized. However, the clear absence of a one-to-one correspondence between the geometries of the organic

used and the structure obtained (1) indicates that other possible roles of the organic also have to be considered.

In the literature at least three roles have been discussed. First, the organic may exert an influence on the gel chemistry by, for example, changing dissolution rates (1,2). It has been argued that templating effects may only become operative when the right gel chemistry is present. Second, the organic can play a stabilizing role by being incorporated in Si-rich zeolite frameworks. In this case it prevents the unfavorable interaction between water and the hydrophobic framework, which would otherwise tend to yield dense materials such as α-quartz (3). Third, the organic can influence the (alumino)silicate equilibria in the synthesis mixture and stabilize possible zeolite precursor species (4).

In the literature there is general agreement, sometimes after prior deviating views (5), that the nucleation of a zeolite takes place in the liquid phase of the synthesis gel and that the growth also involves dissolved nutrients (6-8), which are often thought to consist of approximately 10 T atoms (3,7,8). Thus, a direct link exists between the study of zeolite synthesis and the chemistry of basic (alumino)silicate solutions since these solutions can be considered as model systems for the liquid phase present in a synthesis gel. It is generally accepted that in these types of solutions an equilibrium exists between (alumino)silicates of varying degrees of condensation. Commonly used techniques to characterize these silicate species are chemical trapping by trimethylsilylation and (in-situ) ^{29}Si-NMR spectroscopy. In this way, numerous different silicates have been identified, ranging from monomeric (Si_1) to hexagonal prismatic (Si_{12}) (9). Especially from the NMR work, general trends have become clear, for instance, about the effect of pH and SiO_2 concentration on the average connectivity level. However, while some authors have speculated on the properties of proposed precursor 5-1 secondary-building-unit (SBU) silicate anions (10), which have not yet been positively identified in solution, in general no specific species has been proposed as a zeolite precursor for, say, ZSM-5.

Previously, we have speculated on the possibility that some particularly highly condensed silicate anions, the 'double-n-ring' (DnR) silicates, may be likely candidates for zeolite precursors (3,4,11). On the basis of an observed relationship between the extent of depolymerization of D4R silicates in the synthesis gel and the structure of the zeolites obtained from that gel, a possible precursor role of the D4R silicate has been discussed (11). In another study, the D5R silicate in particular has been considered as a precursor species for the formation of five-ring-rich siliceous zeolites like ZSM-5 (3,4). This proposal was based on the following considerations:

- A shift in the silicate equilibrium towards DnR species upon substitution of large organic cations such as tetraalkylammonium (TAA) for the alkali. These silicates are still present in solution at 90 °C, i.e., close to zeolite formation temperatures. This effect may be based on a favorable electrostatic interaction between the large cations and the condensed DnR silicates. The observed shift parallels the often-facilitated formation of Si-rich zeolites in the presence of organics.

- The observed presence of D5R silicates in actual ZSM-5 forming
  mixtures (12).
- Both the formation of ZSM-5 and the occurrence of defect (mis-
  sing T) sites in the framework can be easily envisaged starting
  from D5R silicates only (3) (see Figure 1).
    In this chapter we will reveal some new findings which are re-
levant to the D5R ZSM-5 synthesis model proposed earlier. The fol-
lowing items will be discussed:
- The composition and dynamic properties of basic silicate solu-
  tions and the implications derived therefrom as to the possibi-
  lity of positively identifying zeolite precursor species.
- The quantification of D5R and other silicates during a silicalite
  synthesis at 95 $^{\circ}$C from clear solution.
- A comparison of the rate of formation of a ZSM-5 phase in the
  presence and absence of different organics.
- The occurrence and distribution of defect sites in ZSM-5 samples
  prepared in different ways and how the Al content affects this.

Experimental

Basic silicate solutions were prepared by using silicic acid (ex
Baker, dried at 350 $^{\circ}$C) and a solution of the organic bases
[25 wt % tetramethylammonium hydroxide (TMAOH), 40 wt % tetra-
ethylammonium hydroxide (TEAOH), 20 wt % tetrapropylammonium hydro-
xide (TPAOH); ex Fluka] and, optionally, dimethyl sulfoxide (DMSO).
A solution of hexamethonium hydroxide [(Me$_3$NC$_6$H$_{12}$NMe$_3$)(OH)$_2$] was
prepared from the bromide salt (ex Sigma) and Ag$_2$O.
    Quantitative chemical trapping of the silicate in solution was
performed by the trimethylsilylation method by using an internal
standard as described earlier (4,11). The results thus obtained
were reproducible to within 20% relative.
    ^{29}Si-NMR spectra were recorded on a Bruker WM-250 (liquid) or
a Bruker CXP-300 Fourier transform magic-angle-spinning (FT MAS)
solid state spectrometer. Resonances are relative to tetramethyl-
silane (TMS). Dynamics of the silicate solutions were studied by
selective excitation techniques by using DANTE-type (13) pulse
sequences.
    Elemental analyses were carried out by using X-ray fluo-
rescence (XRF; Si, Al) and combustion (C, H, N) methods. X-Ray dif-
fraction (XRD) powder spectra were recorded on a Philips PW 1130
instrument.
    Samples 1-7 (silicalite) were prepared in a Teflon bottle at
95 $^{\circ}$C, under static conditions from a homogenized, filtered, and
clear solution of molar composition: 25 SiO$_2$ (ex silicic acid),
9 TPAOH (20 wt %, ex Fluka), 2 NaOH, 450 H$_2$O, and (samples 5-7)
50 vol % DMSO. Synthesis times are indicated in Table I.
    Samples 10-17 were prepared in stirred, Teflon-lined auto-
claves at 190 $^{\circ}$C starting from a homogenized mixture of molar
composition: 40 SiO$_2$ (ex Ketjen sol 40 AS), 1 Al$_2$O$_3$ (ex NaAlO$_2$;
ex ICN, dried at 120 $^{\circ}$C), 5 Na$_2$O, 1000 H$_2$O, and X, with X and the
synthesis times indicated in Table II.
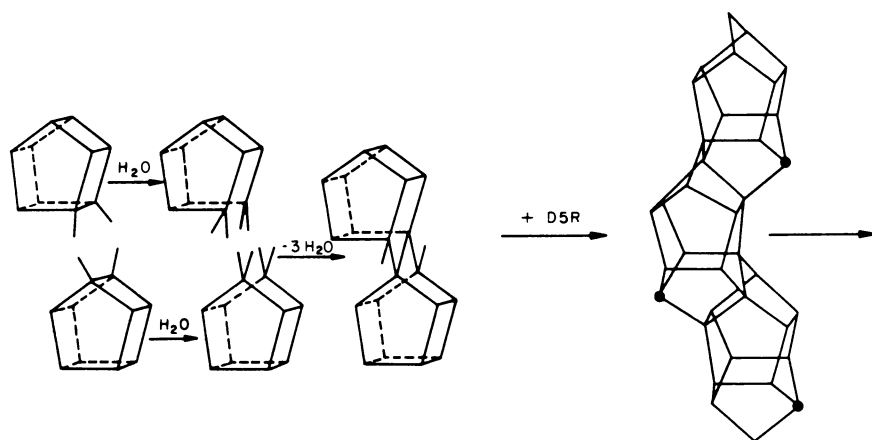
Figure 1.   Formation of ZSM–5, including possible 'missing
            T sites' defects (•), starting from D5R silicates
            only.

Table I. Silicate Composition of a Silicalite-Forming Solution at 95 °C and Product Properties Obtained

Time, h	Composition of Solution, mol %[a]					Properties of Product[b]					Sample Number
	M+D	D4R	D5R	R	P	XRD	Si wt%	$(SiO_2)_x$	$(TPAOH)_y$	$(H_2O)_z$	
Molar Solution Composition: 25 SiO₂/9 TPAOH/2 NaOH/450 H₂O; Non-Stirred											
0	0.8(40)	0.2(9)	0.3(14)	0.7(37)	98	-	-	-	-	-	1
24	2.3(30)	0.9(11)	0.9(11)	5.9(48)	72	100	18	96	4.4	25	2
48	2.5(33)	0.9(12)	0.8(11)	5.8(44)	70	100	20	96	4.4	27	3
96	2.3(33)	0.7(10)	0.8(11)	4.2(46)	69	100	23	96	4.4	30	4
168[c]	2.6(32)	0.9(11)	0.8(10)	4.7(47)	61	100	30	96	4.3	27	-
Molar Solution Composition: 25 SiO₂/9 TPAOH/2 NaOH/450 H₂O + 50 vol % DMSO											
0	0.9(15)	1.5(26)	1.7(29)	1.9(30)	94	-	-	-	-	-	-
24	0.9(12)	1.7(22)	1.8(25)	3.5(41)	89	30	3	96	2.1	46	5
72	1.3(13)	2.1(21)	2.1(21)	4.5(45)	62	85	28	96	3.4	35	6
400[c]	1.8(15)	3.9(33)	2.5(22)	3.8(31)	50	95	38	96	3.5	25	7

a: Absolute percentages are given with, in brackets, the relative amounts, i.e., as if no polymeric silicates and silicalite precipitation were present. M+D = mono- and dimeric silicates; D4R: double-four-ring silicate; D5R: double-five-ring silicate; R = other small silicates; P = polymeric silicates as derived from quantitative chemical trapping procedure. For P the percentage of Si recovered in the products has also been evaluated.

b: XRD: % crystallinity as compared to 100% crystalline TPA silicalite. Si, wt %: Percentage Si recovered (based on elemental analysis). Unit cell: Composition of unit cell (based on 96 Si sites) as derived from elemental analysis.

c: Longer synthesis times do not affect either the silicate composition of the solution or the product properties.

Table II. Properties of Products Obtained at 190 °C
from Synthesis Gel of Molar Composition: 40 SiO_2/1 Al_2O_3/5 NaOH/1000 H_2O/X

X	Time, h [a]	Sample	Cryst., % [b]	Si/Al [c]	Si Recovered, wt %	Organic/Unit Cell [d]
5 NaOH	22	10	75, Z	23	88	-
5 NaOH + 3 wt % Na,H-ZSM-5	8	11	90, Z	22	80	-
5 TPAOH	7	12	100, Z	27	80	3.5
5 TEAOH	40	13	100, Z	30	95	3.8
10 Hexane-1,6-diol	22	14	100, Z	20	85	5.5
3 $NaAlO_2$ + 4 NaOH	22	15	95, M	8	90	-
360 MeOH	50[e]	16	90, I	26	82	-
360 MeOH + 3 wt % Na,H-ZSM-5	16	17	90, Z	29	90	7.5

a: Time when crystallinity reaches its highest value (cf. Figure 6).
b: % Crystallinity, determined by XRD; Z ~ ZSM-5, M ~ mordenite; I ~ ISI-1.
c: Based on elemental analyses.
d: Number of organic molecules per 96 T sites based on elemental analyses.
e: At 170 °C; <10% α-quartz is also obtained.

Samples 20-27 (homogenized mixtures; starting SiO_2 and Al_2O_3 as samples 10-17) were likewise prepared in stirred, Teflon-lined autoclaves, according to the scheme below.

Sample No.	Starting Molar Composition	Synth.Time (h)/ Temp., $^{\circ}$C
20	40 SiO_2\ 1 Al_2O_3\ 5 Na_2O\ 1000 H_2O	22/190
21	same	46/170
22	40 SiO_2\ 1 Al_2O_3\ 2.5 Na_2O\ 1000 H_2O\ 5 NH_3	46/190
23	25 SiO_2[a]\0.31 Al_2O_3\ 1 Na_2O\ 450 H_2O\ 9 TPAOH	32/170
24	25 SiO_2[a]\0.13 Al_2O_3\ 1 Na_2O\ 450 H_2O\ 9 TPAOH	32/170
25	25 SiO_2[a]\0.05 Al_2O_3\ 1 Na_2O\ 450 H_2O\ 9 TPAOH	32/170
26	25 SiO_2\ 2 NH_3\ 450 H_2O\ 5 TPAOH	32/170
27	25 SiO_2\ 2 Na_2O\ 450 H_2O\ 9 TPAOH	70/95

a: ex silicic acid.

Results and Discussion

Basic Silicate Solutions: Composition. In Table III the compositions of some TEAOH and TPAOH silicate solutions in the presence and absence of DMSO as a function of the OH/Si ratio (pH) are compared. DMSO was added since it is known to promote the amount of

Table III[a]. Silicate Distribution in SiO_2/TAAOH/H_2O Solutions. Values in mol % as a function of x; x = OH/Si ratio

Silica Recovered As	x = 0.3		x = 0.7		x = 1.1	
	TEA	TPA	TEA	TPA	TEA	TPA
A. 1 SiO_2/x TAAOH/20 H_2O + 50 vol % DMSO						
Mono- + dimer	1 (12)	0 (2)	1 (2)	1 (1)	1 (1)	0 (1)
D3R	0 (0)	0 (1)	13(16)	7(10)	64(75)	40(52)
D4R	6 (61)	9 (61)	47(60)	37(53)	12(15)	16(21)
D5R	2 (20)	4 (27)	11(14)	13(19)	1 (2)	4 (5)
R	1 (6)	2 (10)	7 (9)	12(17)	6 (8)	15(20)
P	90	85	20	30	15	25
B. Same Composition Without DMSO						
Mono- + dimer	1 (35)	1 (21)	1 (4)	1 (3)	1 (1)	1(1)
D3R	0 (0)	0 (0)	3 (12)	2 (8)	31(60)	16(35)
D4R	1 (25)	1 (22)	6 (27)	7 (28)	5 (8)	9(18)
D5R	1 (25)	1 (22)	6 (22)	6 (23)	2 (2)	3 (6)
R	1 (15)	1 (35)	9 (35)	9 (38)	16(30)	21(41)
P	96	96	75	75	45	50

a: See text for explanation. M+D, D4R, D5R, R,P: see footnote to Table I.

DnR silicates in solution (4). Absolute amounts of silica present
in the form of the various silicates are mentioned, together with
(in brackets) their relative amounts, i.e. as if no polymeric sili-
cates were present. These polymeric silicates, i.e., silicates con-
sisting of more than 10 Si atoms, cannot be characterized by the
chemical trapping method since the silyl esters are not volatile
enough to be detected by GLC/flame ionization detection (FID) (14).
Moreover, ^{29}Si-NMR spectroscopy studies have never been successful
in positively identifying higher molecular weight silicates than
Si_{12} ones (9).

Figure 2 depicts the compositions of the different solutions.
For the polymeric species the absolute amounts are shown; for the
other, smaller silicates the relative amounts. It is evident that,
especially at low OH/Si ratios (i.e., < 0.5, which is a normal
value for Si-rich zeolite synthesis mixtures) the larger part of
the silicate species present in solution consists of uncharacte-
rized, polymeric silicates. The values obtained in the absence of
DMSO (lower part of Table III and Figures 2a and 2b are in good
agreement with literature findings (14).

Basic Silicate Solutions: Dynamics. Exchange reactions between
silicates as well as zeolite formation involve condensation and
hydrolysis reactions between dissolved silicate species. Therefore,
we have extensively studied the dynamics of basic silicate solu-
tions in order to obtain better knowledge of the properties of pos-
sible zeolite precursor species. Our first results were published
earlier (11). Here we have again used selective excitation ^{29}Si-NMR
experiments, applying DANTE-type (13) pulse sequences to saturate a
particular Si resonance belonging to a particular Si site. The rate
of transfer of magnetization from this saturated site to other
sites is then a measure of the chemical exchange rate between the
two sites.

Taking the D4R silicate as an example of DnR silicates in
general, since it is the one that can be obtained in solution in
highest concentration, we have mainly studied the exchange between
this species and smaller silicates. Elevated temperatures were used
(70-90 °C) to partially depolymerize the D4R species to smaller
fragments, from which it would be possible to observe any exchange.
Moreover, the rate of exchange would then be expected to be closer
to that prevailing under synthesis conditions. In Figures 3 and 4
the main results are shown.

Figure 3a shows the ^{29}Si-NMR spectrum, including the precise
composition and the assignments of the various peaks, of a silicate
solution of the organic base hexamethonium hydroxide at 70 °C. As
expected, this bulky organic induces the formation of D4R silicates
in solution. It is frequently used for zeolite synthesis (15). In
Figure 3b, the same solution has been studied by using a pulse
train as inserted; from the spectrum shown in Figure 3a, a spectrum
is subtracted in which the peaks at around -80 ppm have been satu-
rated for different times. The resultant spectrum (Figure 3b) shows
only those peaks which are affected by exchange with the saturated
sites. From this picture the following two conclusions can be
drawn. First, the exchange takes place via the monomeric species,
since the peak at -70 ppm is the first one to emerge. This finding
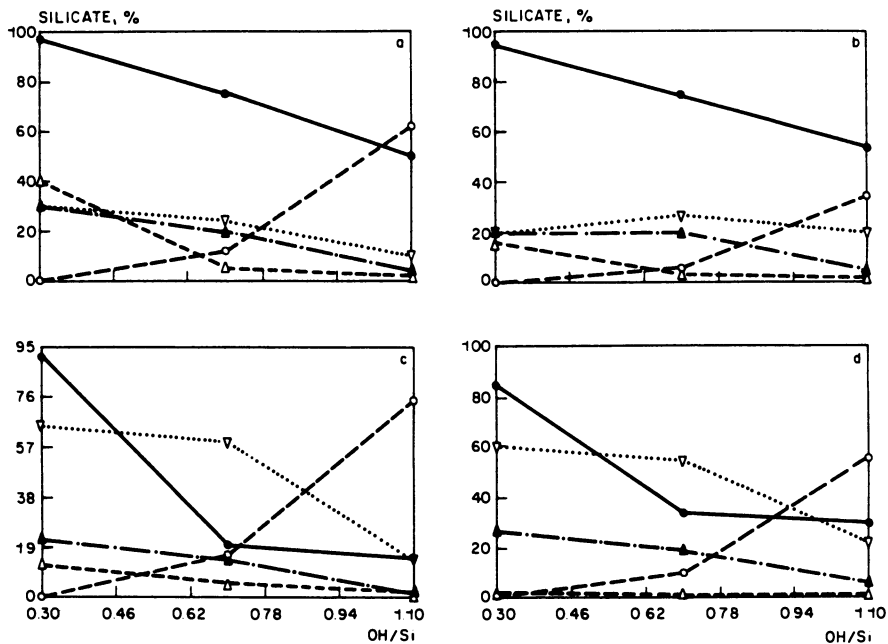is in accordance with earlier line-broadening NMR experiments (16)

Figure 2. Composition of various TEA and TPA silicate solutions ([Si]—2) as a function of the OH/Si ratio. Absolute molar percentages are given for the polymeric species and relative ones for the rest. -Δ- Mono/dimer; -o- D3R; ..∇.. D4R; -.-▲-.- D5R; -•- polymer.
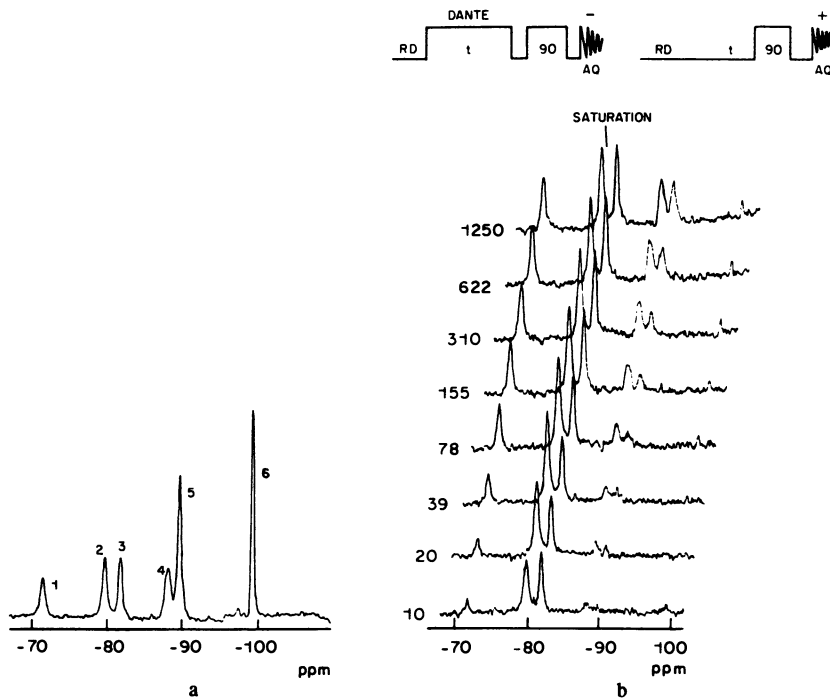a: TEAOH;
b: TPAOH
c: TEAOH + 50 vol % DMSO;
d: TPAOH + 50 vol % DMSO.

Figure 3. ^{29}Si–NMR spectrum of a silicate solution of molar composition: 1 SiO_2\ 1 hexamethonium hydroxide\ 20 H_2O, recorded at 70 $^\circ$C.

   a.   Peaks 1-6 can be assigned to: monomer or Q^0 (1), dimer plus terminally bonded Si sites or Q^1 (2), Si sites that are part of a three-membered ring and have two silicate neighbors or Q_Δ^2 (3), Q^2 (4), D3R and other Q_Δ^3 sites (5), D4R and other Q^3 sites (6).

   b.   Same spectrum after application of pulse train (inserted). Times are saturation times (ms) for peaks 2 and 3.
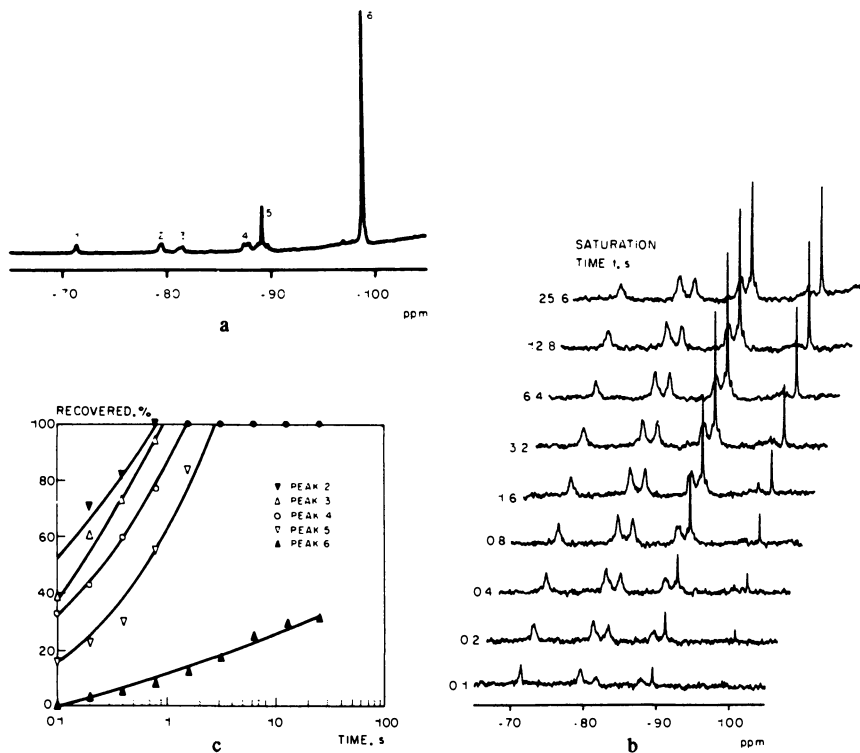
Figure 4. ^{29}Si–NMR spectrum of a silicate solution of molar composition: 1 SiO$_2$\ 1.2 TMAOH\ 17 H$_2$O, recorded at 70 ^{o}C.

   a. Original spectrum.

   b. Same spectrum after application of a pulse train as shown in Figure 3. Peak 1 has been saturated for the time as indicated in the figure.

   c. Rate at which the various peak integrals recover their original values (see a), indicating the extent to which the various silicates participate in the equilibrium.

and electrochemical measurements (17). Second, the D4R (and D3R) silicates barely participate in the exchange after 1250 ms, whereas all other small silicates are in full equilibrium within ≈ 0.5 s; this finding indicates that the DnR species are more stabilized.

In Figures 4a and 4b, analogous spectra are shown for a TMAOH silicate solution at 70 °C but with the monomeric site at −70 ppm being saturated and with a much longer duration of the saturation. Comparing the integrals of the DnR peaks in parts a and b of Figure 4, it then becomes clear that the D3R silicate is in full equilibrium after ≈ 2 s, and that after 25 s 30% of the D4R silicate has participated in the exchange. The rate at which the different silicates participate in the equilibrium is illustrated in Figure 4c. The important conclusion from this part is that for all small silicates the time scale of the exchange (0.1 − 20 s) is very fast compared to that of a zeolite synthesis (1 h − several days).

Three more observations are of interest in this respect. First, increasing the OH/Si ratio of the above-mentioned TMAOH silicate solution to a level of 4 by adding TMAOH decreases all exchange rates by approximately a factor of 3. This finding is in line with an earlier proposal that the mono-deprotonated silicate monomer is the carrier of the exchange (17).

Second, addition of Na^+ ions in the form of $NaNO_3$ to a level of Na/Si = 0.5 to the solution in Figure 4a has no apparent effect on the exchange rates. This indicates that, although Na^+ may have an influence on the overall silicate equilibrium (4), it hardly affects the dynamics of this equilibrium.

Third, addition of 50 vol % of DMSO to the solution with the composition as in Figure 4a increases the stability of the D4R silicate to such an extent that even at 95 °C no other silicates can be detected in solution. As a result, the rate of the exchange reactions could not be studied. It is expected to be relatively slow.

On the basis of the silicate work, the conclusions concerning the possibilities of positively identifying likely zeolite precursor species may be summarized as follows.

First, although the use of bulky organic bases clearly shifts the silicate equilibrium to the DnR species, there may be a large amount (up to more than 90%) of polymeric species present in silicate solutions. This is true especially at low OH/Si ratios (<0.5) or high Si concentrations (>2), i.e., normal values for a zeolite synthesis composition. This range of polymeric silicates cannot at present be characterized satisfactorily, and the presence of zeolite precursor species other than DnR silicates in this range cannot be excluded.

Second, compared to the time scale of a zeolite synthesis, the rate of exchange between all small silicates is very fast. The concentration of possible zeolite precursor species such as the DnR in this silicate range is accordingly expected to be constant throughout a synthesis (vide infra). On this basis, it is very well possible that, for instance, the DnR silicates do play a precursor role; however, a conclusive proof for this will be difficult to obtain (labelling, for example, is not possible).

Moreover, earlier work on low-temperature crystallizations of tetramethylammonium (TMA)-D4R clathrates from solutions in which

the D4R was apparently absent (11) may indicate that, during a zeo-
lite synthesis too, possible precursor species can be present in
sub-detectable amounts.

Silicalite Synthesis from Clear Solution. In order to check
whether the above findings on the presence of polymeric species in
solution and on the fast rate of exchange between the smaller sili-
cates are also applicable in a real zeolite synthesis mixture, we
have studied a silicalite synthesis in more detail. Starting from a
clear, filtered solution of molar composition: 25 SiO_2\9 TPAOH\
2 NaOH\450 H_2O at 95 °C, four identical non-stirred syntheses were
carried out; these syntheses were terminated after different time
intervals. The composition of the solution was quantified at 95 °C
by chemical trapping and the solid phase by XRD and elemental ana-
lyses (wt % Si, C, H, N). In this way a Si mass balance over the
solution and the solid phase during the silicalite synthesis was
obtained. The results are summarized in Table I, which also gives
the results of a similar procedure for an analogous synthesis in
the presence of DMSO. In this latter case, however, we were not
able to filter the solution as thoroughly as in the first one, so
that at the beginning of the synthesis a minor trace of amorphous
material was present.
    From this table the following conclusions can be drawn.
    First, the amount of the different silicates present in the
silicalite-forming solution at 95 °C as determined by chemical
trapping is in good conformity with that derived above from mea-
surements on a TPAOH silicate solution (cf. Table III). Especially
the observation that the larger part of the silicates is present as
non-identifiable polymeric species is of interest.
    Second, the amount of all small silicates present in solution
seems to be constant throughout the duration of the synthesis. This
finding is in line with the fast mutual exchange observed in sili-
cate solutions (vide supra). Moreover, it indicates that if the
zeolite is indeed grown from dissolved small silicates, the equi-
librium between the polymeric and the smaller silicates is rapid
enough to keep the amount of smaller silicates in solution at a
constant level. The zeolite formation stops when the solution is no
longer supersaturated with silica, which in this case means after
about 10 days (see Table I).
    Third, elemental analyses and thermogravimetric measurements
of the products obtained in the absence of DMSO point to the pos-
sible presence of 'missing T sites' defects (3). This is because on
every 96 Si T sites evidently more than the 4 TPA entities expected
for an ideal 'as made' silicalite sample (18) are incorporated.
Interestingly, ^{29}Si-NMR spectroscopy also indicates that a large
amount of defects (35%) are present in these samples (vide infra).
The apparent presence of 'missing T sites' defects may point to the
D5R synthesis model being operative (cf. the introductory comments
and Figure 1).
    The amount of DnR silicates in solution during the silicalite
synthesis in the presence of DMSO is, as expected, much higher than
without DMSO present (see Table I). Nevertheless, the rate of for-
mation of silicalite in the presence of DMSO seems to be somewhat
slower (see Figure 5); thus, if D5R species indeed act as precursor
species, they are highly immobilized. Moreover, the products

obtained exhibit a normal 'as made' TPA-silicalite composition of
~ 3.5 TPA entities per 96 SiO_2 units (19), indicating that presu-
mably no 'missing T sites' defects are present. This observation
is not in line with a possible precursor role of D5R silicates in
this particular synthesis.

<u>Kinetics of Zeolite Formation</u>. Since the D5R synthesis mechanism,
if operative, is clearly disturbed by DMSO (vide supra), we also
carried out a number of time-dependent syntheses in the absence of
DMSO in the hope of being able to relate the kinetics with the D5R
concentration present. Starting from a molar composition of
40 SiO_2\ 1 Al_2O_3\ 5 NaOH\ 1000 H_2O\X at T ~ 190 °C, various orga-
nics and/or seed crystals (X) were added and the solid products
were characterized after various synthesis times. Properties of the
products obtained when the highest crystallinities were reached are
summarized in Table II.
    The crystallization curves for X = 5 NaOH, 5 TPAOH, and 5
TEAOH, respectively, are compared in Figure 6. The use of TPA and
of TEA results in the formation of a stable ZSM-5 phase, obviously
because the organic excludes water from the hydrophobic pores. In
the absence of any organic (X = 5 NaOH), this unfavorable inter-
facial interaction is minimized and, after the prior formation of
ZSM-5, dense phases are obtained [cf. (3)]. That the stabilizing
role of an organic is of prime importance is also indicated by the
observation that when X = 10 hexane-1,6-diol, perfectly stable
ZSM-5 is obtained. In this repect, it is interesting to note that,
when X = 3 $NaAlO_2$ + 4 NaOH, a stable mordenite phase is obtained,
proving that under similar conditions H_2O is very well able to sta-
bilize more Al-rich, hydrophilic frameworks.
    The order for the nucleation rate (see Figure 6: TEA < orga-
nics-free < TPA), and the observation that when X = 5 NaOH + 3 wt %
seed ZSM-5, ZSM-5 is formed about as fast as with X = 5 TPAOH (see
Table II), do not support a precursor role for D5R silicates in all
these synthesis reactions. This is because, on the basis of the D5R
concentrations in analogous silicate solutions, the order TEA ≈ TPA
> organics-free is expected (cf. Table III) (4). If particular zeo-
lite precursors are responsible for the formation of ZSM-5 then,
clearly, TEA has a very retarding effect on their mutual condensa-
tion rate.
    Interestingly, the observed differences between TPA and TEA
provide a qualitative explanation for the finding that the use of
TPA results in ZSM-5 formation over a large range of gel composi-
tions and reaction conditions, whereas the use of TEA does not.
With TPA the very fast nucleation prevents the formation of other
zeolitic phases while the stability prevents transformations to
other products. TEA, on the other hand, may be used for the synthe-
sis of other Si-rich zeolites such as mordenite, ZSM-12, -20, -25,
beta, and Nu-2 (20) as well since it evidently exerts no specific
structure-directing influence during nucleation. Depending on the
precise gel composition and synthesis conditions, it can thus easi-
ly be envisaged that other zeolites may form which are stabilized
by TEA incorporation.
    The subtle effect the gel parameters can have in the absence
of a specific structure-directing organic like TPA [cf. (1)], on
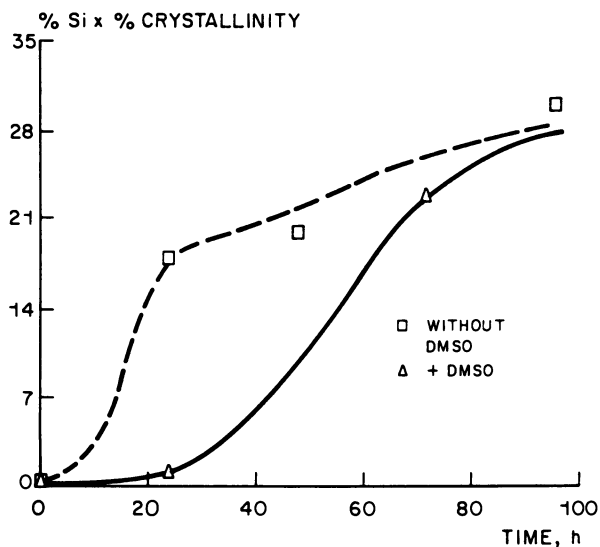
Figure 5.   Comparison of the crystallization curves for the
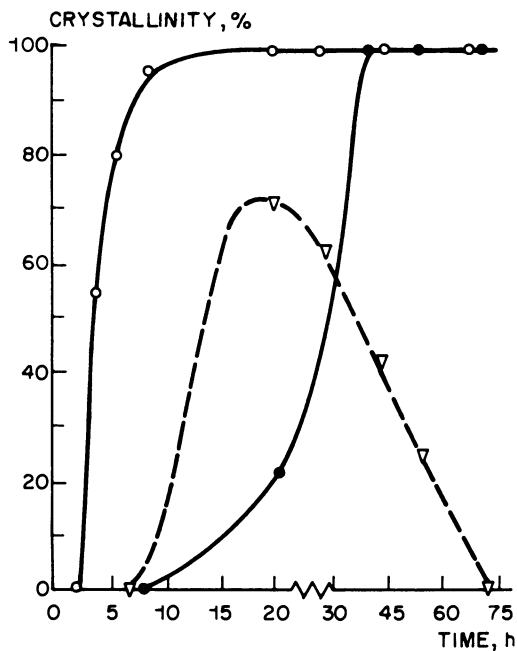   synthesis in the presence and absence of DMSO
            (samples 1-7).

Figure 6.   Crystallization curves for the ZSM-5 syntheses from
            the TEA (-•-) and TPA (-○-) containing mixtures and
            the organics-free one (-▽-).

either the nucleation or the crystallization stage of the synthesis, is further illustrated by the last two entries of Table II. When X = 5 NaOH + 360 MeOH, the gel has changed to such an extent that nucleation of ZSM-5 is prohibited and an ISI-1 phase is obtained instead. Seeding the same mixture with ZSM-5, however, results in the formation of highly crystalline ZSM-5, proving that crystallization of this phase is still very well possible.

Defects. In the literature, various indications [(^{29}Si-NMR (21), IR (22), excessive and Al-independent ion-exchange capacity (23)] of the existence of defect sites in Si-rich ZSM-5 are mentioned. Since the occurrence and distribution of defect sites may give a clue about the operating synthesis mechanism (cf. the introductory comments and Figure 1) they have been studied in closer detail.

First, the dependence of the number of defects on the Al content was determined by ^{29}Si-NMR spectroscopy applied to various ZSM-5 samples having different Si/Al ratios. In Table IV these ratios are indicated, together with the percentage intensity of the ^{29}Si-NMR resonance centered around -103 ppm. This percentage has been obtained from deconvolution of the total NMR intensity into two separate signals, one centered around -103 ppm and one around -113 ppm. Si sites having one Al neighbour (Q^4(1 Al); i.e., non-defect sites) and Q^3 Si sites (sites having only three T site neighbours, i.e., defect sites) contribute to the signal at -103 ppm. The expected percentage intensity of this signal based on the Si/Al ratio is approximately given by (24): 400/(Si/Al). The

Table IV. Properties of Various 'As Made' ZSM-5 Samples
(≥ 90% Crystallinity)

Sample	Si Recovered, wt %	TPA/Unit[a]	Si/Al[b]	-103 ppm,[c] %
11[d]	80	0	22	21
20	82	0	25	16
21	83	0	18	24
22	95	0	22	20
13[d]	95	3.8[e]	30	13
12[d]	80	3.5	27	16
23	63	3.6	31	11
24	55	3.9	72	12
25	62	4.1	220	16
26	94	4.0	>800	20
27[f]	30	4.7	>800	35

a: Number of TPA entities per 96 T sites; based on elemental analyses.
b: Based on elemental analyses.
c: Intensity in ^{29}Si-NMR centered around -103 ppm.
d: cf. Table II.
e: Number of TEA atoms per unit cell.
f: Prepared from clear solution at 95 °C; cf. Table I, samples 1-4.

difference in relation to the actual observed value thus gives the contribution of defect Q^3 sites to this peak. This amount is illustrated in Figure 7, which shows that the number of defects increases from ~0% for ZSM-5, with a Si/Al ratio of ~ 25, to more than 20% for silicalite. This result may indicate that, in the absence of electrostatic $(AlO_4^-)(TPA^+)$ interactions, defects have to stabilize the framework by, for example, allowing $(SiO^-)(TPA^+)$ interactions.

Second, the elemental analyses of the ZSM-5 samples (20-26) prepared via 'standard' synthesis routes do not point to 'missing T sites' defects since these samples contain the normal (19) value of 3.5 - 4 TPA entities per 96 T sites (see Table IV). This observation has been confirmed by thermogravimetric measurements. Therefore, the Q^3 defects in these materials are more likely to originate from hydrolysed SiOSi linkages. Interestingly, the silicalite sample prepared from clear solution at low temperature (sample 27, Table IV) most probably does contain missing T sites defects. This assertion is based on the observed high -103 ppm NMR intensity and the occlusion of more than 4 TPA entities per 96 T sites (see also Table I, samples 1-4).

In Figure 8a some relevant XRD intensities of this material (sample 27) are shown. Also shown are the calculated intensities expected for silicalite which lacks Si on specific pairs of T site positions. Figures 8c and 8d show the calculated intensity patterns for silicalite formed by the most likely cocondensation of D5R silicates only (cf Figure 1: i.e., with missing Si sites on crystallographic positions 1 and 7 or 7 and 12, respectively). From these diffractograms it is clear that, in the present sample (and also in all other samples screened so far), 'missing T sites' defects, if indeed involved, must be randomly distributed through the silicalite framework (cf. Figure 8k). Thus, if the D5R mechanism is operating, scrambling of these types of defects occurs under synthesis conditions in the newly formed material.

Conclusions

Since the formation of five-ring-rich zeolites like ZSM-5 can be easily envisaged starting from D5R silicates only, we have considered in this work the possibility of the D5R being a likely precursor species in either the nucleation and/or the crystallization stage. The results can be summarized as follows.

On the basis of the composition and dynamics of silicate solutions and zeolite synthesis mixtures only, a precursor role for the D5R silicates during both stages cannot be excluded since these species are present in relatively high concentrations during the zeolite synthesis process.

However, the retarded nucleation rate towards ZSM-5 in the presence of DMSO or TEA, relative to TPA (see Figures 5 and 6) is quite unexpected on the basis of the composition of the starting mixture and this finding would seem to refute a precursor role for the D5R during nucleation.

The finding that defects due to missing T sites are present only in a few samples and that, moreover, the defects appear to be randomly distributed does not directly support a precursor role for
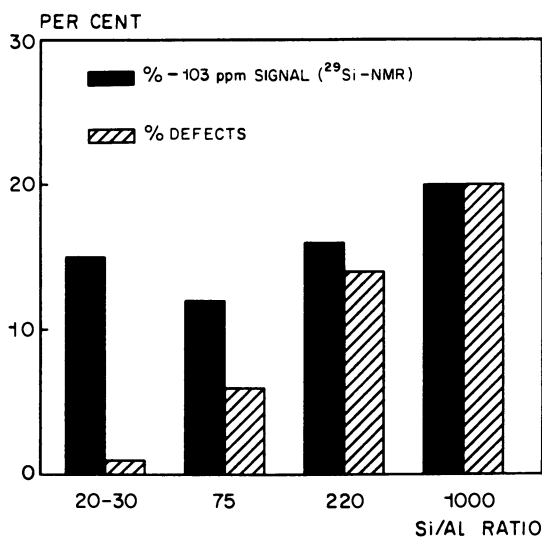
Figure 7. Number of defects in various ZSM-5 samples as a
function of the Si/Al ratio.

INTENSITY

| | | | | | | |
(101)(200)(111)(210)(211)(002)(102)

DIFFRACTION
LINES

a   MEASURED SILICALITE PRECURSOR

b   CALCULATED SILICALITE PRECURSOR

c   do. WITHOUT ATOMS   1 + 7

d   do.   „   „   7 + 12

e   do.   „   „   2 + 12

f   do.   „   „   2 + 8

g   do.   „   „   9 + 10

h   do.   „   „   2 + 5

i   do.   „   „   3 + 4

j   do.   „   „   5 + 7

k   do. 80% OCCUPATION OF Si ATOMS
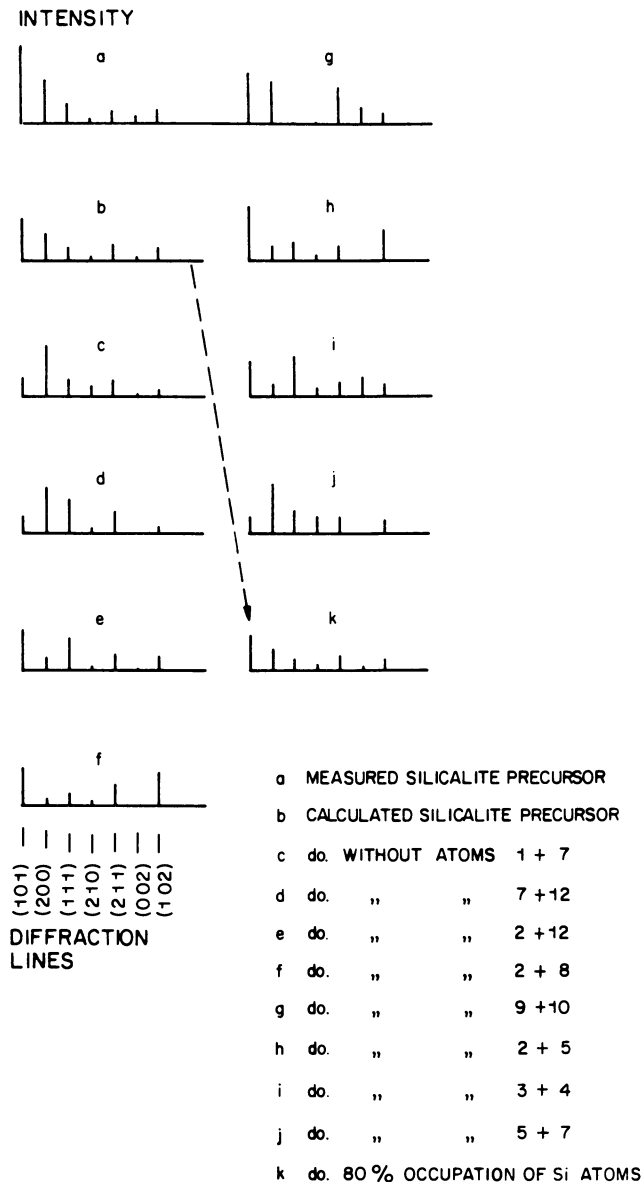
Figure 8.   Measured intensities for selected diffraction lines
of sample 27 compared with calculated ones upon
various pairs of T sites not being occupied. c and d
show the most likely patterns according to the D5R
model (i.e. minus crystallographic T site positions
1 and 7, or 7 and 12, respectively).

D5R species during the crystallization step. The random distribution, however, may be the result of a rapid scrambling of defects under synthesis conditions.

    For these reasons we have come to the tentative conclusion that the D5R silicate condensation mechanism is not generally operative in the synthesis of MFI-type zeolites.

Literature Cited

1. Lok, B.M.; Cannan, T.R.; Messina, C.A. Zeolites 1983, 3, 282.
2. Dewaele, N.; Gabelica, Z.; Bodart, P.; Nagy, J.B.; Giordano, G.; Derouane, E.G . Stud. Surf. Sci. Catal. 1988, 37, 65.
3. Van Santen, R.A.; Keijsper, J.J.; Ooms, G.; Kortbeek, A.G.T.G. ibid. 1986, 28, 169.
4. Groenen, E.J.J.; Kortbeek, A.G.T.G.; Mackay, M.; Sudmeijer, O. Zeolites 1986, 6, 403.
5. Derouane, E.G.; Detremmerie, S.; Gabelica, Z.; Blom, N. Appl. Catal. 1981, 1, 201.
6. Bodart, P.; Nagy, J.B.; Gabelica, Z.; Derouane, E.G. J. Chim. Phys. Phys.-Chim. 1986, 83, 777.
7. Perez-Pariente, J.; Martens, J.A.; Jacobs, P.A. Zeolites 1988, 8, 46.
8. Moudafi, L.; Massiani, P.; Fajula, F.; Figueras, F. ibid. 1987, 7, 63.
9. McCormick, A.V.; Bell, A.T.; Radke, C.J. ibid. 183.
10. See, for example, Aiello, R.; Crea, F.; Nastro, A.; Pellegrino, C. ibid. 549 and Gabelica, Z.; Nagy, J.B.; Bodart, P.; Dewaele, N.; Nastro, A. ibid. 67.
11. Van den Berg, J.P.; De Jong-Versloot, P.C.; Keijsper, J.J.; Post, M.F.M. Stud. Surf. Sci. Catal. 1988, 37, 85.
12. Boxhoorn, G.; Sudmeijer, O.; Van Kasteren, P.H.G. J. Chem. Soc., Chem. Commun. 1983, 1416.
13. Morris, G.A.; Freeman, R. J. Magn. Res. 1978, 29, 433.
14. See, for example: Hoebbel, D.; Garzo, G.; Engelhardt, G.; Ebert, R.; Lippmaa, E.; Alla, M. Z. Anorg. Allg. Chem. 1980, 465, 15; Hoebbel, D.; Garzo, G.; Ujszaszi, K.; Engelhardt, G.; Fahlke, B.; Vargha, A. Z. Anorg. Allg. Chem. 1982, 484, 7; Engelhardt, G.; Hoebbel, D.; Tarmak, M.; Samoson, A.; Lippmaa, E. ibid. 22; Hoebbel, D.; Vargha, A.; Engelhardt, G.; Ujszaszy, K. Z. Anorg. Allg. Chem. 1984, 509, 85; Hoebbel, D.; Vargha, A.; Engelhardt, G.; Ujszaszy, K. Z. Anorg. Allg. Chem. 1985, 521, 61.
15. See, for example, zeolites EU-1 (U.S. patent 4593138), TPZ-3 (European patent 51318), ZSM-12 (U.S. patent 4585639), ZSM-48 (European patent 142317), and ZSM-50 (European patent 127399).
16. Kinrade, S.D.; Swaddle, T.W. J. Chem. Soc., Chem. Commun. 1986, 120.

17. Sjoberg, S.; Ohman, L.O.; Ingri, N.; <u>Acta Chem. Skan.</u> 1985, <u>A39</u>, 93.
18. Van Koningsveld, H.; Van Bekkum, H.; Jansen, J.C. <u>Acta Cryst.</u> 1987, <u>B43</u>, 127.
19. Nagy, J.B.; Gabelica, Z.; Derouane, E.G. <u>Zeolites</u> 1983, <u>3</u>, 43.
20. European patent 108271, U.S. patent 3308069, European patent 13630, U.S. patent 3972983, European patent 15702, European patent 55046.
21. See, for example, Boxhoorn, G.; Kortbeek, A.G.T.G.; Hays, G.R.; Alma, N.C.M. <u>Zeolites</u> 1984, <u>4</u>, 15.
22. See, for example, Woolery, G.L.; Alemany, L.B.; Dessau, R.M.; Chester, A.W. <u>Zeolites</u> 1986, <u>6</u>, 14; Dessau, R.M.; Schmitt, K.D.; Kerr, G.T.; Woolery, G.L.; Alemany, L.B. <u>J. Catal.</u> 1987, <u>104</u>, 484.
23. Chester, A.W.; Chu, Y.F.; Dessau, R.M.; Kerr, G.T.; Kresge, C.T. <u>J. Chem. Soc., Chem. Commun.</u> 1985, 289.
24. See, for example, Engelhardt, G.; Lohse, U.; Lippmaa, E.; Tarmak, M.; Maegi, M. <u>Z. Anorg. Allg. Chem.</u> 1981, <u>482</u>, 49.

Chapter 4

Structure and Properties of Aluminosilicate Solutions and Gels

Gillian Harvey[1] and Lesley S. Dent Glasser

Department of Chemistry, University of Aberdeen,
Aberdeen AB9 2UE, Scotland

A range of aluminosilicate solutions were investigated. The gelation behaviour, the species in solution (as observed by NMR) and the zeolite crystallization products are described. The effect of concentration and type of alkali metal cation present in solution gives information about the formation of aluminosilicate complexes and how they interact, under the influence of the cation, to form an aluminosilicate gel, the precursor to zeolite crystallization.

A typical zeolite synthesis involves mixing together silicate and aluminate solutions or sols to form an aluminosilicate gel, usually instantaneously, which is then treated hydrothermally to give the crystalline product. The composition and structure of the aluminosilicate gel are of considerable interest and characterization of the aluminosilicate species present would give insight into the crystallization process.

It is important to know what species are present at the beginning of the reaction. Silicate and aluminate solutions have been well studied so that one can be reasonably sure what species are present in a given solution of known concentration and pH. Aluminate solutions have been shown to contain only one type of ion at high pH; the tetrahedral $Al(OH)_4^-$ ion (1). It is only when the pH drops towards neutral that other, polymeric ions appear which ultimately give way to $Al(H_2O)_6^{3+}$ in acid conditions. The tetrahedral aluminate ion is the important species for normal zeolite synthesis.

Silicate solutions, again at high pH, contain a range of small silicate polymers, formed from corner-sharing tetrahedral SiO_4 units. These polymers depolymerise quickly in response to increased pH or dilution. Rings and cages are the preferred form of the silicate species, while chains larger than trimer are rare (2,3). Various techniques have been used to

---

[1]Current address: Institute for Crystallography and Petrography, ETH, CH–8092, Switzerland

investigate the silicate species in solution; the most successful being trimethylsilylation (4) and ^{29}Si NMR. ^{29}Si NMR using enriched silica and selected Si-Si decoupling has made it possible to identify and quantify many of the small species present (5-7). It was also found that the range of species present is largely independent of the type of alkali metal cation (Na+ - Cs+) present (4).

A crystalline zeolite can also be studied by a variety of methods including crystallography and NMR but the intermediate phase, the gel, has proved very resistant to any type of study. The aim of this work, therefore, was to delay the formation of the gel long enough to investigate the precursor solution because solutions are generally easier to study than gels.

Aluminosilicate solutions, containing sodium or alkylammonium cations, have been studied previously. Guth et al (8-10) studied changes as aluminate and silicate solutions were mixed using pH, conductivity and Laser Raman measurements. They showed that aluminosilicate complexes were formed. Other experiments studied the crystallization of zeolites directly from solution (11-13). In solutions from which zeolites A and X crystallized, it was possible to observe aluminosilicate complexes by ^{27}Al NMR. It was also stated that crystal nuclei, equivalent to one or two unit cells, were present in the solution. Bell et al (14) observed aluminosilicate species by both ^{27}Al and ^{29}Si NMR in solutions of monomeric silicate solutions doped with aluminate. ^{27}Al NMR spectra showed a broadened and shifted Al(OH)$_4^-$ peak, and two additional peaks, attributed to aluminium attached to one and two silicate species. The ^{29}Si NMR spectra show the Q^0 peak (monomeric silicate) considerably broadened and shifted. Such complexes were also observed in tetramethylammoniun aluminosilicate solutions, again by ^{27}Al NMR (15-17). These solutions are much less prone to gelling and so can be prepared much more concentrated than other aluminosilicate solutions. Eventually double-four-ring aluminosilicates crystallize from solution. The ^{27}Al NMR spectra of these solutions showed four distinct peaks which were interpreted as aluminium attached to zero, one, two and three silicate groups.

In this work aluminosilicate solutions containing Na+, K+, Rb+ or Cs+ cations were studied by a range of different methods: the length of time the solution takes to gel, the light scattering behaviour as it gels, and the species present in solution as determined by ^{27}Al and ^{29}Si NMR. The factors that influence the gelation of the solutions were found to be; composition, cation present and the silicate species present at the beginning of the reaction, i.e. the sequence of mixing. All solutions or gels were then treated hydrothermally to investigate the relationship between the gel properties and the type of zeolite produced.

EXPERIMENTAL

Solutions; preparation and composition

Silicate solutions of ratio 1 : 0.6 SiO$_2$: alkali (MOH) were prepared from fumed silica and AnalaR alkali hydroxides. Aluminate solutions were

prepared by direct reaction of aluminium wire and alkali hydroxide. There were two methods of mixing the solutions together:

1) All excess water and alkali were added to the aluminate solution, which was then mixed with the silicate solution. This ensured that the range of silicate species was identical at the start of every reaction.

2) All or some of the excess alkali (22, 44, 66 and 88% of total alkali) was added to the silicate solution, which was allowed to equilibriate and then mixed with the aluminate solution. Thus the silicate species were progressively depolymerised in response to the extra alkali at the beginning of the reaction.

Forty different compositions of solution were studied (Figure 1) with special emphasis on nine representative solutions (shown in the boxes of Figure 1). The compositions of these nine solutions are given in Table I. Solutions containing sodium, potassium, rubidium or caesium ions were studied.
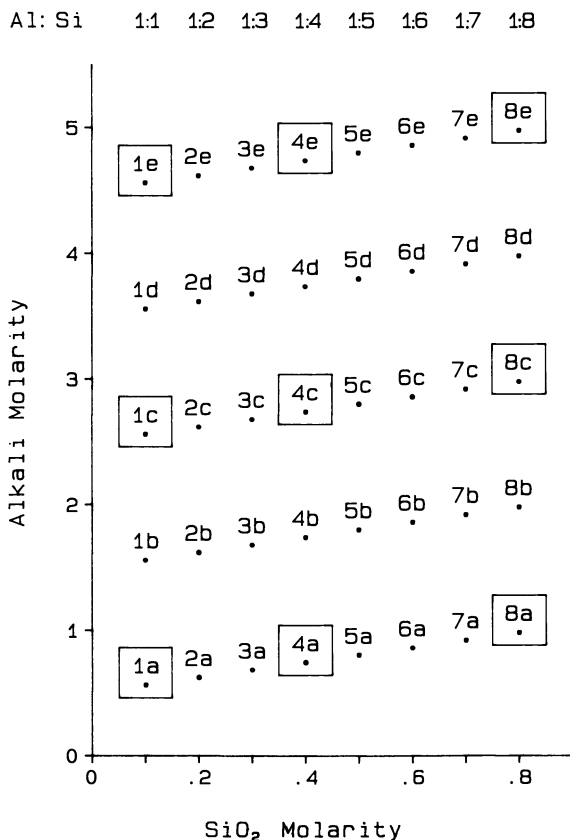
Figure 1: Composition plot for the identification of aluminosilicate solutions. All solutions contain 0.1 M aluminate and variable silica and alkali. The compositions of the solutions indicated by the boxes are given in Table 1.

All solutions were mixed by the first method and studied by means of gelation, light scattering and NMR experiments. Only potassium solutions (which seemed to be representative) were prepared by the second method of mixing and were studied by gelation and NMR experiments.

TABLE I : COMPOSITIONS OF NINE REPRESENTATIVE SOLUTIONS

Solution	Si (M)	Al (M)	Alk (M)	Ratio Si : Al : Alk
1a	0.1	0.1	0.56	1 : 1 : 5.6
1c	0.1	0.1	2.56	1 : 1 : 25.6
1e	0.1	0.1	4.56	1 : 1 : 45.6
4a	0.4	0.1	0.74	4 : 1 : 7.4
4c	0.4	0.1	2.74	4 : 1 : 27.4
4e	0.4	0.1	4.74	4 : 1 : 47.4
8a	0.8	0.1	0.98	8 : 1 : 9.8
8c	0.8	0.1	2.98	8 : 1 : 29.8
8e	0.8	0.1	4.98	8 : 1 : 49.8

Gel time measurements

At the time of mixing all solutions were clear. The "gel time" is defined as the time from mixing to the point when the solution no longer flowed under gravity. The sodium solutions precipitated rather than gelled and so the end point was, somewhat subjectively, taken to be the time taken for the solution to become very cloudy.

Light Scattering Measurements

Light scattering measurements were made on the solutions prepared by the first method of mixing. The measurements were made on a Sofica 42000 Photo Gonio Diffusometer, with unpolarised light of wavelength 545nm. The solutions were filtered (to remove dust and other particles), mixed and placed in the diffusometer as quickly as possible. Scattering increased with time, the limit of detection of the diffusometer was reached at the onset of visible cloudiness and well before gelation. The data obtained was still valuable because changes in the solutions could be observed before any physical changes, such as increased viscosity, were apparent.

NMR

Most of the spectra were run on a Bruker WH-360 MHz spectrometer at the University of Edinburgh. ^{27}Al NMR spectra were obtained with a spectrum frequency of 93.839 MHz, a pulse angle of 90° and an internal D_2O lock and

were plotted relative to an external standard of $Al(H_2O)_6^{3+}$. ^{29}Si spectra, using 88.4% enriched silica, were run with a spectrum frequency of 71.584 MHz, pulse angles between 12º and 18º, an internal D_2O lock and were plotted relative to an external standard of tetramethylsilane. Some of the ^{29}Si spectra were run on a Bruker CP-200 MHz spectrometer at the University of East Anglia, where the spectrum frequency was 39.747 MHz.

Zeolite Crystallization

The gelled mixtures were heated in closed autoclaves at 95ºC for two weeks. The products were identified by x-ray powder diffraction.

RESULTS

Gelation Experiments: Method 1 of Mixing

In these, any additional alkali and water were added to the aluminate solution, so that the initial silicate solution was the same through any series; some gel time experiments for these aluminosilicate solutions have already been described (18-20).

Figure 2 is a three-dimensional representation of the results and shows the dependence of the gel time on composition for potassium aluminosilicate solutions. Gel times do not depend simply on the concentration of any one component. Rather, a "valley" of shortest gel times extends almost diagonally across the plot from low-silica, low-alkali, to high-silica, high-alkali compositions. Values to either side of the "valley" are higher. The longest gel times - up to two weeks - occur in solutions of high-silica, low-alkali content.

Gel times depend strongly on cation type, as does the topography of the "landscape". Sodium aluminosilicate solutions gel much more quickly than potassium; their behaviour can be visualized as a broadening and flattening of the "valley" of Figure 2 until it extends into the high-silica, low-alkali corner. Only the low-silica, high-alkali solutions (top left of the figure) take an appreciable time to gel; for the other compositions, gelation is almost immediate. The behaviour of the rubidium aluminosilicate solutions resembles much more closely that of the potassium solutions, with the "valley" somewhat shifted to the upper left of the plot. The gel times were, on the whole, longer than for potassium. Caesium aluminosilicate solutions gel even more slowly than potassium or rubidium, to the extent that the high-silica, low-alkali solutions had not gelled after one year.

Gelation Experiments - Method 2 of Mixing

The second method of mixing (for potassium solutions only) involved depolymerising the silicate species of the initial silicate solution, by the addition of alkali, throughout a series of experiments, and produced very different results, which do not lend themselves to the type of plot used in Figure 2. This is partly because , in many cases, the gel time is dramatically decreased.
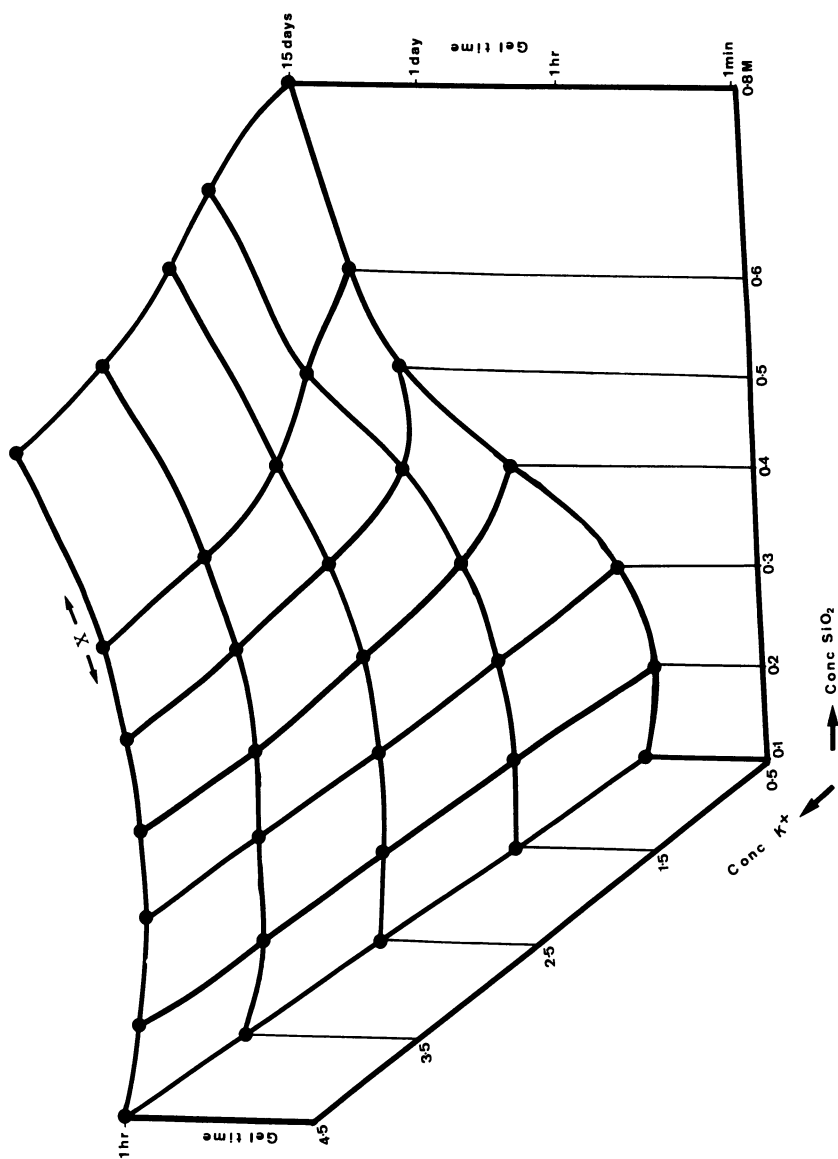
Figure 2: Log(gel time) for potassium aluminosilicate solutions. Each dot represents a solution composition from Figure 1.

Figure 3 shows what happens for compositions !e - 8e as more alkali is added to the silicate solution before mixing with the aluminate. The upper curve corresponds to the line marked "X" in Figure 2, and the others show the effect of progressively increasing the amount of alkali premixed with the silicate solution. The gel times for the least concentrated solutions decrease almost to zero, but as the total amount of silica increases, the change becomes less pronounced until solution 8e is virtually unaffected.

Why is this? Adding more alkali to the silicate solution increases the proportion of small species, particularly monomer (2,3). The compositions with the shortest gel times were thus made using silicate solutions that contained virtually all monomer. The silicate solutions used to prepare the others, which took longer to gel, would have contained an appreciable amount of more highly polymerised species. These points are discussed in more detail later.
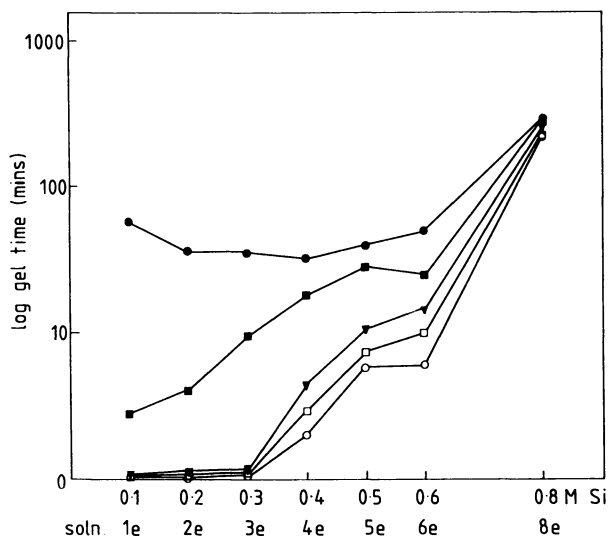
Figure 3: Log(gel time) of potassium aluminosilicate solutions 1e - 8e prepared by Method 2 of mixing. ● = normal mixing as in Method 1, ■ = 22% of total alkali added to silicate solution before mixing with aluminate, ▼ 44% of total alkali, □ = 66% of total alkali and ○ = 88% of total alkali.

Light Scattering

Figure 4 shows the light-scattering curve for nine selected potassium aluminosilicate solutions. Two types of behaviour were apparent. For low-silica solutions, a low, steady amount of scattered light is followed by a sharp increase as the solution becomes cloudy prior to gelling, possibly suggesting a nucleation-and-growth mechanism. There is a direct relation between the persistence of the low value and the observed gel time - the

longer gelation is delayed, the longer the low value persists. The high-silica solutions behave differently in that the light-scattering value increases steadily from the moment of mixing. Here it is the slope of the curve that relates to gel time: the shallower the slope, the longer gelation is delayed.

Similar behaviour was observed for the other cation systems. Sodium solutions show only the first type of behaviour, although only a few could be measured because they gelled so quickly. Caesium solutions, on the other hand, show mainly the second behaviour, i.e. a very slow, steady increase in the amount of scattered light.
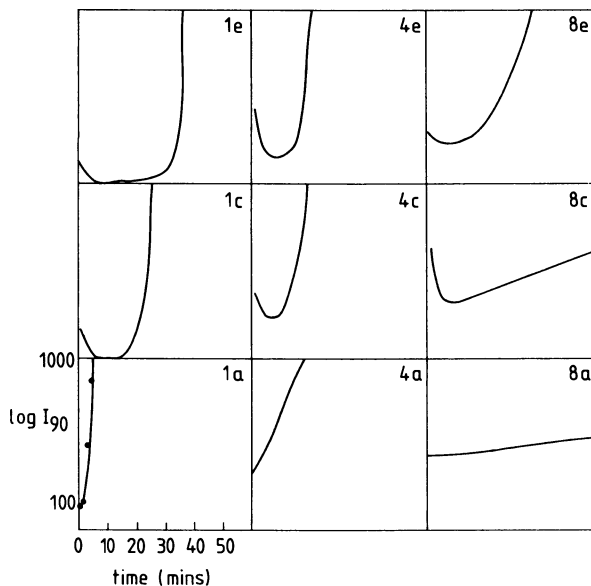
Figure 4: Light scattering curves for potassium aluminosilicate solutions prepared by Method 1 of mixing. All curves are scaled as for solution 1a.

NMR

The NMR results are, in general, not directly comparable with the above results. This is because of the relatively slow time scale of an NMR scan compared with many of the observed gel times. The aluminium spectra could be measured fairly quickly (in about ten minutes) and were less of a problem, but the silicon spectra took longer (up to half the gel time) and at best give a blurred snapshot of the solutions.

Most spectra were measured immediately after mixing, and give information about the species initially present. Attempts were also made to follow changes with time after mixing but with limited success.

Aluminum NMR

This proved extremely informative. Aluminosilicate complexes were observed in every solution studied. Although the spectra measured are of solutions undergoing change, the time taken to collect the data was generally small compared with the gel time. Figure 5 shows spectra for the nine representative potassium aluminosilicate solutions. A summary of the shifts is given in Table II.
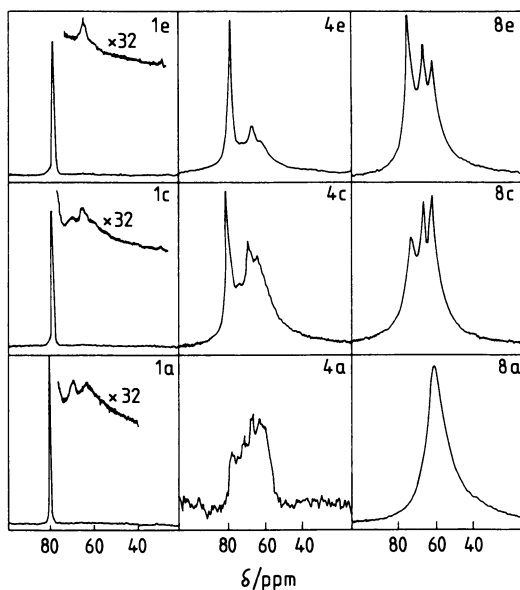
Figure 5: ^{27}Al NMR spectra of potassium aluminosilicate solutions prepared by Method 1 of mixing. Acquisition time was 0.067s and the number of scans averaged 10000. All data was collected in 4K and transformed in 32K.

TABLE II : ^{27}Al NMR CHEMICAL SHIFT RANGES (PPM)[*] FOR ALUMINOSILICATE SOLUTIONS.

Cation	Al(OH)$_4^{-}$[**]	Al(1Si)	Al(2Si)	Al(3Si)	Al(4Si)
Na$^+$	78.85-74.67	-	67.45-66.33	61.74-61.61	-
K$^+$	79.79-72.28	71.39-69.37	66.35-64.10	63.18-60.40	57.21
Cs$^+$	79.64-74.60	70.96-69.52	65.89-63.33	60.60-59.77	58.27

[*] All peaks measured relative to $Al(H_2O)_6^{3+}$
[**] This peak includes the aluminate/silicate association (see text)

Five peaks were observed. These were never all present in the same spectrum. These peaks are comparable to others reported, but no one has reported the observation of as many as five peaks (11-15). The first sharp peak at 80 ppm, which is observed in pure aluminate solutions and is assigned to $Al(OH)_4^-$ persists in many aluminosilicate solutions, although it broadens and shifts (Table II, Figure 6), relative to an aluminate ion in a pure aluminate solution which has a chemical shift of 80 ppm. This type of behaviour could indicate chemical exchange, a loose association between aluminate and silicate species.   The next three peaks, downfield, are always broad but do not shift (Figure 6), and are here interpreted as corresponding to aluminium bonded tetrahedrally to one, two and three silicate groups respectively. These three peaks tend to occur together, with the last two always being more intense than the first. The fifth peak (at around 58 ppm) corresponds to aluminium fully reacted with silicate and tends to occur alone in very slow gelling solutions. It too is rather broad, and this can be interpreted in terms of many overlapping peaks in which the aluminium is bound to a range of silicate species.

Figure 7 shows how the ^{27}Al NMR spectra of solutions of composition 6e (Figure 3) change as alkali is premixed with silicate (Gelation experiments - Method 2 of mixing). As the amount of silicate monomer present at the beginning of the reaction increases, the 80 ppm peak becomes relatively more intense, and shifts downfield and broadens. This points to a loose association of aluminium and silicate monomer, an arrangement that promotes gelling. We return to this point in the discussion.
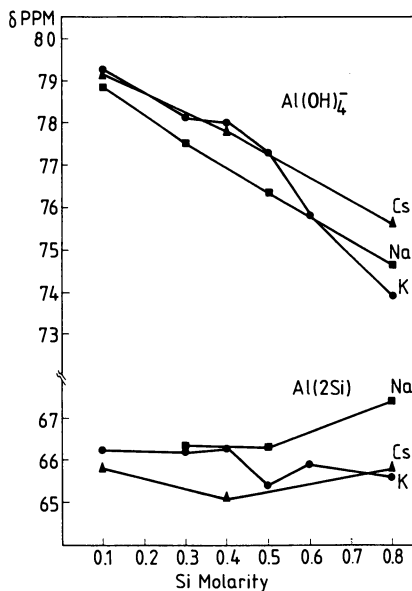
Figure 6: Variation of the chemical shifts (ppm) of $Al(OH)_4^-$ and Al(2Si) peaks with silica content for aluminosilicate solutions 1e - 8e.
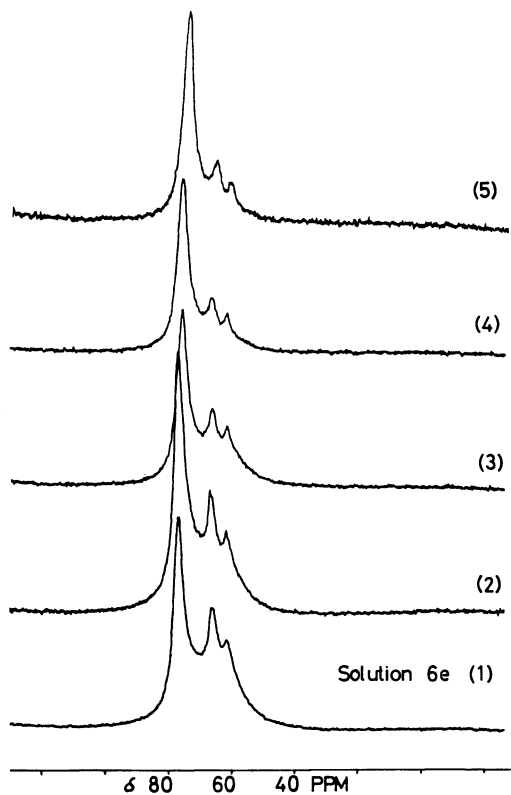
Figure 7: ^{27}Al NMR spectra of potassium aluminosilicate solution 6e prepared by Method 2 of mixing. Acquisition time was 0.067s and the number of scans averaged 6000. All data was collected in 4K and transformed in 32K. Spectrum 1 = normal mixing as in Method 1, 2 = 22% of excess alkali added to the silicate soltuion before mixing with aluminate, 3 = 44% of excess alkali, 4 = 66% of excess alkali and 5 = 88% of excess alkali.

Figure 8 shows the changes in the spectrum of a potassium aluminosilicate solution (4b) as it begins to cloud and gel. As this happens peaks assigned to the higher complexes reduce relative to the first peak. This is surprising but may indicate that the higher complexes are drawn preferentially into the gel, and are then no longer detectable by NMR.

Silicon NMR

Observations were restricted to slow-gelling solutions with high concentrations of silicate, i.e. an excess of silicate over aluminate. Careful comparison of silicate and aluminosilicate solutions of the same silicate and alkali content showed some differences in the ^{29}Si NMR spectra due to the presence of aluminate. For example, the differences between the spectra of caesium silicate and aluminosilicate solutions (Figure 9) are in the broadening and shifting of existing peaks; no new peaks appear. The monomer (Q^0) peak is particularly affected. The ^{27}Al NMR spectrum of the same aluminosilicate solution shows a large amount of the peak interpreted as loose association of aluminium with silicate monomer.

The depolymerization of silicate species under the influence of dilution or increased alkali seems to be unaffected by the presence of aluminate. However, even with enriched ^{29}Si, the spectra take time to measure and so information about kinetics is lost and the spectra relate to the solutions some time after mixing.
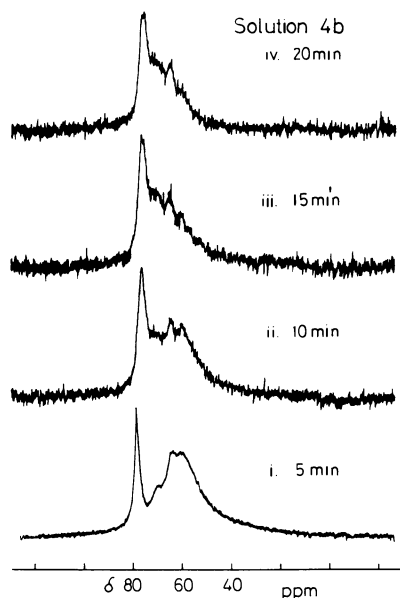
Figure 8: ^{27}Al NMR spectra of potassium aluminosilicate solution 4b over time. Acquisition time was 0.067s and the number of scans 5000 for each spectrum. All data was collected in 4K and transformed in 32K.
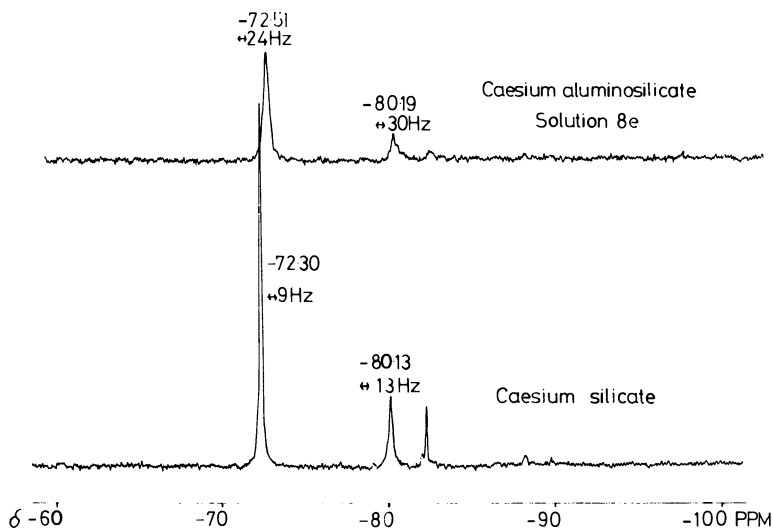
Figure 9: ^{29}Si NMR spectra of caesium silicate (0.8M Si, 4.98M CsOH) and aluminosilicate solution 8e plotted on an absolute intensity scale; aluminosilicate relative to silicate. Acquisition time was 1.359s and the number of scans was 500 for each.

TABLE III : FRAMEWORK DENSITIES OF ZEOLITE PRODUCTS

Framework Type	Framework Density
ANA	18.2
CAB	14.6
EDI	16.6
FAU	12.7
GIS	15.4
LTA	12.9
LTL	16.4
OFF	15.5
SOD	17.2

Zeolite Crystallization

Most solutions produced zeolites; all were known structures (Table III). The products for each cation system are shown in Figure 10. The relationship between the gelation behaviour and the zeolite produced is that the quickest gelling solutions produce the most open frameworks.

DISCUSSION

Any interpretation of the results must reconcile the observations on gelation and light scattering with the NMR results, and explain the shape of the "valley" topography (Figure 2) of gel times.
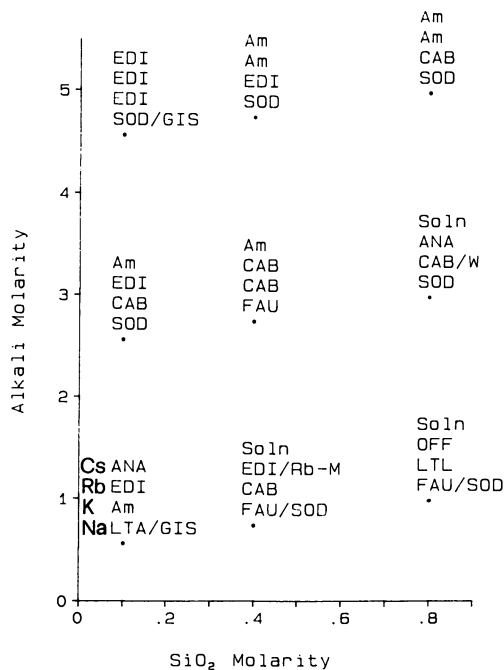
Figure 10: Zeolite products from thermal treatment of gelled solutions. Zeolites are identified by the structures codes given in ref 21. Am is amorphous, Soln indicates no solid product was obtained and zeolites W and Rb-M are described in refs 22 and 23.

We begin with the observations on the potassium solutions, both because they have been studied in most detail, and also because they show the typical "valley" topography in their gel times. The light scattering curves for the low-silica, high-alkali solutions indicate a typical nucleation-and-growth mechanism, with nucleation apparently being the rate-determining step. The high-silica, low-alkali solutions, in contrast, exhibit slow, steady growth, suggesting that sufficient nuclei are present from the start, and that availability of nutrient is the rate determining factor. The short gel times observed in the "valley" are then explained by the presence of sufficient quantities of both nuclei and nutrient.

The shortest gel times of all are observed (Figure 3) when the silicate solution is premixed with sufficient alkali to depolymerise it entirely to monomer. Figure 7 shows that increasing the amount of monomer increases the amount of aluminate/silicate association. This species seems to be critical for gel formation, being both the nutrient and the precursor to forming nuclei. When it is present in large quantities, gelation is almost instantaneous.

However, aluminium appears to complex preferentially with any larger silicate species that are present, and these complexes, once formed, polymerise further only slowly. In Method 1, where the initial silicate solution is quite highly polymerized, the long gel times observed in the presence of excess silica are the result of a lack of nutrient, all available aluminium being already bound to the larger silicate units. The ^{27}Al NMR spectra confirm this interpretation.

Why should aluminium preferentially react with the larger silicate species? The reason may be due to the charge density of the silicate anions. A monomeric (Q^0) ion could theoretically carry a charge of up to -4, although even in very alkaline solutions it will probably be protonated to some extent. Dimer, and other Q^1 units, can carry a maximum of three negative charges per silicon, but Q^2 and Q^3 silicons can carry at most two and one negative charges respectively. Thus the larger the silicate species, the smaller its average negative charge per silicon, and the easier it will be for it to approach the $Al(OH)_4^-$ group.

Once bonded to the aluminate group, such large species may well wrap themselves around the central aluminium and react further; this is consistent with the observation that the peaks assigned to Al(2Si) and Al(3Si) are always more intense than the Al(1Si) peak (Figure 5). In this way, the aluminate reacts without breaking Si-O-Si bonds, consistent with Hoebbel's (16) observation on the formation of double-four-ring aluminosilicates.

Any later rearrangement in response to dilution or increased alkalinity occurs by breaking Si-O-Si bonds; Al-O-Si bonds are not normally cleaved in alkaline solution. The high-silica, low-alkali solutions thus have very long gel times (Figure 2, for solutions containing K+, Rb+ or Cs+) because they are unable to rearrange to provide the free aluminate essential for the formation of nutrient. Gelation is then solely dependent on the coagulating ability of the cation.

The coagulating ability - bringing together aluminosilicate complexes and promoting their reaction - of the various cations reflects their water-clustering ability, sodium being much better than potassium or rubidium, while caesium is hopeless. The aluminosilicate complexes probably substitute for some of the water shell, and are thereby drawn together to form the gel. In this way, the cation determines the insolubility of the aluminosilicate species and therefore the rate of precipitation or gelation.

This is consistent with the observation that in zeolite structures the cation is partially coordinated to the framework and never wholly surrounded by water molecules. Moreover, this intimate association of aluminosilicate and cation species may well be the template for the crystallising zeolite.

ACKNOWLEDGMENTS:

REFERENCES

1. J.W. Akitt, N.W. Greenwood, B.L. Khandelwal and G.D. Lester, J. Chem. Soc. Dalton Trans., 1972, 604.
2. L.S. Dent Glasser and E.E. Lachowski, J. Chem. Soc. Dalton Trans., 1980, 3, 393.
3. L.S. Dent Glasser and E.E. Lachowski, J. Chem. Soc. Dalton Trans., 1980, 3, 399.
4. N.H. Ray and R.J. Paisted, J. Chem. Soc. Dalton Trans., 1983, 475.
5. R.K. Harris and C.T.G Knight, J. Chem. Soc. Faraday Trans. 2, 1983, 79(10), 1525.
6. R.K. Harris and C.T.G Knight, J. Chem. Soc. Faraday Trans. 2, 1983, 79(10), 1539.
7. A.V. McCormick, A.T. Bell and C.J. Radke, Zeolites, 1987, 7, 183.
8. J.L. Guth, P. Caullet and R. Wey, Bull. Soc. Chim. Fr., 1974, 1758.
9. J.L. Guth, P. Caullet and R. Wey, Bull. Soc. Chim. Fr., 1974, 2363.
10. J.L. Guth, P. Caullet, P. Jacques and R. Wey, Bull. Soc. Chim. Fr., 1980, 1-121.
11. S. Ueda, N. Kageyama and M. Koizumi, Proc. 6th Int. Zeolite Conf., Reno, Nevada, Butterworths, 1984, 905.
12. P. Wengin, S. Ueda and M. Koizumi, Proc. 7th Int. Zeolite Conf., Tokyo, Kodansha-Elsevier, 1986, 177.
13. S. Kasahara, K. Itabashi and K. Igawa, Proc. 7th Int. Zeolite Conf., Tokyo, Kodansha, Elsevier, 1986, 185.
14. A.V. McCormick, A.T. Bell and C.J. Radke, Proc. 7th Int. Zeolite Conf., Tokyo, Kodansha-Elsevier, 1986, 247.
15. D. Mueller, D. Hoebbel and W. Gessner, Chem. Phys. Letts., 1984, 84, 25.

16. D. Hoebbel, G. Garzo, K. Ujszaszi, G. Engelhardt, B. Fahlke and A. Vargha, Z. Anorg. Allg. Chem., 1982, 484, 7.

17. G. Engelhardt, D. Hoebbel, M. Tarmak, A. Samoson and E. Lippma, Z. Anorg. Allg. Chem., 1982, 484, 22.

18. L.S. Dent Glasser and G. Harvey, Proc. 6th Int. Zeolite Conf., Reno, Nevada, Butterworths, 1984, 925.

19. L.S. Dent Glasser and G.Harvey, Chem. Comm., 1984, 664.

20. L.S. Dent Glasser and G.Harvey, Chem. Comm., 1984, 1250.

21.   W.M. Meier and D.H. Olson, Atlas of Zeolite Structure Types, Butterworth, 1987.

22. R.M. Barrer and N. McCallum, J. Chem. Soc., 1953, 4029.

23. R.M. Barrer and J.W. Baynham, J. Chem. Soc., 1956, 2882.

Chapter 5

Applications of NMR Spectroscopy to the Study of Zeolite Synthesis

Alexis T. Bell

Center for Advanced Materials, Lawrence Berkeley Laboratory and Department of Chemical Engineering, University of California, Berkeley, CA 94720

NMR spectroscopy is a powerful technique for identifying the structure and concentration of silicate and aluminosilicate anions in gels and solutions used for zeolite synthesis. A review is presented of the types species that have been observed and the dependence of the distribution of these species on pH and the nature of the cations present.

The synthesis of zeolites occurs from solutions or gels containing a broad spectrum of silicate and aluminosilicate anions. Since some of these species resemble secondary building units, it has been postulated that zeolite formation is nucleated by the condensation-polymerization of SBU's and that subsequent crystal growth proceeds via the addition of SBU's to the surface of the growing crystallites [1]. Because the growth of a given zeolite involves only one SBU, or at most a small number of SBU's, there has been a strong interest in identifying the conditions which maximize the concentration of a desired SBU.

NMR spectroscopy is ideally suited for characterizing the silicate and aluminosilicate species present in the media from which zeolites are formed. The nuclei observable include ^{29}Si, ^{27}Al, and all of the alkali metal cations. The largest amount of information has come from ^{29}Si spectra [1-3]. This nucleus has a spin of 1/2, no quadrupole moment, and a chemical shift range of about 60 ppm. As a consequence, it is possible to identify silicon atoms in specific chemical structures. ^{27}Al, on the other hand, is a spin 3/2 nucleus and has a sizeable quadrupole moment. This results in broad lines and limits the amount of information that can be extracted from ^{27}Al spectra.

In this paper we shall summarize our recent findings concerning the nature and distribution of species present in silicate and aluminosilicate solutions and gels. Particular attention will be focused on establishing the effects of pH, cation composition, Si/Al ratio, and solvent composition.

Silicate Solutions

Figure 1 illustrates a high resolution ^{29}Si spectrum for a sodium silicate solution [4,5]. The individual resonances comprising this spectrum are grouped into bands each of
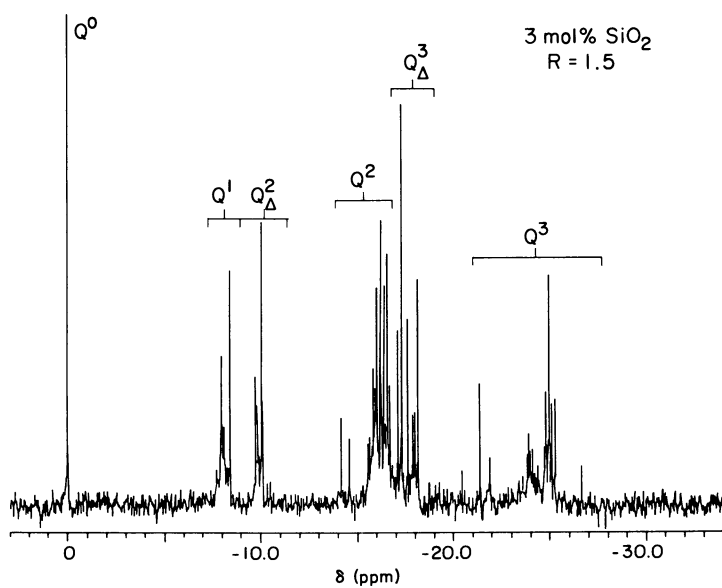
Fig. 1 ^{29}Si NMR spectrum of a 3.0 mol% SiO_2, R = 1.5 sodium silicate solution.

which is designated as Q^n. In this notation, Q represents a silicon bonded to four oxygen atoms forming a tetrahedron. The superscript n indicates the connectivity of the designated tetrahedron to nearest-neighbor tetrahedra. Thus, Q^0 denotes the monomeric anion SiO_4^{4-}, Q^1 end-groups of chains, Q^2 middle groups in chains or cycles, Q^3 chain branching sites, and Q^4 three-dimensionally cross-linked groups. The degree of protonation is ignored in this description.

Many of the individual lines observed in spectra such as those shown in Figure 1 can be assigned to specific silicate structures based on spectra of well defined silicate species and detailed NMR studies of the homonuclear spin-spin coupling of ^{29}Si nuclei in ^{29}Si-enriched silicate solutions [6-8]. Such studies have revealed that the chemical shift of a given silicon atom depends on its connectivity, the length of the Si-O bonds, and the angle of Si-O-Si bonds, as well as the pH of the medium and the cation type. As a consequence the transference of assigments made for one silicate solution to another must be carried out with caution.

Approximately 85% of the of the peak area shown in Figure 1 can be assigned to 19 specific silicate structures [4,5]. A schematic of these structures is presented in Table I, together with the chemical shift for each distinct silicon atom. It is evident from this table that silicate oligomers tend to occur as single and multiple ring structures, rather than as linear chains.

If proper care is taken in the acquisition of Si NMR spectra, then all of the disolved silicon will be expressed in the spectrum. In this case, the peak integral is directly related to the fraction of Si present as that spin, and the molar concentration of the anion is given by the ratio of the peak integral and the number of such identical spins in an anion.

The distribution of silicon amongst the different structures listed in Table I is a strong function of the silicate ratio, R, where R = $[SiO_2]/[Na_2O]$. The dependence of anion mole percentages on silicate ratio is given in Table II. The response of the anion distribution to the silicate ratio falls inot one one of three general classes. For monomer (1), dimer (2), linear trimer(3), cyclic trimer (4), branched cyclic trimer (7), bridged cyclic trimer (9), and pentacyclic heptamer (16), the anion percentages decrease monotonically with increasing silicate ratio. The linear tetramer (5), cyclic tetramer (6), branched cyclic tetramer (8), bicyclic pentamer (10), tricyclic hexamer (11), cis- and trans-tricyclic hexamers (12,13), and hexacylic octamer (18) each exhibit a maximum mole percentage as the silicate ratio increases. Only the cubic octamer (17) and the double hexamer (19) show monotonic increase in mole percentage.

From Table II it is apparent that there are distinct ranges of the silicate ratio in which particular anions are maximized. These ranges are not governed by anion size alone. For example, the large pentacyclic heptamer is present only at silicate ratios typically characterized by high concentrations of monomer and dimer. The connectivity distribution suggests that anions with higher average connectivity tend to achieve maximum concentration at high silicate ratio. For example, the pentacyclic heptamer level is maximum at lower R than the hexacyclic octamer. Furthermore, for anions with the same number of Si atoms, a linear structure will establish maximum level at lower R than will a cyclic structure; this relationship is evidenced by the behavior of the linear and cyclic trimers and tetramers. Finally, structures with only trimeric cyclic units peak at lower R than structures with both cyclic trimeric and larger cyclic units. As the number of three-membered rings decreases or the the number of other rings increases, so does the value of R at the maximum level. This trend may be the result of

Table I. Assignment of ^{29}Si NMR Peaks

No.	Structure	R = 1.0	1.5	2.0	2.5	3.0
1	· A	18.0	6.0	~5.0	6.0	5.0
2	⟶ A	5.2	1.5	1.2	0.9	1.1
3	B A	2.4	1.0	1.2	0.7	0.7
4	▷ A	2.8	1.6	0.6	0.3	~0
5	A B	1.0	1.1	0.5	~0	~0
6	A	~0	0.3	1.2	0.6	n.o.
7	B C A	2.0	1.0	0.9	0.2	~0
8	C B D A	2.0	2.1	3.3	1.8	1.7
9	A B	0.5	0.5	0.5	~0	~0
10	B C D A	1.0	1.7	~0	~0	~0
11	B C A	~0	0.8	1.8	0.8	0.6
12	B A	~0	0.4	0.3	~0	~0
13	B A	~0	0.4	0.3	~0	~0
14	B A	0.3	0.5	0.7	~0	~0
15	A	0.4	0.6	1.4	0.3	0.3
16	C A B	0.4	~0	~0	~0	~0
17	A	0	0	0.1	n.o.	n.o.
18	A B C	0.2	0.3	0.2	n.o.	n.o.
19	A	0	0.1	0.2	0.2	0.3

n.o. - not observable

Table II. Effect of Silicate Ratio on the Percentage of SiO_2 in a Given Silicate Ion

No. (i)	Structure	$|\delta_{Si}|$ (ppm) Peak iA	Peak iB	Peak iC	Peak iD
1	• A	0	0	–	–
2	⊷ A	8.20–8.70	–	–	–
3	∧ B A	7.90–8.20	16.80–16.83	–	–
4	▷ A	10.02–10.12	–	–	–
5	⌒⌄ A B	7.95–8.28	a	–	–
6	☐ A	16.01–16.19	–	–	–
7	B ▷ C • A	7.80–8.10	9.70–9.80	18.09	–
8	C ◇ B D A	a	15.66–15.96	a	24.02–24.10
9	◇ A B C	14.06–14.28	21.90–22.05	–	–
10	B ☐ C A	9.79–9.89	16.31–16.53	16.95–17.25	–
11	B ▢ D A C	15.94–16.11	16.42–16.59	17.48–17.75	24.77–24.92
12	▽ B A	10.38–10.43	a	–	–
13	▢ B A	10.55–10.57	18.12	–	–
14	◈ B A	14.45–14.68	21.29–21.53	–	–
15	▢ A	17.11–17.43	–	–	–
16	C ⬠ B A A	a	17.22	18.79	–
17	▱ A	27.50	–	–	–
18	B ⬡ A C	a	20.62	26.82	–
19	A ⬡	25.41–25.48	–	–	–

a   Not positively identified

b   Capital letter identifies specific Si spin environments

bond-angle stability. Higher R solutions may encourage the predominance of larger Si-O-Si bond angles.

At a fixed silicate ratio, the distribution of silicate structures is affected by the nature of the cation. An illustration of this effect is shown in Figure 2 for the alkali metal cations [9]. As the size of the cation increases, the extent of oligomerization increases. This trend is clearly seen in Figure 3, which represents the distribution of Si among different connectivity states. Since the pH of silicate solutions is unaffected by the nature of the cation, the influence of cation size on the extent of oligomerization has been ascribed to the formation of cation-anion pairs. Results from alkali metal cation NMR spectroscopy provide direct evidence for the presence of cation-silicate anion pairs and indicate that the extent of pair formation increases with increasing cation size [10]. It has been proposed that the formation of such pairs stabilizes the anionic species to hydrolysis and explains the increase in oligomerization with increasing pair formation.

When organic cations are used instead of alkali metal cations, the distribution of silicate species observed at a given silicate ratio is narrower. Figure 4 shows a series of spectra for tetraalkylammonium (TAA) silicate solutions. The solution prepared with tetramethylammonium hydroxide (TMAOH) exhibits four dominant features which in order of increasing shielding are due to monomer, dimer, cyclic trimer, bicyclic hexamer (D3R), and cubic octamer (D4R). As the length of the alkyl branches increases, the D4R structure rapidly disappears and the spectrum is dominated by the smaller silicate oligomers. The strong dependence of the concentration of D4R on the structure of the TAA cation is observed when only one of the four methyl groups in TMA^+ is substituted, as can be seen in Figure 5. Since TAA^+ cations are large compared to alkali metal cations, extensive cation-anion pairing is not expected. As a consequence the observed effect of cation structure on the distribution of silicate species must be ascribed to other causes. One hypothesis is that the hydrophobic surface of TAA^+ cations plays a role in organizing monomeric silicate anions into larger structures. The exact means by which this occurs is not understood and is a subject of current research.

The reactivity of silicate anions can be determined from the rate of Si exchange between anions. Attempts to estimate Si exchange rates from an analysis of ^{29}Si NMR lineshapes have been made, but the accuracy of this technique has been limited by the current understanding of ^{29}Si spin relaxation mechanisms [11-13]. Accurate determinations of the rate of Si exchange between anions can be obtained, however, from an analysis of selective spin inversion experiments [14-16]. Figure 6 illustrates the spectra resulting from the selective spin inversion of the monomer peak in a potasssium silicate solution containing only monomer, dimer, and cyclic trimer anions [16]. These spectra are interpreted on the assumption that Si exchange occurs via the followingt wo reactions:

1.   M + M = D
2.   M + D = c-T

where M = monomer, D = dimer, and c-T = cyclic trimer. The rate coefficients for reactions 1 and 2 can be determined from simulations of the time evolution of inverted spins. Of significant interest is the recent observation that these rate coefficients are a function of the nature of the cation. As can be seen in Figure 7, the rate coefficient for reaction 1 is greatest for K^+ and the rate coefficient for reaction 2 is greatest for Na^+. The effects of cations on the dynamics of Si exchange have been attributed to the formation of cation-anion pairs.
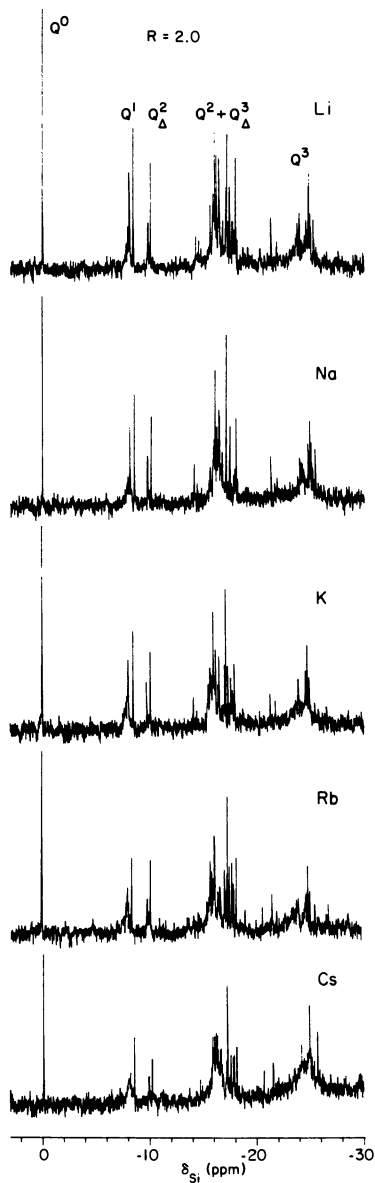
Fig. 2 ^{29}Si NMR spectra of 3.0 mol% SiO_2, R = 2.0 alkali metal silicate solutions.

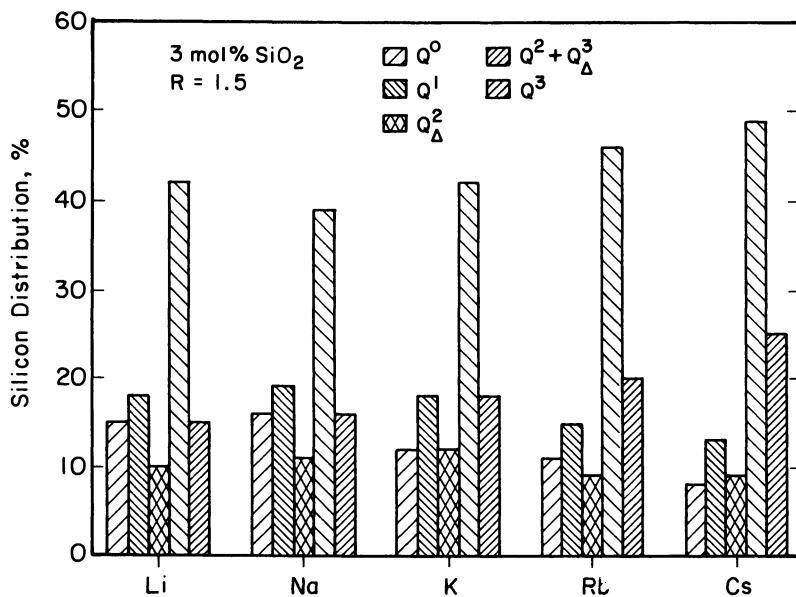Fig. 3 The influence of the cation on the distribution of Si among the connectivity states at the composition 3.0 mol% SiO_2, R = 2.0.
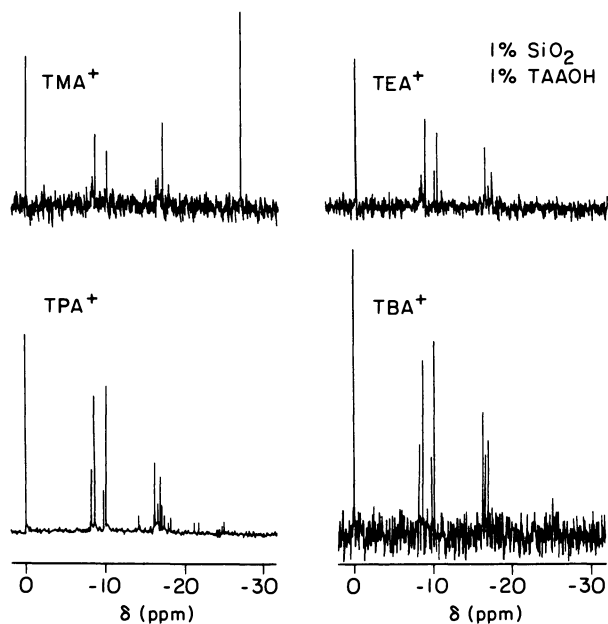
Fig. 4 ^{29}Si NMR spectra of 1.0 mol% SiO_2, R = 2.0 TAA silicate solutions prepared with TMAOH, TEAOH, TPAOH, and TBAOH.

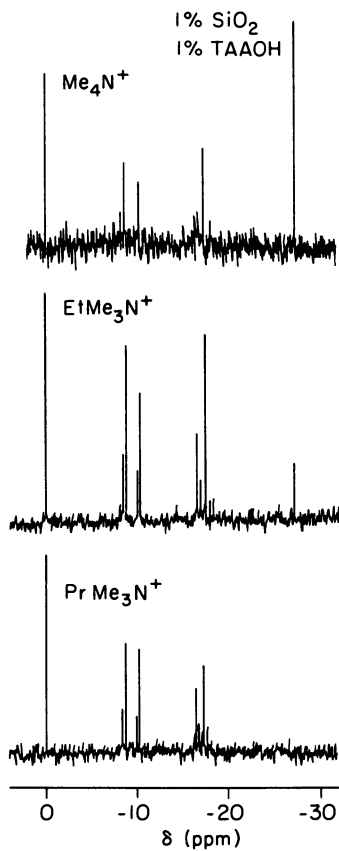Fig. 5 ^{29}Si NMR spectra of 1,0 mol% SiO$_2$, R = 2.0 TAA silicate solutions prepared with Me$_4$NOH, EtMe$_3$NOH, and PrMe$_3$NOH.
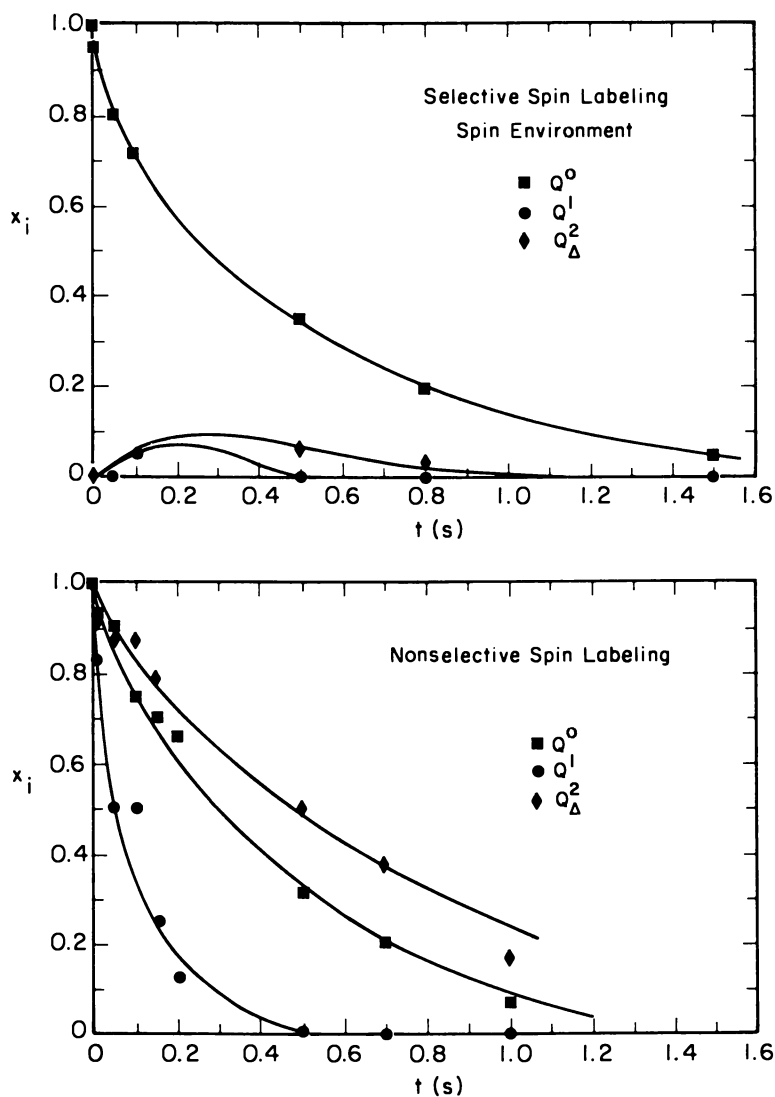
Fig. 6 The fraction of inverted spins in Q^0, Q^1, and Q^2_Δ environments as a function of time following selective or nonselective spin inversion of a potassium silicate solution.
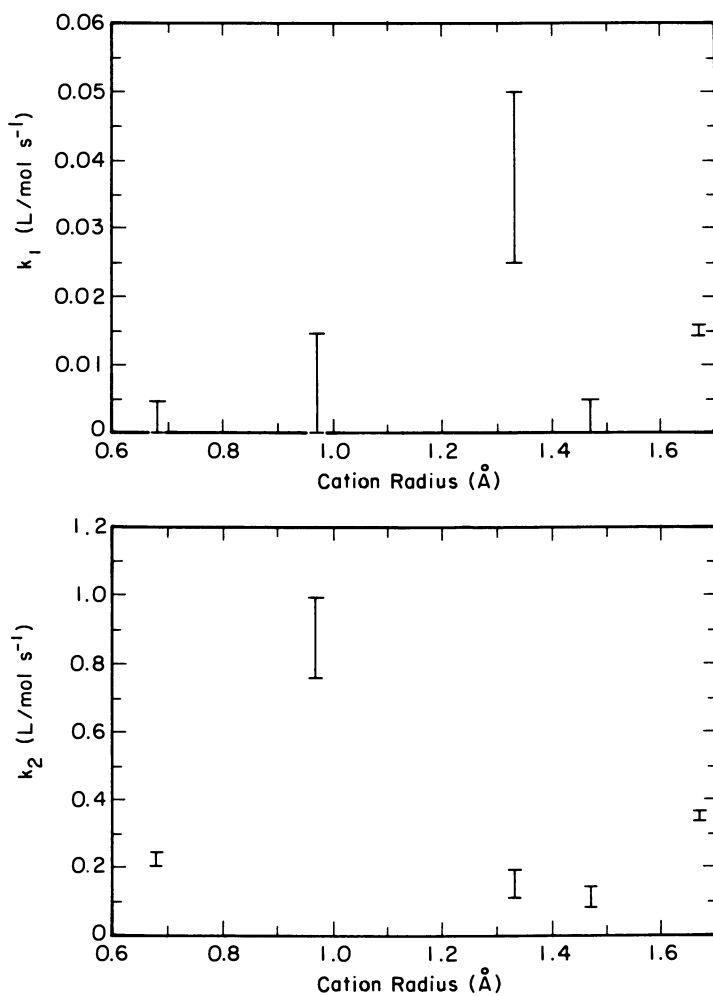
Fig. 7 The dependence of k_1 and k_2 on cation radius.

Aluminosilicate Solutions

The silicate species discussed in the preceding section can react with aluminate anions, $Al(OH)_4^-$ to produce aluminosilicate anions. ^{29}Si NMR spectra of solid silicates and aluminosilicates indicate that the replacement of Si by Al in the second coordination sphere of a give Si causes a low-field shift of about 5 ppm. Since each Si atom can have up to four metal atoms in its second coordination spere, fifteen possible $Q^n(mAl)$ structural units can be envisioned. The estimated chemical shift ranges for these units are given in Table 3 . It is apparent from this table that the ^{29}Si spectrum of an aluminosilicate solution in which Al and Si atoms were statistically distributed would be much more complex than that of an analogous solution containing only silicate species.

Because of the quadrupolar nature of Al, ^{27}Al NMR spectra of aluminosilicate solutions exhibit broad lines from which it is possible to determine the coordination of Al and its connectivity with Si, but the precise environment of each Al atom cannot be defined.   A peak for $Al(OH)_4^-$ is observed at 75 - 79 ppm, and up to three peaks in the range 58 - 72 ppm which have been assigned to various $Al(OSi)_n(O^-)_{4-n}$ building units.

The structure of aluminosilicate species formed upon mixing silicate and aluminate solutions is a strong function of the compositions of both solutions and the nature of the cation. Figure 8 shows a series of ^{29}Si and ^{27}Al spectra taken after addition of sodium aluminate to a silicate solution containing only momeric silicate anions [17]. The presence of aluminate anions results in no new features in the ^{29}Si spectrum, but only an upfield shift in the one observable peak. The ^{27}Al spectrum shows a weak feature upfield of the strong peak for $Al(OH)_4^-$. The observation of only a single ^{29}Si peak suggeests that the Si atoms are in rapid exchange between isolated $[Si(OH)_{4-x}O_x]^{x-}$ species and aluminosilicate structures. Based on the position of the ^{29}Si peak in the solution prepared with a Si/Al ratio of 2, the aluminosilicate species is proposed to be an aluminodisilicate anion.

^{29}Si and ^{27}Al spectra obtained upon addition of sodium aluminate to a solution containing monomer, dimer, and cyclic trimer silicate anions is shown in Figure 9 [17]. The ^{29}Si spectrum of the aluminosilicate solution shows a preferential attenution of the peak associated with the cylic trimer, while the ^{27}Al spectrum shows the appearance of features atributable to Al atoms attached to one and two silicate tetrahedra. The higher reactivity of the cyclic trimer may be due to the strained character of the three membered ring.

Studies of aluminate reaction with TAA silicate solutions have also yielded interesting results. For example, Englehardt and Michel [2] have shown convincing evidence for a D3R struture containing one Al atom in a TEA aluminosilicate solution. In other studies, Engelhardt et al. [18] have found that TMA silicate soulutions containing primarily D4R units do not react with TMA aluminate solutions at room temperature. Upon heating, though, the DAR silicate structure decomposes to produce a variety of aluminosilicate species.

Aluminosilicate Gels

At the concentration levels characteristic of zeolite synthesis, highly viscous gels are formed upon mixing silicate and aluminate solutions. The use of liquid-line NMR techniques to observe such gels results in very broad spectral features due to the fact

Table III. Estimated ^{29}Si Chemical Shift Ranges of Q^n and Q^n(mAl) Structural units of Silicate and Aluminosilicate Anions in Solutions (18)

Q unit	Structure	$-\delta$ (ppm)[a]	Q unit	Structure	$-\delta$ (ppm)[a]
Q^0	O OSiO O	66–73	Q^3(3Al)	O AlOSiOAl O Al	ca 85
Q^1	O OSiOSi O	76–83	Q^4	Si O SiOSiOSi O Si	103–120
Q^1(1Al)	O OSiOAl O	ca 75			
Q^2	O SiOSiOSi O	86–91	Q^4(1Al)	Si O SiOSiOAl O Si	97–105
Q^2(1Al)	O SiOSiOAl O	ca 85			
Q^2(2Al)	O AlOSiOAl O	ca 80	Q^4(2Al)	Si O AlOSiOAl O Si	92–99
Q^3	O SiOSiOSi O Si	95–101	Q^4(3Al)	Al O AlOSiOAl O Si	88–94
Q^3(1 Al)	O SiOSiOAl O Si	ca 95	Q^4(4 Al)	Al O AlOSiOAl O Al	83–87
Q^3(2Al)	O AlOSiOAl O Si	ca 90			

[a]Shift ranges of the central Si atom referenced relative to TMS
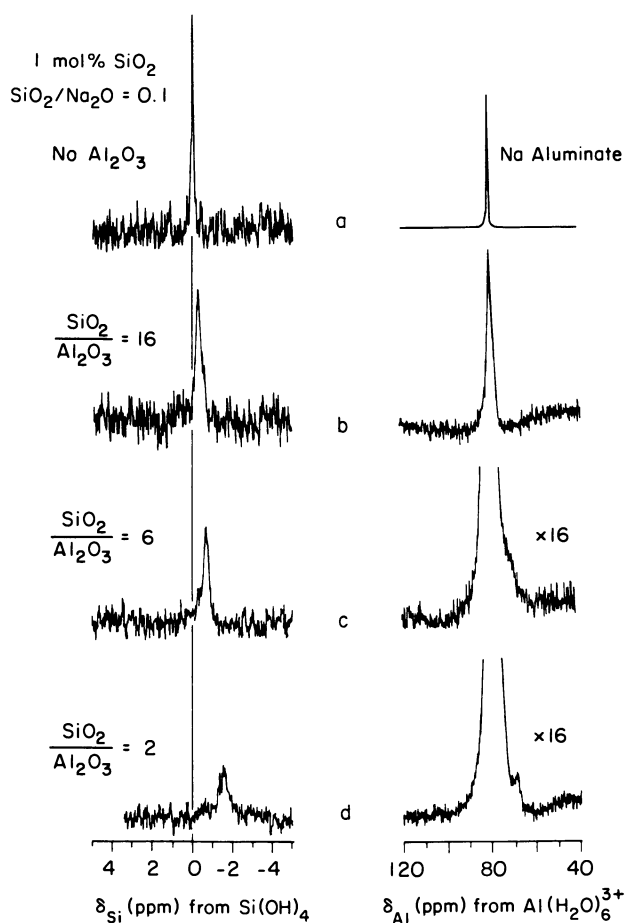
Fig. 8   (a) A ^{29}Si NMR spectrum of a monomeric Na silicate solution of the composition 1.0 mol% SiO$_2$, R = 0.1 and an ^{27}Al spectrum of a monomeric Na aluminate solution of the composition 1 M NaAlO$_2$; (b)-(d) ^{29}Si and ^{27}Al spectra of aluminosilicate solutions with increasing Al concentration. ^{29}Si spectral frequencies are referenced to Si(OH)$_4$ and Al spectral frequencies are referenced to the octahedral Al^{3+} ion in an aqueous solution of AlCl$_3$.

Fig. 9 (a) ^{29}Si spectrum of a Na silicate solution of the composition 3.0 mol% SiO$_2$, R = 0.4, [SiO$_2$]/[Al$_2$O$_3$] = 0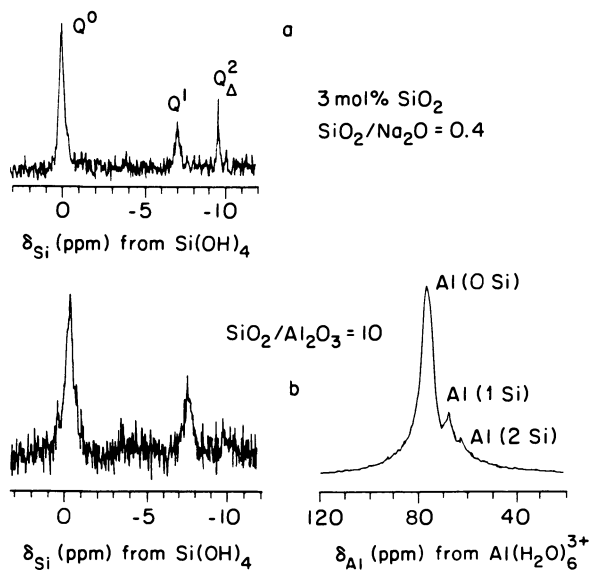. (b) ^{29}Si spectrum of a Na silicate solution of the composition 3.0 mol% SiO$_2$, R = 0.4, [SiO$_2$]/[Al$_2$O$_3$] = 10.0.

that dipolar and quadrupolar interactions and CSA are not fully averaged out. It has been shown recently that these limitations can be overcome by use of MAS-NMR [19]. Figure 10 shows a series of ^{29}Si spectra of gels used to synthesize NaY zeolite. The synthesis mixture has a nominal composition of 4.1 Na$_2$O: 1.0 Al$_2$O$_3$: 13.1 SiO$_2$: 189 H$_2$O and is made from silica sol, sodium aluminate solution, sodium hydroxide solution, and demineralized water. The freshly prepared mixture is homogenized using a turbine mixer and then aged at room temperature. The broad peak at -40 ppm, which is characteristic of Q^4 Si atoms appears to be unaffected by mixing of the reagents. Upon aging of the freshly prepared gel at room temperature, the silica sol dissolves, resulting in a decrease in the intensity of the Q^4 peak and the progressive appearance of peaks indicative of silicon in Q^0, Q^1, Q^2, and Q^3 environments. The time evolution of these peaks, which is shown in Figure 10, suggests that dissolution of the sol produces monomeric silicate anions which then undergo condensation-polymerization to form oligomeric silcate and aluminosilicate structures. Futher changes in the spectra occur upon heating of the gel to 100 C, as may be seen from Figure 10. The shift in the distribution of peak intensities is indicative of further polymerization of the dissolved anions. X-ray diffraction of the recovered solids shows that crystalline zeolite begins to appear after 48 h of heating and that crystallization is completed after 112 h. During this period the composition of the gel changes very little, but the NMR spectra do show progressive evidence for NaY zeolite.
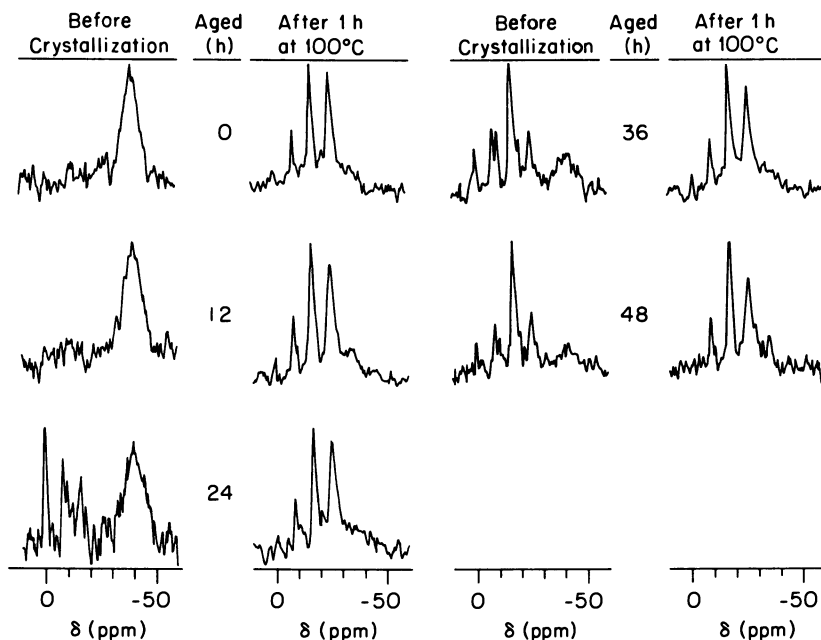

Fig. 10 ^{29}Si MAS-NMR spectra of a sodium silicate gel (nominal composition 4.1 Na$_2$O: 1.0 Al$_2$O$_3$: 13.1 SiO$_2$: 189 H$_2$O) taken after aging the gel at 20 C and heating for 1 h at 100 C.

Conclusions

High resolution ^{29}Si NMR spectroscopy can provide considerable insights into the structure and distribution of silicate and aluminosilicate anions present in solutions and gels from which zeolites are synthesized. The narrowness of individual lines and the sensitivity of the chemical shift to details of the local chemical environment make it possible in many instances to identify exact chemical structures. Studies using ^{29}Si NMR have shown that the distribution of anionic structures is sensitive to pH and the nature of the cations in solution. Alkali metal cation NMR has demonstrated the formation of cation-anion pairs the formation of which is postulated to affect the dynamics of silicate and aluminosilicate formation and the equilibium distribution of these species. ^{27}Al NMR has proven useful in identifying the connectivity of Al to Si, but because of quadrupolar broadening cannot be used to define the precise environment of Al atoms.

Literature Cited

1. Barrer, R. M. The Hydrtothermal Chemistry of Zeolites; Academic Press: London, 1982.
2. Engelhardt, G; Michel, D. High Resolution Solid State NMR of Silicates and Zeolites; Wiley: New York, 1987.
3. Harris, R. K.; Knight, C. T. G. J. Mol. Struc. 1982, 78, 262.
4. McCormick, A. V.; Radke, C. J.; Bell, A. T. in New Developments in Zeolite Science and Technology; Murakami, Y; Iijima, A; Ward, J. W., Eds.; Studies in Surfasce Science and Catalysis Vol 26; Elsevier: 1986; New York, p 247.
5. McCormick, A. V.; Radke, C. J.; Bell, A T. Zeolites, 1987, 7, 183.
6. Harris, R. K.; Knight, C. T. G. J. Chem. Soc., Farad. 2, 1983, 79, 1525.
7. Harris, R. K.; Knight, C. T. G. J. Chem. Soc., Farad. 2, 1983, 79, 1539.
8. Harris, R. K.; O'Connor, M. J.; Curzon, E. H.; Howrath, O. W. J. Mag. Res., 1984, 57, 115.
9. McCormick, A. V.; Radke, C. J.; Bell, A. T. J. Phys. Chem.,in Perspectives in Molecular Sieve Science, Advances in Chemistry Series No. 368; American Chemical Society: Washington, DC, 1988, p 222.
10. McCormick, A. V.; Radke, C. J.; Bell, A. T. J. Phys. Chem., in press.
11. Harris, R. K.; Jones, J.; Knight, C. T. G.; Newman, R. H. J. Mol. Liq., 1984, 29, 63.
12. Engelhardt, G; Hoebbel, D. J. Chem. Soc., Chem. Comm., 1984,514.
13. Kinrade, S. D.; Swadle, T. W. J. Chem. Soc., Chem. Comm., 1986, 120.
14. Griffiths, L; Gundy, C. S.; Plaisted, R. J. J. Chem. Soc., Dalton Trans., 1986, 2265.
15. Creswell, C. J.; Harris, R. K.; Jageland, P. T. J. Chem. Soc. Chem. Comm., 1984, 1261.
16. McCormick, A. V.; Radke, C. J.; Bell, A. T. J. Phys. Chem., in press.
17. McCormick, A. V.; Radke, C. J.; Bell, A. T. J. Phys. Chem., in press.
18. Engelhardt, G.; Hoebbel, D.; Tarmak, M.; Samoson, A. Lippmaa, E. Z. Anorg. Allg. Chem., 1982, 484, 22.
19. Ginter, D. S.; Bell, A. T.; Radke, C. J. J. Mag. Res., in press.

Chapter 6

Observed and Calculated Silicate and Aluminosilicate Oligomer Concentrations in Alkaline Aqueous Solutions

P. Caullet and J. L. Guth

Laboratoire de Matériaux Minéraux, Unité Associée au Centre National de la Recherche Scientifique No. 428, Ecole Nationale Supérieure de Chimie, 3 rue Alfred Werner, 68093 Mulhouse Cedex, France

A model which enables one to calculate oligomer concen-
trations, provided that those of the monomeric $Si(OH)_4$
and $Al(OH)_4^-$ species are known, has been developed. The
equilibrium constants needed are the product of a poly-
merization factor and of an ionization factor. The
polymerization constants for the formation of a Si-O-Si
or a Si-O-Al bond were estimated from solubility data.
Whereas Al-OH groups do not ionize, the ionization
constants of the silanol functions depend, probably in
a very complicated way, on the precise structure of the
oligomer. These constants were estimated partially on
the assumption of existing analogies between polysili-
cic and other inorganic acids. The various constants
used in the model were refined by comparison of the
calculated concentrations with the available experimen-
tal data. The model was then applied to determine the
influence of the chemical composition on the oligomer
distribution . The found relationships agree with the
usual observations in zeolite synthesis.

The study of alkaline silicate and aluminosilicate solutions is of
fundamental importance for a better understanding of the mechanism
of zeolite synthesis [1,2]. Real progress has been realized during
the last fifteen years thanks to the use of new techniques such as
the trimethylsilylation [3,4] of polysilicic acids (followed by a
chromatographic separation of the derivatives) and, even more, ^{29}Si
and ^{27}Al NMR spectroscopy [5-11]. The latter techniques have enabled
the identification of about twenty types of oligomers in silicate
solutions and in some cases estimates of their respective concentra-
tions. The investigation of alkaline aluminosilicate solutions is

much less advanced because these solutions are only stable at very
low silicate and aluminate concentrations.

The model presented here allows a calculation of the concentra-
tions of all the ionized forms of any oligomer species from the con-
centration values of Si(OH)$_4$ and Al(OH)$_4^-$ and from the pH value (the
simulation programs written in BASIC are available from the au-
thors). A communication describing the initial development of this
model appeared in 1984 (12).

The first part of the present paper is related to the alkaline
silicate solutions and represents the main point of our work. The
second part concerns the alkaline aluminosilicate solutions which
were studied less extensively.

ALKALINE SILICATE SOLUTIONS

It is clearly established that, in these solutions, the silicon is
in tetrahedral coordination (13). The simplest form of silica in
solution is the monosilicic acid Si(OH)$_4$. Polymerization results
from the condensation of two silanol groups with the elimination
of a water molecule. A whole series of silicate anions, of various
polymerization and ionization degrees, are thus connected through
dynamic equilibria. The equilibria are governed by the normal chemi-
cal parameters, namely the silica concentration, the pH and the
cation type.

All the studies show that, as a general rule, the formation of
more highly polymerized species is favoured by decreasing pH at
constant silica concentration and increasing silica concentration at
constant M$_2$O/SiO$_2$ ratio (14,15).

Our model applies to sodium or potassium silicate solutions at
room temperature. According to the few experimental data available
(16,17,18) these solutions show similar behaviour.

Four points will be successively developed :
- the principles of the calculation of the oligomer species concen-
  trations,
- the choice of parameters,
- comparison of calculated and experimental results,
- silica distribution in solution.

PRINCIPLES   Any oligomer species containing t silicon tetrahedra,
ℓ bonding oxygens and bearing a negative charge i is assumed to be
in equilibrium with the Si(OH)$_4$ monomeric species according to

$$(a) \quad t \; Si(OH)_4 + i \; OH^- \underset{}{\overset{K\ell,i}{\rightleftharpoons}} \; Si_tO_{(\ell+i)} \; OH^{-i} \; \left[2(2t-\ell)-i\right] \; +(\ell+i) \; H_2O$$
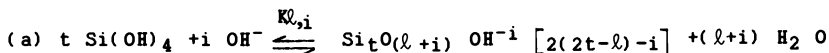
The activity of each species, i.e. $\left[\,t,\ell,i\,\right]$, is thus expressed by

$$\left[t,\ell,i\right] = K_{\ell,i} \; \left[Si(OH)_4\right]^t \; \left[OH^-\right]^i$$

In order to simplify the calculations, activity will be replaced by
concentration.

The equilibrium constant $K_{\ell,i}$ is considered to be equal to the
product of a polymerization constant Kp and an ionization constant

Ki. The pH of the solutions in the present study was determined by using a "high-alkalinity" glass electrode, taking due precautions to avoid carbonation of the solutions.

Depending on the case considered, the monosilicic acid concentration is
- either independent of pH when the silicate solution is in equilibrium with the amorphous silica according to
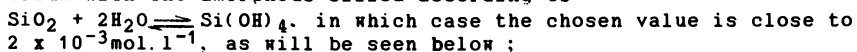 $SiO_2 + 2H_2O \rightleftharpoons Si(OH)_4$. in which case the chosen value is close to $2 \times 10^{-3} mol.l^{-1}$, as will be seen below ;

- or calculated from the monomeric silica concentration if at equilibrium the system contains no solid silica. This implies a knowledge of the pH value and of the ionization constants of $Si(OH)_4$.

CHOICE of PARAMETERS   Ionization constants of $Si(OH)_4$

As only the pk_1 and pk_2 values were determined experimentally (19, 20), we have assumed, in order to estimate pk_3 and pk_4 , that the difference between the pk values of two successive ionizations is constant by analogy with the behaviour of other inorganic polyacids.

While the scattering of pk_1 experimental values around an average of 9.8 is rather small, the uncertainty on the pk_2 value is larger with one set of values around 11.8 and another one   around 12.4. The choice of the pk_2 value to be used in our calculation was made on the basis of the following experimental observations. According to Freund (21) the $SiO_2(OH)_2^{2-}$ species prevails in sodium silicate solutions for a pH of about 13.5 while the $SiO_3(OH)^{3-}$ species begins only to appear for pH values close to 14. These data are supported by other authors (17,22). The best agreement between the calculated distribution of the various ionized forms of $Si(OH)_4$ versus pH (figure 1) and these experimental observations was obtained for $pk_2 = 12.4$, which led us to retain this value.

Ionization constants of polysilicic acids. The ionization constant Ki for equilibrium a) of a species of ionization degree i is the product of i ionization constants k_i corresponding to successive dissociation reactions. We assume that all tetrahedra within any species dissociate once before the second possible dissociation of any tetrahedron occurs, and so on for successive dissociations.

As a general rule the overall acidity of inorganic polyacids seems to increase with polymerization degree (20). For instance the pk_1 of disilicic acid is estimated to be 9.05 (23), while that of silica gel is close to 7 (24,25). On the other hand it is reasonable to think that the pk of the nth ionization (first, second or third) is not the same for all tetrahedra and increases slightly with increasing i. Already ionized silanol groups indeed make the dissociation of the other neighbouring silanol functions more difficult (26). This is corroborated for instance by the pk_i values of polyphosphoric acids. Moreover in this particular case, the acidity of cyclic polymers seems to diminish more quickly with increasing i than that of linear polymers, because on the average the OH groups are nearer to each other and the interactions are stronger. The algorithm used for the computation of pk_i (see below) is based in part upon these observations and was refined according to the results of computer simulations.
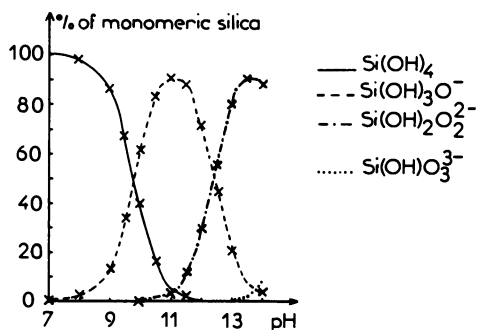
Figure 1 : Computed distribution of the ionized forms of Si(OH)4 versus pH. (pk_1 = 9.8 ; pk_2 = 12.4 ; pk_3 = 15 ; pk_4 = 17.6)

Finally, we arrived at the following assumptions :
- the first tetrahedron that ionizes for the first, second or third time is characterized by the same pk values for all oligomers. These values are smaller than those of $Si(OH)_4$, but their increments are identical : $pk_1 = 9.4$; $pk_2 = 12.0$; $pk_3 = 14.6$
- the pk's of the other tetrahedra of the oligomer which ionize afterwards for the first, second or third times, increase over a 1.7 unit interval beyond the respective values of pk_1, pk_2. and pk_3 for the first tetrahedron. The value of the interval was assumed to be lower than the pk value difference between two successive ionizations of the same tetrahedron (i.e. 2.6) and was chosen partly on the basis of the pk_i values of some polyphosphoric acids. The value finally adopted, i.e. 1.7., was obtained by an iterative procedure that compared calculated and experimentally observed oligomer concentrations. In the case of linear polymers the increase of pk is regular, the pk interval between two successively ionizing tetrahedra being equal to $1.7/(n_i-1)$ (n_i refers to the number of tetrahedra able to ionize at least i times). In the case of cyclic species, once the first tetrahedron is ionized, the pk's of 1st, 2nd or 3rd ionization of the others tetrahedra are equal and increased by 1.7 units with regard to pk_1, pk_2 and pk_3 respectively. For example. the pk_i values corresponding to the linear and cyclic trimers are given in Table I.

Table I : pk_i values of linear and cyclic trimers

	Linear trimer			Cyclic trimer		
Tetrahedron no.	1	2	3	1	2	3
pk_1	9.4	10.25	11.1	9.4	11.1	11.1
pk_2	12.0	12.85	13.7	12.0	13.7	13.7
pk_3	14.6	16.3	-	-	-	-

Polymerization constant. The polymerization constant k corresponds to the following equilibrium :

$$\equiv Si-OH + HO-Si \equiv \overset{k}{\rightleftharpoons} \equiv Si-O-Si\equiv + H_2O$$

k was assumed to depend neither on the polymerization degree, nor on the mean connectivity ($\overline{Q} = 2\ell/t$) nor on the charge carried by the species. The Kp constant of equilibrium a) is thus expressed by $Kp = k^\ell$.

An estimate of k can be made from the solubility of amorphous silica at pH 7, that is $2 \times 10^{-3} mol.l^{-1}$ (19), according to

$$SiO_2 + 2H_2O \overset{k'}{\rightleftharpoons} Si(OH)_4$$
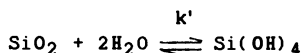
It should be noticed that such a formulation is not exact, because according to our calculations, the dissolved silica is not wholly monomeric, but is about 10% polymerized.

The dissolution reaction (change in free enthalpy : $\Delta G'$) implies the breaking of two Si-O-Si bonds (per silicon atom) and the formation of four silanol groups (with disappearance of two water molecules). On the other hand the polymerization reaction (change in free enthalpy : ΔG) corresponds to the formation of a Si-O-Si bond (and a water molecule) and to the disappearance of two silanol groups. It can thus be written to a first approximation :

$$\Delta G = - \frac{\Delta G'}{2} = - RT \ln k = \frac{1}{2} RT \ln k' = \frac{1}{2} RT \ln\left[Si(OH)_4\right]$$

hence k = 22.5

Considering that the oligomers found experimentally are composed of a rather small number of silicon atoms, a slightly larger value, i.e. k = 25 was finally adopted.

COMPARISON between CALCULATED and EXPERIMENTAL RESULTS   We will discuss first the study made by Dent Glasser et al.(4), although the technique used, namely trimethylsilylation followed by chromatography of the formed derivatives, may have disturbed the initial distribution of the oligomers. The most interesting experimental data were obtained by ^{29}Si NMR spectroscopy. The papers of Harris et al.(9) and of Mc Cormick et al.(10) will be discussed at length further on.

Comparison with the results obtained by Dent Glasser et al (4). These authors studied the influence of silica concentration (at constant pH) and of pH (at constant silica concentration) on the concentrations of the oligomers (t = 1 to t = 8). At constant silica concentration (0.5 mol.1^{-1}) the concentrations of small oligomers (t = 1 to t = 4) decrease with decreasing pH while the concentrations of species with higher degrees of polymerization (t = 6 and t = 8) reach maxima at pH 12 (Figure 2a). The latter species may appear as intermediates during the polymerization process.

In our calculations we have taken into account the oligomers identified by NMR spectroscopy in solutions of analogous compositions (9,10). We have checked that the concentrations of the other theoretically possible species are indeed completely negligible.

On the whole, the experimentally observed evolutions are well reproduced by our computations (Figure 2b). Agreement between experimental and calculated concentrations is good except for the trimer and hexamer species. For these oligomers containing three-membered rings the computed values are probably overestimated because the strains existing in these cycles are not taken into account in our model. The calculated concentrations for hexamers are about five times too high at pH 11 and 12 and could not be shown in Figure 2b. Dent Glasser et al. show also in a single example that the de-
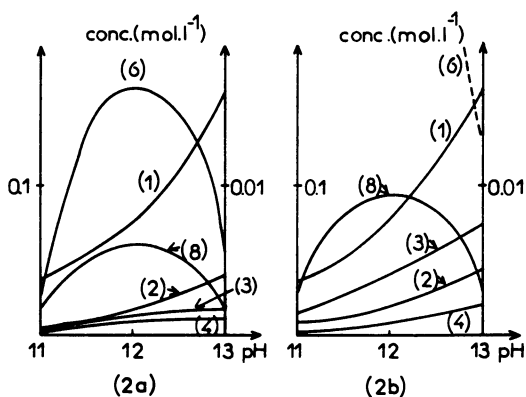
Figure 2 : Experimental (a) and calculated (b) concentrations ($mol.1^{-1}$) of various oligomers (in brackets is given the number of silicon tetrahedra)

Note : On y-axis, the left scale refers to species with 1 to 4 silicon tetrahedra, the right scale to higher polymers (t = 6 and t = 8).

crease of the overall silica concentration at constant pH results in a depolymerization of the oligomer species, in agreement with our calculated results.

Comparison with the experimental data obtained by Harris et al. (9). Three potassium silicate solutions with a constant silica concentration(0.65 mol.l^{-1}) and a variable pH were studied by these authors. Eighteen oligomers, consisting of 1 to 8 silicon tetrahedra, were identified and their relative concentrations were determined. Assuming that the analysis of the NMR spectrum has taken into account the largest part of the silicate species really arising, the calculation of the absolute concentrations is straightforward. The proposed structure of these species will be described later in paragraph entitled "Structure of the silicate oligomers".

The general features found by Harris et al. are analogous to those of Dent Glasser et al. With increasing pH at constant silica concentration, the concentrations of small oligomers (t < 4) increase whereas those of oligomers containing 5 to 8 silicon tetrahedra diminish. The evolution of each tetramer's concentration depends, in fact, on its precise nature.

There is good agreement between the observed concentrations and the calculated ones according to our model only in the case of the less alkaline solution (pH = 12.53 ; molar ratio K/Si = 1). For both other solutions - pH = 13.58 (K/Si = 1.5) and pH = 13.80 (K/Si = 2) - the discrepancies are relatively important, the calculated values being systematically underestimated. In our opinion these descrepancies are due to the fact that the monomeric silica concentration given by Harris et al. and used in our calculation, is probably too low. In comparing data of Harris et al. for the monomer concentration with those of Dent Glasser et al.(the overall silica concentrations are close) it appears that the agreement is rather good in the case of the less alkaline solution. On the other hand the values given by Harris et al. seem to be too low for the two most alkaline solutions. Indeed, the fact that the proportion of monomeric silica indicated by Harris et al. decreases slightly (the whole silica concentration being constant) as the pH increases from 12.53 to 13.58 is at variance with the usually observed trends (14,15). Keeping in mind these remarks, we have given here only the calculated results referring to the less alkaline solution (table II). The agreement between experimental and calculated values is quite satisfactory.

Comparison with the results of Mc Cormick et al. (10). The five sodium silicate solutions studied by these authors have the same silica concentration (about 1.65 mol.l^{-1}) and various pH values (13.67 ; 13.30 ; 12.60 ; 11.86 and 11.54 according to our own measurements). They identified the same oligomers as did Harris, and proposed an additional 12 silicon-tetrahedra hexagonal prismatic species.

In spite of the precautions taken by Mc Cormick et al. it seems to us that some reservations must be maintained concerning the precision of the experimental values of the oligomer concentrations. Indeed in the case of the less alkaline solutions ($SiO_2/Na_2O \geqslant 2$) the signal to noise ratio becomes less favourable. Thus the measurement of the intensity of each individual peak and consequently the

integration of all Si peaks becomes less precise. Accordingly the experimental monomer concentration might be inaccurate in some cases. Indeed the observed variation of the monomer concentration versus pH (Figure 5 in reference [10]) is surprising since the constancy over an interval of more than one pH unit (12.6 to 11.54) is rather unexpected.

Table II : Experimental ([9]) and calculated concentrations of oligomers in a potassium silicate solution (0.65 mol.l^{-1} SiO_2, pH = 12.53)
(* value taken as a basis in our computations)

Number t of tetrahedra of the oligomers	Experimental concentrations (mol.l^{-1})	Calculated concentrations (mol.l^{-1})
1	0.1	0.1*
2	2 x 10^{-2}	2.6 x 10^{-2}
3	2.3 x 10^{-2}	4.8 x 10^{-2}
4	1.7 x 10^{-2}	1 x 10^{-2}
5	1.5 x 10^{-2}	0.5 x 10^{-2}
6	2.6 x 10^{-2}	3.2 x 10^{-2}
7	3.5 x 10^{-3}	4.2 x 10^{-3}
8	4.1 x 10^{-3}	2.7 x 10^{-3}

Taking into account these remarks, only the values calculated by using our model for the three most alkaline solutions are compared to the corresponding experimental results (Table III). The general evolutions with pH are analogous and moreover agree with those shown by Harris et al. However, while the agreement remains acceptable for the small oligomers (t < 4) it becomes rather poor for the other oligomers (t > 4). These relatively disappointing results can probably be explained by the fact that the solutions studied here are much more concentrated in silica than those of Harris et al. This favours the formation of more polymerized species, some of which may be unidentified, and strengthens the reservations stated before concerning the precision of the experimental concentrations of the species. As well the assumption made in our calculations that the activities and concentrations are identical, is less justified

as the ionic strength of the solutions increases. Finally the pH measurement of such very alkaline solutions becomes difficult.

Table III : Experimental ($\underline{10}$) and calculated concentrations of oli-
gomers in a sodium silicate solution (1.65 mol. 1^{-1} SiO_2)
(* t : number of tetrahedra in oligomers)
(** value taken as a basis in our calculations)

t*	pH = 12.60		pH = 13.30		pH = 13.67	
	exp. conc.	calc. conc.	exp. conc.	calc. conc.	exp. conc.	calc. conc.
1	0.08	0.08**	0.11	0.11**	0.30	0.30**
2	1.4×10^{-2}	1.7×10^{-2}	2.3×10^{-2}	1.4×10^{-2}	8.4×10^{-2}	6.8×10^{-2}
3	2.8×10^{-2}	2.4×10^{-2}	4.3×10^{-2}	1.1×10^{-2}	8.6×10^{-2}	10.6×10^{-2}
4	4.1×10^{-2}	4.2×10^{-3}	3.8×10^{-2}	2.1×10^{-3}	4.9×10^{-2}	6×10^{-2}
5	6.2×10^{-2}	1.5×10^{-3}	7.1×10^{-2}	7×10^{-5}	5.7×10^{-2}	8×10^{-4}
6	6.9×10^{-2}	2.9×10^{-3}	4.7×10^{-2}	6×10^{-5}	1.1×10^{-2}	5.4×10^{-4}
7	≈ 0	7×10^{-4}	≈ 0	3×10^{-6}	6.6×10^{-3}	3×10^{-5}
8	4.7×10^{-3}	2.8×10^{-4}	4.1×10^{-3}	1×10^{-7}	2.5×10^{-3}	6×10^{-7}
12	3.4×10^{-3}	2×10^{-7}	2×10^{-3}	2×10^{-12}	≈ 0	2×10^{-11}

In the following section the structure of the silicate oligo-
mers will be considered in more detail.

STRUCTURE of the SILICATE OLIGOMERS   The experimentally identified
species ($\underline{9,10,11}$) are comprised of a rather small number of silicon
tetrahedra (t < 12). They are for instance linear (t = 1 to 4), cy-
clic (t = 3 and 4), bicyclic oligomers (t = 6,8 and 12) consisting
of 2 identical rings. There are, in addition, more complex species
related to the cyclic trimer and tetramer and other polycyclic
forms (t = 7 and 8).
     The values given in Table IV and referring to the potassium
silicate solution already considered before (paragraph entitled
"Comparison with the experimental data obtained by Harris at al.")
show a good agreement between experimental and calculated concentra-
tions for the main oligomers. Satisfactory agreement was found as
well for the other species not mentioned in Table IV.
     Two essential observations which are confirmed by analysis of
the results of Mc Cormick et al.($\underline{10}$) can be deduced from this table:
- the concentration of species of a given type (linear, cyclic or

bicyclic) diminishes with increasing number t of tetrahedra,
- for constant numbers of tetrahedra the concentration of oligomers
is larger for strongly connected species (bicyclic with $\overline{Q}$ = 3). As
well, the order of magnitude of the concentrations is the same for
trimers and tetramers according to whether they are linear or cy-
clic. Our calculations seem to show that the difference becomes
larger for species with higher polymerization degree (t > 4), the
formation of linear oligomers being favoured relative to the forma-
tion of cyclic species.

Table IV : Experimental ($\underline{9}$) and calculated concentrations of oligo-
            mers in a potassium silicate solution
            (0.65 mole SiO_2 per liter, pH=12.53)
            (*t : number of tetrahedra in oligomers)
            (n.o.: non observable)

t*	Linear species		Cyclic species		Bicyclic species	
	exp. conc.	calc. conc.	exp. conc.	calc. conc.	exp. conc.	calc. conc.
1	0.1	0.1	-	-	-	-
2	2×10^{-2}	2.7×10^{-2}	-	-	-	-
3	1.3×10^{-2}	1.3×10^{-2}	10^{-2}	3.5×10^{-2}	-	-
4	n.o.	6.8×10^{-3}	6.4×10^{-3}	1.9×10^{-3}	-	-
5	n.o.	3.4×10^{-3}	n.o.	1×10^{-4}	-	-
6	n.o.	1.7×10^{-3}	n.o.	5.4×10^{-6}	5.1×10^{-3}	1.9×10^{-2}
8	n.o.	4.1×10^{-4}	n.o.	1.5×10^{-8}	n.o.	1.4×10^{-3}
12	n.o.	2.2×10^{-5}	n.o.	1.3×10^{-13}	n.o.	6.8×10^{-6}

        In conclusion, in spite of some reservations, it is possible
with our computational model to account correctly for the general
evolutions and in most cases the estimates are close to experimental
values. In the next part our model will be applied, with the requi-
red modifications, to the study of alkaline aluminosilicate solu-
tions.

ALKALINE SOLUTIONS CONTAINING SILICATE and ALUMINATE IONS

Generally the solubility of alkaline aluminosilicates in alkaline
medium is much lower than that of silica. This is related to the
chemical behaviour of aluminum. At pH larger than 11 this element
exists solely as tetrahedral $Al(OH)_4^-$ ions ($\underline{27}$). The Al-OH functions

are not ionizable and remain available for polymerization, whatever the pH. Experimental data relating to the oligomers present in alkaline aluminosilicate solutions are therefore very scarce, with practically no quantitative information. The only clearly stated qualitative information is the apparent existence of aluminosilicate anions (15, 28, 29). Under such conditions the application of our model claims only here to predict some general trends (30).

Analogously to the calculation principle used for silicate species, the activity of an aluminosilicate oligomer can be expressed by

$$[ts. ta. \ell s. \ell a. i] = K_{\ell s. \ell a. i} \left[Si(OH)_4 \right]^{ts} \left[Al(OH)_4{}^- \right]^{ta} \left[OH^- \right]^i$$

ts and ta being respectively the number of silicon and aluminum tetrahedra, ℓs and ℓa being respectively the number of Si-O-Si and Si-O-Al bonds. All assumptions made for the silicate solutions are used here.

Thus $K_{\ell s. \ell a. i} = Kp \; Ki = k_s{}^{\ell s} \; k_a{}^{\ell a} \; Ki.$

Further, the polymerization constant k_s (referring to the formation of a siloxane bond) and the ionization constant Ki are assumed not to be modified by the presence of aluminum atoms. The k_a value, corresponding to the formation of a Si-O-Al bond, was estimated by iteration according to values originating from a semi-quantitative experimental study (29) and was found to be 35. The following results are based upon an example from this study.

The variation of oligomer concentrations as a function of polymerization degree and connectivity is analogous to the variation observed for silicate solutions. Nevertheless some specific features become apparent.

Alkaline aluminosilicate solutions with a Si/Al ratio close to one, exist only at much lower concentrations than do silicate solutions for a given pH. This results directly from the general expression giving the activity of an oligomer. Indeed, as pH increases, the $Si(OH)_4$ concentration becomes very low whereas the $Al(OH)_4{}^-$ concentration remains practically constant and at a much higher level.

A direct consequence of this is that, for a given conformation, the most stable oligomer will be the one containing the highest number of aluminum atoms, provided it is consistent with Loewenstein's rule (31). This trend becomes weaker as the pH decreases or the overall Si/Al ratio in solution increases, in agreement with the usual observations made in zeolite synthesis (32). These correlations are shown in table V referring to the cyclic tetramers. The numbers in brackets represent the concentration ratio between the species considered and the purely silicic form.

A last important feature concerns the bicyclic species. Our calculations show that their formation is favoured when both constitutive rings contain each an even number of tetrahedra. The concentration of oligomers made of two four- or six-membered rings is respectively larger than the concentration of species containing two three- or five-membered rings. This behaviour is directly related to Loewenstein's rule and can be related to the fact that the frame-

work of alumina-rich zeolites. which are synthesized in alkaline medium. can be built in most cases with even-membered rings of te-trahedra.

Table V : Concentration of the cyclic tetramers in an alkaline aluminosilicate solution ($[$monomeric silica$] + [Al(OH)_4^-]$ = 0.02 mol.l^{-1})

Monomeric silica/Al(OH)$_4^-$ molar ratio	Composition of the species	Concentration of the species (mol.l^{-1})	
		pH = 12	pH = 13
	4 Si.0 Al	6.7×10^{-7} (1)	2.6×10^{-8} (1)
1	3 Si.1 Al	3.7×10^{-5}(55)	5.1×10^{-6} (200)
	2 Si.2 Al	2×10^{-3}(3020)	9.7×10^{-4}(37000)
	4 Si.0 Al	7.3×10^{-6} (1)	2.9×10^{-7} (1)
10	3 Si.1 Al	4.1×10^{-5}(5.5)	5.6×10^{-6} (19)
	2 Si.2 Al	2.2×10^{-4}(30)	1.1×10^{-4}(380)

CONCLUSION

The model presented here allows. in principle. the determination of the concentration of any oligomer species in an alkaline silicate solution provided that the monomeric silica concentration and the pH are known. Due to their greater complexity and experimental diffi-culty. the investigation of aluminosilicate solutions corresponds only to an extension of this model and it was dealt with in a sim-plified way.

Several recent NMR studies have allowed the identification of about twenty silicate oligomers and quantitative or semi-quantitati-ve estimates of their respective concentrations. In spite of the precautions used by some authors, the measured concentrations and in particular the experimental monomer concentration (used as a basis in our calculations) are probably not always very accurate expecial-ly in the case of the less alkaline or the more concentrated (in silica) solutions. The use of an inert silicon-containing internal standard could perhaps be useful. To this lack of accuracy is added the uncertainty of the pH measurement in such strongly alkaline solutions.

Moreover several assumptions made in the setting up of the cal-culation algorithm for the ionization constants lead to an approxi-mate model. An improvement of our model would be to take into account in a more specific way the precise structure of the oligomers. It should be added that any precise experimental measurement of ioniza-

tion constants, even if only those of the monomer, would be very helpful.

In spite of these problems, our model allows us to account for the experimentally found evolutions. Further, the agreement between measured and computed values is generally satisfactory.

The general trends concerning the oligomers present in the solutions can be summarized as follows. The oligomers consist of a rather small number of tetrahedra (t < 12). For a given type (linear, cyclic, bicyclic) the concentrations of the species diminish as t increases and for a given t the formation of strongly connected species is favoured. Both the increase of silicate or aluminate concentrations and the decrease of pH promote the formation of more polymerized species. In the aluminosilicate solutions the preferentially formed species are those with the highest possible number of aluminum atoms, although this trend becomes weaker as the pH is decreased or the overall Si/Al ratio in solution is increased.

LITERATURE CITED

1. R. M. Barrer, J. W. Baynham, F. W. Bultitude, F. M. Meier, _J. Chem. Soc_, 1959, 195.
2. S. P. Zhdanov, _Proc. 5th Int. Conf. on Zeolites_, (Naples), Heyden, London, 1980, 75.
3. C. W. Lentz, _Inorg. Chem._, 1964, _3_, 574.
4. L. S. Dent Glasser, E. E. Lachowski, _J. Chem. Soc._, Dalton Series, 1980, 393.
5. G. Engelhardt, D. Zeigan, H. Jancke, D. Hoebbel, W. Wieker, _Z. anorg. allg. Chem._, 1975, _418_, 17.
6. S. Sjöberg, L. O. Ohman, N. Ingri, _Acta. Chem. Scand. Ser. A_. 1985, _39_, 93.
7. R. K. Harris, C. T. G. Knight, W. E. Hull, _J. Am. Chem. Soc._, 1981, _103_, 1577.
8. R. K. Harris, C. T. G. Knight, _J. Chem. Soc._, Faraday Trans. 2, 1983, _79_, 1525.
9 . R. K. Harris, C. T. G. Knight, _J. Chem. Soc._, Faraday Trans. 2, 1983, _79_, 1539.
10. A. V. Mc Cormick, A. T. Bell, C. J. Radke, _Zeolites_, 1987, _7_, 183.
11. C. T. G. Knight, _J. Chem. Soc._, Dalton Trans., 1988, 1457.
12. J. L. Guth, P. Caullet, R. Wey, _Studies in Surface Science and Catalysis 24_, Elsevier, Amsterdam, 1985, 183.
13. D. Fortnum, J. O. Edwards, _J. Inorg. Nucl. Chem._, 1956, _2_, 264.
14. R. K. Iler, _The Chemistry of Silica_, J. Wiley and Sons, New-York, 1979, chapter 2.
15. G. Engelhardt, D. Michel, _High-resolution solid-state NMR of silicates and zeolites_, John Wiley and Sons, Chichester, 1987, chapter 3.
16. C. T. G. Knight, _Ph. D. Thesis_, University of East Anglia, 1982.
17. D. Barby, T. Griffiths, A. R. Jacques, D. Pawson, _The modern inorganic chemicals Industry_, Ed. Thompson, London, 1977, 320.
18. N. H. Ray, R. J. Paisted, _J. Chem. Soc._, Dalton Trans., 1983, 475.
19. N. Ingri, Nobel Symposium, 1977, _40_, 3.
20. D. D. Perrin, _Ionisation constants of inorganic acids and bases in aqueous solutions_, IUPAC Chemical Data Series n°29, Pergamon Press, Oxford, 2nd edition, 1982.

21. E. Freund, Bull. Soc. Chim. Fr. , 1973. 2238.
22. J. G. Vail. Soluble Silicates, Reinhold, New-York, 1952.
23. L. W. Cary. B. H. W. S. de Jong, W. E. Dibbe Jr., Geochim. Cosmochim. Acta., 1982, 1317.
24. P. Schindler, H. R. Kamber, Helv. Chim. Acta., 1968, 51, 1781.
25. V. N. Belyakov, N. M. Soltinskii, D. N. Strazhesko, V. V. Strelko, Uhr. Khim. Zh., 1974, 40, 236.
26. D. N. Strazhesko, V. B. Strelko, V. N. Belyakov, S. C. Rubank, J. Chromatogr., 1974. 102, 191.
27. R. L. Moolenaar, J. C. Evans, L. D. Mac Keever, J. Phys. Chem., 1970, 74, 3629.
28. L. S. Dent Glasser, G. Harvey, J. Chem. Soc., Chem. Comm., 1984. 1250.
29. J. L. Guth, P. Caullet, P. Jacques, R. Wey, Bull. Soc. Chim. Fr., 1980, 121.
30. J. L. Guth. P. Caullet, Thesis, Mulhouse, France. 1983.
31. W. Loewenstein. Am. Mineral., 1954, 39, 92.
32. R. M. Barrer. Zeolites, 1981, 1, 130.

Chapter 7

Influence of D$_2$O and Alcohols on the Crystallization of Zeolites

Prabir K. Dutta, Micky Puri, and Christopher Bowers

Department of Chemistry, The Ohio State University, Columbus, OH 43210

The synthesis of zeolites with low Si/Al ratios (1-2) from amorphous aluminosilicate solids (Si/Al:1-5) were explored as a function of reaction time and in D$_2$O and alcohol. The growth and decay of zeolite X and P appear to be independent for the same reaction system. Methanol and ethanol have a profound impact in accelerating the rate of large pore crystal growth at low levels, and more condensed phases at higher levels. The role of alcohol appears to be linked to the stabilization of water structure and cation water complexes which together act as templates for crystal growth. The deceleration of zeolite growth in D$_2$O possibly arises from an isotope effect involving condensation polymerization during zeolite growth.

The mechanism of formation of zeolites is very complex, stemming from the diversity of chemical reactions, including various polymerization and depolymerization equilibria, nucleation and crystal growth processes. The physical and chemical nature of the reactants, which typically involve a source of aluminum and silicon along with hydroxides and salts determine the formation of zeolites. Physical effects such as aging, stirring, and temperature also play an important role. These effects lead to the complexity of zeolite formation, but are also responsible for the large number of frameworks that can be synthesized and the rich chemistry associated with this area.([1,2])
Over the past decades, considerable effort has been focussed on the evaluation of the various parameters that influence zeolite crystallization.([3,4]) More recently, spectroscopic techniques are being used to monitor zeolite growth. These studies include high resolution NMR spectroscopy of silicate and aluminate solutions,([5,6]) solid state NMR spectroscopy of the amorphous phase([7,8]) and Raman spectroscopic studies of solution and solid phases during crystallization.([9-14]) The typical solutions present during zeolite growth contain various oligomeric silicate species, Al(OH)$_4^-$ and minute amounts of aluminosilicate anions, because of

their limited solubility. The amorphous solid phase, present at the early stages of zeolite synthesis, is made up of aluminosilicate rings, whose structure determines to some degree the zeolite being synthesized. For example, in the case of zeolites A and X, four membered rings interconnected in a random fashion comprise the solid amorphous phase,(11,14) whereas for zeolite Y, six membered rings are evident.(12) Spectroscopic studies have been unable to provide information about why and how these elementary building blocks combine to form unique zeolitic structures. This process, under otherwise identical conditions, is strongly influenced by the cation e.g. Na⁺, K⁺ and Cs⁺ promote the formation of zeolite A, chabazite and edingtonite, respectively.(14) Cation-water complexes are thought to act as templates for nuclei formation.(2) In addition, we have proposed that cation-water complexes may stabilize small aluminosilicate anions responsible for forming unique zeolitic structures, primarily due to electrostatic and steric factors.(14) We report here an investigation of zeolite synthesis in aqueous alcoholic mixtures and deuterium oxide, in order to explore the influence of water structure on crystallization. Zeolite synthesis in pure alcoholic solvents have been reported, in which hydroxysodalite is formed as the main component.(15,16)

Experimental Section

Ludox TM (Dupont) or SiO_2 gel (Aldrich) was used as the source of silicon and aluminum powder (~40 mesh) was obtained from Alfa Chemicals. NaOD and D_2O were purchased from Aldrich and used as such. NaOH, NaCl, LiCl (Mallinckrodt), LiOH·H_2O (Baker) and ethanol (U.S.P., Pharmco) were all used as received. All experiments were carried out in Teflon bottles and synthesis was done in an oven without stirring.
    Powder X-ray diffraction patterns were obtained with a Rigaku Geigerflex D/Max 2B diffractometer with Ni filtered CuKα source. Elemental analysis (Si/Al ratios) was done with an energy dispersive X-ray fluorescence spectrometer (Kevex) using direct excitation. Zeolites, whose elemental analysis was known independently was used as calibration. The Raman spectra were obtained by excitation with a Spectra Physics 171 Argon Ion Laser using 50 mW of 457.9 nm radiation. A Spex 1403 monochromator along with a RCA C31034 GaAS PM tube was used to analyze the scattered light.
    In studying the influence of ethanol the synthesis was carried out in a way which allowed the effect of the different cations and varying alcohol content to be explored. Clear solutions of sodium silicate and aluminate were combined to produce a gel. The solutions were obtained by dissolving the appropriate amount of SiO_2 or aluminum powder in a solution of 1M NaOH. The Si/Al ratio of the starting composition was 0.9, 5, and 20 which upon filtration, washing and drying produced materials with Si/Al ratios of 1.33, 1.48 and 4.28, respectively. The gel was filtered and extensively washed with water and was then ion exchanged with either 0.1M LiCl or NaCl and again filtered and washed with water. Two grams of this Li and Na ion exchanged material were placed in 50 mL of 1M NaOH or LiOH solution which contained the appropriate

amount of ethanol. This was then heated to 90-95°C and the X-ray
diffraction pattern was periodically checked.

Results

In this section, we detail our results on the nucleation and growth
of zeolite crystals with Si/Al ratios between 1 and 2. Various
perturbations, including the effects of reaction time, D_2O, CH_3OH
and C_2H_5OH on the zeolite process are examined. A narrow range of
starting compositions and reaction conditions are chosen, so that
the effects of the perturbations can be evaluated with a minimum
set of variables. These results are discussed in the context of
present theories of zeolite growth in the next section.

Zeolite X System. It is well recognized that with a fixed reactant
composition, zeolites of different frameworks can be formed.([17])
For example, zeolites X and P are formed from the same reactants at
100°C and 150°C, respectively. Such phenomena are usually
discussed in terms of successive transformation, with a metastable
phase forming at first and converting successively to the more
stable phase.
      Starting with the composition typical for crystallization of
zeolite X 8.6Na_2O 0.75 Al_2O_3 3SiO_2 556H_2O at 85-90°C, we examined
the formation of zeolite crystals over a period of 32 days.
Throughout the crystallization period, zeolites X and P coexisted.
Figure 1A shows the percent crystallinity as determined from the
powder diffraction patterns and Figure 1B is the Raman spectra of
the solid phase at different times. In order to define percent
crystallinity, we chose the reflection peaks at 2θ=6.12 for zeolite
X and 2θ=28.10 for zeolite P as standards. The curves in Figure 1A
are normalized to the maximum intensity observed for these peaks
during the crystallization period at 2 days for zeolite X and 32
days for zeolite P. Signal from zeolite X maximizes within the
first 48 hours and then rapidly decays to 50% of its peak
intensity, followed by a slower decrease in intensity. Crystals of
zeolite P are observed from the earliest times, but their rapid
growth does not occur until 14-16 days of reaction. The rate of
decrease of zeolite X does not follow the growth of zeolite P.
This is in contrast to the observation of Kostinko, who noted that
the rate of disappearance of zeolite A matches the rate of
appearance of hydroxysodalite.([18]) In order to investigate if any
other species is forming during the reaction, the Raman spectra of
the solid phase was studied. Characteristic bands due to zeolite X
and P are observed throughout the crystallization process, and no
evidence for any intermediate species including the amorphous phase
was observed. However, the sensitivity of Raman spectroscopy
precludes the observation of an intermediate unless it is present
in the concentration range of 5-10 percent. Also, the Raman
scattering from the crystalline phase is more pronounced than the
amorphous phase, primarily due to the sharper bands. Therefore,
during the 6-12 day period, the fate of the disappearing zeolite X
crystals is unclear. However, it is clear that nuclei for zeolite
X and P coexist during the entire cyrstallization period. The
nucleation and growth kinetics favor the initial formation of
zeolite X, which results in a slower growth of zeolite P due to a
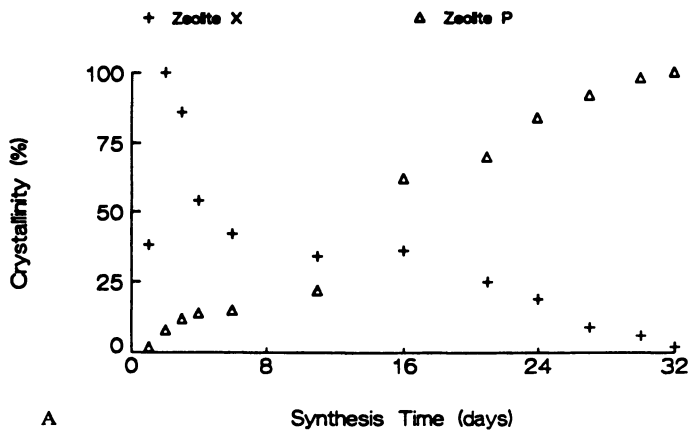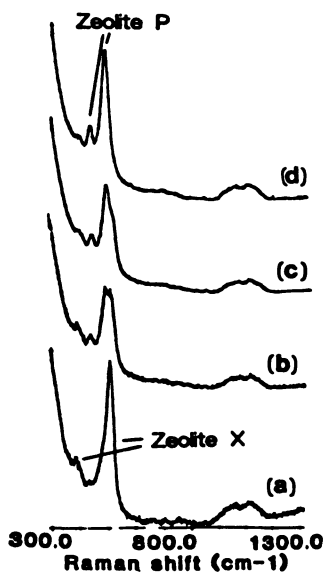
Figure 1. (A) Percent Crystallinity as a function of synthesis time for reactant composition 8.6Na₂O 0.75 Al₂O₃ 3SiO₂ 556 H₂O at 85-90°C. (B) Raman spectra of solid phase at (a) 1 day, (b) 11 days, (c) 20 days, (d) 32 days. Characteristic vibrations of zeolites X and P are marked on the figure.

lack of reactants. These data could also be interpreted to indicate that the nucleation, growth and decay kinetics of zeolites X and P are independent, and can be controlled independently by external factors. These observations are in agreement with the studies of Kerr,(19) who found that the order of mixing of reactants from the same starting composition could result in formation of either zeolite X or P. In order to examine the role of the environment on growth of different crystals from coexisting nuclei, we studied the influence of alcohol and D_2O on the crystallization process.

Zeolite A System. Zeolite A was synthesized at 85-90°C starting with the compositions: $8.6Na_2O$ Al_2O_3 SiO_2 $556H_2O$ and $8.6Na_2O$ Al_2O_3 SiO_2 $556D_2O$. Figure 2A compares the crystallization curves as measured by X-ray diffraction. Good quality zeolite A crystals are obtained in both cases. The major difference between the reactant systems is the slower rate of crystallization in D_2O. However, if the same reaction is carried out in aqueous methanolic solutions at 60-65°C the crystallization is accelerated with increasing methanol concentration. Figure 2B shows the crystallization curves of zeolite A for 0%, 5% and 25% CH_3OH (on a volume by volume basis). At alcohol levels of 50 volume percent or higher, hydroxysodalite crystals are formed at rapid rates (~200 minutes). The role of alcohol on the zeolitization process was examined with ethanol at temperatures of 90-95°C.

Influence of Ethanol. Three different amorphous aluminosilicate solids of Si/Al ratios 1.33, 1.48 and 4.28 were synthesized by mixing sodium silicate and aluminate solutions of various concentrations. These solids were extensively ion-exchanged with LiCl and NaCl solutions. The lithium and sodium containing solids (2g) were then mixed with 50 mL of 1M LiOH and NaOH, respectively. The hydroxide solutions contained 0%, 10%, 25%, 50% and 75% ethanol (volume by volume). These samples were then heated to 90-95°C, and formation of zeolites was monitored by powder diffraction. In one experiment, the lithium aluminosilicate solid was reacted in the NaOH system.

Table I details the results that were obtained. Diffraction measurements were made every hour and the reaction was discontinued if the intensities of the diffracted peaks did not continue to increase. The times on the table indicate the final measurement times. The quality of crystals was determined by comparison with pure crystals and labels of poor, medium and good in the table correspond to ~10%, 50% and 90% of the intensities of the pure crystals.

There are some general trends that can be pointed out. These include:
  (a) No zeolite crystals are formed in the completely lithium system, only crystals of lithium hydroxide or lithium silicate.
  (b) Increasing amounts of alcohol markedly speeded up the crystallization process with optimum speeds at the 25% alcohol content.
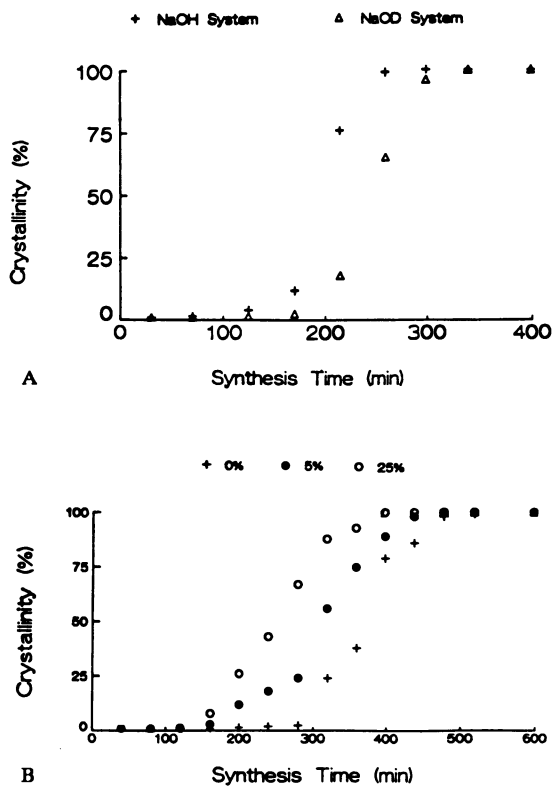
Figure 2. (A) Crystallization kinetics of zeolite A in H$_2$O/NaOH and D$_2$O/NaOD system at 85-90°C. (B) Crystallization kinetics of zeolite A in presence of 0%, 5% and 25% methanol (volume percent) at 60-65°C.

Table I

Synthesis of Zeolites in Aqueous Ethanolic Solutions

Ethanol	Na^+, NaOH (Si/Al = 1.33)	Na^+, NaOH (Si/Al = 1.48)	Na^+, NaOH (Si/Al = 4.28)	Li^+, NaOH (Si/Al = 1.48)
0%	No crystals (24 hours)	No crystals (24 hours)	zeolite Y (medium) (21 hours)	zeolite X,A (poor) (14 hours)
10%	zeolite A,X (poor) (7 hours)	zeolite A (poor) (9 hours)	zeolite Y (good) (15 hours)	zeolite A,X (poor) (14 hours)
25%	zeolite X (good) (9 hours, Si/Al = 1.22)	zeolite X (good) (12 hours, Si/Al = 1.17)	zeolite Y (good) (18 hours, Si/Al = 1.63)	zeolite X (good) (18 hours, Si/Al = 1.12)
50%	zeolite A,X, cancrinite (poor, 9 hours)	zeolite A,X cancrinite (poor, 12 hours)	zeolite Y (poor) (19 hours)	zeolite X (poor) (9 hours)
75%	cancrinite (4 hours)	cancrinite (8 hours)	sodalite (13 hours)	cancrinite (2 hours)

> (c) The yield of total solid product increased
>   with increasing alcohol content, reaching a
>   maximum at the 50% alcohol level.
> (d) At low levels of alcohol, zeolites A, X and Y
>   are formed, whereas at high levels, sodalite
>   and cancrinite are crystallized.
> (e) The presence of both Na$^+$ and Li$^+$ in the system
>   slows down the crystallization process, as
>   compared to the Na$^+$ alone, but the products
>   remain unaffected.

Figure 3 shows the X-ray diffraction patterns observed with the sodium aluminosilicate solid (Si/Al = 1.33) in NaOH. All the data were collected after ~ eight hours (within a span of 30 minutes) of heating and are plotted on the same intensity scale, so they can be compared directly. The yield of total solids in the pure water system was very small (<100 mg) and no crystals were evident. At 10% alcohol, mostly zeolite A and small diffraction peaks due to zeolite X crystals are observed. With 25% alcohol, the crystallization is complete for zeolite X. Fifty percent alcohol shows peaks due to zeolites A, X and cancrinite, whereas at 75% alcohol, cancrinite is the only product.

Discussion

It is clear from the experiments described above that both alcohol and D$_2$O influence the crystallization process. There are some parallels between the alcohol system and previous studies reported in the literature. First, in the case of sodic environments at reactant compositions described in this paper, zeolites A, X, Y, sodalite and cancrinite are formed.[2] So, the presence of alcohol is not modifying the types of frameworks that are being formed, indicating that the precursor aluminosilicate species in aqueous alcoholic solutions and water are similar. The presence of alcohol is influencing the nucleation rate. Second, it has been shown that increasing the hydroxide ion concentration accelerates zeolite growth, whereas at very high concentration of hydroxide ions, more condensed, stable zeolites are formed. Alcohol appears to have a similar effect. In explaining the effect of hydroxide ion, it has been postulated that a higher concentration of OH$^-$ leads to increased concentration of precursor species and thereby formation of more germ nuclei.[2] Third, it has been noted that in the presence of high concentration of salts, sodalite or cancrinite can be formed,[20] analogous to our observation for systems containing high alcohol concentrations.

In order to understand the influence of alcohol on the zeolitization process, it is useful to summarize the structural aspects of alcohol-water mixtures. Considerable work has been done in this area. It is well-recognized that at low alcohol concentrations the viscosity, reciprocal self-diffusion coefficient, the dielectric relaxation time and NMR relaxation times of the water molecules are all greater than that of pure water.[21-24] These observations indicate that addition of alcohol to water at low levels leads to an increased structure of water.[25] This concept is also supported by X-ray diffraction studies[26] and is commonly referred to as hydrophobic hydration.[27] On a molecular level, this effect
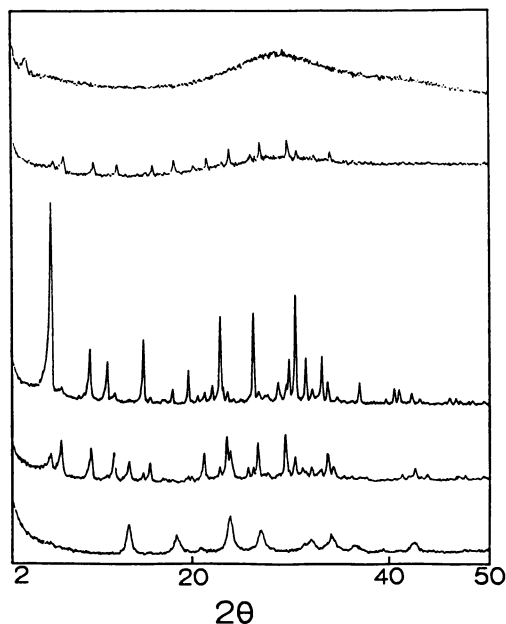
Figure 3. X-ray diffraction patterns as a function of ethanol content for 2g Na aluminosilicate (Si/Al = 1.33) in 50 mL of 1M NaOH with varying ethanol content. From top: 0%, 10%, 25%, 50% and 75% ethanol (volume percent). X-ray patterns taken ~8 hours after reaction at 90-95°C. The intensity axis is the same for all the patterns.

can be pictured as follows. Water is a network liquid with cavities which are constantly forming and collapsing. In the presence of alcohol, these cavities are stabilized by the penetration of the alkyl group into the cages. At higher levels of alcohol, after all these cages get filled, the "free" alcohol molecules bring about the disintegration of water. This model serves to explain the increase in viscosity of water till alcohol levels reach ~40% and subsequent decrease thereafter.(28)

Free energy measurements show that cations are stabilized in alcohol-water mixtures. This is due to the better solvation of the ion because of the inductive effect of the alkyl group from the coordinated alcohol. Anions, on the other hand, are destabilized in alcoholic solutions, due to the same effect.(29)

In discussing zeolite growth, the concept of hydrated cations as templates around which aluminosilicate building blocks can assemble has been recognized.(2,17) We have built on these ideas and proposed that cation-water complexes may actually electrostatically stabilize specific aluminosilicate building blocks.(14) These blocks can then assemble around the cation-water complex. Therefore, any factor influencing the water structure should influence zeolite nucleation and growth. We propose that the alcohol modifies zeolite growth by a combination of at least two factors:

(a) Alcohol influences the structure of water. At levels of alcohol (20-40%), in which the water structure is most rigid, nucleation of large pore zeolites such as zeolite X or Y is facilitated, since the cation-water templates are stabilized. At high levels of alcohol, the water structure is destroyed, leading to the nucleation of more condensed zeolites, such as cancrinite or sodalite. This model is also supported by other observations. Raising the synthesis temperature leads to more condensed zeolites since the structure of water is destroyed.(2) The same effect is also present at high concentrations of salts.(2) Low temperature aging favors the formation of large pore nuclei, since the water is structured.(2)

(b) Alcohol can promote selective solvation.(30) The hydroxide ion, because of its high charge to radius ratio, will be preferentially solvated by the water. The effective concentration of OH⁻ is therefore higher. Such an effect can lead to accelerated growth, as has been noted before. Also, the solubility of silicate species is decreased in aqueous alcoholic solutions, leading to an increased yield of the solid product.(31)

Finally, the solvent isotope effect observed in the crystallization of zeolite A provides further insight into the mechanism. The deuteroxide anion (OD⁻) is a stronger base than OH⁻ and should promote the depolymerization equilibria.(32) Also, D_2O is more structured than H_2O and should promote nucleation.(33) The isotope effect leading to a slower rate of reaction will occur in the condensation polymerization reaction leading to crystal growth, which involves elimination of both H_2O and OH⁻.(2) It is a combination of all these factors that lead to the observed nucleation rate. However, the role of crystal growth reaction appears to have a predominant effect.

Conclusions

In this study, we have shown that both alcohol and D_2O have an important effect on the nucleation and crystal growth of zeolites with Si/Al ratios between 1-2. In the case of alcohol, the formation of large pore zeolites such as zeolites X or Y is markedly accelerated at low alcohol levels. We attribute this to a stabilization of the cation-water complex and structured H_2O which act as templates. However, at high alcohol levels, the structure of water disintegrates and leads to the formation of more condensed zeolites such as sodalite or cancrinite. Synthesis of zeolite A in D_2O is slower than that in water, which primarily arises from the primary and secondary isotope effect during the condensation polymerization reactions necessary for zeolite growth.

Literature Cited

1. Flanigen, E. M. Adv. Chem. Ser. 1973, 121, 119.
2. Barrer, R. M. Zeolites 1981, 1, 130.
3. Kerr, G. T. J. Phys. Chem. 1966, 70, 1047.
4. Culfaz, A.; Sand, L. B. Adv. Chem. Ser. 1973, 121, 140.
5. Harris, R. K.; Knight, C. T. G. J. Chem. Soc. Faraday Trans. 2, 1983, 79, 1525, 1539.
6. McCormick, A. V.; Bell, A. T.; Radke, C. J. Zeolites 1987, 7, 183.
7. Engelhardt, G.; Fahlke, B.; Magi, M.; Lippmaa, E. Zeolites 1983, 3, 292.
8. Engelhardt, G.; Fahlke, B.; Magi, M.; Lippmaa, E. Zeolites 1985, 5, 49.
9. Roozeboom, F.; Robson, H. E.; Chan, S. S. Zeolites 1983, 3, 321.
10. Dutta, P. K.; Shieh, D. C. Appl. Spect. 1985, 39, 343.
11. Dutta, P. K.; Shieh, D. C. J. Phys. Chem. 1986, 90, 2331.
12. Dutta, P. K.; Shieh, D. C.; Puri, M. J. Phys. Chem. 1987, 91, 2332.
13. Dutta, P. K.; Puri, M. J. Phys. Chem. 1987, 91, 4329.
14. Dutta, P. K.; Puri, M.; Shieh, D. C. In Mat. Res. Soc. Symp. Proc.; Treacy, M. M. J.; Thomas, J. M.; White, J. M., Eds.; 1988; Vol. 111, p 101.
15. Bibby, D. M.; Dale, M. P. Nature 1985, 317, 157.
16. van Erp, W. A.; Kouwenhoven, H. W.; Nanre, J. M. Zeolites 1987, 7, 286.
17. Breck, D. W. Zeolite Molecular Sieves; Wiley: New York, 1974, p 248.
18. Kostinko, J. A. ACS Symp. Ser. 1983, 218, 3.
19. Kerr, G. T. J. Phys. Chem. 1968, 72, 1385.
20. Barrer, R. M.; Cole, J. F. J. Chem. Soc. A. 1970, 156.
21. Kay, R. L.; Vituccio, T.; Zawoyski, C.; Evans, D. F. J. Phys. Chem. 1966, 70, 2336.

22. McCall, D. W.; Douglas, D. C. <u>J. Phys. Chem</u>. 1967, <u>71</u>, 987.
23. Haggis, G. H.; Hasted, J. B.; Buchanan, T. J. <u>J. Chem. Phys</u>. 1952, <u>20</u>, 1452.
24. Clifford, J.; Pethica, B. A. <u>Trans. Farad. Soc</u>. 1965, <u>61</u>, 182.
25. Hertz, H. G. <u>Angew. Chem. Intl. Ed</u>. 1970, <u>9</u>, 124.
26. Franks, F. In <u>Hydrogen Bonded Solvent Systems</u>; Corington, A. K.; Jones, P., Eds.; Taylor and Francis: London, 1968.
27. Stengle, T. R.; Hosseini, S. M.; Basiri, H. G.; Williamson, K. L. <u>J. Solution Chem</u>. 1984, <u>13</u>, 779.
28. Beddard, G. S.; Doust, T.; Hudales, J. <u>Nature</u> 1981, <u>294</u>, 145.
29. Bates, R. G. In <u>Solute-Solvent Interactions</u>; Coetzee, J. F.; Ritchie, C. D., Eds.; Marcel Dekker: New York, 1969, p 78.
30. Schneider, H. In <u>Solute-Solvent Interactions</u>; Coetzee, J. F.; Ritchie, C. D., Eds.; Marcel Dekker: New York, 1969, p 301.
31. Iler, R. K. <u>The Chemistry of Silica</u>; Wiley: New York, 1979, p 137.
32. Laughton, P. M.; Robertson, R. E. In <u>Solute-Solvent Interactions</u>; Coetzee, J. F.; Ritchie, C. D., Eds.; Marcel Dekker: New York, 1969, p 399.
33. Heppolette, R. L.; Robertson, R. E. <u>J. Am. Chem. Soc</u>. 1961, <u>83</u>, 1834.

Chapter 8

Influence of Autocatalytic Nucleation on Zeolite Crystallization Processes

B. Subotić

Ruder Bošković Institute, P.O. Box 1016, 41001 Zagreb, Croatia, Yugoslavia

Twenty-eight kinetics of crystallization of different
types of zeolites have been analysed using kinetic
equation: $f_z = K \cdot t_c^q \approx K_o t_c^3 / (1 - K_a\, t_c^3)$ (f_z is the
fraction of zeolite formed at crystallization time
t_c, and K, K_o, K_a, and q are constants). The analysis
showed that the exponent q is a function of the ratio
between number $\bar{N}_a$ of the particles formed by the
growth of nuclei released from the gel during its
dissolution (autocatalytic nucleation) and the number
$\bar{N}_o$ of particles formed by the growth of heteronuclei.
Functional dependences between q, K, K_o, K_a, $\bar{N}_o$,
$\bar{N}_a$, K_g (growth rate constant) and other factors
relevant to zeolite crystallization have been
established and the influences of these factors on the
characteristics of zeolite crystallizing systems have
been discussed.

There is a lot of evidence that the crystallization of zeolites from
aluminosilicate gels is a solution-mediated transformation process
in which the amorphous phase is a precursor for silicate, aluminate
and/or aluminosilicate species needed for the growth of the
crystalline phase (1-9). Generally, it is well known that the
kinetics of most gel-zeolite and zeolite-zeolite transformations can
be expressed mathematically by the simple kinetic equation (1,2,
10-12),

$$f_z = K \cdot t_c^q \tag{1}$$

during the main part of the crystallization (transformation)
process. K and q in Equation (1) are constants for given
experimental conditions. On the other hand, many experimental
studies of zeolite crystallization have shown that linear, size-
-independent crystal growth during the main part of the
crystallization process is typical for most zeolite syntheses (2,5,

6,12-16). In contrast to more or less well defined kinetics of the crystal growth (5,6,12-16), various nucleation mechanisms have been proposed as zeolite particles forming processes. Most authors explained the formation of primary zeolite particles by nucleation in the liquid phase supersaturated with soluble silicate, aluminate and/or aluminosilicate species (1,3,5,7,16-22), with homogeneous nucleation (1,5,7,17,22), heterogeneous nucleation (5,24), cell walls nucleation (16) and secondary nucleation (5) as dominant processes of zeolite particles formation, but the concepts dealing with the nucleation in the gel phase are also presented in the literature (2,6,11,12,14,23-25).

Since some effects, observed during the crystallization of zeolites from gels, as for instance, the autocatalytic nature of zeolite nucleation (2,3,12, Katović, A.; Subotić, B.; Šmit, I.; Despotović, Lj. A. Zeolites, in press) cannot be readily explained only by the classical approaches to the nucleation processes in the liquid phase (2,6,10,12), the objective of this work is to analyse the crystallization kinetics of different types of zeolites by the kinetic equation derived on the basis of Zhdanov's idea on auto-catalytic nucleation (2), in order to explain the influence of auto-catalytic nucleation on zeolite crystallization processes.

Theoretical Approach

Our earlier studies of zeolite-zeolite (10,26) and gel-zeolite (11, 12) transformations have shown that, under the assumption that the crystallization of zeolite is a solution-mediated transformation process (1-9) and that the crystal growth is size-independent (5,6, 12-16), the crystallization (transformation) kinetics can generally be expressed as:

$$f_z = f_z(I) + f_z(II) = m_z(I)/m_z(t_e) + m_z(II)/m_z(t_e) =$$

$$G \varrho N_o K_g^3 t_c^3/m_z(t_e) + \left[G \varrho K_g^3/ m_z(t_e)\right] \int_o^{t_c} (t_c - \tau)^3 d N_\tau \qquad (2)$$

The first term in Equation (2), in which G is the geometrical shape factor of zeolite particles, ϱ is the specific density of zeolite formed, N_o is the number of nuclei (nuclei-I) present in the liquid phase of the system at the very start of the crystallization (transformation) process, $K_g = dL/dt_c$, is the constant of the linear growth rate (and hence, $L = K_g t_c$, where L is the crystal size at crystallization time t_c) and $m_z(t_e)$ is the mass of zeolite formed at the end of the crystallization process, represents the change in the fraction $f_z(I)$ of the mass of zeolite ($m_z(I)$) formed by the growth of the constant number N_o of nuclei-I distributed through the liquid phase of the crystallizing system at the very start of the crystallization (transformation) process ($t \approx 0$). Hence, nuclei-I may be heteronuclei formed in the liquid phase by the rapid heterogeneous nucleation catalysed by the presence of the active centers on impurity particles always present in the liquid phase (27). The second term in Equation (2), in which dN_τ is the

differential number of nuclei (nuclei-II) formed within a
differential time $d\tau$ during the crystallization process and τ is
the time ($0 \leq \tau \leq t$) at which nuclei-II appear and start to grow
($K_g = dL/d\tau$, $L = K_g(t - \tau)$), represents the fraction $f_z(II)$ of the
mass of zeolite ($m_z(II)$) formed by the growth of number N_τ of
nuclei-II formed by some of the time-consumed nucleation processes
during the crystallization. Theoretically, at the constant linear
growth rate of crystals and at constant nucleation rate (i.e.,
homogeneous nucleation in the liquid phase at constant super-
saturation; $dN_\tau = K_n d\tau(28)$), the solution of the second term in
Equation (2) is (1,2,10):

$$f_z(II) = G \varrho K_n K_g^3 t_c^4/4 \, m_z(t_e) = K(II) \, t_c^4 \qquad (3)$$

where K_n is the rate constant of the homogeneous nucleation, and
hence,

$$f_z = G \varrho N_o K_g^3 t_c^3/m_z(t_e) + G \varrho K_n K_g^3 t_c^4/4 \, m_z(t_e) \qquad (4)$$

The Equation (4) can be correlated by Equation (1) with $3 \leq q \leq 4$ (26).
In contrast to the conclusion arising from Equation (4), Zhdanov
found that the numerical value of the exponent q in Equation (1) is
very often grater than 4 in the cases of the crystallization of
zeolites from aluminosilicate gels, which means that the nucleation
rate increases during the autocatalytic stage of the crystallization
process. Zhdanov explained the increase in the particles production
rate $dN_\tau/d\tau$, during the crystallization process by introducing the
possibility of the formation of nuclei not only in the liquid phase
but also the formation of aluminosilicate blocks with ordered
structure in the gel skeleton (2). The specific short-range ordering
of Si and Al inside the amorphous regions of aluminosilicate gels
predicted by Zhdanov (2), has subsequently been experimentally
evidenced by spectroscopic methods (25,29-31). Even, in some cases,
very small particles (with the size below the detection limit by
X-ray diffractometry) of long-range ordered phase have been observed
inside the predominantly amorphous regions of aluminosilicate gels
(32,33). Hence, the dissolution of gel (containing a number N_q of
very small particles of quasicrystalline phase inside the amorphous
matrix) in hot alkaline media should produce both soluble silicate,
aluminate and/or aluminosilicate species and less soluble particles
of quasicrystalline phase (nuclei-II) released from the dissolved
amount of the gel.
    Now, following the assumption that the crystallization of
zeolite from gel is a solution-mediated gel-zeolite transformation
(1-8) and the Kacirek's and Lechert's conclusion (34) that the
growth of crystalline particles inside the gel matrix is
considerably blocked and that they can grow only in the full contact
with the solution phase, the rate $dN_\tau/d\tau$ of the production of
nuclei-II is assumed to be proportional to the amount of the gel
dissolved during the crystallization process (2) and hence, also
proportional to the amount of the crystalline phase formed during
the same time (11). For the described mechanism of the production

(releasing) of nuclei-II, the solution of Equation (2) using an expression for dN_τ in terms of K , q and t_c (see Equation (1)), results in the expression (11):

$$f_z = G \varrho \bar{N}_o \cdot K_g^3 \cdot t_c^3 / (1 - G \varrho \beta \cdot \bar{N}_a \cdot K_g^3 \cdot t_c^3) = K_o \cdot t_c^3 / (1 - K_a \cdot t_c^3) \quad (5)$$

where $\bar{N}_o = N_o/m_z(t_e)$ is the number of particles-I (formed by the growth of nuclei-I), $\bar{N}_a = N_a/m_z(t_e)$ is the number of particles-II (formed by the growth of the number of particles of quasicrystalline phase, released from the mass of gel needed for the crystallization of a unit mass of zeolite (12)), both contained in a unit mass of zeolite at the end of the crystallization process ($t_c \geq t_e$) and

$$\beta = 6/(q+1)(q+2)(q+3) \quad (6)$$

From the set of equations:

$$K_o \cdot t_e^3 / (1 - K_a t_e^3) = \bar{m}_o + \bar{m}_a = 1; \quad K_o \cdot t_e^3 = 1 - K_a \cdot t_e^3$$

$$\bar{m}_o = K_o \cdot t_e^3 = 1 - K_a \cdot t_e^3 \text{ and } \bar{m}_a = 1 - K_o \cdot t_e^3 = K_a \cdot t_e^3 ,$$

arising from Equation (5) under the conditions: $m_z(t_e) = \bar{m}_o + \bar{m}_a = 1$ and $f_z = 1$ for $t_c = t_e$, it can easily be calculated that the ratio between the mass $\bar{m}_a$ of particles formed by the growth of nuclei-II and the mass $\bar{m}_o$ of the particles formed by the growth of nuclei-I, contained in the final product of the crystallization process is:

$$\bar{m}_a / \bar{m}_o = K_a / K_o \quad (7)$$

Since

$$K_a / K_o = G \varrho \bar{N}_a \cdot \beta \cdot K_g^3 / G \varrho \bar{N}_o K_g^3 = \beta \bar{N}_a / \bar{N}_o \quad (8)$$

(see Equation (5)), the combination of Equations (7) and (8) gives:

$$\beta = \bar{N}_o \bar{m}_a / \bar{N}_a \bar{m}_o \quad (9)$$

showing that β is the ratio of average masses of particles-I and particles-II present in the system at the end of the crystallization process.
The solution of Equation (6) in q gives:

$$q = \left[3/\beta + (9/\beta^2 - 1/27)^{1/2} \right]^{1/3} + \left[3/\beta - (9/\beta^2 - 1/27)^{1/2} \right]^{1/3}$$

$$- 2 \approx (6/\beta)^{1/3} - 2$$

and hence, in accordance with Equation (9),

$$q \approx \left[6 \bar{N}_a \cdot \bar{m}_o / \bar{N}_o \cdot \bar{m}_a \right]^{1/3} - 2 \quad (10)$$

Equation (10) shows that the value of the exponent q in Equation (1) is the function of the ratio $\bar{N}_a \cdot m_o(t_e)/\bar{N}_o \cdot m_a(t_e)$ indicating that the numerical value of the exponent q increases with the increasing $\bar{N}_a/\bar{N}_o$ ratio, as evidenced experimentally by the analysis of the kinetics of crystallization of zeolite A from differently aged gels (12).

Results and Discussion

Twenty-eight kinetics of crystallization of different types of zeolites (A (2,12,13,35,36), X (2,6,37), L (38), P (34), ZSM-5 (39-41), synthetic mordenite (2,42) and offretite (43)), synthetized by various authors under various experimental conditions, have been analysed by using Equations (1) and (5).
    The numerical values of the exponent q in Equation (1) were calculated by the slope of log f_z versus log t_c plots, and the intersections of the straight lines with the abscissa represent the numerical values of log K, i.e., log f_z = log K + q log t_c. In all the kinetics analysed, log f_z versus log t_c plots were linear up to $f_z \approx 0.7 - 0.8$ (autocatalytic stage of the crystallization process; see Figures 1 - 3), with linear correlation coefficients not lower than 0.98.
    The numerical values of the constants K_o and K_a in equation (5) were calculated as average values,

$$K_o = \left\{ \sum_{i=1}^{n-1} \sum_{j=i+1}^{n} \left[1/(t_c^3)_j - 1/(t_c^3)_i \right] \Big/ \left[1/(f_z)_j - 1/(f_z)_i \right] \right\} \Big/ (n-1)! \qquad (11)$$

$$K_a = \left\{ \sum_{i=1}^{n-1} \sum_{j=i+1}^{n} \left[(f_z)_j/(t_c^3)_j - (f_z)_i/(t_c^3)_i \right] \Big/ \left[(f_z)_j - (f_z)_i \right] \right\} (n-1)! \qquad (12)$$

obtained by the solution of $(n-1)!$ sets of equations: $(f_z)_i - K_a(f_z)_i (t_c^3)_i = K_o(t_c^3)_i$ and $(f_z)_j - K_a(f_z)_j (t_c^3)_j = K_o(t_c^3)_j$, derived from Equation (5). For values $(f_z)_i = 0.025$ up to 0.975 and $(f_z)_j = 0.05$ up to 1 with steps $\Delta(f_z)_i = \Delta(f_z)_j = 0.025$, the corresponding values of $(t_c^3)_i$ and $(t_c^3)_j$ were calculated as: $t_c^3 = (f_z/K)^{3/q}$, using the corresponding numerical values of K and q from Table I. The ratio $\bar{N}_a/\bar{N}_o$ for each kinetics analysed, was calculated by the combination of Equations (6) and (8), i.e.,

$$\bar{N}_a/\bar{N}_o = K_a(q+1)(q+2)(q+3)/6 \cdot K_o \qquad (13)$$

using the previously determined numerical values of K_a, K_o and q.
    The numerical values of q, K, K_a and K_o, calculated as described above, for each kinetics analysed, are listed in Table 1. Figures 1 - 3 show the correlations between the experimental data and the f_z values calculated by Equation (1) (Figures A) and by Equation (5) (Figures B) and the corresponding numerical values of K, q, K_a and K_o from Table I. A very good agreement between the measured values and the values of f_z calculated by Equation (1) and
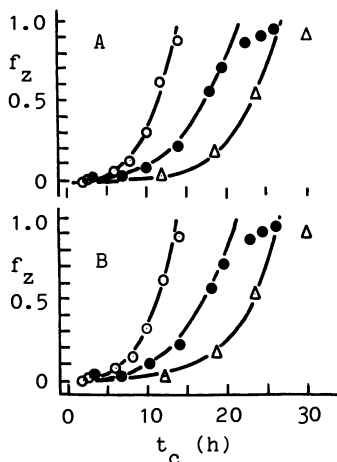
Figure 1. Kinetics of crystallization of zeolite X, o (37), zeolite L, ● (38) and offretite, Δ (43), correlated by Equation (1) (solid curves in Figure A) and by Equation (5) (solid curves in figure B), respectively, using the corresponding values of K, q, K_o and K_a from Table I.
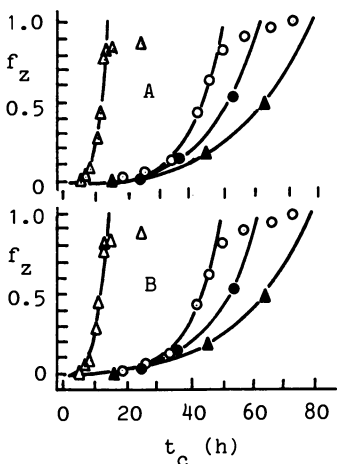
Figure 2. Kinetics of crystallization of ZSM-5, Δ (39), zeolite L, o (38), offretite, ● (43) and synthetic mordenite, ▲ (42), correlated by Equation (1) (solid curves in Figure A) and by Equation (5) (solid curves in Figure B), respectively, using the corresponding values of K, q, K_o and K_a from Table I.
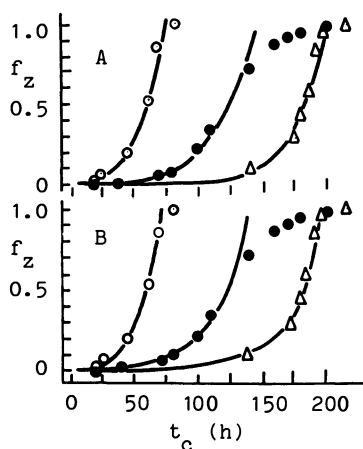
Figure 3.   Kinetics of crystallization of ZSM-5, o (41), zeolite
X, ● (6) and zeolite Pc, Δ (34), correlated by Equation (1)
(solid curves in Figure A) and by Equation (5) (solid curves in
Figure B), respectively, using the corresponding values of K, q,
K_O and K_a from Table I.

Table I   Numerical values of constants K, q, K_o and K_a obtained by the analysis of crystallization kinetics of different types of zeolites

Type of zeolite	K	q	K_o/h^{-3}	K_a/h^{-3}	ref.	Fig.
SM	1.660E-6	3.055	2.031E-6	1.059E-7	42	6
L	6.166E-5	3.15	8.845E-5	1.248E-5	38	2B
X	1.527E-4	3.316	2.881E-4	8.457E-5	37	4
ZSM-5	6.237E-7	3.325	2.047E-6	6.178E-7	41	1B
A	*2.130E-1	*3.60	1.928E-1	1.055E-1	12	2
A	10.839	3.725	4.4812	2.9418	35	7
OFFRT.	1.558E-7	3.803	2.703E-6	1.957E-6	43	2
A	*3.800E-2	*3.90	4.900E-2	3.957E-2	12	2
A	*7.080E-2	*3.98	7.955E-2	6.969E-2	12	2
A	8.000E-1	4.30	4.400E-1	5.044E-1	2	5
X	2.908E-10	4.417	1.641E-7	2.041E-7	6	3
ZSM-5	9.226E-6	4.45	1.961E-4	2.493E-4	39	3
A	*1.290E-2	*4.45	2.589E-2	3.292E-2	12	2
SM	4.440E-5	4.50	5.989E-4	7.863E-4	2	5
X	2.240E-4	4.60	1.921E-3	2.682E-3	2	5
L	6.918E-9	4.80	3.427E-6	5.347E-6	38	2A
A	*2.360E-3	*4.84	1.002E-2	1.597E-2	12	2
A	*4.060E-3	*4.85	1.409E-2	2.255E-2	12	2
OFFRT.	9.948E-8	4.892	2.130E-5	3.484E-5	43	2
ZSM-5	1.884E-4	5.0	2.360E-3	4.067E-3	40	1
A	*4.260E-4	*5.10	4.093E-3	7.388E-3	12	2
A	*4.840E-4	*5.25	4.803E-3	9.253E-3	12	2
A	*2.300E-4	*5.35	3.339E-3	6.702E-3	12	2
A	*4.640E-5	*6.22	2.399E-3	6.486E-3	12	2
A	9.521E-4	6.379	1.082E-2	3.016E-2	13	5
A	25.41	6.95	1.0254	3.3643	35	7
Pc	3.909E-17	7.12	2.999E-8	1.024E-7	34	2
A	3.129E-5	7.73	3.938E-3	1.533E-2	36	7

OFFRT.: offretite; SM: synthetic mordenite

* The values used from Reference 12 by permission of the Elsevier Science Publishers.

Small differences between values K_o and K_a in this Table and in Table 2 in Reference 12 are the result of the use of the improved computer program for the calculation of the values presented here.

Equation (5), respectively, during the main parts of the
crystallization processes (autocatalytic stage) indicates that
Equation (1) is equivalent to Equation (5) and that both kinetic
forms are suitable for the kinetic analysis of the autocatalytic
stage of zeolite crystallization.

Figure 4 shows the dependence of the numerical value of q on
the ratio $\bar{N}_a/\bar{N}_o$. Each point in the Figure represents the relation
between the numerical values of q and the corresponding numerical
value of the ratio $\bar{N}_a/\bar{N}_o$, both calculated for each of the analysed
twenty-eight kinetics, by the procedure explained. The numerical
value of q tends to 3 when the numerical value of the ratio $\bar{N}_a/\bar{N}_o$
tends to zero ($\bar{N}_a \rightarrow 0$), and this a marginal case in which zeolite is
formed by the growth of nuclei-I only. In this case, the kinetics of
crystallization can be expressed by the first term of Equation (2),

$$f_z = f_z(I) = G \varrho N_o K_g^3 t_c^3 / m_z(t_e) = G \varrho \bar{N}_o K_g^3 t_c^3 = K_o t_c^3 .$$

q versus $\bar{N}_a/\bar{N}_o$ is a monotonic function indicating that all
crystallization processes analysed possibly take place by the
simultaneous growth of nuclei-I and nuclei-II, respectively, but
with different parameters (crystal growth rate, absolute numbers of
nuclei-I and nuclei-II, respectively, etc.), whose interrelations
are expressed by Equation (5). The numerical value of q depends
neither on the absolute numbers N_a and N_o nor on the crystal growth
rate (the same or similar values of q for very different values of
pairs K_o and K_a; see Table I.), but on the ratio $\bar{N}_a/\bar{N}_o$ only. Hence,
the value of q can be expressed as the function of $\bar{N}_a/\bar{N}_o$ only and
vice versa, as represented by the solid curve in Figure 4,
calculated by the semi-empirical equation,

$$\bar{N}_a/\bar{N}_o = (1 - 1.82 \times 10^5 \, q^{-11})(1.394 \, q - 2.393)^3 \qquad (14)$$

derived by the analysis of q and K_o and K_a values listed in Table I.
Equation (14) enables the direct determination of the ratio $\bar{N}_a/\bar{N}_o$
from the numerical value of q, without the previous calculation of
the numerical values of K_o and K_a.

Figure 5 shows the relations between fractions $\bar{N}_o/\bar{N}_z$ and
$\bar{N}_a/\bar{N}_z$ ($\bar{N}_z = \bar{N}_o + \bar{N}_a$) on the number of particles-I and particles-II
respectively, and the fractions $\bar{m}_o/m_z(t_e)$ and $\bar{m}_a/m_z(t_e)$ of mass of
zeolite formed at the end of the crystallization process (by
the growth of nuclei-I and nuclei-II, respectively). The rapid
increase in the number $\bar{N}_a$ of particles-II relative to the number of
all particles present in the system (particles-I + particles-II)
influences very slightly the fraction $\bar{m}_a$ of their mass in the final
product, as well as the numerical value of q, so that $\bar{m}_o/m_z(t_e) >$
$\bar{m}_a/m_z(t_e)$ and q < 4 for $\bar{N}_a/\bar{N}_z < 0.97$. This means that particles-I
(formed by the growth of nuclei-I), even in small proportions,
influence the overall crystallization process much more than
particles-II, i.e., $\bar{m}_o/m_z(t_e) = 0.95$ and $\bar{m}_a/m_z(t_e) = 0.05$ for
$\bar{N}_a/\bar{N}_z = 0.52$; $\bar{m}_o/m_z(t_e) = 0.876$ and $\bar{m}_a/m_z(t_e) = 0.124$ for $\bar{N}_a/\bar{N}_z =$
0.76; $\bar{m}_o/m_z(t_e) = 0.646$ and $\bar{m}_a/m_z(t_e) = 0.354$ for $\bar{N}_a/\bar{N}_z = 0.939$ (see
Figure 5). A good illustration for the influence of nuclei-I and
nuclei-II on the crystallization of zeolites is shown in Figure 6.
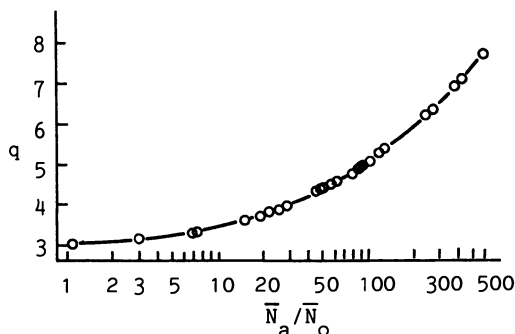
Figure 4. Dependence of the numerical value of the exponent q in Equation (1) on the ratio $\bar{N}_a/\bar{N}_0$ of particles-II and particles-I contained in a unit mass of zeolite at the end of the crystallization process.
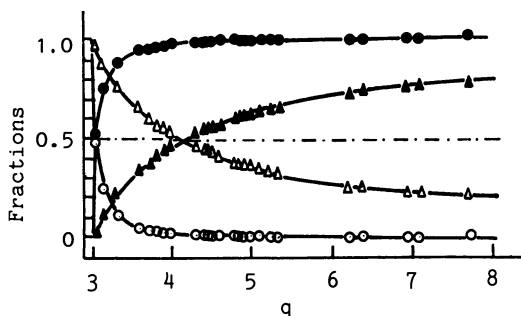
Figure 5. The relations between fractions $\bar{N}_0/\bar{N}_z$ of particles-I (o), $\bar{N}_a/\bar{N}_z$ of particles-II (●), $\bar{m}_0/m_z(t_e)$ of the mass of particles-I (Δ) and $\bar{m}_a/m_z(t_e)$▲ of the mass of particles-II and the value of the exponent q.
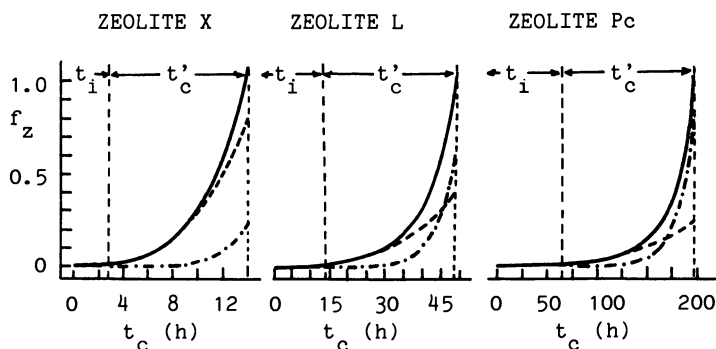
Figure 6. Change in fractions f_z (I) (dashed curves), f_z (II) (dash-dotted curves) and $f_z = f$ (I) + f (II) (solid curves) during the crystallization of zeolites (X, L, Pc) with different fractions of particles-I and particles-II in the crystallizing system.

The change in fraction $f_z(I) = K_o t_c^3$ (dashed curves), $f_z(II) = K_o t_c^3 / (1 - K_o t_c^3) - K_o t_c^3$ (dash-dotted curves) and $f_z = f_z(I) + f_z(II)$ (calculated by Equation (5); solid curves), during the crystallization of zeolite X (see Figure 1B; o), zeolite L (see Figure 2B; o) and zeolite Na-Pc (see Figure 3B; Δ) was analysed using the corresponding numerical values of constants K_o and K_a from Table I. The analysis of the kinetics of crystallization of zeolite X shows that 77 % of the mass of zeolite ($\bar{m}_o/m_z(t_e) = 0.77$) has been formed by the growth of nuclei-I, although their number in the crystallization system is about 7 times lower than the number of nuclei-II ($\bar{N}_a/\bar{N}_o = 7.09$, $\bar{N}_a/\bar{N}_z = 0.875$). In the case of crystallization of zeolite L in which the number of nuclei-II is about 80 times higher than the number of nuclei-I ($\bar{N}_a/\bar{N}_o = 79.99$, $\bar{N}_a/\bar{N}_z = 0.988$), 39 % of the mass of zeolite L has been formed by the growth of nuclei-I. Finally, during the crystallization of zeolite Na-Pc in which the number of nuclei-II is even more than 400 times higher than the number of nuclei-I ($\bar{N}_a/\bar{N}_o = 426.5$, $\bar{N}_a/\bar{N}_z = 0.998$), still 23 % of the mass of zeolite Na-Pc has been formed by the growth of nuclei-I.

The duration of the "induction period" t_i , relative to the overall crystallization time $t_e = t_i + t_c'$ (see Figure 6) at a constant crystal growth rate, increases with the ratio $\bar{N}_a/\bar{N}_o$ in the crystallizing system, i.e., $t_i/t_e = 0.2$ for $\bar{N}_a/\bar{N}_o = 7.09$ (q = 3.316, zeolite X), $t_i/t_e = 0.275$ for $\bar{N}_a/\bar{N}_o = 79.99$ (q = 4.8, zeolite L) and $t_i/t_e = 0.325$ for $\bar{N}_a/\bar{N}_o = 426.5$ (q = 7.12, zeolite Pc).

The observed effects, visualized in Figures 5 and 6 are possibly the consequence of the "inactivity" of nuclei-II hidden by the undisolved amount of gel, i.e., the crystallization process starts by the growth of nuclei-I which are in full contact with the liquid phase from the beginning of the crystallization process, and the nuclei-II start to grow after their releasing from the amount of gel disolved during the crystallization process.

Now, knowing the strong influence of particles (nuclei-I) on the overall crystallization kinetics, the increase of the crystallization rate with the gel ageing at ambient temperature (6,12,13,44,45) can be explained by the increase in the number of nuclei-I and/or the number of nuclei-II, respectively, during the gel ageing (11,12). The recrystallization of the gel (the dissolution of small particles of the gel and the growth of large ones) (6) during its ageing at ambient temperature releases the number $\bar{N}(a)$ of particles of quasicrystalline phase (nuclei-II) from the dissolved gel particles. Since it is reasonable to assume that the growth rate at ambient temperature is negligible in comparison to the growth rate at crystallization temperature, the particles of quasicrystalline phase released from the gel during its ageing (and being in full contact with the liquid phase after the releasing) become new nuclei-I, i.e., $\bar{N}_o = \bar{N}(ht) + \bar{N}(a)$ at crystallization time t_c for any ageing time t_a, where $\bar{N}(ht)$ is the number of nuclei-I formed by rapid heterogeneous nucleation in the liquid phase during the precipitation of the gel ($\bar{N}_o = \bar{N}(ht)$ for $t_a = 0$). Thus, the ageing of gel at ambient temperature decreases the ratio $\bar{N}_a/\bar{N}_o$ at constant or increasing total number of nuclei (12), causing the shortening of the induction period of the crystallization and the increase of the overall

crystallization rate, respectively, as shown in Figure 6 and in Reference 12.

The existance of two kinds of particles, namely those formed by the growth of nuclei-I and nuclei-II, respectively, can explain why in some cases the particles size distribution of the crystalline product is bimodal (1,2,12,19,40,46). In the absence of nuclei-II ($\bar{N}_a$ = 0, q = 3), the particles size distribution is determined only by the size of particles-I ($\bar{N}_o/\bar{N}_z$ in Figure 5). Since all nuclei-I start to grow at the same time (τ = t $\approx$ 0), their size is more or less uniform in the final product (see Figures 6 and 7 in Reference 13). For q = 3 to q = 3.7 the number of particles-II (fraction $\bar{N}_a/\bar{N}_z$ in Figure 5) increases sharply from 0 to 0.95, and for such values of q bimodal distribution by number can be expected. Since it has been shown from the analysis of the crystallization kinetics that the numerical value of q is greater than 3.7 for most kinetics analysed (see Table I and Figure 5), the bimodal distribution by number can be expected only in a limited number of final products of the crystallization. For q > 3.6, the fraction $\bar{N}_o/\bar{N}_z$ of particles-I is negligible and thus, the particle size distribution is determined only be the size of particles-II. Since nuclei-II start to grow at different times (after their releasing from the dissolved amount of gel), particles-II are nonuniform in size (see Figures 3 and 4 in Reference 13). The bimodal distribution by mass is to be expected for all values of q (except for q = 3); $\bar{m}_a$ = 0 and for very high q values; $\bar{m}_o \rightarrow$ 0), as it is deducible from Figure 5 and experimentally evidenced earlier (12).

The analysis of the kinetics of crystallization of different types of zeolites has indicated that the autocatalytic stage of the crystallization process can be mathematically expressed by Equation (1) and Equation (5), respectively. Thus, it can be concluded that the constants K and q in Equation (1) are functions of the particulate characteristics of the crystallizing system. The analysis of the relation between the constants K, q, K_o and K_a from Table I., resulted in the empirical relation:

$$K/(K_o + K_a)^{q/3} = \varphi(q) = 1/(1.227 - 6.612 \ q^{-3.07}) \qquad (15)$$

Now, combining Equations (1), (5) and (15) one obtains,

$$K = \varphi(q)\left[G \ \varrho \ (\bar{N}_o + \beta \ \bar{N}_a)\right]^{q/3} K_g^q \qquad (16)$$

and thus,

$$f_z = \varphi(q)\left[G\varrho(\bar{N}_o + \beta \ \bar{N}_a)\right]^{q/3}(K_g t_c)^q = K \cdot t_c^q \qquad (17)$$

It can readily be calculated that in the absence of the particles of quasicrystalline phase, hidden by the gel matrix ($\bar{N}_a$ = 0, q = 3, $\varphi(q)$ = 1, see Equation (15)), Equation (17) is reduced to the form identical to the first term of the Equation (2) characteristic for the crystallization systems in which the change in the fraction of zeolte is caused by the growth of the constant number of nuclei-I.

Conclusion

The analysis of the kinetics of crystallization of different types of zeolites from aluminosilicate gels points to the conclusion that the crystallization takes place by the simultaneous growth of the constant number $\bar{N}_O$ of nuclei-I present in the system at the very start of the crystallization process and the number $\bar{N}_a$ of nuclei-II released from the gel disolved during the crystallization process. Some characteristics of the crystallization systems such as the duration of the "induction period", the shortening of the "induction period" and the increase of the crystallization rate, respectively, with the gel ageing and the bimodal size distributions in the specific cases have been discussed and explained in relation to the ratio $\bar{N}_a/\bar{N}_O$ of particles (nuclei)-II and particles (nuclei)-I present in the crystallizing systems.

Literature Cited

1. Ciric, J. J. Colloid Interface Sci. 1968, 28, 315.
2. Zhdanov, S. P. In Molecular Sieve Zeolites-I; Gould, R. F., Ed.; Advances in Chemistry Series No. 101; American Chemical Society: Washington, DC, 1971; p 20.
3. Meise, W.; Scwochow, F. E. In Molecular Sieves; Meier, W. M.; Uytterhoeven, J. B., Eds.; Advances in Chemistry Series No. 121; American Chemical Society: Washington, DC, 1973; p 169.
4. Cournoyev, R. A.; Kranich, W. L.; Sand, L. B. J. Phys. Chem. 1975, 79 1578.
5. Freund, E. F. J. Crystal. Growth 1976, 34, 11.
6. Zhdanov, S. P.; Samulevich, N. N. Proc. Fifth Int. Conf. Zeolites, 1980, p 75.
7. Thompson, R. W.; Huber, M. J. J. Cryst. Growth 1982, 56, 711.
8. Fahlke, B.; Starke, P.; Wieker, W.; Wendlandt, K. P. Zeolites 1987, 7 209.
9. Barrer, R. M. Hydrothermal Chemistry of Zeolites; Academic Press: London, 1982; p 145.
10. Subotić, B.; Sekovanić, L. J. Cryst. Growth 1986, 75, 561.
11. Subotić, B.; Graovac, A. In Zeolites - Synthesis, Structure, Technology and Application; Držaj, B.; Hočevar, S.; Pejovnik, S., Eds.; Studies in Surface Science and Technology No. 24; Elsevier: Amsterdam, 1985; p 199.
12. Bronić, J.; Subotić, B.; Šmit, I.; Despotović, Lj. A. In Innovation in Zeolite Material Science; Grobet, P. J.; Mortier, W. J.; Vansant, E. F.; Schulz-Ekloff, G., Eds.; Studies in Surface Science and Catalysis No. 37; Elsevier: Amsterdam, 1988; p 107.
13. Seo, G. Hwahak Konghak 1985, 23, 295.
14. Zhdanov, S. P.; Feoktisova, N. N.; Janj, E. Izv. Akad. Nauk. SSSR, Ser. Khim. 1986, 8, 1720.
15. Tassopoulos, M.; Thompson, R. W. Proc. 7th Int. Conf. Zeolites, 1986, p 153.
16. Lowe, B. M. In Innovation in Zeolite Material Science; Grobet, P. J.; Mortier, W. J.; Vansant, E. F.; Schulz-Ekloff, G., Eds.; Studies in Surface Science and Catalysis No. 37; Elsevier: Amsterdam, 1988; p 1.

17. Kerr, G. T. J. Phys. Chem. 1966, 70, 1047.
18. Chao, K. J.; Tasi, T. C.; Chen, M. S. J. Chem. Soc. Faraday Trans. 1. 1981, 77, 547.
19. Narita, E.; Sato, K.; Yatabe, N.; Okabe, T. Ind. Eng. Res. Prod. Res. Dev. 1985, 24 507.
20. Thompson, R. W.; Dyer, A. Zeolites 1985, 5, 292.
21. Huang, C. L.; Yu, W. C.; Lee, T. Y. Chem. Eng. Sci. 1986, 41 625.
22. Dixon, A. G.; Thompson, R. W. Zeolites 1986, 6 154.
23. McNicol, B. D.; Pott, G. T.; Loos, K. R. J. Phys. Chem. 1972, 76, 3388.
24. Deweale, N.; Bodart, P.; Gabelica, Z.; Nagy, J. B. Acta Chimica Hungarica 1985, 119 233.
25. Dutta, P. K.; Shieh, D. C.; Puri, M. J. J. Phys. Chem. 1987, 91, 2332.
26. Subotić, B.; Škrtić, D.; Šmit, I.; Sekovanić, L. J. Cryst. Growth 1980, 50 498.
27. Walton, A. G. In Nucleation; Zettlemoyer, A. C., Ed.; Marcel Dekker Inc.: New York, 1969; p 225.
28. Nielsen, A. E. Kinetics of Precipitation; Pergamon: Oxford, 1964; p 18.
29. Ruren, X.; Jianmin, Z. Chem. J. Chin. Univ. 1982, 3, 287.
30. Engelhardt, G.; Fahlke, B.; Mäggi, M.; Lippmaa, E. Zeolites 1983, 3 292.
31. Okumura, O.; Tsuruto, Y.; Satoh, T. Gypsum and Lime 1987, 206, 23.
32. Gabelica, Z.; Nagy, J. B.; Debras, G.; Derouane, E. G. Acta Chimica Hungarica 1985, 119, 275.
33. Bursill, L. A.; Thomas, J. M. In Recent Progress Report and Discussions; Sersale, R; Colella, C., Aiello, R., Eds.; Fifth International Symposium on Zeolites; Giannini: Napoli, 1981; p 25.
34. Kacirek, H.; Lechert, H. J. Phys. Chem. 1975, 79, 1589.
35. Subotić, B.; et al. Hem. Ind. 1981, 35, 323.
36. Subotić, B.; Šmit, I.; Sekovanić, L. Proc. Fifth Int. Conf. Zeolites, 1980, p 10.
37. Tatič. M.; Držaj, B. In Zeolites - Synthesis, Structure, Technology and Application; Držaj, B.; Hočevar, S.; Pejovnik, S., Eds.; Studies in Surface Science and Catalysis No. 24; Elsevier: Amsterdam, 1985; p 129.
38. Tsitsichvili, G. V.; et al. Zh. Fiz. Khim. 1979, 53, 1719.
39. Mostowicz, R.; Sand, L. B. Zeolites 1982, 2, 143.
40. Mostowicz, R.; Sand, L. B. Zeolites 1983, 3, 219.
41. Katashane, A. N.; Hegde, S. G.; Kulkarni, S. B. Zeolites 1986, 6, 253.
42. Culfaz, A.; Sand, L. B. In Molecular Sieves; Meier, W. M.; Uytterhoeven, J. B., Eds.; Advances in Chemistry Series No. 121; American Chemical Society: Washington, DC, 1973; p 140.
43. Mondafi, I.; Massiani, P.; Fajula, F.; Figueras, F. Zeolites 1987, 7 63.
44. Polak, F.; Stobiecka, E. prace Chem. 1976, 21, 291.
45. De Kimpe, C. R.; Kodama, H. Clay Minerals 1984, 19, 237.
46. Gabelica, Z.; Blom, N.; Derouane, E. G. Appl. Catal. 1983, 5, 227.

Chapter 9

Role of Gel Aging in Zeolite Crystallization

A. Katović, B. Subotić, I. Šmit, Lj. A. Despotović, and M. Ćurić

Ruder Bošković Institute, P.O. Box 1016, 41001 Zagreb, Croatia, Yugoslavia

The tetragonal form of zeolite P crystallized as the
first crystalline phase and subsequently transformed
into the cubic form of zeolite P when freshly prepared
gel was heated at 80°C, while zeolite X and the cubic
form of zeolite P crystallized simultaneously from
gels aged at 25°C for 1 day and more. The increase in
the ageing time shortened the induction periods of
zeolite X and zeolite P and increased the yield of
zeolite X crystallized, respectively. The effects
observed were explained by the formation of particles
of quasicrystalline zeolite P and zeolite X inside
the gel during the ageing at ambient temperature and
by the growth of particles of quasicrystalline
phase during the crystallization step.

It is well known that the low-temperature ageing of aluminosilicate
gel precursor markedly influences the course of zeolite crystalliza-
tion at the appropriate temperature (1-10). The primary effects of
the gel ageing are the shortening of the induction period and the
acceleration of the crystallization process (1-5), but in some
cases the gel ageing also influences the type(s) of zeolite(s)
formed (1,6,7,10).
    Thus, in many syntheses the gel ageing (8-11) or the addition
of the "crystal direction agent" (aged, X-ray amorphous alumino-
silicate gel) (7,12-14) is a necessary step needed for the obtaining
of the desired type of zeolite at the desired reaction rate.
    It is well known that zeolites of type NaP co-crystallize with
faujasites (15,16). The typical reaction sequence under the
appropriate synthesis condition is (17): amorphous ⟶ faujasite ⟶
gismondine type Na-P. However, in some cases, zeolite Na-P appears
as the first crystalline phase when freshly prepared gel has
been heated at the appropriate temperature (15,18); in these
cases, faujasite can be crystallized either by adding the seed
crystals into the freshly prepared gel (6,13,18) or by ageing the
gel at ambient temperature prior to the crystallization at the

appropriate temperature (6,8,19). While the influence of the gel ageing on the kinetics of crystallization can generally be explained by the increase in the number of nuclei formed in the gel phase or/and in the liquid phase during the ageing (2-6), the explanation of the effect of the gel ageing on the type of zeolite formed requires the study of chemical and structural changes in both the liquid phase and the solid phase of the reaction mixture during the ageing and the crystallization, respectively. Thus, the objective of this work is to investigate the chemical and structural changes in the solid and the liquid phase of the reaction mixture during its ageing as well as during the crystallization process, in order to explain why zeolite X crystallizes only from the aged gel of given composition. The influence of the gel ageing on the crystallization rates of zeolites X and P will also be discussed.

Experimental

Aluminosilicate gels, having a molar composition 4.24 $Na_2O \cdot Al_2O_3 \cdot$ 3.56 $SiO_2 \cdot 230.6$ H_2O, were prepared by slow pouring of 150 ml of diluted water-glass solution (1.715 molar SiO_2, 0.65 molar Na_2O), thermostated at $25°C$, into a plastic beaker containing 150 ml of vigorously stirred sodium aluminate solution (0.482 molar Al_2O_3, 1.39 molar Na_2O) thermostated at $25°C$. The aluminosilicate gels were aged at $25°C$ for given times (t_a = 0 to 10 dyas). After ageing for a predetermined time t_a, the gel was poured into a stainless-steel reaction vessel and heated to crystallization temperature ($80°C$). The moment the gel was added into the preheated reaction vessel was taken as the zero time (t_c = 0) of the crystallization process. The reaction mixture was stirred with a teflon-coated magnetic bar driven by a magnetic stirrer. At ageing times t_a = 0 to 10 days before the crystallization process (t_c = 0 at $25°C$), as well as the times t_c after the beginning of the crystallization process (at $80°C$), aliquots of the reaction mixture were drawn off and centrifuged in order to separate the solid from the liquid phase and to stop the crystallization process, respectively.

Aliquots of the clear liquid phase above the sediment were used to measure Si and Al concentrations by atomic absorption spectrometry (Perkin-Elmer atomic absorption spectrometer, model 3030B) and for the determination of the degree of Si poly-condensation in the liquid phase by molybdate method (20).

The solid phase, after having been washed and dried in the dessicator at room temperature up to the constant weight, was used for analyses.

The fractions f_G of gel, f_{Pc} of zeolite Na-Pc and f_X of zeolite X in the powdered solid samples were taken by Philips diffractometer with CuK-α radiation in the region of Bragg's angles 2θ = $10°$ - $46°$. The weight fractions were calculated by the mixing method (21) using the measured integral intensity of the amorphous maximum (2θ = $17°$ - $39°$) and the sharp maximum corresponding to the diffraction from (533) crystal lattice planes of zeolite X, as well as the sharp maximum corresponding to the diffraction from (310) crystal lattice planes of zeolite Na-Pc.

The average values of crystallite size were determined by the integral width of the diffraction maximums corresponding to the

diffraction from (642) and (533) crystal lattice planes of zeolite X and by the integral width of the diffraction maximums corresponding to the diffraction from (310) and (211) crystal lattice planes of zeolite Na-Pc, using the Scherrer formula (22).

Si and Al contents in the solid samples were determined by measuring of Si and Al concentrations in the solutions obtained by the dissolution of the solids (75 mg) in 50 ml of 2N HCl.

Scanning-electron micrographs of the samples were taken with a Jeol JSM-940 scanning-electron microscope.

Infrared transmission spectra of the solid samples were measured by the KBr wafer technique. Spectra were recorded on a Perkin-Elmer infrared spectrometer, model 580 B.

Results and discussion

Figure 1 shows the kinetics of the crystallization of zeolite X (Figure 1A) and zeolite Na-Pc (Figure 1B), respectively, at 80°C from the gels aged at 25°C for 1, 3, 5, 7 and 10 days. In all cases, zeolite X appears as the first crystalline phase, thereafter zeolite Na-Pc co-crystallizes with zeolite X. After the maximal yield of zeolite X crystallized has been attained, the fraction f_X of zeolite X slowly decreases as the consequence of the spontaneous transformation of zeolite X into more stable zeolite Na-Pc (17). The induction periods of both zeolite X and zeolite Na-Pc shortens and the maximal yield of zeolite X increases, respectively, with the increased time of gel ageing. All kinetics of zeolite X and zeolite Na-Pc, respectively, can be mathematically expressed by the simple kinetic equation (5,23-26),

$$f_z = K \cdot t_c^q \qquad (1)$$

during the interval of the increasing crystallization rate. Here, f_z is the mass fraction of zeolite crystallized at the crystallization time t_c , and K and q are constants for given experimental conditions. The numerical values of the constants K and q, calculated by the log f_z versus log t_c plots (25) using the corresponding experimental data from Figure 1, are listed in Table I.

Table I. Numerical values of the constants K and q which
          correspond to the kinetics of crystallization of
          zeolite X and zeolite Na-Pc, respectively, from
          aluminosilicate gels aged for various times t_a

Time of gel ageing (t_a/d)	Zeolite X		Zeolite Na-Pc	
	K	q	K	q
1	-	-	7.84 E-9	9.86
3	-	-	2.78 E-7	7.83
5	6.34 E-4	4.01	2.21 E-6	7.27
7	1.28 E-3	4.36	-	-
10	1.35 E-3	4.69	-	-
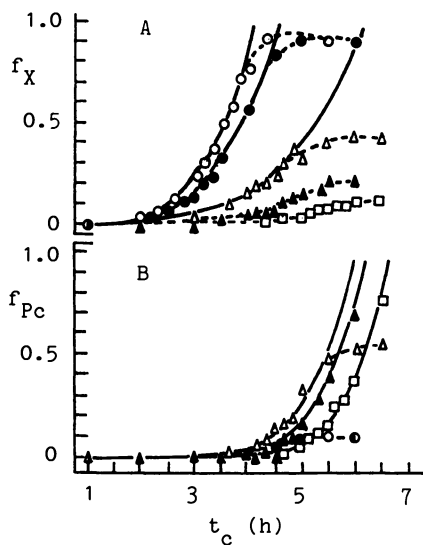
Figure 1. Kinetics of crystallization of zeolite X (Figure A) and zeolite Na-Pc (Figure B) at 80°C, from the aluminosilicate gels aged for t_a = 1 d (□), t_a = 3 d (▲), t_a = 5 d (△), t_a = 7 d (●) and t_a = 10 d (○) at 25°C. f_X and f_{Pc} are mass fractions of zeolite X and zeolite Na-Pc crystallized at crystallization time t_c. Solid curves represent the kinetics of crystallization, calculated by Equation (1) and the corresponding values of the constants K and q from Table I.

There are three typical groups of the crystallization kinetics:
I. zeolite Na-Pc is the dominant product of the crystallization
from the gels aged for 0 to 3 days, II. the mixture of approximately
same amounts of zeolite X and zeolite Na-Pc crystallizes from the
gel aged for 5 days (see scanning-electron micrograph in Figure 5)
and III. zeolite X is the dominant product of the crystallization
from the gels aged for 7 and 10 days. The scanning-electron micro-
graph in the Figure 5 shows that the microcrystals of zeolite X can
be clearly distinguished from the typical spherulites of zeolite P
in the final product of the crystallization.

Figures 2 - 4 show the changes in chemical characteristics of
the liquid and the solid phase, respectively, during the crystal-
lization from the gels aged for t_a = 1 d (group I., see Figure 2),
for t_a = 5 d (group II., see Figure 3) and for t_a = 10 d (group
III., see Figure 4). In all analyzed cases, the concentration of
both silicon and aluminum in the liquid phase increase little from
t_c = 0 up to $t_c \leqslant$ 1 h as the consequence of the increase in the
solubility of the gel with increasing temperature (heating from
25°C up to 80°C). After the crystallization temperature has been
reached, the concentration $C_{Al}(L)$ of the aluminum in the liquid
phase keeps constant during the main part of the crystallization
process while the concentration $C_{Si}(L)$ of the silicon in the liquid
phase keeps constant during the induction period of the crystal-
lization only. The gel-crystal transformation is followed by the
increase in the concentration $C_{Si}(L)$ up to the maximal value
$C_{Si}(L)_{max}$ and by the simultaneous decrease in the Si/Al molar
ratio in the solid phase, respectively. Hence, it is reasonable to
assume that the increase in the concentration of silicon in the
liquid phase, during the crystallization, is the consequence of the
releasing of soluble silicate species from the solid phase due to
the lower Si/Al ratio in the crystalline phase(s) ([Si/Al]$_s \fallingdotseq$ 1.305)
than in the starting aluminosilicate gels ([Si/Al]$_s \fallingdotseq$ 1.4), as
shown in Figures 2C-4C. At the crystallization time when about
70 % of the gel has been transformed into the crystalline phase(s),
the rate of crystallization starts to deccelerate simultaneously
with the sudden decrease in the concentrations of both silicon and
aluminum in the liquid phase. This is probably the consequence of
the decrease in the particle growth rate(s) (see Figure 6) caused
by the decrease in the solute concentration at the time when the
rate of deposition of the soluble species from the liquid phase
onto the surfaces of the growing particles becomes higher than the
rate of feeding of the solution with new soluble species (5,26).
The chemical changes in the liquid phase and the solid phase,
respectively, clearly indicate that the crystallization of zeolite
X and zeolite Na-Pc, respectively, from gels is a solution-mediated
transformation process in which the amorphous phase is a precursor
for silicate, aluminate and/or aluminosilicate species needed for
the growth of the crystalline phase(s) (2,16,19,23-26).

Table II. shows that the concentrations C_{Si} and C_{Al} of
silicon and aluminum in the liquid phase of the gel as well as the
molar ratio [Si/Al]$_s$ of silicon and aluminum in the solid phase of
the gel keeps approximately constant during the ageing at 25°C,
indicating that the chemical equilibrium between the solid and the
liquid phase of the gel has been attained for $t_a \leqslant$ 1 d. After the
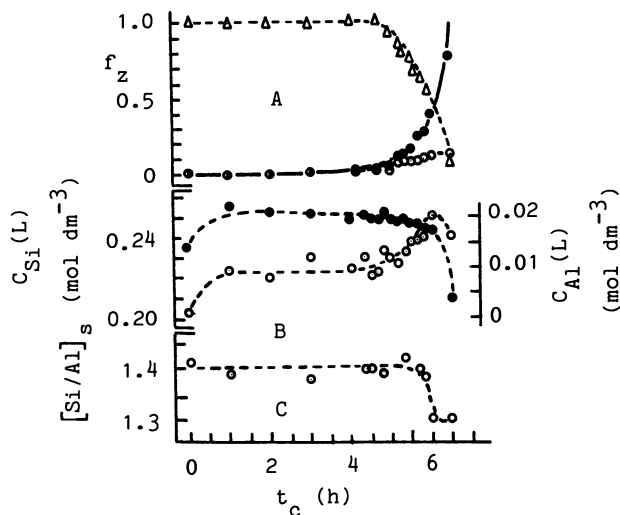
Figure 2. The changes in: A. mass fractions f_X of zeolite X (o), f_{Pc} of zeolite Na-Pc (●) and f_G of gel (Δ), B. concentrations $C_{Al}(L)$ of aluminum (●) and $C_{Si}(L)$ of silicon (o) in the liquid phase and C. molar ratio $[Si/Al]_s$ in the solid phase (o), with the crystallization time t_c, during the crystallization from the gel aged for t_a = 1 d.
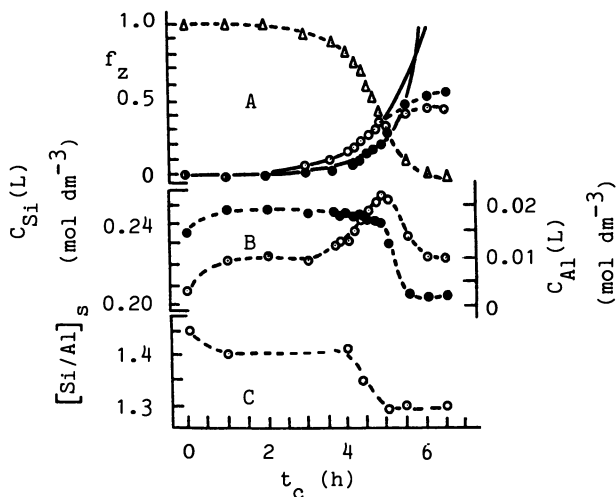
Figure 3. The changes in: A. mass fractions f_X of zeolite X (o), f_{Pc} of zeolite Na-Pc (●) and f_G of gel (Δ), B. concentrations $C_{Al}(L)$ of aluminum (●) and $C_{Si}(L)$ of silicon (o) in the liquid phase and C. molar ratio $[Si/Al]_s$ in the solid phase (o), with the crystallization time t_c, during the crystallization from the gel aged for t_a = 5 d.

Figure 4. The changes in: A. mass fractions f_X of zeolite X (o), f_{Pc} of zeolite Na-Pc (●) and f_G of gel (▲), B. concentrations $c_{Al}(L)$ of aluminum (●) and $c_{Si}(L)$ of silicon (o) in the liquid phase and C. molar ratio $[Si/Al]_s$ in the solid phase (o), with the crystallization time t_c, during the crystallization from the gel aged for t_a = 10 d.
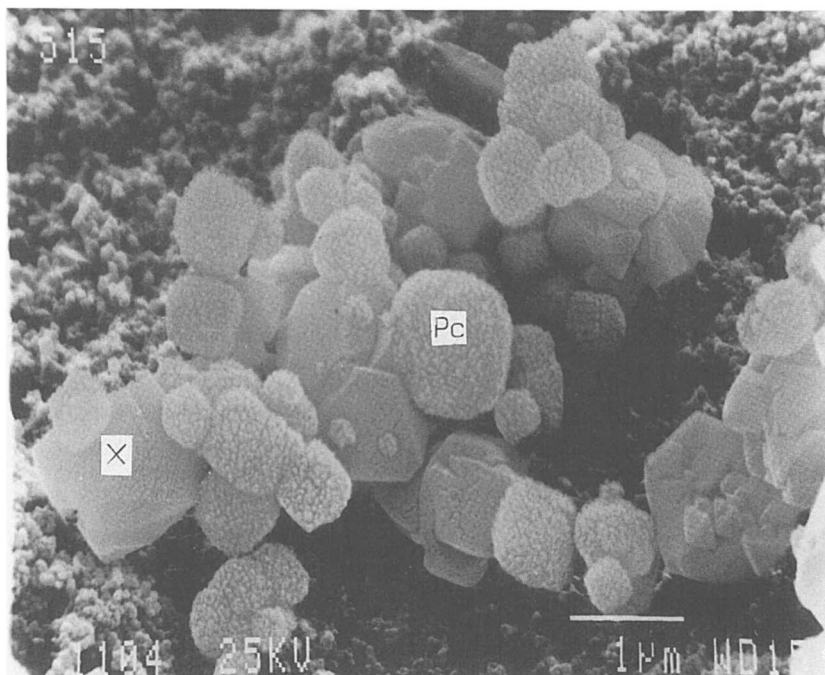
Figure 5. Scanning-electron micrograph of the solid sample drawn off the reaction mixture at the end of the crystallization process from the gel aged for t_a = 5 d; t_c = 6.5 h, f_X = 0.43, f_{Pc} = 0.57.
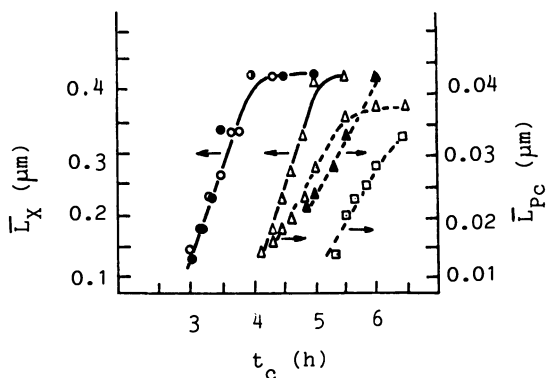
Figure 6. The changes in the average size $\bar{L}_X$ of the crystallite of zeolite X (solid curves) and in the average size $\bar{L}_{Pc}$ of zeolite Na-Pc (dashed curves) with the crystallization time t_c, during the crystallization from gels aged for 1 (□), 3 (▲), 5 (△), 7 (●) and 10 (○) days.

crystallization temperature has been reached, the concentrations of both silicon and aluminum in the liquid phase slowly increase, thereafter their average values $\overline{C_{Si}}(L)$ and $\overline{C_{Al}}(L)$ keep approximately constant during the induction period of the crystallization or even, during the main part of the crystallization process (for aluminum) (see Figures 2-4), and are not markedly influenced by the gel ageing, as shown in Table III. Also, the maximum value $C_{Si}(L)_{max}$ of the silicon concentration in the liquid phase, attained during the crystallization, is not markedly influences by the ageing of the gel, as shown in Figures 2B-4B and in Table III.

Table II. Characteristics of the aluminosilicate gels of 4.24 $Na_2O \cdot Al_2O_3 \cdot 3.56\ SiO_2 \cdot 230.6\ H_2O$ batch composition aged for various times t_a at 25°C

t_a/d	C_{Si}/mol dm^{-3}	C_{Al}/mol dm^{-3}	[Si/Al]$_s$	R/min^{-1}
1	0.203	0.0150	1.42	1.22
2	0.203	0.0141	1.39	1.11
3	0.213	0.0137	1.40	1.23
5	0.209	0.0145	1.45	1.27
7	0.199	0.0142	1.43	1.27
10	0.186	0.0144	1.41	–

Table III. Chemical composition of the liquid phase during the crystallization from the gels aged for various times t_a

t_a/d	$\overline{C_{Al}}(L)$/mol dm^{-3}	$\overline{C_{Si}}(L)$/mol dm^{-3}	$C_{Si}(L)_{max}$/mol dm^{-3}
1	0.0210	0.224	0.251
2	0.0199	0.221	0.262
3	0.0162	0.237	0.267
5	0.0190	0.223	0.255
7	0.0170	0.216	0.262
10	0.0160	0.203	0.239

The measuring of the degree of polycondensation of silicate anions in the liquid phases of the gels aged fro 1, 2, 3, 5, 7 and 10 days, as well as in the liquid phases of the crystallizing systems, has shown that in all the cases the logarithm ln UR, of the percentage of SiO_2 unreacted with molybdic acid is a linear function of the reaction time t , with the slopes R = d(ln UR)/dt between 1.11 min^{-1} and 1.27 min^{-1} (see Table III.). It has been appreciated from the results obtained, that the liquid phase of the reaction mixture contains a mixture of monomeric silicate species (60 % – 80 %), dimeric silicate species (20 % – 40 %) and possibly, low-"molecular" aluminosilicate species that give monosilicic acid and disilicic acid, respectively, in an acidic degradation (20,27,28).

   Figure 6 shows that the average growth rate of zeolite X ($\overline{K_g}(X) = d\overline{L}_X/dt_c \approx 3 \times 10^{-5}$ cm/h) and of zeolite Na-Pc ($\overline{K_g}(Pc) = d\overline{L}_{Pc}/dt_c \approx 1.6 \times 10^{-6}$ cm/h), respectively, is constant during the

crystallization process and independent on the gel ageing. The independence of the growth rates $\overline{K_g}(X)$ and $\overline{K_g}(Pc)$ on the increase in the silicon concentration during the crystallization indicates that the excess of silicon, produced in the liquid phase during the dissolution of the gel and its partial transformation into crystalline products with lower Si/Al molar ratio, exists in the form of "inactive" monosilicic and disilicic acids (8) and hence, does not participate in the reactions at the surfaces of the growing crystals (Katović, A.; Subotić, B.; Šmit, I.; Despotović, Lj. A. Zeolites, in press). Thus, it is reasonable to assume that the growth process takes place by the reaction of low-"molecular" aluminosilicate species from the liquid phase at the surfaces of growing zeolite particles and that the aluminum concentration (in the form of "reactive" aluminosilicate species) is the determining factor of the growth rate of the particles of zeolite X and zeolite Na-Pc, respectively.

Now, the constancy of the crystal growth rate of both zeolite X and zeolite Na-Pc indicates that the shortening of the induction periods of the crystallization of both zeolites is the consequence of the increase in the number of nuclei during the gel ageing. The simultaneous crystallization of zeolite X and zeolite Na-Pc under almost identical chemical conditions indicates that the nuclei of zeolite X and the nuclei of zeolite Na-Pc exist as separate entities. The analysis of the crystallization kinetics of zeolite X and zeolite Na-Pc, respectively, shows that the numerical value of the exponent q in Equation (1) is greater than 4 in all kinetics (see Table I.), which means that the nucleation rate increases during the crystallization process. The changes in the crystallization kinetics with the gel ageing, at constant chemical composition of the reaction mixture, indicate that the structural changes in the solid phase of the gel, during its ageing, should be responsible for the effects observed.

Figure 7 shows that the X-ray diffractogram of the solid phase of freshly prepared gel (0-0) exhibits the amorphous maximum at the 2θ angle corresponding to the diffraction from (310) crystal lattice planes of zeolite Na-Pc (strongest X-ray diffraction maximum of zeolite Na-Pc; see Figure 1 in: Katović, A.; Subotić, B.; Šmit, I.; Despotović, Lj. A. Zeolites, in press). Figure 8 shows that the IR spectra of the solid phase of freshly prepared gel (spectra a), as well as the IR spectra of the solid phases of gels aged for 5 d (spectra b) and for 10 d (spectra c) have a broad band with the maximum at 600 cm^{-1}, indicating the presence of D4R secondary building units of zeolite Na-Pc (29). These findings lead to the assumption that the mixing of silicate and aluminate solutions produces the predominantly amorphous aluminosilicate gel containing a number $(N_a)_{Pc}$ of very small particles of quasicrystalline phase having a structure close to the structure of the cubic modification of zeolite P. Such particles of the qusicrystalline phase, probybly formed by the polycondensation processes inside the gel matrix during its precipitation, can be potential nuclei (nuclei-II) for the crystallization of zeolite Na-Pc. At the same time (during the gel precipitation) a number $(N_o)_{Pc} = N(ht)$ of nuclei (nuclei-I) is assumed to be formed in the liquid phase by the heterogeneous nucleation, catalyzed by the presence of the active centers at the
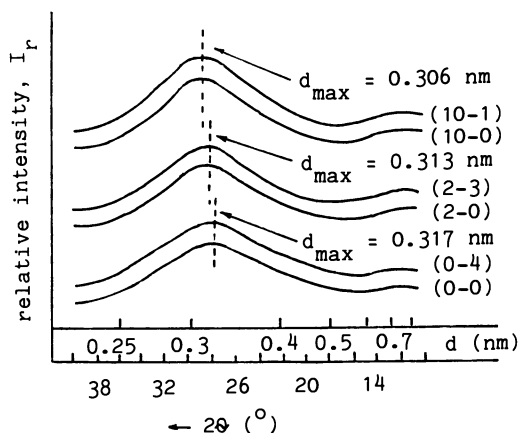
Figure 7. X-ray diffractograms (relative intensities I_r versus Bragg's angles 2θ and versus X-ray diffraction spacings d) of the solid phase of the gels aged at 25°C for t_a = 0 (0-0), t_a = 2 d (2-0), and t_a = 10 d (10-0) and of the same gels heated at 80°C for t_c = 4 h (0-4), t_c = 3 h (2-3) and t_c = 1 h (10-1).
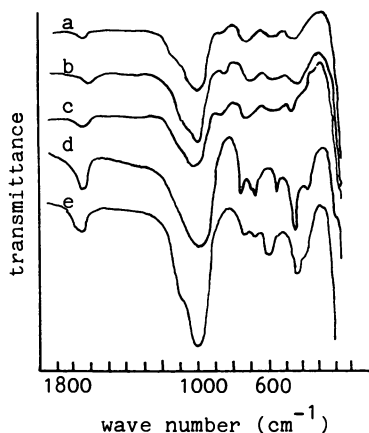
Figure 8. IR spectra of the solid phase of the gels aged at 25°C for t_a = 0 (a), t_a = 5 d (b), t_a = 10 d (c) as well as the IR spectra of zeolite X (d) and zeolite Na-Pc (e).

impurities always present in the liquid phase (30). Hence, after the gel has been precipitated, the system contains a number $(N_o)_{Pc} = N(ht)$ of nuclei-I distributed through the liquid phase and a number $(N_a)_{Pc}$ of nuclei-II distributed inside the solid phase of the gel. Since the positions of the amorphous maximums and their intensities do not change during the induction period (see Figure 7 and Figure 1 in Katović, A.; Subotić, B.; Šmit, I.; Despotović, Lj. Zeolites, in press), it is reasonable to conclude that the particles of quasi-crystalline phase (nuclei-II), distributed inside the gel matrix, cannot grow, or their growth is considerably deccelerated due to the slow material transport inside the gel matrix in comparison with the rate of material transport in the liqid phase. Such conclusion is in accordance with Kacirek's and Lechert's finding (18) that the growth of crystalline particles inside the gel matrix is blocked considerably and that they can grow only in full contact with the solution phase. On the other hand, the shift in the position of the amorphous maximum in the X-ray diffractograms of the solid phase of variously aged gels toward lower X-ray diffraction spacings (see Figure 7), indicates that structural changes take place in the solid phase of the gel during its ageing. At this moment, we do not know the fine mechanism of these changes, but on the basis of the the Raman spectroscopic study of the ageing of the gel prepared for the crystallization of zeolite Y (31), it is reasonable to assume that the structural changes obseved are the consequence of the slow formation of six-membered aluminosilicate rings, their ordering into sodalite cages and the possible formation of particles of quasi-crystalline phase (nuclei-II) with the structure near to the structure of faujasite, inside the gel matrix.

Now, assuming that the freshly prepared gel contains only the nuclei of zeolite P (no zeolite X crystallization) (Katović, A.; Subotić, B.; Šmit, I.; Despotović, Lj. A. Zeolites, in press), its ageing at ambient temperature causes two effects: (i) the formation of six-membered aluminosilicate rings and their ordering into quasi-crystalline faujasite (nuclei-II of zeolite X) and (ii) the recrystallization of the gel (the dissolution of small and the growth of large particles of the gel) (2), releases the number $N(a)_{Pc}$ of particles of quasicrystalline zeolite Na-Pc and the number $N(a)_X$ of quasicrystalline particles of faujasite from the dissolved gel particles. Since the crystal growth rate at ambient temperature is assumed to be negligible in comparison with the growth rate at crystallization temperature, the particles of the quasicrystalline phase released from the gel during its ageing (and being in the full contact with the liquid phase), become new nuclei-I, i.e., $(N_o)_{Pc} = N(ht) + N(a)_{Pc}$ and $(N_o)_X = N(a)_X$ at crystallization time $t_c = 0$ for any ageing time t_a, where $N(ht)$ is the number of nuclei-I of zeolite Na-Pc formed in the liquid phase by heterogeneous nucleation during the gel precipitation ($(N_o)_{Pc} = N(ht)$ for $t_a = 0$ and $t_c = 0$). Similar process of the increase in the number of nuclei-I during the gel ageing was observed in zeolite A crystallizing system (5).

The heating of the reaction mixture induces the growth of nuclei-I of both zeolites from the solution supersaturated with soluble aluminosilicate species. Since the growth rate of zeolite X is considerably greater than the growth rate of zeolite Na-Pc (see Figure 6), zeolite X appears as the first crystalline phase. The

starting growth of nuclei-I exhausts the soluble species from the liquid phase causing the dissolution of a part of the gel in order to keep the solid - liquid equilibrium. The particles of quasi-crystalline faujasite and zeolite P, respectively (nuclei-II of both zeolites), which are released from the dissolved amount of the gel, start to grow from the supersaturated solution. The increase in the number of nuclei (that are in the full contact with the liquid phase) accelerates the formation of the crystalline phase and at the same time accelerates the rate of the gel dissolution and the rate of the releasing of new nuclei-II. The consequence is an "explosive" rate of the outcoming of nuclei-II from the gel and the increase in the crystallization rate during the autocatalytic stage of the crystallization (5,24,25). The described crystallization process can be mathematically expressed by Equation (1) with q 4 (5,24,25) or by the equivalent kinetic form:

$$f_z = G \varrho \bar{N}_o K_g^3 t_c^3 / (1 - G \varrho \beta \bar{N}_a K_g^3 t_c^3) = K_o t_c^3 / (1 - K_a t_c^3) \qquad (2)$$

earlier derived (25) on the basis of Zhdanov's idea on autocatalytic nucleation (2,24). Here, G is the geometrical shape factor of zeolite particles, ϱ is the specific density of zeolite formed, $\bar{N}_o$ is the number of particles-I (formed by the growth of nuclei-I), $\bar{N}_a = \eta$ is the number of particles-II (formed by the growth of the particles of quasicrystalline phase released from the gel during the crystallization process), both contained in a unit mass of zeolite formed at the end of the crystallization process, K_g is the constant of the linear growth rate of zeolite particles and $\beta = 6/(q+1)(q+2)$ (q+3). The numerical values of the constants $K_o = G \varrho \bar{N}_o K_g^3$ and $K_a = G \varrho \beta \bar{N}_a K_g^3$, calculated by the procedure described earlier (25), as well as the ratios $\bar{N}_a / \bar{N}_o = K_a / \beta K_o$, are listed in Table IV. as functions of time t_a of the gel ageing.

Table IV. The change in the numerical values of K_o, K_a and $\bar{N}_a / \bar{N}_o$ with the time t_a of the gel ageing

t_a/d	zeolite X			zeolite Na-Pc		
	K_o/h^{-3}	K_a/h^{-3}	$\bar{N}_a / \bar{N}_o$	K_o/h^{-3}	K_a/h^{-3}	$\bar{N}_a / \bar{N}_o$
1	–	–	–	5.56 E-4	3.09 E-3	1533
3	–	–	–	8.50 E-4	3.67 E-3	775
5	2.35 E-3	2.13 E-3	32	1.11 E-3	3.92 E-3	464
7	5.14 E-3	6.15 E-3	50	–	–	–
10	6.52 E-3	9.58 E-3	72	–	–	–

Figures 2A-4A show that the fractions f_X and f_{Pc}, calculated by Equation (2) and the corresponding values of the constants K_a and K_o from Table IV. (solid curves in Figures 2A-4A) agree very well with the measured fraction during the autocatalytic stages of the crystallization processes, thus indicating that the crystallization of zeolite X and zeolite Na-Pc, respectively, from variously aged gels takes place by the mechanism described above.

Conclusions

The analysis of the experimental data and the numerical values of the constants K_o and K_a and the ratios $\bar{N}_o/\bar{N}_a$ for the crystallization of both zeolite X and zeolite Na-Pc, leads to the following conclusions:

The total number of nuclei of zeolite Na-Pc (number of nuclei-I + number of nuclei-II = $\bar{N}_o + \bar{N}_a = K_o/G \varrho K_g^3 + K_a/\varrho G \beta K_g^3$; see Equation (2)), does not change, or slightly decreases during the ageing of the gel. A part of quasicrystalline particles of zeolite Na-Pc (nuclei-II) releases from the gel and becomes nuclei-I during the gel ageing so that the ratio $\bar{N}_o/\bar{N}_a$ for zeolite Na-Pc decreases with the gel ageing (see Table IV.). The high ratios $\bar{N}_o/\bar{N}_a$ for zeolite Na-Pc indicate that only very small proportion of the particles of quasicrystalline zeolite P has been released from the gel during its ageing, and this is a possible reason for the long induction period of the crystallization of zeolite Na-Pc.

The number of particles of quasicrystalline faujasite (nuclei-II of zeolite X) increases inside the gel matrix during the gel ageing. A part of the particles of quasicrystalline faujasite releases from the gel during its ageing and becomes nuclei-I for the crystallization of zeolite X. The increase of the ratio $\bar{N}_o/\bar{N}_a$ during the gel ageing indicates that the rate of the formation of the particles of quasicrystalline faujasite inside the gel matrix is greater than the rate of their outcoming from the gel during its ageing (recrystallization).

The absence of the IR band at 560 cm^{-1} (characteristic for D6R secondary building units of zeolite X) (29) and the presence of the broad band with the maximum at 600 cm^{-1} (characteristic for D4R secondary building units of zeolite P) (29) even in the IR spectra of the solid phase of the gel aged for 10 d (see Figure 8c), as well as the much lower values $\bar{N}_o/\bar{N}_a$ for zeolite X than the values $\bar{N}_o/\bar{N}_a$ for zeolite Na-Pc (see Table IV.), indicate that the total number of nuclei (nuclei-I + nuclei-II) of zeolite Na-Pc is much greater than the total number of nuclei of zeolite X, for all the gels examined.

The shortening of the induction periods of the crystallization of both zeolite X and zeolite Na-Pc is most probably the consequence of the increase in the number of nuclei-I of both zeolites with the ageing of the gel.

The increase in the yield of zeolite X crystallized, with the gel ageing, is the consequence of the increase in the total number of nuclei of zeolite X at constant, or even decreasing total number of zeolite P, during the gel ageing.

The high yields of zeolite X crystallized from the systems aged for 5 days and more, in which the total number of nuclei of zeolite P is considerably greater than the total number of nuclei of zeolite X, are most probably influenced by the much greater growth rate of zeolite X particles relative to the growth rate of zeolite Na-Pc particles and by relatively low $\bar{N}_o/\bar{N}_a$ ratio for zeolite X compared with the $\bar{N}_o/\bar{N}_a$ ratio for zeolite P (see Table IV.). For illustration, it is easy to calculate by Equation (2) and the data in Table IV. that in the case when the total number of nuclei of zeolite Na-Pc ($\bar{N}_o/\bar{N}_a$ = 464) would be 2000 times greater than the total number of nuclei of zeolite X ($\bar{N}_o/\bar{N}_a$ = 32), and when the growth rate of zeolite

X particles would be 10 times higher than the growth rate of zeolite Na-Pc particles, 50 % of zeolite X and 50 % of zeolite Na-Pc would be formed at the end of the crystallization process.

Literature Cited

1. Polak, F.; Cichocki, A. In Molecular Sieves; Meier, W. M.; Uytterhoeven, J. B. Eds.; Advances in Chemistry Series No. 121; American Chemical Society: Washington, DC, 1973; p 209.
2. Zhdanov, S. P.; Samulevich, N. N. Proc. 5th Int. Conf. Zeolites, 1980, p 75.
3. Lechert, H. In Structure and Reactivity of Modified Zeolites; Jacobs, P. A., Ed.; Elsevier: Amsterdam, 1984; p 107.
4. Seo, G. Hwahak Konghak 1985, 23 295.
5. Bronić, J.; Subotić, B.; Smit, I.; Despotović, Lj. A. In Innovation in Zeolite Materials Science; Grobet, P. J.; Mortier, W. J.; Vansant, E. F.; Schulz-Ekloff, G., Eds.; Studies in Surface Science and Catalysis No. 37; Elsevier: Amsterdam, 1988; p 107.
6. Kasahara, S.; Itabashi, K.; Igawa, K. In New Developments in Zeolite Science Tachnology; Murakami, Y.; Iijima, A.; Ward, J. W., Eds.; Proc. 7th Int. Conf. Zeolites; Kodansha Ltd.:Tokyo, 1976; p 185.
7. Nicolas, S.; Massiani, P.;Vera Pacheco, M.; Fajula, F.; Figueras, F. In Innovation in Zeolite Material Science; Grobet, P. J.; Mortier, W. J.; Vansant, E. F.; Schulz-Ekloff, G., Eds.; Studies in Surface Science and Catalysis No. 37; Elsevier: Amsterdam, 1988; p 115.
8. Dewaele, N.; Bodart, P.; Gabelica, Z.; Nagy, J. B. Acta Chimica Hungarica 1985, 119, 233.
9. Cichocki, A. J. Chem. Soc. Faraday Trans. 1 1985, 81,1297.
10. Kühl, G. H. Zeolites 1987, 7,451.
11. Occelli, M. L.; Pollack, S. S.; Sanders, J. V. In Innovation in Zeolite Material Science; Grobet, P. J.; Mortier, W. J.; Vansant, E. F.; Schulz-Ekloff, G., Eds.; Studies in Surface Science and Catalysis No. 37; Elsevier: Amsterdam, 1988; p 45.
12. Albers, E. W.; Vaughan, D. E. W. U. S. Patent 3 947 482, 1976.
13. Ruren, X.; Jianmin, Z. Chem. J. Chin. Univ. 1982, 25, 349.
14. Qinhua, X.; Shulin, B.; Jialu, D. Scientia Sinica 1982, 25, 349.
15. Kerr, G. T. J. Phys. Chem. 1968, 72, 1385.
16. Freund, E. F. J. Cryst. Growth 1976, 34, 11.
17. Barrer, R. M. Hydrothermal Chemistry of Zeolites; Academic Press: London, 1982; Chapter 6, 6.
18. Kacirek, H.; Lechert, H. J. Phys. Chem. 1975, 79, 1589.
19. Fahlke, B.; Starke, P.; Wieker, W.; Wendlandt, K. P. Zeolites 1987, 7, 209.
20. Thilo, E.; Wieker, W.; Stade, H. Z. anorg. allg. Chem. 1965, 340, 260.
21. Zevin, L. S.; Zavyalova, L. L. Kolichestvenniy Rendgenographcheskiy prazoviy analiz; Nedra: Moskva, 1974; p 37.
22. Klug, H. P.; Alexander, L. E. X-ray Diffraction Procedures; Wiley: New York, 1954; p 491.
23. Ciric, J. J. Colloid Interface Sci. 1986, 28, 315.

24. Zhdanov, S. P. In Molecular Sieve Zeolites-I; Gould, R. F.; Ed.; Advances in Chemistry Series No. 101; American Chemical Society: Washington, DC, 1971; p 20.
25. Subotić, B.; Graovac, A. In Zeolites: Synthesis, Structure, Technology and Application; Držaj, B.; Hočevar, S.; Pejovnik, S., Eds.; Studies in Surface Science and Catalysis No. 24; Elsevier: Amsterdam, 1985; p 199.
26. Subotić, B.; Sekovanić, L. J. Cryst. Growth 1986, 75, 561.
27. O'Connor, T. L. J. Phys. Chem. 1961, 65, 1.
28. Wieker, W.; Fahlke, B. In Zeolites: Synthesis, Structure, Technology and Application; Držaj, B.; Hočevar, S.; Pejovnik, S., Eds.; Studies in Surface Science and Catalysis No. 24; Elsevier: Amsterdam, 1985; p 161.
29. Flanigen, E. M.; Szymanski, H. A.; Khatami, H. In Molecular Sieve Zeolites-I; Gould, R. F., Ed.; Advances in Chemistry Series No. 101; American Chemical Society: Washington, DC, 1971; p 201.
30. Walton, A. G. In Nucleation; Zettlemoyer, A. C., Ed.; Marcel Dekker Inc.: New York, 1969; p 225.
31. Dutta, P. K.; Shieh, D. C.; Puri, M. J. Phys. Chem. 1978, 91, 2332.

Chapter 10

Silicate Species with Cagelike Structure in Solutions and Rapid Solidification with Organic Quaternary Ammonium Ions

Isao Hasegawa[1] and Sumio Sakka[2]

[1]Institute for Chemical Research, Kyoto University, Gokasho, Uji-City, Kyoto-Fu 611, Japan

[2]Division of Molecular Engineering, Graduate School of Engineering, Kyoto University, Sakyo-Ku, Kyoto-City, Kyoto-Fu 606, Japan

Organic quaternary ammonium ions are effective in forming silicate anions with cage-like structures. Formation of these silicate anions in solutions with the aid of the ammonium ions and the abrupt formation of silicate solids with the cubic octameric silicate structure ($Si_8O_{20}^{8-}$) from the solutions are described.

Synthesis of silica-based materials with controlled skeleton structures, such as zeolites, requires controlling the structure of oligomeric silicate species at the first reaction step. Organic quaternary ammonium ions, which are known as organic templates in zeolite synthesis ($\underline{1}$), have a role in making up the specific structures of silicate anions, whereas silicate anions randomly polymerize in aqueous solutions containing alkali metal ions, resulting in the presence of silicate anions with different structures.

A number of studies on the structures of silicate species in organic quaternary ammonium silicate solutions and solids ($\underline{2-27}$) indicated that the silicate anions with cage-like structures, such as $Si_6O_{15}^{6-}$ (double three-membered ring), $Si_8O_{20}^{8-}$ (double four-membered ring) and $Si_{10}O_{25}^{10-}$ (double five-membered ring) were formed. Such silicates with cage-like structures will be utilized as starting materials both in the dissolved state and in the solid state.

It is possible to obtain such silicates as solids by evaporation to dryness of the organic quaternary ammonium silicate aqueous solutions. In this case, however, the process is very slow and accordingly a problem of impurity incorporation arises. It was reported that silicate solids consisting of the double four-membered ring structure were abruptly separated out after an exothermal reaction on stirring the mixture of (2-hydroxyethyl)trimethylammonium hydroxide aqueous solution and tetraethoxysilane ($\underline{26}$).

In the first section of this paper, formation of silicate species with cage-like structures in organic quaternary ammonium silicate solutions are reviewed. In the last section, the process of the rapid selective formation of the silicate solids having the

double four-membered ring structure from the solutions is described,
which has been investigated in the current study.

Formation of Silicate Anions with Cage-like Structures by Organic
Quaternary Ammonium Ions

In this section, some factors affecting the formation of silicate
species with cage-like structures are described.

Effect of the Structure of Organic Quaternary Ammonium Ions. The
tetramethylammonium ion ($N^+(CH_3)_4$), first introduced in zeolite
synthesis by Barrer and Denny (30), and Kerr and Kokotailo (31), is
effective in forming the cubic octameric silicate anion ($Si_8O_{20}^{8-}$,
cubic octamer) (2-16). In the tetramethylammonium silicate aqueous
solutions at higher SiO_2 concentrations or cation-to-silica molar
ratios (abbreviated to the N/Si ratios), the cubic octamer is
singularly formed.
    The organic quaternary ammonium ions with three methyl groups
and another functional group (the ammonium ions in which another
functional group for one methyl group of tetramethylammonium ions is
substituted), such as (2-hydroxyethyl)trimethylammonium
($N^+(CH_3)_3C_2H_4OH$), phenyltrimethylammonium ($N^+(CH_3)_3C_6H_5$) and
benzyltrimethylammonium ($N^+(CH_3)_3CH_2C_6H_5$) ions, also form the cubic
octamer selectively (12,13,22), although they do not form the same
zeolites (32). This suggests that the interaction of silicate anions
and the organic quaternary ammonium ions during the selective
formation of the cubic octamer is not influenced by a bulky group on
the ammonium ion, and only three methyl groups on an organic
quaternary ammonium ion are essential, regardless of the other
functional group being hydrophilic or hydrophobic.
    By using the ammonium ions with four alkyl groups larger than
the methyl group, the other types of silicate anions with cage-like
structures are formed. For example, in tetraethylammonium
($N^+(C_2H_5)_4$) silicate aqueous solutions, the prismatic hexameric
silicate anion ($Si_6O_{15}^{6-}$, prismatic hexamer) is formed (13,14,17,18).
    The silicate anion with a double five-membered ring structure is
mainly formed as a crystalline solid from the tetra-n-butylammonium
($N^+(n-C_4H_9)_4$) silicate solutions whose N/Si ratios range from 0.78 to
1.0 (20,21). Pyridinium ions are also effective in forming silicate
anions with cage-like structures (27).

Effect of the Structure of Silicon Sources. Hoebbel et al. used
silicic acid sols, silicic acid gels, or Aerosil as a silica source
of tetramethylammonium silicate aqueous solutions (9). In the
solutions at the conditions that a N/Si ratio is 1.0 and SiO_2
concentration is ca. 1.4 mol dm^{-3}, the distributions of silicate
anions are almost the same, and the cubic octamer is a dominant
species, although the degradation rates of the silica sources are
different. This suggests that the cubic octamer is formed in the
tetramethylammonium silicate aqueous solution, regardless of the type
of silica source with tetra-functionality. Tetraalkoxysilanes
($Si(OR)_4$, R denotes an alkyl group) can be used as a silica source as
well (4,12,14).
    When methyltriethoxysilane ($CH_3Si(OC_2H_5)_3$), a tri-functional
silane, is used as a silica source and is added to (2-hydroxyethyl)-
trimethylammonium hydroxide aqueous solutions, however, the species

with the cubic octameric structure is not formed (Hasegawa, I.; Sakka, S., unpublished data.). In the solutions, a number of methylsilsesquioxane species, formed by the hydrolysis of methyltriethoxysilane, with different structures are present even under the conditions where the cubic octamer is dominant in the aqueous silicate solutions. This indicates that the use of a silica source with tetra-functionality is required for the selective structure formation with the aid of organic quaternary ammonium ions.

Effect of Temperature. The temperature of a silicate solution also affects the polymerization of silicate anions in the solution. The distribution of silicate anions in an organic quaternary ammonium silicate solution at a fixed N/Si ratio and SiO_2 concentration varies with the temperature of the solution (7,8,13,14,16). Ray and Plaisted (8) reported the temperature dependence of the distribution of silicate anions in the tetramethylammonium silicate aqueous solution at a N/Si ratio of 2/3 and a SiO_2 concentration of 1.0 mol dm^{-3}. The amount of the cubic octamer in the solution decreases with increasing temperature, and the cubic octamer practically disappears above 50 $^{\circ}$C, indicating that the cubic octamer is unstable at higher temperatures. However, Groenen et al. (14) found that the cubic octamer remained in a significant concentration even at 85 $^{\circ}$C, which was close to the temperature of actual zeolite formation, in the tetramethylammonium silicate aqueous solution at a N/Si ratio of 1.0 and a SiO_2 concentration of 1.3 mol dm^{-3}.

Effect of Water. The tetramethylammonium ion also contributes to the selective formation of the cubic octamer in methanolic silicate solutions, prepared by mixing a solution of tetramethylammonium hydroxide in methanol, a small amount of water and tetraalkoxysilane (15). In this solution, the amount of water present in the solution has an important role. The cubic octamer is formed when the H_2O/Si ratio is above 4.0. As tetraethoxysilane is used as a silica source, water is consumed for the hydrolysis of tetraethoxysilane, and the ratio of 4.0 corresponds to the amount of water for the complete hydrolysis of tetraethoxysilane. It should be noted that, above the ratio of 4.0, the recovery of the cubic octamer increases with increasing H_2O concentration although the N/Si ratio and SiO_2 concentration are kept constant, indicating that the presence of water is necessary for the selective formation. Tetraalkylammonium ions are known as the structure forming agents for water; the structure of water around the ion has a certain degree of order (33). Briefly, it appears that the selective formation of silicate species results from the cooperation of organic quaternary ammonium ions and water.

Effect of Water-Miscible Organic Solvent. The distribution of silicate species is different in the aqueous and methanolic system of tetramethylammonium silicate solutions, although the N/Si ratio and SiO_2 concentration are the same. In the aqueous solutions at lower SiO_2 concentrations, low-molecular weight species, such as the monomer and dimer, are present together with the cubic octamer (5,12). In contrast, in the methanolic solutions at lower SiO_2 concentrations, highly cross-linked polymeric species are present along with the cubic octamer (Hasegawa, I.; Sakka, S.; Sugahara, Y.;

Kuroda, K.; Kato, C. J. Chem. Soc., Chem. Commun. in press.).
Moreover, the amount of the cubic octamer formed in the methanolic
system at higher SiO_2 concentrations is larger than that in the
aqueous system (15), suggesting that methanol increases the degree of
polymerization of silicate species and stabilizes the higher
molecular weight species. It is reported that dimethyl sulfoxide
$((CH_3)_2SO)$ also has such an effect (14,34).

Effect of Addition of Sodium Ions to Tetramethylammonium Silicate
Aqueous Solution. In zeolite synthesis, alkali metal cations are
combined with organic quaternary ammonium ions to produce zeolites
with different structures from the one produced with only the organic
quaternary ammonium ion (1). It is then expected that other types of
silicate species are formed in the silicate solutions when organic
quaternary ammonium ions and alkali metal cations coexist. In such
silicate aqueous solutions, however, alkali metal cations only act to
suppress the ability of the organic quaternary ammonium ions to form
selectively silicate species with cage-like structures (13,14,28,29).
     Sodium ions added to the tetramethylammonium silicate aqueous
solutions as an aqueous sodium hydroxide solution inhibit the
formation of the cubic octamer (13,28,29). The amount of the cubic
octamer in the solutions decreases with increasing amount of sodium
ions added. When the concentration of the sodium ion is higher than
twice that of the tetramethylammonium ion, no cubic octamer is formed
in the system, and the distribution of silicate anions in the
solutions becomes almost the same as that in the silicate solutions
containing only sodium ions (29). Engelhardt and Rademacher reported
that the amount of the cubic octamer formed in sodium
tetramethylammonium silicate aqueous solutions decreased with
increasing Na/(Na+N) molar ratio, in other words, as
tetramethylammonium ions were displaced by sodium ions in keeping the
amount of OH^- ions fixed (28). This means that OH^- ions do not cause
the decrease in the amount of the cubic octamer but only sodium ions
cause. Considering that water, with the aid of tetramethylammonium
ions, is necessary for the selective formation of the cubic octamer,
the decrease in the amount of the cubic octamer with increasing
amount of sodium ions may be explained by the destruction of the
interaction between tetramethylammonium ions and water molecules by
sodium ions which consume water for the hydration.

Rapid Solidification of Organic Quaternary Ammonium Silicates

In this section, the results of our study on the rapid solidification
of organic quaternary ammonium silicates are presented.

Experimental

Preparation of Solutions. Tetraethoxysilane is used as a silica
source. By adding tetraethoxysilane to a tetramethylammonium or a
(2-hydroxyethyl)trimethylammonium hydroxide aqueous solution, two
kinds of mixtures in which a N/Si ratio was 1.0 and a SiO_2
concentration was 2.22 mol kg^{-1} were prepared. For comparison,
another mixture consisting of tetraethoxysilane and a sodium
hydroxide aqueous solution with a Na/Si molar ratio of 1.0 and a SiO_2
concentration of 2.22 mol kg^{-1} was prepared.

Analytical Procedure. The structures of silicate anions in the solutions and solids have been examined with the trimethylsilylation technique combined with gas-liquid chromatography and ^{29}Si NMR. The molecular weight distribution was measured by applying gel permeation chromatography to the trimethylsilylated derivatives.

The method of Lentz (35,36) was adopted for trimethylsilylation of the aqueous silicate solutions. The mixture of conc. hydrochloric acid, water, 2-propanol and hexamethyldisiloxane was used as the trimethylsilylating reagent. Trimethylsilylated derivatives obtained were adaptable to gas-phase analysis. The distribution of silicate species in solutions, which was analyzed quantitatively by the trimethylsilylation technique combined with gas-liquid chromatography, was expressed as the SiO_2 recovery, that is, the percentage of silica as a silicate species in total silica component in the solutions.

For trimethylsilylation of the silicate solids, the method of Götz and Masson (37) was used. The mixture of chlorotrimethylsilane, hexamethyldisiloxane and 2-propanol was used as the trimethylsilylating reagent. Conditions for gas-liquid and gel permeation chromatographies were described elsewhere (12).

^{29}Si NMR spectra were recorded with JEOL GSX-400 and FX-200 spectrometers. The spectra of the silicate solutions were recorded at 79.42 MHz using a pulse angle of 45°, a delay time of 5 s and an acquisition time of 0.084 s with a GSX-400. A teflon-made tube was used as sample holder. The spectra of the silicate solids were acquired at 39.64 MHz under conditions of magic angle spinning using a delay time of 6 s and an acquisition time of 0.2048 s. Chemical shifts are given with reference to an external sample of tetramethylsilane.

Results and Discussion

Organic Quaternary Ammonium Hydroxide-Tetraethoxysilane Mixture. The variation in the temperature of the mixture of (2-hydroxyethyl)tri-methylammonium hydroxide aqueous solution and tetraethoxysilane with the stirring time is shown in Fig. 1. The temperature of the mixture gradually rises. It is noticed that the exothermal reaction starts at ca. 29 $^{\circ}$C. Before the exothermal reaction, the mixture is heterogeneous, consisting of two phases, an organic phase of tetraethoxysilane and an aqueous phase of (2-hydroxyethyl)trimethyl-ammonium hydroxide solution. The mixture becomes a single phase solution just when the temperature of the solution reaches a maximum of ca. 61 $^{\circ}$C. When the temperature is lowered, solids begin to precipitate. The whole solution completely solidifies into a mass of wet powder when the temperature drops to 44 $^{\circ}$C.

In the mixture of tetramethylammonium hydroxide aqueous solution and tetraethoxysilane, almost the same tendency is seen in the variation in the temperature with the stirring time as seen in the mixture containing (2-hydroxyethyl)trimethylammonium ions described above. With decreasing temperature, the silicate solids are also deposited from the solution which has become a single phase after the exothermal reaction.

Sodium Hydroxide-Tetraethoxysilane Mixture. The exothermal reaction in the mixture of sodium hydroxide aqueous solution and

tetraethoxysilane also starts at ca. 29 $^{\circ}$C, the same temperature as that for the mixture containing the organic quaternary ammonium ions. The solution becomes turbid just when the exothermal reaction starts. At the maximum temperature (61 $^{\circ}$C), viscous sol starts to precipitate, indicating that the hydrolysis of tetraethoxysilane and the random polymerization of the hydrolyzed product take place very rapidly when the temperature of the solution reaches a maximum.

Reaction Process. In order to elucidate the reaction process before the exothermal reaction, gas-liquid chromatography was performed on both the top and bottom phases of the sample containing (2-hydroxyethyl)trimethylammonium ions. The top phase was analyzed by direct injection into a gas chromatograph. The bottom phase was analyzed after trimethylsilylation by the method of Lentz. Throughout the reaction, only tetraethoxysilane is detected from the top phase. The gas chromatograms of the trimethylsilylated derivatives obtained from the bottom phase at various time intervals are shown in Fig. 2. After 1 h of stirring, only the monomer (SiO_4^{4-}) is detected, which would have been formed by the hydrolysis of tetraethoxysilane. After 2 h of stirring, the small peak corresponding to the dimer ($Si_2O_7^{6-}$) appears. It is assumed that the amount of hydrolyzed product of tetraethoxysilane increases with time, and the polymerization proceeds in the bottom aqueous phase. As the exothermal reaction occurs after 200 min of stirring, the cubic octamer and the species with molecular weights higher than the cubic octamer are recovered from the bottom phase. As indicated with the mixture containing sodium ions, it appears that the polymerization of silicate species following the hydrolysis of tetraethoxysilane proceeds abruptly when the exothermal reaction occurs. Actually, the amount of tetraethoxysilane in the top phase decreases pronouncedly as the temperature rises, and the mixture becomes a single phase within a few minutes of the exothermal reaction.

The quantitative analysis performed on the distribution of silicate anions obtained at the maximum temperature in the single phase solution with the trimethylsilylation technique combined with gas-liquid chromatography indicates that the recovery of monomer is 0.2% and that of the cubic octamer is 10.3%. The other low-molecular weight species are not recovered from the solution. It is assumed that the rest of silica component is present as the species with molecular weights higher than the cubic octamer. The presence of higher molecular weight species at the maximum temperature is clearly seen from Fig. 3 showing the gel permeation chromatogram of the trimethylsilylated derivatives obtained from the single phase solution at the maximum temperature.

In the investigation of the distribution of silicate anions in the (2-hydroxyethyl)trimethylammonium silicate aqueous solutions at a N/Si ratio of 1.0 and different SiO_2 concentrations, it was reported that the recovery of the cubic octamer increased with increasing SiO_2 concentration, and the recovery was ca. 93 % in the solution at a SiO_2 concentration of 1.75 mol dm^{-3} (12). The recovery of the cubic octamer in the present single phase solution is too low compared to the SiO_2 concentration of the solution high at 2.22 mol kg^{-1}. The low recovery of the cubic octamer from the solution at the maximum temperature may be attributed to the high temperature of the
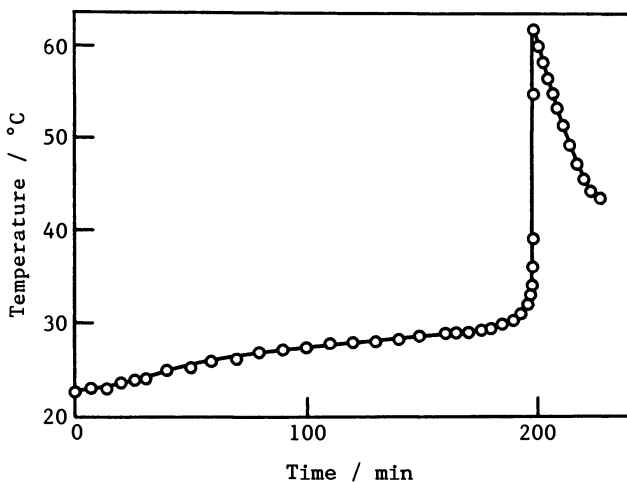
Figure 1. Variation in the temperature of the mixture of (2-hydroxyethyl)trimethylammonium hydroxide aqueous solution and tetraethoxysilane with the stirring time. (Reproduced with permission from Ref. 26. Copyright 1988 The Chemical Society of Japan.)
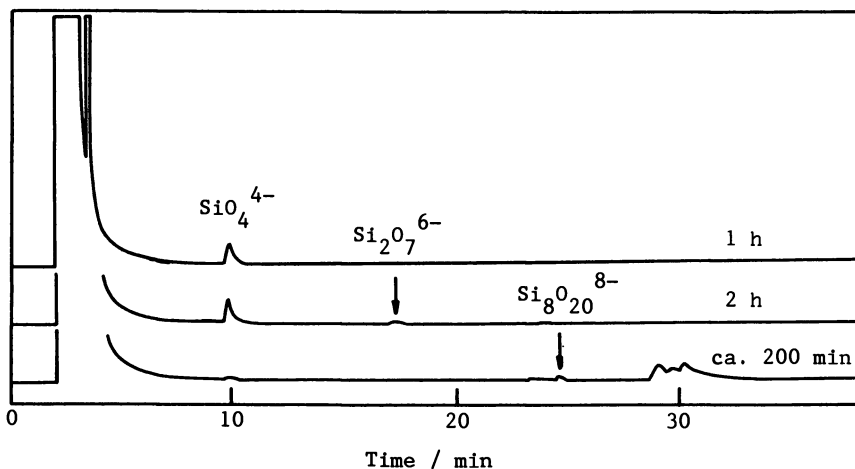
Figure 2. Gas chromatograms of the trimethylsilylated derivatives obtained from the bottom aqueous phase of the mixture containing (2-hydroxyethyl)trimethylammonium ions at various time intervals.
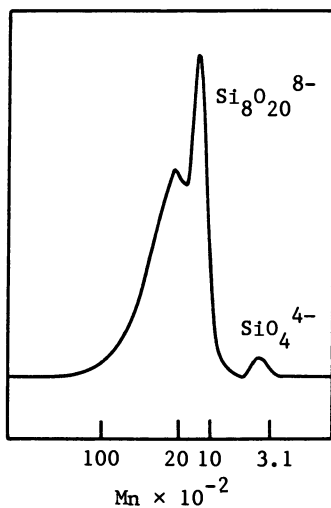
Figure 3. Gel permeation chromatogram of the trimethylsilylated derivatives of silicate species in the single phase solution containing (2-hydroxyethyl)trimethylammonium ions at the maximum temperature of ca. 61 °C.

solution. It is known that the amount of cubic octamer in
tetramethylammonium silicate aqueous solutions diminishes with the
rise of temperature of the solutions (7,8,13,14,16).

Silicate Skeleton Structure of the (2-Hydroxyethyl)trimethylammonium
Silicate Solid. Figure 4 shows the ^{29}Si magic angle spinning NMR
spectrum of the solid formed from the (2-hydroxyethyl)trimethyl-
ammonium hydroxide–tetraethoxysilane mixture after standing in a
desiccator for dryness. Only one sharp peak appears at -98.74 ppm
which is assigned to the silicate building unit of the tri-branching
group, $Si(OSi)_3(O^-)$. The value of the chemical shift is in intimate
agreement with that of tetramethylammonium silicate,
$Si_8O_{20}(N(CH_3)_4)_8$, which has the double four-membered ring structure
in the silicate skeleton (-97.7 or -99.3 ppm) (38,39). One large
peak assigned to $Si_8O_{20}(Si(CH_3)_3)_8$ appears on the gas chromatogram of
the solid trimethylsilylated by the method of Götz and Masson. These
indicate that the solid consists only of the cubic octameric silicate
structure.
     The mixture of tetramethylammonium hydroxide and
tetraethoxysilane also gives the solid consisting only of the
$Si_8O_{20}^{8-}$ silicate skeleton structure.
     Although the silicate skeleton structure of the (2-
hydroxyethyl)trimethylammonium silicate solid, deposited from the
solution, consists of the $Si_8O_{20}^{8-}$ silicate structure solely, the
recovery of the cubic octamer from the solution at the maximum
temperature is only 10.3%, indicating that the selective formation of
silicate structure in the solid is promoted very rapidly with
lowering temperature.

Re-heating of the (2-Hydroxyethyl)trimethylammonium Silicate Solid.
When the (2-hydroxyethyl)trimethylammonium silicate solid is heated
again, the solid melts into a single phase solution in several
minutes. This solution solidifies again on cooling. The solid
obtained after re-heating and cooling also consists of the $Si_8O_{20}^{8-}$
silicate structure, showing that the transition between the solid and
the single phase solution of (2-hydroxyethyl)trimethylammonium
silicate with temperature is reversible.
     ^{29}Si NMR spectrum of the solution, obtained by re-heating of the
solid at ca. 50 $^{\circ}$C, is shown in Fig. 5. Gel permeation chromatogram
of the trimethylsilylated derivatives of silicate species in the
solution is almost the same as that shown in Fig. 3, and the presence
of species with molecular weights higher than the cubic octamer is
confirmed. A very small peak observed at -90.1 ppm is assigned to
the prismatic hexamer, possibly formed by the depolymerization of the
cubic octamer. Main peaks observed at the range between -99.5 and
-100 ppm are attributed to tri-branching units in the silicate
structures. The large sharp peak at -99.5 ppm is assigned to the
cubic octamer. The other peaks, seen at the range between -99.6 and
-100 ppm, would be assigned to the higher molecular weight species,
which are confirmed by gel permeation chromatography. This might
indicate that the higher molecular weight species consist solely of
tri-branching units and have cage-like structures larger than the
double four-membered ring, such as the double five- or six-membered
ring structure.
     It is conjectured that, on heating, silicate species with larger
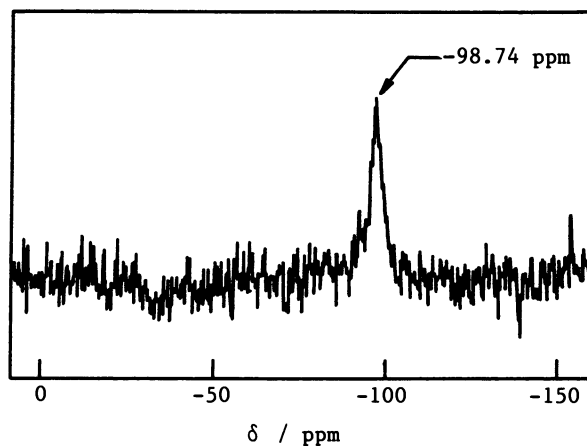
Figure 4. Solid state ^{29}Si magic angle spinning NMR spectrum of (2-hydroxyethyl)trimethylammonium silicate. (Reproduced with permission from Ref. 26. Copyright 1988 The Chemical Society of Japan.)
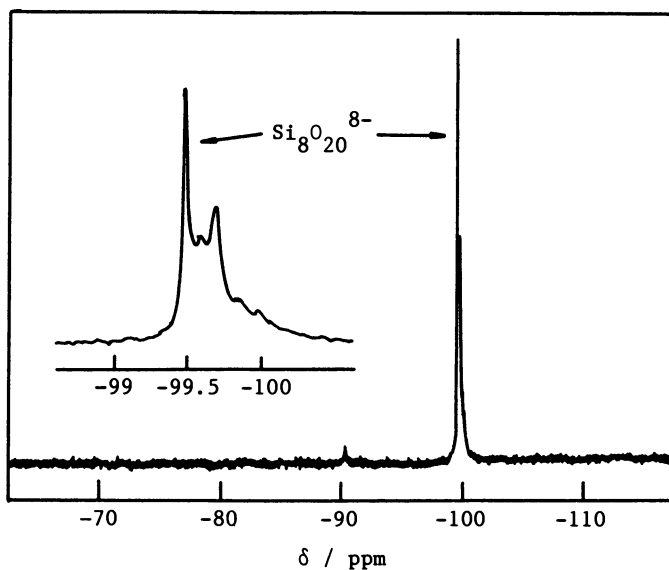
Figure 5. ^{29}Si NMR spectrum of the solution obtained by re-heating the (2-hydroxyethyl)trimethylammonium silicate solid at ca. 50 $^{\circ}$C.

rings would be formed by cleavage of some of the siloxane bonds in the cubic octamer and subsequent reformation, and on cooling, the cubic octamer would be easily formed by the combination of silicate species with larger rings. This would explain the rapid and reversible transition between the solid and solution of (2-hydroxyethyl)trimethylammonium silicate.

In the mixture of sodium hydroxide and tetraethoxysilane, viscous sol precipitates at the maximum temperature. The sol formation shows that polymeric silicate species with uncontrolled structures are formed. It should be recalled that the sodium ion is not effective in controlling the structure of silicate species. In the mixture of organic quaternary ammonium hydroxide and tetraethoxysilane, a single phase solution is obtained at the maximum temperature. This suggests that the structure of higher molecular weight species in the solutions containing organic cations at the maximum temperature is different from that formed in the mixture containing sodium ions. It seems that the structure of higher molecular weight species in the solution containing the organic quaternary ammonium ions at the maximum temperature is also controlled by the organic cations, possibly resulting in the rapid solidification of organic quaternary ammonium silicates.

Conclusions

Tetramethylammonium or (2-hydroxyethyl)trimethylammonium silicate solid, consisting solely of the $Si_8O_{20}{}^{8-}$ silicate structure, was abruptly separated out by cooling the single phase solution which was obtained after an exothermal reaction by mixing the organic quaternary ammonium hydroxide aqueous solution and tetraethoxysilane. The change between the solid and the solution was reversible and very rapid.

Acknowledgments

Literature Cited

1. Lok, B. M.; Cannan, T. R.; Messina C. A. Zeolites 1983, 3, 282.
2. Hoebbel, D.; Wieker, W. Z. Anorg. Allg. Chem. 1971, 384, 43.
3. Hoebbel, D.; Wieker, W. Z. Anorg. Allg. Chem. 1974, 405, 267.
4. Rademacher, O.; Zschuppe, M.; Scheler, H. Z. Chem. 1978, 18, 341.
5. Hoebbel, D.; Garzó, G.; Engelhardt, G.; Vargha, A. Z. Anorg. Allg. Chem. 1982, 494, 31.
6. Harris, R. K.; Knight, C. T. G. J. Mol. Struct. 1982, 78, 273.
7. Engelhardt, G.; Hoebbel, D. Z. Chem. 1983, 23, 33.
8. Ray, N. H.; Plaisted, R. J. J. Chem. Soc., Dalton Trans. 1983, 475.
9. Hoebbel, D.; Starke, P.; Vargha, A. Z. Anorg. Allg. Chem. 1985, 530, 135.
10. Dutta, P. K.; Shieh, D. C. J. Raman Spectrosc. 1985, 16, 312.
11. Knight, C. T. G.; Kirkpatrick, R. J.; Oldfield, E. J. Chem. Soc., Chem. Commun. 1986, 66.

12. Hasegawa, I.; Kuroda, K.; Kato, C. Bull. Chem. Soc. Jpn. 1986, 59, 2279.
13. Thouvenot, R.; Hervé, G.; Guth, J. -L.; Wey, R. Nouv. J. Chim. 1986, 10, 479.
14. Groenen, E. J. J.; Kortbeek, A. G. T. G.; Mackay, M.; Sudmeijer, O. Zeolites 1986, 6, 403.
15. Hasegawa, I.; Sakka, S.; Kuroda, K.; Kato, C. J. Mol. Liq. 1987, 34, 307.
16. Groenen, E. J. J.; Emeis, C. A.; van den Berg, J. P.; de Jong-Versloot, P. C. Zeolites 1987, 7, 474.
17. Hoebbel, D.; Garzó, G.; Engelhardt, G.; Ebert, R.; Lippmaa, E.; Alla, M. Z. Anorg. Allg. Chem. 1980, 465, 15.
18. Hoebbel, D.; Vargha, A.; Fahlke, B.; Engelhardt, G.; Z. Anorg. Allg. Chem. 1985, 521, 61.
19. Cavell, K. J.; Masters, A. F.; Wilshier, K. G. Zeolites 1982, 2, 244.
20. Hoebbel, D.; Wieker, W.; Franke, P.; Otto, A. Z. Anorg. Allg. Chem. 1975, 418, 35.
21. Hoebbel, D.; Vargha, A.; Engelhardt, G.; Újszászy, K. Z. Anorg. Allg. Chem. 1984, 509, 85.
22. Schlenkrich, F.; Beil, E.; Rademacher, O.; Scheler, H. Z. Anorg. Allg. Chem. 1984, 511, 41.
23. Schlenkrich, F.; Ziemens, O.; Rademacher, O.; Scheler, H. Z. Chem. 1984, 24, 130.
24. Ziemens, O.; Schlenkrich, F.; Rademacher, O.; Scheler, H. Z. Chem. 1984, 24, 130.
25. Rademacher, O.; Schlenkrich, F.; Ziemens, O.; Scheler, H. Z. Chem. 1984, 24, 131.
26. Hasegawa, I.; Sakka, S. Chem. Lett. 1988, 1319.
27. Rademacher, O.; Ziemens, O.; Scheler, H. Z. Anorg. Allg. Chem. 1984, 519, 165.
28. Engelhardt, G.; Rademacher, O. J. Mol. Liq. 1984, 27, 125.
29. Hasegawa, I.; Sakka, S.; Kuroda, K.; Kato, C. Bull. Inst. Chem. Res., Kyoto Univ. 1987, 65, 192.
30. Barrer, R. M.; Denny, P. J. J. Chem. Soc. 1961, 971.
31. Kerr, G. T.; Kokotailo, G. J. J. Am. Chem. Soc. 1961, 83, 4675.
32. Itabashi, K. In Zeoraito no Gosei to Oyo (Synthesis and Application of Zeolite); Tominaga, H., Ed.; Kodansha: Tokyo, Japan, 1987; p 83.
33. Frank, H. S.; Wen, W. -Y. Disc. Faraday Soc. 1957, 24, 133.
34. Boxhoorn, G.; Sudmeijer, O.; van Kasteren, P. H. G. J. Chem. Soc., Chem. Commun. 1983, 1416.
35. Lentz, C. W. Inorg. Chem. 1964, 3, 574.
36. Glasser, L. S. D.; Sharma, S. K. Br. Polym. J. 1974, 6, 283.
37. Götz, J.; Masson, C. R. J. Chem. Soc., A 1970, 2683.
38. Lippmaa, E. T.; Alla, M. A.; Pehk, T. J.; Engelhardt, G. J. Am. Chem. Soc. 1978, 100, 1929.
39. Lippmaa, E.; Mägi, M.; Samoson, A.; Engelhardt, G.; Grimmer, A. -R. J. Am. Chem. Soc. 1980, 102, 1889.

Chapter 11

Role of the Tetramethylammonium Cation in the Synthesis of Zeolites ZK−4, Y, and HS

P. D. Hopkins

Amoco Oil Company, Naperville, IL 60566

The synthesis of three zeolites whose frameworks include the sodalite 14-hedron were investigated. In two reaction series the product changed from zeolite Y to ZK-4 as the TMA/Na ratio in the reactant mixture was increased; in a third series the product changed from gmelinite to omega, and finally to HS as the TMA/Na ratio increased. In agreement with published work, essentially all sodalite cages in ZK-4 occluded a TMA ion. Sodalite cages in Y zeolites were occupied statistically by one TMA or approximately two sodium ions. Mechanisms for the synthesis of the zeolites, that are consistent with these observations, are proposed.

Essentially all of the zeolites that can be synthesized in the presence of the tetramethylammonium cation (TMA) have frameworks that contain one of two types of 14-hedra(1). The most common zeolites synthesized with TMA are ZK-4 (LTA)(2), omega (MAZ)(3), E (EAB)(3), and offretite (OFF)(4). (The three letter code in parentheses following each zeolite is the IUPAC structure code (5). These codes identify each zeolite when first mentioned and are used elsewhere in this paper when structure types, rather than specific products are discussed). ZK-4 consists of sodalite or beta cages (14-hedra type I) joined through double four rings (D4R). Omega consists of columns of gmelinite cages (14-hedra type II). Offretite and E also contain columns of gmelinite cages but have substantial numbers of double six rings (D6R). Molecular modelling

shows that the spherical TMA ion fills the spherical sodalite cage well; TMA also fits in the almost spherical gmelinite cage but somewhat more loosely. These fits suggest that TMA may function as a template during the synthesis of these zeolites as well as acting as the counterion to the negatively charged framework. TMA cannot pass through single 6-rings or 8-rings (S6R, S8R) so any TMA occupying space in either 14-hedron must be incorporated during synthesis.

Offretite, E and omega syntheses are strongly aided by the presence of TMA. Gmelinite cage occupancy by TMA in offretite and omega is near unity(6).

TMA is essential to the synthesis of ZK-4. With TMA products having Si/Al atomic ratios up to about three have been produced(7). Essentially all sodalite units in ZK-4 contain a TMA ion(8). In the absence of TMA the isostructural zeolite A, with Si/Al invariably equal to one, is produced.

Zeolites Y (FAU) and HS (hydroxysodalite, SOD) both contain sodalite units in their framework. Both can be synthesized easily without TMA but can also be synthesized in the presence of TMA(9,10). All sodalite cages in HS were found to contain a TMA(8) but quantitative results were not reported for Y(10). The present work describes synthesis of the three zeolites, ZK-4, HS, and Y, that contain the sodalite unit. These syntheses were carried out to prepare samples for NMR and neutron scattering studies, results of which will be reported elsewhere. Some results of these syntheses are presented here; these results may help to elucidate the role that TMA plays in the synthesis of the three zeolites.

Experimental

Syntheses were carried out according to published procedures(7,9) or procedures developed by us. Reactants employed were Ludox HS-40 colloidal silica (DuPont, 40% Silica), sodium aluminate trihydrate (Nalco or EM), sodium hydroxide, tetramethylammonium hydroxide pentahydrate (Aldrich), and distilled water. All reactant mixtures, except those intended to produce HS, were aged for one or more days at room temperature before heating to ca. 100°C for crystallization. HS synthesis mixtures were not aged. Crystallizations were carried out in three-neck flasks at reflux with stirring or in Teflon bottles placed in a 100°C oven without stirring.

The zeolites were synthesized in one of six reaction series. Reactant ratios for the six series are listed in Table I. Series 1 is one that we have used, in the absence of TMA, to synthesize zeolite Y (FAU). Series 2 is based on a published recipe(7) for synthesis of ZK-4 (LTA). Series 3 is one which we use to synthesize zeolite A (LTA) at the low silica end of the range used here. Series 4 and 5 are Series 3 with added TMAOH or NaOH; each increases the pH approximately equally. Series 6 is based on a published recipe(9) for synthesis of zeolite HS. In Series 1, 2, and 6, substitution of TMAOH for NaOH causes only minor increases in pH.

Table I.   Reactant Ratios

Mole Ratios	Series					
	1	2	3	4	5	6
SiO_2	17.3	9.5	(a)	(a)	(a)	20.3
Al_2O_3	1.0	1.0	1.0	1.0	1.0	1.0
Na_2O	(b)	(b)	1.1	2.0	1.1	(b)
$(TMA)_2O$	(b)	(b)	0	0	1.0	(b)
$Na_2O + (TMA)_2O$	13.6	4.6	1.1	2.1	2.1	7.4
H_2O	445	325	85	85	85	280

(a) Varied from 1 to 8.
(b) Varied with sum indicated in fifth line kept constant.

All products were washed thoroughly and dried at ca. 105°C overnight. Product identities and phase purities were determined by powder XRD. Silicon and aluminum were determined by wet chemical methods, carbon and hydrogen were determined by a combustion process, and sodium was determined by atomic absorption spectroscopy. Framework Si/Al ratios were determined by established XRD correlations for Y(11) and ZK-4(12); some ratios were also determined by ^{29}Si NMR. TMA, in total and in specific locations, was determined by ^{13}C NMR(8).

Results

Effect of the TMA/Na Ratio on the Product.

Changing the TMA/Na ratio in reaction series 1 and 2 had a pronounced effect on the nature of the zeolite product as shown in Table II.

Table II.   Effect of Tetramethylammonium on the Nature
of the Zeolite Product

Series 1		Series 2	
TMA/Na	Product	TMA/Na	Product
0.0	Y	0.0	Y
0.2	Y	0.6	Y
0.4	Y	0.8	Y,ZK-4,E
1.0	Y,ZK-4	1.0	Y,ZK-4,E
2.0	ZK-4	1.2	ZK-4,E
8.8	ZK-4	1.5	ZK-4
		2.5	ZK-4

Both reaction series, employing substantially different reactant ratios, followed the same pattern. When sodium was the predominant cation the synthesis product was Y but when there was more TMA than sodium the product was ZK-4. (A trace of zeolite E was found in Series 2 at TMA/Na ratios near 1.0). Clearly, TMA stabilizes the LTA structure over a wider range of SiO_2/Al_2O_3 reactant ratios than has been reported previously.

The Si/Al atomic ratios of the products from series 1, both Y and ZK-4, were nearly invariant as shown in Table III.

Table III. Si/Al Atomic Ratios in Series 1 Products

Reactant TMA/Na	Product	XRD	NMR
0.0	Y	1.59	--
0.2	Y	1.64	1.71
1.0	Y	1.59	1.86
8.8	ZK-4	1.57	--

The Si/Al ratio for the ZK-4 product from reaction series 2 was 1.92 by XRD, 2.20 by NMR and 2.26 by chemical analysis; the last is in good agreement with a ratio of 2.39 found by chemical analysis of a product from a similar synthesis(6).

The TMA/Na ratio also had an effect on the products synthesized in Series 6 as shown in Table IV.

Table IV. Effect of TMA/Na on Series 6 Products

Reactant TMA/Na	Zeolite Product
0.00	gmelinite
0.24	omega
0.40	omega and HS
0.62	HS
1.39	HS

Synthesis of HS at a TMA/Na ratio of 0.25 had been reported previously(6) but the same reactant mixture has also been reported to produce omega(1). As shown in Table IV we synthesized omega at this TMA/Na ratio, but by increasing the TMA/Na ratio we were able to synthesize HS.

Sodalite Cage Occupancy in Y. The sodalite cage occupancy by TMA of three Y zeolites synthesized in Series 1 was determined by ^{13}C

NMR using the intensity for sodalite cages in ZK-4 (which are completely filled with TMA) as a standard. The results are compared in Table V with values calculated for random filling by one TMA ion or by either two or three sodium ions based on the reactant compositions.

Table V. Sodalite Cage Occupancy by TMA in Y Zeolites

Reactant TMA/Na	^{13}C NMR	Calculated for Random Occupancy by 1 TMA or n Na/Cage	
		n=2	n=3
0.17	26%	25%	33%
0.41	45	45	54
0.99	75	66	74

The results suggest that the sodalite cages of Y synthesized in the presence of TMA are filled by a random process; the fit for two sodium ions/cage is slightly better than for three sodium ions/cage. Sodalite cage occupancy by approximately two sodium ions is consistent with many XRD studies(13).

TMA in Zeolite A Reactant Mixtures. Series 3, 4, and 5 differed only in that the cation and hydroxyl concentrations of Series 3 were increased by adding NaOH (Series 4) or TMAOH (Series 5) to the reactant mixture. Series 5 products maintained higher crystallinity than series 3 products as silica in the reactant mixtures was increased as shown in Figure 1. Series 4 products lost crystallinity faster than those of Series 3 as the silica content increased, proving that the effect observed in Series 5 was due to TMA and not to pH (since the difference in pH between TMAOH and NaOH systems was small). The crystallinity in Figure 1 includes only material having the LTA structure; other crystalline phases appeared in some products but were not included in the crystallinity assessments. Series 3 products became amorphous as the silicon content of the reactant mixture increased. Series 4 changed from A to P (GIS) then to Y and gmelinite (GME) and finally became amorphous. Series 5 changed from ZK-4 to HS. Obviously TMA stabilizes the LTA structure in high silica reaction environments.

Discussion

The facts uncovered here that any synthesis mechanisms must account for are:
1. In two reaction series, with substantially different silica to alumina ratios, the zeolite synthesized changed from Y to ZK-4 as the TMA/Na ratio increased.
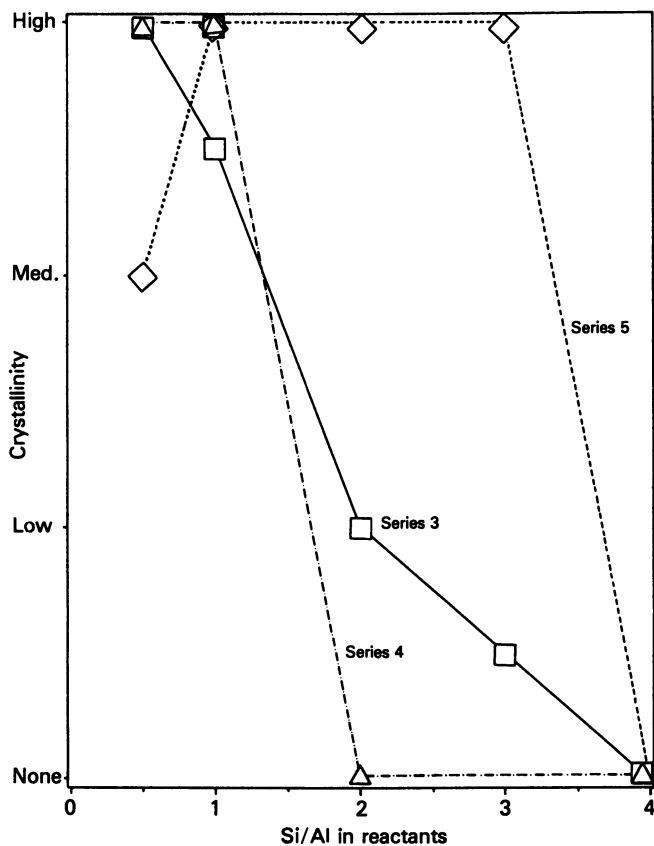
Figure 1. Crystallinity (of the LTA structure) as a function of the Si/Al ratio in the reactant mixture. Series 3, 4, and 5 differ in their Na and TMA contents; see Table I.

2. As the TMA/Na ratio increased in another reaction series the zeolite product changed first from gmelinite to omega and finally to HS.
3. Sodalite units of zeolite Y were filled statistically by one TMA or about two Na ions based on the relative concentrations of the two ions in the reaction medium.
4. The Si/Al atomic ratio of zeolite Y was independent of the amount of TMA incorporated and was comparable to that of a ZK-4 synthesized from a reactant mixture having similar silica and alumina contents.
5. As the silica content of a typical zeolite A reaction mixture was increased, the presence of TMA maintained the product (with the LTA structure) in a higher state of crystallinity than that obtained in its absence.

The first two observations have an important similarity. At low TMA contents in all three series zeolites composed predominantly of double six rings (D6R) are synthesized, zeolite Y in two series and gmelinite in the other. Gmelinite does include the gmelinite 14-hedron in its framework but the framework can be considered as being made up of parallel layers of D6R, the gmelinite cage being the consequence of D6R stacking rather than an important building block. As the TMA content of reaction mixtures increases structures that do not include D6R appear. In two series ZK-4, which may be thought of as built from D4R rather than D6R, appears. In the HS series first omega, in which gmelinite cages are an important part of the framework, appears followed at higher TMA contents by HS, which contains only sodalite cages.

The statistical occupancy of sodalite units in Y implies that joining of D6R, if that is the synthesis mechanism, is not sensitive to the nature of the cation occluded. A reasonable assumption is that sodalite units in Y form without templating but cations are required for charge balancing during some step in the synthesis procedure. The constant alumina content observed in the Y synthesis supports this interpretation.

Stabilization of the LTA structure at high reactant Si/Al ratios by TMA indicates some role for TMA in the synthesis. Published[8] and our own findings that sodalite cages in ZK-4 all contain one TMA suggest that the role is as a template for sodalite cage formation. Templating of sodalite cages apparently is not required for synthesis of zeolite A (Si/Al ratio of one) because the reaction is facile in the absence of TMA.

The observations made here are not sufficient to prove any particular synthesis mechanism. However we may speculate as to mechanisms that are consistent with the observations. The synthesis of LTA probably proceeds by formation of sodalite units from D4R. This mechanism has been postulated before[14,15]. D4R are present in silicate solutions containing sodium[16], potassium[17], and TMA[18] and in aluminosilicate solutions containing TMA[19]. In TMA silicate solutions the fraction of Si in D4R decreases with dilution[20] and in TMA aluminosilicate solutions D4R's decrease with decreasing Si/Al[21]. D4R with strict alternation of Si and Al, as required for zeolite A, can join in only one way and this is apparently facile as no template

is required. However, in situations where D4R contain more Si than Al, a TMA template is required; the template could act to bring the D4R together in the absence of a strong tendency to do so or the TMA could act to stabilize high silica sodalite units which have recently been shown to be less stable than low silica sodalite units(22).

Synthesis of A by a mechanism involving three S4R joined to form a central S6R has been proposed recently(23). The arguments above would also fit this mechanism. However the mechanism using D4R is more satisfactory because it provides the sodalite unit with six D4R to direct further reaction to the LTA structure, but not to FAU or SOD.

Analogously zeolite Y is probably formed by joining of D6R. The formation of Y or gmelinite, in both of which every Si and Al is in a D6R, suggests that D6R are plentiful in reactant mixtures. The existence of D6R in silicate solutions has been inferred(16,24). Joining of D6R to form sodalite units appears to be facile and not affected by the presence of TMA, possibly because the Si/Al ratios of the D6R change in a non-critical range; that is the Si/Al ratio does not approach one or become very large. A similar mechanism, using S6R, has been proposed (25). Again, the D6R mechanism is more satisfying because a sodalite unit with 4 D6R attached is a nucleus only for the FAU structure.

The mechanism of HS formation is less obvious. The stabilizing effect of TMA on high silica sodalite units(22) may have some bearing. The destabilization of D4R and D6R at high Na/Si ratios in solution (high pH?) has been observed(16). HS forms as higher pH than the other zeolites studied here. This may lead to a mechanism involving SnR.

Acknowledgments

Literature Cited

1. Breck, D. W. Zeolite Molecular Sieves; John Wiley: New York, 1974; Table 4.17.
2. Kerr, G. T. Inorg. Chem. 1966, 5, 1537-1541.
3. Aiello, R.; Barrer, R. M. J. Chem. Soc. (A) 1970, 1470-1475.
4. Whyte Jr., T.E.; Wu, E. L.; Kerr, G. T.; Venuto P. B. J. Catal. 1971, 20, 88-96.
5. Meier, W. M.; Olson, D. H. Atlas of Zeolite Structure Types; Butterworths: London, 1987.
6. Barrer, R. M. Hydrothermal Chemistry of Zeolites, Academic Press: London, 1982; 166.
7. Jarman, R. H.; Melchior, M. T.; Vaughan, D. E. W. Intrazeolite Chemistry, Stucky, G. D.; F. G. Dwyer, Eds.; American Chemical Society: Washington, DC, 1983; 267-281.
8. Jarman, R. H.; Melchior, M. T. J. Chem. Soc. Chem. Commun. 1984, 414-416.
9. Jarman, R. H. J. Chem. Soc. Chem. Commun. 1983, 512-513.

10. Hayashi, S.; Suzuki, K.; Shin, S.; Hayamizu, K.; Yamamoto, O. Chem. Phys. Lett. 1985, 113, 368-371.
11. Reference 1, p. 94.
12. Jarman, R. H. Zeolites 1985, 5, 213-216.
13. Mortier, W. J. Compilation of Extra Framework Sites in Zeolites, Butterworth: Guildford, Surrey, UK, 1982; 19-31.
14. Dutta, P. K.; Shieh, D. C. J. Phys. Chem. 1986, 90, 2331-2334.
15. Melchior, M. T. In Intrazeolite Chemistry; Stucky, G. D.; Dwyer, F. G., Eds.; American Chemical Society: Washington, 1983; 243-265.
16. McCormick, A. V.; Bell, A. T.; Radke, C. J. Zeolites 1987, 7, 183-190.
17. Harris, R. K.; Knight, C. T. G. J. Chem. Soc. Faraday Trans. 2 1983, 79, 1539-1561.
18. Hoebbel, D.; Weiker, W. Z. Anorg. Allg. Chem. 1971, 384, 43-52.
19. Groenen, E. J. J.; Kortbeek, A. G. T. G.; Mackay, M.; Sudmeijer, O. Zeolites 1986, 6, 403-411.
20. Hoebbel, D.; Garzo, G.; Engelhardt, G.; Vargha, A. Z. Anorg. Allg. Chem. 1982, 494, 31-42.
21. Hoebbel, D.; Garzo, G.; Ujszaszi, K.; Engelhardt, G.; Fahlke, B.; Vargha, A. Z. Anorg. Allg. Chem. 1982, 484, 7-21.
22. Mabilia, M.; Pearlstein, R. A.; Hopfinger, A. J. J. Am. Chem. Soc. 1987, 109, 7960-7968.
23. Dutta, P. K.; Puri, M.; Shieh, D. C. Microstructure and Properties of Catalysts; M. M. J. Treacy; J. M. Thomas; J. M. White, Eds.; Materials Research Society: Pittsburgh, PA 1988; 101-106.
24. Hoebbel, D.; Garzo, G.; Engelhardt, G.; Ebert, R.; Lippma, E.; Alla, M. Z. anorg. allg. Chem. 1980, 465, 15-33.
25. Dutta, P. K; Shieh, D. C.; Puri, M. J. Phys. Chem. 1987, 91, 2332-2336.

RECEIVED December 22, 1988

Chapter 12

Stabilizing Role of Linear Polyamines as Pore Fillers During the Crystallization of Zeolite NU—10

Concettina Pellegrino, Rosario Aiello, and Zelimir Gabelica[1,2]

Dipartimento di Chimica, Università della Calabria, 87030 Arcavacata di Rende (CS), Italy

We report a first example showing a straightforward correlation between the synthesis efficiency of a zeolite in terms of Al framework incorporation and the pore filling ability of a template. Zeolite Nu-10, prepared from gels of variable Si/Al ratios and using different alkali cations and tetraethylenepentamine (TEPA) as template, incorporates Al in variable amounts governed by the gel composition, provided its framework is stabilized y a complete filling by the polyamine during the growth phase. When TEPA or other less appropriate linear diaminoalkanes are used in such experimental conditions that the resulting Nu-10 framework is only partly filled, a further specific Al incorporation is needed to stabilize the lattice, so that the composition of the zeolite is no longer governed by the initial Si/Al ratio. In each case, structural Si-O⁻ defect groups, imposed by the actual framework Al content, are created and charge compensated by the protonated polyamines and /or by the alkali cations. The latter, incorporated in low and non sequential amounts, play a negligible stabilizing role and only affect the nucleation and growth rates, or sometimes favour crystallization of SiO_2 polymorphs, as side phases.

Quaternary ammonium (Alk_4N^+) ions have been recognized to direct the structure of a wide range of zeolite materials (*1,2*). The (Si, Al)O_2 oxide tetrahedra organize around the organic molecule and provide the initial building blocks of a particular structure.

---

[1]Address correspondence to this author.
[2]Current address: Department of Chemistry, Laboratory of Catalysis, Facultés Universitaires Notre Dame de la Paix, Namur, 61 Rue de Bruxelles, B–500 Namur, Belgium

These primary silicate or aluminosilicate complexes then form, along with the inorganic cations and water molecules, the first zeolite nuclei. At that stage, the guest molecules that especially well fit to the framework zeolite void space, are referred to as templates (*1*) and they usually tend to further act as structure directing agents. It is also presumed that the positively charged centers of the cation specifically interact with AlO_2^- tetrahedra so that the templating effect is further enhanced by such electric-dipole interaction. The resulting structure is completely filled by the organic molecules and these latter are usually found intact in the pore volume of the zeolite.

Zeolites (Pr_4N^+)-ZSM-5 and (Bu_4N^+)-ZSM-11 are among the most famous examples illustrating this concept (*3–5*). Perfectly stabilized by the template, the zeolitic lattice is little influenced by the gel chemistry and can be built over a wide range of Si/Al ratios.

In the presence of minor amounts of Pr_4N^+, poorly crystalline ZSM-5 is obtained (*6*) while in complete absence of template, only limited amounts of ZSM-5 appear after several days of crystallization (*7, 8*). In that case, hydrated sodium ions constitute a poor replacement as template or pore filling agents for Pr_4N^+ (*8*). The crystallization rate of such systems can be considerably increased by addition of amines that then primarily act as pore fillers (*3, 9, 10*) but not necessarily as specific structure directors during nucleation (*3*).

Conversely, in many other cases studied, the stabilization of hydrophobic clathrasils, zeosils and very high silica zeolitic frameworks is induced by neutral guest molecules that only fill the channels and cavities (11, 12). They are thought to form a solid solution on the growing crystals and thereby lower the chemical potential of the framework (*13*). The energy required to stabilize such a framework mostly derives from weak Van der Waals bonds between the guest molecule and the siliceous framework (*12*). In that respect, the templation of ZSM-5 with alcohols (*14*) or ethers (*15*) would also have to be interpreted in terms of a pore filling model.

Between these two extremes, a whole range of guest species may participate in the stabilization of a zeolitic lattice among which (poly)alkylene(poly)amines are the most widely used (*1*). The efficiency of such molecules to direct specifically a structure can be strongly related to their geometry. Slight changes either in the (poly)amine chain length (*16–19*) or in the length and position of the side chains (*13, 19*) often produce zeolites with different structures. However, a given zeolitic structure can also be directed by polyamines with variable chain lengths (*18–20*). They then stabilize to a certain degree the framework, partly aspore fillers and partly by interacting electrostatically in their protonated forms with the framework AlO_2^- centers or with SiO^- defect groups. The increment of the framework stability can be brought by other factors, the best known being the Al lattice incorporation. Indeed, isomorphic substitution of Al for Si in a framework results in its net destabilization (*21*) with respect to aluminosilicate lattice stabilized by counterions (*22*) or charge compensating protons (*23*).

The preference of a zeolitic matrix for Al or Si can be qualitatively estimated by deriving "synthesis efficiency curves" that compare the Si/Al atomic ratio of the gel, plotted against that of the zeolite. The efficiency can be good over a wide [e.g.(Pr$_4$N$^+$)ZSM-5 (24)] or restricted [e.g., siliceous mordenite synthesized in presence of trioctylamine (25)] compositional range, or very poor [e.g. faujasite-type zeolites (26, 27)], indicating that in this latter case, other factors than templating effect must play a stabilizing role (27). Generally, however, a good measure for the potency of a template is the range of Si/Al ratios over which it is effective. This is generally interpreted by considering that AlO$_2^-$ negative centers do not request specifically the positive charges from the template to be neutralized.

To our knowledge, a straightforward relation between the synthesis efficiency and the solely pore filling ability of a template has never been established. In the present paper, we describe a situation where the synthesis efficiency of a zeolite can be controlled and optimized by using nonspecific templates, that, under given experimental conditions, fill to various extents the pore volume during growth. We present the selected example of zeolite Nu-10 whose structure involves parallel, one dimensional noninterconnecting channels. This material can be synthesized in presence of various linear polyamines that act as templates with variable efficiency (20, 28-32). Typical preparations demonstrate that, when achieving a complete filling under specific synthesis conditions, molecules of appropriate length such as TEPA sufficiently stabilize the framework as to allow Al to be incorporated in variable amounts, governed by the gel composition. In contrast, a partial filling achieved by TEPA under different conditions or by other less efficient linear diamines results in a need of Al incorporation to stabilize the lattice by interacting with a positive charge, so that the zeolite composition is no longer modulated by the initial Si/Al ratio.

Experimental

Zeolite Nu-10 was prepared from starting gels having the molar composition in the following range: 2-3 M$_2$O, 50-80 M'Cl, Al$_2$O$_3$, 40-100 SiO$_2$, 30-50 R, 3880 H$_2$O, where M and / or M' = Li, Na, K, Rb, Cs; R= tetraethylenepentamine (TEPA) or 1,3 diaminopropane (DP).

Reagents were alkali hydroxydes and chlorides (all A.R. from Merck or Carlo Erba), Aluminum "trihydrate gel Dry Pharm USPXX" (Serva), Precipitated silica (BDH), TEPA, purum, 20% soln (Merck), DP, (A.R., Fluka). All chemicals were used without further purification.

A typical synthesis consists in adding a solution prepared by mixing Al and the alkali hydroxydes to an aqueous solution of the organic template in which solid silica has been dispersed. A third solution containing the alkali chloride dissolved in the remaining distilled water was added to the mixture. The so formed gel was homogenized under stirring for 0.5 h at 25 °C prior to heating at 180 °C in Teflon-coated stainless steel autoclaves, underautogeneous pressure, for various periods of time. A large number of syntheses were run in order to achieve a systematic study of the synthesis of Nu-10 under various conditions, and to describe the appropriate crystallization fields (30, 32). Even under improved crystallization conditions [optimized M/OH$^-$ ratios and use of M chlorides (30)]. Nu-10 very

often co-crystallizes with a variety of other zeolitic materials, mostly mordenite and ZSM-5. In the present study, we have selected a limited series of preparations in the monocationic systems (M = M'), from which an accurate chemical analysis of the as-formed Nu-10 was possible (Table I, samples 1 to 8). The as made solids either consisted of pure Nu-10 having various crystallinities, from which the zeolite crystals could be separated from the remaining amorphous phase by ultrasonic treatment (33), or of Nu-10 contaminated with known amounts of cristobalite. Syntheses in the bicationic mixed systems (M ≠ M') are original and the final composition of the 4 as made solids is given for completeness. Two of them (samples 9 and 11) allowed the determination of Nu-10 composition.

All the solid phases were identified and characterized for crystallinity by X-ray powder diffraction (Philips PW 1730/10 diffractometer, Cu K_α radiation equipped with a PW 1050/70 vertical goniometer and connected to a P.C. computer for quantitative analyses). Crystallinities for Nu-10 and cristobalite were computed by comparing the intensity of the most characteristic diffraction peaks of each sample to that of the corresponding pure 100% crystalline phases used as standards. In some cases calibration curves derived from Nu-10/cristobalite mechanical mixtures were used. Si, Al, and alkali contents were determined either on precursors or calcined samples (900 °C, air flow, 4h) by atomic absorption, using a Perkin-Elmer 380 AA instrument after digestion and dissolution of the samples in H_2SO_4/HF solutions and further elimination of HF by gentle heating at 60 °C for 12 h.

The amounts of occluded template were determined from weight losses measured by heating the pure Nu-10 precursors in air flow from 25 to 900 °C (10 °C min^{-1}) and maintaining the residues isothermally at 900 °C for 4-6 h, in situ, into a Netzsch STA 429 computer controlled thermobalance (combined TG-DTA-DTGA). DTA confirmed the previous findings of Araya and Lowe (20), namely that the organics start to decompose above 200 °C, temperature at which almost all the water was released. Amounts of hydration water and of the occluded organics were calculated accordingly.

Results

Syntheses

Samples 1 to 12 of Table I were synthesized in monocationic or bicationic systems according to the recently optimized conditions, namely by using TEPA as template and different alkali chlorides as mineralizers (30, 32). Diaminoalkanes proved less efficient in yielding pure Nu-10, in agreement with the results of Hogan et al. (29), who showed that 1,6 diaminohexane (DH) and 1,8 diaminooctane (30) were the only organics directing the formation of pure Nu-10, all other diaminoalkanes yielding poorly crystalline Nu-10, often contaminated with cristobalite or kenyalte, 1,3 diaminopropane also yielded only 68% crystalline Nu-10 in the Na system in our conditions, but the absence of other dense phases might be due to the shorter crystallization time (sample 3). Indeed, in most of the cases and even with TEPA, the Na_2O-NaCl system yielded Nu-10 contaminated with cristobalite (sample 4) but most often with ZSM-5. In fact, it was shown that although pure highly crystalline Nu-10 is usually formed under a markedly wide Si/Al range, extending from 15 to

Table I. Various synthesis conditions yielding zeolite Nu-10 (180°C, agitated autoclaves)

Sample N°	Gel composition (moles for 1 Al_2O_3 and 3860 H_2O, unless otherwise stated)	Synth. time	Product (crystallinity)	Ref.
1	$3Li_2O$ $50LiCl$ $100SiO_2$ $30TEPA$	5d	LiNu-10 (65%)	this work
2	$2Li_2O$ $80LiCl$ $100SiO_2$ $40TEPA$	5d	LiNu-10 (60%)	"
3	$2.32Na_2O$ $50NaCl$ $96.3SiO_2$ $33DP$	3d	NaNu-10 (65%)	"
4	$3Na_2O$ $80NaCl$ $100SiO_2$ $50TEPA$	5d	NaNu-10 (60%)+ Crist. (40%)	"
5	$3K_2O$ $50KCl$ $40SiO_2$ $30TEPA$	5d	KNu-10 (100%)	"
6	$3K_2O$ $50KCl$ $60SiO_2$ $30TEPA$	5d	KNu-10 (100%)	"
7	$3K_2O$ $50KCl$ $80SiO_2$ $30TEPA$	5d	KNu-10 (97%)	"
8	$3K_2O$ $50KCl$ $100SiO_2$ $30TEPA$	5d	KNu-10 (100%)	"
9	$3Na_2O$ $50KCl$ $80SiO_2$ $30TEPA$	5d	K,NaNu-10 (55%)+ Crist. (45%)	"
10	$3K_2O$ $50NaCl$ $80SiO_2$ $30TEPA$	5d	K,NaNu-10 (75%)+ Crist. (15%) +ZSM-5 (10%)	"
11	$3Cs_2O$ $50RbCl$ $80SiO_2$ $30TEPA$	5d	RbNu-10 (55%)	"
12	$3Na_2O$ $50RbCl$ $80SiO_2$ $30TEPA$	5d	Na,RbNu-10 (30%)+ Analc. (35%)	"
13	$14.3Li_2O$ $17SiO_2$ $200H$ $850H_2O$	28h	ZSM-5 +Crist.	20
14	" Na_2O " " "	12h	NaNu-10 (88%)	20
15	" K_2O " " "	14h	KNu-10 (100%)	20
16	" Rb_2O " " "	17h	RbNu-10 (90%)	20
17	" Cs_2O " " "	28h	CsNu-10 (65%)+ Crist. (traces)	20
18	$214Na_2O$ $48NaCl$ $84SiO_2$ $25TEPA$ $3421H_2O$	5d	NaNu-10 (100%)	28, ex.7
19	$1SiO_2$(tetramethoxysilane), $4DEA$ $56H_2O$ (Al free)	60d	Silica-ZSM-22 (100%)	12

300 (20, 34), with Na as the only cation, the crucial Si/Al ratio narrows to 28-85 (29) or even more precisely to 34-52 (31). Although not very clear, this poor efficiency of Na could be related to the formation of a less soluble solid gel phase outside the critical composition (20), or rather to a recrystallization of one zeolite nuclei to a less soluble phase like cristobalite or ZSM-5. The presence of this latter thermodynamically more stable zeolite is not really surprising considering that both Nu-10 and ZSM-5 are built up from the same 5-1 SBU.

In the presence of K^+, Nu-10 can be synthesized over a wider Al concentration range (20, 29, 31) and, in our case, a pure well crystalline Nu-10 is formed after 5 days at 180 °C (samples 5 to 8). Considering other alkali cations, the nucleation period was shown to decrease in the series Cs (20h)>Rb (9h)> K (7h)> Na (6h) all other conditions being fixed (20). The corresponding final phases obtained in that case are listed on Table I. Li^+ failed to give Nu-10 (sample 13) and indeed little information on LiNu-10 is available in the literature. In our conditions, the shortest induction period was observed in the Li system and a 60% crystalline LiNu-10 is formed after only about one day (32) but the crystallinity did not increase further for longer heating times (samples 1 and 2). LiCl appeared indispensible to prevent the formation of ZSM-5 (32).

In the presence of Cs, only amorphous phase was detected after 5 days, this being in line with the longer crystallization time needed to obtain poorly crystalline CsNu-10 (sample 17). In contrast, the bicationic Cs_2O-RbCl system yielded more rapidly RbNu-10 (sample 11) while the Na_2O-RbCl system was less efficient in yielding a pure phase (sample 12). Note also that the Na_2O-KCl system only yielded a K bearing Nu-10 (sample 9). This is in agreement with the concept that small cations like Na^+ better act as structure-directing species during nucleation, while structure-breaking cations like K^+ intervene rather as mineralizing agents during crystallization and are therefore preferentially incorporated in the growing lattice (10).

Besides our samples 9 to 12, little further information is available on competitive role of other inorganic ions in bicationic systems, except the observation by Araya and Lowe (20) that addition of traces of Rb^+ to a K^+ bearing gel results in shorter synthesis times. This observation also goes in line with our findings.

Framework composition

Table II gives the unit cell composition of the 10 of our as synthesized samples for which an accurate analysis was possible. Also are included and adapted 3 other Nu-10 samples for which an analysis was available in the literature (samples 14, 15, 18). We also included the composition of silica-ZSM-22, another zeolite possessing the same framework topology as Nu-10 (12), that was synthesized in presence of diethylamine (DA) under very particular conditions (12).

It is surprising that in all cases, the Al/M ratio is very high. This clearly indicates that the AlO_2^- framework negative centers must also be compensated by positive charges stemming from the template molecules. It is indeed probable that under the relatively low pH values that characterize our synthesis batches (11−11.5), the diamines are at least partly protonated (36). Araya and Lowe also concluded

Table II. Chemical composition, synthesis efficiency, pore filling and framework charge balance of some pure Nu-10 samples, synthesized under various experimental conditions, as described in Table I

Sample N°	Unit cell composition of as-synthesized samples	Synthesis efficiency ($Si/Al)_{zeol}$	$(Si/Al)_{gel}$	Pore filling by the organics (%)	Framework charge balance $\overset{+}{M}$	$\overset{+}{R}$	$\bar{Al}$	$\bar{SiO}$
1	$Si_{23.4} Al_{0.6} Li_{0.2} O_{48} (TEPA)_{0.55} H_2O_{0.3}$	39	50	83	0.2	1.1	0.6	0.7
2	$Si_{22.9} Al_{1.1} Li_{0.2} O_{48} (TEPA)_{0.61} H_2O_{1.3}$	21	50	89	0.2	1.22	1.1	0.32
3	$Si_{23.4} Al_{0.6} Na_{0.1} O_{48} (DP)_{0.98} H_2O_{0.4}$	39	48	70	0.1	2.0	0.6	1.5
14	$Si_{23.61} Al_{0.39} Na_{0.06} O_{48} (DH)_{0.87} H_2O_{1.3}$	59	85.7	86	0.06	1.74	0.39	1.41
15	$Si_{23.62} Al_{0.38} K_{0.13} O_{48} (DH)_{0.86} H_2O_{1.04}$	63	85.7	86	0.13	1.72	0.38	1.47
4	$Si_{23.2} Al_{0.8} Na_{0.05} O_{48} (TEPA)_{0.65} H_2O_{1.2}$	29	(30)(a)	98	0.05	1.3	0.8	0.55
5	$Si_{22.8} Al_{1.2} K_{0.25} O_{48} (TEPA)_{0.73} H_2O_{0.7}$	19	20	109	0.25	1.45	1.2	0.5
6	$Si_{23.2} Al_{0.8} K_{0.15} O_{48} (TEPA)_{0.67} H_2O_{0.2}$	29	30	101	0.15	1.35	0.8	0.7
7	$Si_{23.4} Al_{0.6} K_{0.1} O_{48} (TEPA)_{0.68} H_2O_{0.4}$	39	40	103	0.1	1.35	0.6	0.85
8	$Si_{23.53} Al_{0.47} K_{0.05} O_{48} (TEPA)_{0.64} H_2O_{0.1}$	51	50	97	0.05	1.3	0.47	0.9
9	$Si_{23.0} Al_{1.0} K_{0.2} Na_{0.05} O_{48} (TEPA)_{0.67} H_2O_{0.6}$	23	(24)(a)	101	0.2	1.35	1.0	0.55
11	$Si_{23.43} Al_{0.57} Pb_{0.15} O_{48} (TEPA)_{0.67} H_2O_{1.3}$	41	40	100	0.15	1.35	0.57	0.95
18	$Si_{23.46} Al_{0.54} Na_x O_{48} (TEPA)_{0.65} H_2O_y$	43	42	98	x	1.3	0.54	0.76+ x
19	$Si_{24} O_{48} (DEA)_{1.26}$ (Silica-ZSM-22)	∞	∞	96	—	—	—	(2.5)(b)

(a) Recalculated taking into account the known amounts of cristobalite formed

(b) Extrapolated value

that under their conditions (samples 14 and 15) the DH molecules should be occluded in the framework in their diprotonated forms.

To simplify our reasoning and calculations, we will reasonably assume that all the diamines including TEPA bear two positive charges on their extreme amino groups. Any partial (lower) protonation would only result in a systematically lower number of calculated S10⁻ defect groups that complete the charge balance (see later) without thoroughly altering the nature of the discussion.

The chemical analysis allows to calculate the synthesis efficiency in terms of Al incorporation for all samples. In 8 cases, Nu-10 was prepared with nearly 100% efficiency, while 5 other samples show a more important lattice Al incorporation than that predicted from the gel composition (Figure 1).

Pore filling

The next remarkable observation was the close correlation between the synthesis efficiency and the pore filling by the organics incorporated during synthesis. The filling of each sample was calculated from host and guest geometries as follows.

Zeolite Nu-10 was demonstrated to possess the identical framework topology than zeolites ZSM-22 (35), Theta-1 (37), KZ-2 (38) and ISI-1 (39). The complete crystal structure of Theta-1, ZSM-22 and of its Si end-member was elucidated (Table III).

Their unit cell contains 24 T atoms that form a framework constructed from 5-1 SBU and composed of solely 5, 6 and 10 MR, with no 4 MR. The one dimensional elliptical 10 MR channel system runs parallel to the c axis.

Sorption of n-hexane was shown to be a remarkably simple and accurate method to measure the total length of the medium sized channels of a zeolitic matrix, as these molecules perfectly fill the pore system by achieving an end to end configuration (40, 41). From the n-hexane sorption values on Nu-10 reported by Harrison et al. (42) and by Hogan et al. (29), we found respectively 13.3 Å and 12.03 Å for the total length of the channel system per unit cell [the sorption values of Hogan et al. had to be extrapolated for 25 °C (40)].

These values are close to that calculated from the structure, namely 10.08 Å (Table III). This number is obtained from unit cell dimensions, one unit cell containing 1 + 4 × 1/4 = 2 integer channels of 5.04 Å length each running along the c axis. Many nonreproducible n-hexane sorption data reported for other TON type zeolites in the patent literature can be due to the difficulty to remove the last traces of template from sinusoidal shaped channels, so we retained the most reliable value of 12.03 Å calculated from sorption data achieved on pure H-form Nu-10 (29). On the other hand, the degree of porefilling by the templates was calculated from their actual length (TEPA= 18.2 Å; DH= 12.1 Å; DP= 8.5 Å and DEA= 9.1 Å) (12, 19), assuming their all end to end arrangement in the Nu-10 structure at
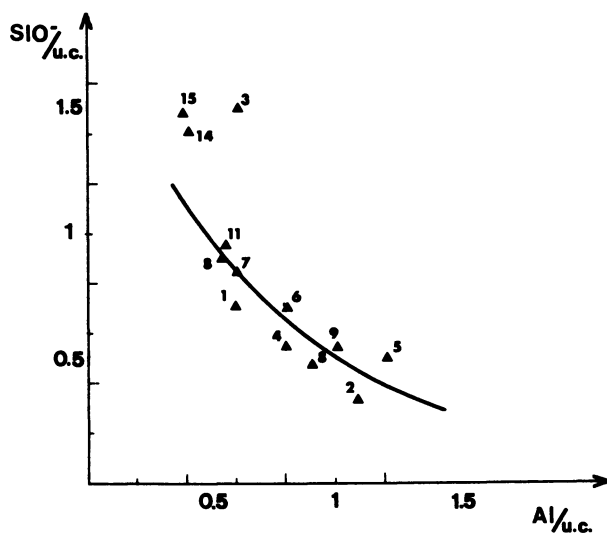
Figure 1. Relationship between Si/Al ratio in the gel and in the Nu-10 zeolites crystallized from it (numbers refer to compositions given in Table II).

Table III. Characteristics of zeolites with TON structure type

Zeolite	Space group	lattice parameters (Å)			channel dimensions (Å)	Reference
		a	b	c		
THETA-1	$Cmc2_1$	13.836(3)	17.415(4)	5.042(1)	—	36
ZSM-22	Cmcm	13.86(3)	17.41(4)	5.04(2)	4.5 x 5.5	35
(Si)ZSM-22	$Cmc2_1$	13.859(3)	17.420(4)	5.038(2)	4.7 x 5.5	12
Nu-10	Cmcm(?)	13.853	17.434	5.04	—	20

the Van der Waals distances (*41*), and neglecting the actual volumes occupied by water and alkali cations because of their rather low amount in each sample (Table II). Such end to end arrangement was directly shown to occur in (Si)ZSM-22 for DEA from the structure data (*12*): the total amount of occluded DEA in the as synthesized materials, 6 wt%, corresponds to a remarkably good pore filling of 96% (Table II). On the other hand, by estimating the diameter of the various diaminoalkane guest molecules, Marler (*12*) concluded that only unbranched flexible aliphatic molecules can fit into the ZSM-22 channels without considerable distortion of the host framework by trhe guest molecule.

Framework charge balance

From the actual organic content and assuming that, in each case, both amino end-group are protonated, it was possible to compute the number of S10$^-$ defect groups created in the structure during crystallization. Owing to the small amount of water released after calcination at 900°C, the presence of OH$^-$ counterions to the positive charges of the organics was estimated to be negligible, as also found in other zeolites (*33*). By contrast, it was established that in usual hydrothermal synthesis conditions leading to various zeolites, fairly large amounts of Si-O-R (R= positively charged template) can be formed, which recondense under calcination to yield a final "healed" structure (*43*).

Figure 2 shows the variation of Si-O-R/ u.c. as a function of Al/u.c. for all the Nu-10 samples. The curve corresponds to what is usually observed in other systems, namely that the number of structural defect groups increases with decreasing framework Al content (*33*). Indeed, the excess of organic cationic species with respect to the number of Al atoms generates structural negative charges following the formal scheme:

$$Si-O-Si + R-NH_3OH \rightarrow Si-O-R' + Si-OH$$
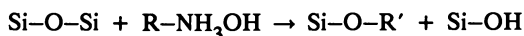
Note also that, although they preferentially neutralize the Al negative charges (*33*), alkali cations can also interact with the lattice:

$$Si-O-Si + M-OH \rightarrow Si-O-M + Si-OH$$
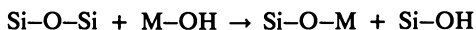
The actual amount of Si-O-D groups (D= H, M or R') can be fairly quantitatively estimated by combining ^{13}C-NMR and TG data (*33*)but it was not the purpose of this work to compute the actual amount of all defect groups, nor to identify them to a particular Si-O-D species.

Finally, samples prepared in presence of diaminoalkanes (No. 3, 14, 15, Table II) do not fit the general curve derived for TEPA-containing zeolites (Figure 2), probably because of the different degree of protonation of these amines.
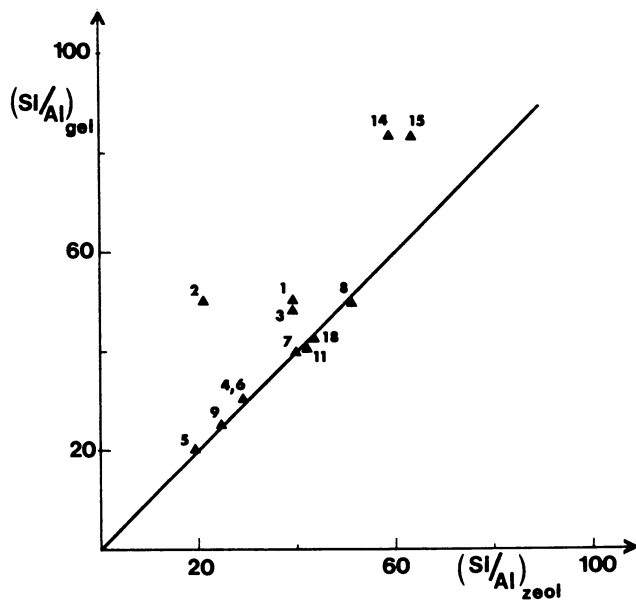
Figure 2.   Variation of the number of SiO^- defect groups, as a function of the number of Al atoms per unit cell of Nu-10 (numbers refer to the composition given in Table II).

Discussion and conclusions

A 100% synthesis efficiency is observed only in the case of zeolites having their pore volume completely filled by the organic template (Table II and Figure 1), irrespective to their alkali or aluminum content or to the nature of the alkali counterions. Except in the case of diethylamine-filled (Si)ZSM-22 (sample 19), all these structures were directed by TEPA, considered along with triethylene-tetramine (TETA), as an excellent templating agent for Nu-10 (*20, 30, 31*). Unfortunately, no other data are available on the potential 100% efficiency of other templates. In fact, many other preparations with different templates, as reported in the first patent describing Nu-10 (*28*), also show a 100% efficiency up to the value for Si/Al= 230 (*44*); but the pore filling was not given.

By contrast, in the Li systems, TEPA does not fill completely the pore system (samples 1 and 2). The same is observed for DH and DP-bearing zeolites (samples 3, 14, 15). These less efficiently filled zeolites show the need to incorporate more Al than the amount provided from the gel composition to stabilize their framework.

Note that the presence of cristobalite as side phase does not influence this behavior (samples 4 and 9). The only consequence due to its formation (probably induced by other variables) is the decrease of the overall Si content in the gel. This does not seem to affect the Nu-10 synthesis efficiency, provided the gel composition is recalculated adequately (Table II).

Obviously, if the nucleation of Nu-10 is governed by both the inorganic cations and the organic templates, the growth is achieved by a total incorporation of the organic molecule that finally perfectly stabilizes the framework. Indeed, the 5-1 SBU precursors to Nu-10 are flexible enough to incorporate one or no Al atoms and yield units of similar stability that ultimately build up the high silica zeolite in a nonpreferential order, according to the actual Si/Al ratio in the precursor gel. Oppositely, 4MR or 6MR precursor species prefer to incorporate an even number of Al atoms (*45*). For example, for the 6MR that are precursors to zeolite ZSM-23, an isomorphic substitution of Al for Si gives a net stabilization in the following order:
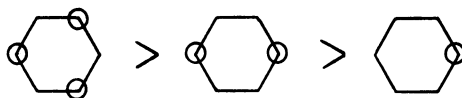
(where ◯ = Al)

The instability of the 2 last species is then compensated by the introduction of exchangeable cations (*21*).

In our particular case, two framework stabilizing possibilities are in competition and a slight change in the synthesis conditions may favour the Al incorporation or the complete pore filling by the organics. Organics with appropriate size and diameter such as TEPA most probably better fit the channel walls than the (shorter) diaminoalkanes, so that no supplementary Al needs to be incorporated. The system then becomes flexible enough as to incorporate Si and Al in amounts given by the gel composition, provided the Si/Al ratio remains within the compositional range where the framework is thermodynamically stable.

The inorganic alkali cations are incorporated in Nu-10 framework in minor and nonregular amounts. This indicates that they probably play a less pronounced

stabilizing role, although they still can exhibit their structure breaking/forming effects as mineralizers during growth. In contrast, lithium is known to favour the easy formation of stable, less soluble aluminate or Al-rich aluminosilicate species. It can be supposed that Al-richer SBU are automatically and exclusively formed in such a system and that they continue to build up the framework along the growth process. The system might then not necessarily be demanding for a complete pore filling, even with TEPA, to get stabilized.

In all cases, the stable frameworks generate a number of SiO^- defect groups, necessary to neutralize the excess of positive charges brought by the pore fillers. It was indeed demonstrated that even larger amounts of such defects do not stabilize a zeolitic framework to a measurable extent (33, 46).

Acknowledgments

Literature Cited

1. Lok, B. M.; Cannan, T. R.; Messina, C. A. *Zeolites* 1983, *3*, 282.
2. Moretti, E.; Contessa, S.; Padovan, M. *La Chimica e l'Industria* 1985, *65*, 21.
3. Gabelica, Z.; Derouane, E.G.; Blom, N., *Appl. Catal.* 1983, *5*, 109.
4. Rollmann, L. D. In *Zeolites, Science and Technology*; Ribeiro, F. R. et al., Eds; M. Nijhoff, Den Haag, 1984, p 109.
5. B.Nagy, J.; Gabelica, Z.; Derouane, E. G.; *Zeolites* 1983, *3*, 43.
6. Calvert, R. B.; Rollmann, L. D., Eur. Patent 101 183, 1981.
7. Nastro, A.; Colella, C.; Aiello, R.; *Stud. Surf. Sci. Catal.* 1985, *24*, 39.
8. Bellussi, G.; Perego, G.; Carati, A.; Cornaro, U.; Fattore, V. *Stud. Surf. Sci. Catal.* 1988, *37*, 37.
9. Calvert, R. B.; Rollmann, L. D.; U.S. Patent 4 495 166, 1985.
10. Gabelica, Z.; Derouane, E. G.; Blom, N. In *Catalytic Materials: Relationship between Structure and Reactivity*; White, T. E., Jr. et al., Eds; ACS Symposium Series N 248; American Chemical Society; Washington, D. C., 1984; p 219.
11. Liebau, F.; Gies, H.; Gunawardane, R. P.; Marler, B., *Zeolites* 1986, *6*, 373.
12. Marler, B. *Zeolites* 1987, *7*, 393.
13. Barrer, R. M.; *Stud. Surf. Sci. Catal.* 1985, *24*, 1.
14. Plank, C. J.; Rosinski, E. J.; Rubin, M. K.; U. S. Patent 4 341 748, 1982.
15. Holderch, W.; Marosi, L.; Mross, W. D.; Schwarzman, M. Eur. Patent 51 741, 1982.
16. Casci, J. L. *Stud. Surf. Sci. Catal.* 1986, *28*, 215.
17. Valyocsik, E. W.; Rollmann, L. D.; *Zeolites* 1985, *5*, 123.
18. Gabelica, Z.; Cavez-Bierman, M.; Bodart, P.; Gourgue, A.; B.Nagy, J.; *Stud. Surf. Sci. Catal.* 1985, *24*, 55.
19. Gunawardane, R. P.; Gies, H.; Marler, B.; *Zeolites* 1988, *8*, 127.
20. Araya, A.; Lowe, B. M.; *Zeolites* 1984, *4*, 280.
21. Mortier, W. J.; Geerlings, P.; Van Alsenoy, C.; Figeys, H. P. *J. Phys. Chem.* 1979, *83*, 855.
22. Sauer, J.; Engelhardt, G.; *Z. Naturforsch.* 1983, *37a*, 277.
23. Derouane, E. G.; Fripiat, J.; *Proc. 6th Intern. Zeolite Conf.*, 1983, p 717.
24. Jacobs, P. A.; Martens, J. A.; *Synthesis of High Silioaluminosilicate Zeolites*; Elsevier: Amsterdam, 1987, p 191.
25. Occelli, M. L.; Pollack, S. S.; Sanders, J. V. *Stud. Surf. Sci. Catal.*, 1988, *37*, 45.

26. See ref. 24, p 344.

27. Gabelica, Z.; Dewaele, N.; Maistriau, L.; B.Nagy, J.; Derouane, E. G. in *Advances in Zeolite Synthesis*, (this volume).

28. Hogan, P. J.; Stewart, A.; Whittam, T. V. Eur. Patent 65, 400, 1981.

29. Hogan, P. J.; Whittam, T. V.; Birtill, J. J.; Stewart, A. *Zeolites* 1984, *4*, 275.

30. Aiello, R.; Nastro, A; Pellegrino, C. *Stud. Surf. Sci. Catal.* 1986, *28*, 255.

31. Le Febre, R. A.; Kouwenhoven, H. W.; van Bekkum, H. *Zeolites* 1988, *8*, 60.

32. Pellegrino, C.; Nastro, A.; Aiello, R. *Proc. 2nd Intern. Conf. Engin. Materials, Bologna*, 1988, in press.

33. B.Nagy, J.; Bodart, P.; Collette, H.; El Hage- Al Asswad, J.; Gabelica, Z.; Aiello, R.; Nastro, A.; Pellegrino, C. *Zeolites* 1988, *8*, 209.

34. Lowe, B. M.; Araya, A.; Eur. Patent 77 624, 1982.

35. Kokotailo, G. T.; Schlenker, J. L.; Dwyer, F. G.; Valyocsik, E. W. *Zeolites* 1985, *5*, 349.

36. See ref. 24, p 119.

37. Barri, S. A. I.; Smith, G. W.; White, D.; Young, D. *Nature* 1985, *312*, 533.

38. Parker, L. M.; Bibby, D. M. *Zeolites* 1983, *3*, 8.

39. Takatsu, K.; Kawata, N. Eur. Patent 87 017, 1983.

40. Derouane, E. G.; Gabelica, Z. *J. Catal.* 1980, *65*, 486.

41. Jacobs, P. A.; Beyer, H. K.; Valyon, J. *Zeolites* 1981, *1*, 161.

42. Harrison, I. D.; Leach, H. F.; Whan, D. A. *Zeolites* 1987, *7*, 28.

43. Boxhoorn, G.; Kortbeek, A. G. T. G.; Hays, G. R.; Alma, N. C. M. *Zeolites* 1984, *4*, 15.

44. See ref. 24, p 244.

45. Guth, J. L.; Caullet, P. *J. Chem. Phys.* 1983, *83*, 155.

46. Van Santen, R. A.; Keijsper, J.; Ooms, G.; Kortbeek, A. G. T. G. *Stud. Surf. Sci. Catal.* 1986, *28*, 169.

Chapter 13

Zeolite Synthesis in the Presence of Fluoride Ions

A Comparison with Conventional Synthesis Methods

J. L. Guth, H. Kessler, J. M. Higel, J. M. Lamblin, J. Patarin, A. Seive, J. M. Chezeau, and R. Wey

Laboratoire de Matériaux Minéraux, Unité Associée au Centre National de la Recherche Scientifique No. 428, Ecole Nationale Supérieure de Chimie, 3 rue Alfred Werner, 68093 Mulhouse Cedex, France

Replacement of OH^- by F^- makes it possible to obtain zeolites in media where pH values can be lowered to acidic ones. Under such conditions MFI-, FER-, MTT-, MTN- and TON-structure type materials could be prepared. This route is especially suited for high-silica materials synthesis, but partial substitution of silicon by B^{III}, Al^{III}, Ga^{III}, Fe^{III}, Ge^{IV} and Ti^{IV} has been possible too. The ease of substitution decreases with increasing stability of the corresponding fluoro-complexes in the solution. As the supersaturation of crystallizing species is lower for fluoride-containing media, the number of phases that could be obtained is smaller (fewer metastable phases), but crystallization is more regular (formation of large crystals with less defects). The choice of templates is therefore more critical. The new medium enables the incorporation of elements sparingly soluble in alkaline solutions (e.g., Fe^{III}) or of cations such as NH_4^+, Co^{2+}. Finally the presence of F in the materials leads to catalytic properties modifications which will be discussed.

In a recent paper (1), our laboratory reported the hydrothermal synthesis of silica-rich, Al, B and (Al+B) MFI-type zeolites in non-alkaline medium (2-4). The very pure materials so obtained exhibit a high crystallinity and a regular morphology which seem to be related to their growth in moderately supersaturated solutions. Their characterization (5,6) and the study of their properties (7) has disclosed differences to zeolites of the same structure and similar composition obtained in alkaline medium.

The development of the synthesis in fluoride medium has been studied in connection with the new possibilities opened by this method (incorporation in the framework of elements sparingly soluble in alkaline medium, synthesis without alkaline cations, new possiblility to directly incorporate cations such as NH_4^+, divalent cations, the good stability of usual templates in this medium,...).

Synthesis and characterization has been specially investigated in the case of

i) MFI structural type materials with a purely siliceous framework, or with silicon partly substituted by trivalent (B, Al, Fe, Ga) or tetravalent (Ge, Ti) elements.

ii) purely siliceous and silicoaluminate zeolites of the structural types FER, TON, MTT and MTN (8).

EXPERIMENTAL

125 ml PTFE-lined steel autoclaves were used. In order to remove any solid which might have been stuck on the coating, a washing with a 50 % HF aqueous solution was performed before every new synthesis. The solid products were carefully examined under the optical polarizing microscope (morphology and size, presence of amorphous impurities). Identification was then performed using powder X-ray diffraction (Philips PW 1130 diffractometer) (1). Calcination in order to decompose and remove the template was monitored by thermogravimetry (Mettler 1 Thermoanalyzer), differential thermal analysis (Setaram M2) or differential scanning calorimetry (Setaram DSC-111). The chemical environment of atoms in the solids was studied by NMR (MAS and CP-MAS). Resonance of ^{11}B, ^{13}C, ^{19}F, ^{27}Al and ^{29}Si nuclei was recorded on a Bruker MSL-300 spectrometer operating at a 7 Tesla magnetic field. Chemical analysis of silicon and of its substituents was performed by atomic absorption spectroscopy after dissolving the material in HF (9). In some cases, a spot analysis and X-ray emission mapping of these elements in the crystals was carried out on a Castaing type (Camebax) electron microscope.

The fluorine content was determined by neutron activation or, after dissolution of the solid, by potentiometry using a F^--selective electrode (10). The catalytic activity was estimated with a methanol conversion test at 370°C and variable W.H.S.V.

RESULTS AND DISCUSSION

CRYSTALLIZATION of ZEOLITES in OH^- or in F^- MEDIA. Due to the low solubility of zeolites, the yield of crystallization is poor when it is carried out from a clear solution. To avoid this drawback, the solution is fed by continuously dissolving a solid which is mostly an oxide or hydroxide gel of the framework-forming elements T (11). Silicate, aluminate and aluminosilicate anions are thus formed by solubilization of the Si and Al sources in the presence of OH^-. The latter is the mobilizing agent used to transfer these elements through the solution : it is consumed on dissolution and regenerated on crystallization. In the new route, this role is played by fluoride (F^-) anions. The crystallization becomes thus possible in neutral and even in acidic media. The liquid phase must further contain species which will generate the microporous volume by occupying the cavities and channels of the framework. These templates are either cations to compensate the negative charges of the framework or neutral species (ion pairs, molecules). Due to their interactions, they stabilize the structure and make crystallization possible. The synthesis process can be represented as follows :

Solid reactants source
(mostly amorphous)

+OH⁻   dissolution   +F⁻

e.g., silicates   Solution containing   e.g., fluosilicates
      +   species for   +
e.g., aluminates   - framework building   e.g., fluoaluminates
                        - micropore filling

-OH⁻   polycondensation   -F⁻

                        crystalline
                        zeolite
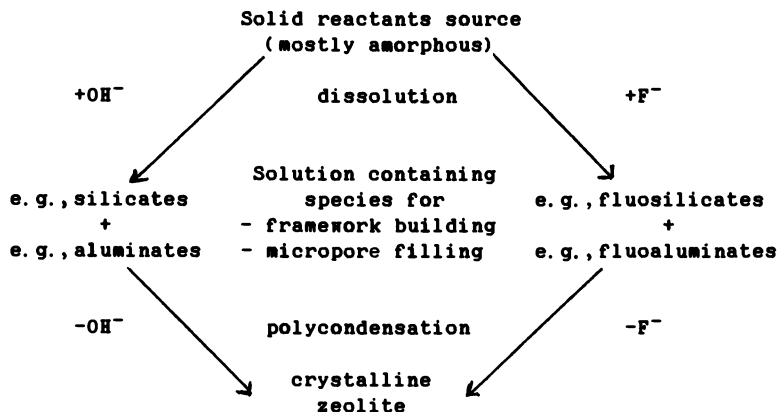
The OH⁻and F⁻ synthesis media are compared in Table I and the zeolites obtained so far in F⁻ media are listed in table II.

Table I. Comparison of the OH⁻ and F⁻ reaction media
used in zeolite synthesis

	OH⁻ medium	F⁻ medium
- pH	> 10	≈ (1-11)
- Mobilizing agents	OH⁻	F⁻
	Bases: NaOH, Pr₄OH,...	Acids: HF,...
	Salts: Na₂CO₃,...	Salts: NH₄F,...
	Molecules: amines,...	Molecules: BF₃,...
- T element sources	Oxides, hydroxides, alkoxides, salts (amorphous or crystalline solids)	
- Template	Ionic compounds (salts, bases): Pr₄NBr,...	
	Molecules : Pr₃ N,...	
- Temperature	> 20°	> 40°
- Duration	From a few hours to several days	

Table II. Zeolites obtained so far in F⁻ media

Structure type	MFI	FER	TON	MTT	LTA**	NU1**
T elements	Si	Si*	Si	Si		
	Si+Be,	Si+Al,	Si+Al*	Si+Al*	Si+Al	Si+Al
	B, Al, Ga,	Fe				
	Fe, Ge, Ti					

* difficult to synthesize ; ** non reproducible synthesis.

MFI-type ZEOLITES. A large number of MFI-type zeolites could be obtained in F⁻ media (2-4, 12-15) according to the described route (1) with $Pr_x NH^+_{(4-x)}$ (Pr = n-propyl, x = 1 to 4) templates and for the T elements quoted above. Pr_4N^+ is the best template (Table III).

Table III. Templating efficiency of $Pr_xNH^+_{(4-x)}$
in the absence and in the presence
of Al substituting for Si

	T = Si	T = Si, Al
Pr_4N^+	MFI	MFI
Pr_3NH^+	MFI	MFI
$Pr_2NH_2^+$	MTT (MFI)	MFI (MTT)
$PrNH_3^+$	MTN (FER) (MFI)	FER (MFI)

( ) generally as a secondary phase.

Crystals are always of good quality and the size exceeds generally the values observed in alkaline-type synthesis. Addition of seeds decreases the crystallization time and allows tailoring of the size. The morphology is the same as for crystals obtained by the usual alkaline route. The length/width ratio decreases with x in the template and the substitution degree of Si (16). The substitution by trivalent elements leads generally to crystals with less flat faces which indicates that crystallization occured in a more super-saturated medium.

PURELY SILICEOUS MFI-type ZEOLITES. Among the templating cations which were used, Pr_4N^+ proved to be the most efficient for easy and fast crystallization. In Table IV are given the crystallographic characteristics of the obtained siliceous MFI-type zeolites (16) as a function of the template.

Table IV. Unit cell formula and crystal parameters
of the siliceous MFI-type zeolites
(as synthesized and (*) calcined)

unit cell formula	a (Å)	b (Å)	c (Å)	ß (°)	u. c. vol.(Å)³
$\|Si_{96}O_{192}\|4Pr_4NF$	20.039(3)	19.928(3)	13.382(3)	90	5344(3)
$\|Si_{96}O_{192}\|4Pr_3NHF$ $8H_2O$	20.048(2)	19.889(2)	13.383(3)	90	5337(3)
$\|Si_{96}O_{192}\|4.8Pr_2NH_2F$ $6.5H_2O$	20.045(4)	19.886(3)	13.379(5)	90	5334(3)
$*Si_{96}O_{192}$	13.383(5)	20.107(4)	19.887(3)	90.63(3)	5351(3)

Water molecules occupy the volume of the channels which is left emp-
ty by the templates carrying less than four propyl groups. The ca-
tionic nature of the templates was established by ^{13}C NMR. Whereas
Pr_4N^+ occupies the straight and zigzag channels (17), the Pr_3NH^+
and $Pr_2NH_2^+$ cations are located preferentially in the zigzag chan-
nels. Such a conclusion could be drawn from the following observa-
tions (16) :
i) b (parallel to the straight channels) decreases, a increases
and c stays constant on going from Pr_4N^+ to $Pr_2NH_2^+$.
ii) The Pr_3NH^+ and $Pr_2NH_2^+$ species decompose according to DSC under
argon at about the same temperature (535 and 515°C). Such a tempera-
ture is much higher than the decomposition temperature of $Pr_2NH_2^+$
occluded in the MTT structure (<400°C) in which this template is
located in straight channels analogous to those of the MFI struc-
ture. A shoulder which appears on the endothermic peak at 518° in
the case of the Pr_3NH^+ template could mean that the first step of
the decomposition would be the removal of the propyl group located
in the straight channels.
iii) The ^{13}C chemical shift of the ß carbon of $Pr_2NH_2^+$ in the MFI-
type structure (δ = 18.2 ppm/TMS) is different from the correspon-
ding value for $Pr_2NH_2^+$ in the MTT-type structure (δ = 20.1 ppm/TMS).
iv) the morphology change indicates an increase of the relative
growth rate along b.
     The decrease of the resolution of the MAS NMR spectra (16) with
decreasing number of propyl groups on the template molecule could be
due
i) in the case of the ^{29}Si spectra : to an increase of the number of
defects on the framework tetrahedral sites and to a large chemical
shift distribution owing to a distribution of interactions between
the Si atoms and the organic species and the water molecules in the
channels.
ii) in the case of the ^{13}C spectra : to increasing mobility of the
template molecule and to interaction with water molecules.
     After removal of the templates by calcination, the ^{29}Si spectra
are very similar for the three samples. The large number of obser-
ved lines (from 16 to 21 depending on the synthesis and the calcina-
tion procedure) proves the good crystal quality of the materials.
     All the preceding samples crystallized after 2 to 7 days from
an AEROSIL silica at 170 - 200°C for template/Si = 0.1 - 0.5 and
F/Si = 0.25 - 1 ratios (pH = 5 - 8). It was necessary to seed (1-
2wt. % seeds) and to use Pr_4NBr when the synthesis was performed
at 80°C. The crystals obtained after 12 days were then small (1-5
µm) quasi hexagonal platelets, showing a 90° twin. Powder X-ray
diffraction showed no difference from the samples prepared between
170°C and 200°C. But the resolution of the ^{29}Si NMR spectra is com-
pletely lost for both the as-synthesized sample and the sample cal-
cined at 550°C. This reveals the presence of defects whose nature
and number could, however, not be determined yet. Nevertheless, as
they do not disap-pear on calcination, this could mean that empty
tetrahedral sites exist beside bridging defects.

MFI-type zeolites with Si PARTLY SUBSTITUTED by T^{III}(T=B, Al, Fe, Ga).
The fluoride route can be used to prepare MFI-type zeolites with

trivalent elements in the framework $(3, 4, 12, 15)$. If T^{III} = B, Al, Fe or Ga (or a combination of these elements), the Si^{IV}/T^{III} ratio varies with synthesis conditions and is always larger than about 10. Beside the Si^{IV}/T^{III} ratio in the reaction mixture, factors favouring incorporation of the T^{III} elements are : increasing of the crystallization temperature and minimizing the $F/(Si^{IV}+T^{III})$ ratio.

This trend, illustrated by some values concerning the incorporation of Al^{III} in Table V, seems to be connected with the nature of the ligands in the T^{III} element complexes in the solution. The polycondensation reactions are probably unfavoured when the $F/(OH, H_2O)$ ratio in these complexes is too high.

Table V. Influence of the F/Si ratio and temperature on the Si/Al ratio in the MFI-type zeolites

(Si/Al) (initial)	F/Si	$\theta(°C)$	% Al (in the zeolite)	Si/Al (in the zeolite)
7	1	150	1.3	30
7	1	200	1.7	19
7	0.25	190	2.5	15
12	1	80	0.3	110
12	1	150	0.9	43
12	1	200	1.3	30
12	0.25	150	1.6	24
12	0.25	200	1.8	21

A study of the distribution of the elements within the crystals could be achieved by X-ray emission mapping, owing to their large size. The most homogeneous intra- and intercrystalline compositions are those with a Si^{IV}/T^{III} ratio between about 20 and 30. This corresponds to nearly 4 T^{III}, i.e., 4 negative charges balanced by the 4 alkylammonium cations in the unit cell. Homogeneity decreases when Si^{IV}/T^{III} increases. There is a concentration gradient ; the core of the crystals being richer in T^{III} than the outer shell. This gradient weakens from Ga^{III} to Fe^{III} and Al^{III}. The stability constants of the fluoride complexes of these elements are increasing in the same order (18). (Table VI)

Table VI. Stability constants of the fluoride complexes for Ga^{III}, Fe^{III} and Al^{III}

	Ga^{III}	Fe^{III}	Al^{III}
pK_1	4.4–4.9	5.2	6.1
pK_2	3.8	3.9	5

(pK_n related to $T^{3+}+n\ F^- \rightleftharpoons (TF_n)^{3-n}$)
In the case of the less stable gallium complexes, the element

will enter the framework quickly, especially if all the gallium is present in the solution. The great stability of fluoaluminate complexes reduces the activity of the "useful species" and hence hinders the rapid incorporation of Al.

When the two elements are competing, it can be shown by X-ray emission mapping that the core of the crystal is saturated with Ga and that Al follows Ga towards the outside (Figure 1). But the degree of substitution and the importance of the segregation will depend on both $T_{Al}^{III}/T_{Ga}^{III}$ and $T_{Si}^{IV}/(T_{Al}^{III} + T_{Ga}^{III})$ ratios in the reaction mixture. Thus, if these ratios are lower than about 1 and 30 respectively, Ga only will be present in the crystals.

The concentration gradient of T^{III} in the crystal can be strongly reduced when Si^{IV} and T^{III} are in the same reactive solid source. Its dissolution, as crystallization progresses, keeps the activity of the elements at a nearly constant level. This is illustrated in the case of the crystallization of Fe^{III}-containing MFI-type zeolites. In Figure 2 can be compared the iron distributions in two zeolites prepared, one from a (Si,Fe)-hydrogel obtained by tetraethoxysilane hydrolysis in the presence of a ferric salt and distillation of the ethanol, the other from a mixture of AEROSIL silica and a ferric salt solution (19). A starting Si/Fe ratio of 70 was used for both experiments and was found too by chemical analysis of the two crystalline samples. It can be seen that the distribution is homogeneous in the first case (Figure 2a,b). On the other hand, the crystals prepared with the AEROSIL silica are heterogeneous (Figure 2c, d) : all the iron which was available in the solution was built in from the outset of the crystallization (iron-rich core and silicon-rich outer shell).

When the synthesis is made in the presence of a divalent cation, such as Co^{2+} or Mg^{2+}, these elements are found in the zeolite crystals. In samples containing from 2.5 to 5 Al/unit cell there are from 0.2 to 1.4 Co or Mg depending on the composition of the reaction mixture (20). These elements are probably in the cationic form in the channels and not in the framework sites as in the pale-blue samples synthesized from alkaline gels with a low Co/Si ratio (21). The cobalt-containing samples are indeed pink-orange before and after removal of the template. This is the colour of the octahedrally coordinated cobalt (II) in aqueous solution. After calcination, the divalent cations can be exchanged with protons of strong acid solutions.

-MFI-type zeolites with Si^{IV} SUBSTITUTED by Ge^{IV} or Ti^{IV}. High substitution degrees could be reached with germanium by using the fluoride synthesis route (up to Ge/Si=2/3) (14). To our knowledge, such values have never been observed previously for the MFI-type structure.

The most favourable pH range lies between 9 and 11. Other oxides containing the main part of Ge co-precipitate with the MFI-type zeolites in neutral or acidic medium. In a very alkaline medium, the formation of soluble germanates restricts the incorporation of germanium in the zeolite. Moreover if the pH is adjusted with alkali or ammonium hydroxide, the corresponding germanates admix with an almost purely siliceous MFI-type zeolite. These difficulties can be
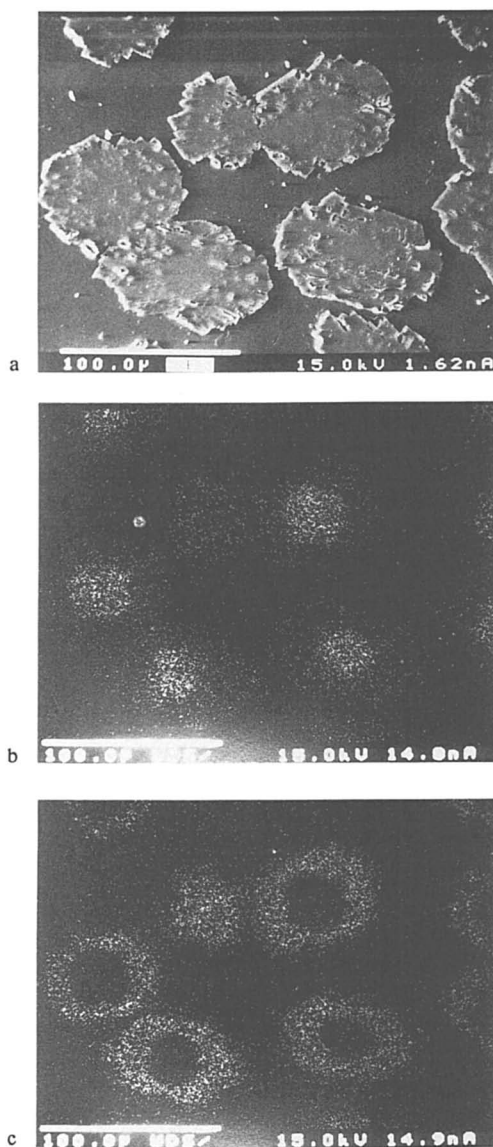
Figure 1 : Section across |Ga,Al,Si|-MFI crystals (a) scanning electron micrograph ; X-ray emission mapping of (b) Ga and (c) Al.
⊢————————⊣ 100 μm
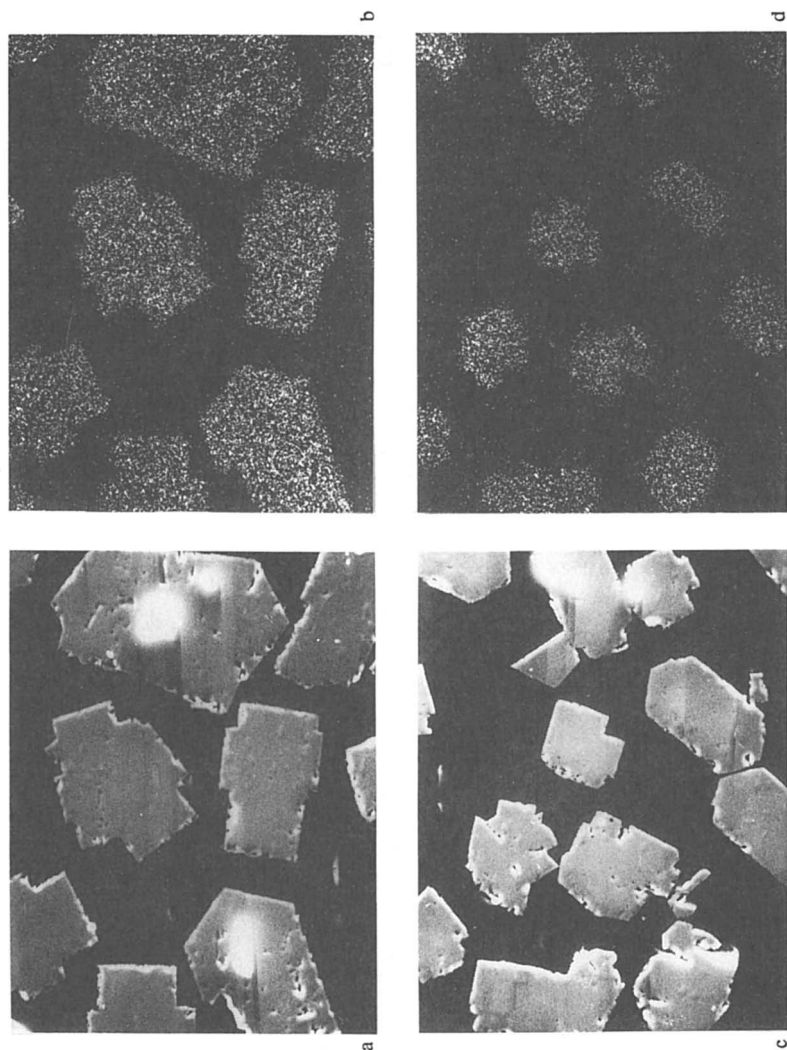
Figure 2 : (a,c) Scanning electron micrographs and (b,d) X-ray emission mapping of Fe in sections across (a,b) homogeneous and (c,d) heterogeneous |Fe, Si| -MFI crystals.

avoided if the pH is adjusted near 10 with an amine such as CH_3NH_2. Under such conditions the presence of F^- allows crystallization to occur within 15 hours at 180°C, with the reaction mixture $GeCl_4$; SiO_2 ; HF ; $0.5 NPr_4Br$; $8 CH_3NH_2$; $35 H_2O$.

The orthorhombic crystals transform into monoclinic ones after elimination of the template at 550°C, in air. Unit cell parameters of the monoclinic materials are a function of the degree of substitution x (Ge/96 tetrahedra) (Table VII).

Table VII. Unit-cell parameters of the monoclinic materials (calcined) vs. the number x of Ge in the unit cell

x	a_o (Å)	b_o (Å)	c_o (Å)	ß (°)	V(Å^3)
0	13.379	20.098	19.878	90.58	5345
17	13.428	20.137	19.939	90.57	5391
32.8*	13.455	20.180	19.968	90.51	5428

* crystals from the reaction mixture given in the text.

The monoclinic-orthorhombic transition temperature of the calcined samples increases linearly from ≈ 80°C (x=0) to ≈ 250°C (x=32.8). It should be noted that the reverse phenomenon is observed when trivalent elements (B, Al, Fe...) are incorporated into MFI-type zeolites : the transition temperature decreases with the substitution degree (22).

The investigation of the substitution of Ti^{IV} for Si^{IV} in the structure of MFI-type zeolites is in progress. The first results show a lower substitution degree, similar to the values obtained with the trivalent elements. This probably results from the stability difference between the germanium and the titanium fluoro-complexes.

FER-, TON-and MTT-type ZEOLITES. The use of amines instead of quaternary ammoniums yields three pentasil zeolites with the FER, TON and MTT structural types (23-25). The first two are obtained with the same amine families (aliphatic linear mono-or diamines). A low Si/Al ratio leads to the FER structure, in agreement with VALYOCSIK et al. (26), whereas a high ratio favours the TON structure. The influence of the carbon chain length (x) of the amine is shown in Figure 3. The composition of the reaction mixture was : (1-y) SiO_2 ; y Al_2O_3 ; 10 H_2O ; $3[CH_3(CH_2)_{x-1} NH_2, HF]$ or $1[NH_2(CH_2)x NH_2, 2HF]$.

For the FER-type zeolite, y ≈ 0.066 and synthesis duration was 14 days at 170°C in a static mode. The TON-type zeolite as obtained for y ≈ 0 and heating for 3 days at 170°C under agitation with 5 wt. % seeds (with respect to silica).

By using monoamines, FER-type and TON-type materials were well crystallized for x equal to 3 or 4 and 4 or 5 respectively. With diamines, the best results were obtained with x equal to 4 or 5 for the FER-type and with x equal to 5 or 6 for the TON-type materials.
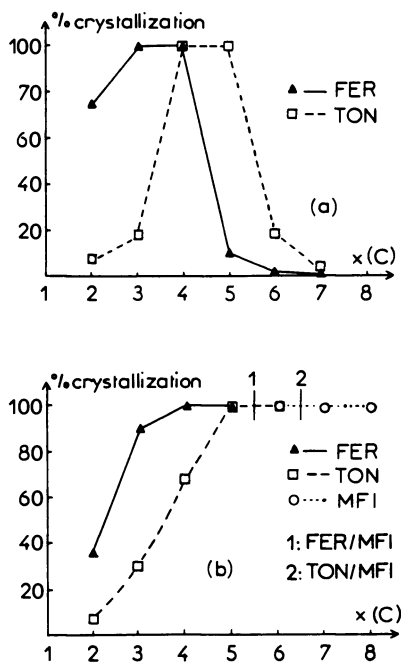
Figure 3 : Crystallization (%) of FER(▲) TON(□) and MFI (o) type materials as a function of the number x of carbons in the mono-amines (a) and in the diamines (b) used as templates.

It is worth noting that with the diamines, MFI-type zeolite was obtained instead of FER-type zeolite for x = 6 and of TON-type zeolite for x = 7. The influence of the agitation and the presence of seeds adds to the influence of the Si/Al ratio in the reaction mixture in directing the crystallization towards FER- or TON types. These three factors were investigated at 170°C for reaction mixtures containing n-butylamine which is able to produce the two structures (Figure 4).

It can be seen that an agitated medium is markedly favourable to the TON-type zeolite, the FER-type zeolite being less sensitive to this factor. The presence of seeds increases the crystallization rate for both zeolites. FER-type zeolites containing Co^{2+} or Mg^{2+} could be prepared with Co^{2+} or Mg^{2+}- exchanged aluminosilicate gels (20). In addition to the above-mentioned templates for TON-type zeolites, two other amines, di-n pentylamine and 1,4-diamino n-pentane, yield the same structure.

A MTT-type structure is obtained by using one of the three following amines, di-propylamine, isopropylamine or pyrrolidine, as template under the same conditions as for the synthesis of TON-type zeolites.

As for all other zeolite crystals prepared with the fluoride route, the crystals of the structure types FER TON and MTT are of very large size in the absence of seeds. The FER-type crystals are aggregates of plates, the size of which can be larger than 200 μm. The other structure types (TON and MTT) show a fibrous aspect, the length being over 100 μm for a diameter below 1 μm (Figure 5).

The chemical analysis and the ^{13}C NMR results show that the template is always present in the cationic form (compensation of framework charges and/or F^- anions in the channels).

OTHER MICROPOROUS SOLIDS. Among the other zeolites which have been obtained by using the fluoride route at pH ≈ 7, appear a MTN-type clathrasil (27), the zeolites NU1 (27) and A (28), and an unknown phase which is probably a novel clathrasil (Figure 5). The MTN-type clathrasil (Figure 5) crystallizes in the presence of Me_4N^+ cations for a Si/Al ratio from 7 to infinity, whereas the zeolite NU1 (Figure 5) is obtained preferentially for Si/Al < 100. It should be noted that the reproducibility of the synthesis of the latter is very poor, the clathrasil phase being formed easily instead. The ^{13}C CP-MAS NMR study of the occluded template shows the presence of Me_4N^+ and Me_3NH^+ cations in the clathrasil, while Me_4N^+ alone is observed for the zeolite NU1. It may thus be assumed that the decomposition of Me_4N^+ into Me_3NH^+ is responsible for the difficult crystallization of zeolite NU1.

The crystallization of zeolite A (structure type LTA) for a pH value lying between 5 and 8 at 170°C is surprising (20). It was obtained from an aluminosilicate gel (Al/Si= 1.2-1.5 ; Na/Al= 0.6-1.2) which was prepared by mixing sodium aluminate and silicate solutions at 5°C. After 3h aging, the pH was adjusted to 3 by using conc. HNO3. The gel was then filtered, washed and dried at 80°C. The reaction mixture was completed by adding water (H_2O/Si = 80-150), a halide (HF/Si = 0.3 or NaCl/Si = 0.8) and zeolite A seeds (2-4 wt. % of the starting gel). The chemical composition and the morphology of the crystals obtained after heating for 264 h at 170°C are

the usual ones (Na/Al=1 ; Si/Al = 1) (28). The thermal stability is however ≈ 100°C higher than the stability of a normal zeolite A. Less defects are presumably present in the material prepared in the neutral medium.

The FLUORINE element in the ZEOLITES SYNTHESIZED in the PRESENCE of F⁻. The fluorine content of the samples is very variable ; it depends on the structure type, on the composition and on the post-synthesis chemical or heat treatments. It may reach 7 wt. %. In the highly siliceous materials, namely in the MFI-type samples, the F content is equal to 1-1.2 wt. % which corresponds to a F/(charge of the template cations) ratio close to one. It may thus be assumed that F is located essentially in the channels as ion pairs. After calcination in air, the F content approaches zero ; however when it is performed in argon, the concentration is close to 0.2 wt. %. For samples containing other elements beside Si, the residual fluorine concentration may be larger. For instance, in the case of a MFI-type sample with a Si/Al ratio of 90 prepared in the presence of Pr_4NBr, there are 0.35 wt. % F after calcination. The F/Al ratio is equal to 1 and the cation exchange capacity approaches 0 (29). No OH bands corresponding to $\equiv Si - \overset{H}{\underset{}{Al}} - Al \equiv$ strong acid sites are visible on the IR spectrum. It may thus be assumed that fluorine is in the framework ($\equiv Si - F - Al \equiv$ or $\equiv Si - F...Al \equiv$). When such a sample is defluorinated by heating in 0.15 N ammonia for 14 h at 170°C and recalcined at 550°C, the resultant cation exchange capaci-ty is consistent with the Si/Al ratio. The modification may be des-cribed by the following reaction :

$$\equiv Si-F...Al\equiv \; + \quad NH_4OH \longrightarrow \; \equiv Si-\underset{H}{\overset{|}{O}}-Al\equiv \; + \quad NH_4F$$
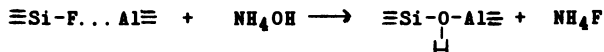
Another MFI-type sample which was obtained from a Mg^{2+} exchan-ged aluminosilicate gel in the presence of a large amount of HF ($1SiO_2$; 0.06 Al_2O_3 ; 0.03 MgO ; 0.003 Na_2O ; 1.2 Pr_3N ; $2.4HF$; 23.5 H_2O — 170°C, 300 h) contained 3.3 Al and 3 F per unit-cell after calcination at 550°C. The replacement of 1.2 Pr_3N + 2.4 HF by 1.1 Pr NH_2 + 1.1 HF in the above reaction mixture led to a FER-type material. According to chemical and thermal (TG, DTA) analysis and to the cation exchange capacity, the chemical formulae of the as-synthesized and calcined samples are respectively the following :

$$Mg_{0.2}(PrNH_3)_{1.8}\left[Si_{33.5}Al_{2.5}O_{71.7}F_{0.3}\right] \; 1.4PrNH_3F \; 1.5H_2O$$
$$\text{and} \; Mg_{0.2} \; H_{1.8}\left[Si_{33.5}Al_{2.5}O_{71.7}F_{0.3}\right] \; 18H_2O.$$
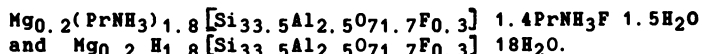
It may then be concluded that 12 % of the negative charges in-duced by Al are not revealed owing to the presence of F (20).

The effect of the addition of F to the starting mixture on the adsorption and the catalytic properties is quite significant. For example, the hydrophobicity of purely siliceous samples is conside-rably enhanced (less Si-OH groups). Figure 6 shows that such a ma-terial adsorbs more n-propanol from a dilute n-propanol + water solution than a material which was prepared in alkaline medium.

The complete or partial cancelling by F of the negative charges induced by the incorporation of trivalent elements such as Al influ-

```
↑
| 20 days (static)                    TON 50%. TON 50%.
|
| FER100%.FER100%.FER+TON                 TON 20%.
| 10
|
|•FER 90%.
|   7      30      35     50     300  Si/Al(starting)
|────────────────────────────────────────────────────→
|                                  •TON100%.
|
| FER60%.              TON100%.         TON 95%.
| 10 days(agitated)   (• in presence of seeds)
↓
```
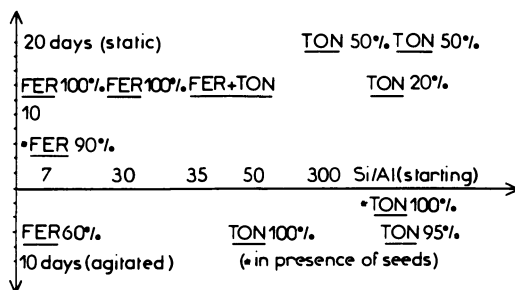
Figure 4 : Influence of starting Si/Al ratio, time, agitation and seeding on FER- and TON-type materials crystallization with n-butylamine template.
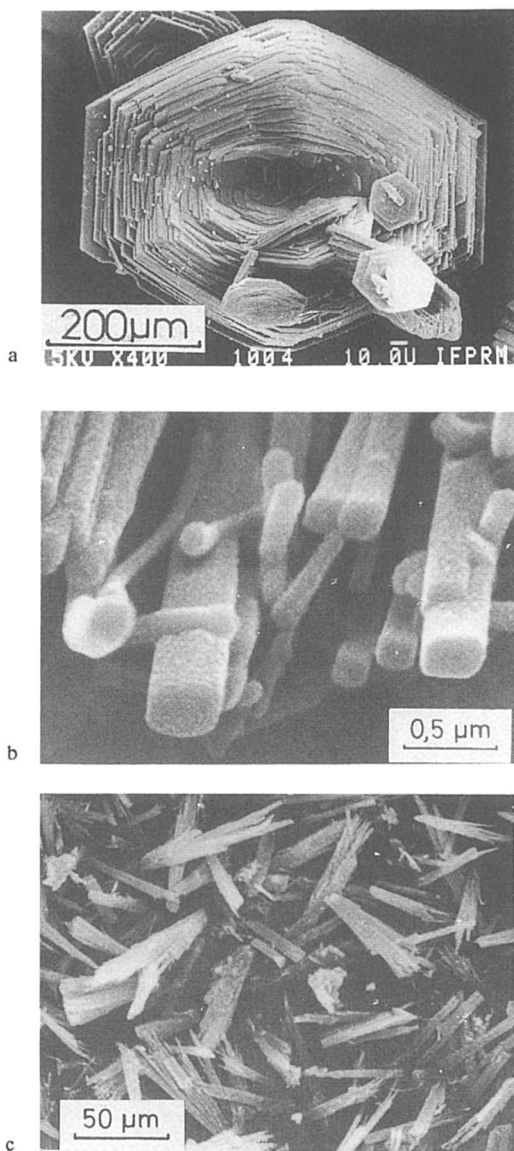
Figure 5. Scanning electron micrographs of (a) FER-, (b) TON-, and (c) MTT-type materials. Continued on next page.

Figure 5. Continued. Scanning electron micrographs of (d) MTN-, (e) NU1-type materials, and (f) of a novel clathrasil.
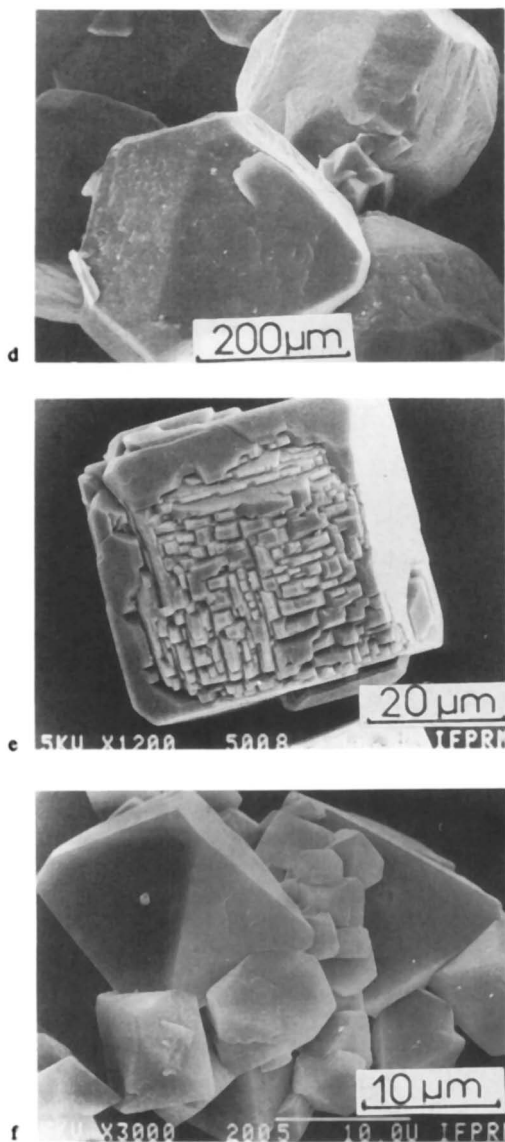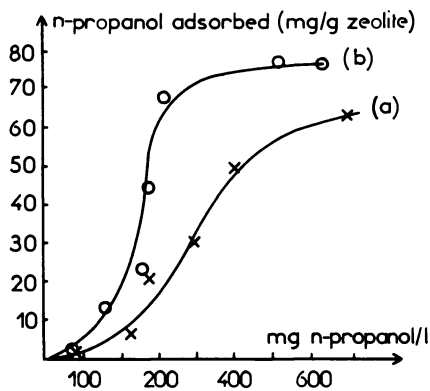
Figure 6 : n-propanol adsorption (from dilute aqueous n-propanol solutions) of MFI-type zeolites prepared (a) in alkaline medium and (b) in fluoride medium .

ences the acid catalysis properties. It was found, for example, that methanol to hydrocarbon conversion was very low on the above-mentioned Mg-MFI sample containing 3.3 Al and 3 F per unit cell. The conversion reached however 100 % on the defluorinated recalcined sample. A FER-type sample which was prepared by using conditions close to the conditions employed for the above FER-type sample (2.5Al and 0.3F per unit cell) but containing Co^{2+} instead of Mg^{2+}, showed a methanol conversion yield of about 100 %, which decreased slowly with increasing time-on-stream (90 % conversion after 26h, W.H.S.V. = 0.4). The activity of the same sample which was first de-fluorinated and recalcined, decreased more rapidly owing to strong and rapid coking on the acid sites which were available from the outset. In contrast, in the case of the non-defluorinated sample, the formation of water during the conversion leads to the gradual elimination of F and thus makes the acid sites slowly available.

CONCLUSIONS

By using fluoride anions in zeolite synthesis, it is possible to extend the usual alkaline pH range to a neutral or acidic one.
    The replacement of OH^- by F^- for the formation of soluble fra-mework building species facilitates the incorporation of T elements which are sparingly soluble (e.g., Fe^{III}, Ti^{IV}) or do not polycon-densate easily (e.g., Ge^{IV}) in alkaline medium. The nature of the soluble species is still not well known, i.e., coordination and type of the other ligands beside F^- (e.g., H_2O, OH). Particularly, the F/(other ligands) ratio seems to be critical. A compromise has to be found, a low fluoride content hinders solubilization and a high content prevents polycondensation. The compromise leads to systems which are less supersaturated than for alkaline media. Hen-ce, fewer metastable phases are obtained. This is however also an advantage since better controlled nucleation and slower growth rate yield crystals with fewer defects and with controlled size. The relative stability of the fluoro-complexes of the elements which were studied, is strongly in favour of silicon incorporation. This F^- route is therefore well suited for obtaining silica-rich mater-ials, i.e., of the pentasil type. But the small number of framework negative charges leads to fewer templating cation-framework inter-actions. This, and the lower supersaturation, make the synthesis more critical and enhance the role of the template for the stabili-zation of the zeolite stucture. Choice of the template becomes thus more critical. A good steric and chemical fit to the framework has to be reached in order to increase the favourable interactions and also those between the species which are present in the pores. It should be mentioned further that many organic species such as the quaternary ammonium ions are more stable in a neutral medium than in an alkaline one.
    Neutral or acidic pH values make it possible to start with ca-tions which are sparingly soluble in alkaline medium (e.g. divalent cations) or do not exist in such a medium (e.g. NH_4^+). When the NH_4^+ cations replace the usual alkali cations, the materials obtained are therefore alkali-free and a simple calcination yields the acidic form of the zeolite. The cation exchange step is thus bypassed.

Finally a modification of exchange, adsorption and catalytic properties has been found (e.g., increased hydophobicity, cancelling of framework charges).

We thank Dr Z. GABELICA from Namur University for his contribution to the study of the germanium incorporation and Miss A.C. FAUST for the synthesis and the analysis of many samples.

LITERATURE CITED

1. J.L. Guth, H. Kessler, R. Wey, in "New Developments in Zeolite Science and Technology, Proceedings of the 7th Int. Zeolite Conf.". Ed. Y. Murakami, A. Iijima, J.W. Ward, Tokyo 1986, Kodensha-Elsevier, p.121.

2. J.L. Guth, H. Kessler, M. Bourgogne, R. Wey, G.Szabo, Fr. Pat. Appl. 84-07773, 1984.

3. J.L. Guth, H. Kessler, M. Bourgogne, R. Wey, G. Szabo, Fr. Pat. Appl. 84-11521, 1984.

4. J.L. Guth, H. Kessler, R. Wey, A.C. Faust, Fr. Pat. Appl. 85-07978, 1985.

5. H. Kessler, J.M. Chezeau, J.L. Guth, G. Coudurier, H. Strub, Zeolites, 1987, 7(4) 360-366.

6. M. Soulard, S. Bilger, H. Kessler, J.L. Guth, Zeolites, 1987, 7 (5) 463-70.

7. F. Raatz, unpublished results.

8. W.M. MEIER, D.H. OLSON, Atlas of Zeolite Structure Types, 1987, Butterworth.

9. L. Delmotte, Thesis, UHA Mulhouse, 1985.

10. J.L. Guth, R. Wey, Bull. Soc. Fr. Minéralogie et Cristallographie, 92 105-107, 1969.

11. J.L. Guth, P. Caullet, J. Chimie Physique, 1986, 83(3) 155-175.

12. J. Patarin, J.L. Guth, H. Kessler, G. Coudurier, F. Raatz, Fr. Pat. Appl. 86-17711, 1986.

13. J.L. Guth, H. Kessler, J.M. Popa, Fr. Pat. Appl. 87-07187, 1987.

14. Z. Gabelica, J.L. Guth, Fr. Pat. Appl. 88-04367, 1988.

15. A. Seive, J.L. Guth, F.Raatz, L. Petit, Fr. Pat. Appl. 88-06509, 1988.

16. J. Patarin, Thesis, UHA Mulhouse, 1988 ; J. Patarin, M. Soulard, H. Kessler, J.L. Guth, J. Baron, Zeolites (accepted).

17. G.D.Price, J.J. Pluth, J.V. Smith, J.M. Bennet, R.L. Patton, J.A.C.S., 1982, 104 5971-77.

18. A.M. Bond, G.T. Hefter, "Critical survey of stability constants and related thermodynamic data of fluoride complexes in aqueous solutions" Ed. IUPAC, 1980, Pergamon Press.

19. J. Patarin in "Précurseurs moléculaires de matériaux inorganiques - Ecole d'été, Procédés Sol-Gel" Carcans Maubuisson, France, 1987.

20. J.M. Higel, Thesis, UHA Mulhouse , 1987.

21. J.A. Rossin, C. Saldarriaga, M.E. Davis, Zeolites, 1987, 7(4) 295-300.

22. D.G. Hay, H. Jaeger, J.C.S., Chem. Com., 1984, 1433-35.

23. J.L. Guth, A.C. Faust, F. Raatz, J.M. Lamblin, Fr. Pat. Appl. 86-16362, 1986.

24. J. Patarin, J. M. Lamblin, A. C. Faust, J. L. Guth, F. Raatz, Fr. Pat. Appl. 88-06841, 1988.
25. J. Patarin, J. L. Lamblin, A. C. Faust, J. L. Guth, F. Raatz, Fr. Pat. Appl. 88-08105, 1988.
26. E. W. Valyocsik, L. D. Rollmann, <u>Zeolites</u>, 1985, <u>5</u>, 123-125.
27. P. A. Jacobs, J. A. Martens, "<u>Synthesis of high-silica aluminosilicate zeolites</u>", Studies in Surface Science and Catalysis, 1987, Vol. 33, Elsevier, p. 330 and p. 361.
28. D. W. Breck "<u>Zeolite Molecular Sieves. Structure Chemistry and Use</u>", 1974, John Wiley and Sons., p. 272.
29. L. Petit, J. L. Guth, H. Kessler, F. Raatz, Réunion du Groupe Français des Zéolithes, Eveux, 1988 (Poster).

Chapter 14

Cancrinite Crystallization from Alkaline Aluminosilicate Systems Containing Large and Small Cations

C. Colella[1] and M. de' Gennaro[2]

[1]Dipartimento di Chimica, Ingegneria Chimica e Materiali, Università de L'Aquila, 67040 Monteluco di Roio (AQ), Italy
[2]Dipartimento di Scienze della Terra, Università degli Studi di Napoli, Via Mezzocannone 8, 80138 Naples, Italy

Cancrinite crystallization, promoted by the joint pre-
sence in the reaction system of lithium and a large
cation, has been thoroughly investigated, pointing
out the specificity of the cationic couple for the synthe-
sized phase. The products obtained have been characte-
rized by means of X-ray diffraction, chemical, micro-
scopy and thermal analyses. A hypothesis on the mecha-
nism of cancrinite formation has been worked out, also
on the basis of the preliminary results of structural
analysis.

The specificity cation-structure in framework silicates
crystallization has been recognized for a long time, as most
synthesized phases form only if a given cation is present in the
reaction mixture (1). Although it is very seldom clear the mechanism
through which the single cations develop their action, it is likely
that the main role played by them is a templating one, as it is
evident in some instances, especially when syntheses are performed
in the presence of organic cations (1). Referring to syntheses in
polycationic systems, there is evidence that a single cation, often
the larger one (2), normally plays the structure-directing role;
nevertheless cases are known of cationic couples which determine the
formation of specific frameworks, for instance zeolites RHO,
synthesized in mixed Na,Cs systems (3), edingtonite, formed from
Ba+Li (4), EAB and mazzite, both of them obtained in the presence of
sodium and tetramethylammonium (TMA) (5).
    A recent paper (6) reports an interesting case of a felspathoid,
cancrinite, previously obtained in typically sodic environments with
(7) or without added salts (8), synthesized in bicationic systems
formed by lithium and a large alkaline cation (rubidium or cesium).
Such syntheses suggest that cancrinite is a further phase, the

formation of which may depend on the joint presence of two cations and, moreover, that the coupling of a large and a small alkaline cation produces the same result of the presence of sodium hydroxide alone or plus a sodium salt.

This works aims, first of all, to strengthen this assertion, optimizing Cs,Li- and Rb,Li-cancrinite crystallization and extending the investigation also to the couple Tl,Li, inasmuch as Tl^+ ionic radius is very close to that of Rb^+ and as the three large cations behave also in other occasions in a similar way (see for instance the formation of phases belonging to the structural type ABW (9)). Further purposes of this study are: i) to verify that cationic couples, excluding sodium and different from the above three, do not give rise to cancrinite; ii) to characterize the synthesized cancrinites from a physico-chemical point of view; iii) to work out a hypotesis on the role played by the two cations in cancrinite formation.

Experimental

Referring to the reaction conditions previously found (6), synthesis runs were performed at 200°C and at autogenous pressure in sealed teflon containers, rotated for programmed times (usually one day) in a thermostated oven.Particular care has been taken in avoiding the contact of the reaction magma with atmospheric carbon dioxide. Reagent grade chemicals were used for preparing the reaction mixtures and the solutions for ion exchange tests (see below): silica suspension (Ludox, 40% SiO_2), dried aluminum hydroxide (Serva, 61.35% Al_2O_3), concentrated RbOH or CsOH solution (Alfa Products), Tl_2SO_4 (Fluka), $LiOH \cdot H_2O$, NaOH, KOH, $Ba(OH)_2 \cdot 8H_2O$ (Merck), TMA hydroxide solution (Merck), ammonium hydroxide solution (Carlo Erba).

The oxide batch composition tested for cancrinite crystallization was as follows:

$$n\ Li_2O \cdot mMe_2O \cdot Al_2O_3 \cdot 2SiO_2 \cdot 100\text{--}110\ H_2O$$
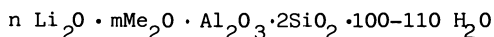
where Me is Rb, Cs, Tl or mixtures of them, n ranges between 1 and 2, m between 2 and 10. Referring in particular to the runs in mixed Li,Ba and Li,NH_4 systems, the ratios 2Ba/2Ba+Li and NH_4/NH_4+Li were systematically varied, ceteris paribus, between 0 and 1, while the total alkalinity ranged between 1 and 4.

At the end of the reaction the products were separated from mother liquors by filtration, washed and dried overnight at 100°C.

X-ray powder diffraction investigations were made in cooperation with P. Norby (Oslo University) and I.G. and E. Krogh Andersen (Odense University). For phase identification and lattice costants determination a Guinier-Hagg camera has been used ($CuK\alpha_1$ =1.5451 Å (10); quartz internal standard a=4.91309 Å, c=5.40426 Å (11). The diagrams were indexed and lattice constants refined by least square

calculations (programme PARAM (12)). Extra framework cation positions were determined by the programmes in the XRS–82 system (13). The data used for these determinations were obtained with a Siemens D5000 diffractometer 4° < 2ϑ<90°, step scan 0.02°, CuKα radiation).The Li,Cs–C (see below) structure has been refined. Refinement of the Li,Tl–C structure is not yet finished, but some conclusive results have been obtained.

Electron microscope examination of the samples was performed on selected Au-coated products, using a Cambridge Stereoscan 250 TP apparatus.

Thermal analysis was carried out on selected samples using a Netzsch STA thermoanalyzer mod. 409.

Ion exchange tests were carried out on selected cancrinites, suspending 0.2 g samples in 60 ml of 1M suitable nitrate solutions and rotating them in teflon containers at 100°C for about 4–6 hours. Solutions were replaced several times, until no change has been recorded in their chemical constitution.

Chemical analyses of original solids and of liquids after ion exchange tests were made using standard procedures : Si and Al have been determined gravimetically; Li,Rb,Cs,Tl by atomic absorption spectrophotometry (Perkin–Elmer 370).

Results

Synthesis Runs. The investigation on the physico–chemical conditions which lead to cancrinite crystallization confirms the previous data (6) indicating that this phase forms in wide ranges of Li/large cation mole ratio and OH^- alkalinity. Moreover the results of the synthesis runs have pointed out that, in agreement with the hypothesis done (see introduction), thallium also shows a noteworthy ability to give rise, when mixed with lithium, to cancrinite. Preliminary tests with TlOH (Fluka) and LiOH have produced good cancrinite, but constantly contaminated by some Tl_2O_3 . So most of the further runs have been carried out using Tl_2SO_4 as source of thallium with a consequent reduction of the total alkalinity of the reaction magma. In this case research has demonstrated that at lower Li/Tl mole ratios (close to 0.2) cancrinite forms readily, while at higher ratios (about 0.7) a phase analogous to Tl–C (4) crystallizes. Runs have been performed also in ternary cation systems (lithium plus two large cations) and in quaternary ones, allowing the mole ratios between the large cations to vary,while leaving constant and equal to 0.67 the mole ratio between lithium and the sum of the other cations.The whole of the results obtained can be summarized as follows (note that the synthetic phases are referred to, indicating the cationic evironment in which they form, a capital letter symbolizing the phase, and, when known, the structure code):

-) in binary cation systems (lithium plus one large cation) cancrinite forms very readily with Cs+ (very good specimens after only four hours), easily with Tl+ , on the contrary Rb+ shows lesser aptitude to give rise to cancrinite: synthesis products are usually badly crystallized and often contain impurities (mostly a phase analogous to K-F, EDI (14);

-) in ternary cation systems it has been confirmed the superior ability of the couple Cs,Tl to those formed by Cs+Rb and Tl+Rb. It looks like Cs + and Tl+ are somewhat interchangeable, so that an optimal ratio between them for cancrinite crystallization is not easily deducible. It should be noted that runs with prevailing cesium give pollucite cocrystallization, while those with more thallium also give rise to the formation of Tl-C (see above);

-) in quaternary cation systems cancrinite formation is strongly hindered. Usually mixtures of phases are obtained with prevailing pollucite, Rb-A, ABW (6) and Tl-C or Tl-F (analogous to K-F , see above), according to the relative abundance of Cs, Rb or Tl, respectively, in the reaction magma.

Among the various cancrinite samples obtained three have been considered for further characterization, namely those formed starting from the magmas having the following oxide composition:

a) $1.4Li_2O \cdot 2.1Cs_2O \cdot Al_2O_3 \cdot 2SiO_2 \cdot 102H_2O$

b) $1.4Li_2O \cdot 7.5Tl_2O \cdot Al_2O_3 \cdot 2SiO_2 \cdot 110H_2O$

c) $1.4Li_2O \cdot 2.1Cs_2O \cdot 7.5Tl_2O \cdot Al_2O_3 \cdot 2SiO_2 \cdot 102H_2O$

The relative products have been referred to as Li,Cs-C, CAN Li,Tl-C, CAN and Li,Tl,Cs-C, CAN, respectively. Figures 1 and 2 report in particular two scanning electron micrographs of the second and the third samples, in which the exagonal cross section of the prismatic cancrinite crystals is well visibile.

Cation specificity has been tested performing syntheses in the same conditions as those giving cancrinite (see the first of three oxide compositions reported above), substituting the small or the large cation with other cations.

Table I summarizes the results obtained, pointing out that cancrinite does not form, if even one of the prescribed cations is absent. The logical exception of this, as it will be discussed later, is the system Na,Cs.

Referring in particular to Ba++ and NH_4^+ , inasmuch as their anhydrous radii are the closest among those of the cations examined, to Rb+ and Tl+ , it has been considered useful to investigate more widely on the phases synthesizable, when they are coupled with lithium (see experimental). Figures 3 and 4 report the respective crystallization fields, from which it is possible to notice that no cancrinite forms at any composition of the reaction system. The phases obtained refer to Li-A, ABW (A) and Li-K (K) (9) in both fields, Ba,Li-M, PHI (4) and Ba-P, analogous to celsian or cymrite (15) in Ba,Li field. Am denotes no crystallization.
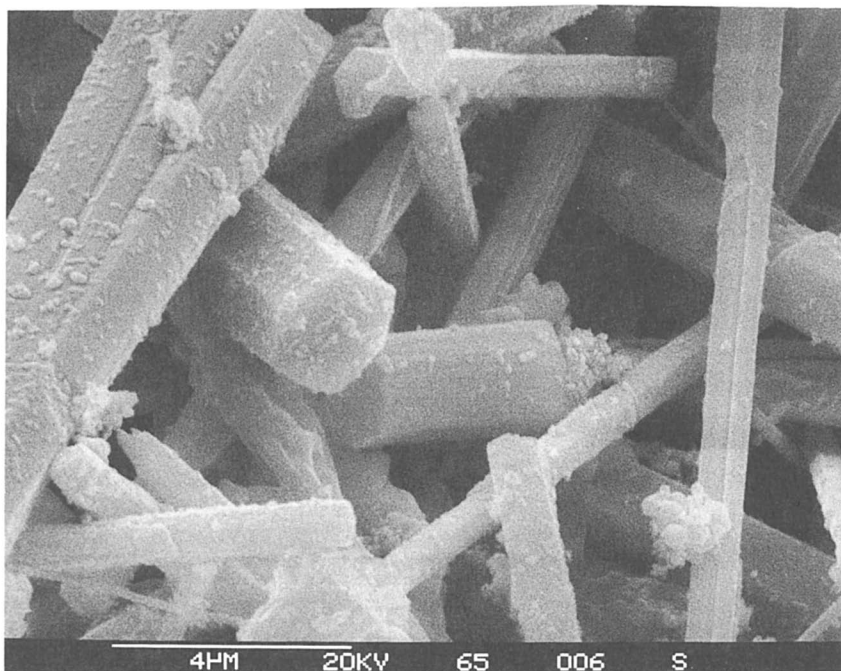
Figure 1. Scanning electron micrograph of cancrinite crystals.
Sample Li,Tl-C (see synthesis section).
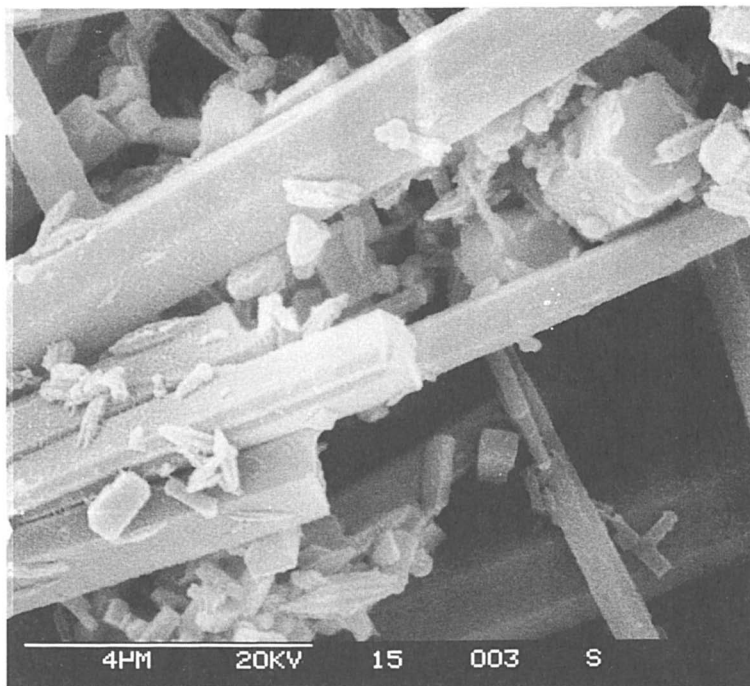
Figure 2. Scanning electron micrograph of cancrinite crystals.
Sample Li,Tl,Cs-C (see synthesis section).
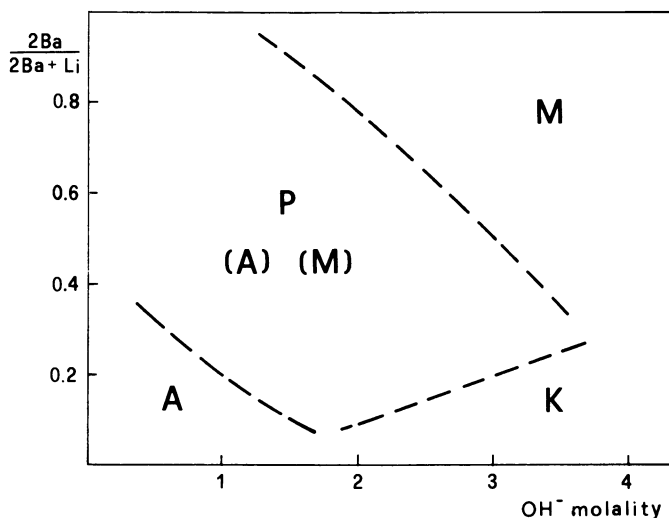
Figure 3. Crystallization field of the phases obtained from magmas with $SiO_2/Al_2O_3 = 2$, reacted for one day at 200°C in the presence of mixed barium and lithium hydroxides. A=Li-A, ABW (9); K=Li-K (9); M=Ba,Li-M, PHI (4), P=Ba-P (4, 15). Phases in parentheses cocrystallize with Ba-P, but usually in lesser amount.
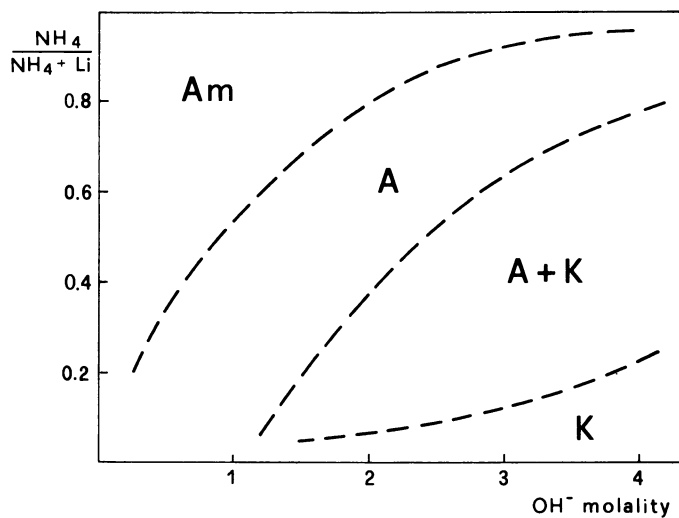
Figure 4. Crystallization field of the phases obtained from magmas with $SiO_2/Al_2O_3 = 2$, reacted for one day at 200°C in the presence of mixed ammonium and lithium hydroxides. A=Li-A, ABW (9); K=Li-K (9). Am denotes no crystallization.

Table I. Phases synthesized in the presence of cationic couples

Binary cation system	Phases obtained and structure type code	References
Li – Na	Like Na-I, SOD	8
Li – K	Like K-M, PHI	14
Li – TMA	No crystallization	–
Na – Rb	Rb-A, ABW + Na-J*	6, 8
Na – Tl	Tl-C**	4
Na – Cs	Na,Cs-C, CAN	This paper
K – Rb	K-F, EDI + Rb-A, ABW	14, 6
K – Tl	Tl –C**	4
K – Cs	Cs-A, ABW	6
Rb – Tl	Rb-A, ABW	6
Rb – Cs	Rb-A, ABW + Cs-P, ANA	6
Cs – Tl	Cs-A, ABW + Cs-P, ANA	6

(*) Hydrated nepheline; (**) Unknown nature.

X-Ray Diffraction Data. The X-ray diffraction powder patterns of the cancrinites, referred to in the synthesis section, have been indexed in accordance with the space group $P6_3$ as found by Jarchow (16). Table II reports the cell parameters of the three synthetic cancrinite samples and of a natural sample (16) for comparison.

Chemical Analysis. Data for the three cancrinite samples on anhydrous basis are shown in Table III. Values of water content are reported in the next section.

Table II. Cell parameters of cancrinite-like phases*

Phase	Cell dimensions, Å		
	a	b	γ
Li,Cs–C	12.433(1)	4.969(1)	120°
Li,Tl–C	12.442(1)	4.988(1)	120°
Li,Tl,Cs–C	12.450(1)	4.998(1)	120°
Cancrinite (16)	12.75	5.1	120°

(*) Standard deviation in parentheses.

Si/Al ratio is near 1 in any sample, in good agreement with the value found in the mineral. Notice that in a previous paper (6) a higher value had been reported, possibly because of the presence in the synthesized products of some unreacted silica, either in mixture

or included (see also Ref. 17). As it is deducible from the data of Table IV, all the cancrinites appear strongly selective for lithium. When the two large cations are in competition, Cs^+ is preferred to Tl^+, in agreement with the already mentioned greater ability of Cs^+ to promote cancrinite crystallization. The data are however consistent with a different role played by the small and the large cation, being evident that the latter may occupy only well defined sites in the structure (most likely cancrinite cages).

Table III. Chemical analysis and molar ratio data for cancrinite samples

Sample	Wt. percent (anhydrous basis)				
	Li_2O	Cs_2O	Tl_2O	Al_2O_3	SiO_2
Li,Cs-C	7.21	22.10	–	32.37	38.31
Li,Tl-C	2.98	–	49.32	21.39	26.30
Li,Tl,Cs-C	5.34	10.11	22.91	28.21	33.43
	Moles per mole Al_2O_3				
Li,Cs-C	0.76	0.25	–	1.00	2.01
Li,Tl-C	0.47	–	0.55	1.00	2.09
Li,Tl,Cs-C	0.65	0.13	0.20	1.00	2.01

Thermal Analysis Data. The thermal behaviour of the synthesized cancrinites is not very significant. The phases contain small amounts of water (roughly 2-2.5%) which is removed smoothly between room temperature and several hundred degrees centigrade. Water is in part readsorbable, but only if the thermal treatment does not exceed 400°C. Thermal stability is limited at about 500°C for Li,Tl-C, while the sample containing cesium appears slightly more stable. The three cancrinites melt at about 900°C.

Ion Exchange Studies. Table V summarizes the data obtained ion exchanging exhaustively the three cancrinite samples for Tl^+, Li^+ or Na^+. It is easily observed that cesium contained in the framework is practically not exchangeable; thallium can substitute for lithium or be substituted by it only partly; only minor amounts of sodium can enter the framework preferably in place of thallium. These observations suggest that Cs^+ and some Tl^+ are located in inaccessible sites (cancrinite cages); Li^+ and some Tl^+ are in the large channel, even if it appears a little obscure why lithium does not exchange for sodium. The explanation of this is given in charge to structural analysis.

Table IV. Comparison between cation molar ratios in the reaction
          magmas and in the crystallized cancrinites

Amorphous and crystalline phases	Cs/Li	Cation molar ratios Tl/Li	Cs+Tl/Li
Magma a	1.50	–	–
Li,Cs–C	0.33	–	–
Magma b	–	5.36	–
Li,Tl–C	–	1.17	–
Magme c	1.50	5.36	6.86
Li,Tl,Cs–C	0.20	0.31	0.51

Table V. Cation molar fractions in the original cancrinite samples
          and after ion exchange

Cancrinite sample	X Li	X Cs	X Tl	X Na
Li,Cs–C	0.760	0.246	–	–
Tl–exchanged	0.568	0.213	0.225	–
Li–exchanged	0.771	0.235	–	–
Na–exchanged	0.720	0.246	–	0.040
Li,Tl–C	0.475	–	0.554	–
Tl–exchanged	0.402	–	0.627	–
Li–exchanged	0.622	–	0.407	–
Na–exchanged	0.466	–	0.395	0.169
Li,Cs,Tl–C	0.648	0.130	0.196	–
Tl–exchanged	0.648	0.130	0.196	–
Li–exchanged	0.768	0.122	0.083	–
Na–exchanged	0.644	0.130	0.180	0.020

The structure of Li,Cs–C and Li,Tl–C. The anion lattice of Li,Cs–C
and Li,Tl–C is similar to that found by Jarchow (16). No attempt has
been made to determine whether the Si/Al arrangement is ordered.

In the Li,Cs–C all cesium ions are located in the cancrinite
cages. They have 12 framework oxygen atoms as neighbours at
distances from 3.2 to 3.8 Å. The lithium ions are situated in the
channels.

In the Li,Tl–C difference electron–density maps there are large
peaks at four positions. These positions we assume to be partially

occupied by thallium ions. The three positions are in the cancrinite cage and have lattice oxygen atoms at distances in the range from 2.5 to 3.1 Å. The fourth position is in the channel and has lattice oxygen atoms at distances from 2.6 to 2.7 Å. The lithium ions and water molecules have not been located, and no attempt has been made to refine parameters of the thallium ions.

Discussion

The results of the present study provide evidence of the different mechanisms through which cancrinite forms in essentially sodium environments with and without sodium salts (18) and in systems containing large and small cations. In the former case there is no evident relationship between shape and dimension of the anion, which may be also OH⁻, and dimension of cancrinite cage; the anion is found both in the wide channel and sometimes in the cage, so that it appears that anion enters the cancrinite structure essentially for charge balancing. In the latter, crystallization is a direct result of the specificity of cancrinite cage for Cs⁺ mainly, but also, even if to a different extent, for Tl⁺ and Rb⁺. The templating action is the one most frequently referred to for explaining the specificity cation-structure. This has been demonstrated in the case of large organic cations (see for instance the excellent fitting of TMA ion in gmelinite and sodalite cages (19) and of TPA ion in ZSM-5 intersection of the channels (20)), while no proof, as far as we know, has been collected before now of a templating action of the rather small anhydrous inorganic cations. In the cancrinite crystallization the evidence is still more convincing, if we consider that three inorganic cations, irrespective of their nature, only on the basis of their rather close dimensions, determine the formation of the same framework structure. The specificity of cancrinite cage for the large ionorganic cation is obviously not valid in general: as matter of fact cancrinite cage is a rather common tertiary building unit, present in erionite, offretite, Linde L, and Losod (besides liottite and afghanite) but these types, when synthesized, are obtained in other cationic environments, in which often K and TMA prevail. Since the ionic radii of these cations are rather different from those of Cs⁺, Tl⁺ and Rb⁺, one must deduce that this structural unit, although favoured by the presence of specific cations, is the result of the arrangement of other simpler building units, rather than the direct precursor of the species which is going to crystallize. In the case of cancrinite an active role should be claimed for lithium, inasmuch as associations of other inorganic cations with Cs⁺, Tl⁺ and Rb⁺ do not lead normally to its crystallization. The exception of sodium must be related likely to the already mentioned possibility that environments of NaOH may give rise to cancrinite. A hypothesis may be then worked out

for lithium, that it is responsible for the formation in solution of the "ladder-like" structural unit, present in cancrinite but also in ABW structural type, another Li-dependent framework structure (9). Figure 5 reports an idealized representation of this chain unit and the possible ways through which, in presence or in absence of the large inorganic cation, cancrinite or Li-A, ABW types form, respectively. It appears evident the templating role of the large cation, while it is still obscure the mechanism of action of lithium in the formation of the chain units.
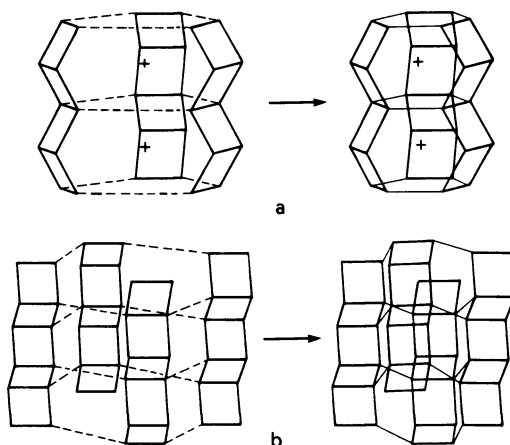
Figure 5. Schematic representation of CAN and ABW types formation from systems containing lithium and including (a) or excluding (b) a large cation (symbolized by +).

Conclusion

Cancrinite crystallization from mixed cationic systems is an example, certainly not generalizable, of the determinant role played by the cations in framework silicate crystallization. In the present case the specificity is even double, because either the small cation (Li^+) or the large one (Cs^+, Tl^+, or Rb^+) are essential for the synthesis and a role for each of them has been hypotized. The completion of the structural analysis, now in progress, may confirm the hypotheses, explaining also some still unclear points.

Acknowledgments

Literature Cited

1. Barrer, R.M. Hydrothermal Chemistry of Zeolites, Academic Press, London 1982, pp 157–170.
2. Khatami H. Proc. 3rd Inter. Conf. on Molecular Sieves, Ed. J. B. Uytterhoeven, Leuven University Press, 1973, p 167.
3. Robson, H.E.; Shoemaker, D.P.; Olgivie R.A.; Manor, P.C. In Molecular Sieves, Eds. W.M. Meier and J.B. Uytterhoeven, Adv. Chem. Series No. 121, Washington, 1973; p 106.
4. Barrer, R.M.; Beaumont R.; Colella C. J. Chem. Soc. Dalton 1976, 934.
5. Aiello R.; Barrer R.M. J. Chem Soc. A 1970, 1470.
6. Colella C.; de'Gennaro M.; Iorio V. In New Developments in Zeolite Science and Technology; Eds. Y. Murakami, A. Iijima and J.W. Ward, Kodansha, Tokyo 1986; p 263.
7. Barrer R.M.; Cole J.F. J. Chem. Soc. A 1970, 1516.
8. Barrer R.M.; White E.A.D. J. Chem. Soc. 1951, 1269.
9. Colella C.; de'Gennaro M. Annali di Chimica 1986, 76, 115.
10. International Tables for X-ray Crystallography. Vol. III, Kynoch Press, Birmingham 1962, p 66.
11. Ibid. p 122.
12. Stewart J.M.; Machin P.A.; Dickinson C.W.; Ammon H.L.; Heck H.; Flack H. The X-RAY 76 SYSTEM. Tech. Rep. TR 446, Computer Center, Univ. of Maryland, College Park, MD 1976.
13. Baerlocher Ch. The X-ray Rietveld System XRS-82, Inst. fur Krystallographie und Petrographie, ETH, Zurich, 1982.
14. Barrer R.M.; Baynham J.W. J. Chem. Soc. 1956, 2882.
15. Colella C. Rend. Acc. Sc. Fis. Mat. (Napoli) 1973, 40, 304.
16. Jarchow O. Zeit. fur Kristall. 1965, 122, 407.
17. Barrer R.M.; Vaughan D.E.W. J. Phys. Chem. Solids 1971, 32, 731.
18. Barrer R.M.; Cole J.F.; Villiger H. J. Chem. Soc. A 1970, 1523.
19. Flanigen E.M. In Molecular Sieves, Eds. W.M. Meier and J.B. Uytterhoeven, Adv. Chem. Series No. 121, Washington 1973, p 119.
20. Nagy J.B.; Gabelica Z.; Derouane E. G. Zeolites 1983, 3, 43.

Chapter 15

Nonaqueous Synthesis of Silica Sodalite

D. M. Bibby, N. I. Baxter, D. Grant-Taylor, and L. M. Parker

Chemistry Division, Department of Scientific and Industrial Research, Private Bag, Petone, New Zealand

The synthesis of ethylene glycol-silica sodalite from the non-aqueous systems SiO_2-Na_2O-ethylene glycol and SiO_2-Na_2CO_3-ethylene glycol is described. Addition of water up to a water/ethylene glycol ratio of 0.05 has no effect, above this sodium metasilicate is produced in increasing amounts until it is the only product at a water/ethylene glycol ratio 0.5. Each sodalite cage contains one ethylene glycol molecule which can be removed by a combination of pyrolysis and high pressure oxidation. These oxidation products can be decapsulated at low pressures to produce a pure silica sodalite.

We describe here the synthesis of silica sodalite containing ethylene glycol in the sodalite cages, a material referred to as ethylene glycol-silica sodalite, EG-SS. We also describe a method for removing the ethylene glycol to leave a pure silica sodalite. Unlike the usual systems for synthesis of zeolitic materials [1] these are non-aqueous, namely silica-sodium hydroxide-ethylene glycol and silica-sodium carbonate-ethylene glycol. Our first syntheses were described elsewhere [2]. Subsequently, a wide range of allowable reagent compositions for successful EG-SS production have been studied and the crystallisation fields are presented here.

The available evidence suggests that the material as synthesised contains one ethylene glycol molecule in each sodalite cage. The high temperature weight loss in thermogravimetric analysis corresponded to nearly two ethylene glycol molecules per unit cell, with a carbonaceous residue in the black calcined material. A neutron diffraction study [3] produced data of such a quality that essentially one ethylene glycol molecule must be present in each cage.

With a free diameter of the sodalite cage of about 6 angstrom, the size of the molecules that can be accommodated is limited. Ethylene glycol, propanol and also tetramethyl ammonium ions (5) can be easily encapsulated. However, molecules such as

propylene glycol or glycerol, which might also be suitable
solvents, would be too large to fit comfortably in the cage.

Experimental

The reagents were redistilled ethylene glycol (EG) (laboratory
reagent), fumed silica (Degussa Aerosil 200), NaOH (laboratory
grade) and Na_2CO_3 (laboratory grade). All reactions were carried
out at a temperature of 170°C, for periods of up to 21 days, in
stainless steel vessels with agitation when the viscosity was low
enough. In syntheses using NaOH where the SiO_2/EG ratio was less
than 0.1, the hydroxide was added as the solid as it rapidly
dissolved in the EG at the reaction temperature. For SiO_2/EG ratios
between 0.1 and 1.0, the NaOH was generally dissolved in the EG
prior to mixing with the SiO_2. For ratios above 1.0, NaOH was
dissolved in methanol and a slurry with the SiO_2 was prepared. The
methanol was then removed at low temperature (below 50°C) in vacuo,
and the appropriate amount of EG was added. In syntheses using
Na_2CO_3 the carbonate was mixed into the reaction mixture in a finely
ground anhydrous form.

Thermogravimetric analysis was performed on a Stanton Redcroft
thermobalance in a flowing oxygen atmosphere at a heating rate of
10°C/minute. Thermal desorption/mass spectrometry (TD/MS) was
carried out using an Extranuclear quadrupole mass spectrometer.[4]
To analyse the evolved gases a mass range of 1 to 100 was scanned,
while the sample was heated in a partial vacuum (ca. 0.1 bar argon)
at 10°C/minute.

The high pressure oxidation studies were carried out in test
vessels (American Instrument Co.) with a working pressure limit of
1000 bar at room temperature and only slightly lower at a
temperature limit of 400°C. High pressure oxygen (commercial grade)
was introduced from a cylinder with up to 140 bar available at room
temperature. The oxygen pressure at 400°C could be calculated from
values of the compressibility factor[6] and the filling pressure at
room temperature. Sample powders were spread thinly along the wall
of the horizontal vessel to reduce any local heating to a minimum.

Sodium analyses were carried out by flame photometric methods
after dissolution of the sample in HF. X-ray diffraction was
carried out on standard powder diffraction equipment.

Results and Discussion

Synthesis of Ethylene Glycol-Silica Sodalite (EG-SS). The
crystallisation field for the system SiO_2-NaOH-EG at 170°C is shown
in Figure 1. At low values of the ratio SiO_2-EG the products were
either clear solutions or translucent gels. At low Na_2O/EG ratios
and high SiO_2/EG ratios no obvious reaction products were found and
the material was still amorphous after reaction. At Na_2O/EG ratios
above 0.025 and SiO_2/EG ratios between 0.05 and 0.5 both β-sodium
silicate and cristobalite were formed. Pure EG-SS was formed at
SiO_2/EG ratios between 0.05 and 3.0 and Na_2O/EG ratios from 0.007 to
0.4. Mixed EG-SS and amorphous material was produced up to a
SiO_2/EG ratio of ca.10.

Assuming that each sodalite cage is occupied by one EG
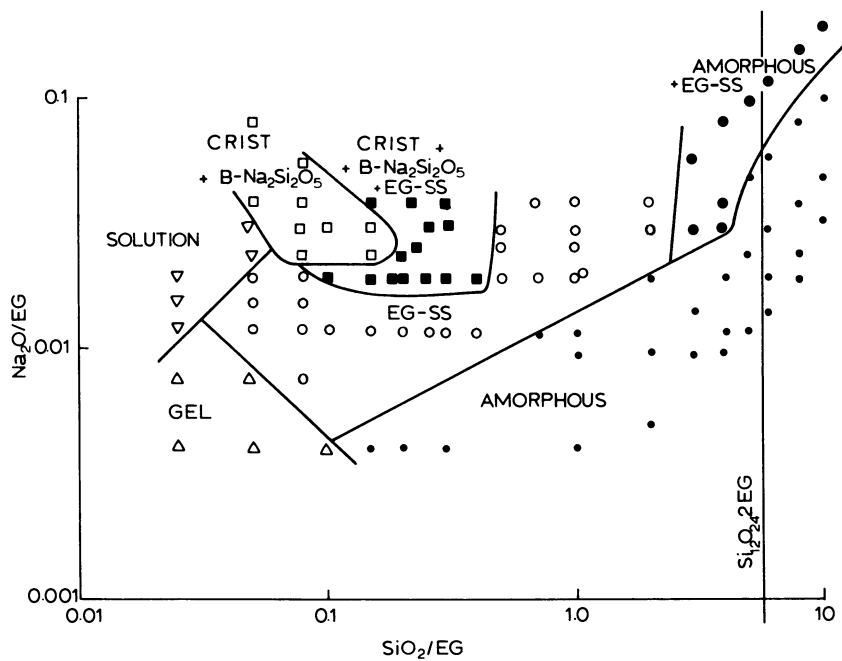
Figure 1. SiO_2/EG versus Na_2O/EG for the system SiO_2:NaOH:EG.

molecule (a unit cell composition $Si_{12}O_{24}.2EG$), the SiO_2/EG ratio
of the pure EG-SS is 5.81. Above this ratio it is inevitable that
EG-SS will be mixed with other products, usually unreacted
material. In practice this work shows that pure EG-SS can be
formed up to $SiO_2/EG = 3$ within the reaction times used here.

As Figure 1 shows, as the amount of EG in the system falls, the
ratio Na_2O/EG has to increase for successful EG-SS synthesis. For
SiO_2/EG ratios below 0.4 the calculated SiO_2/Na_2O ratio varies from
ca. 3 to ca.10. For SiO_2/EG above 0.4 the SiO_2/Na_2O ratio can
increase from ca. 10 to a maximum of ca. 50. Thus as the amount of
EG in the system falls, the proportion of Na_2O required for
successful synthesis of EG-SS also falls.

For values of SiO_2/EG above 1 the reactant mixture has the
appearance of a dry powder. Although EG has a high vapour pressure
at 170°C and was rapidly and uniformly distributed throughout the
reactants, it was clear from preliminary experiments in these "dry"
systems that the NaOH could not be uniformly distributed. It was
for this reason that the procedure of mixing the SiO_2 with the
appropriate amount of NaOH dissolved in methanol was adopted. The
presence of any small residual amounts of methanol in the reactants
after drying in vacuo did not appear to be detrimental.

In the system SiO_2-NaOH-EG, water may be present in trace
amounts as an impurity or as a product of a reaction between NaOH
and EG to form sodium glycolate. In an investigation into the
possibility that water acts as a catalyst, EG-SS was synthesised
from a system where sodium metal was dissolved in redistilled EG
before being mixed with SiO_2 previously dried at 500°C. No
differences were observed in the rate of formation of the EG-SS or
in the purity of the product. However, the experimental
difficulties of ensuring complete removal of water from the system
are such that, as yet, a catalytic role for water cannot be entirely
eliminated.

The effect the deliberate addition of water on the
crystalization of silica sodalite was investigated in a separate
series of experiments where increasing amounts of water were added
to the system. Addition of water up to water/ethylene glycol ratios
of 0.05 had no observable effect, x-ray diffraction showing 100
percent silica sodalite. Above this ratio increasing amounts of
meta sodium silicate were formed until this became the only product
at water/ethylene glycol ratios above 0.5.

The effect of Na_2CO_3 on the SiO_2-Na_2O-EG system was
investigated because of the reported [1] synthesis of cancrinite
from hydrothermal systems containing Na_2CO_3. However, we found no
product here other than EG-SS. Figure 2 shows the crystallisation
field for EG-SS in the system SiO_2-Na_2CO_3-EG. Within the
composition range studied, there appears to be no upper boundary to
the allowable Na_2O/EG ratio over a range of values of SiO_2/EG from
ca. 0.03 to ca.2. Considering the limited solubility of Na_2CO_3 in
EG, this is perhaps not surprising. The EG is essentially saturated
at room temperature at Na_2O/EG ratios >0.02[7]. Above the
saturation ratio the Na_2CO_3 acts as an inert diluent. Although
reaction periods were limited to 21 days, there was no indication
that products other than EG-SS would form.

As seen in Figure 3, powder X-ray diffraction showed that EG-SS
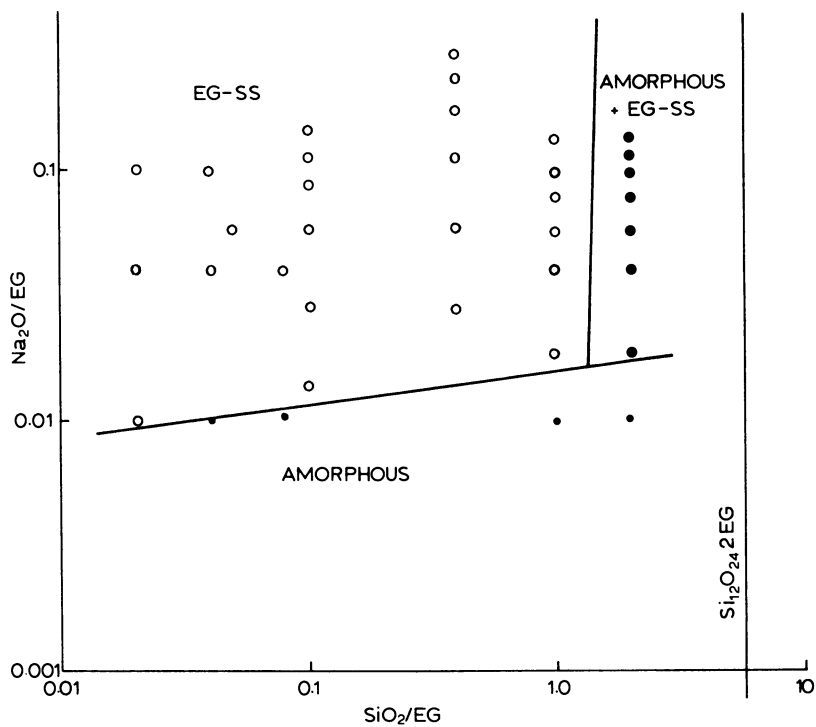
Figure 2. SiO_2/EG versus Na_2O/EG for the system $SiO_2:Na_2CO_3:EG$.
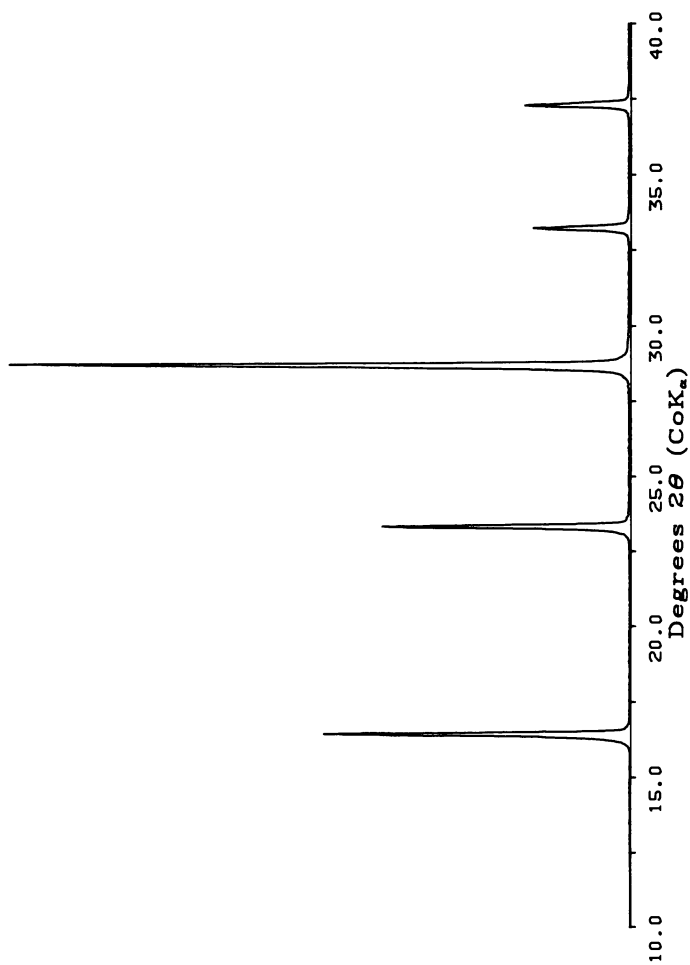
Figure 3. X-ray powder diffraction patterns for EG-SS prepared from the SiO_2:NaOH:EG system.

products from both systems (NaOH and Na_2CO_3) were extremely crystalline. Inspection of a pure EG-SS sample by scanning electron microscopy showed regular cuboctahedra up to 25 microns in diameter (Figure 4). Chemical analysis of the products from either system showed essentially no incorporation of sodium unless aluminium was present, when sodium was present in amounts appropriate to balance the framework charge, as has been reported previously[2,8].

It is difficult to determine the role of the EG in these systems. Clearly it is a reactant since, at the limit, the amount of EG present governs the yield of EG-SS. At low SiO_2/EG ratios it would appear that EG had a similar solvation behaviour to that of water in typical hydrothermal zeolite syntheses. However, at high SiO_2/EG ratios a possible comparison would be with pneumatolysis[1] where reactions take place not in excess solvent but in the presence of small amounts of reactive volatiles which transport the reactants to the crystallising surface. This is supported by the formation of relatively large regular crystals of EG-SS, suggesting that they grow from solution, and indicates that the EG does act as a solvent to transport the silica to the crystallising surface. This solvent need not necessarily be more than a thin layer over the growing surface as long as there is sufficient to bridge the amorphous silica particles and the EG-SS crystals.

As the SiO_2/EG ratio in the reactants approaches the compositional limit of 5.81, and a large proportion of the EG initially present becomes incorporated into the EG-SS solid, the Na_2O/EG ratio increases rapidly. Eventually the Na_2O/EG ratio rises to the point where apparently no further EG-SS formation occurs. At this point, the remaining EG is presumably saturated with sodium silicate and conditions become unfavourable for further conversion of the amorphous silica.

It should be noted that zeolites will form from reactant gels with very low water contents[9] although reaction rates are low. Also, the conversion of the zeolite chabazite in the absence of added water to give a range of other more compact framework structures has been reported. Particularly relevant was the conversion of a silicaceous sodium-form of chabazite to nosean (sodalite) at ca. 300°C.[12]

Removal of Occluded Ethylene Glycol. Since the smallest cross section of the EG molecule is greater than the free dimension of the 6-window of the sodalite cage, the removal of occluded EG to yield a pure SiO_2 sodalite was not straightforward.

Initially removal was attempted by calcination in air or in oxygen but the sodalite became black, with the evolution of large amounts of volatiles, and it remained black even after being heated to 900°C for several days. The formation of a resistant black product on calcination is in contrast to another report[8] that calcination of EG-SS in air at 500°C yielded a white product. Thermogravimetric analysis showed that the majority of the EG was lost but a significant carbonaceous residue remained. The X-ray diffraction pattern of the black silica sodalite showed no change except that the peaks became significantly broader. This suggests the generation of some degree of structural disorder or the
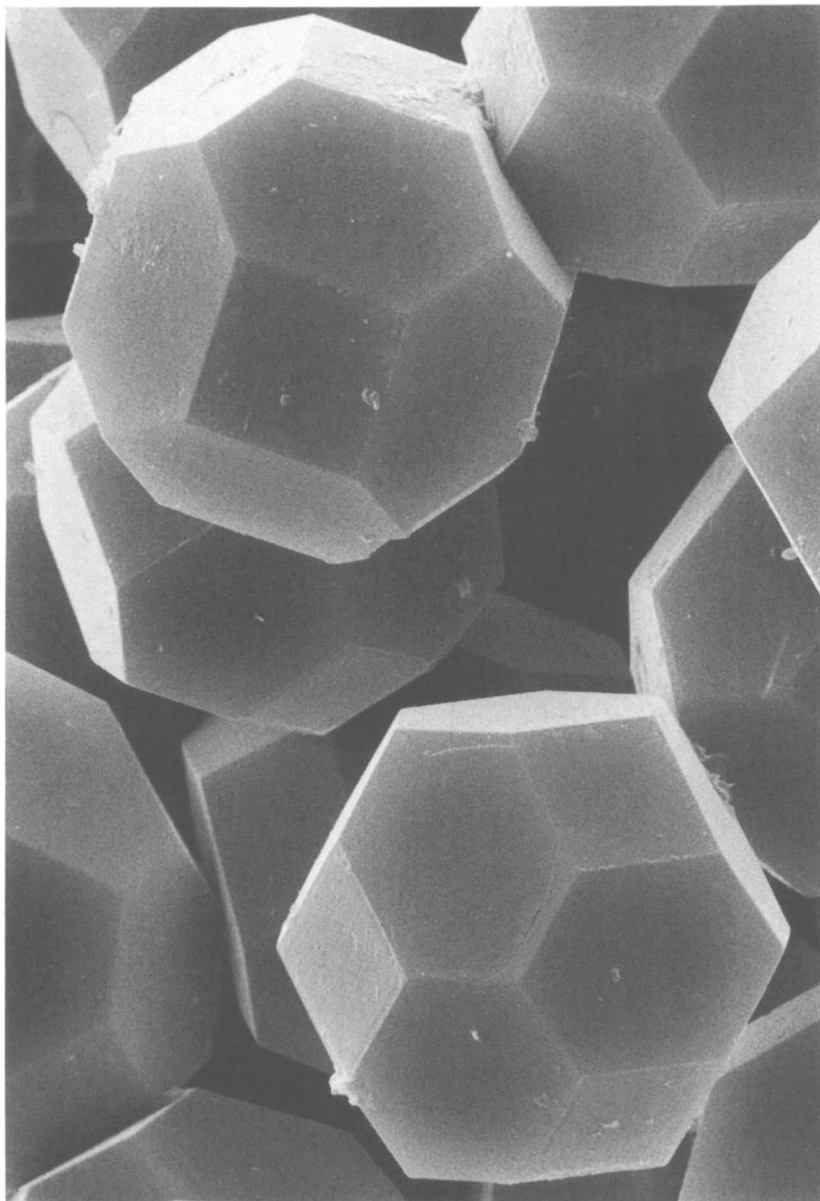
Figure 4.   Scanning electron micrograph of EG-SS prepared from
the SiO_2:NaOH:EG system.

generation of defects arising from the internal forces generated by the decomposition products of the EG, which will have a greater volume than that of the parent molecule. Water generated during the decomposition may also promote some structural breakdown.

A detailed investigation of the volatile decomposition products products was carried out using TD/MS. The results of heating a sample of EG-SS at 10°C/minute are shown in Figure 5. At ca. 400°C there was rapid evolution of large quantities of water, carbon monoxide, carbon dioxide, and hydrogen. The black carbonaceous product clearly still contained oxygen as carbon oxides still continued to be evolved as the temperature was increased, peaking again between 600°C and 700°C. Carbon monoxide production continued to rise from ca. 800°C (not shown here), possibly due to the reduction of the SiO_2 framework by the intimately associated carbonaceous material. The carbonaceous product also dehydrogenated at the higher temperatures, the yield of hydrogen peaking between 600°C and 700°C.

The lack of success in removing the remaining carbonaceous material by oxidation in air is not surprising in view of the diameter of the 6-ring opening (ca. 2.3 A) and cross-sectional diameter of the oxygen molecule (2.8 A). However, there have been studies (10,11) of the encapsulation in zeolites of molecules which, under normal conditions of temperature and pressure, could not penetrate the framework. It has been shown[10] that oxygen can be encapsulated in the sodalite cage of zeolite-A and that argon and krypton (diameters 3.8 and 3.9 A respectively) can be encapsulated in sodalite.[11]

A sample of EG-SS was pyrolysed in vacuo at a heating rate of ca. 2°C/minute from 300°C to 700°C. The resultant black product was then treated with high pressure oxygen for 15 minutes at ca. 400°C. After this treatment, the decapsulated products evolved on heating were analysed using TD/MS. After the first treatment, only carbon dioxide and a small amount of oxygen were evolved with no indication of carbon monoxide. Repeating the high pressure oxygen procedure produced a sample which evolved both oxygen and carbon dioxide in similar quantities (Figure 6). After 5 cycles, a sample was produced which evolved mainly oxygen and which was a light grey in colour.

After pyrolysis, it appeared that most of the sodalite cages still contained some carbonaceous material. On treatment with oxygen at high temperatures, some degree of oxygen encapsulation occurred with the oxygen reacting with the carbon to give carbon dioxide. As shown in Figure 6, this decapsulates from 400°C. On repeating the cycle, the same reaction occurred but this time there were more initially empty sodalite cages which now became occupied with oxygen only and thus on decapsulation both oxygen and carbon dioxide evolved. The ratio of oxygen to carbon dioxide increased with each cycle as the carbonaceous material was removed as carbon dioxide. Water was not observed as any water formed from hydrogen associated with the carbonaceous residue would be desorbed at 400°C or lower during the high pressure oxygen treatment as the water molecule readily passes through the 6-ring opening. The colour of the material darkened slightly during decapsulation. This was probably due to the gas-saturated sodalite having a higher
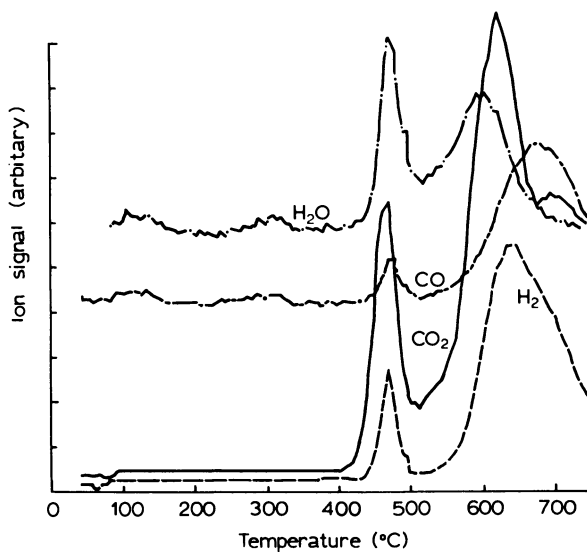
Figure 5: Ion signal versus temperature for EG-SS prepared from
the SiO_2:NaOH:EG system.
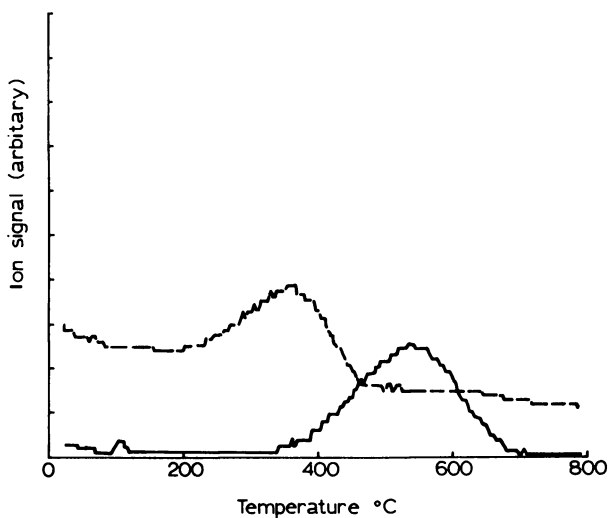
Figure 6. Ion signal versus temperature for pyrolysed EG-SS
containing encapsulated O_2 and CO_2.

refractive index than that of the decapsulated material. The light scattering power of the saturated sodalite would, therefore, be higher and as a result the powdered sample appeared lighter in colour.

Since carbon dioxide decapsulates from 400°C, an extended treatment in high pressure oxygen at that temperature should be effective in removing the carbonaceous residue in one step. A pyrolysed sample of silica sodalite was heated at 400°C in high pressure oxygen for 64 hours. The gases subsequently decapsulated contained predominantly oxygen with a small amount of carbon dioxide. This experiment confirms that during the high pressure treatment carbon dioxide can desorb and be replaced by oxygen. However, the sample was still black after 64 hours and substantially longer times - or possibly higher temperatures would be required for all of the carbon to be oxidised and for the carbon dioxide to be desorbed and replaced with oxygen.

Caution has to be used in the high pressure treatment. As the structure becomes depleted of carbon it tends to collapse to an amorphous solid if temperatures and pressures are increased too rapidly.

Conclusion

The crystallisation fields for synthesis of silica sodalite from two non-aqueous systems have been determined. The silica sodalite synthesised is in a form containing ethylene glycol in the sodalite cages. It has also been shown possible to remove the ethylene glycol from the sodalite cages using a combination of pyrolysis followed by repeated cycles of high temperature, high pressure oxidation.

Acknowledgments

References

1.   Barrer, R.M., "Hydrothermal Chemistry of Zeolites"; Academic Press: New York, 1982.
2.   Bibby, D.M. and Dale, M.P. Nature 1985, 317, 157.
3.   Richardson, J.W. Jr., Pluth, J.J., Smith, J.V., Dytrych, W.J. and Bibby, D.M., J. Phys. Chem. (In Press).
4.   Parker, L.M. and Patterson, J.E., Report No. 2330, DSIR, Chemistry Division, New Zealand, 1983.
5.   Baerlocher, C. and Meier, W.M., Helv. Chim. Acta 1969, 52, 1853.
6.   Perry, J.H. and Chilton, C.H., "Chemical Engineers Handbook", McGraw Hill: New York, 1973.
7.   Stephen, H. and Stephen, T., "Solubility of Inorganic and Organic Compounds"; Pergamon Press: New York, 1963, Vol. 1, Part 1.
8.   van Erp, W.A., Kouwenhoven, H.W. and Nanne, J.M., Zeolites 1987, 7, 286.
9.   Ciric, J., J. Colloid and Interface Sci., 1968, 28, 315.

10.   Fraenkel, D., Ittah, B. and Levy, M., "Zeolites", Eds. Drzaj,
      B., Hocevar, S. and Pejovnik, S., Elsevier Science
      Publishers: Amsterdam, 1985.
11.   Barrer, R.M. and Vaughan, D.E.W., J. Phys. Chem. 1971, 32,
      731.

Chapter 16

Contribution of Propylammonium Species to the Stabilization of the MFI-Type Structure

J. Patarin, H. Kessler, M. Soulard, and J. L. Guth

Laboratoire de Matériaux Minéraux, Unité Associée au Centre National de la Recherche Scientifique No. 428, Ecole Nationale Supérieure de Chimie, 3 rue Alfred Werner, 68093 Mulhouse Cedex, France

Of the numerous organic species leading to the MFI-structure type, the tetrapropylammonium cations are known to be the most efficient. However few thermodynamic data have been determined to corroborate this experimental result. Three highly siliceous MFI-type samples were synthesized by using a fluoride-containing neutral or slightly acidic medium in the presence of tetra-(TPA^+), tri-($TRIPA^+$), or dipropylammonium ($DIPA^+$) cations. Determination of their solution enthalpy in 25% HF enabled their standard enthalpy of formation to be calculated and hence the contribution of the organic species to the stabilization of the structure could be estimated. The results show. as expected. the following stabilization effects: $DIPA^+ \approx TRIPA^+ < TPA^+$.

The favorable influence of organic molecules in the synthesis of MFI-type zeolites is widely recognized. For example. aluminium-containing ZSM-5 can be obtained also in the absence of an organic template (1, 2), but the synthesis of silicate I seems to require the presence of an organic molecule in the reaction mixture (3).

Many studies have been devoted to determining the exact role of these organic species. Stucture directing effects, void-filler effects, and stabilization of specific secondary building units in the solution have been considered (4-6).

Numerous organic species are known to lead to the crystallization of the MFI-type structure (7) but the tetrapropylammonium cations can be considered to be the most specific. To our knowledge no thermodynamic data such as standard formation enthalpies ($\Delta_f H^\circ$) and stabilization energies attributed to the organic species have been published to corroborate this experimental observation. The published thermodynamic data ($\Delta_f G^\circ$, $\Delta_f H^\circ$, $\Delta_f S^\circ$, Cp) are for natural zeolites (8-11) or for organic-free synthetic zeolites. However. some data have been obtained by calculations using lattice energy minimization and extended Hückel theory (12) or by semi-empirical methods based on addition of the thermodynamic functions of the oxide compo-

nents of the zeolite (13) and on correlations between thermodynamic data and structural properties (14).

In order to compare the effect of various organic species, three highly siliceous MFI-type samples containing tetra-, tri- and di-n-propylammonium cations were synthesized according to the new synthesis route that we have developed recently in our laboratory (15-17). In place of the usual alkaline reaction medium, our synthesis uses a neutral or slightly acidic reaction medium in the presence of fluoride. In such a medium, F⁻ acts as a solubilizing agent of silica and of other oxide sources, if any are present, and enters into the channels of the structure with the organic species. Generally, well-formed crystals are obtained without any undesirable additional phase. This route is particularly interesting here because it allows the incorporation of tripropylamine and dipropylamine in the cationic form comparable to the cationic TPA⁺ species. According to the IUPAC recommandations (18) the designations used for the samples are TPA[Si]-MFI, TRIPA[Si]-MFI and DIPA[Si]-MFI.

The standard enthalpies of formation of the samples were obtained by solution calorimetry in 25% HF; also the stabilization effect on the MFI-type structure of the three organic species could be determined. For comparison, an aluminium-containing sample TPA[Si,Al]-MFI was also studied.

EXPERIMENTAL

The products used for the calorimetric measurements and for the synthesis of the MFI-type materials were high purity reagents: 40% aqueous HF (Prolabo); (n-C_3H_7)$_4$NBr (Fluka, purum, 99%); (n-C_3H_7)$_3$N (Fluka, purum, > 98%); (n-C_3H_7)$_2$NH (Fluka, purum, 99%); n-C_3H_7Br (Prolabo, Rectapur, > 97%); AlCl$_3$, 6H$_2$O (Fluka, purum, > 99%); Al(OH)$_3$ (Merck gibbsite, pure, > 98%); SiO$_2$ (Degussa, Aerosil 130, > 98.5%).

SYNTHESIS   The starting molar compositions are given in Table I. The reaction mixture was heated at 170°C in a Teflon-lined stainless steel autoclave for 15 to 50 days depending on the sample.

Table I. Starting chemical molar composition

Sample	SiO$_2$	AlCl$_3$	(C_3H_7)$_4$NBr	(C_3H_7)$_3$N	(C_3H_7)$_2$NH	NH$_4$F	HF (40%)	H$_2$O
TPA[Si]-MFI	1	/	0.125	/	/	0.5	/	30
TPA[Si,Al]-MFI	1	0.033	0.125	/	/	0.5	/	30
TRIPA[Si]-MFI	1	/	/	1	/	/	2	30
DIPA[Si]-MFI	1	/	/	/	1	/	2	30

For the TRIPA$[$Si$]$-MFI and DIPA$[$Si$]$-MFI samples, the amines were first neutralized with HF; seeding (4-5 wt % of the starting SiO$_2$) with finely ground crystals was necessary. In the case of the TRIPA$[$Si$]$-MFI sample, for example, the seeds were obtained as follows. A first reaction mixture containing tripropylamine was seeded with crystals of a TPA$[$Si$]$-MFI sample. After crystallization, new seeds were taken from the obtained crystalline solid for a second synthesis of TRIPA$[$Si$]$-MFI. Therefore, the quantity of seeds of TPA$[$Si$]$-MFI still present in the second seeds and in the final TRIPA$[$Si$]$-MFI sample was negligible. The same procedure was used for the DIPA$[$Si$]$-MFI sample. The synthesis of the latter was rather difficult since the MTT-type (19) zeolite KZ-1 (20) forms easily in the same synthesis conditions. Only two of fifteen attempts yielded a X-ray pure DIPA$[$Si$]$-MFI sample.

After heating, the solids were filtered, washed with water and dried in air at 90°C. Optical and electron microscopy, powder X-ray diffraction, thermal analysis and high resolution solid-state ^{13}C and ^{29}Si NMR spectroscopy were used to check the purity of the samples. Chemical analyses were performed by using atomic absorption spectroscopy (Al and Si) and ion-selective electrodes (F$^-$ and NH$_4^+$) for F$^-$, TPA$^+$, TRIPA$^+$ and DIPA$^+$. The propylammonium cations were first transformed into NH$_4^+$ by heating in conc. H$_2$SO$_4$ (180°C, 2 days) in the presence of Se as a catalyst after the solids had been dissolved in aqueous HF. The water content of the materials was determined by thermogravimetry. The chemical formula per unit cell of the as-synthesized and of the calcined samples is given in Table II.

Table II. Chemical formula per unit cell

TPA$[$Si$]$-MFI	$[(C_3H_7)_4N]_4$ Si$_{96}$ O$_{192}$ F$_4$
TRIPA$[$Si$]$-MFI	$[(C_3H_7)_3NH]_4$ Si$_{96}$ O$_{192}$ F$_4(H_2O)_8$
TRIPA$[$Si$]$-MFI dehydrated	$[(C_3H_7)_3NH]_4$ Si$_{96}$ O$_{192}$ F$_4$
DIPA$[$Si$]$-MFI	$[(C_3H_7)_2NH_2]_{4.8}$Si$_{96}$ O$_{192}$ F$_{4.8}$ (H$_2$O)$_{6.5}$
TPA$[$Si, Al$]$-MFI	$[(C_3H_7)_4N]_4$ Si$_{93}$ Al$_3$ O$_{192}$ F
$[$Si$]$-MFI	Si$_{96}$ O$_{192}$
H$[$Si, Al$]$-MFI	H$_3$ Si$_{93}$ Al$_3$ O$_{192}$ (H$_2$O)$_{28.8}$

The organic-free $[$Si$]$-MFI and H$[$Si, Al$]$-MFI samples were obtained by calcination of the as-synthesized samples performed in air at 550°C. The H$[$Si, Al$]$-MFI sample was hydrated at room temperature in a

water vapor atmosphere (p/p$_0$ = 0.80). The three other calcined sam-
ples are hydrophobic.
        The water of hydratation of the tri- and dipropylammonium ca-
tions occluded in the as-synthesized TRIPA[Si]-MFI and DIPA[Si]-MFI
samples can be removed irreversibly. For instance, the heating of
the TRIPA[Si]-MFI sample in argon at 240°C leads to the dehydrated
TRIPA[Si]-MFI sample.

CALORIMETRIC MEASUREMENTS   Solution calorimetry was performed at
298.2±0.1 K by using a C-80 differential flux calorimeter manufac-
tured by Setaram. The energy equivalent of the calorimetric signal
was determined by electric calibration. The reliability of the
equipment was checked by the dissolution of tris-(hydroxymethyl)
aminomethane (THAM). Agreement within 0.4% with the published value
of +17.75 kJ.mol^{-1} (21) was obtained.
        Both cells (Figure 1), for sample and reference, made of Kel-F,
were designed and manufactured in our laboratory (22). They consist
of a body (a) (inner diameter : 17 mm) fitted into the lower part
with a trough (b) and in the upper part with a plug (c). The whole
is held together by two brass rings (d,e) which are screwed into the
body. The tightness is ensured by two Viton O-rings (f). The volume
available to HF is about 6 ml.
        For the determination of the enthalpies of dissolution of so-
lids in HF, a 5.5 ml aliquot of 25% HF was placed in the sample cell
and the acid was covered with a thin layer (h) of paraffin oil (Pro-
labo, Rectapur) which is inert to HF. The Kel-F capsule (g) con-
taining the solid was placed on the oil layer. Sufficient buoyancy
was ensured by the latter: any attack of the sample powder by HF
vapor or by the solution was thus avoided. The reference cell con-
tained the same volume of HF than the sample cell.
        The heat of solution of tripropylamine and of dipropylamine in
HF was determined by using the same cell with some slight modifica-
tions. Instead of using the sample capsule, the amine was introduced
in the empty lower trough which was then closed with a Teflon sphe-
re. Afterwards, the HF was poured into the volume above the sphere.
A thin Voltalef grease layer on the sphere ensured a tight seal.
        The heat of reaction between tripropylamine and propyl bromide
was determined by using the standard commercial stainless steel
cells from Setaram.
        In all types of measurements, complete mixing of the reactants
was ensured by continuous tumbling of the calorimeter block.

RESULTS AND DISCUSSION

According to chemical analysis (Table II) and CP ^{13}C MAS NMR spec-
troscopy, it can be concluded that the three propylammonium cations
are occluded as ion pairs with F$^-$ in the channels of the structure
of the TPA[Si]-MFI, TRIPA[Si]-MFI and DIPA[Si]-MFI samples. In the
case of the two latter samples, the organic cations are hydrated
(Table II); it will be seen later that the water molecules contribu-
te significantly to the formation enthalpy of both materials. Also,
CP ^{13}C MAS NMR spectroscopy shows for the DIPA Si -MFI sample a
small amount of TRIPA$^+$ beside the DIPA$^+$ cations (molar TRIPA$^+$/DIPA$^+$
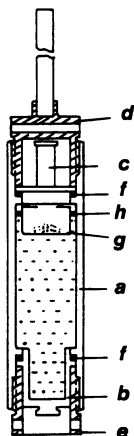
Figure 1. Sample cell: a, body; b, trough; c, plug; d, e: brass rings; f, O-rings; g, capsule; h, paraffin oil layer (22).

$\approx$ 0.10); disproportionation of DIPA$^+$ could have occured under the synthesis conditions (23).

Thermochemical cycles (Figure 2) involving the formation of compounds (α-quartz, gibbsite, amines, tetrapropylammonium bromide, etc.), the dissolution of these compounds and of the MFI-type samples in 25% HF, and the dilution of aqueous HF allow the calculation of the standard enthalpy of formation of the samples.

As an example, in Table III are given the reactions and the corresponding enthalpies used for the derivation of the standard formation enthalpy of the TRIPA[Si]-MFI sample.

Table III : Thermochemical scheme for the derivation of the standard enthalpy of formation of the TRIPA[Si]-MFI sample

REACTIONS	ΔH°(kJ)	Ref
(1) $96Si(s) + 96 O_2(g) \longrightarrow 96SiO_2\,\alpha$-quartz	-87450 ± 136	24
(2) $96\alpha\text{-}SiO_2 + 19453.5HF \bullet 64810.0H_2O \longrightarrow A$	-13016.6 ± 17.3	8
(3) $B \longrightarrow C + 19449.5HF \bullet 64802.0H_2O$	$+13623.7\pm93.2$	22
(4) $2H_2(g) + 2F_2(g) \longrightarrow 4HF(\ell)$	-1214.2 ± 1.0	25
(5) $4HF(\ell) + 13.3H_2O(\ell) \longrightarrow 4HF \bullet 13.3H_2O$	-70.60 ± 0.02	25
(6) $2N_2(g) + 36C(s) + 42H_2(g) \longrightarrow 4(C_3H_7)_3N(\ell)$	-828.6 ± 4.0	26
(7) $4(C_3H_7)_3N(\ell) + A \longrightarrow B$	-244.7 ± 4.5	22
(8) $19449.5HF \bullet 64796.7H_2O + 4HF \bullet 13.3H_2O \longrightarrow 19453.5HF$ $\bullet 64810.0H_2O$	0	22
(9) $19449.5HF \bullet 64802.0H_2O \longrightarrow 19449.5HF \bullet 64796.7H_2O$ $+5.3H_2O\ (\ell)$	≈ 0	25
(10) $4O_2(g) + 8H_2(g) \longrightarrow 8H_2O(\ell)$	-2286.6 ± 0.3	27

$\Delta_f H^\circ(TRIPA[Si]\text{-}MFI) = \Delta H^\circ_9 + \Delta H^\circ_{10} + \Delta H^\circ_4 + \Delta H^\circ_5 + \Delta H^\circ_8 + \Delta H^\circ_1 + \Delta H^\circ_6 + \Delta H^\circ_2 +$

$\Delta H^\circ_7 + \Delta H^\circ_3 = -91487.6 \pm 165.8\ \text{kJ.mol}^{-1}$

$A = 96H_2SiF_6\ 18877.5HF\ 65002.0H_2O$
$B = 4[(C_3H_7)_3NH^+](aq) + 4F^-(aq) + 96H_2SiF_6 \bullet 18873.5HF \bullet 65002.0H_2O$
$C = [(C_3H_7)_3NH]_4Si_{96}O_{192}F_4(H_2O)_8$

Elements $\xrightarrow{\Delta_f H°(Z)}$ As-synthesized or

$(Si, O_2, H_2, C, F_2, N_2, ...)$ calcined sample (Z)

$\Sigma \, \Delta_f H°(\text{compounds})$

quartz, amino compounds, gibbsite,... $- \Delta_{sol.} H°(Z)$

$\Sigma \, \Delta_{sol.} H°(\text{compounds})$

$H_2SiF_{6(aq)} + AlF_6^{3-}{}_{(aq)} + \text{propylammonium}_{(aq)} + F^-{}_{(aq)} \cdots$

$$\Delta_f H°(Z) = \Sigma \, \Delta_f H°(\text{comp.}) + \Sigma \, \Delta_{sol.} H°(\text{comp.}) - \Delta_{sol.} H°(Z)$$
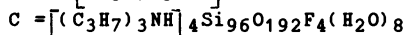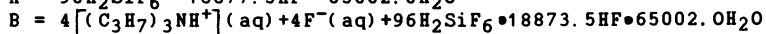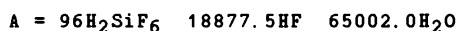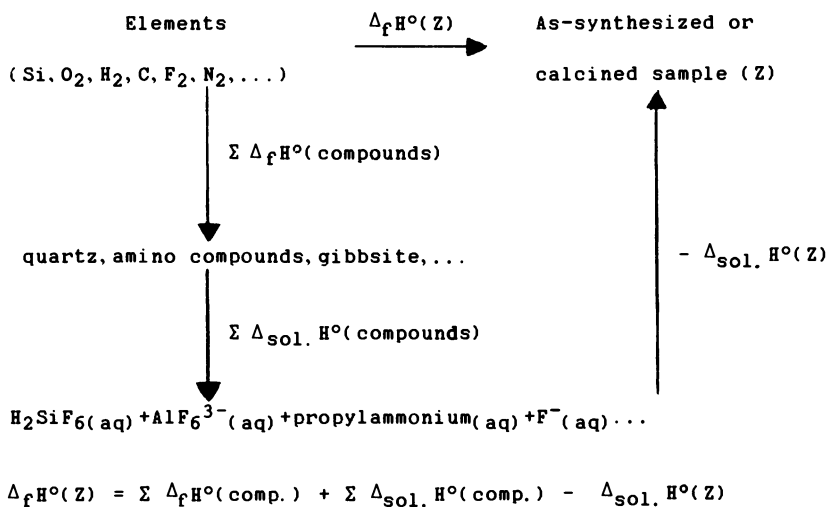
Figure 2. Thermochemical cycle considered for the derivation of
the standard formation enthalpy of the MFI-type samples (Z).

The standard formation enthalpy of many compounds ($H_2O_{(\ell)}$, $(C_3H_7)_3N_{(\ell)}$, etc.) taking part in the cycles are taken from the literature. The standard enthalpy of formation of TPABr (taking part in the cycles relative to the TPA$[Si]$-MFI and TPA$[Si,Al]$-MFI samples is not available; therefore, it had to be determined. Following the synthesis of tetraalkylammonium bromides and iodides (28), the reaction of formation of TPABr was carried out in butanone on starting with tripropylamine and propyl bromide. The other reactions that were considered are the dissolution of TPABr, $(C_3H_7)_3N$, and C_3H_7Br in butanone. The value obtained for $\Delta_f H^\circ$(TPA Br) is -322.9 ± 1.0 kJ.mol^{-1}.

STANDARD SOLUTION ENTHALPY   The measured standard solution enthalpy of α-quartz and of the as-synthesized and the calcined MFI-type samples are as follows :

Sample	$\Delta_{sol.} H^\circ$ (kJ) (per 96 TO$_2$, T=Al, Si)
α-quartz	-13245.1 ± 48.0
TPA$[Si]$-MFI	-12653.0 ± 89.0
TRIPA$[Si]$-MFI	-13623.7 ± 93.2
TRIPA$[Si]$-MFI, dehydrated	-13527.5 ± 91.2
DIPA$[Si]$-MFI	-13688.6 ± 25.9
TPA$[Si,Al]$-MFI	-12628.8 ± 26.8
H$[Si,Al]$-MFI	-13054.8 ± 29.5
$[Si]$-MFI	-13250.8 ± 86.5

The standard deviation of the mean is expressed by $\sigma_{\bar{x}} = \sqrt{\Sigma(x_i - \bar{x})^2/n(n-1)}$, where $\Sigma(x_i - \bar{x})^2$ is the sum of the squares of the deviations from the mean value $\bar{x}$ and n the number of measurements (30).

The solution enthalpy of α-quartz found here ($\Delta_{sol.} H^\circ = -137.97 \pm 0.52$ kJ.mol^{-1}SiO$_2$) is slightly larger than the value published by Johnson et al. (8) (-135.59 ± 0.18 kJ.mol^{-1}). For our further calculations we have chosen this published value since our quartz sample contained traces of cristobalite.

There is a $\approx$ 4% difference between our value of the solution enthalpy of the highly siliceous calcined $[Si]$-MFI sample and the value published recently by Johnson et al. (29) for the dissolution in 24.4% HF of a sample of silicalite I prepared in alkaline medium in the absence of fluoride (-144.93 ± 0.18 kJ/SiO$_2$ for a SiO$_2$/HF ratio equivalent to the ratio used here). Such a difference could be related to the nature of the samples and to morphology differences. Our calcined sample contained traces of fluorine whereas the silica-

lite I sample studied by Johnson et al.(29) was prepared in alkaline
medium in the presence of TPAOH, which may have contained the usual
KOH impurity. Such an alkaline compound, which still may be present
in the calcined solid could lead to an increase in the solution
heat. The crystal size of our sample (80x40x20 μm^3) was much larger
than the size (4μm) of the sample studied by Johnson et al (29).

STANDARD ENTHALPY of FORMATION   The standard enthalpies of forma-
tion of the as-synthesized and the calcined samples are as follows :

Sample	$\Delta_f H°$ (kJ per 96TO$_2$)
TPA[Si]-MFI	-89925.0±163.5
TRIPA[Si]-MFI	-91487.6±165.8
TRIPA[Si]-MFI	-89297.2±164.7
DIPA[Si]-MFI	-91308.3±139.5
TPA[Si, Al]-MFI	-89317.0±136.0
H[Si, Al]-MFI	-95976.2±138.4
[Si]-MFI	-87216.6±162.1

The uncertainty (σ_t) of $\Delta_f H°$ given above is equal to the square
root of the sum of the squares of the standard deviations of the
means for the individual reactions taking part in the thermochemical
cycle considered $\sigma_t = \sqrt{\Sigma \sigma^2 \bar{x}_i}$ (30).
The enthalpy term can be considered here as giving a direct
measure of the lattice energy. Comparison of the $\Delta_f H°$ values ac-
counts for the variations of lattice energy and hence for the stabi-
lity of the structure of the samples.
The as-synthesized TPA[Si]-MFI sample appears to be slightly
more stable than the aluminium-containing TPA[Si, Al]-MFI sample. This
result is in agreement with the semi-empirical calculations of Ooms
et al. (12) which show that in the absence of water, the aluminium-
rich samples are less stable than the purely siliceous ones. However
the observed difference between the $\Delta_f H°$ values is small because
the aluminium content of the TPA[Si, Al]-MFI sample is not very high
(Si/Al = 31).
On the other hand, in agreement with the work of Barrer (31),
it is found for the calcined samples that the H[Si, Al]-MFI sample is
more stable than the highly siliceous [Si]-MFI one; the hydration of
the compensating cations increases the stability of the structure.
The $\Delta_f H°$= -908.5±1.7 kJ.mol^{-1} SiO$_2$ for the [Si]-MFI sample is sligh-
tly larger (absolute value) than the value determined for silicalite
I by Johnson et al. (29) by fluorine-combustion calorimetry (-905.20
±0.84 kJ.mol^{-1} SiO$_2$). Vieillard (14) has published a smaller value
(-900.45±0.28 kJ.mol^{-1} SiO$_2$) which was not determined calorimetri-

cally but semi-empirically by using correlations between thermodynamic data and structural properties such as mean Si-O bond length, mean SiOSi angle and the polarizability of Si and O.

The magnitude of $\Delta_f H°$ for the as-synthesized DIPA[Si]-MFI and TRIPA[Si]-MFI samples is larger than for the TPA[Si]-MFI sample; this observation is unexpected. In fact $\Delta_f H°$ takes into account the enthalpy of formation of the water occluded in the DIPA[Si]-MFI and TRIPA[Si]-MFI samples. The $\Delta_f H°$ of both dehydrated samples are slightly different, and the order of increasing magnitude of $\Delta_f H°$ is then as expected:

DIPA[Si]-MFI dehydr. $\approx$ TRIPA[Si]-MFI dehydr. < TPA[Si]-MFI.
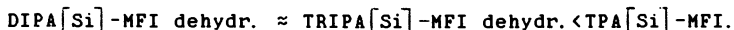
A good estimate of the contribution of the organic species to the stabilization of the as-synthesized samples may be obtained by considering the following initial and final states:

[Si]-MFI(s) +4TPA$^+$(aq) +4F$^-$(aq) $\longrightarrow$ TPA[Si]-MFI(s)

[Si]-MFI(s) +4TRIPA$^+$(aq) +4F$^-$(aq) +8H$_2$O(ℓ) $\longrightarrow$ TRIPA[Si]-MFI(s)

[Si]-MFI(s) +4.8DIPA$^+$(aq) +4.8F$^-$(aq) +6.5H$_2$O(ℓ) $\longrightarrow$ DIPA[Si]-MFI(s)
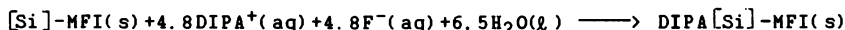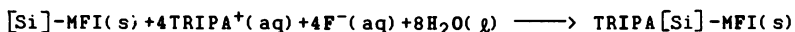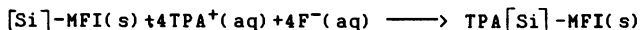
By using the following standard formation enthalpies that were obtained from various thermochemical cycles (this work):

$$\Delta_f H° \ (TPA^+(aq), \ F^-(aq)) \ = \ - \ 527.9 \pm 1.1 \ kJ.mol^{-1}$$
$$\Delta_f H° \ (TRIPA^+(aq), \ F^-(aq)) \ = \ - \ 604.0 \pm 1.5 \ kJ.mol^{-1}$$
$$\Delta_f H° \ (DIPA^+(aq), \ F^-(aq)) \ = \ - \ 571.2 \pm 1.2 \ kJ.mol^{-1}$$
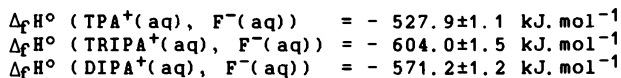
the $\Delta H°$ of stabilization are -596.8 ± 230.3 kJ.mol^{-1}, $+431.6 \pm 231.9$ kJ.mol^{-1} and $+508.0 \pm 213.9$ kJ.mol^{-1} for the TPA[Si]-MFI, TRIPA[Si]-MFI and DIPA[Si]-MFI samples respectively.

It appears that the TPA F ion pair only contributes significantly to the stabilization of the MFI structure. This result agrees with the observed specificity of the three organic species with respect to the MFI-structure type. The tetrapropylammonium species lead to the MFI-type structure alone, whereas the two other species lead also to the structure types MEL (32) and MTT respectively.

CONCLUSION

The determination of the standard enthalpy of formation of the as-synthesized and calcined highly siliceous MFI-type samples made it possible to estimate the interaction between the framework and the organic species. This interaction is significant in the case of the TPAF species only, due presumably to their neat fit into the channels. For the aluminium-containing sample, the stabilizing effect of water molecules, when occluded in the channels, was evidenced.

LITERATURE CITED

1. Chao, K. J.; Tasi, T. C.; Chen, M. S.; Wang, I. J. Chem. Soc. Faraday Trans. I 1981, 77, 547.
2. Tissler, A.; Müller, U.; Danner, A.; Polanek, P.; Unger, K. K.; 27. Diskussionstagung der Arbeitsgemeinschaft Kristallographie, Konstanz, 1988, Vorabdruck aus Zeitschrift für Kristallographie, p. 258.
3. Grose, R. W.; Flanigen, E. M. U. S. Pat. 4061724, 1977.
4. Groenen, E. J. J.; Kortbeek, A. G. T. G.; Mackay, M.; Sudmiejer, O. Zeolites 1986, 6, 403.
5. Flanigen, E. M. Pure Appl. Chem. 1988, 52, 2191.
6. Maretti, E.; Contessa, S.; Padovan, M. Chim. Ind. (Milan), 1985, 67, 21.
7. Lok, B. M.; Cannan, F. R.; Messina, C. A. Zeolites, 1983, 3, 282.
8. Johnson, G. K.; Flotow, H. E.; O'Hare, P. A. G. Am. Miner. 1982, 67, 736.
9. Johnson, G. K.; Flotow, H. E.; O'Hare, P. A. G. Am. Miner. 1983, 68, 1134.
10. Johnson, G. K.; Flotow, H. E.; O'Hare, P. A. G. Am. Miner. 1985, 70, 1065.
11. Bennington, K. O.; Brown, R. R. U. S. Bureau Mines R. I. 1983, 8778.
12 Ooms, G.; Van Santen, R. A.; Jackson, R. A.; Catlow, C. R. A. in Innovation in Zeolite Materials Science; Grobet, P. J.; Mortier, W. J.; Vansant, E. F.; Schulz-Ekloff, G.; Eds.; Elsevier, 1987; p. 317.
13. La Iglesia, A.; Aznar, J. Zeolites 1986, 6, 26.
14. Vieillard, P. Bull. Minéral. 1986, 109, 219.
15. Guth, J. L.; Kessler, H.; Bourgogne, M.; Wey, R. Fr. Appl. 2564451, 1985.
16. Guth, J. L.; Kessler, H.; Bourgogne, M.; Wey, R.; Szabo, G. Fr. Appl. 2567868, 1986.
17. Guth, J. L.; Kessler, H.; Wey, R. in Proc. 7th Int. Zeolite Conf. New Developments in Zeolite Science and Technology; Murakami, Y.; Iijima, A. Ward J. W., Eds; Elsevier, 1986; p. 121.
18. Pure Appl. Chem. 1979, 51, 1091.
19. Rohrman, A. C. Jr.; Lapierre, R. B.; Schlenker, J. L.; Wood, J. D.; Valyocsik, E. W.; Rubin, M. K.; Higgins, J. B.; Rohrbaugh, W. J. Zeolites 1985, 5, 352.
20. Parker, L. M.; Bibby, D. M. Zeolites 1983, 3, 8.
21. Hill, J. O.; Ojelund, G.; Wadso, I. J. Chem. Thermod. 1969, 1, 111.
22. Patarin, J.; Soulard, M.; Kessler, H.; Guth, J. L.; Diot, M. Thermochimica Acta, in press
23. Tapp, N. J.; Bibby, D. M.; Milestone, N. M. Zeolites 1988, 8, 157.
24. Wise, S. S.; Margrave, J. L.; Feder, H. M.; Hubbard, W. N. J. Phys. Chem. 1963, 67, 815.
25. Johnson, G. K.; Smith, P. N.; Hubbard, W. N. J. Chem. Thermod. 1973, 5, 793.
26. Pedley, J. B.; Rylance, J. Computer Analyzed Thermochemical Data. Organic and organometallic compounds; Academic Press, 1977.
27. Codata, J. Chem. Thermod. 1978, 10, 903.
28. Smith, P. A. S.; Frank, S. J. Am. Chem. Soc. 1952, 74, 509.
29. Johnson, G. K.; Tasker, I. R.; Howell, D. A.; Smith, J. V. J. Chem. Thermod. 1987, 19, 617.

30. Rossini, F.D.; Deming, W.E. *J. Wash. Acad. Sci.* 1939, *29*, 416.
31. Barrer, R.M. *J. Phys. Chem. Solids* 1960, *16*, 84.
32. Gabelica, Z.; Derouane, E.G.; Blom, N. *Appl. Catal.* 1983, *5*, 109.

Chapter 17

Effect of Gravity on Silicalite Crystallization

David T. Hayhurst[1], Peter J. Melling[2], Wha Jung Kim[1],
and William Bibbey[2]

[1]Department of Chemical Engineering, Cleveland State University,
Cleveland, OH 44115
[2]Advanced Materials Center for the Commercial Development of Space,
Battelle Columbus Division, 505 King Avenue, Columbus, OH 43201–2693

Silicalite was synthesized from a batch
composition of $2.55Na_2O-5.0TPABr-100SiO_2-2800H_2O$
at 180°C and at times ranging from one to seven
days. Autoclaves containing the synthesis mixture
were centrifuged during reaction, providing an
elevated gravitational force field. Tests were
conducted at 30 and 50G and at normal gravity.
For synthesis performed under elevated gravity,
average and maximum crystal sizes were
substantially greater than those measured under
normal gravity. Average and maximum crystal
lengths were 42 and 132μm for the 1G synthesis.
For the elevated gravity crystallizations, two
separate nucleations and growths were observed.
For 50G, the first growth was rapid, producing
135μm silicalite crystals in two days. The
second crystallization produced larger 200μm
crystals in five days. The maximum crystal
sizes measured were 190 and 300μm for the two
crystallizations. Elevated gravity was also
found to affect product yield. At normal
gravity, crystal yields were less than 5%.
For elevated gravity reactions, these yields
increased to over 55% based on total silica in
the initial reaction mixture. A discussion of
how elevated gravity affects nucleation, growth,
yield and crystal size of silicalite is presented.

The synthesis of large zeolite crystals has received much attention
in both the open and patent literature. The first report on the
growth of large crystals of types A, P and X zeolites was by Ciric
in 1967(1). Recent reports have focused on the pentasil zeolites,
in particular ZSM-5 and silicalite (2-20). The largest
ZSM-5/silicalite crystals are reported to range up to 420 μm in
length (17,19). In each report, investigators have varied and
optimized the chemistry of the reacting mixture in order to

maximize the size. The reaction temperature and degree of agitation have also been considered as reaction variables.

The effect of gravity on crystal growth has recently come under study, particularly in the micro- or zero-gravity regime. Zetterlund and Fredriksson (22) studied the growth of indium antimonide from its melt under microgravity conditions and formulated mathematical expressions form the effects of gravity on freely growing crystals. Rodot et al. (23) have studied the effects of gravitational forces up to 5G on crystals grown from their own melt (Bridgeman Method) and concluded that the quality of the crystals was similar to those grown in space. Studies on the effect of gravity on crystals grown by techniques other than from a crystal melt are more limited. Sand et al. (24) have postulated that the synthesis of zeolites in microgravity would result in the formation of larger crystals as particle settling and thermal convective currents would be avoided. Zeolite nuclei should remain suspended in solution, growth would continue in the nutrient-rich mother-liquor and larger crystals would form. Although microgravity experiments have not been performed, crystallizations conducted in viscous solutions support this hypothesis (24).

As with micro-gravity, reports on the effects of elevated gravity on zeolite crystal growth are absent from the literature. The application of high gravity during crystal growth stratifies the solid and liquid reactants. Nucleation and crystal growth occurs at the solid-liquid interface in contrast to a homogeneous gel as is postulated for microgravity. In this research the effect of applying an external gravitational force during synthesis was studied. The high gravity was achieved by centrifuging the reaction vessels during synthesis. Reactions were carried out using a centrifuge placed in an oven. The effects of elevated gravity on growth rate, crystal size, yield and morphology are presented.

EXPERIMENTAL

Synthesis

The reactants used in this study were a colloidial silica, Ludox AS-40 (Dupont), reagent-grade tetrapropylammonium bromide (Aldrich Chemical Co.) and a 50wt% sodium hydroxide solution (Mallinckrodt Inc.). The reaction mixture had the oxide formula, $2.55Na_2O-5.0TPABr-100SiO_2-2800H_2O$. The mole ratios of the reactants are listed in Table 1. The synthesis batch was prepared using the following procedure. The collodial silica was weighed into a tared plastic beaker. To this, weighed amounts of water, sodium hydroxide solution and tetrapropylammonium bromide were added. The mixture was agitated until a uniform gel was obtained. Reactants were then rapidly transferred into 15-ml teflon-lined Morey-type autoclaves. The vessels were sealed, weighed and placed into an eight position centrifuge contained within a preheated forced convection oven set at 180°C. Weighed vessels were carefully placed to achieve the best possible balance of the centrifuge.

Procedure

The centrifuge was fabricated using an eight position sample bracket mounted within a forced-convection oven. Individual sample

Table 1. Molar Ratios of Reacting Species

Species	Ratio
SiO_2/Al_2O_3*	∞
H_2O/SiO_2	28.0
OH^-/SiO_2	0.051
Na^+/SiO_2	0.051
TPA^+/SiO_2	0.050

*Alumina was not added to the reaction mixture although some
aluminum may be present as a trace impurity in the reagents.

mounts were machined to support the 15-ml autoclaves.
The centrifuge was rotated at a pre-determined speed using a high-
torque Lightning Mixer motor mounted outside the oven using
graphite bearings. Rotational speed was maintained with a
Reliance Electric variable speed controller. Gravitational
forces in excess of 100G were obtainable using this centrifuge,
although the preferred operating range was 10 to 50G.

The centrifuge was rotated at predetermined speeds yielding
different gravitational forces. A set speed was maintained
throughout the experiment. At daily intervals, the centrifuge
was stopped, and a vessel was removed from the oven. The vessel
was replaced with a vessel of similar weight (loaded with water),
then the crystallization was continued.

The product vessel was quenched to room temperature using
cold tap water. The autoclaves were immediately opened, and the
pH of the mother liquor was measured. The solid products were
placed in a Buchner funnel, washed a minimum of three times with
100ml of distilled water, and dried overnight at 110°C.

Product yield was measured for all runs. The yield was
determined by emptying the entire contents of the autoclave into
a pyrex beaker. Sodium hydroxide solution (100ml, 0.1N) was
added to the beaker, and the slurry was heated to boiling (100°C)
for one hour to completely dissolve the amorphous solids. The
remaining purified silicalite crystals were dried at 110°C. The
weight of silica initially charged to the autoclave was
calculated from the initial colloidal silica. The ratio of the
final weight of purified silicalite crystals to the initial
weight of silica charged to the autoclave gives the product yield.

Analysis
Phase identification of the product crystals was performed by
powder x-ray diffraction, using $CuK_{\alpha 1}$ radiation. The instrument
was a Philips Model PW1730/10 x-ray generator equipped with a PW
1050/70 vertical goniometer. Diffractograms were measured for the
as-synthesized product; that is, crystals plus gel. Crystal size
and morphology were determined by scanning electron and optical
microscopy. The electron microscope was an AMRay Model 1200B
microscope equipped with a KEVEX Model 7000 Energy x-ray dispersion
analyzer for qualitative chemical analysis.

The particle size distribution of the silicalite crystals
was determined using optical microscopy. To analyze size, the
as-synthesized samples (crystals plus gel) were dispersed onto
glass slides from an alcohol suspension and then examined under an
optical microscope using polarized light. Polarized light assists
in the separation of unreacted gel and crystals in the image. The
image was then acquired by a television camera connected to a Traco
Northern 8502 Image analysis system. The image was analyzed using
the Tracor Northern software by first converting the image to a
binary (black-white) image, and then the software analyzes each
particle in the field. Before initiating a test, the system was
calibrated by viewing standard particles. Because of ambiguities
introduced by the use of polarized light, it was necessary to
manually outline many of the particles using a mouse. This allows
for the removal of spurious particles, insuring a true accounting
of all crystals. The image analysis software uses the binary image
to individually analyze each particle (assuming a rectangular
geometry), thereby obtaining a length and width for each crystal.
To assure that meaningful data was being collected, a minimum of
three image fields were collected for each sample.

RESULTS AND DISCUSSION

The mixture used in the study was found to produce only
silicalite. Crystallizations were carried out under normal gravity
and at 30 and 50G. Sample vessels were removed from the
oven/centrifuge assembly at one day intervals and tested for
average crystal length, for the average length of the largest 10%
of the crystals, for crystal yield and for the pH of the mother
liquor. Results are shown in Figures 1, 2, 4 and 5, respectively.
The value for average particle size was determined using the
particle size distribution system described earlier. Three
replicate size distributions were determined for each experimental
run. Each image was found to have from twenty to forty crystals.
An average crystal length was determined by using all the
individual crystal lengths from the three replicates; that is,
averaging a total of 60 to 120 crystal lengths. This average
crystal length is plotted in Figure 1 as a function of reaction
time. Under normal gravity, trace amounts of crystallized product,
having an average crystal length of 93μm, appeared after one day.
This initial growth occurred heterogeneously on the teflon-lined
vessel walls. Few crystals were observed to form in the bulk gel.
At longer times, silicalite was found to crystallize homogeneously
in the gel. These crystals averaged 45 to 60μm in length. It is
interesting to note that at seven days larger silicalite crystals
were found to form, some exceeding 100μm in length. These results
suggest a secondary crystallization forming these larger crystals.
The average crystal lengths determined for the elevated
gravity experiments were substantially greater than those found
for the 1G experiment. At 30 and 50G, the average crystal lengths
were found to be 160 and 156μm respectively as determined by
averaging the mean crystal lengths for reaction times of two to
seven days. For the high gravity runs, large crystals formed in
one day. These crystals were of comparable length to the 1G run.

With increasing reaction times, average crystal length increased to maximums of 192 and 198μm for the 30 and 50G experiments. In both elevated gravity experiments there was an initial formation of relatively large crystals followed two to three days later by a second growth of larger crystals. These results suggest a dissolution of the smaller crystallites providing nutrients for the continued growth of the largest crystals.

Mean crystal sizes for the largest 10% of the crystals were calculated using crystal size distribution data. Results for normal gravity and for the high gravity runs are plotted in Figure 2. The largest crystals were produced at high gravity during the second phase of crystal growth. The average size of the largest 10% was 295 and 297μm for the 30 and 50G runs. In the normal gravity run, some large 130μm crystals were observed forming in one day; although as noted previously, these crystals nucleated heterogeneously on the walls of the teflon autoclave liner. The largest crystals which formed homogeneously at 1G ranged from 50 to 95μm. A second growth, producing larger 100μm crystals, was found to begin at seven days. Although Figures 1 and 2 quantify the differences in average and maximum crystal lengths between normal and elevated gravity syntheses, the effect of gravity on crystal size is best demonstrated by a direct comparison. Optical micrographs of silicalite produced after five days of reaction at 1 and 30G are shown in Figure 3. Both micrographs were taken at identical magnifications of 50X and clearly demonstrate the enhancement in crystal size caused by elevated gravity.

In addition to increasing crystal size, the application of elevated gravity also affects crystal yield. Yields were measured for the 1, 30, and 50G runs. Results are plotted in Figure 4. For synthesis conducted at normal gravity, crystal yields never exceeded 4.3% of the initial charge of silica. For the 30 and 50G preparations, crystal yields of 46.7 and 55.5 were measured. At elevated gravity, it was observed that crystals formed in a layer directly above a dense layer of the amorphous silica gel. With increasing reaction times, the crystal layer thickens while the silica gel layer diminished. At seven days, no separate amorphous silica layer was present. The commercial significance of enhanced product yield using elevated gravity is obvious.

The pH of mother liquor was measured for all three experimental runs. These data are plotted on Figure 5. The alkalinity of the reacting solution was found to decline with time. The pH of the initial mixture was 11.85 declining to less than 10.00 upon completion of the crystallization. The changes in pH with time were found to exhibit minima. For all three cases, the lowest pH values were measured for the reaction times which produced the largest crystals. Under normal gravity, minimum pH values were noted at one and seven days. These times correspond to the formation of the two maximum crystal sizes. Similar trends are observed for the elevated gravity synthesis.

Based on the crystal size, yield and pH data, it is possible to postulate a model for silicalite crystallization in a high gravity environment. The primary effect of applying high gravity during the crystallization is to segregate the collodial silica
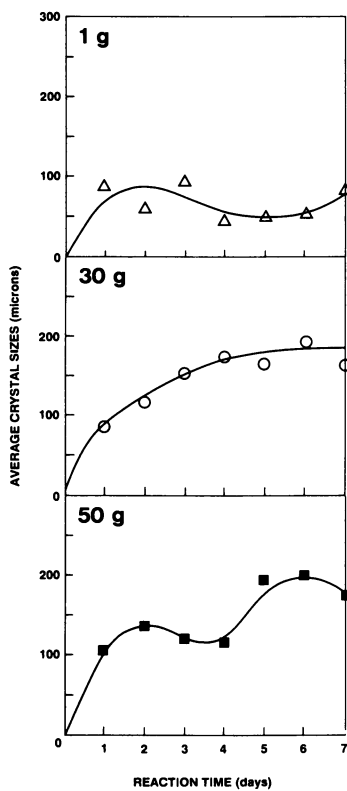
Figure 1. Average crystal size of the 1, 30 and 50G synthesis.
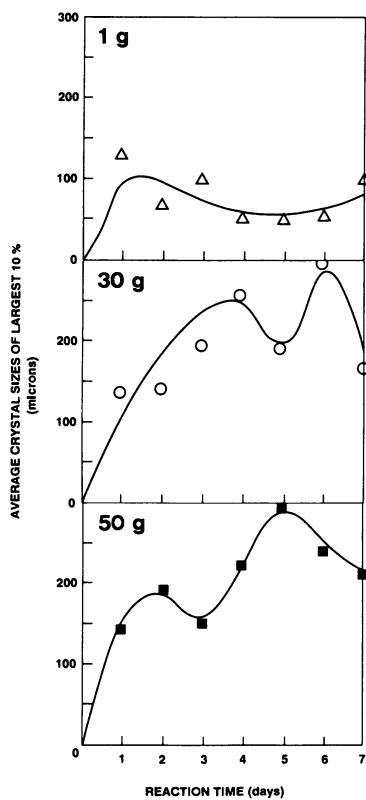
Figure 2.   Average size of largest 10% of crystals synthesized
            at 1, 30 and 50G.
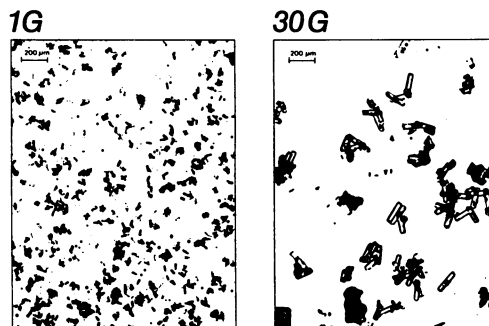
Figure 3.   Optical micrograph of crystals produced after 5 days
            of reaction at 1 and 30G (magnification 50x).
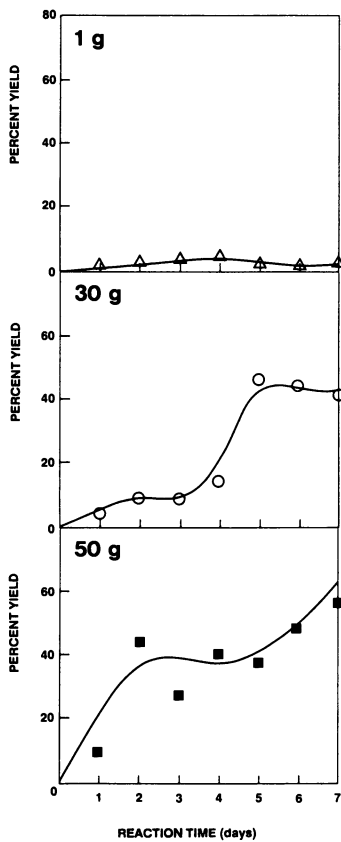
Figure 4.   Yield of crystals synthesized at 1, 30 and 50G.
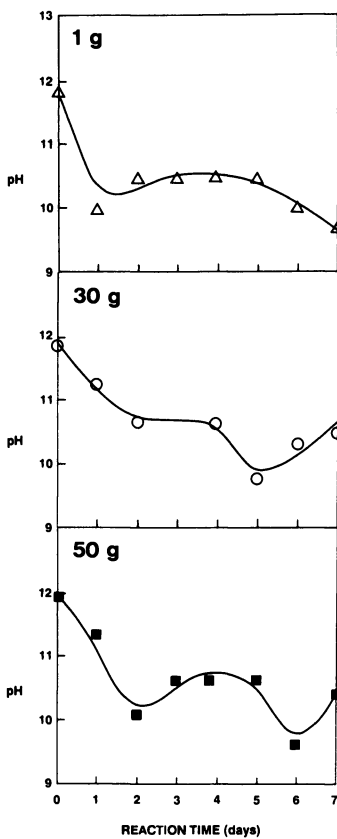
Figure 5. pH of mother liquor for the 1, 30 and 50G synthesis.

from the liquid phase which contains both the template and the alkali. This separation of the solid and liquid phases requires that dissolution, nucleation and crystallization occur only at the interface between the densified solid silica and the alkali solution. This limited interface reduces the number of critical-sized nuclei which form. As crystal growth occurs at a limited number of sites, larger crystals are produced. In this type of crystallization, true solution phase crystallization is expected to predominate. As noted previously, crystals were found to form a layer directly above the densified silica layer in all elevated gravity reactions. With increased reaction time the crystal layer increases in thickness while the silica gel layer diminishes. The reasons for a second crystallization, and increased product yield, are less obvious and require further investigation.

CONCLUSIONS

Results reported in this study demonstrate that the application of an external gravitational force during synthesis profoundly affects the crystal size and product yield of silicalite. Crystals grown under high gravity are substantially larger than those formed under normal gravity. Correspondingly, product yield is enhanced with elevated gravity. Although the scope of this report is limited, the changes in silicalite crystallizaton due to elevated gravity appear to result from the separation of the liquid and solid silica phases; suggesting that solution phase crystallization may predominate. The commercial implications of these results to zeolite producers are equally significant.

ACKNOWLEDGMENTS

LITERATURE CITED

1.   Ciric, J., *Science* 1987, 155, 373.
2.   Nastro, A. and Sand, L.B., *Zeolites* 1983,3, 57.
3.   Mostowicz, R., and Sand, L.B., *Zeolites* 1983, 3, 219.
4.   Mostowicz, R., and Berak, J., *Polish Pat.* 135 293 (1982).
5.   Mostowicz, R. and Sand L.B., *Zeolites* 1982, 2, 143.
6.   Derouane, E.G. et al., *Appl. Catal.* 1981, 1, 201.
7.   Gabelica, Z., Derouane, E.G., and Blom, N., *Appl. Catal.* 1983, 5, 109.
8.   Gabelica, Z., Blom, N., and Derouane, E.G., *Appl. Catal.* 1983, 5, 227.
9.   Gabelica, Z., Derouane, E.G., and Blom, N., *ACS Symp. Ser.* 248, *Am. Chem Soc.*, USA, 1984, p.219.
10. Romannikov, V.N. et al., *Zeolites* 1983, 3, 311.
11. Ghamami, M. and Sand, L.B., *Zeolites* 1983, 3, 155.
12. Pelrine, B.P., US Pat. 4 100 262 (1978).

13. Olson, D.H. and Valyocsik, E.W., Eur. Pat. Appl. 0 026 963 (1981).
14. Kuei-Jung, Chao et al., <u>Zeolites</u> 1986, **6**, 35.
15. von Ballmoss, R. and Meier, W.M., <u>Nature</u> 1981, **289**, 782.
16. Lermer, H. et al., <u>Zeolites</u> 1985, **5**, 131.
17. Hayhurst, D.T. and Lee, J.C.,in <u>New Developments in Zeolite Science and Technology</u> (Eds. Y. Murakami, A. Iijima and J.W. Ward), Kodansha, Tokyo, and Elsevier, Amsterdam, 1986, p. 113.
18. Hou, L.Y., Sand, L.B. and Thompson, R.W. in <u>New Developments in Zeolite Science and Technology</u> (Eds. Y. Murakami, A. Iijima and J.W. Ward), Kodansha, Tokyo, and Elsevier, Amsterdam, 1986, p. 239.
19. Kornatowski, J. <u>Zeolites</u> 1988, **8**, 77.
20. Chen, S.Z., Huddersman, K., Keir, D. and Rees, L.V.C., <u>Zeolites</u> 1988, **8**, 106.
21. Guth, J.L., Kessler, H. and Wey, R. in <u>New Developments in Zeolite Science and Technology</u> (Eds. Y. Murakami, A. Iijima and J.W. Ward), Kodansha, Tokyo and Elsevier, Amsterdam, 1986, p 121.
22. Zetterlund, E.H. and Fredricsson, E., <u>Material</u> <u>Letters</u>, 1982, **1**, p. 127.
23. Rodet, H., Regel, L.L, Ghamami,M., Videskii, I.V., <u>J. Cryst. Growth</u>, 1986, **79**, p. 77.
24. Sand, L.B., Sacco, A., Thompson, R.W. and Dixon, A.G., <u>Zeolites</u>, 1987, **7**, p. 387.

Chapter 18

Crystallization of Pentasil Zeolite in the Absence of Organic Templates

Feng-Yuen Dai[1], Minoru Suzuki, Hiroshi Takahashi†, and Yasukazu Saito

Institute of Industrial Science, University of Tokyo, 7—22—1 Roppongi, Minato-ku, Tokyo 106, Japan

As-synthesized Na-ZSM-5, which possesses an isostructure with TPA-ZSM-5, exhibits a hexagonal-lath-shaped morphology. Liquid phase SiO_2/Al_2O_3 ratio is important in controlling the formation of Na-ZSM-5 and mordenite, and the silica source influences the liquid phase composition. High yield of Na-ZSM-5 is obtained only when a small-sized silica sol is employed. A linear relationship between Na/Al starting atomic ratio and the nucleation rate indicates that charge neutralization of SBU is required for zeolite crystallization.

As ZSM-5 zeolite possesses excellent catalytic properties, synthesis of this material without organic templates would be economically important from the industrial standpoint. ZSM-5 crystals can be synthesized without using expensive and toxic organic templates (1-4). Since the raw materials and hydrothermal synthesis conditions used by several workers are quite different, their starting compositions for organic-free Na-ZSM-5 synthesis are not the same. It is well known that the silica source has a considerable influence on the kind of zeolitic products (5), however, reason for this is not clear. In order to seek optimum conditions for Na-ZSM-5 formation in the absence of organic template, the effects of both starting composition and silica source were examined. Some questions regarding the as-synthesized Na-ZSM-5 characterization were also discussed.

Experimental

Zeolite Crystallization. The raw materials used in the study were: 1) sodium aluminate (Al_2O_3 51.51 wt%, Na_2O 40.24 wt%), sodium hydroxide (10 wt% NaOH aqueous solution), and colloidal silica sols, 2) aluminum sulfate, water glass (SiO_2 24.3 wt%, Na_2O 8.12 wt%, and Al_2O_3 0.023 wt%) and 0.1 N sulfuric acid. For the silica sol, both S-20 L (with particle size of 10-20 nm; SiO_2 20.3 wt %, Na_2O 0.04

[1]Current address: Department of Chemical Engineering, Worcester Polytechnic Institute, Worcester, MA 01609
†Deceased

wt%, Al_2O_3 0.024 wt%) and SI-80 P (70-90 nm; SiO_2 40.8 wt%, Na_2O 0.43 wt%, Al_2O_3 0.030 wt%), obtained from Catalysts & Chemical Industry, Ltd., were used.

The amounts of SiO_2 (0.287 mol) and H_2O (13.15 mol) were kept constant in hydrogels, while those of sodium hydroxide and sodium aluminate were varied appropriately. For example, to adjust a composition of 9.33 Na_2O-1.0 Al_2O_3-70 SiO_2-3213 H_2O, which is typically one for ZSM-5 synthesis (6), a starting gel was prepared by adding sodium aluminate (0.7708 g), 10 wt% NaOH (26.05 g) and H_2O (76.49 g) solution gradually into an aqueous solution of S-20 L (85.10 g) and H_2O (68.86 g), then stirred for 1 h at room temperature. Zeolite crystallization was carried out in a 400 ml Teflon vessel inside an autoclave, under autogeneous pressure at 190 ± 2 °C without agitation. To avoid seed effects, the Teflon vessel was cleaned with hydrofluoric acid prior to each succeeding synthesis.

Characterization of Solid Product. Chemical analysis of solid product was carried out by means of wet method; the SiO_2 component was dissolved with hydrofluoric acid and then evaporated, the contents of Na_2O and Al_2O_3 were determined by flame photometry and atomic absorption spectrophotometry, respectively. The content of SiO_2 was estimated by subtracting the value of loss of ignition (L.O.I.) (at 1200 °C) and the contents of Na_2O and Al_2O_3 from initial mass of solid product.

X-ray powder diffraction (XRD) profile was measured by an X-ray diffractometer (Rigaku Denki, Ltd., D-9 C, equipped with a scintillation counter), using Cu-Kα radiation with the slit system of RS = 0.15 mm and DS = SS = 1/2°; the 2θ scan rate was 1/4 or 1/8 °/min. The 2θ values were adjusted by the Si(111) reflection, using silicon powder (300 mesh) as the internal standard. Crystal morphology of zeolites was observed by means of scanning electron microscopy (Akashi, Ltd., Alpha-10).

The zeolite products with the highest XRD intensities and with the lowest amorphous material impurities were used as the quantitative standards for both Na-ZSM-5 and mordenite. The degree of crystallization was estimated by comparing the sum of the respective XRD peak areas (around 2θ = 20-30°) with those of the standard.

To characterize the organic-free Na-ZSM-5, the following samples (with similar SiO_2/Al_2O_3 ratios of ca. 50) were prepared (7). TPA-ZSM-5 (A_1) was synthesized from starting composition of 2.0 TPA_2O-1.0 Al_2O_3-65 SiO_2-3000 H_2O at 170 °C for 48 h with stirring, using tetrapropylammonium bromide (TPABr) as the TPA source. The sample A_1 was calcined at 620 °C for 3 h to obtain an organic-free zeolite (B_1). To obtain DEA-ZSM-5 (A_1'), zeolite B_1 was first degassed at 150 °C for 1 h in a glass tube, and then excess amount of diethylamine (DEA) was vacuum-transferred into the glass tube to immerse the zeolite B_1 at 15 °C for 12 h. Na-ZSM-5, synthesized at 190 °C for 16 h from 8.75 Na_2O-1.0 Al_2O_3-70 SiO_2-3150 H_2O system, was converted into its hydrogen-form (B_2) through ammonium-exchange (15 °C for 12 h) and calcination (540 °C for 4 h), followed by loading DEA (15 °C for 12 h) to give a DEA-zeolite (A_2), and finally by calcining the sample A_2 (540 °C for 4 h) to yield another organic-free zeolite (B_2'). To view clearly the XRD profile changes, the XRD region of 2θ = 22-25° was enlarged by using a 2θ scan rate of 1/8 °/min.

^{29}Si NMR Characterization of Silicate Species. NMR spectra were measured on a JEOL GX-270 NMR spectrometer at 53.69 MHz (8); the

gated decoupling mode was applied to avoid the Nuclear Overhauser effect (NOE). ^{29}Si chemical shift was referred to the internal standard of tetramethyl silane (TMS), which was mixed with chloroform in volume ratio TMS/CHCl$_3$ = 1/3, sealed in a 5 mm glass tube and settled into each 10 mm Teflon sample tube. The pulse width and pulse interval were 10 μs and 6 s, respectively. 500-800 FID decays were accumlated to gain sufficient S/N ratios.

Results and Discussions
Characteristics of Na-ZSM-5.
The XRD profiles of as-synthesized, TPA- and Na-ZSM-5 are not exactly identical (Figure 1). Around the main-peak region of 2θ = 23.0-23.5°, Na-ZSM-5 zeolite gives a well-resolved profile in contrast with TPA-ZSM-5; such a profile has been accepted as grounds for the ZSM-8 assignment (9). The structure of ZSM-8 has been suggested to be an intergrowth of ZSM-5 and ZSM-11 (10). A question arises therefore, whether as-synthesized Na-ZSM-5 belongs to TPA-ZSM-5 or so-called ZSM-8. When the as-synthesized TPA-ZSM-5 is calcined to decompose the organic species in the skeleton, the main peaks split well and resemble that of Na-ZSM-5 (Figure 1). Decomposition and readsorption of organic species for both TPA- and Na-ZSM-5 were therefore examined, to elucidate the effect of organic species.

As shown in Figure 2a, only five significant peaks appeared around the region of 2θ = 22.0-25.0° for either TPA- or Na-ZSM-5. When sample A_1 was converted into B_1, the position of its strongest peak (marked as (1)) remained unchanged, whereas other peaks ((2)-(5)) were slightly shifted toward higher angles. On the contrary, incorporation of DEA into the sample B_1 producing A_1', induced the peak shifts toward lower angles. The trends of the peak shifts due to content of organics were observed also for zeolites prepared from Na-ZSM-5, as can be seen in Figure 2b, where the XRD profile changes $B_2 \rightarrow A_2 \rightarrow B_2'$ are shown.

Since both kinds of siliceous zeolites exhibit high stability against thermal treatment, as can be seen in the reversible changes of XRD profiles from A_1 to A_1' or from B_2 to B_2', no topological changes in the host skeleton occur throughout these conversion processes. These profile changes can therefore be attributed to lattice expansion induced by the guest organic amine.

Over the XRD region of 2θ = 5-50°, all the positions of calcined-(TPA)-ZSM-5 (B_1) coincided well (within error of ± 0.02°) with those of H-ZSM-5 (B_2). Furthermore, for both kinds of zeolites (SiO$_2$/Al$_2$O$_3$ ≈ 50), no doublet peaks appeared at 2θ = 24.4, 29.2, and 48.6° throughout the above treatments. This is in agreement with the previous data (11), which showed that neither calcination nor ion exchange change the orthorhombic symmetry of as-synthesized ZSM-5 zeolites with SiO$_2$/Al$_2$O$_3$ ≤ 147.

On these grounds, it is concluded that the as-synthesized Na-ZSM-5 possesses an isostructure with TPA-ZSM-5 but differs in framework topology from the so-called ZSM-8 structure.

Hexagonal-lath-shaped crystals (Na-ZSM-5) are always obtained from the organic-free system, whereas sphere-like or crossed-discus (twinned) crystals (TPA-ZSM-5) are easily formed in the system containing TPABr (Figure 3). From XRD measurements of the lath-shaped Na-ZSM-5, certain peak intensities were found to be sensitive to the manner of mounting the specimen onto an X-ray sample holder.
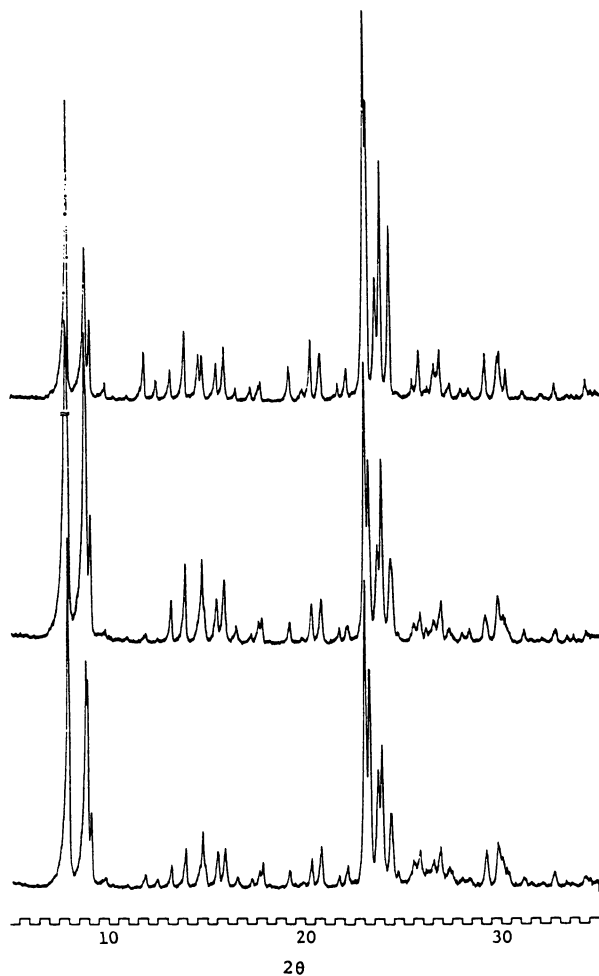
Figure 1. XRD profiles of as-synthesized TPA-ZSM-5(top),
Na-ZSM-5(bottom) and calcined-(TPA)-ZSM-5(middle).

a)

b)
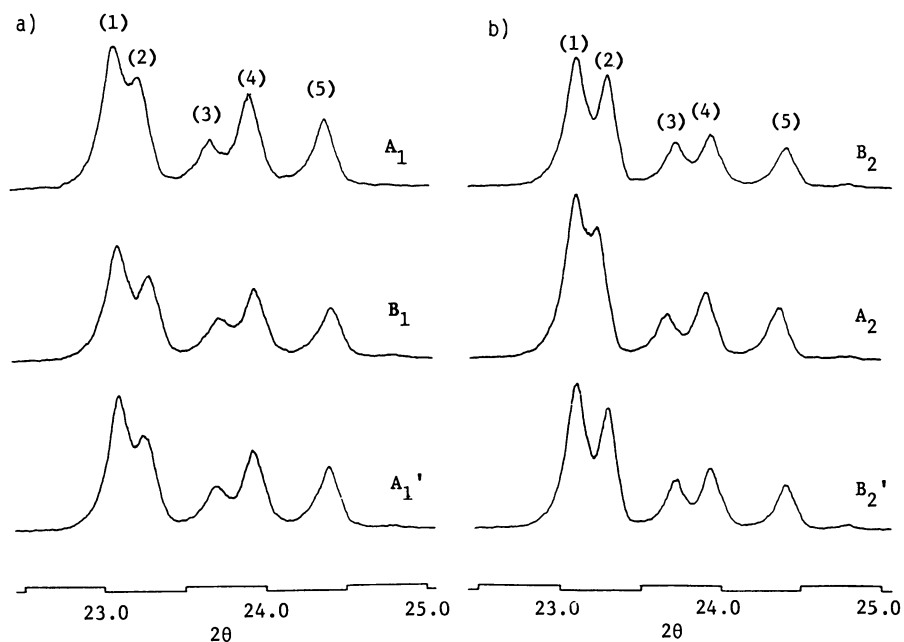
Figure 2. Effect of guest organic amine on the XRD profiles of
both TPA-ZSM-5(a) and Na-ZSM-5(b).
(Reproduced with permission from Ref. 7. Copyright 1988
Bull. Chem. Soc. Jpn.)
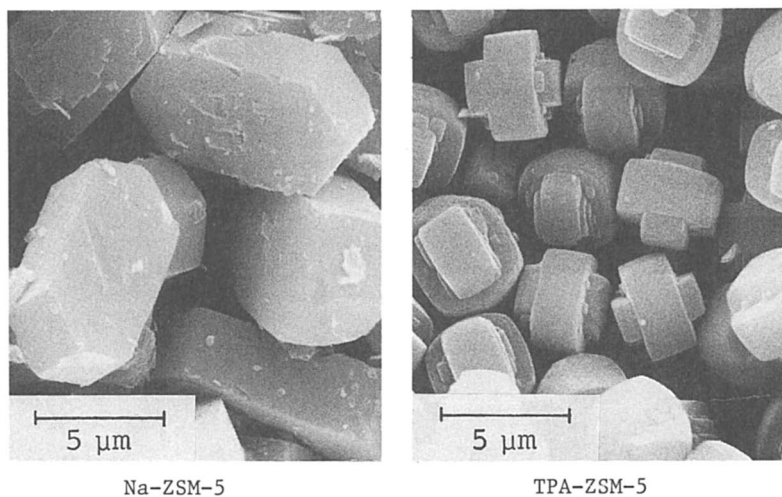
Na-ZSM-5   TPA-ZSM-5

Figure 3. SEM morphologies of Na-ZSM-5 and TPA-ZSM-5.
(Reproduced with permission from Ref. 7. Copyright 1988
Bull. Chem. Soc. Jpn.)

With regard to the sphere-like TPA-ZSM-5, such a phenomenon has never been experienced previously. Those specific XRD peaks, sensitive to the specimen pressing, were summarized in Table I, together with the corresponding Miller Indices of ZSM-5 (12). The peaks that diminished in intensity were classified to belong to the group of ($h0l$) reflection, whereas those intensified - to the ($0k0$) group.

It is conceivable that the hexagonal-flat planes of crystals are apt to orient parallel to the board surface of XRD sample holder due to the preferred orientation by pressing. The peaks of diffraction planes that are parallel to the hexagonal flat planes can therefore be intensified. This supports the view that the hexagonal flat planes of Na-ZSM-5 crystal belong to the (010) reflection plane. Since those planes with ($0k0$) Miller Indices intersect perpendicularly the 'b' axis, the straight 10-membered-ring channels of ZSM-5 (elongated along the 'b' axis (13)) are therefore deduced, to penetrate perpendicularly the hexagonal flat planes of the Na-ZSM-5 crystals.

Correlation of Starting Composition with Crystallization of Pentasil Zeolites. Zeolites were synthesized at 190 °C for 24 h, by using the S-20 L sol as the silicate source. The starting compositions were varied systematically within the molar-ratio ranges of $10.0 \leq SiO_2/Al_2O_3 \leq 100$ and $0.11 \leq Na_2O/SiO_2 \leq 0.26$, as shown in the extended triangle diagram (Figure 4). ZSM-5 (marked as ● hereafter) is formed preferentially to mordenite (○) at high SiO_2/Al_2O_3 and Na_2O/SiO_2 starting ratios. Phase transformation ZSM-5 → ZSM-5 + mordenite → mordenite is induced easily by increasing the Na_2O/SiO_2 or decreasing the SiO_2/Al_2O_3 ratios.

Table II summarizes the anaytical data of ZSM-5 prducts synthesized in the organic-free system (at 190 °C for 24 h). At the starting SiO_2/Al_2O_3 molar ratio of 100, ZSM-5 crystals were accompanied by large quantities of amorphous gel (observed by SEM), and small amount of α-quartz (observed by XRD), and, therefore, they were not suitable for elemental analysis. For the starting SiO_2/Al_2O_3 ratio higher than 100, ZSM-5 phase was not obtained and only amorphous aluminosilicate gel and α-quartz were formed. The maximum SiO_2/Al_2O_3 ratio of ZSM-5 crystals obtained in this study was 49.3.

It is concluded that the optimum compositions which yield a high amount of crystals are: SiO_2/Al_2O_3 = 50-70, Na_2O/SiO_2 = 0.13-0.20 for ZSM-5, and SiO_2/Al_2O_3 = 20-25, $Na_2O/SiO_2 \geq 0.20$ for mordenite (when the S-20 L sol is used as silica source) (6).

Significance of Silica Source on Controlling Pentasil Zeolite Phase The use of different silica sources often produces different zeolitic products, even from the same starting composition (5,8). For instance, when compositions of SiO_2/Al_2O_3 = 50 and Na_2O/SiO_2 = 0.13 were used, silica sols with small particle sizes (10-20 nm) gave pure ZSM-5 phase, whereas large particle sizes of sols (35-55 and 70-90 nm) produced mordenite in high extent (6). This could be rationalized by assuming that the zeolite precusor appeared in the liquid phase, since the liquid composition plays an important role in controlling the type of zeolite which is formed (14). Large-sized silica sol dissolves more difficult than the silica sol with small particles (15), and therefore a lower SiO_2/Al_2O_3 ratio of liquid composition is induced by the large-sized particles. This favors the formation of low-silica mordenite rather than ZSM-5. This point of view is consistent with the fact that formation of mordenite phase is pre-determined by decreasing the starting SiO_2/Al_2O_3 ratio.

Table I. Effect of Preferred-Orientation on XRD of
Na-ZSM-5 Crystal

$(h\ k\ l)$	2θ	$(I/I_0)^a$	
		normal setting	extreme pressing
1 0 2	13.90	76	47
2 0 2	15.86	69	49
1 0 3	20.34	40	28
3 0 3	23.91	219	156
0 4 0	17.79	38	69
0 5 1	23.25	436	526
1 5 1	23.68	186	213
0 10 0	45.46	57	73

a) The intensity of (111) reflection ($2\theta = 9.08°$) was
used as I_0, because this was the strongest peak
insensitive to the preferred orientation.
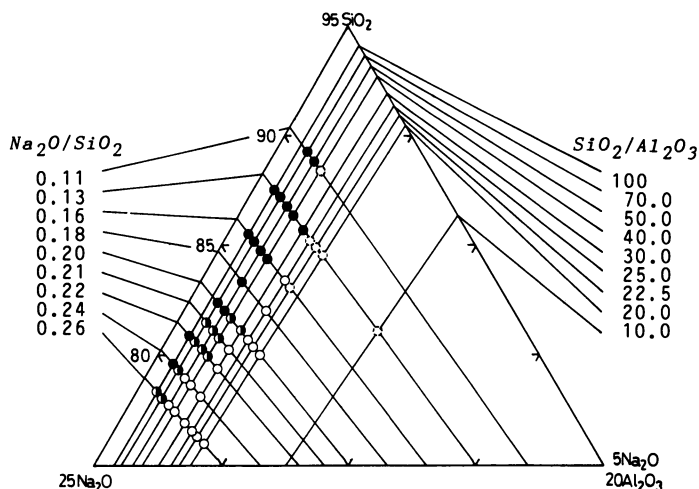
Figure 4. Formation fields of pentasil zeolites of Na-ZSM-5 and
mordenite in the absence of organic templates.
(Reproduced with permission from Ref. 6. Copyright 1986
Kodansha Ltd., Japan)

Table II. ZSM-5 Crystals Synthesized in
Na_2O-Al_2O_3-SiO_2-H_2O System

hydrogel		solid product	
SiO_2/Al_2O_3	Na_2O/SiO_2	% ZSM-5[a]	SiO_2/Al_2O_3
100	0.22	50	——
100	0.16	60	——
100	0.13	56	——
70	0.20	88	37.4
70	0.16	97	44.3
70	0.13	95	49.3
50	0.20	78	33.4
50	0.13	85	39.2

a) Degree of crystallization estimated by XRD method.

Figure 5 summarizes the zeolite phases synthesized from water glass, S-20 L and SI-80 P sols in the range of SiO_2/Al_2O_3 = 8-100, at 190 °C for 48 h, at constant H_2O/SiO_2 (45.9) and Na_2O/SiO_2 (0.13) ratios. For the water glass, Na_2O/SiO_2 = 0.32 can not be reduced. In order to reduce the pH values of hydrogels prepared from water glass, an appropriate amount of sulfuric acid was added.

At the starting ratio of SiO_2/Al_2O_3 = 40.0, for example, a pure mordenite phase was obtained from the SI-80 P sol, whereas the S-20 L gave the coexisting phases of ZSM-5 and mordenite. The water glass produced ZSM-5 + mordenite + α-quartz phases. It is apparent that there is a lower-limit of SiO_2/Al_2O_3 starting ratio necessary to form zeolite for each silica source. This minimum ratio for producing either ZSM-5 or mordenite increased in the order of water glass < S-20 L < SI-80 P. Silicate components in water glass are expected to contribute immediately to the liquid composition without a subsequent dissolution process. Therefore, water glass would increase the SiO_2/Al_2O_3 ratio of liquid phase more rapidly than the silica sols would, providing thus the lowest minimum SiO_2/Al_2O_3 ratio among these silica sources. The small-sized sol (S-20 L) could produce more readily avaliable silicate species in the alkaline solution than the large sol (SI-80 P), and give the lower minimum SiO_2/Al_2O_3 ratio.

^{29}Si NMR spectra of these three kinds of silica sources, together with the alkaline silicate solutions are shown in Figure 6. The alkaline silicate solutions were prepared by dissolving the silica sols with the sodium hydroxide aqueous solutions, at room temperature for 1 h, giving the following compositions: H_2O/SiO_2 = 45.9 and Na_2O/SiO_2 = 0.13 (SiO_2 = 14.33 mmol). These experimental conditions were similar to the conditions for preparation of the starting gel for zeolite synthesis, except for addition of aluminates.

The water glass gave at least five distinct ^{29}Si NMR peaks similar to previous data ([16,17]). Those peaks have been assigned as Q^0-Q^4. No Q^0-Q^2 peaks were found in the NMR spectra of both S-20 L and SI-80 P sols, in contrast to the water glass (Figure 6a). A broad band which appeared around -112 ppm was also assigned to the Q^4 ([18]). After the silica sols dissolved in the sodium hydroxide aqueous solution for 1 h at room temperature, the S-20 L sol gave four additional peaks of Q^0-Q^3, whereas Q^0 and weak peaks of Q^1 and Q^2 were generated from the SI-80 P (no significant changes of these spectra occurred within 3 h after the NMR measurements had been started).

Because no NOE was operative at the present NMR conditions, the peak intensities should correspond to the amounts of dissolved silicate species. NMR study supported the evidence that the small-sized sol (S-20 L) gave more silicate species than the large sol (SI-80 P) did. Also, the nature of the dissolved silicate species from different sols was not the same, as can be seen from Figure 6b, where the species from the S-20 L contain the middle group (Q^2) and branching group (Q^3) in larger quantity than species from the SI-80 P (Figure 6b). This could be also attributed to the particle sizes. It has been pointed out that the appearance of the Q^2 and Q^3 groups are important to the zeolite crystallization ([19]). From Figure 6, it can be seen that the amount of these groups are increasing in the order of SI-80 P < S-20 L < water glass, providing strong evidence to support the above viewpoint in explaining the results of Figure 5.
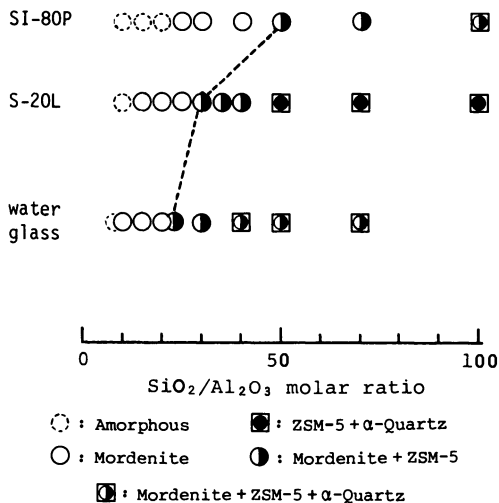
Figure 5.   Effect of silica source on zeolite crystallization.
(Reproduced with permission from Ref. 8.   Copyright 1988
Chem. Lett.)
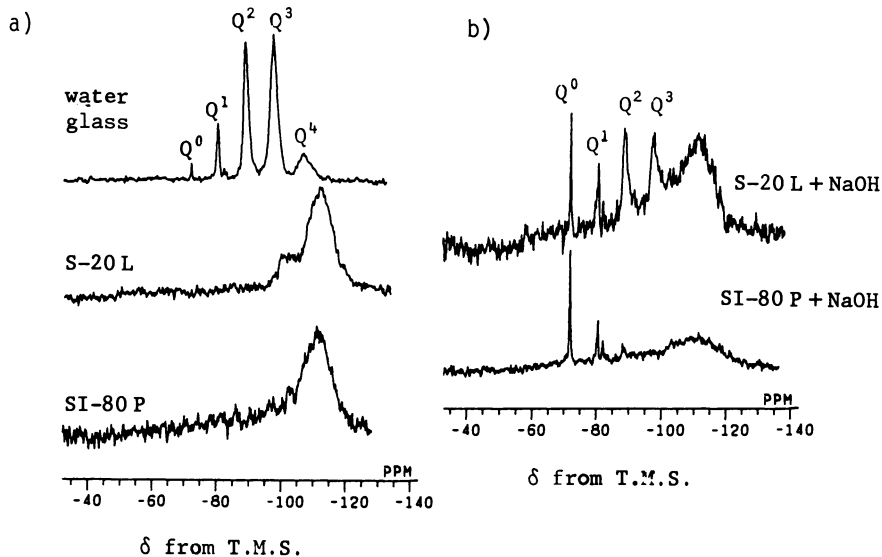
Figure 6. ^{29}Si NMR spectra of a) water glass, silica sols of
different particle sizes, and b) alkaline solutions of those sols.
(Reproduced with permission from Ref. 8.   Copyright 1988
Chem. Lett.)

Although water glass contains sufficient amounts of Q^2 and Q^3 groups, it is not the best source for pure ZSM-5 crystallization in the absence of organic templates. We had succeeded in the synthesis of pure Na-ZSM-5 crystals in high extent, using only the S-20 L sol, whereas the contamination with mordenite was inevitable by using either water glass or the SI-80 P sol (8). The activity of silicates in water glass is considered to be very high, therefore, they react easily with aluminates producing an aluminosilicate species with lower SiO_2/Al_2O_3 ratios that favor the occurrence of low-silica precursors.

It is suggested, therefore, that choosing the proper silica source is essential to synthesize pure ZSM-5 in the organic-free system. The proper silica source would be the silica sol with small particle sizes such as 10-20 nm, or one that could produce silicate species with appropriate amounts of Q^2 and Q^3 groups in the alkaline solution.

Initiation of Zeolite Crystallization. An induction period (t_i) is always observed at zeolite crystallization, and is accepted to be the period necessary for the formation of zeolite nuclei (20). The inverse value of induction period, $1/t_i$, is called the rate of nucleation. The crystallization curves were plotted as the degree of crystallization (estimated by the XRD method) versus synthesis time. The values of t_i were obtained by extrapolating the time when crystal growth started.

From the starting compositions that are within the range stated above (Figure 4), several values of t_i were examined and plotted against the Na/Al atomic ratio in starting composition (Figure 7). The value of t_i decreases as a function of the Na/Al value, along each curve A, B, and C. The molar ratios of Na_2O/H_2O for curve A, B, and C are 0.0029, 0.0044, and 0.0058, respectively. The addition of NaCl without changing the alkali content increases only the magnitude of Na/Al ratio to a higher value along the same line. Addition of NaCl to hydrogel of composition 1 and 2 resulted in compositions 1' and 2', respectively.

A linear relationship was found between the rate of nucleation ($1/t_i$) and the Na/Al atomic ratio, as shown in Figure 8. The following features are worth mentioning: 1) For constant amount of alkali in hydrogel, the nucleation rate of zeolite increases linearly with increasing Na/Al atomic ratio of the hydrogel. 2) The slope of each line increases with increasing the alkali content. 3) The addition of NaCl, which is known as a mineralizer, increases the Na/Al value. 4) All straight lines intercept at the origin (0,0), suggesting that zeolite nucleation will never start when the Na/Al atomic ratio of hydrogel is zero.

The postulate (21), that the crystal framework of zeolite is formed by the progressive additions of secondary building units (SBU) instead of single $(Si,Al)O_4$ tetrahedra, is widely accepted. The silicate species observed by ^{27}Si NMR (Figure 6) could be related to the SBU-like species. Assuming that an SBU consists of at least one $(AlO_4)^-$ anion, its charge compensation with a Na^+ cation would be required. The Na/Al ratio could be realized as the encounter probability between Na^+ cation and $(AlO_4)^-$ anion, or in terms of the probability between Na^+ cation and SBU. The Na/Al ratio can be increased by addition of either NaOH or NaCl.
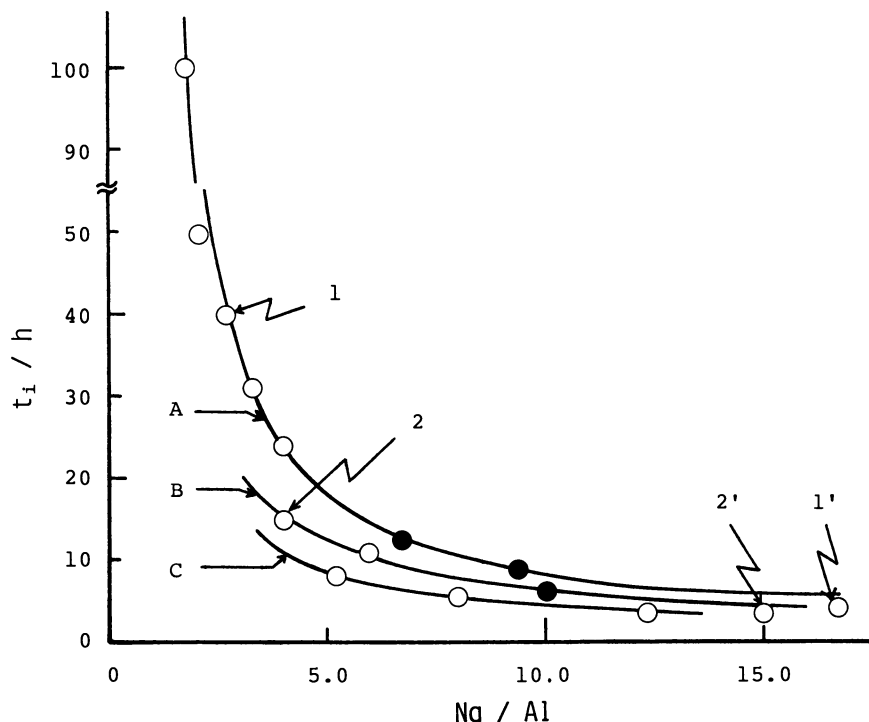
Figure 7. Relationship between Na/Al starting atomic ratio and induction period.
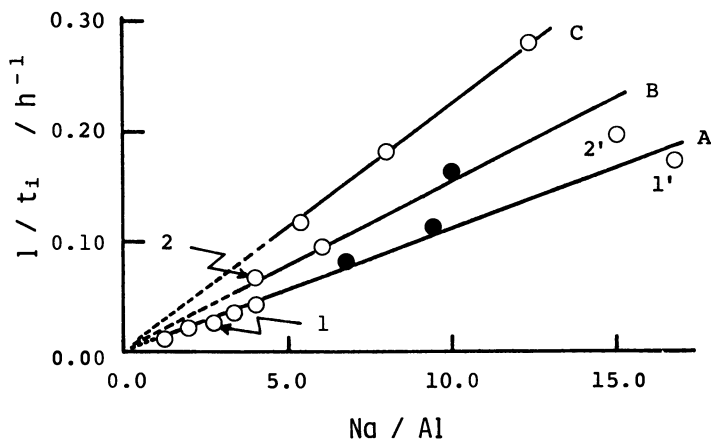
Figure 8. Relationship between Na/Al starting atomic ratio and nucleation rate.
(Reproduced with permission from Ref. 6. Copyright 1986 Kodansha Ltd., Japan)

As germ nuclei must reach a critical size before becoming viable for spontaneous further growth (22), species of the charge-stablized SBU would be required to compose the critical-sized germ nuclei.

Literature Cited

1. Chao, K.-J. Proc. Nat. Sci. Conc., Taiwan, 1979, 3, 233.
2. Grose, R. W.; Flanigen, E. M. U.S. Patent 4,257,886, 1981.
3. Nastro, A.; Colella, C.; Aiello, R. In Studies in Surface Science and Catalysis 24 - Zeolites: Synthesis, Structure, Technology, and Application; 1985; Elsevier, Amsterdam; pp 39-46.
4. Berak, J. M.; Mostowicz, R. In Studies in Surface Science and Catalysis24 - Zeolites: Synthesis, Structure, Technology, and Application; 1985; Elsevier, Amsterdam; pp 47-54.
5. Barrer, R. M.; Denny, P. J. J. Chem. Soc. 1961, 983.
6. Dai, F.-Y.; Suzuki, M.; Takahashi, H.; Saito, Y. Proc. 7th Int. Zeol. Conf. 1986, p 223.
7. Dai, F.-Y,; Suzuki, M.; Takahashi, H.; Saito, Y. Bull. Chem. Soc. Jpn. 1988, 61, 3403.
8. Dai, F.-Y.; Deguchi, K.; Suzuki, M.; Takahashi, H.; Saito, Y. Chem. Lett. 1988, 869.
9. Lechert, H. In Zeolite: Science and Technology; Ribeiro, F. et al., Ed.; NATO ASI Ser. Ser. E. 80, 1984; pp 158-161.
10. Gabelica, Z.; Nagy, J. B.; Bodart, P.; Debras, G.; Derouane, E. G.; Jacobs, P. A. In Zeolite: Science and Technology; Ribeiro, F. et al., Ed.; NATO ASI Ser. Ser. E. 80, 1984; pp 193-210.
11. Nakamoto, H.; Takahashi, H. Chem. Lett. 1981, 1013.
12. Ballmoos, R. In Collection of Simulated XRD Powder Patterns for Zeolite; Butterworth, UK, 1982; pp 74-75.
13. Olson, D. H.; Lawton, S. L.; Kokotailo, G. T.; Meier, W. M. J. Phy. Chem. 1981, 85, 2238.
14. Zhdanov, S. P. In Molecular Sieve Zeolite-I; Gould, R. F. Ed.; Advances in Chemistry Series No. 101; American Chemical Society: Washington, DC, 1971; p 20.
15. Iler, R. K. In The Chemistry of Silica; John Wiley & Son, New York, 1979; pp 45-55.
16. Marsmann, H. C. Z. Naturforsch. B, 1974, 29, 495.
17. Engelhardt, G.; Fahlke, B.; Mägi, M.; Lippmaa, E. Zeolites 1985, 5, 49.
18. Lippmaa, E.; Mägi, M.; Samoson, A.; Engelhardt, G.; Grimmer, A.-R. J. Am. Chem. Soc. 1980, 102, 4889.
19. Groenen, E. J. J.; Kortbeek, A. G. T. G.; Mackay, M.; Sudmeijer, O. Zeolite 1986, 6, 403.
20. Breck, D. W. J. Chem. Edu. 1964, 64, 678.
21. Barrer, R. M.; Baynham, J. W.; Boltitude, F. W.; Meier, W. M. J. Chem. Soc. 1959, 195.
22. Barrer, R. M. In Hydrothermal Chemistry of Zeolite; Academic Press, London, 1982; Chapter 4.

Chapter 19

Crystal Growth Regulation and Morphology of Zeolite Single Crystals of the MFI Type

J. C. Jansen, C. W. R. Engelen[1], and H. van Bekkum

Department of Organic Chemistry, Delft University of Technology, Julianalaan 136, 2628 BL Delft, Netherlands

Crystal growth phenomena in zeolite MFI formation have been monitored. Two new single crystal forms of zeolites of the MFI type are reported. Pyramidal single crystals were found to grow at the surface of gel spheres, the formation of which is thought to be induced by the decomposition of tetrapropyl-ammonium ion during zeolite synthesis and by the presence of trivalent metal ions. The pyramidal crystals are shown to be precursors of the cube-shaped ZSM-5 single crystals described earlier. Another morphology known for MFI-type single crystals, the elongated prismatic habit is shown to transform into a shelf-shape morphology when increasing amounts of boric acid are added to the synthesis mixture.

Synthesis procedures to obtain large zeolite crystals are well developed (1,2). In particular much attention has been paid to the synthesis of ZSM-5 crystals (3-6). Elongated prismatic (Fig. 1a) and cubic-shaped orthorhombic (Fig. 1b) ZSM-5 crystals of sizes between 2-50 μm were reported in the first recipes (7) in the patent literature. Later on, systematic studies have led to excellent synthesis prescriptions for the growth of large crystals of the prismatic (8) as well as of the orthorhombic form (9). The synthesis parameters which are dominant in the crystallization of pure ZSM-5 single crystals, are still under study (10,11).

[1]Current address: Exxon Chemical Holland BV, P.O. Box 7335, 3000 HH Rotterdam, Netherlands
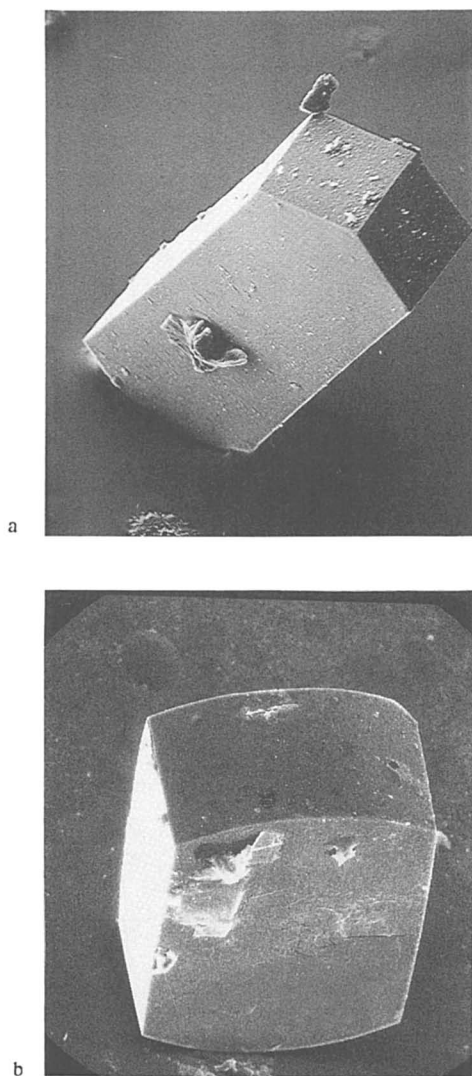
Figure 1. Four different single crystal forms of ZSM-5.
(a) Elongated prismatic; (b) cubic-shaped orthorhombic.
Continued on next page.
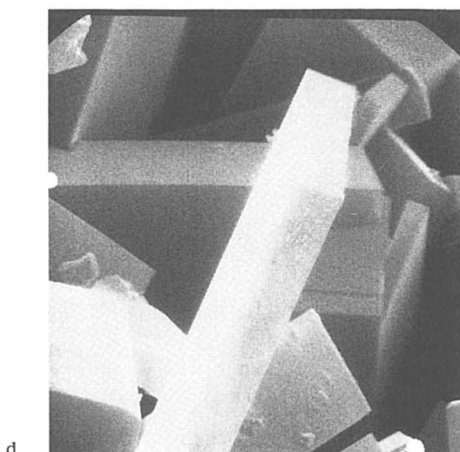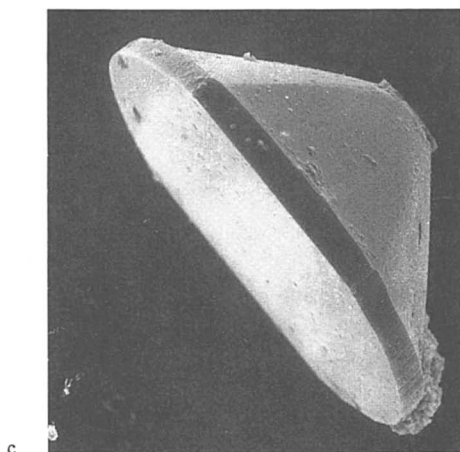
Figure 1. Continued. (c) Pyramidal shaped and (d) shelf-like shaped.

A full understanding of zeolite growth principles is difficult because hydrothermal crystallization of zeolites takes place in heterogeneous reaction media. Domains differing in composition and in viscosity exist in the same reaction mixture and can give rise to different products due to local differences in supersaturation, in ion transport velocity, etc. For this reason it is often difficult to correlate the crystal shape and type to the starting synthesis parameters because the crystal morphology, composition and size will reflect the local crystal growth conditions. So far only the crystal growth history of crystals with the elongated prismatic form is well described. The objective of our studies is to identify local crystal growth conditions which lead to different crystal forms of ZSM-5 by influencing nucleation and growth behaviour. In this paper we report on two new morphologies (Fig. 1c, 1d) of single crystals of the MFI type. Growth history as well as relation to the morphologies reported earlier (Fig. 1a, b) will be discussed.

Experimental

Materials. Table I lists the starting chemicals together with the concentration of the main inorganic impurities.

Table I. Inorganic impurity contents (in ppm)of source chemicals applied

	Al	Ti	Cr	Fe
SiO_2, Aerosil 200,* Degussa	440	90	10	110
SiO_2, FO Optipur, Merck*			$< 10^{-3}$	< 0.01
NaOH, Merck	< 5			< 5
aq. NaOH, Suprapur, Merck	< 0.05			< 0.05
TPA.Br, Janssen*	0.2	0.18	0.004	0.2

* Regularly used chemicals.

Synthesis. Two types of synthesis formulations were applied. The first one is the synthesis procedure as described by Lermer et al. (9) resulting in large cubic ZSM-5 crystals (Fig. 1b) with composition (molar ratio) in the clear starting solution as follows:

	SiO_2	Al_2O_3	Na_2O	TPA_2O	H_2O
(I)	12	<0.5	20	20	2000

The other formulation yielding elongated or shelf-shaped ZSM-5 crystals (Fig. 1a and d, respectively) has the following molar composition:

	SiO_2	B_2O_3	Na_2O	TPA_2O	H_2O
(II)	12	0-2.5	4.5	4.5	2000

Crystallizations were performed at 180 $^\circ$C, in Teflon-lined autoclaves of 35 ml capacity.

Characterization. The TPA concentration in the reaction mixtures
was determined by Induced Coupled Plasma Atomic Emission
Spectroscopy (ICPAES) carbon analysis, which was preceded by
n-hexane extraction in order to remove tripropylamine.
- Al, Cr, Fe, Ti were analyzed in the reactants and intermediate
  products with ICP and Atomic Absorption Spectroscopy (AAS).
- Al-ZSM-5 single crystals were characterized by Elecron Probe Micro
  Analysis (EPMA) on a JEOL XRAY microanalyzer (Superprobe 733).
- B-ZSM-5 as well as Al-ZSM-5 single crystals were for particular
  characterization embedded in resin and subsequently polished.

Results and discussion

Growth of ZSM-5 crystals from gel spheres. The events that take
place during the hydrothermal treatment of synthesis mixture (I),
with regularly used chemicals, see Table I, but *without* added
alumina, are shown in Figures 2a and 2b. Initially the silica is,
considering the high OH/SiO_2 ratio of the synthesis mixture, mainly
present as monomers (12). During the first day about two thirds of
the TPA^+ reacts with OH^- according to the Hoffmann degradation
reaction yielding tripropylamine and propene. The decrease in pH
accompanying this reaction induces polymerization of the silica
monomers to silica sol particles. When Aerosil 200 silica is used,
transparent silica bodies up to several mm in size are formed after
the first day (see Figure 3a). According to SEM observations (see
Figure 3b) these gel spheres are composed of close-packed particles
of about 200-400 Å in diameter. The silica bodies therefore have
been formed by aggregation of the earlier formed sol particles. As
estimated from the decrease in SiO_2 concentration, some 5-10 percent
of the original silica is converted into the gel bodies.
    During hydrothermal treatment of a very pure synthesis mixture
composed of Optipur SiO_2, Ultrapure NaOH (both of Merck), TPA-Br,
and water with a resistance higher than 10^{18} ohm, no gel bodies were
formed at 180 °C not even after two weeks. This implies (13) that
the aggregation of the silica sol particles to gel bodies is
facilitated by the presence of T-atoms other than Si. It has been
proposed (14) that trivalent cations - which are present in the
Aerosil source (cf. Table I), adsorb onto the sol surface and cause
the formation of interparticle bonds which is observed as gelation.
Indeed chemical analysis by AAS showed the following non-Si elements
to be present in the gel bodies: Cr - 63 ppm, Fe - 538 ppm, Al - 588
ppm, Ti - 513 ppm (concentrations relative to Si); the total ratio
Si/T being 588 (T = Cr^{3+}, Fe^{3+}, Ti^{4+}, and Al^{3+}). Assuming that the
T-atoms are adsorbed onto the surfaces of the sol particles, this
would mean for a 400 Å particle with density 2 g/cm^3 that each
T-atom occupies 440 $Å^2$ outer surface, which is a realistic figure
(15). The concentration of Al in the gel bodies is about equal to
the corresponding concentration in the silica source (Aerosil) which
is according to Table I the main supplier of inorganic impurities.
By contrast, the concentrations of Cr, Fe and Ti are higher than the
initial ones mentioned in Table I. The water content of the gel
bodies as determined by AAS and TGA measurements ranged from 30 to
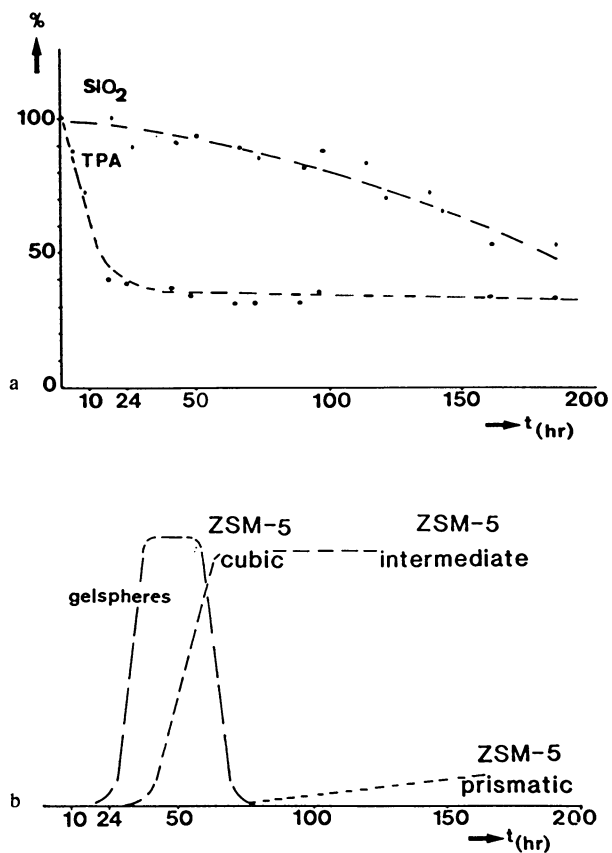
Fig. 2. Hydrothermal treatment of synthesis mixture I without
        added alumina at 180 ^{0}C.
        a. The solution concentrations of silica and
           tetrapropylammonium ion (TPA) as measured by ICP
           versus time;
        b. The formation of solid phases as observed by
           light-microscope.
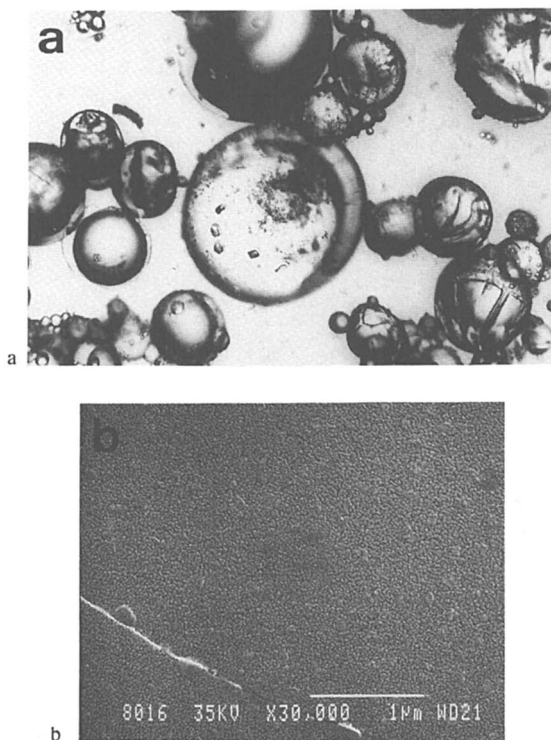
Fig. 3. a. Light micrograph (50 x) of silica bodies formed during
the first days of hydrothermal treatment of synthesis
mixture I without added alumina at 180 °C;
b. SEM picture (30,000 x) of a fracture plane of a silica
body.

50%. Surprisingly TPA could not be detected by FTIR, either on the outer surface, in the diffuse reflection mode, or in flakes from the interior of the gel spheres in the transmission mode.

After about two days, see Figures 4 and 5a, crystallization is observed at the surface of the gel spheres. Pyramids of which the basal plane coincides with the sphere surface penetrate into the sphere body. Despite the supersaturation of the silica source no abundant nucleation is observed on the sphere surface. According to XRD and FTIR measurements the pyramids consist of ZSM-5 framework with TPA as guest molecules.

The fact that ZSM-5 framework formation is strongly promoted by TPA[+] and the observation that just a relatively low number of pyramids is present in the sphere surface are in harmony with DRIFT measurements on the sphere surface which do not indicate the presence of TPA. Thus it is concluded that the concentration of TPA[+] is low in the cation layer of the gel sphere surface.

The orientation of the pyramids, see Figure 4, is unique. Generally, the ac plane which is the largest crystal plane, is parallel to the surface of the gel sphere. As shown in Scheme I(a) the crystal a direction is initially relatively large with respect to the crystal c direction. Apparently crystallization proceeds favorably in the a direction under the actual crystal growth conditions. The continuous TPA strings and silica layers in the crystal a direction might be the stabilizing factor (16). The c direction, under more homogeneous crystal growth conditions the longest ZSM-5 crystal dimension, is initially relatively small as shown in Scheme I(a) and Figure 4. The absence of flat crystal faces in the c direction of the pyramid crystal and the smoothly curved ends of the crystal suggest a volume diffusion controlled crystallization mechanism. The mechanism is most likely imposed (17) by the extremely high supersaturation prevailing.

After some time a new ac plane is observed at the top of the pyramid as shown in Figure 5b (by arrows) and Scheme I(b). The new a/c crystal dimension ratio deviates strongly from the a/c ratio of the plane. It is therefore suggested that the local crystal growth conditions are changed. The new a/c ratio resembles the a/c ratio of the final cube-shaped crystals. As shown in Figure 5c,d and Scheme Ic the pyramidal crystal is now growing in the a and c crystal direction, apparently in the liquid interface which also provides supply of TPA from the liquid phase. At last the well known cubic-shaped ZSM-5 crystal is formed, Figure 5e and Scheme I(d).

Two types of crystals can be grown, depending upon the history of the pyramid. As depicted in Figure 1c and Figure 6 massive and hollow pyramids are observed, respectively. The massive as well as the hollow pyramids both result in ZSM-5 cubic-shaped crystals, shown in Figure 5d for the hollow species. As separate pyramids are observed in the synthesis mixture, after 48 h, holes of such pyramids must be present in the surface of the gel spheres, as marked in Figure 7. We postulate that a preorientation of silica with TPA in the wall of such holes restarts a pyramid crystallization. The pyramid growth process is then analogous to the solid pyramid growth. At last a ZSM-5 crystal with a hollow ac plane
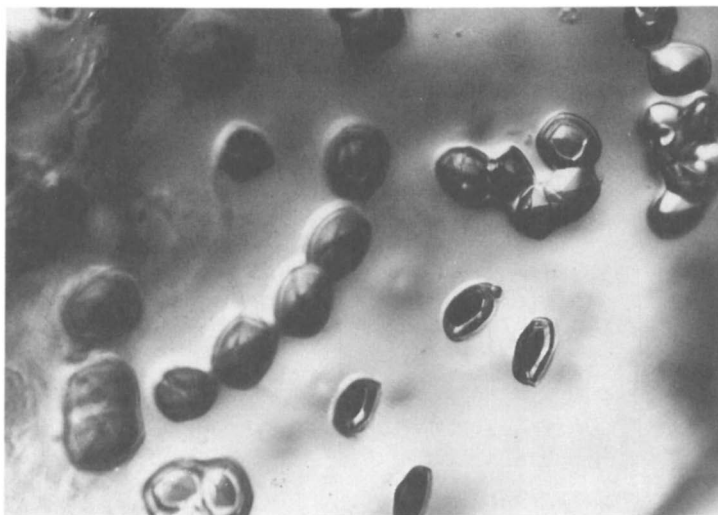
Fig. 4. Light micrograph (50 x) of the lower surface of a silica
gel body present after 2 days hydrothermal treatment;
ZSM-5 crystals with a pyramidal shape penetrate (upwards)
into the body. The a-c plane is for all depicted crystals
parallel to the outer surface of the silica body.
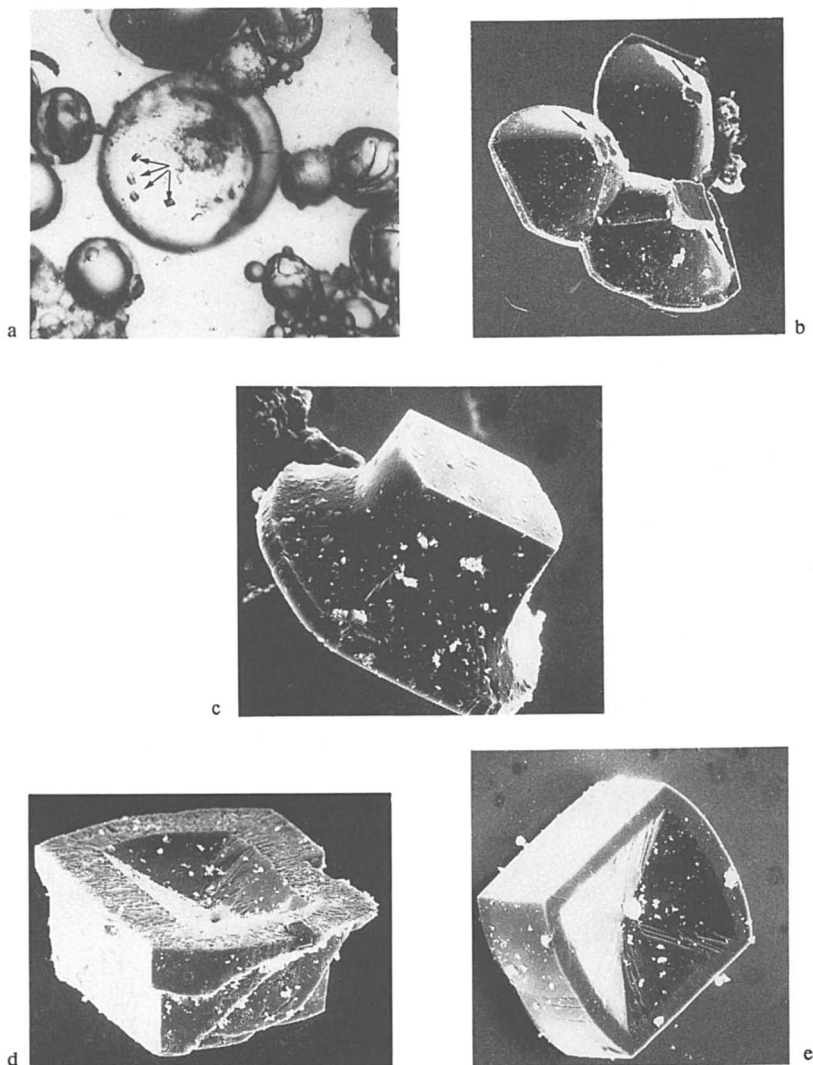
Fig. 5. Genesis of a cubic ZSM-5 crystal.
    a. Small ZSM-5 pyramids (light micrograph - 30 x) present
       on surface of gel bodies, see arrows;
    b. Development of a new a-c plane on the top of the
       pyramids (SEM picture - 150 x), see arrows;
    c and d. Growth of the pyramids mainly in the a and c
       direction (SEM - 600 x);
    e. Full grown hollow cubic ZSM-5 crystal (SEM - 240 x).

a/c ratios		**views on gelsphere surface**	
Pyramidal crystals		perpendicular	along
basal plane	2nd a/c plane		
3			
1	.4		
.8	.6		
.7	.7		
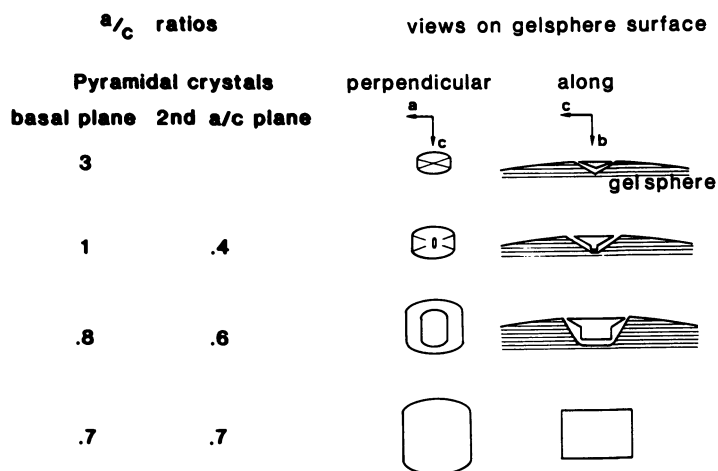
Scheme I.   Average a/c ratios of developing pyramid crystals with transition into cubes and schematic drawing of growth process in the gel spheres.
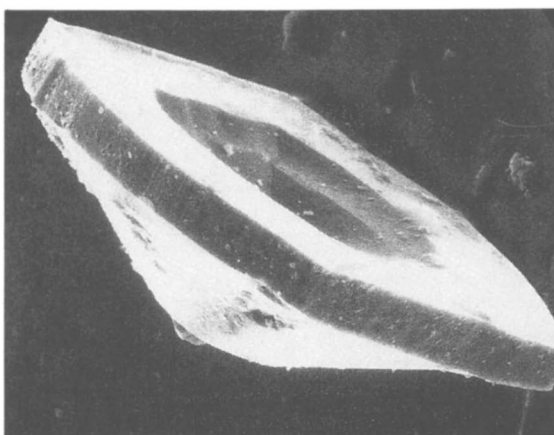
Fig. 6. SEM picture (360 x) of a pyramidal ZSM-5 crystal with pyramid-shaped hole.
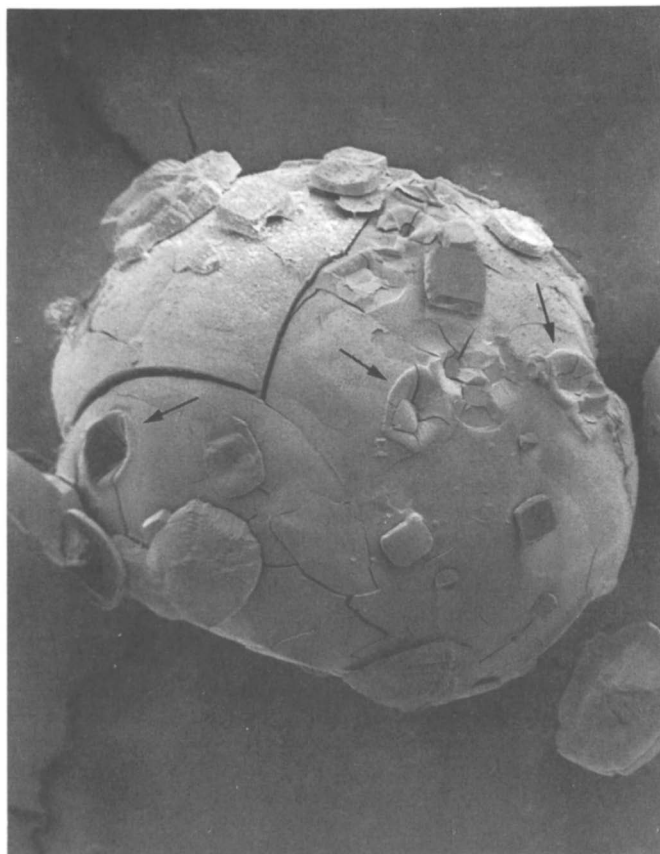
Fig. 7. SEM picture (100 x) of a gel sphere covered with ZSM-5
         pyramids penetrating the gel surface (only the ac planes
         are visible) and holes (see arrows) where pyramids have
         been present.

is observed, see Figure 5e. As shown in Figure 8 several
intermediate crystal forms of ZSM-5 elongated and cubic-shaped
crystals are possible. Extreme forms with respect to a/c crystal
dimension ratio and crystal faces in c direction are the left and
right crystals in this series. The well known elongated prismatic
crystal form of ZSM-5 is observed in relatively homogeneous crystal
growth conditions. As described above the cubic form is grown in
heterogeneous crystal growth conditions. Intermediate crystal forms
might be developed when both crystal growth conditions have been
present, the probable growth order being from cubic to elongated. As
cubic crystals are developed in gel spheres an enrichment of crystal
faces in the c direction is possible when the gel spheres are
consumed and the crystal growth conditions become more homogeneous.
It is supposed that a change from heterogeneous to homogeneous
crystal growth conditions, thus crystal growth in a gel sphere to
crystal growth in solution, influences the concentration and
gradient of isomorphously substituted framework Si. The Al gradient
occurring in elongated shaped ZSM-5 crystals is well documented
(17). By contrast the Al distribution *among* and within the cube-
shaped crystals, shows a more homogeneous pattern as depicted in
Figure 9. Figure 9a presents the Al/uc of seven crystals, with
different sizes, of the same batch prepared according to Lermer et
al. (9). According to linear crystal growth theory small crystals
are formed later than large crystals. A homogeneous distribution
among the crystals was observed. Figure 9b presents the EMPA
scanning pattern on two planes of the largest crystal. No
heterogeneity was found, regarding the Al distribution. The
homogeneous pattern might be due to crystal growth in a gel phase
with a homogeneous Al distribution. To establish T-atom distribution
in the cube-shaped crystals it is imperative that no homogeneous
crystal growth conditions have been started in the last period of
the hydrothermal crystallization. As the cube crystallization is
finished when the gel spheres are consumed the actual [Si] and Si/Al
ratio of the remaining synthesis mixture will then be opportune.
Consequently a further growth of the original cube crystal will
change the crystal shape and the Al distribution. The
crystallization time of the cube crystals in this study was 4 days
and no Al gradient was found. On the other hand cubic crystals which
were grown 10 days indeed were reported to exhibit an Al gradient
(18).
     The main differences between the elongated and cube-shaped
crystal forms are in the different faceting in the crystal
c-direction and the relatively short crystal c dimensions of the
cubic crystal. In terms of crystal growth it is plausible that the
elongated crystal growth is governed by the framework topology. The
growth is relatively slow in directions perpendicular to framework
layers with high tetrahedral density, the pentasil layers in the ac
and bc plane being examples (16). A 001 plane is generally not
observed. The crystal <u>c</u> direction flat facets are h0l planes, though
hkl planes have also been observed. It is well known that increasing
supersaturations of crystal building molecules can change the
crystal form. In the gel sphere crystallization it appears that the
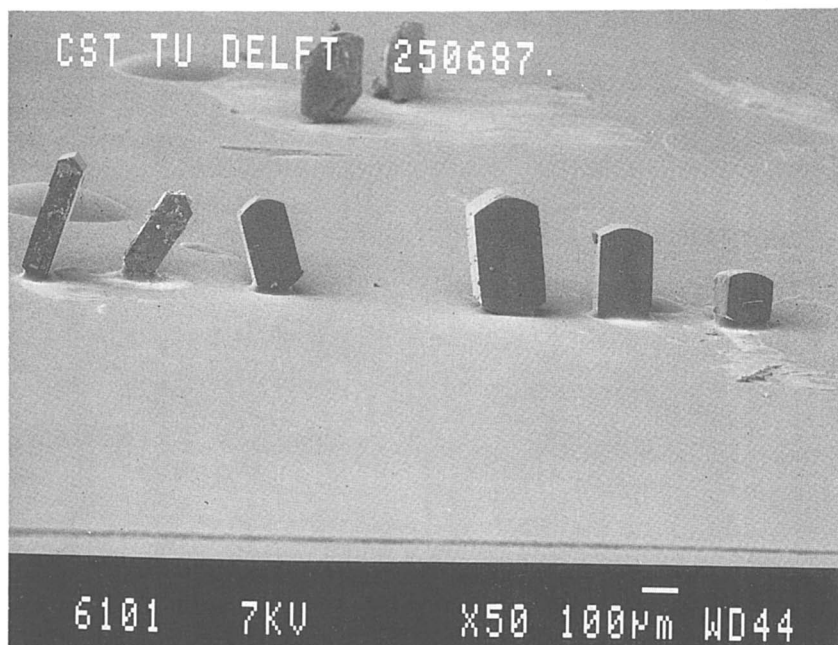
Fig. 8. Scala of shapes of ZSM-5 crystals.
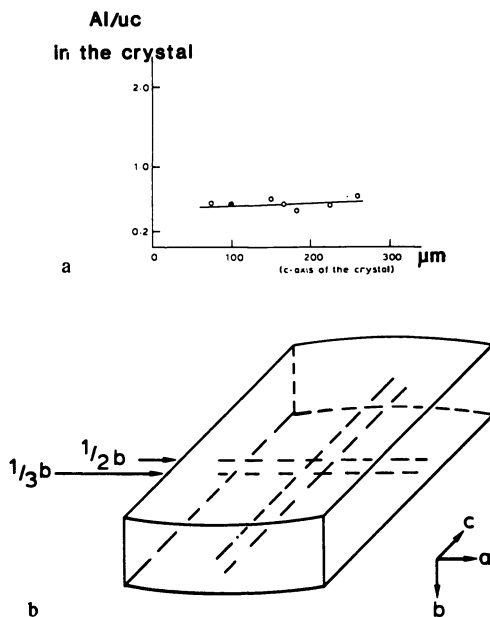
Al/uc

in the crystal

Fig. 9. Al distribution among and within cubic-shaped ZSM-crystals.
  a. Al/u.c. of cubic ZSM-5 crystals grown from the same
     synthesis mixture as function of the c-dimension;
  b. EMPA Al-scanning pattern at half and one third height
     within a cubic ZSM-5 crystal. The ac planes were
     exposed by polishing the crystal in the b direction.

crystal form is a function of the above mentioned mechanism which is, however, partly overruled by the extremely high silica supersaturation resulting in smooth curved ends of the crystal in the relative short c-direction.

Effect of borate additive on ZSM-5 morphology. If crystal morphology is studied in relation to isomorphous substitution of Si by T-atoms in the framework then it looks like homogeneous crystal growth conditions should be present. By adding boric acid to the reaction mixture (II) the elongated crystal morphology of Figure 1a was found to be changed as a function of the concentration of the borate source. Scheme II presents schematically the crystal morphology changes observed. At higher boron concentrations the ac plane develops strongly with respect to the bc plane. At the higher boron concentration applied shelf-type crystals (Fig. 1d) are formed. It is suggested that all crystal faces are involved in a crystal growth inhibition by the presence of $B(OH)_3/B(OH)_4^-$, as the build-in of B as a T-atom - trigonal or tetrahedral - will constitute an irregularity at the growing crystal surface which will hamper.

It is well described that crystal growth inhibition is caused by special additives. The pentasil layers of the ac plane and bc plane are more or less identical. The ac plane pentasil layers, however, are generated via a crystallographic mirror plane operation, the bc plane pentasil layers not. As the crystal growth rate of both layers is decreased by the BO_3/BO_4 presence the above mentioned difference in the stacking of the pentasil layers will be reflected in the a/b crystal dimension ratio (16). Presently a detailed study is being carried out regarding this interesting effect on morphology exerted by borate (19).

In conclusion two new single crystal forms of zeolites of the MFI type have been observed which can be interrelated on the basis of crystal growth consideration with two existing morphologies.
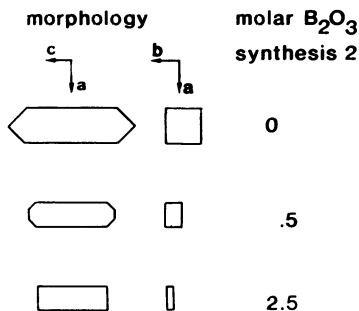
Scheme II. Morphology of B-ZSM-5 crystals as a function of the boron concentration in the synthesis formulation.

References

1. Ciric, J. <u>Science</u> <u>1967</u>, 689.
2. Charnell, J. F. <u>J. of Cryst. Growth</u> 1971, <u>8,</u> 291-294.
3. Erdem A.; Sand, L. B. <u>Proc. 5th IZC</u>; Rees, L. V., Ed.; Heyden, <u>1980</u>, 64-72.
4. Gabelica, Z.; Derouane, E. G. <u>A.C.S. Symposium Series</u> 1987, <u>248</u>, 219-251.
5. Mostowicz, R.; Berak, J. M. <u>Stud. Surf. Sci. Cat.</u> ; Drzaj, B.; Hocevar S.; Pejovnik, S., Eds.; Elsevier: Amsterdam, 1985, Vol. 24, pp 65-72.
6. Kuehl, G. H. <u>Eur. Pat. Appl.</u> 0,0093519 (1983).
7. Argauer R. J.; Landolt, G. R. <u>U.S. Patent</u> 3,702,886 (1972).
8. Hayhurst D. T.; Lee, J. C. <u>Proc. 7th IZC</u>; Murakami, Y.; Iijima A.; Ward, J. W., Eds.; Elsevier: Tokyo, 1986, pp 113-120; Hayhurst, D. T.; Aiello, R.; Nagy, J. B.; Crea, S.; Giordano, G.; Nastro, A.; Lee, J.C. <u>A.C.S. Symp. Series</u> 1988, <u>368</u>, 277-291.
9. Lermer, H.; Draeger, M.; Steffen, J.; Unger, H. K. <u>Zeolites</u> 1985, <u>5</u>, 131-134.
10. Bodart, P.; Nagy, J. B.; Gabelica, Z.; Derouane, E. G. <u>J. Chem. Phys.</u> 1986, <u>83</u>, 777-790 and literature cited therein.
11. Lowe, B. M. <u>Stud. Surf. Sci. Cat.</u>; Goubet, P. G.; Mortier, W. M.; Vansant, E. F.; Schulz-Ekloff, G., Eds.; Elsevier: Amsterdam, 1988, <u>37</u>, 1-12.
12. Dentglasser, L. S.; Lachowski, E. E. <u>J. Chem. Soc. Dalton</u> <u>1980</u>, 393-398.
13. O'Melia, C. R.; Stumm, W. <u>J. Colloid and Interface Sci.</u> 1967, <u>23</u>, 437-477. Allen, L. H.; Matijević, E. <u>J. Colloid and Interface Sci.</u> 1970, <u>35</u>, 67-76.
14. Lamer, V. K.; Healy, T. W. <u>Rev. Pure Appl. Chem.</u> 1963, <u>13</u>, 112. Hahn, H. H.; Stumm, W. <u>Adv. Chem. Ser.</u> 1968, <u>79</u>, 91 (American Chemical Society).
15. Iler, R.K. <u>J. Colloid Interface Sci.</u> 1976, <u>55</u>, 25.
16. A more theoretical study has been undertaken and will be published.
17. Ballmoos R. von; Meier, W. M. <u>Nature</u> 1981, <u>289</u>, 782-783.
18. Chao, K.-J.; Chern, J.-Y. <u>Zeolites</u> 1988, <u>8</u>, 82-85.
19. Jansen, J. C.; Ruiter, R. de; Bekkum, H. van. To be presented for the 8th IZC, Amsterdam, 1989.

Chapter 20

Synthesis of Pentasil Zeolites With and Without Organic Templates

W. Schwieger[1], K.-H. Bergk[1], D. Freude[2], M. Hunger[2], and H. Pfeifer[2]

[1]Sektion Chemie der Martin-Luther-Universität Halle-Wittenberg, Schlossberg 2, DDR–4020 Halle, German Democratic Republic
[2]Sektion Physik der Karl-Marx-Universität Leipzig, Linnestrasse 5, DDR–7010 Leipzig, German Democratic Republic

Magic-angle-spinning nuclear magnetic resonance spectroscopy (MAS ΓR) yields quantitative information about Brönsted acidity and structural defects in zeolites. We have studied samples of pentasil zeolites synthesized with and without organic templates using 1H and 27Al NMR. The influence of mono-, di- and tri-n-alkylamine and tetraalkylammonium compounds (alkyl = methyl, ethyl, propyl and butyl) upon the rate of crystallization, yield and the properties of the products is discussed. By varying the SiO_2/Al_2O_3 ratio and the lengths of the period of crystallization at 175 °C, $H_2O/SiO_2=30$, $Na_2O/SiO_2=0.1$ we have arrived optimal reaction conditions for a template-free synthesis of zeolites of ZSM-5 type at $SiO_2/Al_2O_3=30$-50 and 36-48 h. In all samples the concentration of non-acidic hydroxyl groups (silanol groups) is much higher than could be accounted for by the number of terminal hydroxyls on the external surface of the crystallites. In the H-form of the zeolites the number of acidic OH groups is equal to the number of framework aluminium atoms. We demonstrate that it is possible to synthesize defect-free zeolites of type ZSM-5 without an organic template.

The synthesis of pentasil zeolites is supported by organic cations. Argauer et al. (1) first described syntheses with tetraalkylammonium and tetraalkylphosphonium compounds. The organic cations may not only initiate and sustain a certain crystallization process but also may lead to products of a new structure. This "templating" behaviour is explained by the structure-directing effect of the organic cations in the process of crystallization (2,3).

In the past numerous syntheses were described using compounds which were assumed to possess this templating property. A few references are given in Table I, beginning with the classic templates, going to more simple molecules and ending with the template-free synthesis. A group-specific arrangement is presented in Table II.

Table I. Organic compounds, which were mostly used in syntheses of zeolites of pentasil-type. Abbreviations are TPA[+] for tetrapropylammonium cation, TEPA[+] for triethylmonopropylammonium cation, TBA[+] for tetrabutylammonium cation, TBP[+] for tetrabutylphosphonium cation, TPA for tripropylamine and C_6DN for hexamethyldiamine

Product	Group of compounds	Preferred comp.	References
ZSM-5	tetraalkylammonium cation	TPA[+]	(1,4,5)
		TEPA[+]	(6,7)
	trialkylamine and alkylhalogenide	TPA and propylchloride	(8-11)
ZSM-11	tetraalkylammonium or tetraalkylphosphonium cation	TBA[+]	(12)
		TBA[+], TBP[+]	(5)
ZSM-5 like	alkanolamine	$NH_2CH_2CH_2OH$	(13-15)
	diamine	C_6DN	(16)
	mono-n-alkylamine	propylamine	(17-19)
	alcohols and ammonia	C_4H_9OH	(20)
	alcohols	C_4H_9OH	(21)
	template-free		(22,23)

Table II. The different types of organic compounds, which can be used for the syntheses of pentasil zeolites

Type	Examples	References
organic cations	R_4N^+, R_4P^+	(1,4,5,7)
	polymeric cationic compound	(24)
organic molecules	diamine	(16)
	amine	(17-19)
	alcohols	(20,21)
	dioxane	(25)
	2-aminopyridine	(26)
organic anions	alkylbenzolsulfonate	(27)
	polymeric anionic compound	(28,29)

In consideration of the fact that even a template-free synthesis is possible it is not easy to understand that all different groups of compounds should have the same structure-directing effect. For a more plausible explanation we must consider the reaction mixture as a whole and discuss the combined effects of all components. Table III is an attempt to systematize the effects of different components.

Table III. The influence of the relative (referred to SiO_2) amount
of different compounds of the reaction mixture upon the
properties of the reaction mixture and of the product

Molar ratio	Properties
Al_2O_3/SiO_2	composition of the network
H_2O/SiO_2	viscosity, concentration of hydroxyde ions
OH^-/SiO_2	molecular weight of silicates, conc. of hydroxide ions
Na^+/SiO_2) R_4N^+/SiO_2)	cation distribution, templating effect, Al-content

To draw conclusions concerning the templating effect of different
molecules, comparable conditions for the crystallization process must
be used. In this paper we present a systematic investigation on the
effect of mono-, di- and tri-n-alkylamine and tetraalkylammonium
compounds   (alkyl = C_1 - C_4) upon the rate of crystallization, yield
and the properties of the products. Also the field of a template-
free synthesis is studied. The products were characterized by magic-
angle-spinning nuclear magnetic resonance spectroscopy (MAS NMR) and
X-ray diffraction.

Experimental

The template containing samples were synthesized using a procedure
based on those given by Union Carbide (30). The batch composition
expressed in mole ratios was as follows:

$$1 \ R_2O * 4.1 \ Na_2O * 50 \ SiO_2 * 0.417 \ Al_2O_3 * 691 \ H_2O$$
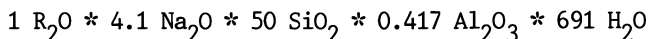
with R = C_iN, $(C_i)_2N$, $(C_i)_3N$, $(C_i)_4N^+$ and $C_i = C_1-C_4$ = methyl-butyl.
Some of the samples were synthesized without Al_2O_3.   The syntheses
with tetrapropylammonium iodide ($TPA^+ J^-$) as template were carried
out with a varying SiO_2/Al_2O_3 ratio in the range 25 - 400. The batch
composition of the template-free synthesis was

$$4 \ Na_2O * 1 \ Al_2O_3 * x \ SiO_2 * 1200 \ H_2O$$
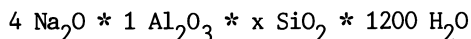
where x varies from 10 to 100.
Sodium silicate, sodium aluminate and NaOH were obtained from
VEB Chemiekombinat Bitterfeld. The organic templates were guaranteed
reagents. At first NaOH was diluted in water and then sodium silicate
and sodium aluminate in liquid or diluted form were added under
stirring. Afterwards, the organic compound was added under vigorous
stirring. The obtained mixture was stirred for further 15 min and
then distributed over several autoclaves in portions of 50 cm^3 per
autoclave. The crystallization was conducted in a furnace at 175 °C.
The reaction vessels were placed on rotating shafts. After the time
of crystallization the autoclave was quickly cooled down. The pro-
ducts were filtered, washed and dried at 100 °C. The procedure of the
template-free synthesis was different in only one point: To the
diluted aqueous solution of sodium silicate the sodium aluminate was
added.

The synthesized samples were analyzed by X-ray powder diffraction for qualitative and quantitative phase identification. The unit used was a Philips Model with a vertical goniometer and a scintillation counter, utilizing Ni-filtered CuK$_\alpha$ radiation. For quantitative phase identification an external standard sample of α-Al$_2$O$_3$ was used. The percentage crystallization was calculated using the averaged peak intensities at $2\Theta=35.2°$ and $2\Theta=47.3°$ of the reference sample and the peak intensity at $2\Theta=23.2°$ for the sample under study (31).

X-ray and aluminium MAS NMR measurements were carried out on samples rehydrated in a desiccator over an aqueous NH$_4$Cl solution. A portion of the zeolites synthesized with organic templates was heated for 5 h at 600 °C to remove organic compounds. The Na$^+$/H$^+$ ion exchange was carried out at room temperature with an aqueous solution of 0.5 N HCl. The preparation of ^{1}H MAS NMR samples was performed under shallow bed activation conditions in a glass tube of 5.5 mm inner diameter and 10 mm height of the zeolite layer. The temperature was increased at a rate of 10 K/hr. After maintaining the samples at the final activation temperature of 400 °C under a pressure below 10^{-2} Pa for 24 hrs., they were cooled and sealed.

NMR measurements were performed on a home-made spectrometer HFS 270 and on a BRUKER spectrometer MSL 300. As a reference for intensity measurements of the aluminium NMR a well-characterized sample of ZSM-5 with a framework Si/Al-ratio of 15 was used. The total concentration of OH groups in the activated samples was determined by comparison of the maximum amplitude of the free induction of the samples with those of a capillary containing an aqueous solution in a probe with a short ring-down time. To separate the relative intensities of different lines in an ^{1}H MAS NMR spectrum quantitatively, the signals of the spinning side bands were added to the main signal. The home-made MAS equipment for the rotation of the fused glass ampoules was carefully cleaned to avoid spurious proton signals.

Results and Discussion

Synthesis. Figure 1 shows the crystallization of template-containing zeolites as a function of time. The aluminium-free syntheses using TEA$^+$, TPA$^+$ and TBA$^+$ as template give products with pentasil structure (silicalite I or II) without other phases. TMA$^+$ and all other amines mentioned above yield in the aluminium-free syntheses as the first crystalline phase only magadiite, an aluminium-free sheet silicate. The aluminium containing syntheses give different phases with pentasil structure, sheet structure and an amorphous phase. Table IV presents the maximum percentage crystallization of the pentasil phase. The value of about 100% for TEA$^+$, TPA$^+$, TBA$^+$, di-and tri-n-propylamine and di- and tri-n-butylamine proves that these syntheses yield only the pentasil phase. X-ray diffraction analysis shows that TPA$^+$ and TBA$^+$ lead to the ZSM-5 and ZSM-11 structure type, respectively. Figure 2 shows a comparison of the X-ray diffraction patterns. The most intense diffraction lines occur at $2\Theta=20°-27°$. Going from the tetraalkylammonium to the alkylamine compounds a splitting of the 23.2° line can be observed. The form of the splitted line seems to be typical for the template. Similar patterns have been measured for the following zeolites of pentasil type (32): NU-5 (EP 54 386), ZSM-8 (NL 7 014 807) and ZETA-1 (DE 2 548 695). It is not clear whether the
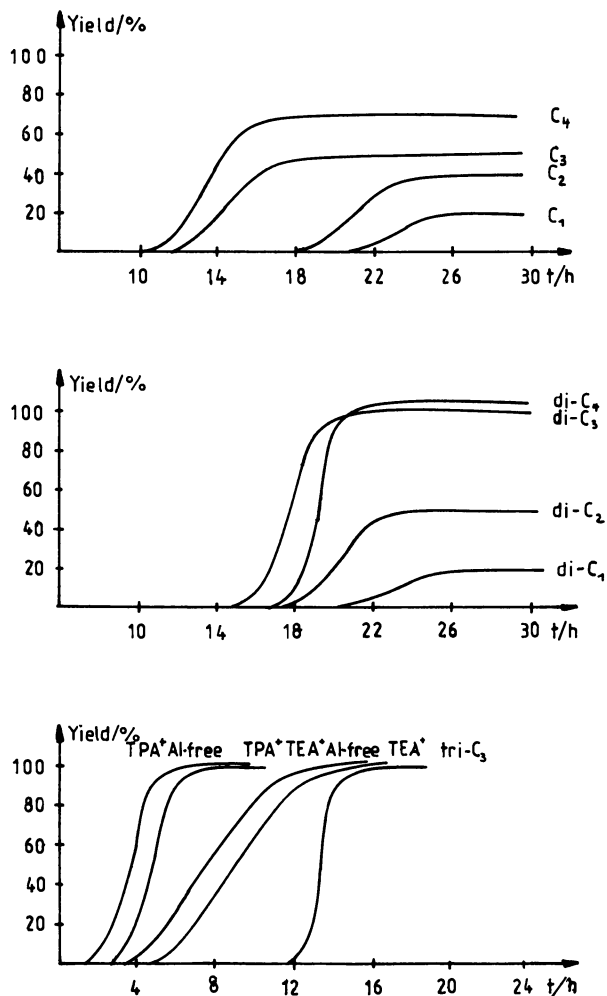
Figure 1. Yield of pentasil zeolites (percentage crystallization) as a function of time. Abbreviations are C_4 for mono-n-butylamine, C_3 for mono-n-propylamine, C_2 for mono-n-ethylamine, C_1 for mono-n-methylamine, di-C_4 for di-n-propylamine, di-C_3 for di-n-propylamine, di-C_2 for di-n-ethylamine, di-n-C_1 for di-n-methylamine, TPA$^+$ Al-free for the aluminium-free synthesis with the tetrapropylammonium cation, TPA$^+$ for tetrapropylammonium cation, TEA$^+$ Al-free for the aluminium-free synthesis with the tetraethylammonium cation, TEA$^+$ for tetraethylammonium cation and tri-C_3 for tri-n-propylamine.
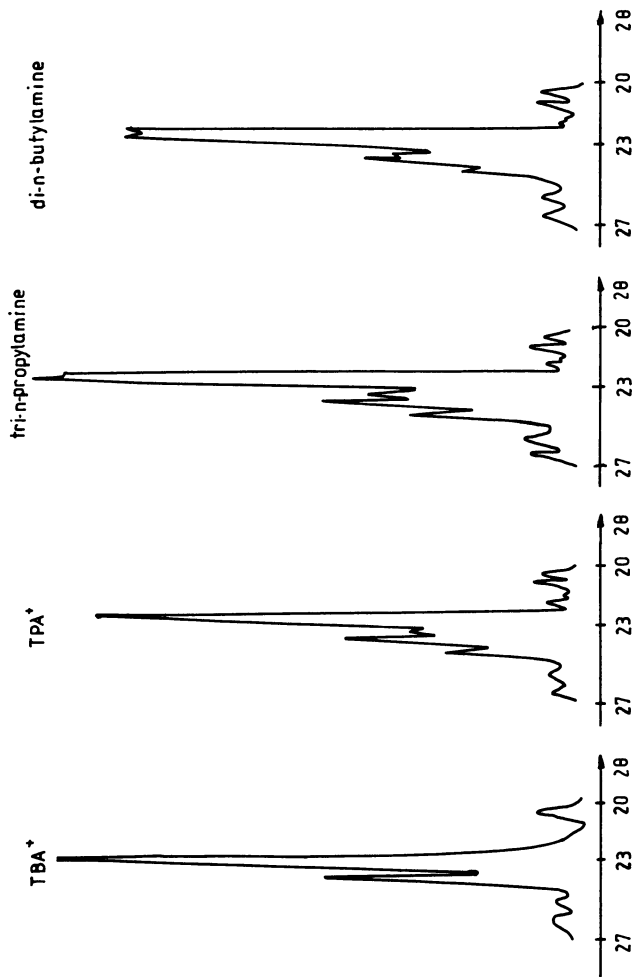
Figure 2. X-ray diffraction patterns.

Table IV. The yields of syntheses measured in mass% of crystalline pentasil in dependence on the template. The experimental error is about $\pm 10\%$

Template	methyl	ethyl	propyl	butyl
mono-n-alkylamine	21	40	50	70
di-n-alkylamine	20	55	100	100
tri-n-alkylamine	11	77	106	101
tetraalkylammonium cation	23	90	100	103

patterns are due to a special phase or due to an intergrowth ZSM-5/ZSM-11, cf. (33,34).

Magadiite apart from pentasil phases can be found in zeolites synthesized with mono-n-methyl-, -ethyl-, -propyl- or -butylamine, with di-n-methyl-, -ethyl- or -propylamine, with tri-n-methyl- or -ethylamine and with tetramethylammonium iodide. Table IV shows that the zeolite content increases with the number of carbon atoms per group and with the number of alkyl groups.

Values describing the kinetics of crystallization with organic compounds are presented in Table V. Figure 3 shows how the values t_o = induction period, t_g = period of growth and k = percentage crystallization per hour can be determined from the curves presented in Figure 1. Aluminium decelerates the synthesis as can be shown by comparison of the aluminium-containing and the aluminium-free syntheses using TPA^+ and TEA^+ as template. Compounds containing the propyl group give the best structure directing effect and among them the shortest induction period has beeen found for TPA^+ and the maximum crystallization rate for tri-n-propylamine.

Table V. The induction period t_o, the period of growth t_g, the crystallization rate k (percentage crystallization per hour) and the maximum percentage crystallization (mpc) in dependence on the different templates used in pentasil syntheses

Template	t_o (h)	t_g (h)	k (% h^{-1})	mpc (%)
mono-n-methylamine	20.8	3.5	6	21
mono-n-ethylamine	18.8	4.2	10	40
mono-n-propylamine	12.7	3.6	14	50
mono-n-butylamine	11.8	3.2	22	70
di-n-methylamine	21.0	4.1	5	20
di-n-ethylamine	18.8	2.9	19	55
di-n-propylamine	16.0	2.2	46	100
di-n-butylamine	18.5	2.0	50	100
tri-n-propylamine	13.2	0.9	118	106
TEA^+	6.0	4.0	24	98
TPA^+	4.3	1.0	100	100
TEA^+ (Al-free)	5.2	4.2	25	104
TPA^+ (Al-free)	3.0	0.5	216	108

Figure 4 presents the isothermal phase transformation diagram of the template-free syntheses in which the SiO_2/Al_2O_3 ratio and the time t of crystallization are varied. The SiO_2/Na_2O and H_2O/SiO_2 ratios are 10 and 30, respectively. The pentasil phase could only be synthesized for $n = SiO_2/Al_2O_3 = 30 - 50$ and $t = 36 - 72$ h. Outside of this area amorphous material, mordenite, sheet structures similar to kenyaite, quartz and crystobalite can be found. For values of n less than 25 the crytalline product is mordenite. For $30 < n < 50$ a yield of 95% (related to the SiO_2 content) ZSM-5 type, which was proved by X-ray diffraction pattern, could be found. Depending on n and the crystallization time, t, a more or less large amount of amorphous material is produced. This is shown in Figure 5. A long crystallization time causes recrystallization and is harmful to the yield of ZSM-5 products.

The influence of the compounds in the crystallization mixture upon the morphology of crystallites is illustrated by the scanning electron micrographs presented in Figures 6-8. Figure 6 shows that in the aluminium-free syntheses TPA^+ gives spherical crystallites with a diameter of 2-3 μm and TEA^+ gives rhombic crystallites with sizes of about 1x2x5 μm. Figure 7 demonstrates the influence of the SiO_2/Al_2O_3 ratio on the morphology. With increasing ratio the size and the smoothness of the crystallites increase. The template-free synthesized zeolites with a SiO_2/Al_2O_3 ratio of 30 show flaking surfaces (see Figure 8).

In conclusion the syntheses performed in this work show:
- The real structure directing effect is caused by the TEA^+, TPA^+, and TBA^+ cations. These cations cause the structure directing effect also in the aluminium-free syntheses.
- Amines support the synthesis of aluminium containing pentasils in dependence on their number of carbon atoms.
- A template-free synthesis can be performed in a limited range of the SiO_2/Al_2O_3 ratio. Based on these results a zeolite of pentasil-type is industrially produced by Chemiekombinat Bitterfeld, GDR.

NMR-characterization. Corbin et al. (35) were able to show by a systematic study that ^{27}Al MAS NMR gives the true Si/Al ratio with a mean error of 10 %, if two conditions are met: a) The amount of paramagnetic species is less than 0.05 % and b) the sample does not contain "NMR-invisible" aluminium. Chemical analyses of the samples under study showed that condition one is fulfilled. If samples contain "NMR-invisible" aluminium a difference between the concentration determined by chemical analysis and the framework aluminium concentration determined by NMR should be observed. From the absence of such a difference we conclude that "NMR-invisible" aluminium species do not exist in our samples. Also a line at the position of about 0 ppm due to octahedrally coordinated non-framework aluminium and a broad line at about 30 ppm due to tetrahedrally coordinated non-framework aluminium (36) could not be observed. The values for the concentration of framework aluminium atoms derived from the intensities of the line at about 60 ppm (see below) are in good agreement with those corresponding to the amount of alumina used in the synthesis mixtures. In conclusion, through the ^{27}Al MAS NMR measurements it was possible to show that all aluminium atoms are incorporated in tetrahedrally oxygen coordinated framework positions.
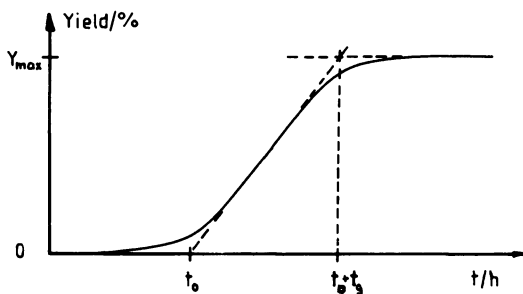
Figure 3. Crystallization as a function of time. t_o denotes the induction period, t_g the period of growth and the rate of crystallization, k, can be calculated using the maximum percentage crystallization, Y_{max}, by $k = Y_{max}/t_g$.
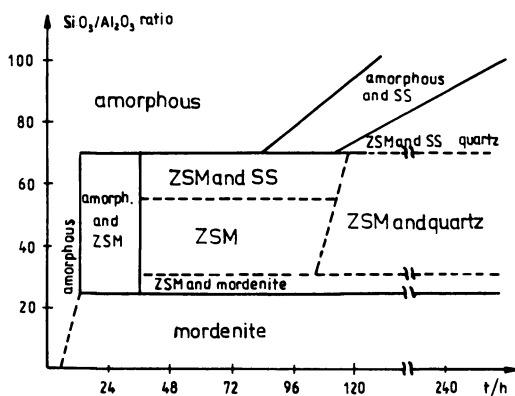
Figure 4. Isothermal phase transformation diagram of the template free syntheses. SS denotes sheet structures.
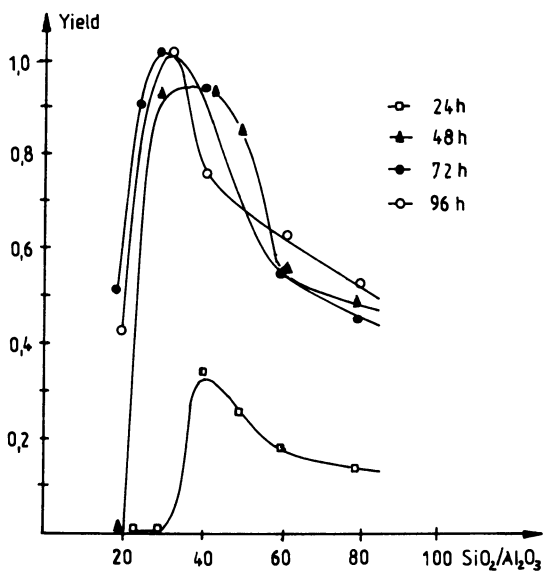
Figure 5. Yield of pentasil zeolites as a function on the SiO_2/Al_2O_3 ratio for different crystallization times.
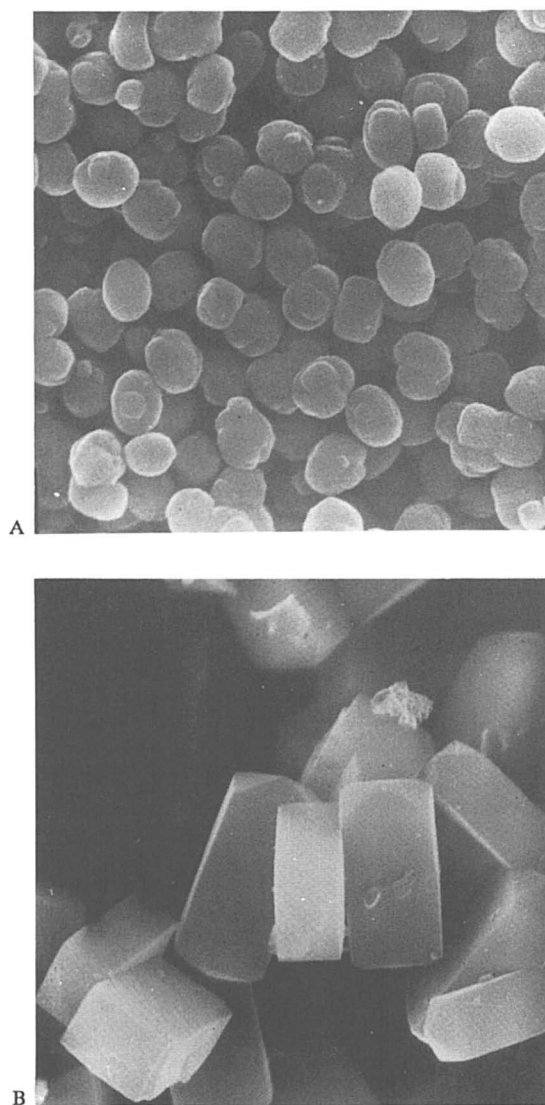
Figure 6. Scanning electron micrographs of the products of the aluminium-free syntheses with TPA[+] (A) and TEA[+] (B) as template.
(3000 x)
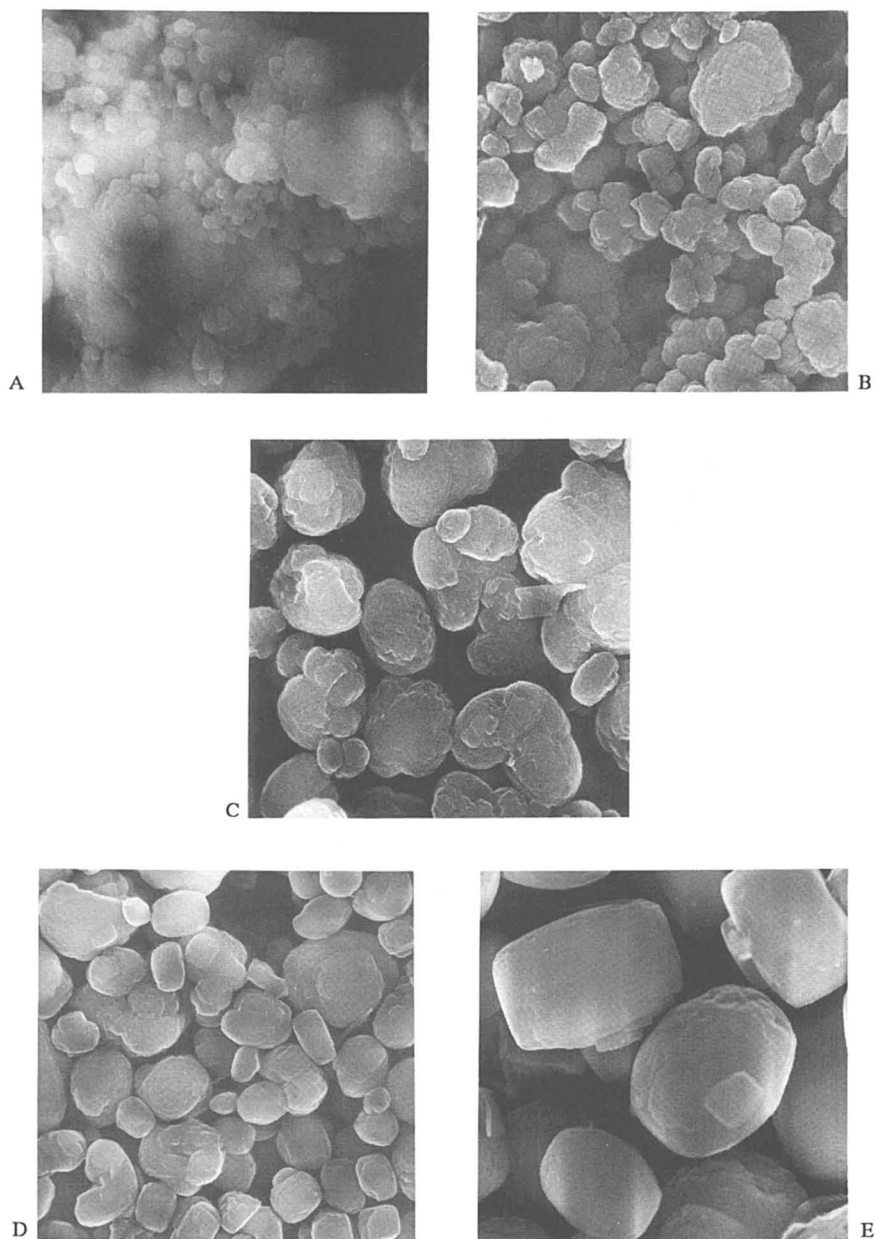
Figure 7. Morphology of pentasil zeolites synthesized with TPA^+ as template in dependence on the SiO_2/Al_2O_3 ratio of 25 (A), 50 (B), 100 (C), 200 (D) and 400 (E).   (5000x)
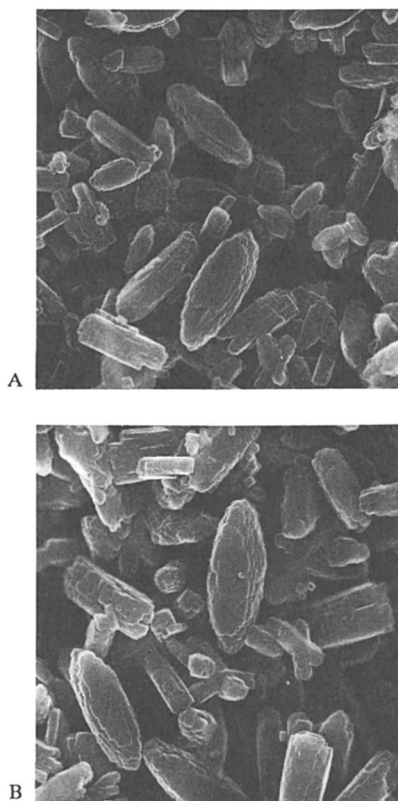
Figure 8. Scanning electron micrographs of the products of the
template-free syntheses performed at 175 °C (A) and 200 °C (B).
                                                            (8000x)

The line width of the corresponding ^{27}Al MAS NMR signal is determined by second-order quadrupole interaction. That means, it is determined by the deviation from the ideal tetrahedral symmetry of the AlO_4 units. The highest degree of symmetry resulting in a line width of 7±1 ppm (at 6.3 T) is observed for the pentasil phase. The quartz phase, mordenite and the amorphous phase gave line widths of 9 ppm, 14 ppm and 18 ppm, respectively. The shift of the centre of gravity of the lines with respect to the resonance position of the aluminium-hexaaquo complex is 47-56 ppm. Taking into account the quadrupole correction for the shift, which has a maximum value equal to the line width (37) a chemical shift of ca. 60 ppm results for all lines.

Therefore, through a measurement of the chemical shift of the ^{27}Al MAS NMR line it is not possible to distinguish between different phases in the product. The amorphous and the crystalline phases give a difference only in the line width.

^{1}H MAS NMR spectra are presented in Figure 9. Two different signals can be seen in the spectra of the hydrogen forms. Line (a) at 2 ppm is due to non-acidic hydroxyl groups (silanol groups) at the outer surface of zeolite crystallites, at framework defects and in the amorphous part of the sample. Line (b) at 4.3 ppm is caused by bridging (acidic) OH groups (38). Further lines due to different types of acidic OH groups or AlOH groups on non-framework aluminium species (38), could not be observed in these spectra. Values for the concentration of framework aluminium atoms and of the hydroxyl protons giving rise to lines (a) and (b) are presented in Tab. 6. The number of terminal OH groups per gram of dried zeolite, n_T, is calculated by $n_T = 0.12 \times 10^{20} d^{-1}$, where d denotes the diameter of the crystallites (μm).

The intensities of line (a) in Table VI show that for all specimens the values for the concentration of SiOH groups are much greater than the values obtained from a calculation of the number of terminal OH groups. The extremely high concentration of silanol groups observed for TPA$^+$/ZSM-5 zeolites is in accordance with our previous findings (38,39). The number of these SiOH groups is larger, by a factor of up to 1000, than the number which is necessary to terminate the external crystal surface. From the absence of amorphous material (within the accuracy of the X-ray measurements) it follows that up to 8% of the framework Si are present as SiOH groups. This means, that the ZSM-5 synthesis with TPA$^+$ as template leads to a highly disturbed lattice with a high concentration of non-intact Si-O-Si bonds. The enhanced concentrations of SiOH groups in the hydrogen form of the zeolites indicate that, after sample calcination, about half the defect sites are present as Si-O-Na, the other half being present as internal silanol groups. The treatment with 0.5 N HCl leads to the exchange of Na$^+$ cations on the defect sites with H$^+$, thus forming a maximum number of silanol groups. This behaviour can be explained (36) by the following reaction scheme of a defect site:

```
Na   TPA                    Na   H                       H    H
 |    |                      |    |                       |    |
 O    O      850 K, 10 h     O    O     0.5 N HCl, 15 h   O    O
 |    |     ─────────────►   |    |    ─────────────────► |    |
 Si   Si                     Si   Si                      Si   Si
/I\  /I\                     /I\  /I\                     /I\  /I\
```
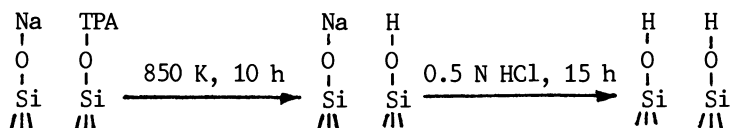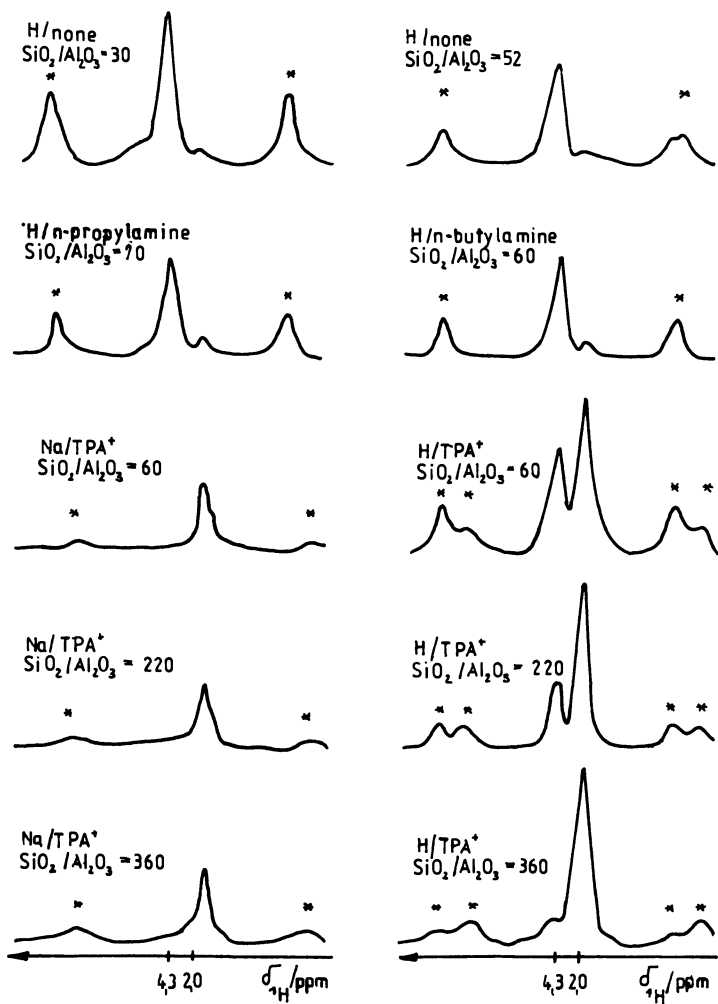
Figure 9. ^{1}H MAS NMR spectra. * denotes spinning sidebands.

Table VI. Concentrations of hydroxyl species and framework aluminium atoms in the hydrogen (H) or sodium (Na) form of pentasil zeolites synthesized with different organic templates and without organic templates

Form/Template	Crystallite diameter (μm)	SiO_2/Al_2O_3 ratio	Concentration (10^{20} species per gram)		
			Protons, line (a)	Protons, line (b)	Framework Al atoms
H/none	3.2	30	0.6	4.9	5.8
H/none	3.0	52	0.5	3.2	3.6
H/mono-n-propylamine	1.2	70	0.4	3.2	2.7
H/mono-n-butylamine	1.1	60	0.5	3.5	3.2
Na/TPA$^+$	1.7	60	1.5	0.0	3.2
H/TPA$^+$	1.7	60	3.7	3.5	3.2
Na/TPA$^+$	1.5	220	1.3	0.0	0.9
H/TPA$^+$	1.5	220	3.6	1.2	0.9
Na/TPA$^+$	2.1	360	1.6	0.0	0.6
H/TPA$^+$	2.1	360	3.8	0.5	0.6

Since a hydrothermal treatment at 1100 K for 5 days leads to a healing of the zeolitic framework, most of the internal SiOH groups must be vicinal: Neighbouring framework defects (vicinal SiOH groups) are transferred via dehydration into intact Si-O-Si bonds (36).

By contrast, ZSM-5 specimens from organic-free batches and those synthesized by n-butyl- and n-propylamine possess relatively intact lattices with only a small concentration of internal silanol groups (see Figure 9 and Table VI).

Concerning the concentration of Brönsted sites (acidic bridging OH groups) we found that for the hydrogen form of the zeolites the number of bridging hydroxyl groups is in good agreement with the number of framework aluminium atoms.

Literature Cited

1. Argauer, R. J.; Landolt, G. R. U.S. Patent 3 702 886, 1972.
2. Flanigen, E. M. Adv. Chem. Series 1973, 121, 119.
3. Rollmann, L. D. Adv. Chem. Series 1978, 173, 176.
4. Dwyer,Y. N.; Jenkins, E. E. U.S. Patent 3 941 871, 1976.
5. Chen, Y. N.; Miale, N. J.; Readan, J. W. U.S. Patent 4 112 056, 1978.
6. Kalkarmi, S. B.; Shitalkar, V. B.; Katasthane, A. N.; Borade, R. B.; Datunasamg, P. Zeolites 1982, 2, 133.
7. Borade, R. B.; Chandrankar, A. J.; Kulkarni, S. B.; Ratasany, P. Indian. J. Technol. 1983, 21, 358.
8. Schwartz, A. B. Patent BP 1 365 318, 1974.
9. Rollmann, L. D. Patent DE 2 817 577, 1978.
10. Dwyer F. G.; Klocke, D. J. Patent DE 2 822 725, 1978.
11. Gabelica, Z.; Derouane, E. G. ACS Symp. Ser. 1985, 248, 219
12. Chu, P.; Woodbury, N. J. U.S. Patent 3 709 979, 1973.
13. Ball, W. J.; Palmer, V. W.; Stewart, P. G. Patent EP 2900, 1979.

14. Ball, W. J.; Palmer, V. W.; Stewart, P. G.
    Patent EP 2899, 1979.
15. Ball, W. J.; Palmer, V. W.; Stewart, P. G.
    U.S. Patent 4 346 021, 1982.
16. Rollmann, L. D.   U.S. Patent 4 108 881, 1978.
17. Rubin, M. V.; Rosinski, E. J.; Plank, Ch. J.
    Patent DE 2 442 240, 1975.
18. Rubin, M. V.; Rosinski, E. J.; Plank, Ch. J.
    U.S. Patent 4 151 189, 1979.
19. Bremer, H.; Reschetilowski, W.; Son, D. Q.; Wendland, K.-P.;
    Nau, P.-N.; Vogt, F.   Z. Chem. 1981, 21. 77.
20. Post, M. F. M.; Nanne, J. M.   Patent DE 2 913 552, 1979.
21. Post, M. F. M.; Nanne, J. M.   Can. Pat. 1 135 679, 1982.
22. Roscher, W.; Bergk, K.-H.; Pilchowski, V.; Schwieger, W.;
    Wolf, F.; Fürtig, H.; Hädicke, U.; Höse, W.; Krüger, W.;
    Chojnacki, K.-H.   Patent DD-WP 207 186, 1984.
23. Roscher, W.; Bergk, K.-H.; Pilchowski, V.; Schwieger, W.;
    Wolf, F.; Fürtig, H.; Hädicke, U.; Höse, W.; Krüger, W.;
    Chojnacki, K.-H.   Patent DD-WP 207 185, 1984.
24. Kerr, G. T.; Rollmann, L. D.   Patent DE 2 705 436, 1978.
25. Klotz, M. R.   U.S. Patent 4 377 502, 1983.
26. Whittam, T. V.   Patent EP 59359, 1982.
27. Hugiwara, H.; Kiyozumi, Y.; Kurila, M.; Sato, T.; Shimudu, H.;
    Szuki, K.; Shin Ch.   Chem. Letters 1981, 11, 1653.
28. Roscher,W.; Bergk, K.-H.; Pilchowski, V.; Schwieger, W.;
    Wolf, F.; Fürtig, H.; Hädicke, U.; Höse, W.; Krüger, W.;
    Chojnacki, K.-H.   Patent DD-WP 207 184, 1984.
29. Lowe, B. M.; Aroya, M.   Patent EP 77624, 1983.
30. Grose, R. W.; Flanigen, E. M.   U.S. Patent 4 061 724, 1977.
31. Bergk, K.-H.; Schwieger, W.   Abstr. Internat. Conf. on Zeolites,
    Portoroze, 1984.
32. Jacobs, P.; Martens, A. I. A.   In Synthesis of Highsilica
    Aluminosilicate Zeolites;   Dellmann B. and Yales, I. T. Eds.;
    Studies in Surface Science and Catalysis, Vol. 35,
    Elsevier (1987).
33. Kokotailo, G. T.;   Meier, W. M.   Chem. Soc. Spec. Publ.
    1980, 33, 13
34. Koningsveld, H. van; Jansen, J. C.; Bekkum, H. van
    Zeolites 1987, 7, 564.
35. Corbin, D. R.; Burgess, B. F.; Vega A. J.; Farlee, R. D.
    Analytical Chemistry 1987, 59, 2722.
36. Hunger, M.; Kärger, J.; Pfeifer, H.; Caro, J.; Zibrowius, B.;
    Bülow, M.;   Mostowicz, R.   J. Chem. Soc., Faraday Trans.I,
    1987, 83, 3459.
37. Freude, D.; Haase, J.; Klinowski, J.; Carpenter, T. A.;
    Ronikier, G.   Chem. Phys. Letters 1985 119, 365.
38. Freude, D.; Hunger M.; Pfeifer, H.   Proceedings of the Fourth
    International Symposium on Magnetic Resonance in Colloid and
    Interface Science, Münster, July 1986; Z. Physik. Chem. NF
    1987, 152, 171.
39. Hunger, M.; Freude, D.; Fröhlich, T.; Pfeifer, H.; Schwieger, W.
    Zeolites 1987, 7, 108.

RECEIVED December 22, 1988

Chapter 21

Synthesis of VPI–5

Mark E. Davis[1], Consuelo Montes[1], and Juan M. Garces[2]

**[1]Department of Chemical Engineering, Virginia Polytechnic Institute
and State University, Blacksburg, VA 24061
[2]Dow Chemical Company, Midland, MI 48640**

We report here, for the first time, the synthetic
procedures used to crystallize the
aluminophosphate molecular sieve VPI-5. Two
synthesis methods are illustrated. The step by
step procedures are discussed in detail and
reveal the precise nature of synthesizing VPI-5.

The first discovery of a zeolite was recorded in 1756 ($\underline{1}$). Since
that time numerous natural and synthetic zeolites, silica
polymorphs, and aluminophosphate-based molecular sieves have been
reported. The largest ring in these materials consists of 12
tetrahedral (12 T) atoms. This boundary has been in existence for
over 180 years since the first zeolite to contain 12 T-atom rings,
gmelinite, was discovered in 1807 ($\underline{1}$). Recently, we have
synthesized the first molecular sieve with rings that possess
greater than 12 T-atoms ($\underline{2},\underline{3}$). Virginia Polytechnic Institute
number 5 (VPI-5) is a family of aluminophosphate based molecular
sieves with the same three-dimensional topology. The extra-large
pores of VPI-5 contain unidimensional channels circumscribed by
rings which have 18 T-atoms and possess free diameters of
approximately 12 Å ($\underline{2},\underline{3}$).
    We report here, for the first time, the synthesis procedures
used to crystallize the extra-large pore, aluminophosphate,
molecular sieve VPI-5. Synthesis techniques for crystallization
of element substituted VPI-5 are forthcoming (Davis, M. E., et
al., Zeolites '89, in press)

<u>Experimental Section</u>

Pseudoboehmite alumina (Catapal-B) and 85 wt% H_3PO_4 were used
exclusively as the aluminum and phosphorus starting materials.
Aqueous (55 wt%) tetrabutylammonium hydroxide (TBA) and
n-dipropylamine (DPA) were purchased from Alfa and Aldrich,
respectively.

A typical synthesis procedure involves the following steps: (i) alumina is slurried in water, (ii) phosphoric acid is diluted in water, (iii) the phosphoric acid solution is added to the alumina slurry, (iv) the aluminophosphate precursor mixture is aged at ambient conditions, (v) an organic is added to the precursor mixture and aged with rapid agitation to form the final gel, which (vi) is charged into the autoclave and heated. The gel composition can be written as

$$x \ R \bullet y \ Al_2O_3 \bullet z \ P_2O_5 \bullet g \ H_2O.$$

Exploratory syntheses were accomplished in 15 ml Teflon-lined autoclaves which were statically heated at autogenous pressure in forced convection ovens. Larger autoclaves (300 ml, 600 ml, and above) have also been successfully employed. At specified times, the autoclaves were removed from the oven, quenched in cold water, and the pH of the contents measured. Product VPI-5 was recovered by slurrying the autoclave contents in water, decanting the supernatant liquid, filtering the white solid, and drying the crystals in ambient air.

A Stoe I2 X-ray diffractometer was used to collect X-ray powder diffraction data. Figure 1 illustrates the X-ray powder diffraction pattern for VPI-5. Scanning electron micrographs were obtained using a Cambridge Instruments Stereoscan 200 scanning electron microscope.

Results and Discussion

We have synthesized VPI-5 with a variety of organic agents such as amines and quaternary ammonium cations. The synthesis procedure depends upon the type of organic agent and we will illustrate an "amine" synthesis with DPA and a "quat." synthesis with TBA. Table I lists reproducible procedures. We have provided an example of a "small" scale synthesis (DPA) and a fairly "large" scale synthesis (TBA) to show that these procedures can be scaled-up. Below we discuss the essential details of these two procedures. VPI-5 that has been crystallized with the use of DPA and TBA will be denoted DPA-VPI-5 and TBA-VPI-5, respectively.

Synthesis Using DPA. The synthesis of DPA-VPI-5 is summarized in Table I and is fully described as follows. Upon combining the alumina slurry with the phosphoric acid solution, the pH of the precursor mixture rises with aging (see Fig. 2). Thus, the phosphoric acid is slowly reacting with the alumina. The pH stabilizes around 1.2-1.3 after approximately 1.5 hours. This aging process is important for the formation of VPI-5. If the precursor mixture is not aged and all other steps of the procedure followed, H3 (4,5) is usually crystallized. H3 is an aluminophosphate hydrate (AlPO₄ • 1.5 H₂O) first synthesized by d'Yvoire (4). The structure of H3 has been solved (5) and contains 4,6, and 8 membered rings. Aging times as long as approximately 10 hours still yield VPI-5. Upon addition of the DPA to the stirring precursor mixture the pH immediately increases to above 3 and then gradually climbs to a final value of approximately 3.75 (see Fig. 2). Again, the aging of the complete
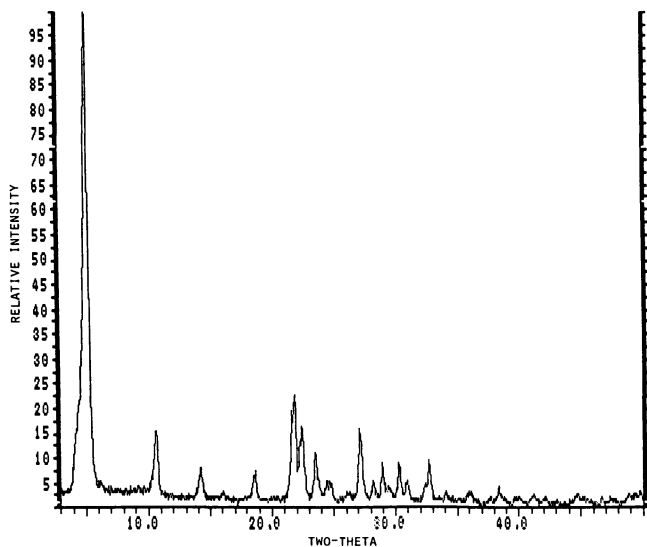
2Θ	d(Å)	I/I₀(%)
5.38	16.43	100
9.32	9.49	2
10.75	8.23	14
14.26	6.21	6
16.16	5.48	2
18.68	4.75	6
21.76	4.08	20
21.92	4.05	22
22.39	3.97	14
22.56	3.94	15
23.59	3.77	10
24.46	3.64	4
26.12	3.41	2
27.17	3.28	16
28.19	3.17	5
28.96	3.08	7
29.48	3.03	4
30.28	2.95	8
30.88	2.90	5
32.71	2.74	7
34.05	2.63	2
35.86	2.50	3
38.32	2.35	3

Figure 1. X-ray powder diffraction pattern of VPI-5.

Table I. Synthesis Procedures for VPI-5 With DPA and TBA

DPA

1. 6.9 g of pseudoboehmite are slurried in 20 g of water

2. 10 g of water are added to 11.5 g of phosphoric acid

3. The phosphoric acid solution is added to the alumina slurry to form a precursor mixture

4. The precursor mixture is aged for 1.5-2 hours at ambient conditions with agitation

5. 5.1 g of DPA are added to the precursor mixture and the resulting gel aged with agitation for 1.5-2 hours at ambient conditions

6. The reaction mixture is heated at 142°C for 20-24 hours

gel composition: DPA $\cdot$ Al$_2$O$_3$ $\cdot$ P$_2$O$_5$ $\cdot$ 40 H$_2$O

TBA

1. 55 g of pseudoboehmite are slurried in 150 g of water

2. 100 g of water are added to 90 g of phosphoric acid

3. The phosphoric acid solution is added to the aluminium slurry to form a precursor mixture

4. The precursor mixture is aged for 1.5-3 hours at ambient conditions with no agitation

5. 186 g of 55 wt% TBA are added to the precursor mixture and the resulting gel vigorously agitated for approximately 2 hours at ambient conditions

6. The reaction mixture is heated at 150°C for 24 hours

gel composition: TBA $\cdot$ Al$_2$O$_3$ $\cdot$ P$_2$O$_5$ $\cdot$ 50 H$_2$O

gel is important. Since the pH slowly rises during this time period, a chemical reaction is occurring. If the gel is aged for too long of period, e.g., 24 hours, H3 is crystallized rather than VPI-5.
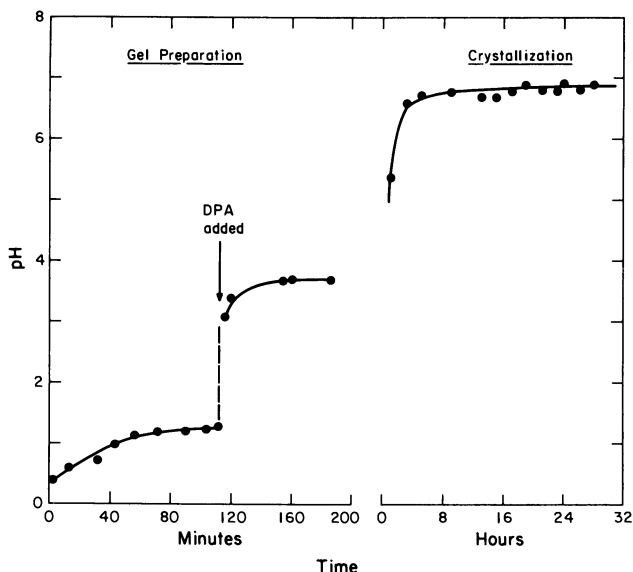
Figure 2. pH versus time for the synthesis of DPA-VPI-5.

The crystallization of VPI-5 occurs at 142°C, and the crystallization time is fast. From Figures 2 and 3 it is observed that within five hours the pH of the autoclave contents has reached a plateau and the product is quite crystalline. In Figure 3 we illustrate the degree of crystallinity estimated from X-ray powder diffraction data as a function of time. Since VPI-5 quickly crystallizes, the values shown at short times are rough estimates only. Notice, however, that the DPA-VPI-5 is not stable for long periods of time in the mother liquor, and that the loss of crystallinity is not accompanied by a change in pH. We specify a crystallization time of 20-24 hours in Table I since we have observed that slight variations in the procedure normally lengthen the time for the onset of crystallization. However, we almost always observe the highest crystallinity in the samples which have been crystallized for 20-24 hours.

The crystallization temperature can be varied ± 5°C with no adverse effects. At temperatures above 150°C VPI-5 forms with H3 then quickly decomposes and ultimately $AlPO_4$-11 is crystallized. At temperatures around 125°C the solid product is amorphous at 24 hours but eventually forms H3 after several days.

Table II illustrates the effect of gel composition on the final product crystallized using the procedure listed in Table I.

Table II. Variation in Gel Composition With DPA Synthesis

Preparation	DPA	Al_2O_3	P_2O_5	H_2O	Result
1	1.0	1.00	1.00	40	VPI-5
2	1.0	1.10	1.00	40	VPI-5
3	1.0	0.90	1.00	40	VPI-5
4	1.0	0.75	1.00	40	VPI-5 + H3
5	1.0	1.25	1.00	40	unknown*
6	1.0	1.00	0.75	40	unknown*
7	1.0	1.00	1.25	40	H3 + unknown*
8	1.0	1.00	1.00	35	VPI-5 with slightly lower crystallinity
9	1.0	1.00	1.00	45	VPI-5 + H3**
10	0.5	1.00	1.00	40	H3
11	2.0	1.00	1.00	40	amorphous

*Most likely dense phase aluminophosphate
**Required longer crystallization time
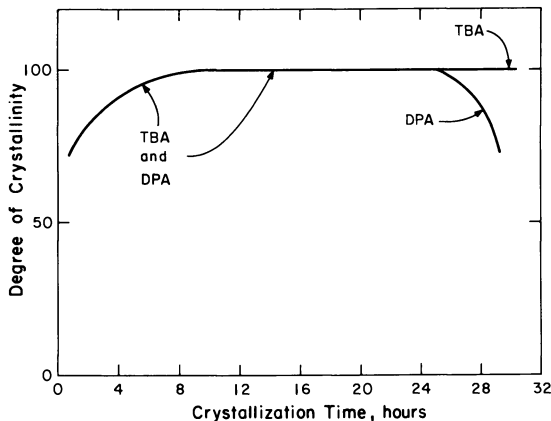
Figure 3. Degree of crystallinity estimated from X-ray powder diffraction data versus crystallization time.

Notice that small compositional variations (preparations 1-3) are allowable. However, ± 25% variations in gel composition do not crystallize pure DPA-VPI-5. It is interesting to note that the water content is important and that excess DPA (preparation 11) hinders the crystallization of VPI-5.

Synthesis With TBA. As with the DPA-VPI-5 crystallization, the TBA synthesis involves the use of a precursor aluminophosphate mixture. (This is summarized also in Table I.) However, there is an important distinction between the two types of syntheses during step 4. When TBA is used, the precursor mixture is not agitated. The quiescent mixture exhibits a pH profile in time nearly that with agitation (see Figures 2 and 4). If the precursor mixture is agitated during aging, either TBA-VPI-5 is formed and accompanied by H3 or only H3 is crystallized.

The precursor gel is vigorously agitated just prior to the addition of TBAOH. When the TBAOH is combined with the aluminophosphate mixture the pH instantly rises to around 5. The final pH is dependent upon the degree of mixing during addition of TBAOH. Incomplete mixing produces pH's below 5 and can lead to the formation of impure TBA-VPI-5 (with small amounts of H3 present).

The TBA gel crystallizes VPI-5 rapidly and reaches a final pH equivalent to that observed with DPA (see Figures 3 and 4). For reasons similar to those outlined in the DPA synthesis, we specify approximately 24 hours of crystallization time when using TBA (in Table I). Notice that the TBA-VPI-5 does not decompose in the mother liquor. We have observed that the TBA-VPI-5 is stable in the mother liquor for many days. It is interesting that the final pH of the TBA and DPA syntheses are approximately the same yet the TBA-VPI-5 is stable while the DPA-VPI-5 is not.
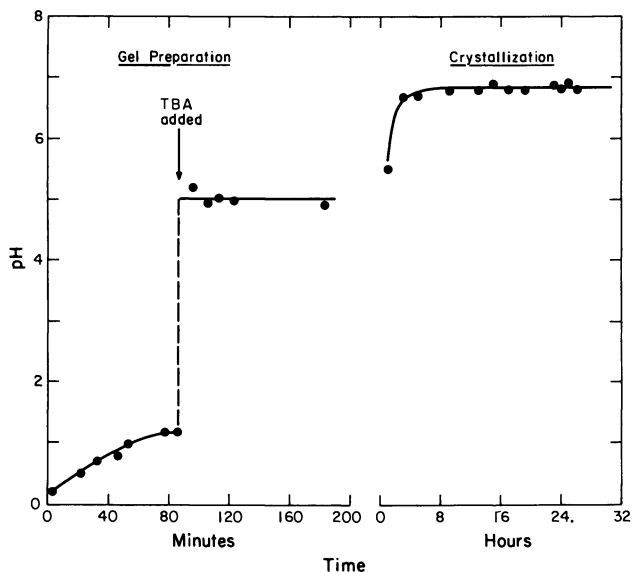
Figure 4. pH versus time for the synthesis of TBA-VPI-5.

Morphology. Figures 5, 6, and 7 show scanning electron micrographs which illustrate the morphology of TBA-VPI-5, DPA-VPI-5, and H3 respectively. The TBA-VPI-5 crystals have "needle-like" morphology and are aggregated into bundles. The crystals are approximately 10 microns in length and are submicron in diameter. We suspect that the c-axis and thus the 12 Å pore is oriented in the direction of the needle length. On the other hand, the DPA-VPI-5 shows large spherical aggregates (greater than 100 microns). Inspection of these aggregates reveals particles which adopt a variety of morphologies. Spheres of approximately 5 microns are observed as well as needles (see Figure 6b). From adsorption experiments (ref. 3, sample 1 = TBA-VPI-5, sample 2 = DPA-VPI-5), it has been determined that the void volume of TBA-VPI-5 is equivalent to DPA-VPI-5. Therefore, the 5 micron spheres in DPA-VPI-5 are not impurities but must also be DPA-VPI-5 with a different or very small crystal habit. The morphology of H3 is illustrated since it typically is the impurity present when VPI-5 is not crystallized properly. H3 is observed as spherical aggregates of approximately 20 micron diameter. These aggregates are easily distinguished from TBA-VPI-5 by optical microscope. However, since DPA-VPI-5 grows in large spherical aggregates it is more difficult to differentiate from H3 with only a optical microscope. However, we presently are able to do so and use the difference in size ($\sim 100~\mu$ versus $\sim 20~\mu$) as the distinguishing feature.

Adsorption. Table III shows the adsorption capacity of $AlPO_4$-5 and VPI-5 for various adsorbates. All values listed are obtained at $P/P_o = 0.4$. The data for $AlPO_4$-5 (except for
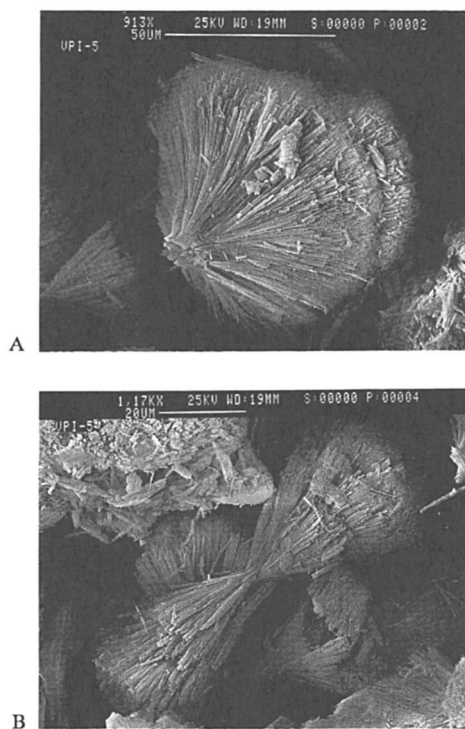
Figure 5. Scanning electron micrographs of TBA-VPI-5. (A) bar size is 50 microns, (B) bar size is 20 microns.
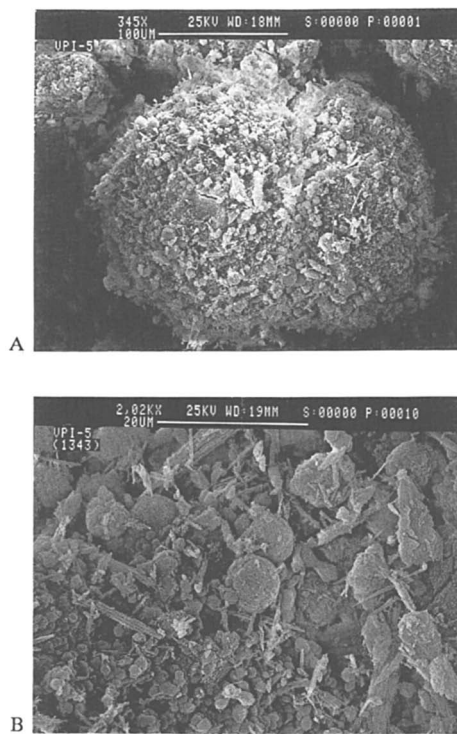
Figure 6. Scanning electron micrographs of DPA–VPI–5. (A) bar size is 100 microns, (B) bar size is 20 microns.
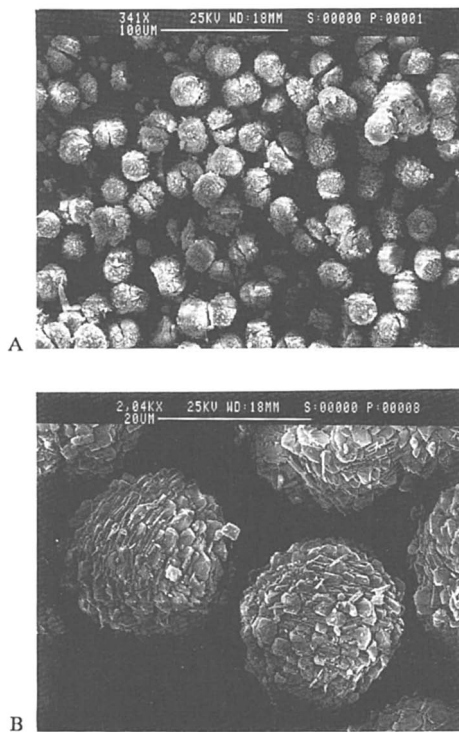
Figure 7. Scanning electron micrographs of H3. (A) bar size is 100 microns, (B) bar size is 20 microns.

Table III. Adsorption capacity of molecular sieves at P/P_o = 0.4[a]

Kinetic Diameter, Å	Adsorbate[b]	Capacity, cm^3/g	
		$AlPO_4$-5[c]	VPI-5
3.46	O_2	0.146	0.228
4.30	n-Hexane	0.139	0.198
6.00	Cyclohexane	0.145	0.156
6.20	Neopentane	0.137	0.148
8.50	Triisopropylbenzene	0.021[a]	0.117

[a] From Davis et al., J. Am. Chem. Soc., submitted.

[b] Adsorption at room temperature except for O_2 which was performed at either liquid N_2 or O_2 temperatures.

[c] From ref. 6.

triisopropylbenzene) are from Union Carbide (6). The VPI-5 data were obtained using a McBain-Bakr apparatus and the samples were activated by heating to 350°C under vacuum overnight (Davis et al., J. Am. Chem. Soc., submitted). $AlPO_4$-5 adsorbs oxygen and the hydrocarbons listed except for triisopropylbenzene. The triisopropylbenzene is too large to penetrate the 12 T-atom ring. Notice that the adsorption capacity of $AlPO_4$-5 is the same, within experimental error, for all adsorbates listed. VPI-5 reveals two phenomena not observed for $AlPO_4$-5. First, triisopropylbenzene is adsorbed. Second, the adsorption capacity monotonically decreases with increasing adsorbate size. Since VPI-5 contains pores that are slightly larger than 12 Å, all adsorbates other than triisopropylbenzene have the possibility of fitting more than one molecule across the diameter. In other words, packing of adsorbate molecules may be important in these extra-large pores. Further evidence to support this ideas is provided elsewhere (Davis et al., J. Am. Chem. Soc., submitted).

Perfluorotributylamine (PFTBA) has a kinetic diameter greater than 10 Å ($\sim$ 10.5 Å). After repeated attempts to adsorb PFTBA into VPI-5, we were convinced that our data were influenced by extracrystalline adsorption. Thus, we performed PFTBA desorption experiments utilizing a thermogravimetric analyzer in which the off-gas was transferred into a mass spectrometer. $AlPO_4$-5 was used for comparison since PFTBA cannot adsorb in a 12 T-atom ring. $AlPO_4$-5 and VPI-5 were loaded with PFTBA. Next, $AlPO_4$-5 was heated to 100°C in flowing helium in the apparatus described previously. After several hours, a stable weight was obtained (PFTBA loss observed in the mass spectrometer). Upon heating $AlPO_4$-5 to 550°C, no further weight loss was observed. Thus, PFTBA can be desorbed from an $AlPO_4$ surface by flowing helium at 100°C. The same treatment was employed for VPI-5. After reaching a stable weight in flowing helium at 100°C, the sample was heated to 550°C. Several higher temperature desorption peaks were due to the loss of PFTBA. We interpret this result to indicate that PFTBA can adsorb within the 18 T-atom rings of VPI-5. Thus, adsorption of molecules with kinetic diameters above 10 Å is possible with VPI-5.

Acknowledgments

Literature Cited

1. Breck, D. W., *Zeolite Molecular Sieves*; Wiley: New York, 1974; p. 188.
2. Davis, M. E.; Saldarriaga, C.; Montes, C.; Garces, J.; Crowder, C. *Nature* 1988, *331*, 698.
3. Davis, M. E.; Saldarriaga, C.; Montes, C.; Garces, J.; Crowder, C. *Zeolites* 1988, *8*, 362.
4. d'Yvoire, F. *Bull. Soc. Chim* 1962, 1762.
5. Pluth, J. J.; Smith, J. V. *Nature* 1985, *318*, 165.

6.   Wilson, S. T.; Lok, B. M.; Messina, C. A.; Flanigen, E. M.
     <u>Proceedings of the Sixth International Zeolite Conference</u>,
     Butterworths: Survey, 1985; p. 97.

RECEIVED December 22, 1988

Chapter 22

Synthesis of Microporous Silicoaluminophosphates in Hexanol–Water Biphasic Systems

Johan A. Martens, Bart Verlinden, Machteld Mertens, Piet J. Grobet, and Peter A. Jacobs

Laboratorium voor Oppervlaktechemie, Katholieke Universiteit Leuven, Kardinaal Mercierlaan 92, B–3030 Heverlee, Belgium

Microporous silicoaluminophosphates are synthesized in the hexanol-water biphasic system using tetrapropylammonium hydroxide (Pr_4N-OH) and dipropylamine (Pr_2N) as templates. The outcome of the crystallization depends on phase separation and agitation during synthesis. MCM-1 crystallizes in a broad range of conditions and in the presence of Pr_4N-OH or Pr_2N. The mechanism of Si substitution in and the ion-exchange and catalytic properties of MCM-1 materials are influenced by the template used. A silicon-free homolog of MCM-1 exists and was formerly denoted as $AlPO_4$-H_3. The structural identity of MCM-1 and $AlPO_4$-H_3 is demonstrated. The crystallization of $AlPO_4$-H_3 from an inorganic synthesis mixture is an example of the growth of microporous aluminophosphates in absence of template. The intracrystalline void structure of MCM-1 is determined with the decane test.

Crystalline microporous silicoaluminophosphates have been patented as SAPO-n (1) or MCM-n (2) materials. The SAPO materials crystallize from an aqueous medium in the presence of organic templates, the MCM materials from a biphasic medium, using similar templates. Most of the actually known MCM's and SAPO's are crystallographically different apart from SAPO-34, SAPO-44, SAPO-47 and MCM-2 which have the chabasite topology (2,3). The structure of other MCM materials is presently unknown.

From the available literature it appears that the Si, Al and P ordering in the two groups of microporous silicoaluminophosphates should be different. The anhydrous chemical composition of SAPO-n corresponds to (1):
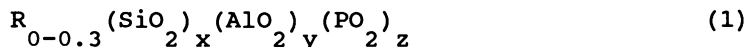
$$R_{0-0.3}(SiO_2)_x(AlO_2)_y(PO_2)_z \qquad (1)$$

in which R is the template molecule. A SAPO-n material can be considered to originate from Si substitution into an hypothetical aluminum phosphate framework (4,5). The predominant substitution mechanisms are Si for P (mechanism 2) and two Si atoms for one Al and one P simultaneously (mechanism 3). Si substitution for Al (mechanism 1) does not occur with SAPO's (4). The negative charge of a SAPO is, therefore, proportional to the mole fraction of Si incorporated via mechanism 2, as mechanism 3 does not create any lattice charge. The general anhydrous formula of MCM-n is (2):

$$R_v M_{x/m}^{m+} (AlO_2)_{1-y}^{-} (PO_2)_{1-x}^{+} (SiO_2)_{x+y} N_{y/n}^{n-} \qquad (2)$$
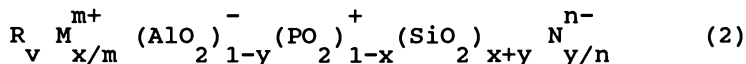
When the incorporation of Si is again considered as a replacement of Al and/or P in an hypothetical aluminum phosphate lattice, the MCM formula precludes isomorphic substitution via mechanism 3 and allows only for mechanism 1 and 2 to occur. According to the MCM formula, SiO_2 tetrahedra replace AlO_2^- and introduce positive framework charge, which is neutralised by the anions N^{n-} or replaces PO_2^+ and creates negative framework charge, which is neutralised by the cations M^{m+}.

As a result of these suggested differences in isomorphic substitution mechanism, SAPO and MCM materials should have different ion-exchange and catalytic properties. SAPO's are cation exchangers and potential Brønsted acid catalysts. MCM's are expected to be cation and/or anion exchangers and are potential Brønsted acid, Brønsted base or Brønsted acid/base catalysts.

In this work the potential of biphasic synthesis mixtures for the synthesis of microporous silicoalumino-phosphates is investigated. The influence of emulsification of the synthesis mixture, agitation and temperature on the crystallization is studied. The structural identity of MCM-1 and $AlPO_4$-H_3, which is an aluminum phosphate hydrate that crystallizes in absence of template, is demonstrated. Special attention is paid to the mechanism of Si substitution in MCM-1, to its catalytic activity and its intracrystalline void structure.

Experimental

Materials. The components of the biphasic synthesis mixture were hexanol (HEX), tetraethyl orthosilicate (TEOSi), orthophosphoric acid (85%), Pr_2N and Pr_4N-OH (25%), all from Janssen Chim., pseudoboehmite (Vista, 70% Al_2O_3, 30% H_2O) and water. These compounds were mixed in the following way. To hexanol first TEOSi was added and subsequently phosphoric acid, pseudoboehmite, the template and water. The synthesis mixtures were transferred into autoclaves with a capacity of 120 ml. Agitation was performed by rotating the autoclaves at 50

rpm. After crystallization the slurries were filtered, and the solid products washed and dried.

$AlPO_4-H_3$ was prepared according to experiment No.3 of ref.6. From pseudoboehmite, phosphoric acid and water a 100 ml aqueous solution containing 10 g of Al_2O_3 and 38 g of P_2O_5 was prepared. This solution was diluted seven times and refluxed under vigorous stirring during 3 h. $AlPO_4-H_3$ was recovered by filtration, washing and drying.

Methods. X-ray powder diffraction (XRD) patterns were recorded using a modified Siemens type F diffractometer, automated and equipped with a McBraun position sensitive detector (22).

Scanning electron micrographs were taken with a Phillips instrument.

MAS NMR spectra were obtained with a Bruker 400 MSL spectrometer. The experimental conditions used in the ^{29}Si DEC, ^{29}Si CP, ^{27}Al, ^{27}Al CP and ^{31}P DEC were as follows:

Parameter	^{29}Si		^{27}Al	^{31}P
	DEC	CP	CP	DEC
MAS frequency (MHz)	79.5		104.2	161.9
Pulse length (μs)	3	5.2	0.6	4
Repetition time (s)	3	5	0.1	10
Spinning rate (kHz)	3		3	5
CP MAS contact time (ms)	–	5	– 0.5	–
Decoupling (ms)	1			1
Number of scans	18000	10000	3000	48

Infrared spectra were recorded on a PE-580B instrument with data station. Lattice vibration spectra were obtained using the KBr technique. Hydroxyl spectra were scanned on self-supporting wafers of the samples mounted in a vacuum cell. Spectral averaging was usually 9 times.

The as-synthesized materials were converted into bifunctional catalysts by heating in inert atmosphere at 723 K, impregnation with $Pt(NH_3)_4Cl_2$ solution to obtain a 1% by weight loading with Pt and activation in flowing oxygen and hydrogen at 673 K. A description of the reactor used for decane conversion was given previously (7). The H_2/decane molar ratio in the feed was 100 and W/F_O was 2 kg h mole^{-1}. The use of the catalytic conversion of decane to characterize the void volume of microporous crystals was described previously (8-10).

Results and Discussion

Influence of Agitation and Synthesis Temperature of a Two Phase System. A synthesis mixture with the following molar composition per mole of Al_2O_3:

$(HEX)_{4.28}(TEOSi)_{0.36}(P_2O_5)_{0.75}(Pr_2N)_{1.03}(H_2O)_{30.75}$
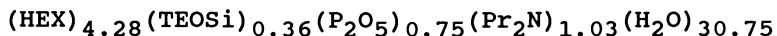
is a two phase system which does not emulsify. It will be further denoted as mixture A. It was autoclaved under different conditions of temperature, time and agitation. The crystallization products obtained are listed in Table I. MCM-1, MCM-9, SAPO-11 and mixtures thereof were obtained depending on the nature of the hydrothermal treatment (Table I). In Figures 1-3 the XRD patterns of the respective phases are compared to literature data. The patterns of MCM-1 and SAPO-11 are in agreement with literature. Some of the line positions in the pattern of MCM-9 are shifted with respect to data from the patent literature and supplementary diffractions of medium intensity are found at 2θ values of 6.7 and 13.5.

Table I. Influence of Temperature, Time and Agitation on the Nature of the Crystallization Products from Mixture A

Exp. No.	T_1[a] (K)	T_2 (K)	t_2 (h)	T_3 (K)	t_3 (h)	T_4 (K)	t_4 (h)	Agit.[b]	Product	Purity[c] (%)
1	–	403	24	443	24	–	–	Y	MCM-1	100
2	–	423	24	473	24	–	–	Y	MCM-1+SAPO-11	50+50
3	298	403	24	448	24	458	24	Y	MCM-1	100
4	298	418	24	458	24	–	–	Y	MCM-1	100
5	–	473	48	–	–	–	–	Y	MCM-1+SAPO-11	60+40
6	298	403	24	458	24	–	–	Y	MCM-1	100
7	–	403	24	443	24	–	–	N	MCM-9+U[d]	70
8	–	403	24	443	72	–	–	N	MCM-1+SAPO-11	90+10
9	–	403	24	443	72	–	–	N	MCM-1+SAPO-11	60+40
10	–	393	24	443	24	–	–	N	MCM-1+U[d]	60
11	–	393	24	443	96	–	–	N	MCM-1+U[d]	30
12	298	403	24	458	24	–	–	N	MCM-1+SAPO-11	80+20
13	298	403	24	458	24	–	–	N	SAPO-11	80
14	298	403	24	458	24	–	–	N	SAPO-11	60
15	–	408	24	458	24	–	–	N	SAPO-11	60
16	–	408	24	473	24	–	–	N	SAPO-11+MCM-1	70+30
17	–	423	24	473	24	–	–	N	MCM-1+SAPO-11	70+30
18	–	423	48	473	120	–	–	N	MCM-1+SAPO-11	50+50
19	–	458	48	–	–	–	–	N	MCM-1+SAPO-11	60+40

a, T(emperature), t(ime), using a temperature increase of 0.1 K s^{-1} between two T_i values, t_1=0 h; b, Y(es), N(o); c, from XRD; d, unidentified phase.

When synthesis mixture A is agitated, MCM-1 crystallizes as a pure phase if the temperature in the first step of the hydrothermal treatment is low (Nos.1,3,4 and 6). When this temperature is 423 K or higher, co-crystallization of SAPO-11 is observed (Nos.2 and 5). MCM-9 was obtained under static conditions after heating at 403 K and at 443 K for one day (No.7). When the heating period at the second temperature is prolonged MCM-9 is transformed into a mixture of MCM-1 and SAPO-11

(Nos.8 and 9). MCM-1, SAPO-11 or a mixture of both were obtained in all other syntheses performed without agitation (Nos.10-19). The crystallization of SAPO-11 seems to be favoured generally when a high temperature step (>443 K) is involved (Nos.12-19) or after prolonged heating at 443 K (Nos.8 and 9). It seems that MCM-9 and MCM-1 are unstable with respect to SAPO-11 and accordingly the following successive phase transformations must occur:

MCM-9 -> MCM-1 -> SAPO-11.
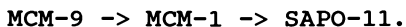
The importance of stirring of biphasic systems during synthesis becomes apparent when comparing the results from experiments Nos.1 and 7. Under static conditions MCM-9 crystallizes (No.7) while after agitation MCM-1 is obtained (No.1). A SEM photograph of MCM-1 No.1 is shown in Figure 4. The MCM-1 crystals are about 1 μm large. The picture also shows a high degree of crystallinity and homogeneous morphology of the crystals.

Synthesis in non-Emulsifying Conditions with Pr_2N using Increasing Amounts of Si. Mixtures were prepared with the following molar composition :

$$(HEX)_{4.28} (Al_2O_3)_{1.00} (P_2O_5)_{0.75} (Pr_2N)_{1.03} (H_2O)_{30.75}$$
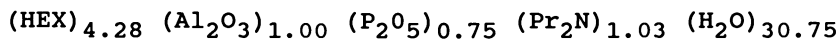
and containing various amounts of TEOSi. The amount of hexanol had to be increased when more than 0.8 mole of TEOSi were used. All mixtures were stirred during the hydrothermal treatment. The products obtained are listed in Table II. When no TEOSi was added to the synthesis mixture, ALPO-11 was obtained (Nos.20 and 21). With 0.095 mole of TEOSi, the same crystalline phase was obtained and denoted as SAPO-11, although the incorporation of Si in the material was not verified (No.22). Pure MCM-1 crystals were obtained when the amount of TEOSi was between 0.36 and 0.65 mole per mole Al_2O_3 (Nos.4,24-28). With higher amounts of TEOSi co-crystallization of MCM-1 with an unidentified phase (Sample No.29) or with SAPO-11 (Samples Nos.30 and 31) or poorly crystalline MCM-1 (Sample No.32) was obtained. Thus, under the present experimental conditions, the Si content of the mixture for MCM-1 crystallization cannot be varied widely.

Synthesis in Emulsifying Conditions with Pr_4N-OH. The results of the syntheses performed with mixtures containing Pr_4N-OH are presented in Table III. The different molar ratios of the components of the synthesis mixture were varied around those given in the original patents on MCM-1 (11), MCM-3 (12) and MCM-4 (13) synthesis. MCM-1 was obtained in all experiments (Nos.33-36). In experiment No.34, traces of other unidentified crystalline phases have co-crystallized.

The synthesis mixture in all instances was an emulsion. With this synthesis mixture there seems to be

MCM-1

No.6		Ref.11	
d(nm)	I/I$_o$	d(nm)	I
0.976	33	0.967	m
0.695	100	0.686	vs
0.657	77	0.649	s
0.490	40	0.486	s-vs
0.428	80	0.425	vs
0.341	47	0.339	m
0.308	66	0.306	vs
0.295	16	0.293	w
0.291	19	0.289	w
0.269	37	0.268	m
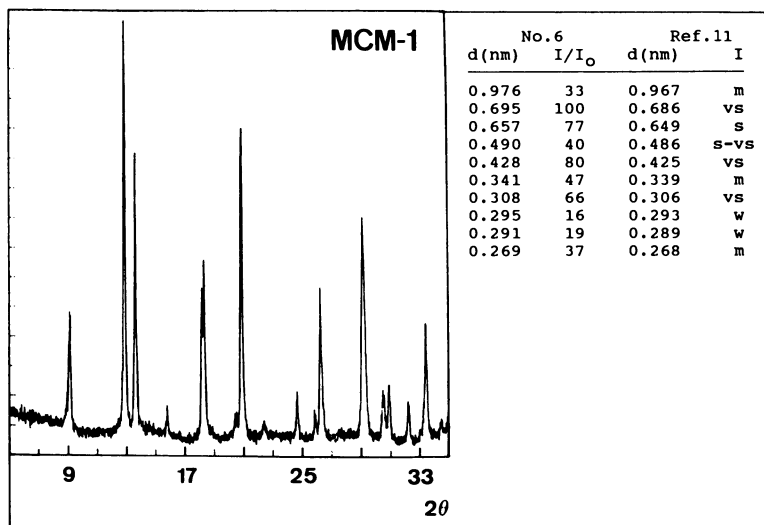
Figure 1. XRD pattern of MCM-1 sample No.6 and comparison of the line positions and intensities with the data from ref.11.

MCM-9

No.7		Ref.25	
d(nm)	I/Io	d(nm)	I/Io
1.650	100	1.641	100
1.084	32	1.084	7
0.948	44	0.933	15
0.824	43	0.820	31
0.670	28	0.668	8
0.629	28	0.617	14
0.568	46	0.565	13
0.550	25	0.546	5
0.489	30	0.474	14
0.438	29	0.434	15
0.417	24	0.421	54
0.395	71	0.394	43
0.386	43	0.383	25
0.380	27	0.377	20
0.361	25	0.359	9
0.340	26	0.339	6
0.330	35	0.328	32
0.318	22	0.316	10
0.313	31	0.309	14
0.308	31	0.303	9
0.297	30	0.295	19
0.269	22	0.263	7
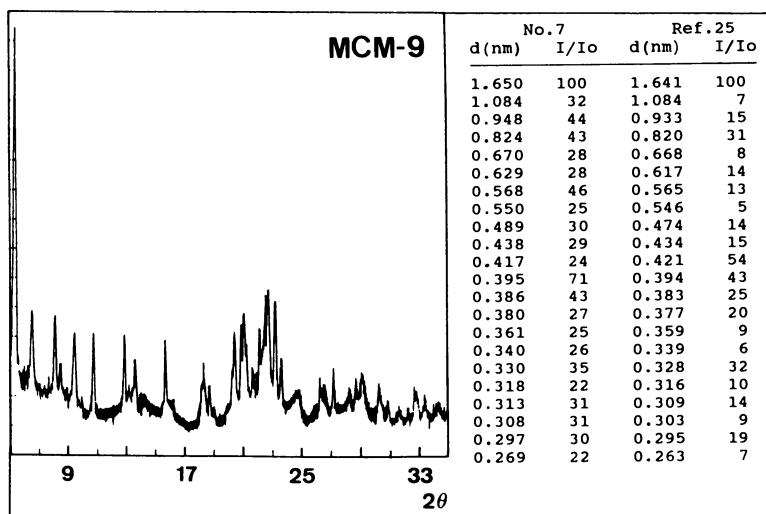
Figure 2. XRD pattern of MCM-9 sample No.7 and comparison of the line positions and intensities with the data from ref.22.

SAPO-11

No.13		Ref.1	
d(nm)	I/Io	d(nm)	I/Io
1.097	38	1.085	34
0.940	54	0.931	49
0.665	40	0.666	16
0.568	33	0.564	30
0.437	58	0.432	50
0.424	100	0.423	100
0.402	55	0.400	58
0.392	78	0.393	75
0.386	58	0.383	67
0.308	30	0.302	9

2θ
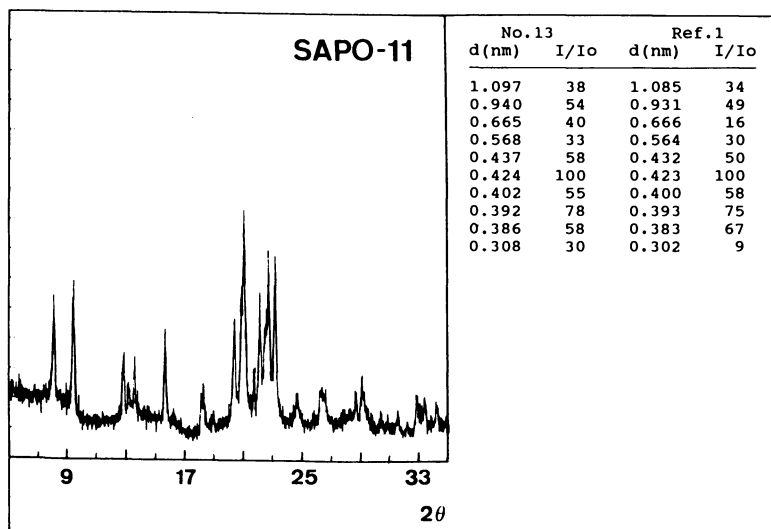
Figure 3. XRD pattern of SAPO-11 sample No.13 and comparison of the line positions and intensities with the data from ref.1.

Figure 4. Scanning electron micrograph of MCM-1 sample No.1.

no influence of agitation on the crystal phase obtained. The morphology of the MCM-1 crystals obtained with Pr_4N-OH is shown in Figure 5. The size of the crystals is around 1 μm. The nature of the template (Pr_2N or Pr_4N-OH) also seems unable under these conditions to influence the morphology and dimensions of MCM-1 crystals (Figures 4 and 5).

Table II. Crystallization Products from Stirred Mixtures with Molar Compostion per Mole of Al_2O_3
$(HEX)_{4.28}$ $(TEOSi)_x$ $(P_2O_5)_{0.75}$ $(Pr_2N)_{1.03}$ $(H_2O)_{30.75}$

Exp. No.	TEOSi x	T_1[a] (K)	T_2 (K)	t_2 (h)	T_3 (K)	t_3 (h)	T_4 (K)	t_4 (h)	Product
20	0	298	418	24	458	24	–	–	ALPO-11
21	0	298	408	24	458	96	–	–	ALPO-11
22	0.095	298	408	24	458	96	–	–	SAPO-11
23	0.24	298	408	24	458	96	–	–	MCM-1+SAPO-11
4	0.36	298	418	24	458	24	–	–	MCM-1
24	0.39	298	403	24	448	24	458	24	MCM-1
25	0.42	298	403	24	448	24	458	24	MCM-1
26	0.49	298	403	24	448	24	458	24	MCM-1
27	0.51	298	403	24	448	24	458	24	MCM-1
28	0.65	298	403	24	448	24	458	24	MCM-1
29[d]	0.81	298	403	24	448	24	458	24	MCM-1 + U[b]
30	0.84	298	418	24	458	24	–	–	MCM-1+SAPO-11
31[d]	0.97	298	403	24	448	24	458	24	MCM-1+SAPO-11
32[d]	1.13	298	403	24	448	24	458	24	MCM-1+AM[c]

a, T(emperature), t(ime), using a temperature increase of 0.1 K s^{-1} between two T_i values; b, unidentified phase; c, amorphous; d, with (HEX) = 5.14.

Table III. Synthesis with Pr_4N-OH under Stirring[a]

Ref. Exp. No.	11 1	11 3	12 1	13 1	– 33	– 34	–[b] 35	– 36
HEX	4.38	6.0	8.6	3.8	4.38	8.6	3.8	3.8
TEOSi	0.36	0.49	0.70	0.31	1.07	0.70	0.31	0.31
P_2O_5	0.75	1.02	1.46	1.18	0.75	1.46	1.19	1.19
Al_2O_3	1.00	1.00	1.00	1.00	1.00	1.00	1.00	1.00
Pr_4NOH	0.77	1.06	1.51	0.67	0.77	1.21	0.67	0.67
H_2O	42.2	57.7	82.4	39.2	60.2	88.3	48.9	48.9
T (K)	433	453	423	423	448	423	423	423
t (h)	72	168	72	168	72	120	192	192
	MCM-1	MCM-1	MCM-3	MCM-4	MCM-1[c]	MCM-1	MCM-1	MCM-1

a, all synthesis mixtures were emulsified; b, under static conditions; c, containing trace of unidentified phase.

Figure 5. Scanning electron micrograph of MCM-1 sample No.34.

Characterization of $AlPO_4-H_3$ and MCM-1. In 1961 d'Yvoire reported on the synthesis of aluminum phosphate hydrates (6). $AlPO_4-H_3$ is of particular interest among these materials. Literature data on the XRD line positions and relative intensities for $AlPO_4-H_3$ and MCM-1 are collected in Figure 6. The materials show identical XRD patterns and thus should have the same structure type.

Infrared spectroscopy of the lattice vibrations of $AlPO_4-H_3$ and MCM-1 synthesized with Pr_4N-OH and Pr_2N are shown in Figure 7. The identity of the structures is also clear from those data.

The ^{27}Al, ^{27}Al CP and ^{31}P MAS NMR spectra of $AlPO_4-H_3$ are shown in Figure 8. A sharp ^{27}Al line is observed at 41.2 ppm. In aluminum phosphates ^{27}Al lines in the range 41-29 ppm are ascribed to tetrahedrally co-ordinated Al (14). An additional ^{27}Al signal appears with maxima at -11, -16, -19 and -24 ppm. This signal according to its position can be assigned to octahedrally co-ordinated aluminum. The 41 ppm line and those in the range -11 till -26 ppm are also visible under CP, indicating that protons (structural water) are in the vicinity of Al. The aluminum phosphate hydrates variscite and metavariscite have structures composed of alternating Al and P, with Al and P exhibiting octahedral and tetrahedral co-ordination, respectively (15,16). The formula of variscite and metavariscite is $AlPO_4 \cdot 2H_2O$. The two waters of hydration occupy cis positions in the co-ordination sphere of aluminum. With metavariscite the ^{27}Al MAS NMR chemical shift is -13.2 ppm (14) and with variscite it is -12.5 (17), which is in the range found for $AlPO_4-H_3$. With $AlPO_4-H_3$ the shape of the octahedral ^{27}Al line suggests the presence of a well-defined octahedral Al complex deviating from axial cylindrical symmetry and which is subjected to quadrupolar interaction. The ^{27}Al lines in the range from -11 till -24 ppm can be assigned to Al containing two water molecules in cis position in its octahedral co-ordination shell. The chemical formula of $AlPO_4-H_3$ is $AlPO_4 \cdot 1.50H_2O$ (6,18). Accordingly, not every Al atom can take two water molecules in its co-ordination shell. This necessitates the presence of tetrahedral aluminum, justifying the 41.2 ppm ^{27}Al signal. The ratio of the intensity of the line at 41.2 ppm to the sum of those between -11 and -24 ppm is 1.00 ± 0.05. Therefore, the structure should contain an equal amount of octahedrally and tetrahedrally co-ordinated Al. From the 1.50 mole of hydration water, only 1.00 mole is in the co-ordination shell of Al, corresponding to twice the amount of Al(VI).

The ^{31}P spectra consist of two lines at -24 and -26 ppm with equal intensity (Figure 8). Dense aluminium phosphates and AlPO-n materials generally show a single symmetrical line in the range from -19 till -30 ppm, consistent with the presence of tetrahedral phosphorus (14). $AlPO_4-H_3$ is actually the first aluminum phosphate for which a ^{31}P spectrum with two tetrahedral lines is
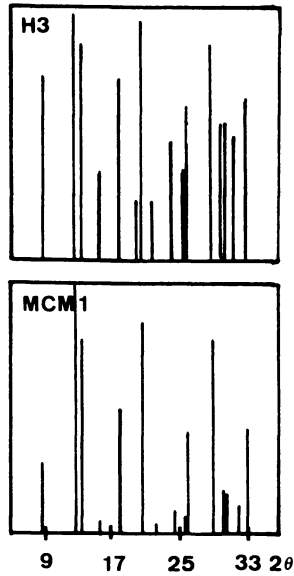
Figure 6. XRD line positions and relative intensities for $AlPO_4-H_3$ (data adapted from ref.6) and for MCM-1 (data from ref.11).
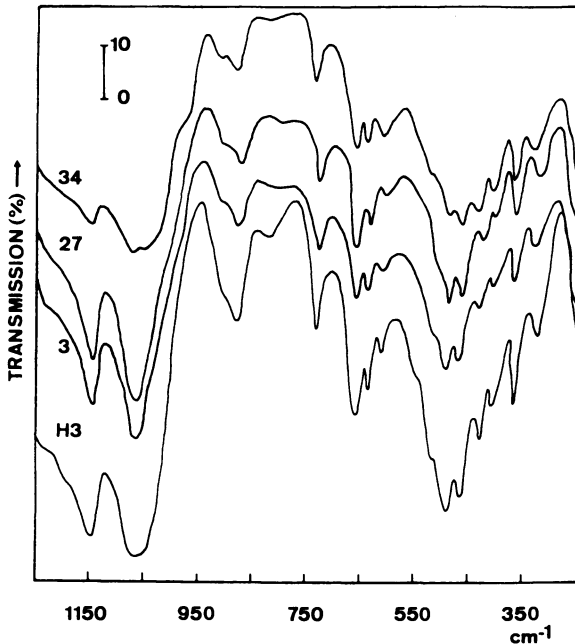
Figure 7. Infrared lattice vibration spectra of $AlPO_4-H_3$, MCM-1 synthesized with Pr_2N (samples Nos.3 and 27) and with Pr_4N-OH (sample No.34).
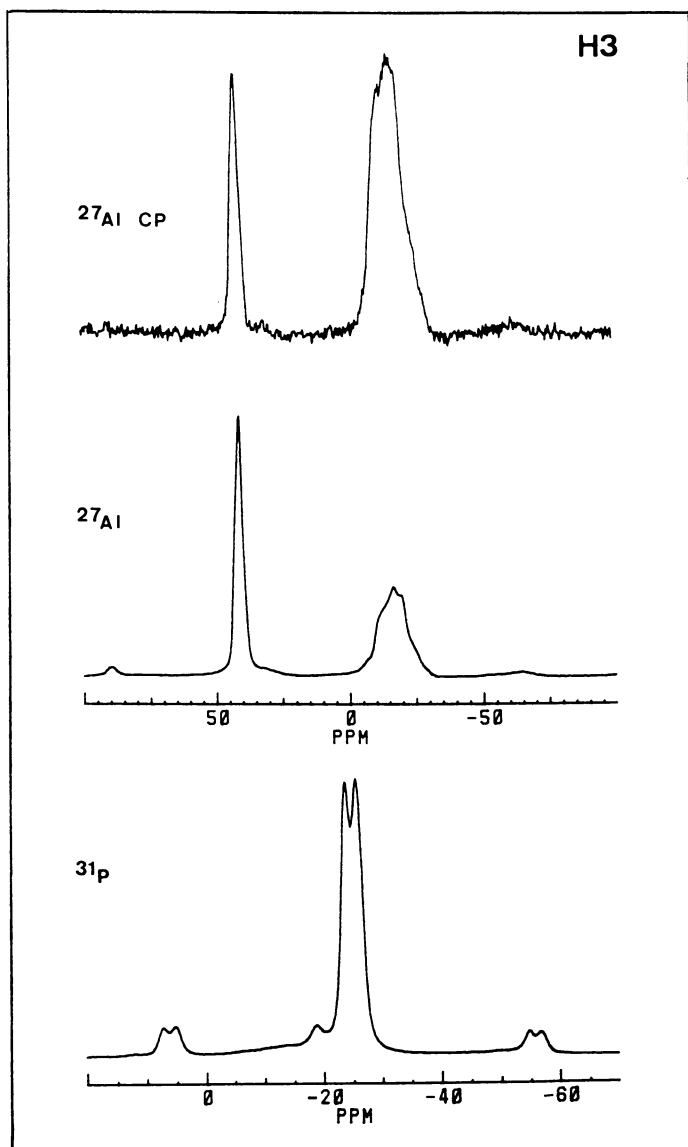
Figure 8. ^{27}Al, ^{27}Al CP, and ^{31}P MAS NMR spectra of AlPO$_4$-H$_3$.

reported. The two line spectrum could result from different co-ordinations of P with Al(IV) and Al(VI).

The ^{27}Al and ^{31}P MAS NMR spectra are in agreement with the structural data available in literature ([18-20]). AlPO$_4$-H$_3$ contains PO$_4$ tetrahedra alternating between AlO$_4$ and AlO$_4$(H$_2$O)$_2$ octahedra ([18]). When the water molecules are ignored the structure can be regarded as a 4-connected tetrahedral framework, containing 6^3 and 4.8^2 two-dimensional nets joint by up-down linkages ([18]).

The ^{27}Al, ^{29}Si, ^{29}Si CP and ^{31}P MAS NMR spectra of MCM-1, prepared with Pr$_2$N in experiment No.27 are shown in Figure 9. The ^{29}Si signal is very broad. Using ^{29}Si CP MAS NMR it becomes narrower and restricted to the -80 till -120 ppm range, which is typical for Si in zeolites ([21]) and SAPO's (22). The ^{29}Si spectrum of SAPO-5, e.g., consists of a line at -92, ascribed to Si(4Al) co-ordination and -112 ppm, representing Si(4Si). The ^{29}Si spectrum shown in Figure 9 suggests that the co-ordination and the T-atom positions of Si in MCM-1 are much more complex.

The ^{27}Al spectrum shows a sharp line at 41.2 ppm, a broad signal around 7 ppm and additional signals from -11 till -24 ppm. We have experienced that the broad line around 6 ppm arises from non-ideal synthesis conditions, when an excess of amorphous Al is present in the sample. Chemical analysis (Table IV) confirms that there is an excess of Al in the product, when the Al T-atom fraction exceeds 50%. Apart from the 7 ppm signal, the ^{27}Al spectrum of MCM-1 is very similar to that of AlPO$_4$-H$_3$. The intensity ratio of the 41.2 ppm line to the sum of the lines between -11 and -24 ppm is 1.07 ± 0.05. This indicates that within experimental error the proportion of Al(IV) to Al(VI) is fixed by the framework topology and does not change with the incorporation of Si.

With MCM-1, ^{31}P lines at -24 and -26 ppm are observed, as expected (Figure 9). The incorporation of Si does not influence the relative amounts of the two types of P atoms, giving rise to -24 and -26 ppm signals, respectively.

The ^{29}Si, ^{27}Al and ^{31}P MAS NMR spectra of MCM-1 sample No.34 prepared with Pr$_4$N-OH are shown in Figure 10. Apparently, the replacement of Pr$_2$N with Pr$_4$N and the differences in chemical composition (Table IV) do not influence the ^{29}Si and ^{27}Al line positions. The intensity ratio of the 41.2 ppm line to the sum of those between -11 and -24 ppm is 0.98 ± 0.05. If Si is incorporated in the lattice, it does not influence the proportion of Al(IV) to Al(VI). In the ^{31}P MAS NMR spectrum the most intense signals are at -24 and -26 ppm. Signals at higher field (1,-7 and -19 ppm) should be assigned to P not incorporated in the crystals which cannot be removed by washing. The intensity ratio of the two major ^{31}P lines is again close to unity, as observed for AlPO$_4$-H$_3$ and MCM-1 prepared with Pr$_2$N.
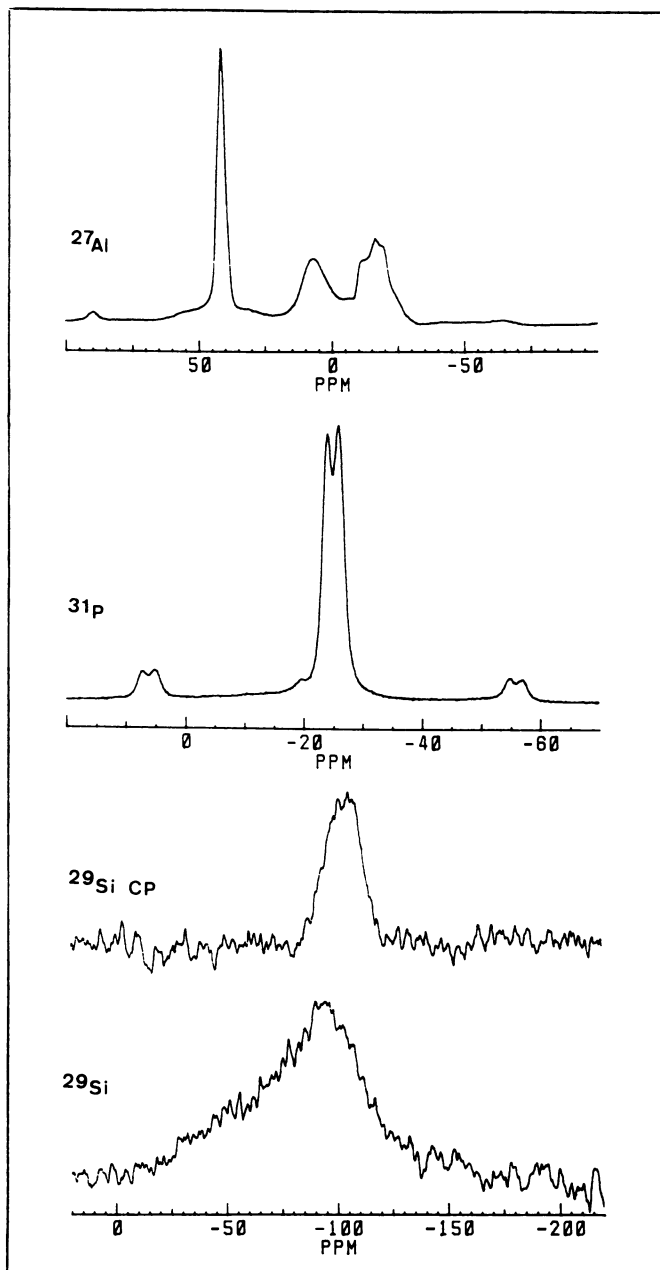
Figure 9. ^{27}Al, ^{29}Si, ^{29}Si CP and ^{31}P MAS NMR spectra of MCM-1 sample No.27.

<u>Conditions for AlPO$_4$-H$_3$ and MCM-1 Synthesis.</u> From previous section it can be concluded that as far as the coordination of Al is concerned, AlPO$_4$-H$_3$ is a hybrid between the aluminum phosphate hydrates like variscite and metavariscite and the aluminophosphate molecular sieves. It can be expected that the synthesis conditions under which it crystallizes will also be intermediate between those of hydrates and molecular sieves. Literature together with the present new data seem to confirm this.

<u>i. pH of Gel</u>. According to the data of d'Yvoir (<u>6</u>), AlPO$_4$-H$_3$ crystallizes from inorganic synthesis mixtures with composition:

$$(Al_2O_3)_{1.00} \ (P_2O_5)_{2.73} \ (H_2O)_x,$$
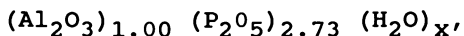
x ranging from 42 to 3,600. The pH of the solution was in all experiments lower than 2.5. Under these conditions AlPO$_4$-H$_3$ is metastable and appears in the following sequence of successive phase transformations:

amorphous -> AlPO$_4$-H$_1$ -> AlPO$_4$-H$_2$ -> AlPO$_4$-H$_3$ -> metavariscite and variscite.

Wilson et al. reported after 24 h heating at 423 K the synthesis of AlPO-5 in the following system (<u>23</u>):

$$(Pr_3N)_{1.0} \ (Al_2O_3)_{1.0} \ (P_2O_5)_{1.0} \ (H_2O)_{40}.$$
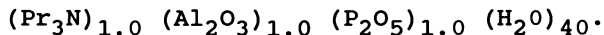
AlPO$_4$-H$_3$ co-crystallized with AlPO-5 and metavariscite when in the gel the (Pr$_3$N)/(Al$_2$O$_3$) ratio was decreased from 1.0 to 0.6. A concommittant decrease of the initial pH occurred from 3.0 to 2.3. The importance of gel pH was further illustrated by adding to the gel 0.5 mole of HCl, or by increasing the amount of P$_2$O$_5$ to 1.2 mole per mole Al$_2$O$_3$. After these changes, AlPO$_4$-H$_3$ co-crystallized with AlPO-5 and AlPO$_4$-tridimite, or with metavariscite, respectively.

The crystallization of MCM-1 occurs at low pH too. The pH of mixture A from which MCM-1 succesfully crystallizes (Table I) was 2.4.

<u>ii. Temperature.</u> The conditions of temperature at which AlPO$_4$-H$_3$ crystallizes are illustrated by the data of Wilson et al. (<u>23</u>). AlPO$_4$-H$_3$, variscite and metavariscite were formed after heating a gel at 373 K for 168 h with composition:

$$(Pr_3N)_{1.0} \ (Al_2O_3)_{1.0} \ (P_2O_5)_{1.0} \ (H_2O)_{40}.$$
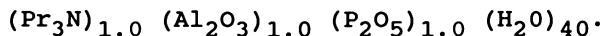
After a reaction of 24 h at 398 K AlPO$_4$-H$_3$ appears together with AlPO-5 and metavariscite. Pure AlPO-5 crystallizes at higher temperatures (423 and 473 K). If in this gel Pr$_3$N is replaced with Pr$_4$N-OH, metavariscite is obtained after 384 h of heating at 328 K. Metavariscite, AlPO$_4$-H$_3$ and variscite are formed at 373 K and a reaction time of 168 h. After 24 h at 398 K AlPO-5

crystallizes together with $AlPO_4-H_3$. The use of higher temperatures results in AlPO-5 formation.

Wilson et al. concluded that high synthesis temperatures are necessary to overcome the tendency of Al to be octahedrally co-ordinated in acidic media (23). From the data of Table I it follows that the same rule applies for silicoaluminophosphates. When a high temperature step is involved in the synthesis, the crystallization of SAPO-11 containing only Al(IV) is favoured over MCM-1, having Al(VI) next to Al(IV).

iii. Agitation. Stirring is an important synthesis parameter in the crystallization of $AlPO_4-H_3$. We experienced that for $AlPO_4-H_3$ synthesis according to the recipe of d'Yvoir (6) mechanical stirring was necessary during reflux of the synthesis mixture. Without stirring only amorphous solids could be recovered. The crystallization of MCM-1 from biphasic mixtures which are not emulsified seems also to be favoured if the synthesis mixture is stirred (Table I).

Table IV. Chemical composition of MCM-1

Exp. No.	Si (%)	Al (%)	P (%)	N (%)	Template[a] (%)	T-atoms/ template molecule[a]
MCM-1 synthesized with Pr_4N-OH						
33	6.6	45.0	48.4	0.88	11.7	17
34	6.2	36.1	57.7	0.74	9.8	22
MCM-1 synthesized with Pr_2N						
1	12.0	51.5	36.5	0.38	2.7	50
3	9.2	54.5	36.3	0.55	4.0	33
25	11.8	53.6	34.6	–	–	–
26	12.0	53.0	35.0	–	–	–
27	13.3	51.5	35.2	0.64	4.6	29
28	18.0	48.9	33.1	0.59	4.3	29

a, assuming no template degradation.

Isomorphous Substitution of Si in MCM-1. In Table IV the chemical composition of some of the MCM-1 materials of Tables I-III is given. When MCM-1 is synthesized with Pr_4N-OH the fraction of P is higher than of Al (Nos.33 and 34). According to the MCM formula given in eqn. 2, MCM-1 sample No.33 should have cation- as well as anion-exchange capacity, the latter being highest. The P content of MCM-1 sample No.34 exceeds 50% (Table IV). If amorphous P present in the sample (Figure 10) is taken into account, the actual lattice P content should be lower. Anyway, Si substitution in this structure appears to occur via mechanism 1 and the material should behave as an anion exchanger. When MCM-1 is synthesized with Pr_2N, the Al fraction is close to 50% and Si seems to replace P (mechanism 2). The materials are, therefore,
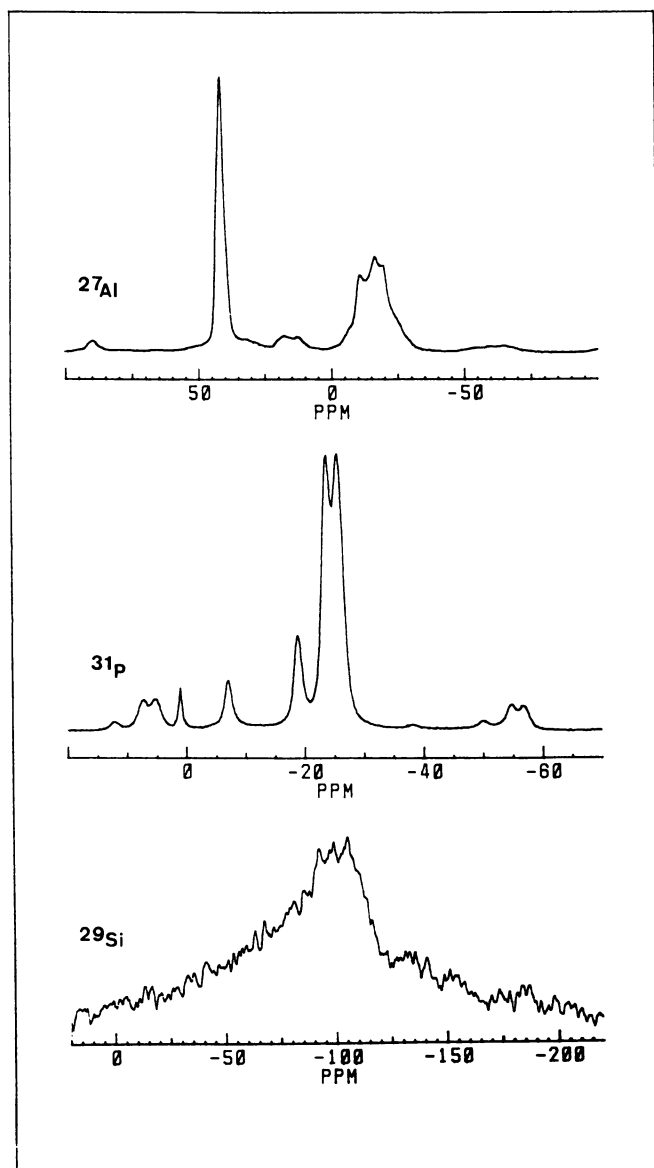
Figure 10. ^{27}Al, ^{29}Si and ^{31}P MAS NMR spectra of MCM-1 sample No.34.

cation exchangers. Infrared spectroscopy indicates that the as-synthesized MCM-1 contains residual dipropyl-ammonium cations vibrating at 1460 cm^{-1} (Figure 11). Pr$_2$N shows an infrared band at 1560 cm^{-1}.

Hydroxyl Groups in AlPO$_4$-H$_3$ and MCM-1. The infrared spectra of the hydroxyl vibrations of AlPO$_4$-H$_3$ and MCM-1 are shown in Figure 12. AlPO$_4$-H$_3$ does not contain infrared active hydroxyl groups. In MCM-1 synthesized with Pr$_2$N hydroxyl groups are observed at 3740 and 3670 cm^{-1}. These bands shift to 3620 and 3450 cm^{-1}, respectively, upon adsorption of benzene, which acts as a hydrogen bond acceptor molecule (spectra not shown). This indicates that the Brønsted acidity of the 3670 cm^{-1} hydroxyls is higher than of the ones at 3740 cm^{-1}. Therefore, the 3740 cm^{-1} hydroxyls should be ascribed to silanol groups and the 3670 cm^{-1} bands to bridging Si-OH-Al. The appearence of the latter hydroxyl groups in the MCM-1 materials is consistent with Si substitution according to mechanism 2.

MCM-1 sample No.34 synthesized with Pr$_4$N-OH shows hydroxyl vibrations at 3740 cm^{-1} and 3670 cm^{-1}. The chemical composition given in Table IV suggests that isomorphous substitution according to mechanism 2 does not occur in this material. If the 3670 cm^{-1} band represents Al-OH-Si groups, there should be a contribution of mechanism 2 and the P content should be lower than 50%. An alternative explanation is that the 3670 cm^{-1} band in this sample represents P-OH groups, associated with the excess of P in the sample.

Catalytic Activity of MCM-1. For selected MCM-1 samples the temperature at which 5% isomerisation of decane is obtained is given in Table V. MCM-1 catalysts are active when synthesized with Pr$_2$N. The activity of sample Nos.1 and 27 is comparable. These samples have a similar chemical composition (Table IV) and contain strong Brønsted acid sites, visualised by 3670 cm^{-1} infrared bands (Figure 12). Sample No.3 contains less Si (Table IV) and is less active.

The reaction temperature necessary to obtain 5% isomerisation of decane with MCM-1 sample No.33 prepared with Pr$_4$N-OH is about 100 K higher than with the MCM-1 prepared with Pr$_2$N (Table V). The very weak Brønsted acidity is consistent with the virtual absence of isomorphous substitution mechanism 2 in this sample.

In conclusion, it seems that in MCM-1 besides the isomorphic substitution mechanism 2, which is found in SAPO's, mechanism 1 can also be operative. In MCM-1 synthesized with Pr$_4$N-OH according to the latter mechanism Al is replaced with Si. The presence of both octahedral and tetrahedral Al in MCM-1 could be the reason for this unexpected behaviour.
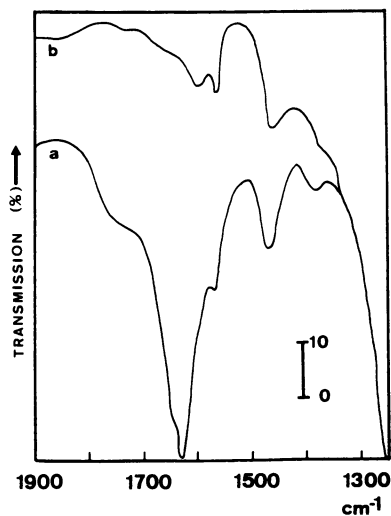
Figure 11. Infrared spectrum of the organic material
in MCM-1 sample No.1 at 295 K (a) and after evacuation
at 400 K (b).
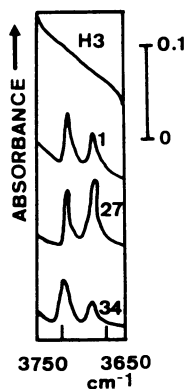
Figure 12. Infrared spectrum of the hydroxyl groups of
AlPO$_4$-H$_3$ and MCM-1 samples Nos. 1, 27 and 34.

Table V. Temperature ($T_{5\%}$) necessary to reach 5%
isomerisation of decane over MCM-1

Exp. No.	$T_{5\%}$ (K)
MCM-1 synthesized with Pr_2N	
3	538
1	527
27	510
MCM-1 synthesized with Pr_4N-OH	
33	636

Pore filling in $AlPO_4$-H_3 and MCM-1. The MCM-1 samples synthesized with Pr_4N-OH contain 17 to 22 mol T-atoms per mol Pr_4N (Table IV, Nos.33 and 34), which is comparable to the 26 mol T-atoms found per Pr_4N molecule in AlPO-5 (24). It indicates that the potential void volume in the MCM-1 framework is at least comparable to that of AlPO-5. The stoicheometry of $AlPO_4$-H_3 is $AlPO_4 \cdot 1.50H_2O$, corresponding to 17.7 weight-% of H_2O. As discussed above there is 11.8 weight-% of structural water (in the co-ordination sphere of octahedral Al) and the remaining 5.9 weight-% is zeolitic water. Apparently, this fraction in MCM-1 can be replaced with 10 to 12% of Pr_4N (Table IV, Nos.33 and 34). The template content of the MCM-1 samples synthesized with Pr_2N is much lower (Table IV, Nos.1, 3, 27 and 28) and consequently, the number of T-atoms per Pr_2N molecule is systematically higher (Table IV). As Pr_2N is a smaller molecule than Pr_4N-OH, this means that the void volume of the MCM-1 crystals is only partially filled with Pr_2N in these instances. The chemical nature of the additional pore filling molecules was not determined. The presence of water is most likely. It was not verified whether hexanol was also present in these crystals.

Void Structure of MCM-1 Determined with the Decane Test. The results from the decane test for determining the void structure are presented in Table VI. The test could not be applied to MCM-1 synthesized with Pr_4N-OH as this material is too weakly acidic.

The first criterion allows to discriminate between 10-and 12-MR structures (9). MCM-1 behaves like a 12-MR zeolite. The second criterion allows to make a ranking according to the size of the windows (10). MCM-1 is among the most shape-selective 12-MR zeolites. A CI[*] of 2.0 and 1.8 is situated between that of offretite (CI[*]=1.8) and ZSM-12 (CI[*]=2.2) and corresponds, therefore, to a window size of about 0.6 nm. Important differences are found in the values of criterion 3 and 4, indicating that the voids of the different materials are significantly different. In this respect, there seems to be no relation with the Si content. According to Criterion 5 MCM-1 is

intermediate between 10- and 12-MR zeolites. Criteria 6
to 8 should be considered with caution. All catalysts
exhibit hydrogenolysis and therefore the application of
these criteria is not allowed (8,9). For MCM-1 sample
No.27 which is the most active catalyst (Table V) and
exhibits almost no hydrogenolysis, the isopentane yield
is in agreement with large pore characteristics (Table
VI). The molar values obtained in criterion 7 and 8 are
equal indicating that secondary hydrocracking occurs (9).
As this phenomenon is not strongly pronounced, the pore
system could be bi- or tridimensional. Definite proof for
this could be obtained if a more acidic MCM-1 catalyst
were available.

   $AlPO_4-H_3$ is an 8-MR structure (18). Consequently, the
largest pore openings in MCM-1 should also be 8-MRs. The
results of the decane test suggest that the pores of MCM-
1 become enlarged after calcination.

Table VI. Characterization of the Pore Structure of MCM-1
using the Hydroconversion of Decane

	Exp. No.			Zeolites	
1	27	3		10-MR	12-MR
1. Ethyloctanes in monobranched isomers at 5% isomerisation (%)					
7.6	8.4	7.7		< 1.0	> 5
2. 2-/5-methylnonane ratio at 5% isomerisation					
2.0	1.8	1.8		> 2.7	1.0-2.2
3. 3-/4-ethyloctane at 5% isomerisation					
0.6	0.7	0.9			
4. 4-propylheptane in monobranched isomers at 75% conversion					
2.6	1.4	1.8		0.0	> 0
5. Multibranched isomers at maximum isomerisation (%)					
18	27	19		3-11	>26
6. Mole isopentane/100 mole C10 cracked at 35% cracking					
*	26	*		11-21	>37
7. Mole C3/100 mole C10 cracked - mole C7/100 mole C10 cracked/2 at 35% cracking					
*	2.9	*			
8. Mole C4/100 mole C10 cracked - mole C6/100 mole C10 cracked					
*	3.1	*			

*, hydrogenolysis superimposed.

   Wilson et al. have stated that in absence of organic
template molecules no microporous aluminum phosphates can
be synthesized (24). The synthesis of $AlPO_4-H_3$ from an
inorganic gel is a clear exception to this statement.
Aluminum-rich zeolites are generally crystallized in
absence of organic molecules. The synthesis of high-
silica zeolites in absence of organic molecules is very
difficult, in agreement with the hydrophobic nature of

their intracrystalline surface. Aluminum phosphates with fully cross-linked tridimensional frameworks are moderately hydrophilic (24). As the dehydrated forms of $AlPO_4-H_3$ are very hydrophilic (6) it is in our opinion not surprising that the presence of organic template molecules is not required.

Conclusions

   $AlPO_4-H_3$ is the aluminum phosphate homolog of MCM-1. The framework topology of MCM-1 and $AlPO_4-H_3$ is the same. A characteristic structural feature of $AlPO_4-H_3$ and MCM-1 materials is the presence of an equal amount of Al(IV) and Al(VI) in the framework. $AlPO_4-H_3$ is, therefore, a hybrid between the aluminum phosphate hydrates, containing Al(VI) and the aluminophosphate molecular sieves, containing Al(IV). For the same reason MCM-1 can be distinguished from the SAPO-n family of materials. In the co-ordination shell of Al(VI) in $AlPO_4-H_3$ and MCM-1, two structural water molecules are present in cis position. Phosphorus is present in two different and equally abundant co-ordinations with Al(IV) and Al(VI). The co-ordination and the T-atom positions of Si in MCM-1 are complex. The isomorphous substitution mechanisms are probably Si for Al (mechanism 1) and Si for P (mechanism 2). MCM-1 materials in which mechanism 2 is operative are active in hydrocarbon conversion reactions catalysed by Brønsted acidity.
   The presence of Al(VI) in $AlPO_4-H_3$ explains why it crystallizes at lower temperatures than AlPO-n materials as the tendency of Al to be octahedrally co-ordinated in acid media is only maintained at low synthesis temperatures. Alternatively, at higher temperatures the crystallization of $AlPO_4-H_3$ can be favoured by decreasing the pH of the gel. For the same reason, the temperature and/or gel pH at which MCM-1 crystallizes are lower than for the synthesis of SAPO's. $AlPO_4-H_3$ can be synthesized with the same templates as MCM-1, or in absence of template. The synthesis of the microporous aluminum phosphate $AlPO_4-H_3$ from an inorganic gel is a clear exception to the statement that "in absence of organic template molecules no microporous aluminum phosphates can crystallize" (24). The crystallization of MCM-1 from biphasic mixtures which are not emulsified is favoured if the synthesis mixture is stirred. Stirring is also an important parameter in the synthesis of $AlPO_4-H_3$ from an inorganic gel. If the synthesis mixture is emulsified agitation seems to be less important.
   Calcined MCM-1 behaves catalytically like a 12-MR structure with 0.6 nm pore openings.

Acknowledgments

Literature Cited

1. Lok, B.M.; Messina, C.A.; Patton, R.L.; Gajek, R.T.; Cannan, T.R.; Flanigen, E.M. U.S. Patent 4 440 871, 1984.
2. Derouane, E.G.; Valyocsik, E.W.; Von Ballmoos, R. Eur. Patent Appl. 146 384, 1984.
3. Flanigen, E.M., Lok, B.M.; Patton, R.L.; Wilson, S.T. In New Developments in Zeolite Science and Technology, Proceed. 7th Int. Zeolite Conf.; Murakami, Y; Lijima, A.; Ward, J., Eds., Kodansha, Elsevier, Amsterdam, Oxford, New York, Tokyo, 1986, p.103.
4. Lok, B.M.; Messina, C.A.; Patton, R.L.; Gajek, R.T.; Cannan, T.R.; Flanigen, E.M. J. Am. Chem. Soc. 1984, 106, 6092.
5. Flanigen, E.M.; Patton, R.L.; Wilson, S.T. Stud. Surf. Sci. Catal. 1988, 37, 13.
6. d'Yvoir, F. Bull. Soc. Chim. 1961, 372, 1762.
7. Jacobs, P.A.; Uytterhoeven, J.B.; Steijns, M.; Froment,G.; Weitkamp, J., Proceed. 5th Int. Conf. Zeolites, Rees, L.V.C., Ed. Heyden, London, 1980, p.607.
8. Martens, J.A.; Tielen, M.; Jacobs, P.A.; Weitkamp, J., Zeolites, 1984, 4, 94.
9. Martens, J.A.; Jacobs, P.A., Zeolites, 1986, 6, 334.
10. Jacobs, P.A.; Martens, J.A., In New Developments in Zeolite Science and Technology, Proceed. 7th Int. Zeolite Conf.; Murakami, Y; Lijima, A.; Ward, J., Eds., Kodansha, Elsevier, Amsterdam, Oxford, New York, Tokyo, 1986, p.23.
11. Derouane, E.G.; Von Ballmoos, R. Eur. Patent Appl. 146 385, 1984.
12. Derouane, E.G.; Von Ballmoos, R. Eur. Patent Appl. 146 386, 1984.
13. Derouane, E.G.; Von Ballmoos, R. Eur. Patent Appl. 146 387, 1984.
14. Blackwell, C.S.; Patton, R.L. J. Phys. Chem. 1984, 88, 6135.
15. Kniep, R.; Mootz, D. Acta Cryst. 1973, B29, 2292-4.

16. Kniep, R.; Mootz, D.; Vegas, A. <u>Acta Cryst</u>. 1977, <u>B33</u>, 263-5.
17. Kotsarenko, N.S.; Mastikhin, V.M.; Mudrakovskii, I.L.; Shmachkova, V.P. <u>React. Kinet. Catal. Lett.</u> 1986, <u>30,2</u>, 375.
18. Pluth, J.J.; Smith, J.V. <u>Nature</u> 1985, <u>318</u>, 165.
19. Keller, E.B. <u>Doctoral Thesis</u>, ETH Zurich, 1987.
20. Meier, W.M.; Olson, D.H. <u>Atlas of Zeolite Structure Types</u>, Second Edition, Butterworths, 1987, 26.
21. Engelhardt, G.; Michel, D. <u>High-Resolution Solid-State NMR of Silicates and Zeolites</u>, John Wiley & Sons, Chichester, 1987.
22. Martens, J.A.; Mertens, M.; Grobet, P.J.; Jacobs, P.A.; <u>Stud. Surf. Sci. Catal.</u> 1988, <u>37</u>, 97.
23. Wilson, S.T.; Lok, B.M.; Messina, C.A.; Flanigen, E.M.; in <u>Proceed. 6th Int. Zeolite Conf</u>., Olson, D.; Bisio, A., Eds., Butterworths, 1984, p.97.
24. Wilson, S.T.; Lok, B.M.; Messina, C.A.; Cannan, T.R.; Flanigen, E.M.,In <u>Intrazeolite Chemistry</u>, Stucky, G.D.; Dwyer, F.G., Eds., <u>ACS Symp.Ser.218</u>, 1983, p.79.
25. Derouane, E.G.; Von Ballmoos, R. Eur. Patent Appl. 146 389, 1984.

Chapter 23

Synthesis and Characterization of Metal Aluminophosphate Molecular Sieves

Stephen T. Wilson and Edith M. Flanigen

Union Carbide Corporation, UOP Molecular Sieve Technology Department, Tarrytown Technical Center, Tarrytown, NY 10591

Novel metal aluminophosphate molecular sieves (MeAPO–n) have been synthesized, where Me can be the divalent form of Co, Fe, Mg, Mn, or Zn, or trivalent Fe. These MeAPO molecular sieves have tetrahedral frameworks containing metal, aluminum, and phosphorus, and exhibit a wide range of compositions within the general formula $0 - 0.3$ R : $(Me_xAl_yP_z)O_2$ where x, y, and z represent normalized mole fractions with $x = 0.01-0.25$, $y = 0.15-0.52$ and $z = 0.35-0.6$ and R refers to the organic template, an amine or quaternary ammonium salt. The structures can be envisioned as hypothetical $AlPO_4$ frameworks with metal incorporated into some of the Al sites. The anionic framework charge generated by such substitution leads to Bronsted acidity. The 18 reported MeAPO structure–types include structures topologically related to zeolites, $AlPO_4$, and SAPO molecular sieves as well as novel structures. The catalytic properties of MeAPO's are both metal and structure dependent, and as acidic catalysts they range in activity from low to high.

The history of molecular sieve synthesis encompasses some 40 years and includes the preparation of aluminosilicate zeolites (1), phosphorus–substituted aluminosilicates (2,3), and the microporous silica polymorphs (4). More recently, the compositional and structural range of molecular sieves has been significantly increased by the discovery of crystalline microporous aluminophosphate–based frameworks, beginning with the aluminophosphates (5–7) or $AlPO_4$–n molecular sieves. This initial discovery was followed by the silicoaluminophosphates (8), titanium aluminophosphates (9), metal aluminophosphates (10–13), and metal silicoaluminophosphates (14) designated SAPO–n, TAPO–n, MeAPO–n, and MeAPSO–n, respectively. The acronym SAPO is derived from $(Si_xAl_yP_z)O_2$ and TAPO, MeAPO, and MeAPSO are derived

similarly where the T = Ti and Me = Metal as described. The
suffix "n" denotes a specific structure type or framework topology.

The MeAPO family described here marks the first demonstrated
incorporation of the divalent forms of cobalt (CoAPO), iron
(FAPO), magnesium (MAPO), manganese (MnAPO), or zinc (ZAPO) into
microporous frameworks during synthesis.

Experimental

The synthesis of a MeAPO molecular sieve typically uses an aqueous
reaction mixture formed by combining a dissolved form of the
divalent metal, orthophosphoric acid, a reactive alumina, and an
amine or quaternary ammonium templating agent (R). The metal is
typically introduced as the acetate or sulfate salt, or as the
metal oxide dissolved in dilute phosphoric acid. A synthesis
mixture is prepared in one of two ways:

1) An alumina source (e.g., pseudo-boehmite or aluminum
   isopropoxide) is mixed with dilute orthophosphoric acid, then
   combined with an aqueous solution containing the metal salt.
   Finally the template, an amine or quaternary ammonium
   hydroxide, is added.

2) The alumina source is combined with an aqueous solution of the
   metal salt first, then dilute orthophosphoric acid is added,
   and finally the template.

Typical reaction mixtures have the molar composition:

$$y \text{ R} : 2x \text{ MeO} : (1-x) \text{ Al}_2\text{O}_3 : \text{P}_2\text{O}_5 : 40 \text{ H}_2\text{O}$$

where y = 1.0 - 2.5, and x = 0.005 - 0.333. These reaction
mixtures are then heated quiescently at a temperature of
100-200°C for sufficient time to crystallize the MeAPO molecular
sieve. The particular time/temperature conditions depend on the
metal, the template, and the structure-type. In many cases a
given reaction mixture will produce the same structures with each
metal although the time/temperature conditions may vary. The
template R is occluded in the MeAPO product during synthesis and
appears essential to the synthesis of these novel phases. It can
be removed thermally at 400-600°C.

Structures

There are 18 reported MeAPO structure-types (Table I). Eight of
these are zeolite structure analogs (17, 20, 34, 35, 37, 43, 44,
47) which were subsequently observed in AlPO$_4$-based materials.
Seven structure-types were first identified in the AlPO$_4$ (5, 11,
14, 16, 31), SAPO (41), or MeAPSO (46) families (14,15). The
remaining structures (36, 39, 50) were first observed in the MeAPO
family. The x-ray powder diffraction patterns characteristic of
the structure-types 5, 11, 17, and 20 (6,16,17); and 14, 18, and
31 (7) have been previously published. The x-ray powder patterns

for the structure-types 16, 46, and 50 (both calculated and observed) are included in recent reviews of AlPO₄-based structures (16,17). For the remaining novel structures 36, 39, and 41, x-ray powder patterns are shown in Figures 1-3.

The 34 (18), 44 (19), and 47 (19) types are all now known to be structures with the chabazite framework topology (as determined by single-crystal methods) but prepared with different templates, TEAOH, cyclohexylamine, or N,N-diethyl-ethanolamine, respectively. As initially prepared, there was sufficient variation in the x-ray powder patterns of the as-synthesized forms for different framework topologies to be considered. Once calcined, the three species exhibit essentially identical powder patterns, consistent with the framework topology. Other properties vary substantially among the three species. There still remains the possibility of unique, template mediated, framework siting for the metal in these and other templated forms of the chabazite topology.

Table I. Typical Templates and Structure-Types for MeAPO
          Molecular Sieves

MeAPO Species	Structure Type	Typical Template	Pore Size (nm)
5	AlPO₄-5	N,N-diethylethanolamine	0.8
36	Novel	tripropylamine	0.8
37	Faujasite	TPAOH + TMAOH	0.8
46	MAPSO-46	di-n-propylamine	0.7
50	Novel	di-n-propylamine	0.8
11	AlPO₄-11	di-n-propylamine	0.6
31	AlPO₄-31	di-n-propylamine	0.7
41	SAPO-41	di-n-propylamine	0.65
14	AlPO₄-14	isopropylamine	0.40
17	erionite	quinuclidine	0.43
34	chabazite	tetraethylammonium	0.43
35	levynite	quinuclidine	0.43
39	novel	di-n-propylamine	0.40
43	gismondine	di-n-propylamine	0.43
44	chabazite	cyclohexylamine	0.43
47	chabazite	N,N-diethylethanolamine	0.43
16	AlPO₄-16	quinuclidine	0.3
20	sodalite	tetramethylammonium	0.3

Synthesis

The structure-template relationships previously observed in the AlPO₄ family are compounded now by the participation of the metal in synthesis. At one extreme the template

d(A)	I	d(A)	I
11.2	100	4.03	13
10.8	31	3.95	14
6.54	4	3.72	5
5.59	11	3.27	12
5.39	31	3.15	7
4.64	13	3.08	6
4.27	34	2.80	7
4.10	15	2.58	5

Figure 1.   X-ray Powder Diffraction Pattern of MAPO-36.

d(A)	I	d(A)	I
9.34	33	3.01	15
6.60	64	2.95	35
4.91	54	2.74	14
4.18	87	2.64	10
3.94	100	2.36	10
3.30	7	1.78	5
3.11	10		
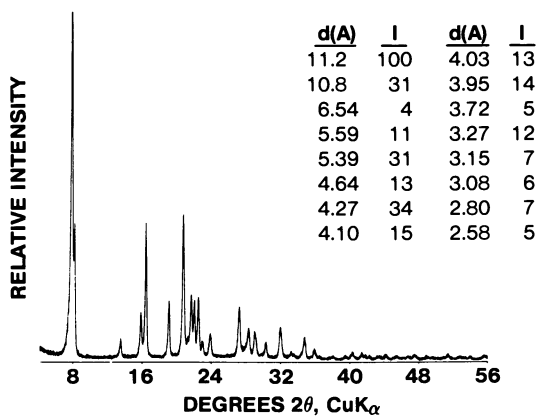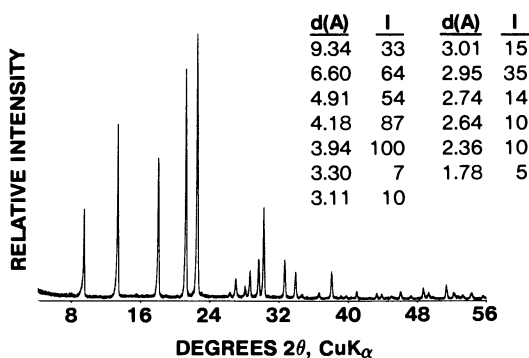
Figure 2.   X-ray Powder Diffraction Pattern of MAPO-39.

d(A)	I	d(A)	I
12.9	20	3.88	23
9.08	20	3.83	18
6.47	20	3.53	14
4.86	9	3.46	17
4.31	5	3.03	12
4.21	100	2.39	9
4.01	64		
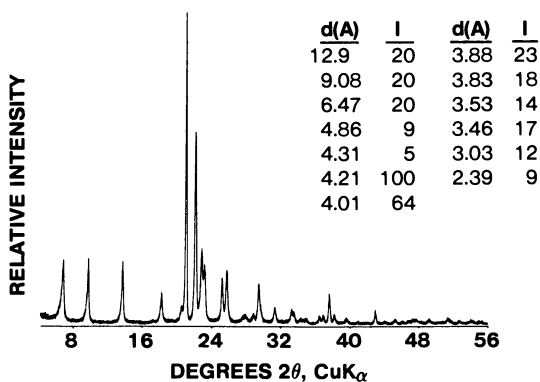
Figure 3.   X-ray Powder Diffraction Pattern of MAPO-41.

tetramethylammonium (TMAOH) behaves consistently across all the $AlPO_4$-based families, producing the sodalite or 20 structure-type under most conditions. At the other extreme, di-n-propylamine templates at least seven structure-types depending on synthesis conditions and gel composition.

Tetramethylammonium (TMAOH). Tetramethylammonium yields the 20 structure-type over a wide range of gel composition and temperature (Table II). Using a reaction mixture prepared with magnesium acetate:

1.0 TMAOH : 2x MgO : (1-x) Al_2O_3 : P_2O_5 : 40 H_2O : 4x HOAc
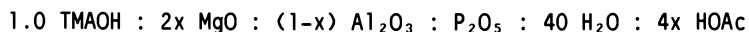
where x = 0.083, 0.167, and 0.333, the 20 structure is the only type observed at 100, 150, or 200°C. Gel and product analyses for samples prepared at 200°C are expressed as mole fractions, normalized to 1 mole of total product oxide, TO_2.

The product oxide compositions reflect the gel composition and each exhibits TMA contents up to, but not exceeding, one TMA per sodalite cage (or 0.167 TMA/TO_2). Product 3 exhibits an analysis consistent with occupation of 1/6 of the framework T-sites by Mg, with one TMA per sodalite cage. The framework charge is completely balanced by occluded TMA^+. The remaining products have lower framework charge and less than one TMA per sodalite cage. The amount of TMA^+ occluded is nevertheless greater than the calculated framework charge and this excess charge is probably balanced by negatively charged species, such as phosphate or hydroxide, occluded in some of the sodalite cages.

Table II. Reaction Mixture and Product Analyses for MAPO-20
Structures (TO_2 formula, anhydrous basis)

		TMA	: (Mg	Al	P $)O_2$	TO_2/R	Framework Charge*
1)	Gel	0.250	0.042	0.458	0.500		
	Product	0.131	0.041	0.454	0.505	7.6	-0.031
2)	Gel	0.250	0.083	0.417	0.500		
	Product	0.135	0.084	0.401	0.515	7.4	-0.054
3)	Gel	0.250	0.167	0.333	0.500		
	Product	0.167	0.158	0.330	0.512	6.0	-0.134

*Framework charge calculated from chemical analyses.

Tetraethylammonium (TEAOH). In $AlPO_4$ synthesis, TEAOH templates the structure-types 5 and 18. In SAPO and in MeAPO synthesis, structures 5 and 34 are produced. Both 18 and 34 have pore systems controlled by 8-rings and both have comparable, large void volumes. The presence of the Me or Si in the gel composition

favors structure-type 34 over 18. In MeAPO synthesis the rate of crystallization of the 34 structure depends on the metal. The metals Mg, Co, and Zn readily form pure 34 at 100°C in 2-4 days from the gel composition:

1.0 TEAOH : 0.4 MeO : 0.8 Al_2O_3 : P_2O_5 : 55 H_2O :
4.8 iPrOH : 0.8 HOAc

where the acetic acid and isopropanol derive from the metal acetate salt and aluminum isopropoxide (AIP) used as reactants. Under similar conditions, MnAPO-34 requires more than 7 days to crystallize and FAPO-34 fails to crystallize in 21 days. Higher temperatures are required to crystallize FAPO-34. The elemental analysis of three MeAPO's prepared from the above gel at 100°C are shown below (expressed as normalized TO_2 fractions):

Species	TEAOH : (	Me	Al	P	$)O_2$	TO_2/R	Framework Charge
ZAPO-34	0.083	0.095	0.396	0.509		12	-0.077
MAPO-34	0.079	0.095	0.400	0.505		13	-0.085
CoAPO-34	0.108	0.085	0.407	0.508		9	-0.069

These analyses and others are consistent with the occupancy of each chabazite cage by one TEA molecule, i.e. 1 TEA/12 TO_2.([15])
    Using a different gel composition, with pseudo-boehmite instead of AIP, the effects of gel metal concentration and crystallization temperature on MAPO-34 synthesis with TEAOH can be illustrated (Figures 4 and 5). Reaction mixtures were prepared differing only in Mg concentration (x):

  1.0 TEAOH : x MgO : 0.8 Al_2O_3 : 1.0 P_2O_5 : 40 H_2O : 2x HOAc

The initial gel pH ranged from 3.5 - 4.5, increasing with Mg content. At 100°C and a 2 day reaction time (Figure 4), the lowest Mg concentration (0.05) yields primarily template-free aluminophosphate hydrate structure-types such as metavariscite and variscite ($AlPO_4$: 2 H_2O) and H_3 ($AlPO_4$: 1.5 H_2O) ([20,21]).
As the Mg concentration is increased toward 0.25, MAPO-34 becomes the major product and then the only product. At higher Mg concentrations non-microporous, Mg-rich structures increase at the expense of MAPO-34.
    The same series of gel compositions digested for 5-7 days at 100°C show similar behavior, except for the greater prominence of the H_3 structure-type at the expense of metavariscite and variscite structures.
    This series of gels crystallized at 150°C for 3 days yields exclusively mixtures (Figure 5). When no Mg is present, only the 5 and 18 structures are observed. At the lowest Mg concentration (0.05) the 18 structure coexists with the 34, and as the Mg concentration increases, the relative amount of MAPO-34 increases as the MAPO-5 decreases. At the highest Mg concentration examined the ratio of MAPO-5 to MAPO-34 is about 2:1.
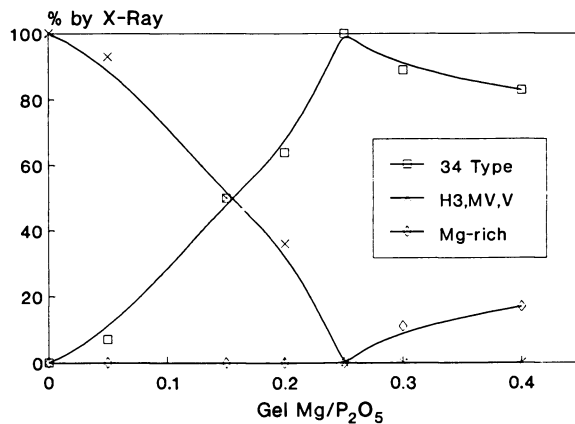
Figure 4.   Product Distribution vs. Gel Mg Concentration in MAPO-34 Synthesis with TEAOH (100°C, 2 Days).
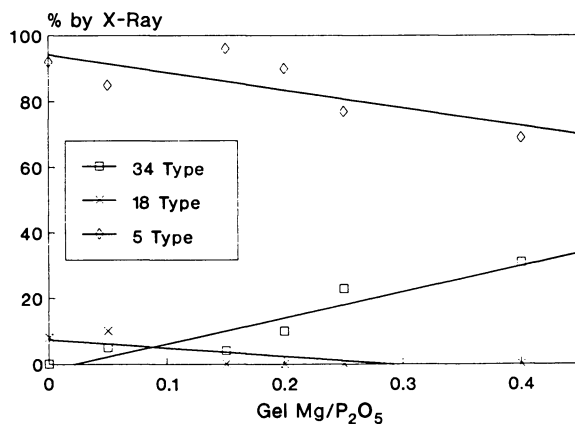
Figure 5.   Product Distribution vs. Gel Mg Concentration in MAPO-34 Synthesis with TEAOH (150°C, 3 Days).

   To summarize these results, at constant template concentration and higher gel Mg concentrations, Mg-rich, non-molecular sieve structures seem to nucleate at the expense of MAPO-34. At gel concentrations of 0.4 and below, some MAPO-34 is formed as long as there is any Mg in the gel.

   These observations suggest that under this set of conditions there is a preferred range of gel compositions for making pure MAPO-34 with TEAOH. Reaction mixtures outside the preferred range produce mixtures containing at least some MAPO-34 but the amount of MAPO-34 declines as the Mg content of the gel deviates too far in either direction. The tendency of gels with low Mg concentrations to give mixtures rather than simply a pure, low Mg MAPO-34 also suggests that MAPO-34 has a preferred product stoichiometry. The products obtained along with the MAPO-34 are typical of low Mg or Mg-free gels, i.e., MAPO-5 and aluminophosphates such as H_3 or metavariscite. It is possible that some Mg is also incorporated in Al sites of these aluminophosphate structures.

<u>Quinuclidine (QUIN)</u>. The template quinuclidine yields the structure-types 16 and 17 (ERI) in $AlPO_4$ synthesis and types 16, 17, and 35 (LEV) in SAPO and MeAPO synthesis. Typical synthesis gels for the preparation of MeAPO-16 and -35 are:

16 – 1.0 QUIN : 0.17 MeO : 0.92 Al_2O_3 : P_2O_5: 40 H_2O :
       0.33 HOAc
35 – 1.0 QUIN : 0.50 MeO : 0.75 Al_2O_3 : P_2O_5: 40 H_2O :
       1.00 HOAc

   In general, higher crystallization temperatures (150–200°C) and lower gel Me favor structures 16 and 17. Since these structures are also templated in the absence of Me, a broad compositional range is easier to achieve. The 35 structure is favored at low temperatures (100°C) and higher gel Me concentrations. Table III shows typical gel and product compositions for MeAPO-16 and MeAPO-35. The four gel compositions shown for MeAPO-35 produce product compositions that mirror the gels, and demonstrate compositional latitude for this framework also.

   Despite the variation in framework composition, both the 16 and 35 structure-types show characteristic ratios of approximately 10 and 9, respectively, for the number of TO_2 units per template. These values are completely consistent with structural knowledge. For the 16 structure (<u>19</u>) there are 10 TO_2 per cage and room for 1 QUIN in each. For the 35 structure there are 9 TO_2 per cage and room for 1 QUIN in each. The remaining structure templated by QUIN, 17, also possesses 9 TO_2 per QUIN but 2 QUIN occupy each large cage.

Table III.   Elemental Compositions of Gel and Product for Typical
             MeAPO-16 and -35 (TO$_2$ Formula, Anhydrous Basis)

16-TYPE		QUIN	: (Me	Al	P)O$_2$	TO$_2$/R
Gel		0.250	0.042	0.458	0.500	
Products	CoAPO	0.094	0.050	0.456	0.495	10.6
	MnAPO	0.103	0.050	0.456	0.494	9.7
	MAPO	0.099	0.051	0.462	0.486	10.1
35-TYPE						
Gel		0.250	0.050	0.450	0.500	
Products	FAPO	0.130	0.040	0.470	0.490	7.7
Gel		0.250	0.100	0.400	0.500	
Products	CoAPO	0.099	0.104	0.377	0.519	10.1
	MnAPO	0.112	0.104	0.390	0.506	8.9
	MAPO	0.092	0.121	0.397	0.481	10.9
Gel		0.250	0.125	0.375	0.500	
Products	CoAPO	0.110	0.117	0.366	0.517	9.1
	MnAPO	0.110	0.130	0.371	0.499	9.1
Gel		0.250	0.132	0.342	0.526	
Product	ZAPO	0.109	0.131	0.354	0.514	9.2

Tripropylamine (Pr$_3$N).   As in the case of AlPO$_4$-5, MeAPO-5 is
readily synthesized with a variety of templates, including
tripropylamine (Pr$_3$N), tetrapropylammonium (TPAOH),
tetraethylammonium (TEAOH), N,N-diethylethanolamine (DEEA),
2-methylpyridine, and triethanolamine. Of these, Pr$_3$N and TPAOH
also template an additional novel, large pore structure,
designated 36. The two structure-types are frequently observed in
admixture and the relative selectivity of the Pr$_3$N for 5 or 36
appears to depend on the metal. Using the gel composition:

1.0-1.5 Pr$_3$N : 0.17 MeO : 0.92 Al$_2$O$_3$: P$_2$O$_5$: 40 H$_2$O : 0.33 HOAc

and digesting at 150°C for 24 hours, the product structure-types
are:

Me	Unseeded	Seeded
Mg	36	36
Zn	36	36
Co	5 > 36	36
Mn	5	36 > 5

(where the amount of 36-type seed is equal to 10 wt.% of starting
oxides).
    Under these conditions Mg and Zn form pure MeAPO-36 more
readily than Co and Mn. Higher gel Pr$_3$N levels are effective in

favoring the 36 structure, and seeding of the reaction mixture with a 36 structure-type of any composition also accelerates nucleation of 36. Product analyses of typical MeAPO-36 are shown in Table IV. Variation in the framework composition of the 36 structure can be induced by changing the gel composition. The packing density of the Pr_3N stays relatively constant at 1 Pr_3N per 20 TO_2, a value that is essentially identical to that of Pr_3N in the 5 structure-type.

Table IV. Elemental Compositions of Gel and Product for Typical MeAPO-36 (TO_2 Formula, Anhydrous Basis)

		Pr_3N : (Me	Al	P)O_2	TO_2/R	Framework Charge
Gel		0.375	0.042	0.458	0.500		
Products	MAPO	0.045	0.038	0.460	0.500	22	-0.044
	MnAPO	0.048	0.060	0.436	0.504	21	-0.052
	CoAPO	0.056	0.045	0.465	0.490	18	-0.065
Gel		0.204	0.102	0.408	0.490		
Product	MAPO	0.047	0.102	0.413	0.485	21	-0.135

Di-n-propylamine (DPA). Di-n-propylamine templates at least 7 structure-types in MeAPO synthesis. This multiplicity of possible structures makes the job of preparing one structure, free of competing structures more challenging. Fortunately, other synthesis factors can be used to focus the structure-directing effect of the template. Such factors as metal type, template concentration, metal concentration, crystallization temperature, and seeding can be used to influence structure formation.

The synthesis conditions observed to favor formation of a particular structure-type are shown in Table V.

Table V. Trends in Synthesis Conditions Favoring Structure Formation with Di-n-Propylamine

Structure Type	Template Conc.	Metal Conc.	Temp. °C	Seed
11	Low	Low	200	x
31	Low	Low	200	x
39	Low	High	150	
41	High	Low	200	x
43	High	High	150	
46	High	High	150	
50	High	High	150	

Synthesis conditions that yield essentially pure MAPO examples for six of these structures are shown in Table VI.

Table VI. Typical Synthesis Conditions for Crystallization of MAPO Structures with DPA. (Molar Formula)

Type	DPA	MgO	Al_2O_3	P_2O_5	H_2O	Time	Temp.	Seed
11	1.0	0.17	0.92	1.0	50	24	200	
31	1.5	0.20	1.00	1.0	60	24	150	x
39	1.0	0.40	0.80	1.0	40	24	150	
41	2.0	0.30	0.85	1.0	50	24	200	x
46	2.0	0.30	0.85	1.0	50	168	150	
50	2.5	0.30	0.85	1.0	50	144	150	

(Reactants include pseudo-boehmite alumina and magnesium acetate).

Typical product analyses of some of these structure-types are shown below (TO_2 formula, anhydrous basis):

Species	DPA :	(Me	Al	P	$)O_2$	TO_2/R	Framework Charge
11	0.050	0.042	0.453	0.505		20	-0.032
39	0.054	0.096	0.406	0.498		19	-0.100
41	0.048	0.052	0.451	0.497		21	-0.058
46	0.118	0.130	0.370	0.500		8	-0.130
50	0.183	0.211	0.310	0.479		5	-0.253

In general, the structures with highest void volume (lowest values of TO_2/R) are favored by high gel template concentrations.

Characterization

Chemical Analysis. The chemical analyses of these and other MeAPO molecular sieves are consistent with tetrahedral frameworks in which Me and Al occupy 50% of the T sites and P, the other 50%. All of the available structural evidence on $AlPO_4$ and MeAPO also supports frameworks based on alternating (Al,Me) and P in the lattice T sites. The negative framework charge produced by such an incorporation pattern is balanced primarily by the positively charged template and, secondarily, by other occluded species, such as H^+ or Me^{2+}.

Based on geometrical considerations alone, frameworks with a Me fraction greater than 0.125 must have some phosphorus atoms bonded to at least two metal atoms through oxygen. Of the species described herein, examples of structure-types 20, 35, 46, and 50 fit this criterion. The refinement of the data and the chemical analysis for CoAPO-50 (19) are consistent with this pattern of framework incorporation.

Electron microprobe analysis was carried out on selected MeAPO samples. These samples were mounted in epoxy resin, polished, and

carbon coated. Elemental analyses were determined by both energy dispersive and wavelength dispersive techniques using standards and reported correction procedures. The electron microprobe analyses were carried out on individual crystallites of typical morphology. The results are shown in Table VII. In all cases, P constituted approximately 50% of the T atoms and (Al+Me), 50%. Multiple spot analyses (spot size = 5 μm) of some of the larger crystals indicated compositional uniformity from edge to center with no pronounced zoning. Where available, bulk chemical analyses compared very favorably with those from the electron microprobe.

Table VII. Comparison of Electron Microprobe and Bulk Chemical Analyses for Selected MeAPO Molecular Sieves

Species	Normalized Elemental Ratio			Technique*
	Me	Al	P	
MnAPO–11	0.03	0.46	0.51	1
	0.04	0.43	0.53	2
MnAPO–44	0.15	0.34	0.50	1
	0.14	0.33	0.52	2
	0.14	0.36	0.51	3
MAPO–47	0.09	0.39	0.51	1
	0.13	0.37	0.51	2
	0.11	0.39	0.50	3
CoAPO–47	0.11	0.38	0.51	1
	0.10	0.37	0.53	2
	0.11	0.39	0.50	3
CoAPO–5	0.03	0.47	0.51	1
	0.03	0.46	0.51	2

*Technique: 1=Energy Dispersive, 2=Wavelength Dispersive, 3=Bulk Chemical.

X-Ray Crystallography. Single crystal structure determinations for the Me containing frameworks MnAPO–11 (22); CoAPO–50, CoAPO–44, CoAPSO–44, MAPSO–46, CoAPO–47 (19); and MAPO–43 (23) have been described. In all of these determinations the metal was found to be in the framework.

Adsorption. The adsorption properties for selected AlPO$_4$–based molecular sieves are summarized in Table VIII. The adsorption data are arranged for each structure-type in order of increasing adsorbate size. The large pore structure-types (5, 36, 46) with pores defined by 12-rings of oxygen readily adsorb neopentane (kinetic dia. 0.62 nm). The 5 and 46 structure-types have been

Table VIII. Typical Adsorption Pore Volumes For Selected AlPO$_4$–Based Structure Types

		Adsorption Capacity (cc/100g) [a]						
Adsorbate =		H$_2$O	O$_2$	n-butane	n-hexane	isobutane	cyclohexane	neopentane
Kinetic Dia. (nm) =		0.265	0.346	0.43	0.43	0.50	0.60	0.62
P/Po =		0.9	0.9	0.4	0.3	0.3	0.5	0.6
Temp.(C) =		22	-183	22	22	22	22	22
Structure	Ring Size [b]							
5	12	26	16	13				12
36	12	31	21	14				13
46	12	35	30		28			26
11	10	18	13		11		11	2
31	10 or 12	21	13		11		9	11
41	10 or 12	21	12		10		8	11
34	8	33	27	23				
35	8	31	17	1				
39	8	23	9	1				
44	8	35	25	25	10	2		
47	8	35	27					
16	6	28	4	1				
20	6	32	2	1				

a) Determined by standard McBain-Bakr gravimetric techniques after calcination at 500–600°C in air. Samples activated at 350°C, 0.01 torr, prior to measurement.

b) Number of tetrahedral atoms (Al, P, Me) in ring controlling pore size. When structure not known, estimated from adsorption measurements.

determined by single crystal methods (24,19). The 5 structure has a unidimensional cylindrical pore structure with a diameter of ca. 0.8 nm. The 46 structure has a three-dimensional pore structure with 12-ring channels parallel to the c-axis intersecting 8-ring channels perpendicular to this axis.

Of the medium pore structures (11,31,41), only the 11 structure has been published (22,25) and it has parallel, elliptical, non-intersecting 10-ring channels. Adsorption data indicate that cyclohexane is readily adsorbed but neopentane is excluded. The other two structures show less differentiation between cyclohexane and neopentane and may, in fact, have elliptical 12-ring pores.

The small pore (8-ring) structures all adsorb oxygen but only the chabazite-types and levynite adsorb n-butane or n-hexane and the rate of adsorption is very strongly dependent on particle size. Larger adsorbates are completely excluded. The very small pore structures (6-ring) adsorb only water and exclude oxygen.

Catalytic Activity. As shown above, the negative framework charge of the MeAPO molecular sieves as synthesized is balanced, at least in part, by the positively charged organic template. On calcination, protonic species are formed by the thermal decomposition of the template. To assess catalytic cracking activity and Bronsted acidity, selected MeAPO species (Table IX) were tested for n-butane cracking (26). Factors influencing the measured activity include structure-type, metal type, and framework metal content. Comparing the large pore structures, the maximum activity decreases across the series: 36 > 46 > 5. For a given structure and metal type the activity can be varied with

Table IX.   Maximum n-Butane Cracking* Values (k_A) for Selected
           MeAPO Molecular Sieves

Structure	Metal					Framework Me Fraction
	Co	Fe	Mg	Mn	Zn	
5	0.4	0.9	1.3	1.2		0.04-0.05
36	13.8		30.3	6.8		0.04-0.05
46	2.5		5.9			0.13-0.17
11		1.4	0.5	0.5		0.04-0.05
31	3.7		4.2	2.4		0.02-0.04
41	1.3		0.6	0.4		0.04-0.05
34	23.2	0.6	35.7	5.2	12.5	0.08-0.10
47	6.5					0.12
39			0.05			0.09

* Samples previously calcined in air, then activated in situ under flowing helium at 500°C for one hour. Feedstock is 2 mole% n-butane in helium at 500°C.

framework metal concentration. At comparable metal concentrations the 36 structure exhibits considerably greater activity than the corresponding 5-type.

For the medium pore structures (11,31,41) the maximum activity appears to decrease somewhat across the series: 31 > 11 = 41. Among these, the framework metal concentration has the most pronounced effect on the activity of the 31 structure-type.

The relative activities of the various 34 structures show a decrease in the maximum value for each metal in order: Mg > Co > Zn > Mn > Fe. This relative ordering of the metals also appears true for other structures, such as 36, 46, and 31, although the data are less complete. The 39 structure-type excludes n-butane (based on adsorption data) and, accordingly, shows a very low butane cracking activity, consistent with essentially no catalytic activity due to the external surface.

Thermal Stability. Most MeAPO molecular sieves exhibit good thermal stability, retaining crystallinity after a 400-600°C air calcination to remove the organic template. The ultimate thermal stability depends on structure-type, metal type, and metal concentration.

Conclusions

Along with AlPO$_4$ and SAPO, the MeAPO molecular sieves have extended the structural and compositional variety found among the growing numbers of AlPO$_4$-based molecular sieves. Both the metal and the organic template exert a primary influence on structure-formation during synthesis. Despite the similarities in the behavior of the five metals in synthesis, each still has a distinct "personality", e.g., in structure selection with a given template or in the rate of crystallization. In addition to Bronsted acidity discussed here, potentially useful properties imparted by the presence of metal in framework sites include ion exchange and metal specific behavior, such as redox activity.

Acknowledgments

Literature Cited

1.   Breck, D.W. Zeolite Molecular Sieves; Wiley: New York, 1974.
2.   Flanigen, E.M.; Grose, R.W. In Molecular Sieve Zeolites-I; Advances in Chemistry Series No. 101; American Chemical Society: Washington, DC, 1971; pp. 76-101.
3.   Artioli, G.; Pluth,J.J.; Smith, J.V. Acta Crystallogr. 1984, C40, 214-217.

4.   Grose, R.W.; Flanigen, E.M. U.S. Patent 4 061 724, 1977.
     Flanigen, E.M.; Bennett, J.M.; Grose, R.W.; Cohen, J.P.;
     Patton, R.L.; Kirchner, R.M.; Smith, J.V. Nature (London)
     1978, 271, 512-516.
5.   Wilson, S.T.; Lok, B.M.; Messina, C.A.; Cannan, T.R.;
     Flanigen, E.M. J. Am. Chem. Soc. 1982, 104, 1146-1147.
6.   Wilson, S.T.; Lok, B.M.; Messina, C.A.; Cannan, T.R.;
     Flanigen, E.M. In Intrazeolite Chemistry; Stucky, G.D.;
     Dwyer, F.G., Eds.; ACS Symposium Series No. 218; American
     Chemical Society: Washington, DC, 1983; pp 79-106.
7.   Wilson, S.T.; Lok, B.M.; Messina, C.A.; Flanigen, E.M. In
     Proc. Sixth International Zeolite Conference; Olson, D.;
     Bisio, A., Eds.; Butterworths: Guildford, Surrey, UK, 1984;
     pp. 97-109, 1985, pp 97-109.
8.   a) Lok, B.M.; Messina, C.A.; Patton, R.L.; Gajek, R.T.;
     Cannan, T.R.; Flanigen, E.M. U.S. Patent 4 440 871, 1984. b)
     Ibid. J. Am. Chem. Soc. 1984, 106, 6092-3.
9.   Lok, B.M.; Marcus, B.K.; Flanigen, E.M. U.S. Patent 4 500
     651, 1985.
10. Wilson, S.T.; Flanigen, E.M. U.S. Patent 4 567 029, 1986.
     b) Messina, C.A.; Lok, B.M.; Flanigen, E.M. U.S. Patent 4
     544 143, 1985.
11. Wright, L.J.; Milestone, N.B. Eur. Pat. Appl. 0 141 662,
     1985.
12. Pyke, D.R.; Whitney, P.; Houghton, H. Applied Catalysis 1985,
     18, 173-190.
13. Bond, G.C.; Gelsthorpe, M.R.; Sing, K.S., J. Chem. Soc.,
     Chem. Commun. 1985, 1056-7.
14. Flanigen, E.M.; Lok, B.M.; Patton, R.L.; Wilson, S.T.
     Pure & Appl. Chem. 1986, Vol. 58; No. 10, pp 1351-58.
15. Flanigen, E.M.; Patton, R.L.; Wilson, S.T. In
     Innovation in Zeolite Materials Science; Grobet, P.J.;
     Mortier, W.J.; Vansant, E.F.; Schulz-Ekloff, G., Eds.; Stud.
     in Surf. Sci. and Cat. Vol. 37; Elsevier: New York, 1988; pp
     13-27.
16. Bennett, J.M.; Dytrich, W.J.; Pluth, J.J.; Richardson, J.W.,
     Jr.; Smith, J.V. Zeolites 1986, 6, 349-61.
17. Ibid., in press, 1989.
18. Ito, M.; Shimoyama, Y.; Saito, Y. Acta. Crystallog. 1698,
     C41, 1698-1700.
19. Bennett, J.M.; Marcus, B.K. In Innovation in Zeolite
     Materials Science; Grobet, P.J.; Mortier, W.J.; Vansant,
     E.F.; Schulz-Ekloff, G., Eds.; Stud. in Surf. Sci. and Cat.
     Vol. 37; Elsevier: New York, 1988; pp 269-79.
20. d'Yvoire, F. Bull. Soc. chim. France 1961, pp 1762-76.
21. Pluth, J. J.; Smith, J. V. Acta. Cryst. 1986, C42, 1118-20.
22. Pluth, J. J.; Smith, J. V.; Richardson, J. W., Jr. J. Phys.
     Chem. 1988, 92, 2734-38.
23. Pluth, J.J.; Smith, J.V.; Bennett, J.M. J. Am. Chem. Soc., in
     press.

24. Bennett, J.M.; Cohen, J.P.; Flanigen, E.M.; Pluth, J.J.; Smith, J.V. In Intrazeolite Chemistry; Stucky, G.D.; Dwyer, F.G., Eds.; ACS Symposium Series No. 218; American Chemical Society: Washington, DC, 1983; pp 109-18.
25. Bennett, J.M.; Richardson, J.W., Jr; Pluth, J.J.; Smith, J.V. Zeolites 1987, 7, 160-2.
26. Rastelli, H., Jr.; Lok, B.M.; Duisman, J.A.; Earls, D.E.; Mullhaupt, J.T. Can. J. Chem. Eng. 1982, 60, 44-9.

Chapter 24

Significant Parameters in the Synthesis of Large Alkaline-Free MFI-Type Zeolites and AFI-Type Aluminophosphates

U. Müller, A. Brenner, A. Reich, and K. K. Unger

Institut für Anorganische Chemie und Analytische Chemie, Johannes Gutenberg-Universität, P. O. Box 3980, D–6500 Mainz, Federal Republic of Germany

Factorial experiments were successfully employed to determine significant synthesis variables allowing the crystallization of large $AlPO_4$-5 and ZSM-5 crystals. Growth of AFI-type aluminophoshate up to 500 μm in length was achieved using a molar reaction composition of 0.5 Pr_3N - Al_2O_3 - P_2O_5 - 300 H_2O. Crystal size and yield were countercurrently affected by the water content during the synthesis . The alkaline-free crystallization of 300 μm uniform MFI-type zeolites at high conversion was possible in a batch of 6.5 $(TPA)_2O$ - 282 $(NH_4)_2O$ - 96 SiO_2 - 1400 H_2O. Decreasing water content and increasing ammonia concentration improved both crystal size and yield. Length growth rates reached 3.0 ± 0.6 μm/h. Increasing the aluminium content caused a decrease in the size and yield of ZSM-5 after four days along with a reduction in the crystal aspect ratio compared to aluminium-free runs. Preliminary results with alkaline-free preparations of DOH-, DDR-, MTN-, and MEL-type zeolites indicate, that large crystals with sharp particle size distributions are frequently observed in ammonia-based zeolite synthesis processes.

Large crystals of molecular sieve materials are of profound interest both for academic studies and special industrial applications. Investigations regarding single crystal structure refinement ([1]), the determination of anisotropic electrical, magnetic or optical properties ([2]), the description of diffusion processes ([3,4]) or the elaboration of intrinsic adsorption properties ([5,6]) are based on the use of uniform large specimens with a distinct morphology. Large zeolite crystals with a rather small nonselective external surface might be useful in shape-selective catalysis ([7]) or in fluidized-bed reactions as binder-free and self-supporting adsorbents. Moreover, a certain crystal size and shape is required for the manufacture of

zeolite-membranes (<u>8</u>) or the employment of molecular sieves as substrates for semiconductors (<u>9</u>).

However, during the crystallization of zeolites and related materials, complex multicomponent mixtures, e.g. of silica, alumina, mineralizers, water and organic templates, are hydrothermally reacted. Nucleation and growth of crystals can be dependent upon chemical composition as well as kinetics or equilibrium conditions existing in the solid, liquid, and gas phase. Given these considerations, the most efficient method of studying the impact on the results when two or more synthesis parameters , hereafter called "factors", were to be changed is obtained by factorial experiments (<u>10</u>). Accordingly, a trial is designed where sets of different synthesis variables are arranged in specific treatment combinations, enabling an assessment of the effects of changing the level of a factor independently of all others and possible interaction effects. Thus the required information is extracted with a pre-selected degree of statistical certainty at a minimum expenditure of effort and costs. If significant effects are elucidated, they can be directly employed as starting values to further improve synthesis by means of central composite design or Simplex-variation procedures, finally yielding optimum conditions for the desired response, regarding crystal size, morphology or product yield.

This study aims to demonstrate, that statistic factorial design can be used in order to determine significant compositional parameters in the rapid growth of large high-silica ZSM-5 zeolite (<u>11</u>) and $AlPO_4$-5 aluminophosphate crystals (<u>12,13</u>).

Experimental

Zeolite ZSM-5. Zeolite samples were crystallized from a gel containing colloidal silica (Ludox AS-40), deionized water, aluminiumtriisopropylate (ATIP, Merck), as source of aluminium, and tetrapropylammonium bromide, (TPABr, Aldrich). Ammonia solutions were prepared by saturating a thermostated aqueous solution with gaseous NH_3 (98% purity). Contents of 25%, 32%, and 47% w/w of ammonia were obtained and gravimetrically controlled. The components were added in the sequence: TPABr, SiO_2, alumina source, water and ammonia solution. The mixture was vigorously agitated, sealed and left for four days at a temperature of 453 K to react. Li-NH_4-ZSM-5 was grown using a procedure described elsewhere (<u>14,15</u>).

Aluminophosphate $AlPO_4$-5. $AlPO_4$-5 was obtained from compositions containing pseudoboehmite (Pural SB, Condea) which was added to aqueous phosphoric acid (Merck, 85%) and deionized water. Finally, tripropylamine (Aldrich) was continuously added to the stirred solution. The crystallization time was limited to 72 hours.

Crystallization was carried out with 50 ml of reaction mixtures in 100 ml steel autoclaves lined with Teflon under static conditions. All isolated products were characterized by X-ray diffraction, scanning electron microscopy, and electron microprobing (Camebax, CAMECA). Selected samples were employed for nitrogen adsorption and microcalorimetry at 77 K. After calcination at 823 K, catalytic activity and selectivity of HZSM-5 samples were monitored using the disproportionation of ethylbenzene as a test reaction. The

particle size distribution was obtained using optical microscopy on
300 to 800 individual crystals.

Results and Discussion

Synthesis of large AFI-type crystals. For these studies of the
crystallization of large AFI-type aluminophosphate crystals, the
reaction temperature T, the concentration of tripropylamine Pr_3N,
and the amount of water were chosen as operational variables.
Synthesis runs were performed with each of these "factors" at a high
(+) and a low (-) level, for molar compositions with b Pr_3N - Al_2O_3
- P_2O_5 - c H_2O as indicated in Table I:

Table I. Compositional Factors and Levels investigated for
the Synthesis of $AlPO_4$-5 crystals

Factor	High Level	Low Level
A: T (K)	453	423
B: Pr_3N	3.0	0.5
C: H_2O	300	50

Table II summarizes the 2^3 possible treatment combinations. Run (1)
denotes a synthesis with all factors at their lowest level. Product
yields, see Table II , and maximum crystal sizes along the (001)
axis (Table III) represent mean values from duplicated sets of each
trial. The "effect" column lists the impact of a factor, positive or
negative, on the response, viz. product yield and crystal length,
for the case that the level of this factor is raised from a medium
to a high level. Calculation procedures have been described in the
literature (10).

Table II. Treatment Combinations for the Influence of
Different Factors on the $AlPO_4$-5 Product Yield

Combination	Factor A	Factor B	Factor C	Yield % w/w	Effect	Significance 95%
1	423	0.5	50	85	27.0	
a	453	0.5	50	17	-10.0	-
b	423	3.0	50	42	- 1.5	-
ab	453	3.0	50	34	5.5	-
c	423	0.5	300	3	-17.5	+
ac	453	0.5	300	9	9.0	-
bc	423	3.0	300	18	5.0	-
abc	453	3.0	300	8	- 9.5	-

Finally, all effects were evaluated by "Student t-test" and "F-test"
methods, in order to check whether these effects were simply due to
experimental error rather than being statistically significant.
Decisions are based on a certainty of at least 95% .Significant

variables in the following tables have been marked (+) in the last column.

Referring to Table II, factor C, the water content, obviously strongly influences the yield of $AlPO_4$-5. This effect is negative in sign which means that increasing the water content during the crystallization causes a significant decrease in yield. It should be noted, that this result is strictly valid only for the experimental conditions and compositions as listed in Table I.

Table III. Treatment Combinations for the Influence of Different Factors on the $AlPO_4$-5 Crystal Size

Combination	Factor A	Factor B	Factor C	Size μm	Effect	Significance 95%
1	423	0.5	50	98	161.4	
a	453	0.5	50	25	-29.4	-
b	423	3.0	50	30	-29.4	-
ab	453	3.0	50	13	78.4	-
c	423	0.5	300	500	119.9	+
ac	453	0.5	300	140	6.9	-
bc	423	3.0	300	135	9.4	-
abc	453	3.0	300	350	64.9	-

Regarding the crystal size in Table III, it was observed that again factor C, the amount of water in the synthesis mixture exerts a strong influence. However, high water concentrations are conducive to the growth of large crystals, since the effect is positive. Results obtained so far illustrate, that either high product yields or large crystals of $AlPO_4$-5 can be prepared by the method under investigation. Within the boundaries of these treatment combinations, neither the synthesis temperature nor the concentration of tripropylamine proved to be significant parameters for the growth of large $AlPO_4$-5 crystals. the hexagonal rod-like shape of large crystals of AFI-type is illustrated in Figure 1, whereas the normalized particle size distribution of a typical sample is depicted in Figure 2. A similar crystal morphology has already been reported by Wilson et al. (13) using tetrapropylammonium cations as an organic template.

Adsorption properties of large AFI-type crystals are consistent with the micropore structure which have been discussed elsewhere (16)(6).

Synthesis of large ZSM-5 Crystals. Preliminary studies led to the investigation of a synthesis mixture with a molar composition expressed in oxide ratio: 6.5 $(TPA)_2O$ - b $(NH_4)_2O$ - c Al_2O_3 - SiO_2 - a H_2O. Table IV illustrates the factors which were examined.
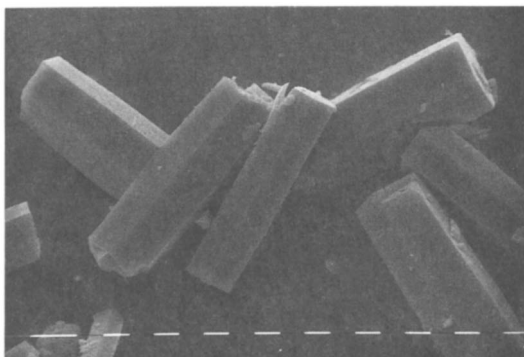
Figure 1.   Scanning Electron Micrograph of Large $AlPO_4$-5
            Crystals (scale bar: 10 μm).
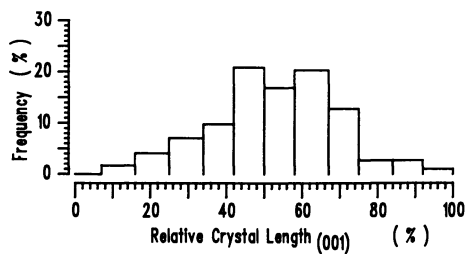
Figure 2.   Particle Size Distribution of Large $AlPO_4$-5
            Crystals.

Table IV. Compositional Factors and Levels for the
Synthesis of ZSM-5 Crystals

Factor	High Level	Low Level
A: H_2O	3200	1400
B: $(NH_4)_2O$	282	141
C: Al_2O_3	0	1

Product yield, see Table V, was found to be significantly dependent upon the ammonia content. High concentrations caused increases in the yield of ZSM-5.

Table V.   Treatment Combinations for the Influence of
Different Factors on the ZSM-5 Product Yield

Combination	Factor A	Factor B	Factor C	Yield % w/w	Effect	Significance 95%
1	1400	141	1	76.0	66.1	
a	3200	141	1	1.4	- 9.4	-
b	1400	282	1	83.2	24.3	+
ab	3200	282	1	88.4	10.6	-
c	1400	141	0	47.5	3.8	-
ac	3200	141	0	42.2	7.9	-
bc	1400	282	0	95.2	0.8	-
abc	3200	282	0	94.8	- 9.5	-

High ammonia concentrations are not only responsible for maximum product yields but together with low water and aluminium concentrations, they appear far more important for the growth of large crystals (see Table VI). Figure 3 presents a scanning electron micrograph of large uniform NH_4-ZSM-5 crystals. Compared to a previously synthesized Li-NH_4-ZSM-5, see Figures 4 and 5, the particle size distribution of solitary crystals from the alkaline-free composition was found to be markedly narrow, see Figure 6, which hints at a short nucleation period. It is obvious from Table VI, that a high water content leads to a decrease in the size of the crystals.

The treatment combination "bc" of Table VI was chosen in order to monitor the growth kinetics of NH_4-ZSM-5. Table VII summarizes the results and compares the growth rates with the data found by various other investigators with different systems. Strong influences of OH^- concentration on growth rates have already been observed by Hou et al. for NH_4-TPA mixtures ([17]) and by Lowe ([20]) and Hayhurst et al. ([18]) for Na-TPA systems. The latter group recorded even faster crystallization and shorter induction periods in Na^+-free synthesis
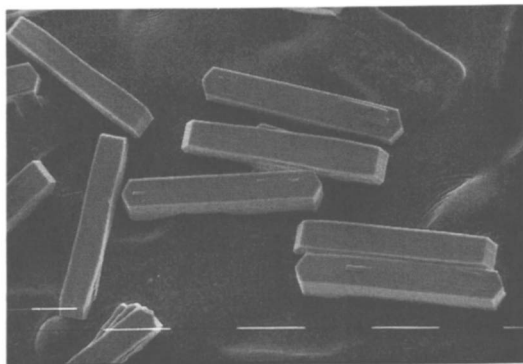
Figure 3.   Scanning Electron Micrograph of Large NH_4-ZSM-5
Crystals (scale bar: 100 μm).
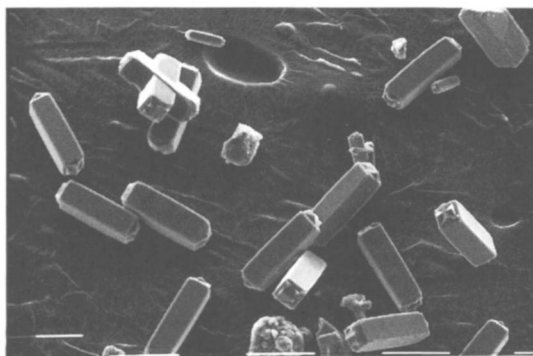
Figure 4.   Scanning Electron Micrograph of Large Li-NH_4-ZSM-5
Crystals (scale bar: 100 μm).
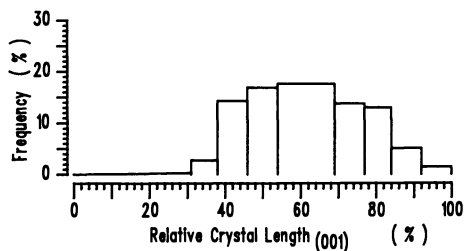
Figure 5.   Particle Size Distribution of Large Li-ZSM-5
           Crystals.
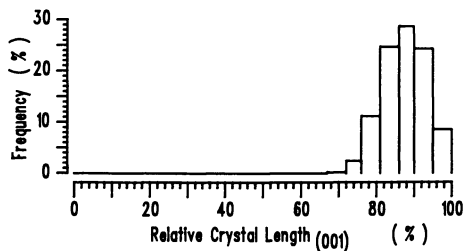
Figure 6.   Particle Size Distribution of Large NH_4-ZSM-5
           Crystals.

processes. With an alkaline-free, highly active composition of 6.5 $(TPA)_2O$ - 282 $(NH_4)_2O$ - 96 SiO_2 - 1400 H_2O it was possible to rapidly grow large and uniform crystals at a maximum conversion.

Table VI. Combinations for the Influence of Different Factors on the Crystal Size of ZSM-5

Combination	Factor A	Factor B	Factor C	Size μm	Effect	Significance 95%
1	1400	141	1	105	155.5	
a	3200	141	1	18	-33.3	+
b	1400	282	1	232	60.8	+
ab	3200	282	1	123	- 9.0	-
c	1400	141	0	133	36.0	+
ac	3200	141	0	122	15.8	-
bc	1400	282	0	285	2.8	-
abc	3200	282	0	225	- 3.5	-

Upon addition of aluminium, it could be seen that not only the crystal size for a given reaction time tended to be smaller compared to an aluminium-free synthesis run, see Table VI, but that the crystal morphology was significantly affected.

Table VII. Comparison of Crystal Growth Rates

System	Rate $\mu m/h$	Reference
1.9 $(TPA)_2O$-1.3 Na_2O-96 SiO_2-960 H_2O	1.3	19
3.8 $(TPA)_2O$-96 SiO_2-960 H_2O	2.2	21
12.8 $(TPA)_2O$-192 $(NH_4)_2O$-96 SiO_2-2400 H_2O	0.6	16
6.5 $(TPA)_2O$-282 $(NH_4)_2O$-96 SiO_2-1400 H_2O	3.0	Table VI
2.4 $(TPA)_2O$-3.4 Na_2O-96 SiO_2-3600 H_2O-384 EtOH	2.0	20

With increasing aluminium content during the reaction, the product crystals became more globular in shape. Table VII summarizes the influence of Al with respect to the aspect ratio, defined as the ratio of crystal length (001) to crystal width (100). Concerning crystal habits in Na-TPA compositions, no influence of Al-concentration was observed by Mostowicz and Berak ([22]). Hayhurst et al. ([18]) reported a dependency of product aspect ratios on the alkalinity in sodium containing reaction mixtures. Contrarily, observations of NH_4-ZSM-5 reactions given in Table VIII clearly indicate, that even a duplicated amount of $(NH_4)_2O$, runs "c" and "bc", has no statistical significant impact on the aspect ratio.

Table VIII. Influence of Aluminium Content on Crystal
            Morphology for NH$_4$-ZSM-5

Combination	Factor A	Factor B	Factor C	Aspect Ratio	Effect	Significance 95%
1	1400	141	1	3.13	5.12	
a	3200	141	1	1.27	-0.06	
b	1400	282	1	3.71	-0.40	-
ab	3200	282	1	2.06	-0.17	-
c	1400	141	0	7.69	2.59	+
ac	3200	141	0	9.99	0.81	-
bc	1400	282	0	6.20	-0.74	-
abc	3200	282	0	6.90	-0.23	-

Microprobe analysis of HZSM-5 samples from a Li-NH$_4$-TPA system
(sample A), see Figure 7, gave rise to a characteristic composi-
tional zoning of Al in the outer rim of the crystals. HZSM-5 from
alkaline-free processes (sample B), see Figure 8, had a more homo-
geneous aluminium distribution throughout the crystals.
     Evaluating the catalytic shape-selectivities of these materials
by use of the disproportionation of ethylbenzene (23,24) at 523 K at
a conversion of 2% in differential reactor mode, it was observed
that larger crystals of sample A gave 85% para-diethylbenzene and
15% meta-diethylbenzene. The smaller crystals of sample B with the
smoother aluminium gradient yielded 96% para-diethylbenzene and only
4% meta-isomer. In a second series, samples of crushed large
crystals with mean sizes of 1-10 μm were examined. No increase in
activity was observed as is expected when the reaction is controlled
by the diffusion limitation of molecules in the large crystals.
However, this treatment created larger non-selective external
surface area and hence a smaller selectivity of 87% para-diethyl-
benzene for sample B was recorded.
     These results, at least for the test reaction applied, are
encouraging for the feasability of large crystals as catalysts.
Thus, the advantages of the crystallization of NH$_4$-ZSM-5, viz. large
uniform crystals, maximum conversion at high growth rates and smooth
Al-zoning profiles with only few external surface active sites were
successfully combined for the one-step manufacture of a HZSM-5
catalyst, see Figure 9, directly grown as a shell on pre-shaped
silica beads (25).

Summary and Conclusion

The amount of water present during the synthesis of large AFI-type
aluminophosphate crystals was found to be of significant importance.
However, yield of AlPO$_4$-5 and crystal size were countercurrently
influenced. It follows that at least with tripropylamine, either few
large crystals or maximum conversions into small particle AlPO$_4$-5 is
possible.
     With regard to MFI-type zeolites, statistic factorial design
proved to be extremely helpful. For alkaline-free systems, factors
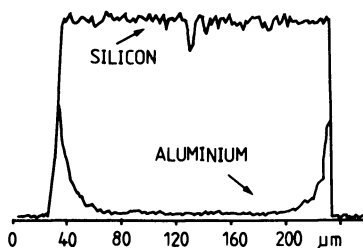
Figure 7.   Electron Microprobe Analysis Across a ZSM-5 Crystal
            of Sample A (bulk analysis Si/Al = 65).
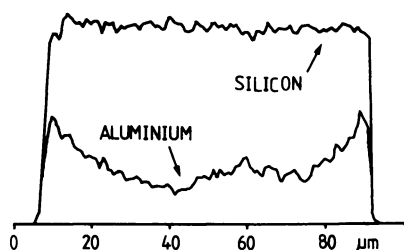
Figure 8.   Electron Microprobe Analysis Across a ZSM-5 Crystal
            of Sample B (bulk analysis Si/Al = 42).
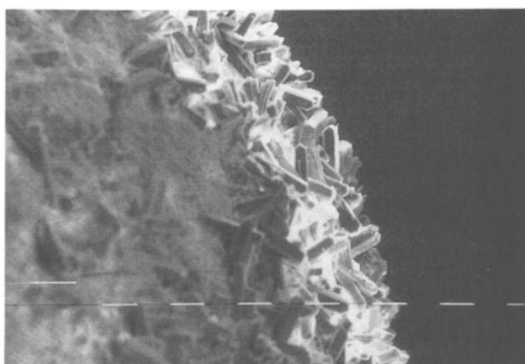
Figure 9. Scanning Electron Micrograph of a Fragment of an Alkaline-Free HZSM-5 Shell Grown on a Pre-Shaped Silica Pellet (scale bar: 10 μm).

were detected which enable the rapid synthesis of large uniform ZSM-5 crystals out of reaction compositions with high ammonia and low water contents. Aluminium affects the crystal aspect ratio. Moreover, for the ammonia based reaction mixtures, a more homogeneous Al-gradient across the HZSM-5 crystal is obtained, which assures improved shape-selective behavior in the catalytic conversion of ethylbenzene. Using organic templating molecules other than TPABr, several synthesis characteristics remained. With amino-adamantane, large DOH-type crystals (see Fig. 10) could be synthesized as well as large ZSM-58 (DDR-type) following addition of aluminium. Tetramethylammonium nucleated large crystals of ZSM-39 (MTN-type) and tetrabutylammonium favored the synthesis of uniform MEL-type zeolites. Independent of the template, all these ammonia based crystallization processes had a high product yield, narrow particle-size distribution and a rapid growth.

Factorial experiments can successfully serve to determine significant synthesis parameters for aluminophosphates and zeolites. Future studies will also focus on the underlying mechanisms of the nucleation and growth of high-silica zeolites out of alkaline-free ammonia containing reaction mixtures.
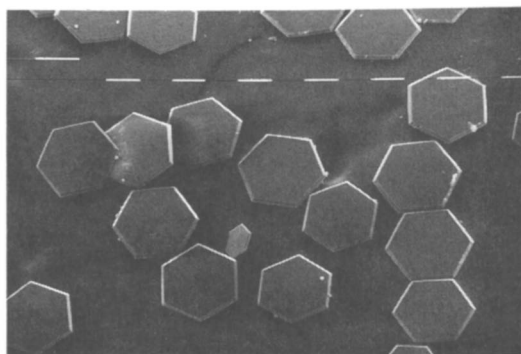
Figure 10. Scanning Electron Micrograph of Large Crystals of DOH-Type (scale-bar: 100 μm).

Acknowledgments

Literature Cited

1. Lermer, H.; Dräger, M.; Steffen, J.; Unger, K. K. Zeolites 1985, 5, 131.
2. Cox, S. D.; Gier, T. E.; Stucky, G. D.; Bierlein, J. J. Am. Chem. Soc. 1988, 110, 2987-8.
3. Bülow, M.; Struve, P.; Rodzus, Ch.; Schirmer, W. Proc. 5th Int. Zeolite Conf., Naples 1980, pp 580-591.
4. Beschmann, K.; Kokotailo, G. T.; Riekert, L. In Characterization of Porous Solids, Unger, K. K.; Rouquerol, J.; Sing, K. S. W.; Kral, H., Eds.; Elsevier: Amsterdam, 1988; pp 355-65.

5. Müller, U.; Unger, K. K.; In <u>Characterization of Porous Solids</u>, Unger, K. K.; Rouquerol, J.; Sing, K. S. W.; Kral, H., Eds., Elsevier: Amsterdam, 1988; pp 101-108.

6. Müller, U.; Unger, K. K.; Pan, D.; Mersmann, A.; Rouquerol, J.; Rouquerol, F.; Grillet, Y. <u>Proc. Int. Symp. "Zeolites as Catalysts, Sorbents and Detergent Builders"</u>; Weitkamp, J.; Karge, H.-G., Eds.; Elsevier: Amsterdam, 1989, pp 625-34.

7. Hölderich, W.; Hesse, M.; Naumann, F. <u>Angew. Chem.</u> 1988, <u>100</u>, 232. <u>Angew. Chem. Int. Ed. Engl.</u> 1988, <u>27</u>, 226.

8. Te Hennepe, H. J. C.; Bargeman, D.; Mulder, M. H. K.; Smolders, C. A. In <u>Characterization of Porous Solids</u>; Unger, K. K.; Rouquerol, J.; Sing, K. S. W.; Kral, H., Eds.: Elsevier: Amsterdam, 1988, pp 411-20.

9. Terasaki, O.; Yamazaki, K.; Thomas, J. M.; Ohsuna, T.; Watanabe, D.; Sanders, J. V.; Barry, J. C. <u>Nature</u> (London) 1987, <u>330</u>, 58-60.

10. Davies, O. L.; <u>The Design and Analysis of Industrial Experiments;</u> Longman: London, 1979; pp.247-439.

11. Olson, D. H.; Kokotailo, G. T.; Lawton, S. L.; Meier, W. M. <u>J. Phys. Chem.</u> 1981, <u>85</u>, 2238-43.

12. Bennett, J. M.; Cohen, J. P.; Flanigen, E. M.; Pluth, J. J.; Smith, J. V.; In <u>Intrazeolite Chemistry</u>; Stucky, G. D.; Dwyer, F. G., Eds.; ACS Symp. Ser. No. 218, American Chemical Society, Washington, DC, 1983, pp 109-118.

13. Wilson, S. T.; Lok, B. M.; Messina, C. A.; Cannan, T. R.; Flanigen, E. M. In <u>Intrazeolite Chemistry</u>; Stucky, G. D.; Dwyer, F. G., Eds.; ACS Symp. Ser. No. 218, American Chemical Society, Washington, DC, 1983, pp 79-106.

14. Müller, U.; Unger, K. K. <u>Zeolites</u> 1988, <u>8</u>, 154-6.

15. Nastro, A., Sand. L. B.; <u>Zeolites</u> 1983, <u>3</u>, 219.

16. Müller, U.; Unger, K. K.; <u>Z. Kristallogr.</u> 1988, <u>182</u>, 190-2.

17. Hou, L.-Y.; Sand, L. B.; Thompson, R. W. <u>Proc. 7th Int. Zeolite Conf.</u> Tokyo 1986, pp 239-246.

18. Hayhurst, D. T.; Aiello, R.; Nagy, J. B.; Crea, F.; Giordano, G.; Nastro, A.; Lee, J. C. In <u>Perspectives in Molecular Sieve Science;</u> Flank, W. H.; Whyte, Th. E., Eds.; ACS Symp. Ser. No. 368, American Chemical Society, Washington, DC, 1983, pp 277-291.

19. Crea, F.; Nastro, A.; Nagy, J. B.; Aiello, R. <u>Zeolites</u> 1988, <u>8</u>, 262.

20. Lowe, B. M.; In <u>Innovation in Zeolite Materials Science</u>; Grobet, P. J.; Mortier, W. J.; Vansant, E. F.; Schulz-Ekloff, G., Eds.; Elsevier: Amsterdam, 1988, pp 1-12.

21. Hayhurst, D. T.; Nastro, A.; Aiello, R.; Crea, F.; Giordano, G. <u>Zeolites</u> 1988, <u>8</u>, 416-422.

22. Mostowicz, R.; Berak, J. M. In <u>Zeolites - Synthesis, Structure, Technology and Application</u>; Drzay, B.; Hocevar, S.; Pejovnik, S., Eds; Elsevier: Amsterdam, 1985, pp 65-72.

23. Karge, H.-G.; Weitkamp, J.; Ernst, S.; Girrbach, U.; Beyer, H. K., <u>Studies Surface Science Catalysis</u> 1984, <u>19</u>, pp 101-111.

24. Girrbach, U. Ph D. Thesis, Gutenberg-Universität, Mainz, 1987.

25. Danner, A.; Müller, U.; Unger, K. K.; Hölderich, W. DE 3728451, 1987; EP 88113655, 1988.

Chapter 25

Disordered Pentasil-Type Borosilicates

Synthesis and Characterization

Giovanni Perego, Giuseppe Bellussi, Angela Carati, Roberto Millini, and Vittorio Fattore

Eniricerche S.p.A., 20097 San Donato Milanese, Italy

The synthesis of pentasil-type borosilicates, referred to as BOR-E, from hydrogels containing a binary mixture of $Me_4N^+/(n-Pr)_4N^+$, $Et_4N^+/(n-But)_4N^+$ or $Me_4N^+/(n-But)_4N^+$ cations is described. Mirror plane-based stacking faults, randomly distributed in the ZSM-5-type (BOR-C) inversion center-based stacking of pentasil layers were identified in the framework structure of BOR-E by X-ray diffraction analysis. The probability of the occurrence of stacking faults, p, was estimated from X-ray diffraction data following a method developed for structure determination of a ZSM-11 type borosilicate (BOR-D). p ranges from 0 to 0.2, compared to 0 and 0.25 determined for BOR-C and BOR-D, respectively. The probability is dependent on both the cation pair used in the reaction mixture and the resulting relative abundance of the cations within the pores.

Pentasils constitute a well known family of porotectosilicates. The framework structure of the members of this family, based on five membered rings of tetrahedra, can be described in terms of two different stackings of layer pairs related by an inversion center (i-type) and mirror simmetry (σ-type), respectively (1) . ZSM-5 aluminosilicate, the parent borosilicate BOR-C (2), and the pure silica analog Silicalite-1 (3), represent the most important members; their framework structure is based on i-type stacking (4).

For another member, the ZSM-11 aluminosilicate, a crystal structure was proposed based on σ-type stacking (5). However, a more recent X-ray investigation of BOR-D, the parent borosilicate structure, clearly demonstrated that the ZSM-11-type framework is really built up of a disordered layer sequence of i and σ-type stackings (6). Evidence of intergrowth of i-type and σ-type was obtained also by high-resolution electron microscopic imaging and electron diffraction in pentasil-type aluminosilicates, which were crystallized from hydrogels containing a mixture of tetrapropylammonium and tetrabutylammonium hydroxides (7) or tetrabutylammonium bromide with varying amounts of sodium and potassium hydroxides (8).

Pentasil-type borosilicates with different extents of disorder in the framework, referred to as BOR-E (9), were obtained in our laboratories using binary mixtures of different quaternary ammonium cations.

The present paper describes the synthesis and structural characterization of BOR-E, based on X-ray diffraction data.

EXPERIMENTAL

Synthesis

All crystallization reactions were performed at 170°C during 7-14 days, in a stainless steel autoclave equipped with a device for stirring. Hydrogels were obtained by dissolving boric acid in aqueous solution containing tetralkylammonium hydroxides (from Fluka) and RPE grade sodium hydroxide (from Carlo Erba), followed by tetraethylorthosilicate (Dynasil A, from Dynamit Nobel) addition. The molar composition of the precursor hydrogel was:

$$10SiO_2 \cdot B_2O_3 \cdot 2.5(R_4NOH, R_4'NOH) \cdot 0.8NaOH \cdot 380H_2O$$
$$(R: Me, Et, n\text{-}Pr; R': n\text{-}Pr, n\text{-}But).$$
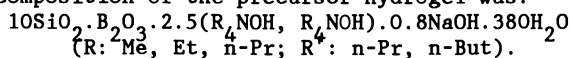
After calcination in air at 550°C the crystals were reacted with ammonium acetate solution and finally converted to the H-form by calcination of the NH_4^+-exchanged crystals in air at 550°C. More details are reported elsewhere (9).

Chemical analysis was carried out on the as-synthesized samples, using conventional methods. The content of R_4N^+ and $R_4'N^+$ was easily derived by taking into account the weight fractions of nitrogen and carbon obtained from elemental analysis. A list of the crystallized samples, together with their chemical composition, is reported in Table I.

X-ray analysis

X-ray powder patterns were recorded by the step-scanning procedure on a Philips diffractometer equipped with a pulse-height analyzer using CuKα radiation.

The powder pattern of H-BOR-E is intermediate between the patterns of H-BOR-C and H-BOR-D (see Figure 1). In particular, the intensities of the reflections with h+k+l=2n+1 (according to the unit cell characteristic of H-BOR-C) are lower in the pattern of H-BOR-E with respect to the pattern of H-BOR-C and are accompanied by some line broadening (see for example 133 at 2θ ≈ 24.5° in the patterns of Figure 1). The intensities of the remaining reflections are practically invariant. Moreover a partial coalescence of hkl and khl reflections is observed in the pattern of H-BOR-E. These effects occur to varying extent in the patterns of different samples of H-BOR-E. The trend observed in the pattern of H-BOR-D is similar to that observed in the pattern of H-BOR-E, but the extent of the phenomenon is more pronounced for the latter.

The above mentioned features of the X-ray diffraction pattern of H-BOR-E are presumably due to the same structural disorder occurring in BOR-D and in the related ZSM-11-type frameworks. Consequently, a fit of the experimentally observed patterns was attempted using the

Table I. Unit cell composition for borosilicates precursors

Sample	x[b] (c)	(d)	R_4N^+	$R_4'N^+$	B	Si	p[e]
R: n-Pr R': n-But							
1	1	1	3.5	-	4.9	91.1	0.0
2	0	0	-	4.3	4.4	91.6	0.25
3	0.33	>0.99	3.5	-	2.9	93.1	0.0
4	0.50	0.67	2.4	1.2	3.7	92.3	0.0
5	0.67	>0.99	3.6	-	3.0	93.0	0.0
R: Et R': n-Pr							
6	1	1	4.5	-	4.3	91.7	0.0
7	0.50	0.24	0.9	2.9	3.2	92.8	0.0
8	0.67	0.12	0.4	3.1	3.1	92.9	0.0
R: Me R': n-Pr							
9	0.50	0.18	0.7	3.3	4.1	91.9	0.03
10	0.66	0.32	1.5	3.1	4.3	91.7	0.05
11	0.75	0.36	1.5	2.7	3.9	92.1	0.09
12	0.80	0.32	1.4	2.9	5.3	90.7	0.08
R: Et R': n-But							
13	0.50	0.46	1.7	2.0	3.8	92.2	0.07
14	0.66	0.60	2.3	1.5	3.8	92.2	0.08
15	0.75	0.62	2.4	1.5	3.7	92.3	0.10
16	0.80	0.60	2.3	1.5	4.1	91.9	0.09
R: Me R': n-But							
17	0.50	0.35	1.4	2.6	4.1	91.9	0.14
18	0.50	0.37	1.5	2.5	4.2	91.8	0.17
19	0.50	0.41	1.6	2.3	4.5	91.5	0.15
20	0.50	0.42	1.7	2.3	4.1	91.9	0.13
21	0.50	0.44	1.8	2.2	4.0	92.0	0.11
22	0.50	0.48	2.0	2.2	4.3	91.7	0.12
23	0.25	0.50	1.9	1.9	4.9	91.1	0.10
24	0.50	0.53	2.1	1.9	4.4	91.6	0.08
25	0.75	0.58	2.4	1.8	4.1	91.9	0.16
26	0.25	0.60	2.6	1.8	4.6	91.4	0.20

Number of atoms or groups/u.c.[a]

(a) $Na^+ < 0.1$ ions/u.c. .
(b) $x = nR_4N^+/(nR_4N^+ + mR_4'N^+)$.
(c) Reaction mixture.
(d) Crystal.
(e) Stacking fault probability, see text.
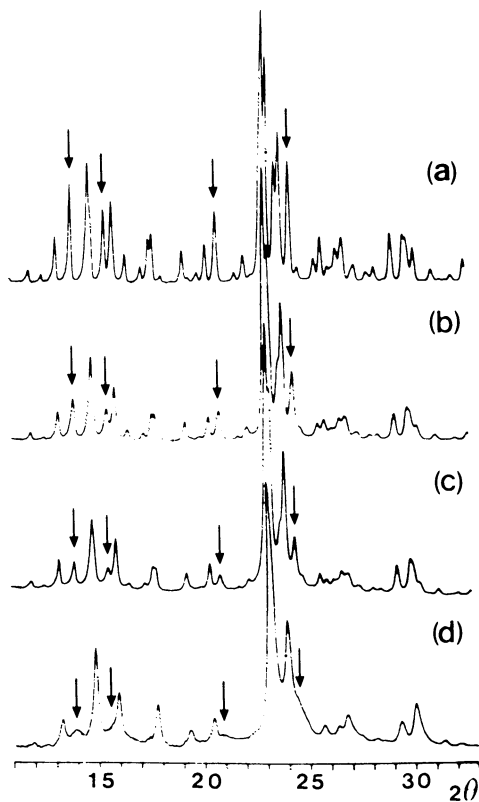
Figure 1. Selected portion of X-ray powder patterns of (a) H-BOR-C, sample 1, (b) H-BOR-E, sample 13, (c) H-BOR-E, sample 21 and (d) H-BOR-D, sample 2. Arrows indicate the position of sharp reflections of H-BOR-C, which have their intensity reduced in H-BOR-E, while becoming diffuse in H-BOR-D.

model successfully applied to the crystal structure determination of H-BOR-D (6).

Calculation of the scattered intensity

Calculation of X-ray profiles was performed in steps of 0.04° throughout the 6-50° 2θ angular region by applying the procedure used in the structure determination of H-BOR-D (6). In this procedure the instrumental broadening was simulated by convoluting the sample profiles with two Lorentzian line functions, with a 2:1 intensity ratio and a full width at half maximum of 0.1° 2θ, representing the contribution of $K\alpha_1$ and $K\alpha_2$ lines, respectively.

The calculated patterns were scaled by equating the intensities to the experimental values after integrating over the 11-50° 2θ angular range and subtracting the background. The angular range below 11° was neglected because it is very sensitive to the presence of extra-framework species. Calculation of intensities was performed by considering tetrahedral sites to only be occupied by Si. The isotropic temperature parameter B was fixed at 1.0 and 2.0 for Si and O, respectively.

The disordered model as well as the expression derived for calculation of scattered intensities were described previously (6).

Very briefly, the model is based on a pentasil layer sequence in which the prevailing i-type stacking is interrupted by σ-type stacking faults. In the crystal lattice description adopted for ZSM-5 (4) the layers lie in the b-c plane while being stacked along a. p is the probability of a stacking fault occurrence and p* the probability of a general layer to be at a crystal boundary. Both the stacking faults and the crystal termination are regarded as purely random independent events according to Bernoullian statistics. L_b and L_c are average crystal size along the b and c directions, respectively.

According to the expression used for the calculations ("Equation 15" in (6)) the scattered intensity is characterized by a Lorentzian line profile. The atomic fractional coordinates reported for the crystal structure of ZSM-5 (4) were used as intrinsic atomic parameters for the pentasil layers as was done for the structure determination of H-BOR-D.

The calculations were performed for four selected samples, characterized by different intensities for the reflections with h+k+l=2n+1, using the trial and error method. Firstly, L_b, L_c, p* and unit cell parameters were adjusted to fit the diffraction profile of reflections with h+k+l=2n (invariant intensity). Subsequently, a value was selected for p, in order to fit the intensities of reflections with h+k+l=2n+1. Due to the high sensitivity of the calculated profile to any variation of p, the estimated value of p has confidence limits of ± 0.02. The best fit, identified by the lowest value of the intensity disagreement factor, R (see Figures 2 and 3), was obtained using the values listed in table II. As for the case of H-BOR-C and H-BOR-D, the resulting values of unit cell parameters are significantly lower than the corresponding parameters characteristic of the pure silica analog, Silicalite-1, which supports framework incorporation of boron. A slight difference between the values of a and b parameters exists for H-BOR-E and
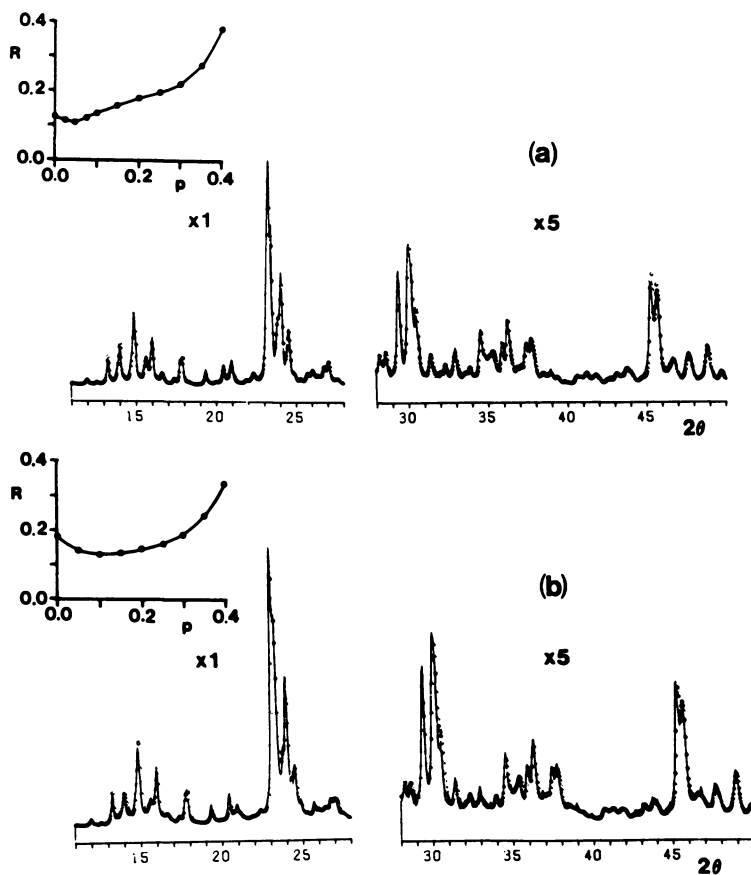
Figure 2. Experimental (—) and calculated (●●) X-ray diffraction profile for H–BOR–E, sample 10 (a) and 23 (b). The insets show a plot of the intensity disagreement factor (see Table II) vs. the fault probability parameter, p.
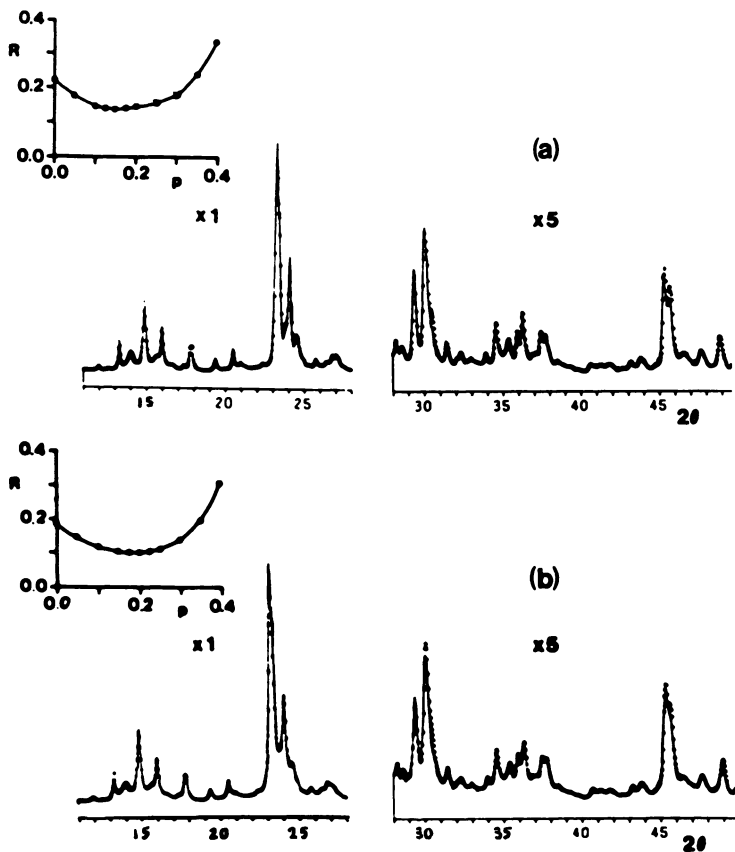
Figure 3. Experimental (--) and calculated (●●) X-ray diffrac-
tion   profile for H-BOR-E, samples 19 (a) and 26 (b). The
insets show a plot of the intensity disagreement factor (see
Table II) vs. the fault probability parameter, p.

H-BOR-D, though reduced with respect to H-BOR-C, in agreement with an excess of i-type stackings occurring in both structures (see table II).

Table II. Values of the structural parameters[a] obtained in the best fit of X-ray scattering profile for selected samples of H-BOR-E

					Unit cell parameters				
Sample	p	p*	L_b	L_c	a(Å)	b(Å)	c(Å)	V(Å^3)	R
	(b)	(c)	(d)	(d)					(e)
10	0.05	0.019	300	300	19.991	19.822	13.338	5285.4	0.11
23	0.10	0.024	250	300	19.979	19.832	13.326	5280.2	0.12
19	0.15	0.026	250	350	19.973	19.835	13.340	5284.8	0.14
26	0.20	0.033	200	300	19.968	19.835	13.350	5287.4	0.10
BOR-D[f]	0.25	0.037	300	300	20.02	19.92	13.35	5324.0	0.09
BOR-C[f]					20.01	19.82	13.35	5294.6	
Silicalite-1[g]					20.117	19.874	13.371	5345.5	

(a) According to "Equation 15" in (6).
(b) Stacking fault probability.
(c) Crystal termination probability along a (stacking direction).
(d) Average crystal size along b (L_b) and c(L_c).
(e) Intensity disagreement factor.
(f) Ref. (6).
(g) Monoclinic, α = 90.62°, Ref.(2).

p values were found to correlate well with intensity variations in the experimental patterns. In particular, a linear correlation was verified for the ratio between the intensity of 102 reflection (2θ≈14°) and the intensity of 301-031 multiplet (2θ≈15°), see Figure 4. The resulting regression of Figure 4 was used for determining the value of p for all other samples investigated.

Results and discussion

H-BOR-E was crystallized using Me_4N^+/(n-Pr)$_4N^+$, Et_4N^+/(n-But)$_4N^+$ and Me_4N^+/(n-But)$_4N^+$ binary mixtures. Both alkylammonium cations of each pair contained in the reaction mixture were found in precursor with only few exceptions. In most cases their molar ratios were found to be significantly different from the corresponding ratio in the reaction mixture. The results are summarized in Table III.

For the Et_4N^+/(n-Pr)$_4N^+$ cation pair the formation of the ordered structure of BOR-C is consistent with expectation, the same structure being formed in the presence of the individual cations. The (n-But)$_4N^+$ cation favors the formation of disordered framework structures, evident from the synthesis of BOR-D, when mixed with Me_4N^+ and Et_4N^+ but not (n-Pr)$_4N^+$. In the latter case, the (n-Pr)$_4N^+$ cation is greatly favored in the crystallization process and the
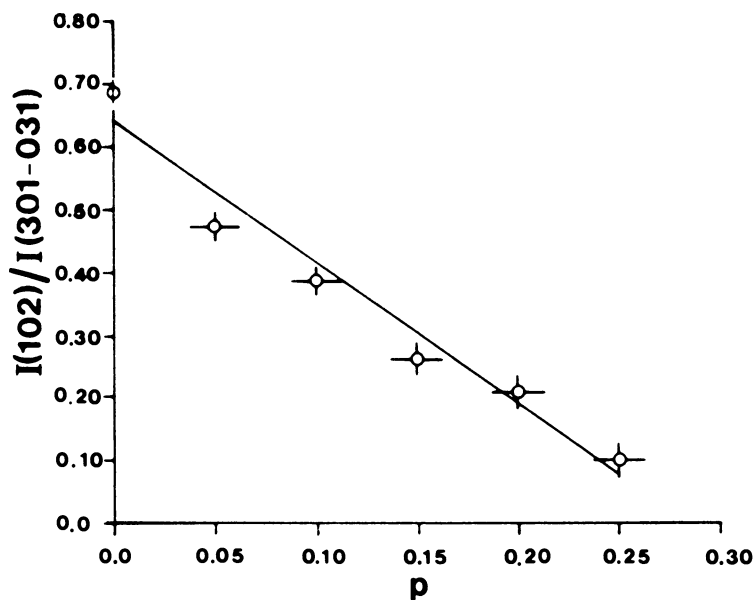
Figure 4. Variation of the ratio between the intensity of the reflections occurring at $2\vartheta \approx 14°$ and $2\vartheta \approx 15°$, respectively, in the X-ray powder pattern of H-BOR-E, as a function of the fault probability parameter, p.

ordered BOR-C phase is formed. Probably BOR-E may be obtained by working with a large excess of $(n-But)_4N^+$ cations in the reaction mixture. A similar behaviour was observed when the synthesis of disordered pentasil-type aluminosilicates from the $(n-Pr)_4n^+/(n-But)_4N^+$ system was attempted (7).
The most interesting results concern the behaviour of Me_4N^+.

This cation favors the formation of BOR-A (Nu-1-type framework), when used alone in the reaction mixture (2). In the above binary mixtures, it behaves differently, leading to the formation of pentasil-type structure, even when its concentration greatly exceeds that of the other alkylammonium cation in the reaction mixture.

Moreover, this cation seems to be more efficient than $(n-But)_4N^+$ in producing the formation of BOR-E. As a matter of fact, BOR-E is easily obtained from the $Me_4N^+/(n-Pr)_4N^+$ system, but not from the $(n-But)_4N^+/(n-Pr)_4N^+$ system.

Table III. Summary of the results

Cation pair R_4N^+ , $R_4'N^+$		$x^{(a)}$	Borosilicate phase	$p^{(b)}$
R: Et	R': n-Pr	0	BOR-C	0
		0 ÷ 0.2	BOR-C	0
		1	BOR-C	0
n-Pr	n-But	0	BOR-D	0.25
		0.7 ÷ 1	BOR-C	0
Me	n-Pr	0	BOR-C	0
		0.2 ÷ 0.4	BOR-E$_{(c)}$	0.03 - 0.09
		1	BOR-A$^{(c)}$	
Et	n-But	0	BOR-D	0.25
		0.4 ÷ 0.6	BOR-E	0.07 - 0.10
		1	BOR-C	0
Me	n-But	0	BOR-D	0.25
		0.3 ÷ 0.6	BOR-E$_{(c)}$	0.08 - 0.20
		1	BOR-A$^{(c)}$	

(a) Cations abundance in the precursor, $x=nR_4N^+/(nR_4N^+ + mR_4'N^+)$. (b) Frequency of stacking faults, see text.
(c) Nu-1 type, Ref.(2).

The stacking fault probability ,p, in H-BOR-E depends on both the cation pair used in the reaction mixture and the resulting cation abundance, defined by the molar fraction $x=nR_4N^+/(nR_4N^+ + mR_4'N^+)$ within the pore structure of the precursor. In the $Me_4N^+/(n-But)_4N^+$ system, p decreases linearly from 0.25 (H-BOR-D phase, x=0) to ca. 0.1 for x=0.5. For higher values of x, the trend is inverted

abruptly, p going up to 0.2 for x=0.6 (see Figure 5a). A linear dependence of p on x is also observed for the $Me_4N^+/(n-Pr)_4N^+$ system (Figure 5b). For the $Et_4N^+/(n-But)_4N^+$ system, values of 0.08 - 0.10 are observed for x≈0.6 (see Table I and III) near those expected for a linear variation between the values characteristic of H-BOR-D (x=0, p=0.25) and H-BOR-C (x=1, p=0), respectively.

The occurrence of a σ-type stacking fault in the framework of pentasils may be regarded as a 'twin' involving two domains of ZSM-5 type. Such a 'twin' probably occurs frequently in pentasil-type crystals, though it is not easily detected by X-ray analysis when present at low abundance (p<0.02). The good fit obtained for the X-ray diffraction patterns of H-BOR-E adds support to the validity of the model already successfully applied for the structure determination of H-BOR-D. On the other hand, the alternative model postulated for structures intermediate between ZSM-5 and ZSM-11, based on high resolution electron microscoping imaging (7), seems unfavorable with respect to the present model especially for a high fault frequency. The former model, based on two slabs of ZSM-5 joined together in such a way that one of these is rotated 90° around [001] axis, requires two-dimensional disorder and many of the Si-O-Si linkages cannot be formed at the twin plane, due to steric hindrance. Obviously, the occasional presence of some faults of this type cannot be excluded in the structure of H-BOR-E.

No macroscopic inhomogeneity is evident from the scanning electron micrographs of H-BOR-E samples, see Figure 6. The particles are nearly spherical with a morphology resulting from an aggregation of tablet-shaped small crystals. The substantial structure homogeneity of H-BOR-E is also confirmed by the results obtained with the Me_4N^+-containing systems. In fact, we must concede that inhomogeneities in the crystallized solid could originate from partitioning of the two types of cations during the crystallization process. In this case the nucleation of BOR-A by Me_4N^+ cations, would be expected.

When considering the results obtained in the present investigation, it seems quite difficult to account for the occurrence of stacking faults in the framework of pentasils simply by the different molecular size of the tetralkylammonium cations trapped within the pores. In fact, the phenomenon occurs in the presence of tetrabutylammonium or tetramethylammonium cations which have the largest and the smallest molecular size, respectively, among the organic bases investigated. It is possible that crystallization kinetics or hydrophilicity of the quaternary ammonium cations play some role. In any case, additional experiments are needed to provide a reasonable explanation.

The frequency of σ-type stackings is lower than 0.25, the value determined for the structure of H-BOR-D, in all of the samples obtained in the present investigation. The excess of i-type stackings commonly found in the framework of pentasils, suggests that this type of stacking is favoured with respect to the σ-type at least under the conditions usually adopted for the synthesis of these materials.
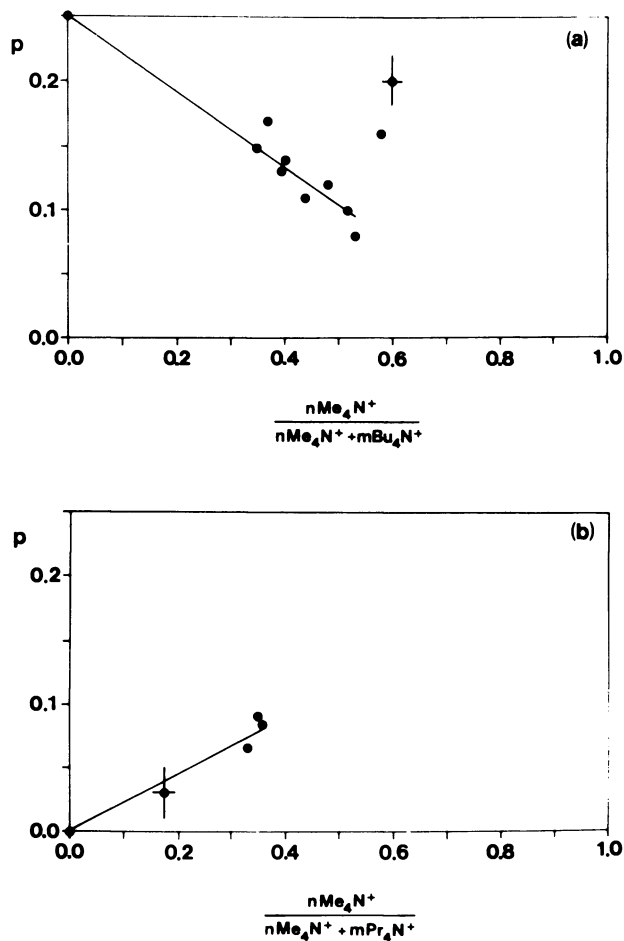
Figure 5. Variation of the fault probability parameter, p, in the framework of H–BOR–E, as a function of the molar fraction of R_4N^+ cations, x (see Table I), in the precursors, for the different R_4N^+/R'_4N^+ systems.
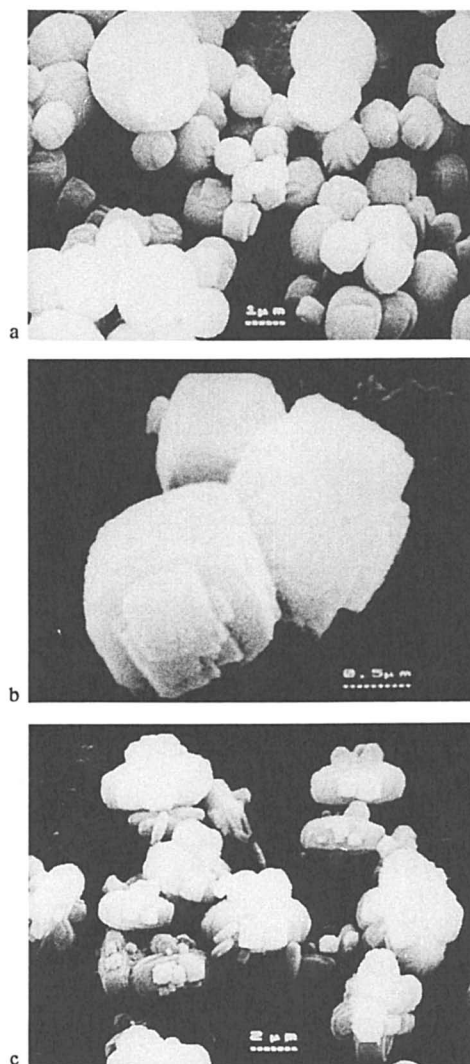
Figure 6. Scanning electron micrographs of H-BOR-E, samples 11 (a), 15 (b) and 18 (c).

Literature Cited

1. Kokotailo, G.T.; Meier, W.M. <u>Chem. Soc. Spec. Publ.</u> 1980, <u>33</u>,133.
2. Taramasso, M.; Perego, G.; Notari, B. <u>Proc. Fifth Int. Conf. on Zeolites</u>; Rees, L.V.C., Ed.; Heyden and Sons: London 1980; p. 40.
3. Flanigen, E.M.; Bennet, J.M.; Grose, R.W.; Cohen, J.P.; Patton, R.L.; Kirchner, R.M.; Smith, J.V. <u>Nature</u> (London) 1978, <u>271</u>, 512.
4. Olson, D.H.; Kokotailo, G.T., Lawton, S.L., Meier, W.M. <u>J. Phys. Chem.</u> 1981, <u>85</u>, 2238.
5. Kokotailo, G.T.; Chu, P.; Lawton, S.L.; Meier, W.M. <u>Nature</u> (London) 1978, <u>275</u>,119.
6. Perego, G.; Cesari, M.; Allegra, G. <u>J. Appl. Cryst.</u> 1984, <u>17</u>, 403.
7. Millward, G.R.; Ramdas, S.; Thomas, J.M.; Barlow, M.T. <u>J. Chem: Soc. Faraday Trans. 2</u> 1983, <u>79</u>, 1075.
8. Jablonski, G.A.; Sand, L.B.; Gard, J.A. <u>Zeolites</u> 1986, <u>6</u>, 396.
9. Taramasso, M.; Perego, G.; Fattore, V. Br. Patent 2 120 226, 1985.

Chapter 26

Isomorphous Substitution of Boron in Mordenite and Zeolite Y

Thomas R. Gaffney, Ronald Pierantozzi, and Mark R. Seger

Air Products and Chemicals, Inc., Allentown, PA 18195

Synthetic limits on the extent of isomorphous
substitution often limit our ability to modify the
catalytic properties of zeolites. Here we describe
two methods of substituting boron into mordenite,
which together allow a wide range of substitution
levels to be effected. Direct crystallization of
mordenite from gels which contain borates results
in low levels of boron incorporation into the
framework structure. The level of boron
substitution is primarily determined by the
SiO_2/Al_2O_3 ratio of the gel. Boron cannot
compete with aluminum for a site in a growing
crystallite, but boron will incorporate into
mordenites crystallized from aluminum deficient
gels. Using a post-synthetic treatment of
dealuminated mordenite and zeolite Y, we obtained
higher levels of boron substitution for aluminum.
Boron-11 NMR experiments and silicon-29 cross
polarization NMR experiments indicate that borate
anions condense with hydroxyl nests and become part
of the framework structure. The level of
substitution is limited by the hydroxyl nest
content of the dealuminated mordenite. The alpha
test establishes that the n-hexane cracking
activity of boron substituted mordenites is
determined exclusively by the aluminum content.

When applied to zeolites the term "isomorphous substitution"
refers to the replacement of silicon or aluminum atoms by
elements with ionic radii and coordination requirements which are
compatible with the T (tetrahedral) sites of the zeolite
structure. One method of preparing isomorphously substituted
zeolites is to include a reactive source of the replacement

element in the synthesis gel. If the solution chemistry of the
reactive species is compatible with gel formation and
crystallization processes, then an isomorphously substituted
zeolite may crystallize. For this to occur, the substituting
element must be able to compete with Si or Al for addition to the
growing crystallite. The substituting element does not need to
be involved in the nucleation process, but it must not interfere
with nucleation for crystallization to occur. When isomorphous
substitution can be controlled, it can be used to enhance
desirable properties into zeolite catalysts and adsorbents. A
review on isomorphous substitution and its potential catalytic
implications recently appeared (1). We now report our attempts
to prepare boron substituted mordenites and zeolite Y directly
from gel precursors, and by post-synthetic treatment of
crystalline mordenite and zeolite Y.

Experimental

Hexane (99% n-hexane) was obtained from Aldrich. Silica was
obtained as a 30% Colloid (LUDOX-HS, 30 wt% SiO_2) from DuPont.
Aluminum hydroxide, boron oxide, and sodium metaborate were
obtained from Alfa Products. Boric acid was obtained from
J. T. Baker. Commercial samples of mordenite and zeolite Y were
obtained from the Norton and Union Carbide Companies,
respectively. A specific example which illustrates the typical
procedure used for preparing mordenite and zeolite Y from gels is
given below.

Solid state ^{11}B and ^{29}Si MAS NMR spectra were obtained
using a Bruker CXP-200 spectrometer and a Doty multinuclear
double air bearing MAS probe. The samples were run as powders
loaded into sapphire rotors with Kel-F endcaps, and were spun at
the magic angle at approximately 3 kHz. Boron and silicon NMR
chemical shifts are relative to boron trifluoride etherate and
tetramethylsilane, respectively. The ^{11}B NMR spectra were
collected with and without using a solid echo pulse sequence (2)
with a 10 ms delay between 90° pulses. The repetition times
utilized for ^{11}B and ^{29}Si MAS NMR were 1 s and 10 s,
respectively; ^{29}Si CPMAS NMR utilized 1.5 s repetition times
and decoupling field strengths exceeding 50 kHz. The contact
times utilized for ^{29}Si CPMAS were varied from 100 μs to
10 ms, with 1 ms giving strong CP intensity.

Direct Synthesis. A solution was prepared by dissolving
$Al(OH)_3$, B_2O_3, and NaOH in deionized water. This solution
was slowly added to silica sol (30 wt%) with stirring, to give a
gel with the composition 22.9 SiO_2:Al_2O_3:3.2 Na_2O:0.91 B_2O_3:460
H_2O. The gel was stirred for 10 min, and then heated at 165°C
for 48 h in a stirred, Teflon lined, stainless steel pressure
vessel. After 48 h the reactor was cooled to room temperature,
and the product was separated by filtration and washed with
copious quantities of water and dried at 120°C. The X-ray powder
pattern of the product is characteristic of mordenite, with no
extraneous peaks.

Zeolite Y gels were prepared by the same procedure outlined above. These gels were aged for 24 h at room temperature prior to crystallization. They were crystallized at 95°C for 64 h in polypropylene bottles without stirring (3). The products were separated by filtration, washed with copious amounts of water, and dried at 120°C.

<u>Post-Synthetic Boron Incorporation</u>. The acid form of mordenite (Zelon 900H) was heated at 90°C in 14 M nitric acid for 24 h with stirring. The product was washed with water to a neutral pH. The samples were analyzed for Na, Si, and Al content by x-ray fluorescence spectroscopy. The extent of dealumination was found to vary for different lots of Zelon 900H. For a given lot, the extent of dealumination increased with acid extraction time. The extent of dealumination was controlled by adjusting the extraction time. Boron oxide (1.50 g B_2O_3) was dissolved in 140 mL of 0.25 M KOH. Dealuminated mordenite (25 g; Si/Al = 64) was added to the solution, and the pH was adjusted to 13 by addition of KOH. The resulting suspension was stirred at 80°C for 24 h in a Teflon lined Parr pressure vessel. The product was separated by filtration, thoroughly washed with deionized water, and dried at 120°C. The composition of the product was determined by XRF and atomic absorption spectroscopy.

Zeolite Y was dealuminated with EDTA according to a published procedure (4). Boron oxide (0.15 g) was dissolved in 140 mL of 0.22 M KOH. Zeolite Y (5 g, Si/Al = 9.1) was suspended in the solution. The suspension was heated at 80°C for 24 h in a Teflon vessel. Products were washed thoroughly with deionized water and dried at 120°C. The chemical composition of products prepared by direct synthesis and by post-synthetic methods are listed in Table 1.

Table 1. Chemical Composition of Boron Substituted
Mordenite Samples

Method of Preparation	Weight % (Dry Basis)				
	SiO_2	Al_2O_3	Na_2O	K_2O	B_2O_3
Direct Synthesis	80.7	12.1	7.81	0.04	0.02
Direct Synthesis	85.7	8.9	5.91	0.01	0.11
Direct Synthesis	88.1	7.1	5.38	0.01	0.29
Direct Synthesis	87.9	6.7	5.03	0.01	0.66
Direct Synthesis	88.3	5.9	4.18	0.01	0.57
Post-Synthetic Substitution	76.7	11.9	–	10.2	0.07
Post-Synthetic Substitution	91.1	8.3	–	a	0.52
Post-Synthetic Substitution	94.0	4.7	–	a	1.22
Post-Synthetic Substitution	88.9	1.26	–	6.1	3.68

a) Sample analyzed in the acid form.

Mordenite samples that were not in the acid form were exchanged into the ammonium ion form by three successive treatments with 0.2 M NH$_4$NO$_3$ at room temperature for 4 h prior to catalytic testing. The acid form of the zeolites was generated by heating the ammonium form at 540°C in air for one hour. The published procedure for the alpha test (5) was used with modification. Hexane (20% in helium) was passed over the catalysts (1g) at a superficial flow rate (F) of 34.1 mL/min. The effluent gases were sampled after the catalyst was on stream for 3.0 min. First order rate constants and alpha values were calculated as previously described (5).

Results and Discussion

Direct Synthetic Substitution

Mordenite. It has been reported that partial substitution of boron in mordenite occurs when boric acid is added to the synthesis gel (6,7). Evidence for boron substitution for aluminum in mordenite samples prepared in borosilicate glass reactors has also appeared (8). We sought to determine the extent of boron substitution into the mordenite framework which can be affected by direct synthesis.

Mordenite can be synthesized from gels comprised of Na$_2$O, Al$_2$O$_3$, SiO$_2$, and H$_2$O (9–13). More siliceous products are formed as the SiO$_2$/Al$_2$O$_3$ and SiO$_2$/Na$_2$O ratios are increased (13). The range of mordenite compositions which can be prepared as pure phases by this method are represented in Formula 1.

$$Na_x[(SiO_2)_{48-x}(AlO_2)_x] \cdot yH_2O \quad x = 3\text{--}8 \tag{1}$$
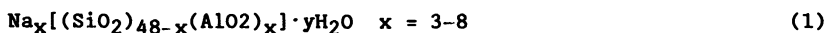
Gels in the composition range SiO$_2$/Al$_2$O$_3$ = 10–25 and SiO$_2$/Na$_2$O = 0.1–0.3 crystallize to give pure mordenite. We carried out syntheses in which B$_2$O$_3$ replaced varying amounts of Al$_2$O$_3$ in the gels. Figure 1 correlates the SiO$_2$/Al$_2$O$_3$ ratio of the products with the ratio in the gel. The straight line plot shows that the silica to alumina ratio of the product is determined by the silica to alumina ratio of the gel. Inclusion of reactive borates in the gel (circles in Figure 1) has no effect on the amount of aluminum incorporated into the mordenite structure. Apparently boron cannot successfully compete with aluminum for lattice sites in the growing crystallites. Boron does not interfere with the crystallization of mordenite when 50% or less of the Al$_2$O$_3$ in the gel is replaced by B$_2$O$_3$. However, higher levels of B$_2$O$_3$ result in co-crystallization of non-microporous phases, such as aluminum borate and sodium borosilicates.

Although boron cannot successfully compete with aluminum for sites in the mordenite structure, the more siliceous products contain significant amounts of boron. Figure 2 shows the B$_2$O$_3$ content of the products as a function of the SiO$_2$/Al$_2$O$_3$ ratio in the gel and in the product. It is clear that if enough aluminum is available in the gel to form an
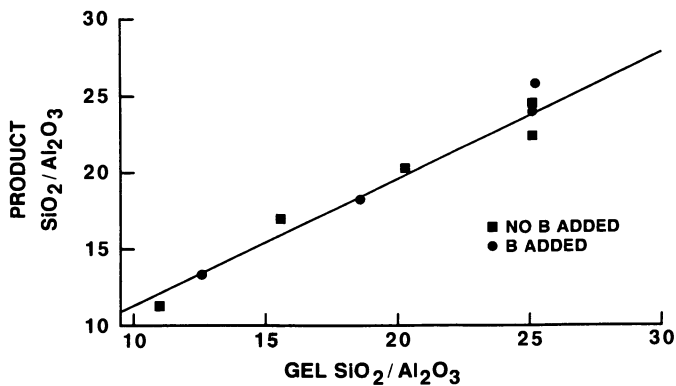
Figure 1. SiO_2/Al_2O_3 ratio of mordenite product versus gel composition.
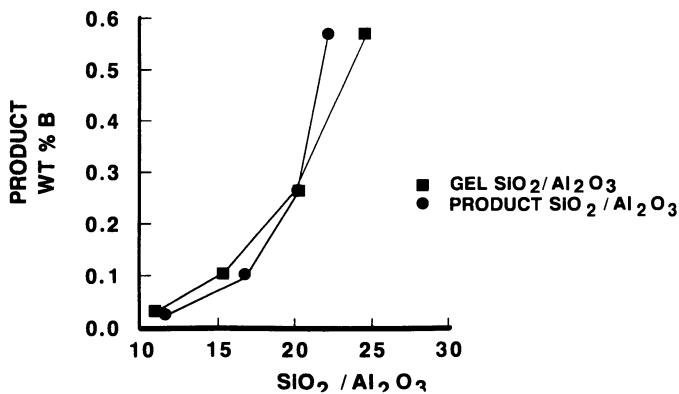
Figure 2. Boron content versus SiO_2/Al_2O_3 ratio for boron substituted mordenites.

Al saturated mordenite (x = 8 in Formula 1), the product contains only trace amounts of boron. As the SiO_2/Al_2O_3 ratio of the gel increases, and insufficient Al is present to form the aluminous mordenite end-member, the boron content of the product rises dramatically. The upper limit on the SiO_2/Al_2O_3 level at which pure mordenite forms, which is approximately 25, determines the upper limit on boron substitution level.

For the most siliceous preparations, the mole % boron in the product is proportional to the mole % boron in the gel. Figure 3 shows the correlation between wt % boron in the gels and products. The amount of boron which substitutes into the mordenite structure increases with increasing boron concentration in the gel, and decreases with increasing aluminum content in the gel. The level of substitution is much more dependent on the aluminum content in the gel than on its boron content. The explanation for this is found in the higher affinity of the structure for aluminum. Boron and aluminum compete for a limited number of sites in the mordenite structure as it forms. When enough aluminum is available to form an aluminum saturated mordenite structure (x = 8, Formula 1) then boron substitution does not occur. The most highly substituted material prepared by this method is $Na_{4.5}[(SiO_2)_{43.5}(AlO_2)_{3.9}(BO_2)_{0.6}]$. Similar results have been reported (14) for crystallization of ZSM-5 from gels which contain aluminum and boron.

<u>Faujasite</u>. Zeolite Y was prepared from Na_2O, Al_2O_3, SiO_2, and H_2O derived gels using Breck's method (3). We prepared four gels in which 0, 5, 10, and 25% of the molar amount of Al_2O_3 used to prepare zeolite Y was replaced by B_2O_3. The gels were crystallized under identical conditions. The yield of crystalline product decreased with increasing boron content in the gel. The major phases formed from the boron doped gels were α-$Al_2O_3 \cdot OH$ (boehmite) and sodium aluminum silicate hydrate; however, the undoped parent gel yielded highly crystalline zeolite Y as the only crystalline product. In contrast to the mordenite system, addition of B_2O_3 to the gel inhibits nucleation or crystallization of zeolite Y. Earlier work showed that another synthetic faujasite, zeolite X, can be crystallized from borate containing gels, but that borate is occluded in the zeolite pores, and is not incorporated into the framework structure (15,16).

<u>Characterization of Substituted Boron</u>. We used solid state ^{11}B NMR and X-ray diffraction data to distinguish occluded borates from boron substituted into the zeolite framework. When an element replaces aluminum or silicon in a zeolite structure, the local coordination environment changes to accommodate the new ion. Since B^{3+} is a much smaller ion than Al^{3+}, the unit cell axes contract when boron replaces aluminum in the framework. The ionic radii of trivalent B and Al in a tetrahedral environment are 0.25 Å and 0.53 Å, respectively (1). The magnitude of the contraction is dependent upon the level of substitution (17).

The lattice constants of a boron substituted mordenite sample with SiO_2/Al_2O_3 = 25.3 and $SiO_2/(Al_2O_3 + B_2O_3)$ = 22.5
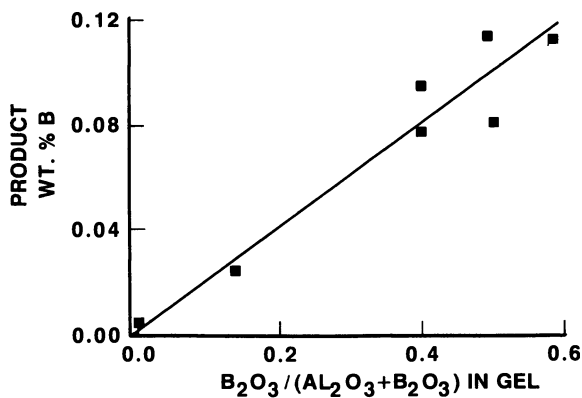
Figure 3. Boron substitution level versus gel composition for boron substituted mordenites.

were refined from corrected XRD data, obtained using corundum as an internal standard. Table 2 shows the variation in the unit cell dimensions of mordenite as a function of the SiO_2/Al_2O_3 ratio of the sample (13,18). The unit cell values for the boron containing sample, designated "synthetic", are well below the values of mordenite and aluminum deficient mordenite samples. In each dimension, the value is significantly lower than would be expected if the structure were comprised of Si and Al with extra-lattice boron occluded in the pore system.

Table 2:   Unit Cell Dimensions of Mordenites and
Boron Substituted Mordenites

Sample	Si/Al	Si/B	a($\overset{\circ}{A}$)	b($\overset{\circ}{A}$)	c($\overset{\circ}{A}$)	V($\overset{\circ}{A}^3$)
a	5.0	∞	18.11	20.53	7.528	2798
a	12.5	∞	18.11	20.38	7.49	2764
Synthetic	12.7	90	18.05	20.34	7.46	2741
b	60.0	∞	18.06	20.26	7.46	2730
Post-Synthetic	59.9	14	17.84	20.03	7.36	2627

a) Literature values from (13)   b) Literature value from (18)

Solid state ^{11}B NMR is a very sensitive probe of the site symmetry of boron (8,19). For solid samples, the quadrapolar interaction gives rise to resonance lineshapes that are very dependent on the symmetry of the boron environment, even if Magic Angle Spinning (MAS) techniques are used. Boron atoms located at sites of tetrahedral symmetry have vanishingly small electric field gradient (EFG) anisotropies, and thus have very narrow MAS NMR lineshapes. Trigonal boron sites however, have large EFG anisotropies and give rise to very broad MAS lineshapes in powder samples.

Figure 4a is a ^{11}B MAS NMR spectrum of a mordenite sample prepared from an aluminum deficient gel which contained B_2O_3. The sharpness of the peak indicates a tetrahedral boron location, and the chemical shift agrees with previously reported values for boron in a zeolite framework (8). In contrast, extra-lattice boron in mordenite (vide infra) gives a broad resonance, as shown in Figure 4b.

The NMR and X-ray diffraction data are only consistent with substitution of boron into the framework structure of the mordenite. Although we prepared boron substituted mordenite directly from modified gels, direct synthesis has severe limitations. The solution chemistry of the substituting element can interfere with zeolite nucleation and crystallization, as

observed for boron in faujasite-type syntheses. In syntheses
where there is no apparent interference with the crystallization
processes, the amount of substitution that occurs may be limited
by the solubility of the replacement element in the gel during
crystallization. The intrinsic affinity of the crystallizing
solid for depleting one gel species relative to others may also
limit substitution. Because of these limitations, it was only
possible to prepare mordenites which contain low levels of boron
by direct synthetic methods.

Post-Synthetic Substitution

Methods for isomorphously substituting preformed zeolite
structures have the potential for allowing a wider range of
compositions to be prepared. When the zeolite structure is
already formed, the compatibility of the solution chemistries of
the replacement element with aluminum and silicon is not a
concern, and nucleation and crystallization are not required.
    Several methods were attempted for effecting isomorphous
substitution in preformed crystalline zeolites. Decationized
samples of mordenite and zeolite Y were refluxed with boric acid,
sodium metaborate, and B_2O_3 in aqueous solutions with pH
varying between 4 to 12. The products exhibit broad ^{11}B NMR
signals which are characteristic of boron in a trigonal
environment (Figure 4b). After thorough washing only trace
amounts of boron (ca. 0.03%) remain in the product. Boron
apparently cannot displace aluminum or silicon from the framework
of a preformed structure under these conditions.
    When treated under the proper conditions, aluminum can be
removed from zeolites without loss of crystallinity (20). It has
recently been demonstrated that for zeolite Y the extra-lattice
aluminum is incorporated into the framework when the sample is
treated with KOH (21). We sought to determine if dealuminated
zeolite frameworks are reactive, and are isomorphously
substituted when treated with borate salts in basic medium.
After we completed our studies, a report of boron incorporation
into zeolite Y using similar methods appeared (22).

Mordenite. We dealuminated mordenite with acid and treated the
product with B_2O_3 in basic solution. The products obtained
contain high levels of boron. The amount of boron in the product
is dependent upon the level of dealumination of the mordenite.
Figure 5 is a plot of the boron content of the product versus the
Si/Al level of the starting material. More heavily dealuminated
samples contain more boron after a KOH/B_2O_3 treatment. The
data point off of the curve (circle in Figure 5) is for a
synthetically prepared siliceous mordenite, whereas the data
points on the curve are for acid dealuminated (siliceous)
mordenites. It is clear that materials which have the same
aluminum content prepared by these two methods react differently
with borate anions. An acid dealuminated mordenite with Si/Al =
12 takes up almost ten times as much boron than its synthetically
prepared analogue.
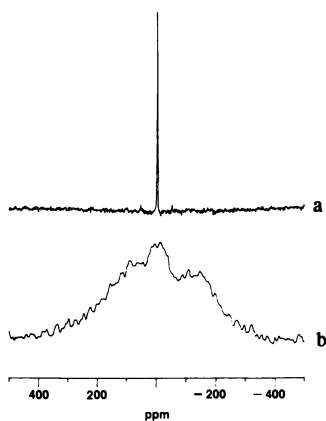
Figure 4. Solid state ^{11}B NMR spectra of boron substituted mordenite (a), and extra-lattice boron occluded in mordenite (b).
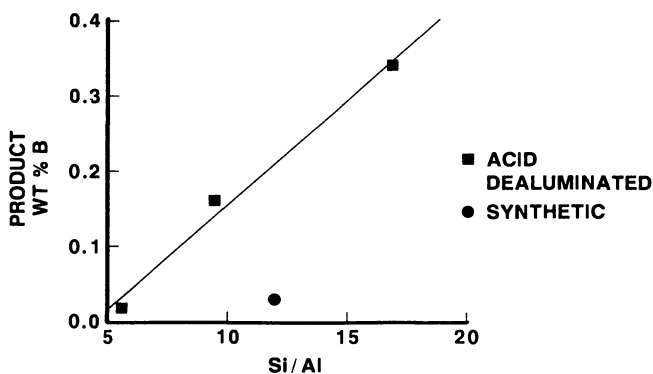
Figure 5. Boron uptake of synthetic and dealuminated mordenites.

The observed reactivity difference between zeolites and acid dealuminated zeolites is directly attributable to the presence of intrazeolitic hydroxyl nests in the acid treated samples. Two resonances are present in the ^{29}Si MASNMR spectra of acid dealuminated mordenites (Figure 6), which we assign to silicon with no nearest neighbor aluminum atoms (-112 ppm), and to SiOH "nests" (-103 ppm). Cross polarization (CP) NMR techniques corroborate the assignment of the resonance at -103 ppm (vide infra). The spectra in Figure 6 demonstrate that the -103 ppm resonance is enhanced by the cross polarization technique, confirming the presence of hydroxyl nests in our dealuminated samples. Figure 7 shows the spectra of the same sample after treatment with B_2O_3/KOH. The resonance at -111 ppm is broadened, presumably due to the presence of boron and aluminum atoms in sites adjacent to Si, and the CP resonances have almost disappeared. These two changes are consistent with boron reacting at the internal hydroxyl nest position as shown in Scheme 1.

Scheme 1:   Framework Substitution

```
          Si                                          Si
          /                                           /
          O                                Si         O
          H                                /          |
                                           O
Si—OH      HO—Si    B(OH)4⁻ ,      Si—O—B—O—Si   + 4H2O
                                           |
          H                                O
          O                                 \
           \                                Si
          Si
```
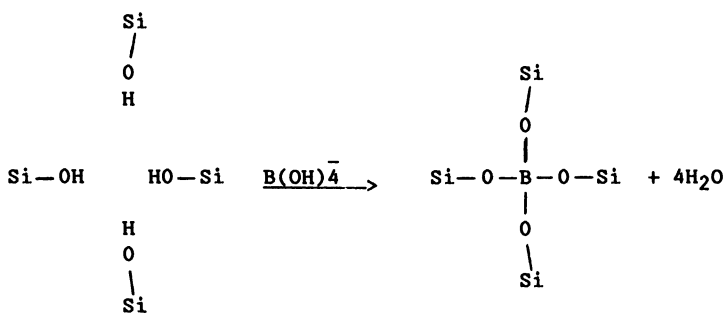
The ^{11}B NMR spectrum of this sample contains a single narrow resonance centered at -3.2 ppm, which is characteristic of boron in a tetrahedral coordination environment in the framework structure. The ^{29}Si NMR spectra of a synthetically prepared siliceous mordenite with the same Si/Al ratio is shown in Figure 8. No CP resonances are present, which indicates that hydroxyl nest concentration in this material is very low compared to the acid treated sample. These data confirm that hydroxyl nests, generated by the removal of Al from the zeolite structure, are reactive sites for isomorphous substitution. Aluminum deficient, preformed zeolites which do not contain hydroxyl nests, i.e. synthetically prepared samples, do not undergo isomorphous substitution when treated in a similar fashion.

The amount of boron substitution achieved using this post-synthetic method is approximately six times higher than the most heavily substituted mordenite prepared by direct synthesis from gels (vide supra). If this post-synthetic treatment
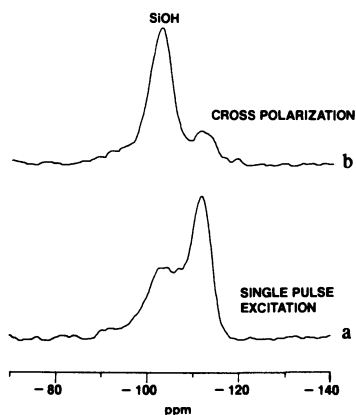
Figure 6. Single pulse excitation and cross polarization ^{29}Si NMR spectra of dealuminated mordenite.
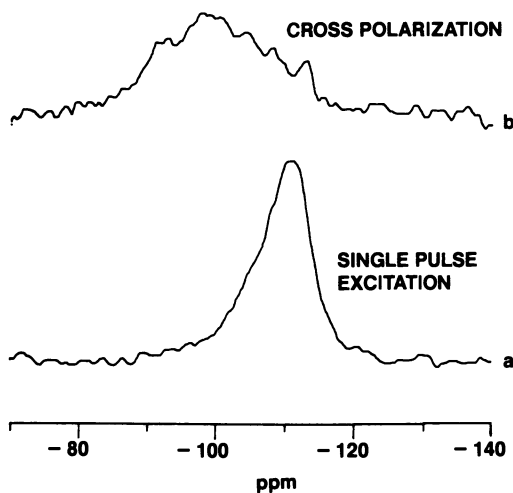
Figure 7. Single pulse excitation and cross polarization ^{29}Si NMR spectra of boron mordenite prepared from dealuminated mordenite.
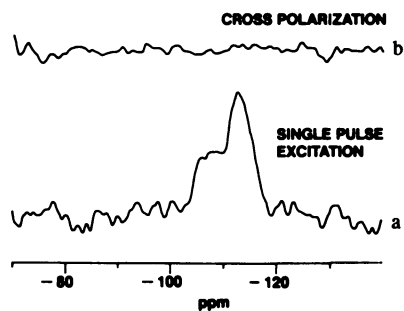
Figure 8. Single pulse exitation and cross polarization
^{29}Si NMR spectra of synthetic mordenite.

produces a structurally substituted zeolite, then the unit cell axes should exhibit a large contraction upon KOH/B_2O_3 treatment. The lattice constants of the material with $K_{3.9}[(SiO_2)_{44.1}(AlO_2)_{0.7}(BO_2)_{3.2}]$ were refined from corrected XRD data, and are listed in Table 2 along with the constants for mordenite and synthetically prepared boron substituted mordenite. The large contraction of the unit cell observed for the heavily borated material is strong evidence for structural substitution of boron in these materials. The unit cell volume of the highly substituted structure (K^+ ion form) is 6.1% smaller than the cell volume of the aluminum analogue (H^+ form). Only a 1.6% contraction is attributable to the removal of aluminum. The major reduction in unit cell volume (-4.5%) results from boron pulling the oxygen atoms in hydroxyl nests closer together, as depicted in Scheme 1. It must be noted that although this comparison is between different ion forms, the potassium form should have a larger unit cell than the acid form if no structural substitution occurred (23).

Zeolite Y. We also substituted boron into dealuminated zeolite Y. We dealuminated zeolite Y by EDTA treatment using standard methods (4). The presence of hydroxyl nests in the product was confirmed using ^{29}Si CPMAS NMR spectroscopy. The dealuminated material incorporated 33 times more boron than zeolite Y when treated with KOH/B_2O_3. These data are summarized in Table 3. The boron substituted faujasite exhibits a single sharp resonance in the ^{11}B NMR spectrum, consistent with structural substitution. Since the substitution level was low and would not be expected to cause large shifts in the diffraction pattern, no corrected XRD data were obtained on substituted zeolite Y.

Zeolite Y does not recrystallize in KOH solutions (24). Our results are in agreement with this for Y, but for dealuminated Y zeolite there is a decrease in the Si/Al ratio when treated with B_2O_3 in KOH solution (Table 3). We found a similar trend in the mordenite system. Apparently these zeolite structures are more susceptible to recrystallization when dealuminated. Preparation of boron substituted zeolite Y by post-synthetic substitution demonstrates that this method may be used to prepare materials which are not readily available by direct synthetic procedures.

Table 3:   Substitution Levels of Zeolite Y and
Dealuminated Zeolite Y

Sample	Starting Material Si/Al	Product Si/Al	ppm B
Zeolite Y	2.6	2.7	15
Dealuminated Y	9.1	5.9	500

NMR Methods. The cross polarization technique was used to transfer magnetization from ^{1}H to [29]Si. Spin temperature alteration ensures that only silicon atoms with a strong dipolar (through-space) interaction with protons will appear in the CPMAS spectrum. Only silicon atoms near immobile hydrogens (i.e., not exchanging in the NMR time scale) will be detected. Comparison of the FTMAS and CPMAS spectra in Figure 6 shows a strong enhancement of the -103 ppm peak with only a weak enhancement of the -112 ppm peak assigned to Si(0Al). Application of the same experimental method to mordenite prior to acid dealumination failed to detect any CP signal, indicating that the hydrogen atoms present in the hydrated sample were all involved in rapid chemical exchange. Furthermore, it also demonstrates that the protons involved in the cross polarization to silicon in the acid dealuminated sample are not from the adsorbed water of hydration.

The variation of the [29]Si CPMAS spectrum was examined as the contact time for the cross polarization experiment was changed. The most intense CP signal was obtained with relatively short contact times, indicative of short silicon-hydrogen internuclear distances. Maximum CP intensity in the -103 ppm peak occurred at about 1 to 2 ms, suggesting ^{1}H to [29]Si distances of a few angstroms or less for this type of silicon. The Si(0Al) peak at -112 ppm showed a less intense CP signal, but with maximum enhancement occurring at longer contact times, indicative of a greater average distance to immobile hydrogen atoms.

The presence of the broad signal arising from trigonal extra-lattice boron species can only be reliably detected by using a solid echo pulse sequence (2). The broad lineshape in Figure 4b, attributed to trigonal boron, was not detected by the simpler one-pulse NMR method. There are reports in the literature that trigonal framework boron atoms may be present in some dehydrated calcined zeolites (25). The broad signals attributed to trigonal framework boron reversibly disappear upon rehydration of the zeolite sample, indicating conversion back to tetrahedral symmetry (25) As the samples analyzed by ^{11}B MAS NMR were all hydrated, no trigonal framework boron species were observed.

Catalytic Properties. The Bronsted acid sites in zeolites are associated with bridging hydroxyl groups adjacent to aluminum atoms (5). Substitution of other trivalent elements for aluminum greatly affects the strength of these Bronsted acid sites, and there is a growing body of experimental data (1) which indicates that aluminosilicates are stronger acids than borosilicates. Previously, a quantitative test based on n-hexane cracking (alpha test) was developed and used to assess the strong acid properties of zeolites (5). We used the alpha test to compare the strong acidity of substituted and unsubstituted mordenites.

We found the acidity of chemically dealuminated mordenites shows a large variation with aluminum content (Figure 9). The alpha values decrease over five orders of magnitude as the aluminum content decreases from four aluminum atoms per unit cell down to 0.8 Al/unit cell. If the Bronsted acid sites associated with boron are of equal strength as those associated with

aluminum, then the alpha values of unsubstituted and substituted samples in which SiO_2/Al_2O_3 (unsubstituted) is equal to $SiO_2/(Al_2O_3+B_2O_3)$ (substituted) should be equal. The activity measured for the heavily substituted material is almost identical to the sample with the same aluminum content, and is over four orders of magnitude lower than would be expected if boron sites are as acidic as aluminum sites (circle in Figure 9). This clearly illustrates that only aluminum contributes to the hexane cracking activity of these materials under the experimental conditions used. The presence of framework boron has no affect on the strong acid character of the catalyst. The presence of framework boron may still increase the number of weak and medium acid sites, but the alpha test will not be sensitive to these sites, especially when strong acid sites associated with aluminum are present.

The alpha values of synthetically prepared mordenites are within the range of 10^5-10^6. There is only a small variation in a values of siliceous mordenite as the aluminum content of the material varies. This is in contrast to dealuminated mordenites, which exhibit a much larger variation in alpha values as the aluminum content varies. These catalytic results on synthetic and acid dealuminated mordenites indicate that factors other than the total aluminum content must contribute to the variation in activity of the catalysts. The linear correlation of alpha versus aluminum content reported for some zeolites (26) does not apply to the acid dealuminated samples. Evidence has been presented for the presence of both Bronsted sites and Lewis sites enhancing the strong acidity of zeolite catalysts (27). The presence of extra-lattice aluminum in acid dealuminated mordenite samples was confirmed by ^{27}Al NMR spectroscopy. The presence of both framework aluminum and extra-lattice aluminum in the acid treated materials may account for the wide variation in alpha values as a function of aluminum content.

The synthetic boron substituted mordenites have alpha values similar to the aluminosilicate analogues. This is not surprising since boron replaces only 10% of the aluminum in these materials. For boron to affect the alpha values of these samples, the acid strength of a B-OH proton would have to be much greater than for a Al-OH proton, which is clearly not the case.

Conclusions

We prepared boron substituted mordenite by direct synthesis from gel precursors and by post-synthetic substitution into dealuminated mordenite. Direct substitution is favored in aluminum deficient gels, but exacting crystallization requirements for mordenite formation limit the amount of boron that can be incorporated into the framework structure. Higher substitution levels were achieved using a post-synthetic treatment. Boron substituted zeolite Y could not be prepared by a similar direct synthetic method, but post-synthetic methods were effective at providing low substitution levels. This demonstrates the more general utility of post-synthetic substitution methods. The hexane cracking activity of
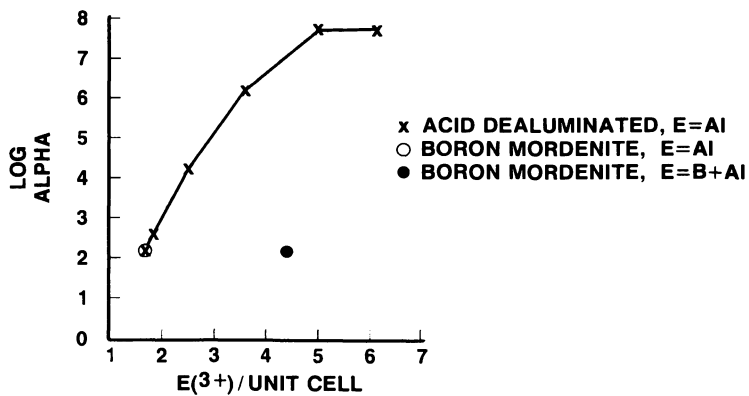
Figure 9.   n-Hexane cracking activity of mordenites.

substituted and unsubstituted mordenites is consistent with
strong acid sites associated with aluminum, but not boron.

Acknowledgments

Literature Cited

1. Tielen, M.; Geelen, M.; Jacobs, P. A. Acta Phys Chem, 1985,
    31 (1-2), 1-18.
2. Boden, N. In Determination of Organic Structure by Physical
    Methods; Nachod, F. C., Ed.; Academic: New York, 1971,
    Vol.4, p 51-137.
3. Breck, D. W. U.S. Patent 3 130 007, 1964.
4. Kerr, G. T. J. Phys. Chem. 1968, 72(7), 2594-6.
5. Miale, J. N.; Chen, N.Y.; Weisz, P. B. J. Catal., 1966, 6,
    278-87.
6. Ione, K. G.; Duc Tien, N.; Klyueva, N. B.; Vostrikova, L. A.
    Catalysis Sci. Tech., 1985, 281-6.
7. Klyueva, N. V.; Duc Tien, N.; Ione, K. G. React. Kinet.
    Catal. Lett., 1985, 29 (2), 427-32.
8. Gabelica, Z.; Nagy, J. B.; Bodart, P.; Debras, G. Chem.
    Lett., 1984, 1059-62.
9. Bajpai, P. K. Zeolites, 1986, 6(1), 2-8.
10. Bajpai, P. K.; Rao, M. S.; Gokhale, K. V. G. K. Ind. Eng.
    Chem. Prod. Res. Dev., 1978, 17(3), 223-7.
11. Domine, D.; Quobex, J. In Molecular Sieves; Barrer, R. M.,
    Ed.; Soc. of Chem. Industry: London, 1968; p 78.
12. Sand, L. B. In Molecular Sieves; Barrer, R. M., Ed.; Soc.
    of Chem. Industry: London, 1968; p 71.
13. Itabashi, K.; Fukushima, T.; Igawa, K. Zeolites, 1986,
    6(1), 30-4.
14. Bodart, P.; Nagy, J. B.; Gabelica, Z.; Derouane, E. G.
    Appl. Catal., 1986, 24, 315-8.
15. Barrer, R. M.; Freund, E. F. J.C.S. Dalton Trans., 1974,
    1049-53.
16. Shannon, R. D. Acta Crystallogr., 1976, 32(5), 751-67.
17. Taramasso, M.; Perego, G.; Notari, B. Proc. 5th Int. Conf.
    Zeolites, 1980, p 40.
18. Olsson, R. W., Rollmann, L. D. Inorg. Chem., 1977, 16, No.
    3, 651-4.
19. Gabelica, Z.; Debras, G.; Nagy, J. B. Stud. Surf. Sci.
    Catal., 1984, 19, 113-21.
20. Scherzer, J. ACS Symp. Ser. 1984, 248 (Catal. Mater. Relat.
    Struct. React), 157-200.
21. Liu, X.; Klinowski, J.; Thomas, J. M. J. Chem. Soc. Chem.
    Commun. 1986, 582-584.

22. Klinowski, J.; Hamdan, H.; Sulikowski, B.; Man, P. P.; Carr, S. W. 194th ACS National Meeting, New Orleans, LA, August 30 - September 4, 1987.
23. Mortier, W. J., Compilation of Extraframework Sites In Zeolites; Butterworth & Co.: Great Britain, 1982, pp 55-6.
24. Barrer, R. M. Hydrothermal Chemistry of Zeolites; Academic: London, 1982.
25. Kessler, H.; Chezeau, J. M.; Guth, J. L.; Strub, H.; Coudurier, G. Zeolites, 1987, 7(4), 360-6.
26. Haag, W.O.; Lago, R. M.; Weisz, P. B. Nature, 1984, 309, 589-91.
27. Beyerlein, R. A.; McVicker, G. B.; Yacullo, L. N.; Ziemiak, J. J. J. Phys. Chem., 1988, 92(7), 1967-70.

Chapter 27

Hydrothermal Isomorphous Substitution of Boron in Zeolite ZSM–5/Silicalite

Bogdan Sulikowski[1] and Jacek Klinowski

Department of Chemistry, University of Cambridge, Lensfield Road, Cambridge CB2 1EW, England

We report (i) isomorphous substitution of boron, by *secondary* synthesis, into silicalite and into highly siliceous (Si/Al>400) ZSM-5; and (ii) an improved *direct* synthesis of zeolite (Si,B) -ZSM-5. The chemical status of B in the boronated products depends upon reaction conditions. Careful control of the con- centration of the base, the borate species and of the duration of treatment, allows the preparation of samples containing only 4-coordinated B or a mixture of 3- and 4-coordinated B in various relative concentrations. The products were characterized by magic-angle-spinning (MAS) NMR and infrared (IR) spectro- scopies and by powder x-ray diffraction (XRD).

Elements such as B, Ga, P and Ge can substitute for Si and Al in zeolitic frameworks. In naturally-occurring borosilicates B is usually present in trigonal coordination, but four-coordinated (tetrahedral) B is found in some minerals and in synthetic boro- and boroaluminosilicates. Boron can be incorporated into zeolitic frameworks during synthesis, provided that the concentration of aluminium species, favoured by the solid, is very low. (B,Si)-zeolites *cannot* be prepared from synthesis mixtures which are rich in aluminium. Protonic forms of borosilicate zeolites are less acidic than their aluminosilicate counterparts (1-4), but are active in catalyzing a variety of organic reactions, such as cracking, isomerization of xylene, dealkylation of arylbenzenes, alkylation and disproportionation of toluene and the conversion of methanol to hydrocarbons (5-11). It is now clear that the catalytic activity of borosilicates is actually due to traces of aluminium in the framework (6). However, controlled substitution of boron allows fine tuning of channel apertures and is useful for shape-selective sorption and catalysis.

[1]On leave from the Institute of Organic Chemistry and Technology, Kraków Technical University, Poland

We have earlier addressed the problem of the post-synthesis insertion of aluminium in zeolites ZSM-5 (12) and Y (Hamdan, H.; Sulikowski, B.; Klinowski, J. J.Phys.Chem., (in press)). The substitution of gallium in silicalite-II has also been achieved (13). It was therefore of considerable interest to establish whether boron can also be incorporated into silicate frameworks *after* the completion of synthesis. We report isomorphous substitution of boron into zeolite ZSM-5 by mild hydrothermal treatment with borate species.

Experimental

Materials. The parent zeolite (Si,Al)-ZSM-5 was synthesized according to Argauer and Landolt (14), calcined in air at 500°C, and subjected to two-fold ion exchange with aqueous 1M NH_4Cl. The 86% ammonium-exchanged zeolite was washed and dried. It had Si/Al=47.6 (by wet chemical analysis). Dealuminated ZSM-5 was prepared by two-fold steaming of a NH_4-ZSM-5 at 540°C for 2 h each time followed by extraction of aluminium with 2M HCl under reflux, washing and drying. The product (De-ZSM-5) had Si/Al>400.

Silicalite was synthesized according to Grose and Flanigen (15), using tetrapropylammonium hydroxide and Ludox AS-40 as a source of silicon. The product was washed, dried and calcined in air at 600°C giving crystalline silicalite with Si/Al=563 as determined by x-ray fluorescence (XRF) and atomic absorption (AA).

Starting materials for the direct synthesis of (Si,B)-ZSM-5 were fumed silica (Cabosil), tetrapropylammonium bromide (TPA-Br), ammonium fluoride and orthoboric acid (16). The source of silica was mixed with TPA-Br and water and then a mixed solution of NH_4F and H_3BO_3 was added under vigorous stirring. The resultant gel was homogenized for 1.5 h and transferred into a Teflon-lined stainless steel autoclave which was then heated at 200°C for 17 days. Zeolite crystals were washed, dried at 60°C and hydrated in a desiccator.

Hydrothermal treatment with borate species. The boronation procedure was as follows: first, solution A was prepared by dissolving 7.75 g of B_2O_3 in 100 ml KOH (pH≈8). The ^{11}B NMR spectrum of this solution (not shown) consists of one signal at 19.9 ppm (from $BF_3 \cdot Et_2O$), corresponding to trigonal boron (17). 1.5 g of the zeolite was then placed in a polypropylene bottle and 20 ml of solution A added (zeolite/B_2O_3 = 0.9) and the final pH of the suspension was adjusted with additional amounts of KOH. The bottles were tightly capped and kept in an oven at the desired temperature for 24-42 h without stirring. The products were thoroughly washed with distilled water, dried at 80°C and hydrated in a desiccator. The conditions of the hydrothermal treatment are summarized in Table I.

Table I. Conditions of hydrothermal treatment of dealuminated ZSM-5
(samples 1-2) and silicalite (samples 3-9), chemical shift (CS) and
full-width-at-half-maximum (FWHM) of the ^{11}B MAS NMR signals

Sample	(g)	B_2O_3 (g)	KOH conc. (M)	Temp. (oC)	Time (h)	^{11}B MAS NMR CS (ppm[‡])	FWHM (Hz)
1	0.5*	0.20	0.08	80	24	-3.97	93
2	0.2*	0.43	0.01	80	40	-3.84	91
3	1.5	1.55	<0.01	80	24	-3.97	115
4	1.5	1.55	0.03	80	24	-3.96	109
5	1.5	1.55	0.05	80	24	-3.92	104
6	1.5	1.55	0.16	80	42	-3.94	92
7	1.5	1.55	0.10	80	42	-3.93	95
8	1.5	1.55	0.50	28	25	-	-
9	1.5	1.55	2.00	28	25	-	-

* dealuminated ZSM-5 (Si/Al>400).
‡ from external $BF_3 \cdot Et_2O$.

Magic-angle-spinning NMR. ^{11}B MAS NMR spectra were measured at
128.33 MHz using a Bruker MSL-400 multinuclear spectrometer. Samples
were spun in Vespel rotors at 4-5 kHz using air as the spinning gas. Radio-
frequency pulses of 2 μs duration were applied with 300 ms recycle delay.
Short pulses are necessary if quantitative spectra of quadrupolar nuclei are
to be obtained (18). From 6000 to 24000 transients were acquired for each
spectrum, and all spectra were recorded under the same conditions. [11]B
chemical shifts are quoted in ppm from external $BF_3 \cdot Et_2O$. A calibration
curve was prepared using known amounts of the as-prepared (Si,B)-ZSM-5.
The samples were also analyzed by AA. The samples were hydrated in the
desiccator over saturated NH_4NO_3 solution prior to measurement.

X-ray diffraction. XRD patterns were acquired on a Philips PW1710 vertical
goniometer using $CuK\alpha$ radiation selected by a graphite monochromator
in the diffracted beam. All the samples were fully hydrated before XRD
diffractograms were measured. Silicon powder was used as an internal
standard.

Infrared spectra. IR absorption spectra in the framework vibration region
(400-1400 cm^{-1}, resolution 1 cm^{-1}) were obtained with a Nicolet MX-1
Fourier transform spectrometer using the KBr pellet technique.

Results and Discussion

Silicalite (samples 3-9) and dealuminated ZSM-5 (samples 1-2) were sub-
jected to hydrothermal treatment under mild alkaline conditions at
various boron-to-zeolite ratios, temperatures and times of treatment (see
Table I). To consider the question of the status of boron in the boronated
samples we have used ^{11}B MAS NMR, a technique capable of providing
direct information on the type of short-range environment of the nucleus.
        Typical ^{11}B MAS NMR spectra of boronated samples 1 and 7 are
shown in Figure 1. The spectrum of boronated sample 1 prepared from
dealuminated ZSM-5 consists of one narrow signal centred at -3.97 ppm.
The spectrum of boronated silicalite contains a second broad signal [see
Figure 1(b)]. We shall address first the question of the origin of the sharp
^{11}B NMR signals with the chemical shift at about -3.9 ppm (Table I). In
borosilicates boron can adopt either three- or four-fold coordination. In
naturally-occurring borosilicates it is usually present in trigonal
coordination, but four-coordinated (tetrahedral) B is found in some
minerals (such as datolite, garrelsite and reedmergnerite, the boron
analogue of albite (22)) and in synthetic boro- and boroaluminosilicates.
Tetrahedral boron in the boro- and boroaluminosilicates gives rise to a
sharp signal with a chemical shift in the range of -3.3 to -4.0 ppm from
$BF_3 \cdot Et_2O$ (2,4,23-25). In minerals such as kernite and inderite, BO_3 and
BO_4 groupings can be unambigously distinguished by NMR. Moreover,
relative spectral intensities were in excellent agreement with both x-ray
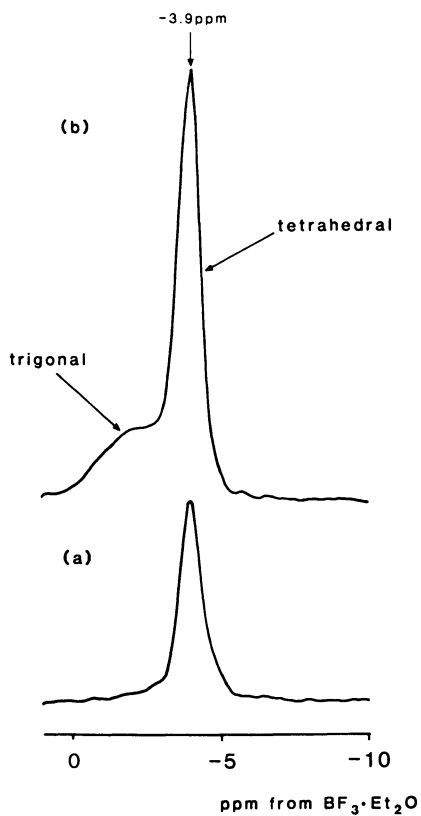
Figure 1. ^{11}B MAS NMR of boronated samples in the absolute intensity mode. (a) sample 1; (b) sample 7.

studies and chemical composition (26). Accordingly, the sharp signal at about -3.9 ppm in the boronated samples is assigned to tetrahedrally coordinated framework boron.

In order to check this conclusion further, a number of (Si,B)-ZSM-5 zeolites were prepared *via* direct synthesis. The crystals of B-ZSM-5 are all very well developed with the length of about 200 μm (Figure 2). In the as-synthesized (Si,B)-ZSM-5 the chemical shift of boron is -3.95 ppm with FWMH=94 Hz [Figure 3 (b)]. The signal is narrow and symmetric because of small quadrupole interactions of tetrahedral ^{11}B. The signals at -3.9 ppm in the spectra of boronated samples are also narrow (91 to 115 Hz, see Table I and Figure 1) and are clearly due to tetrahedrally coordinated framework boron.

The assignment of the second broad signal in Figure 1 (b) for sample 7 is less straightforward. One possibility is that it corresponds to three-coordinated boron. Trigonal boron is usually observed in dehydrated (Si,B)-ZSM-5 (2,4). Upon dehydration of the borosilicates with ZSM-5 structure containing framework *tetrahedral* boron atoms, the coordination of boron changes to trigonal and in completely dehydrated (Si,B)-ZSM-5 zeolites nearly all the boron exists as BO_3 units, although small amounts of tetrahedral sites were reported by Kessler et al. even in fully dehydrated samples (16). The ^{11}B spectrum of a dehydrated (Si,B)-ZSM-5 shows a typical quadrupolar pattern composed of two distinct peaks (both corresponding to *the same* kind of boron) with a centre of gravity at approximately -5 ppm. In partially dehydrated zeolites the quadrupolar pattern of trigonal boron is superposed onto a symmetric signal from tetra-hedrally coordinated boron. Moreover, upon complete *rehydratation* of borosilicate only one signal was always observed thus indicating that the lower symmetry units BO_3 transform fully to BO_4 groupings (2,4). Since our samples 1-9 were completely hydrated before the NMR spectra were recorded, but the broad signal is still present in most samples, we conclude that it comes from non-framework BO_3 units in amorphous species present within the zeolite channels. The broad signal was also found in the spectrum of Pyrex glass [see Figure 3 (a) and refs. 4, 23 and 26] and in the spectra of a variety of boron minerals (26).

Table II gives the absolute intensities of NMR signals and the concentration of tetrahedral and trigonal boron sites. The boron content of the samples was calculated from spectral intensities. It follows that the amounts of boron introduced into silicalite/ZSM-5 during hydrothermal treatment are relatively small, between 0.17-0.50 B atoms per unit cell. Of this amount up to 0.36 B/u.c. was found in tetrahedral coordination (sample 6, treated with 0.16M KOH for 42 h). There is also a systematic decrease of the (tetrahedral) boron line width from 115 to 91 kHz (Table I) with the increase alkalinity of the treatment.

Temperature of treatment is also important. The optimal temperature for the reinsertion of *aluminium* into ultrastable zeolite Y is 60-80°C (Hamdan, H.; Sulikowski, B.; Klinowski, J. J.Phys.Chem., (in
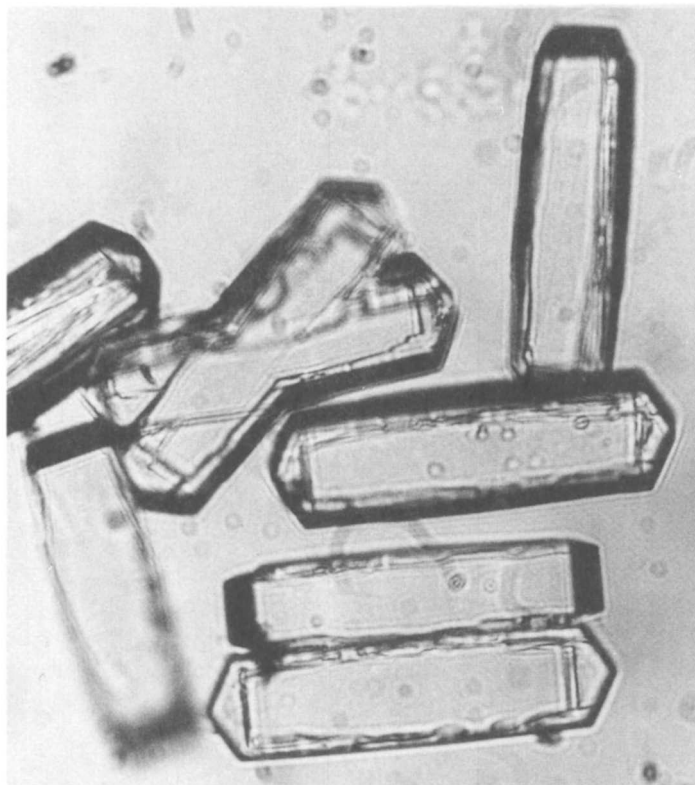
Figure 2. Optical microscope photograph of (Si,B)-ZSM-5 prepared by direct synthesis (14) and containing 2.2 boron atoms per unit cell. The crystals are remarkably well developed and uniform in size (ca. 200μm long), but are all intimately twinned.
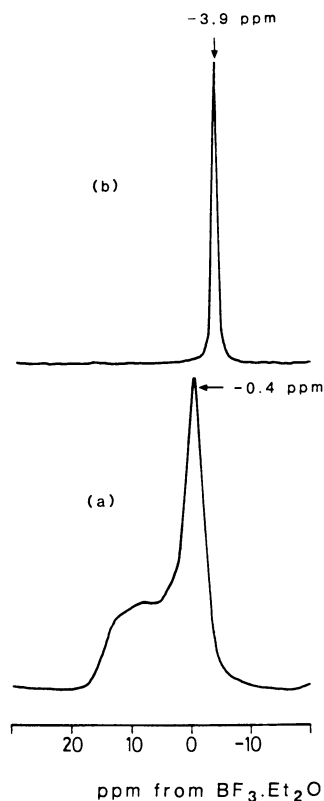
Figure 3. ^{11}B MAS NMR spectra (not in the absolute intensity mode). (a) Pyrex glass; (b) as-prepared (Si,B)-ZSM-5 (2.2 boron atoms per unit cell).

Table II.   Relative ^{11}B spectral intensities

Sample	Relative total intensity	Tetrahedral boron (%)	Trigonal boron (%)	Boron atoms per unit cell (tetrahedral)	(total)
1	77.4	100.0	-	0.17	0.17
2	94.8	75.9	24.1	0.16	0.21
3	177.1	47.8	52.2	0.19	0.40
4	184.0	40.7	59.3	0.17	0.41
5	192.6	38.7	61.3	0.17	0.43
6	222.3	72.7	27.3	0.36	0.50
7	209.7	65.1	34.9	0.31	0.47

press)). However, only traces of boron are present in silicalite treated at room temperature (samples 8 and 9), even though the alkalinity of the boron-ating solution was considerably higher than for other samples. Although unit cell parameters are a linear function of Si/Al (27,28,30) and Si/B ratios (29), the amounts of tetrahedral B are too small to be quantitatively monitored by XRD.

The position of the asymmetric stretch T-O-T vibration in infrared spectra of the framework vibration region (at about 1100 cm^{-1}) is a sensitive probe of Si/Al and Si/B ratios in aluminosilicates (27) or borosilicates (31). Infrared spectra of the boronated samples revealed a slight shift of the asymmetric stretch silicalite band at 1100 cm^{-1} to about 1098 cm^{-1}, consistent with the boron content calculated from NMR line intensities (Jansen et al. (31) reported a 10 cm^{-1} shift upon substitution of 4.1 boron atoms per unit cell of ZSM-5).

The crystallinity of the boronated samples was monitored by XRD. No changes in line intensities were generally observed, which indicates that crystallinity of samples is fully maintained during secondary synthesis. The framework remained intact even when silicalite was treated with concentrated 2M KOH (sample 9). Alkaline treatment with a strong base did, however, induce a change of symmetry. Both the starting silicalite and the sample treated with 0.5M KOH were monoclinic, while sample 9 (treated with 2M KOH) was orthorhombic (see Figure 4). Pure silicalite has 24 crystallographically non-equivalent sites for Si and is monoclinic at room temperature (19-21) (Williams, J.H.; Axon, S.A.; Klinowski, J. Chem. Phys. Lett. (submitted)). It undergoes a transition to an orthorhombic form (with 12 crystallographically non-equivalent sites for Si) at 82°C (20). In ZSM-5, which is nominally isostructural with silicalite, the temperature, T_t, at which the transition occurs depends on the level of "impurities" (i.e. species other than silica, such as the residual aluminium in the framework, cations, adsorbed water and organics). ZSM-5 with relatively high Al contents is orthorhombic at room temperature because the transition occurs at $T_t < 20°C$. The sample of silicalite treated with 2M (but *not* with 0.5M) base solution was orthorhombic, and it is clear that treatment with a strong base introduces sufficient amount of "impurities" for the phase transition to take place below the room temperature.

The disparity in size of the aluminate and the silicate tetrahedra must be the reason why, at least for some frameworks, the range of Si/Al ratios, and therefore the extent of the post-synthesis isomorphous substitution of Al for Si is limited (27). For boron, with the ionic radius of 0.23 Å as compared with 0.51 Å for aluminium, the disparity in size is even greater (2). Quantum chemical calculations predict that the tetrahedral coordination of aluminium is favoured in comparison with BO_4 groupings (32,33). An attempt to insert boron into the framework of ferrierite (34), a structurally related zeolite, was unsuccessful.
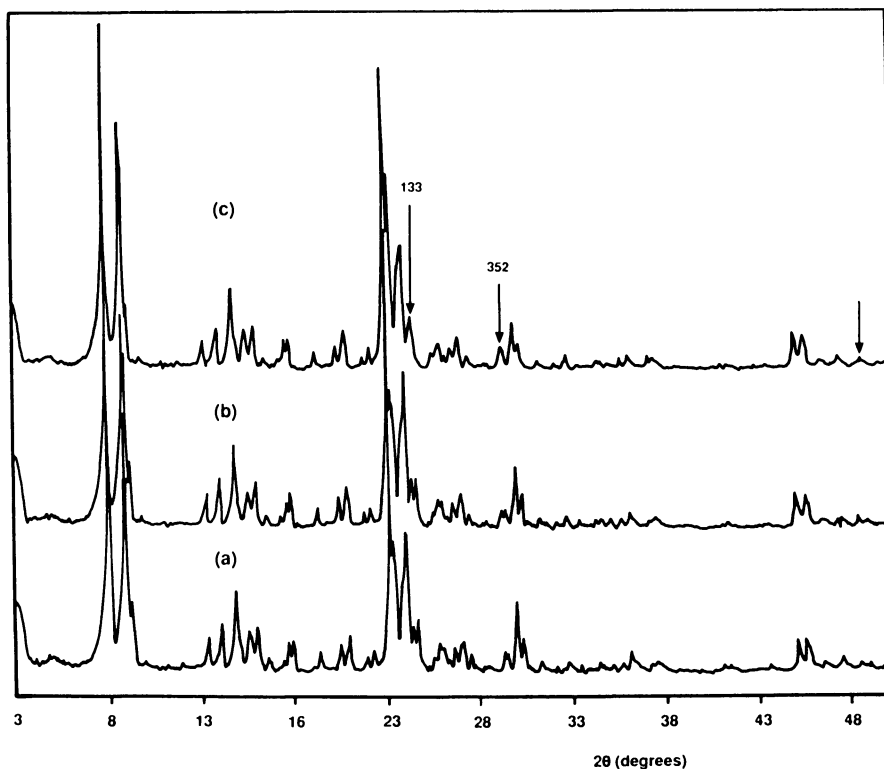
Figure 4. XRD patterns. (a) Parent silicalite; (b) after treatment with borate solution in 0.5M KOH (sample 8); (c) after treatment with borate solution in 2M KOH (sample 9). Arrows indicate peaks which split upon the orthorhombic/monoclinic phase transition.

Acknowledgment

Literature Cited

1.   Scholle, K.F.M.G.J.; Kentgens, A.P.M.; Veeman, W.S.; Frenken, P.; van der Velden, G.P.M. J. Phys. Chem., 1984, 88, 5.
2.   Scholle, K.F.M.G.J.; Veeman, W.S. Zeolites , 1985, 5, 118.
3.   Chu, C.T-W.; Chang, C.D. J. Phys. Chem., 1985, 89, 1569.
4.   Brunner, E.; Freude, D.; Hunger, M.; Pfeifer, H.; Reschetilowski, W.; Unger, B. Chem. Phys. Lett., 1988, 148, 226.
5.   Beyer, H.K.; Borbely, G. in New Developments in Zeolite Science and Technology , Proc. 7th Int. Zeolite Conf., (Murakami, Y.; Iijima, A.; Ward, J.W.; Eds.), Kodansha, Tokyo and Elsevier, Amsterdam, 1986, p. 867.
6.   Chu, C.T-W.; Kuehl, G.H.; Lago, R.M.; Chang, C.D. J. Catal., 1985, 93, 451.
7.   Kaeding, W.W.; Chu, C.; Young, L.B.; Butter, S.A. J. Catal., 1981, 69, 392.
8.   Howden, M.G. Zeolites , 1985, 5, 334.
9.   Borade, R.B.; Halgeri, A.B.; Prasada Rao, T.S.R. in ref. 5, p. 851.
10. Hölderich, W.; Eichborn, H.; Lehnert, R.; Marosi, L.; Mross, W.; Reinke, R.; Ruppel, W.; Schlimper, H. in Proc. 6th Int. Zeolite Conf., (Olson D.H.; Bisio, A.; Eds.), Butterworths, Guildford, 1984, p. 545.
11. Ratnasamy, P.; Hegde, S.G.; Chandwadkar, A.J. J.Catal., 1986, 102, 467.
12. Sulikowski, B.; Rakoczy, J.;Hamdan, H.; Klinowski, J. J.Chem.Soc.,Chem.Commun., 1987, 1542.
13. Xinsheng, L.; Thomas, J.M. J.Chem.Soc.,Chem.Commun., 1985, 1544; Thomas, J.M.; Xinsheng, L. J.Phys.Chem.,1986, 90, 4843.
14. Argauer, R.J.; Landolt, G.R. U.S.Pat. 3,702,886 (1972).
15. Grose, R.W.; Flanigen, E.M. U.S.Pat. 4,061,724 (1977).
16. Kessler, H.; Chezeau, J.M.; Guth, J.L.; Strub, H.; Coudurier, G. Zeolites , 1987, 7, 360.
17. Salentine, C.G. Inorg. Chem., 1983, 22, 3920.
18. Klinowski, J.; Man, P.P. Chem. Phys. Lett., 1988, 147, 581.
19. Fyfe, C.A.; Strobl, H.; Kokotailo, G.T.; Kennedy, G.J.; Barlow, G.E. J.Am. Chem. Soc., 1988, 110, 3373.
20. Klinowski, J.; Carpenter, T.A.; Gladden, L.F. Zeolites, 1987, 7, 73.
21. Endoh, A. Zeolites, 1988, 8, 250.
22. Appleman, D.E.; Clark, J.R. Amer. Mineral., 1965, 50, 1827.
23. Gabelica, Z.; Nagy, J.B.; Bodart, P.; Debras, G. Chem.Lett., 1984, 1059.
24. Bodart, P.; Nagy, J.B.; Gabelica, Z.; Derouane, E.G. Appl. Catal., 1986, 24, 315.
25. Coudurier, G.; Auroux, A.; Vedrine, J.C.; Farlee, R.D.; Abrams, L.; Shannon, R.D. J. Catal., 1987, 108, 1.

26. Turner, G.L.; Smith, K.A.; Kirkpatrick, R.J.; Oldfield, E. J.Magn.Reson., 1986, 67, 544.

27. Anderson, M.W.; Klinowski, J. J.Chem.Soc., Faraday Trans. I , 1986, 82, 1449.

28. Sohn, J.R.; DeCanio, S.J.; Lunsford, J.H.; O'Donnell, D.J. Zeolites, 1986, 6, 225.

29. Coudurier, G.; Vedrine, J.C. in ref. 5, p.643.

30. Kubelková, L.; Seidl, V.; Borbély, G.; Beyer, H.K. J.Chem.Soc., Faraday Trans. I, 1988, 84, 1447.

31. Jansen, J.C.; Biron, E.; van Bekkum, H. in Innovation in Zeolite Materials Science, Proc. Int. Symp., Nieuwpoort (Belgium), Sept. 13-17, 1987, (Grobet, P.J.; Mortier, W.J.; Vansant, E.F.; Schulz-Ekloff, G.; Eds.), Elsevier, Amsterdam, 1988, p.133.

32. Pelmentschikov, A.G.; Zhidomirov, G.M.; Khuroshvili, D.V.; Tsitsishvili, G.V. in Structure and Reactivity of Modified Zeolites, (Jacobs, P.A. et al.; Eds.), Elsevier, Amsterdam 1984, p.85.

33. Derouane, E.G.; Fripiat, J.G. J.Phys.Chem., 1987, 91, 145.

34. Gies, H.; Gunawardane, R.P. Zeolites, 1987, 7, 442.

Chapter 28

Isomorphous Substitution of Iron in the Faujasite Lattice

P. Ratnasamy, A. N. Kotasthane, V. P. Shiralkar,
A. Thangaraj, and S. Ganapathy

National Chemical Laboratory, Pune 411008, India

The crystalline faujasite Y zeolites containing
iron have been prepared. Evidence for the presence
of Fe in the lattice framework is obtained using
XRD, solid state MASNMR (^{29}Si, ^{27}Al and ^{13}C), ESR,
both framework and hydroxyl IR spectroscopies and
DTA. Lattice Fe leads to increase in the XRD unit
cell parameters. Spin echo experiments indicate that
the spin-spin relaxation time of ^{29}Si is shortened
due to the presence of Fe in the framework. CPMASNMR
spectra of ^{13}C atoms in tetraethylammonium-ZSM-20,
a zeolite with a faujasite-like structure, also
exhibit line broadening due to the interaction of
Fe^{3+} with the template ion. DTA studies indicate
that Fe-faujasites have lower thermal stability
than their Al-analogs. The (OH) vibration frequency
shifts from 3540 and 3630 to 3570 and 3643 cm^{-1}
respectively on isomorphous substitution of Al by Fe.
Relative changes in the intensity of the ESR peak
at g = 4.3 at low temperatures also support the
conclusion that iron can be inserted in the fauja-
site lattice positions.

Barrer[1] had reviewed the isomorphous substitution
of Al or Si in the zeolite framework by other
elements such as Ga, Be, B, Fe, Cr, P and Mg. The
substitution of Al by Fe in the ZSM-5 framework is

now well established ($\underline{2-5}$). In 1972, McNicol and
Pott ($\underline{6}$) showed unambiguously that iron impurities in
faujasite zeolites can occupy substitutional lattice
positions. From EPR studies of the Fe^{3+} impurity in
NH_4-faujasite, Derouane et al. ($\underline{7}$) showed that iron
can be simultaneously present in three forms : Fe^{3+}
species in the aluminosilicate framework, Fe^{3+} ions
acting as counterions and Fe_3O_4 or another Fe^{3+}
compound with strong exchange spin-spin interactions,
precipitated on the zeolite. In both the studies, the
iron occurred as an impurity in the zeolite and no
deliberate attempt was made to introduce Fe^{3+} in
lattice positions. Szostak and Thomas ($\underline{8}$) were the
first to deliberately synthesise a condensed phase
zeolite, sodalite, with significant quantities of
iron in the framework ($SiO_2/Fe_2O_3 = 6-30$).

   In the present paper, we report the synthesis of
NaY wherein Al^{3+} has been partially replaced by Fe^{3+}.
Evidence from a variety of techniques including solid
state NMR, IR and ESR spectroscopies as well as
DTA/TG support the conclusion that a significant part
of iron is isomorphously substituted in the lattice
parameter.

EXPERIMENTAL

A: Synthesis of zeolites
The hydrothermal synthesis of the faujasites was
carried out at 373 K in stainless steel autoclaves in
static condition. The faujasites were synthesised
using seeds' of an aluminium ferri-silicate gel. 16
g of the homogeneous seed slurry (aged for 24 hrs at
room temperature) was added to an aqueous gel mixture
containing sodium silicate (86.8 g), sodium aluminate
(5.6 g), aluminium sulphate (7.5 g) and ferric
sulphate (2.1 g). The whole gel mixture was
transferred to an autoclave and stirred for one hr to
get a homogeneous gel. The autoclave was then placed

in an air oven at 373 K and the gel is crystallized
for 11 hrs. The autoclave is then quenched under cold
water to room temperature. The crystallized solid is
filtered, washed and dried at 393 K for 6 hrs. The
zeolites containing varying amounts of Fe^{3+} were
synthesised by changing appropriately the quantities
of aluminium sulphate and ferric sulphate but keeping
the seed slurry concentration essentially the same.

B: Zeolite characterisation

The crystalline phase identification was carried out
by XRD (Philips, PW-1710). The chemical analyses were
performed by a combination of wet chemical, atomic
absorption (Hitachi Z-800) and ICP (Jobin Yuon-JY
VHR) methods. The zeolites were further characterised
by scanning electron microscopy (Cambridge), thermal
analysis (Netzsch, Model STA 490), FTIR (Nicolet 60
SXB) and ESR (Bruker E-2000) spectroscopies. The
FTIR spectra were recorded with the Spectratech
diffuse reflectance attachment. The solid state **MAS**
(for ^{29}Si and ^{27}Al) and CPMAS (for ^{13}C) spectra were
recorded at ambient temperature using a Bruker MSL-
300 FT-NMR spectrometer. For ^{29}Si and ^{27}Al Bloch
decays were averaged 2400 times before Fourier
transformation to get spectra with sufficient S/N.
While acquiring ^{29}Si spectra, a recycle time of 3
sec. was found to be sufficient to give fully relaxed
spectra. MAS was kept at 3.5 KHz. ^{29}Si spectra were
measured   using TMS as the primary reference while
an aqueous solution of $AlCl_3$ provided the reference
peak for ^{27}Al. Spin-echo experiments were carried out
under MAS using the following pulse sequence ($\pi/2)_x - \tau$
($\pi)_y$ with quadrature phase cycling. The second half
of the spin-echo was Fourier transformed, and the
signal intensity decay as a function of   gave T_2
of ^{29}Si.   Adsorption of H_2O and benzene on the
zeolites was measured gravimetrically (298 K, P/P_o =
0.5) using a McBain balance in a conventional BET

system. Five zeolite samples (A-E) were investigated
in this study. Sample A was Linde NaY. Samples B-E
were ferrisilicates. Samples B, C and D were off-
white while sample E was dark yellow indicating the
presence of at least a portion of Fe in non-lattice
position. Sample F was obtained by impregnation of
sample A with Fe_2O_3 and was dark brown in colour. It
contained 3.4% (wt.) of Fe_2O_3.

RESULTS AND DISCUSSION

X-ray diffraction

The chemical composition of Samples A-E is given in
Table I.

Table I. Chemical composition of samples A-E (%
wt.)

Sample	LOI	SiO_2	Al_2O_3	Na_2O	Fe_2O_3
A	28	63.6	23.3	11.9	0.47
B	27	64.2	22.0	12.6	1.06
C	26	63.0	21.3	12.6	3.0
D	26	62.1	19.2	13.4	5.3
E	26	66.0	18.8	6.7	8.6

LOI = Loss on ignition at 1073 K, % wt.

For samples A-C, the lower values of Na/Al indicate
the presence of hydronium ions as charge compensating
ions. The samples were crystalline and all the lines
could be indexed assuming the structure of Linde NaY
(Sample A). The high crystallinity of these samples
is also borne out by their similar values for the
adsorption of H_2O and benzene (30.3, 29.3, 29.3 and
28 wt. % for the adsorption of H_2O and 24.9, 26.6,
24.8 and 22.9 wt.% for the adsorption of benzene on
samples A-D, respectively). The unit cell values,
calculated from the observed XRD patterns, are found
to decrease with increasing Fe content in the solid
(Figure 1, line A). If there had been no Fe
incorporation in the faujasite lattice and the

crystalline framework consisted solely of SiO_4 and AlO_4 tetrahedra, then the unit cell values would have followed line B of Fig. 1. The latter was calculated from the Breck and Flanigen equation

$$\frac{SiO_2}{Al_2O_3} = 2 \times \frac{2.586 - a_o}{a_o - 2.419}$$

Values of (SiO_2/Al_2O_3) were taken from solid state NMR data (presented later). The difference between lines A and B (indicating unit cell expansion) is due to the incorporation of Fe in the lattice framework. However, if all the Fe in the solids were to occupy lattice positions, the unit cell parameters would have been larger than those observed (line A) and would have increased with Fe content. The observed intermediate position of line A leads to the conclusion that only a fraction of Fe is in the faujasite lattice, the balance occupying non-framework positions. Thus, while the observed a_o values are higher than those calculated if no isomorphous substitution had taken place (line B) they are still lower than those expected if all the Fe in the solid occupy lattice positions. The negative slope of line A is due to the SiO_2/M_2O_3 (M = Al + Fe) in the lattice increasing from sample A to sample E. The increasing values of (SiO_2/M_2O_3) in the lattice in samples B through E are also borne out by IR and NMR data (see Table III).

Thermal analysis

The relative crystalline stability of these materials was evaluated by DTA/TG (Fig.2). It is seen that the exothermic peak (indicating the collapse of the faujasite lattice) around 1133 K in NaY(Sample A) progressively shifts to lower temperataures with increasing iron content in the zeolite reaching 1033 K for Sample E indicating that the presence of iron reduces the thermal stability of the lattice
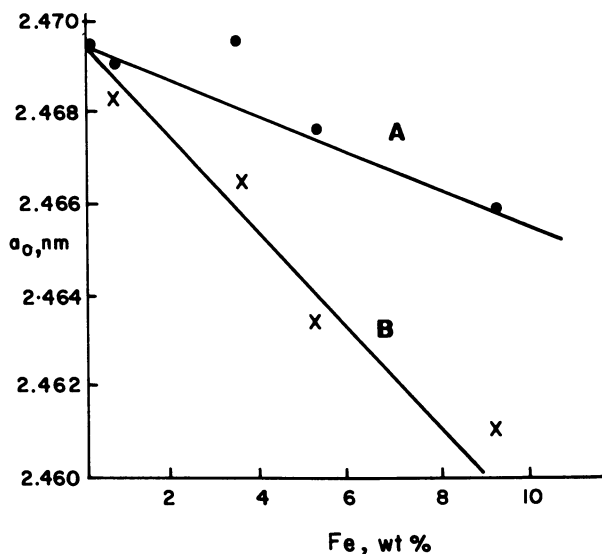
Figure 1. A : Variation of unit cell parameter, a_O with Fe content; B : Calculated values of a_O if no Fe is present in the lattice.
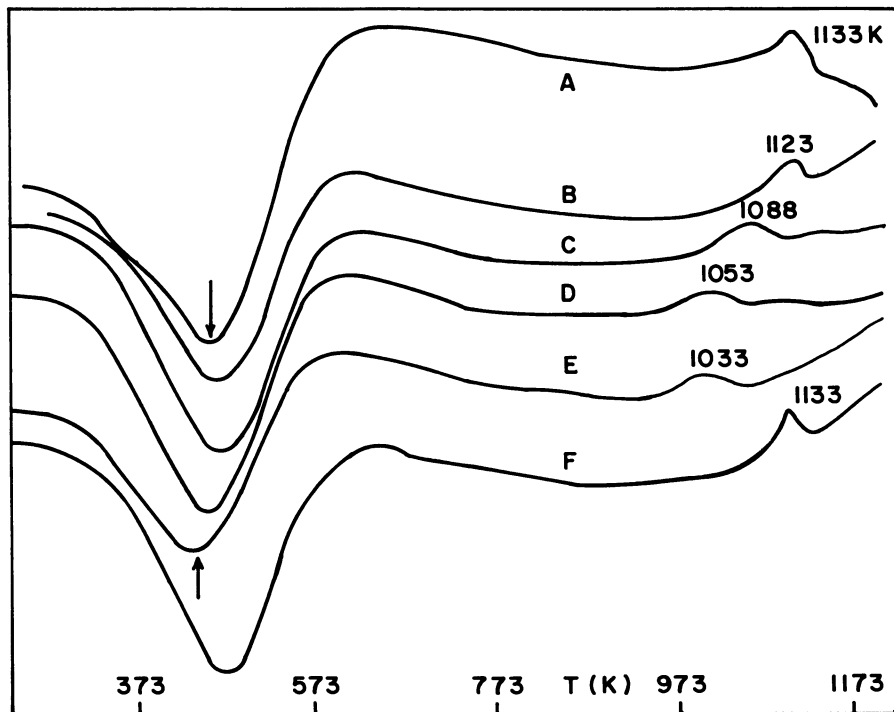
Figure 2. DTA plots of samples A–F (curves A–F, respectively).

framework. The lower thermal stability of the ZSM-5 framework containing Fe^{3+} in lattice positions (compared to the Al analog) is already known (3). A similar observation in the faujasite system (Fig.2) suggests that the observed lower thermal stability of the crystalline lattice may be caused by the presence of iron in it. Iron in non-lattice positions (as Fe_3O_4, for example) does not destabilise the lattice. The exothermic peak for sample F (which has a Fe content similar to Sample C but wherein all the Fe is in non-lattice positions) occurs at the same value as for Sample A (Fig. 2).

IR spectroscopy

The values of some major absorption bands in the framework IR spectra of samples A and C-E are compiled in Table II. On progressive introduction of Fe in the zeolite, the bands at 1020 and 1150 cm^{-1} shift to lower values (Table II). These shifts, due to the asymmetric stretching vibration of T—O—(T = Si, Al or Fe) to lower wavenumbers are consistent with the expected shift when the heavier Fe atom replces Al in the lattice framework (5). The enhancement of the band around 775 cm^{-1} on going from Sample A to E suggests that the SiO_2/M_2O_3 (M = Al + Fe) ratio increases from Sample A to E. This conclusion was also made from the XRD data (see earlier section) and is also supported by the NMR results (see later). The enhanced intensity of this band at higher values of SiO_2/M_2O_3 in the faujasite system has already been reported (5).

The hydroxyl spectrum of the protonic forms (obtained by repeated ammonium exchange with 5N NH_4Cl and calcination at 673 K for 6 hr) of samples A, C and D (curves A-C, Fig.3, respectively) contain bands around 3450, 3630 and 3740 cm^{-1}. The former two had been assigned to acidic, bridging OH groups while the
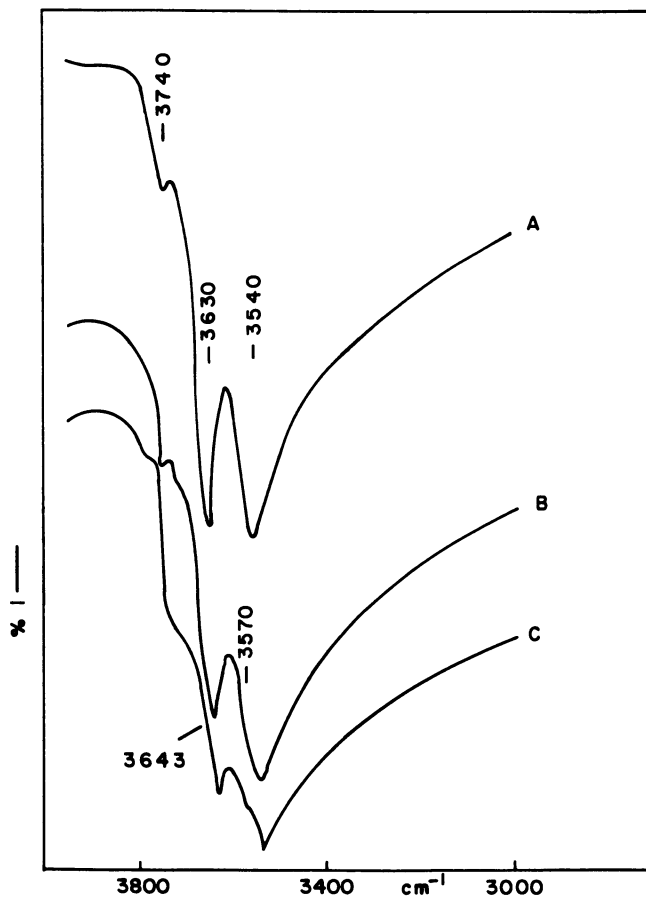
Figure 3.   Hydroxyl vibrations of samples A, C and D
(curves A-C, respectively).

last   is   attributed   to   terminal   Si-OH   or
extra framework silica gel ($\underline{9}$). In samples containing
iron (curves B and C), in addition to the above
bands, shoulders are seen at 3570 and 3643 cm^{-1},
respectively (Fig. 6). In the pentasil system, Chu
and Chang ($\underline{10}$) as well as Kustov et al. ($\underline{11}$) had
observed that when Al is isomorphously replaced by
Fe, the hydroxyl band is shifted from 3610 to 3630
cm^{-1}.   The observed shoulders (Fig. 6) at 3570 and
3643 cm^{-1} are assigned to (OH) vibrations of Si(OH)Fe
groups in the faujasite lattice and constitute
additional evidence for the presence of Fe in the
lattice framework.

Table II.   IR spectra of zeolite samples

Sample	Frequency(cm^{-1}) of band							
A	380	455	500	585	725	775	1020	1150
C	380	460	505	585	715	775	1010	1130
D	385	455	500	575	715	790	1010	1120
E	380	455	505	575	720	790	1010	1120

ESR spectroscopy

While an ESR signal at g = 4.3 cannot be used to
confirm the presence of Fe^{3+} in zeolite lattice posi-
tions ($\underline{12}$), the observation of such a signal is a
necessary consequence of such a presence and may,
hence, lend additional support to any postulate of
isomorphous substitution of Al by Fe.   The ESR
spectra of the samples (Fig. 4) reveal two main
signals at g = 2.0 (broad) and 4.3 (narrow),
respectively.   While the former is attributed to non-
framework, octahedrally-coordinated Fe^{3+}, the latter
is assigned to tetrahedral Fe^{3+} ($\underline{6,7}$) , possibly in
lattice positions. The larger temperature dependence
of the signal at g = 4.3 compared to that of g = 2.0
(Fig. 4) as well as the relative insensitivity of the

former   to   oxidation-reduction   treatments   suggest
that it arises from Fe^{3+} ions in tetrahedral lattice
location. On extraction with oxalic acid, the greater
reduction   in   the   intensity of the g = 2.0 signal
compared   to   at g = 4.3 further supports   the   above
conclusions.

NMR spectroscopy

The ^{27}Al MASNMR spectra of samples A-F revealed the
presence   of   only tetrahedrally coordinated Al;   no
Al_{oct} could be detected indicating that all the Al in
the solid are in lattice positions. Signals due   to
octahedral Al appeared only on hydrothermal treatment
above 773 K. The half band width of the Al_{tet} line of
samples B-E were broader than that of Sample A.   In
addition, spinning side band (SSB) patterns were also
present.

The ^{29}Si spectra of samples A,C and F are given in
Fig.5.   The spectra of the samples B,D and E, were
similar to that of sample C. The NaY system (Sample
A) exhibits 5 peaks which can be assigned to Si(4Al),
Si(3Al), Si(2Al), Si(1Al) and Si(0Al) in agreement
with reported observations (3). The Si/Al ratio
calculated from NMR intensities (14) agreed well with
that   determined by chemical analysis (Table III),
confirming that all the Si and Al are in the lattice
framework. As the Fe concentration is increased, the
peak   at   -84 ppm due to Si(4Al) disappears and the
relative   intensity of the Si(3Al) peak at -89 ppm
(vis-a-vis Si(0Al) peak, for example) decreases
(compare curves A and C in Fig. 5). That these two
effects are due to the substitution of Fe for Al and
not due to occluded iron is revealed on comparing the
spectra of samples C and F (Fig.5). The presence of
Fe_2O_3 in the faujasite cavities of sample F does not
affect   the   relative intensities of Si(nAl) lines
(compare   curves   A and F). An attempt was   made   to
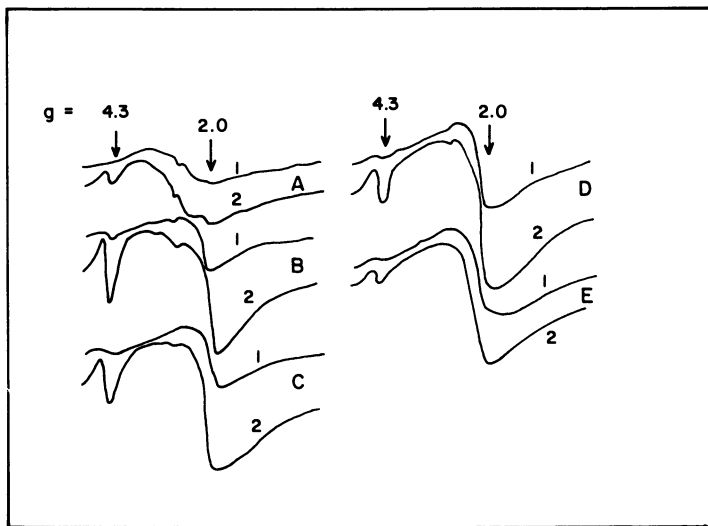
Figure 4.   ESR spectra of samples A-E (curves A-E, respectively) : curves 1 and 2 denote spectra recorded at 198 and 135 K, respectively.
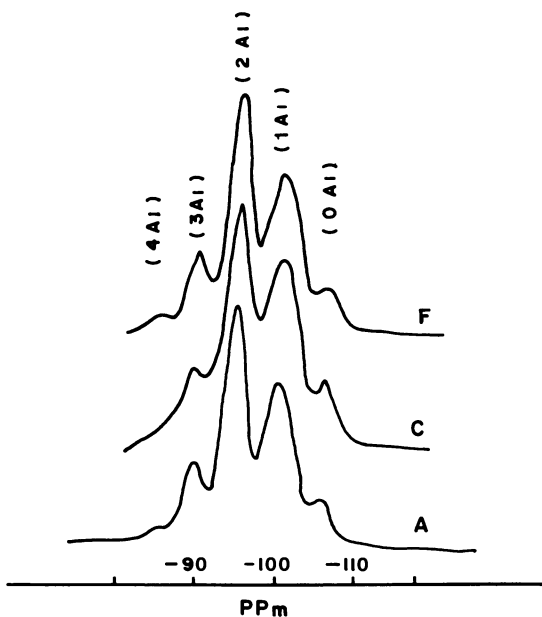
Figure 5. ^{29}Si MASNMR spectra of samples A, C and F (curves A,C and F).

estimate the amount of Fe^{3+} in lattice positions. From the integrated intensities of all the lines due to ^{29}Si the value of Si/(Al+Fe) in the lattice was first calculated (Table III). Assuming that the values of Si/Al from chemical analysis is equal to that in the lattice (since no octahedral Al or amorphous SiO_2 could be detected), Si/Fe ratios in the lattice were calculated (Table III). As the iron concentration increases two additional effects are observed : (1) The line width of the peaks at -99 and -105 ppm, due to Si(1Al) and Si(0Al), respectively, increases; (2) The SSB pattern becomes more pronounced. The origin of the SSB can be traced to the bulk paramagnetic susceptibility of the iron oxide particles in the zeolite pores (15). The ^{13}C CPMASNMR spectra of tetraethyl─

Table III. Comparison of composition data
from chemical analysis and NMR spectroscopy

Sample	$(Si/Al)_C$	$(Si/Al+Fe)_C$	$(Si/Al+Fe)_N$	$(Si/Fe)_N$
A	2.31	2.29	2.32	─
B	2.48	2.32	2.48	─
C	2.52	2.31	2.48	156.2
D	2.76	2.34	2.48	24.5
E	2.98	2.30	2.54	17.2
F	2.52	2.31	2.32	─

Note : The subscripts C and N, refer to data from chemical analysis (Table 1), and NMR spectroscopy, respectively.

ammonium ion in the ZSM-20 system, a zeolite with a faujasite-like crystalline structure, are shown in Fig.6. In the ferrisilicate analog of ZSM-20 (Curve B) the line-broadening is more pronounced for the methylene carbon (35 to 210 Hz) than for the methyl carbon (35 to 140 Hz) consistent with the closer interaction (through the N atom) of the former with

lattice Fe^{3+} further supporting the feasibility of iron substitution in the faujasite lattice. In order to differentiate the inhomogeneous line broadening due to magnetic coupling between Si and Fe, we carried out the Carr-Purcell-Meiboom-Gill (CPMG) version of the Hahn spin echo experiment ([16]). In this experiment the 180° pulse refocusses the inhomogeneity effects contributing to the line broadening. Thereafter, any contribution to Si linewidth due to susceptibility effects (arising from occluded Fe_2O_3 or Fe_3O_4, for example) will be refocussed and the decay of the ^{29}Si spin-echoes will be determined only by spin-spin relaxation of Si nuclei. Fig.7 presents the decay of the spin-echo Si-signal intensity for samples A and D. The T_2 for sample D was only 2.2 compared to 7.8 msecs for sample A. This lower value comes primarily from the Si-Fe nuclear-electron coupling and provides conclusive evidence that Fe is in the framework.

CONCLUSIONS

Isomorphous substitution of iron in the faujasite lattice is indicated by the following facts: (1) An increase in the unit cell parameter, a_o, with increasing Fe concentration (XRD); (2) the lower thermal stability of the crystalline structure of samples B–E, (DTA); (3) The shift to lower wavenumbers of the framework asymmetric stretching frequencies (IR); (4) The observation of Si(OH)Fe groups at 3570 and 3643 cm^{-1} (IR); (5) the detection of the ESR signal at g = 4.3 and its insensitivity to oxidation-reduction treatments as well as extraction with oxalic acid and (6) NMR line-broadening (^{29}Si and ^{13}C), disappearance of the Si(4Al) line as well as an increase in the spin-spin relaxation time, T_2, on incorporation of iron.
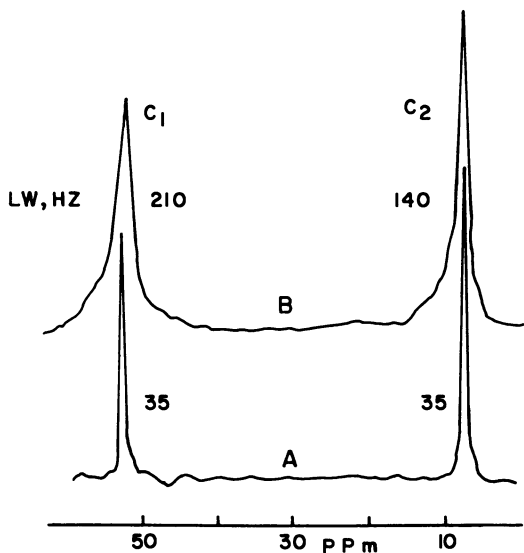
Figure 6. ^{13}C CPMASNMR spectra of alumino- and ferri-silicate ZSM-20 (curves A and B). C_1 and C_2 refer to the methylene and methyl carbon atoms, respectively.
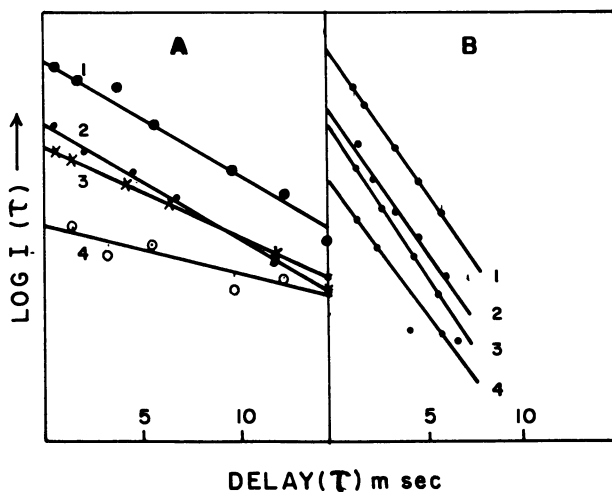
Figure 7. Spin-echo decay of ^{29}Si signals from samples A and D (A and B). Lines 1-4 refer to signals from Si (3Al), Si (2Al), Si (1Al) and Si (0Al), respectively.

Literature cited

1. Barrer, R.M. Hydrothermal chemistry of zeolites, Academic Press, London, 1982, p. 251.
2. Kovenhowen, H.W. and Stork, W.H.J., U.S. Patent, 3 208 395.
3. Ratnasamy, P., Borade, R.B, Sivasanker, S., Shiralkar, V.P. and Hegde, S. G. Proc. of Int. Symp. on Zeolite Catalysts, Siofok (Hungary), 1985, p. 137.
4. Ball, W.J., Dwyer, J., Garforth, A.A. and Smith, W.J., Studies in surface scince and catalysis, 1986, 28, 137.
5. Szostak, R. and Thomas, T.L., J.Catal., 1986, 100, 555.
6. McNicol, B.D. and Pott, G.T., J.Catal., 1972, 25, 223.
7. Derouane, E.G. Mestdagh, M. and Vielvoye, L., J.Catal., 1974, 33, 169.
8. Szostak, R. and Thomas, T.L., J.Chem.Soc., Chem. Commun., 1986, 113.
9. Ward, J.W., J.Catal., 1967, 9, 225.
10. Chu, C.T.W. and Chang, C.D. J.Phys.Chem., 1985, 89, 1569.
11. Kustov, L.M. Kazansky, V.B. and Ratnasamy, P., Zeolites, 1987, 7, 79.
12. Kucherov, A.V. and Slinkin, A.A., Zeolites, 1988, 8, 110.
13. Engelhardt, G., Attenburg, W., Hoebbel, D. and Wieker, W., Z.Anorg. Allg.Chemie., 1977, 437, 249.
14. Engelhardt, G., Lohse, U., Lippmaa, E., Tarmak, M. and Magi, M., Z.Anorg.Allg.Chemie, 1981 482., 49.
15. Oldfield, E., Kinsey, R.A., Smith, K.A., Nicholas, J.A. and Kirkpatrick, R.J., J.Mag. Resonance, 1983, 51, 325.
16. Slichter, C.P. Principles of magnetic resonance, 1980, Springer-Verlag, p. 254.

Chapter 29

Zeolite Chemistry

Substitution of Iron or Titanium for Aluminum in Zeolites via Reaction with the Respective Ammonium Fluoride Salts

Gary W. Skeels and Edith M. Flanigen

Union Carbide Corporation, Tarrytown Technical Center, Tarrytown, NY 10509

A novel chemistry is described for the substitution of iron and/or titanium for aluminum in a number of zeolite frameworks. The reaction of zeolites with an aqueous solution of the ammonium fluoride salt of the metal under relatively mild conditions yields zeolites that are dealuminated, contain substantial quantities of either iron or titanium and are essentially free of defect structure.

The reaction of zeolites with an aqueous fluorosilicate solution under relatively mild conditions has been shown to yield zeolites with silicon enriched frameworks which are essentially free of structural defects (1). As a result of the treatment, the framework topologies of the respective zeolites are relatively unchanged, but the zeolite compositions which are produced either do not occur naturally or are not synthesized directly. The fluorosilicate treatment process has been termed "Secondary Synthesis".

Breck has reviewed the early literature where Ga^{3+}, P^{5+}, and Ge^{4+} were potentially incorporated into a few zeolite structures via a primary synthesis route (2). Evidence has also been presented to show that the small amounts of Fe^{3+}, typically present in both natural and synthetic zeolites, are located in framework tetrahedral positions (3). A more recent review of "isomorphic substitution" in zeolites, via primary synthesis methods, speculates on the potential impact of such substitutions on catalysis (4). The vast majority of work has been related to the high silica zeolites, particularly of the ZSM-5 type. Another approach to substitution of metal atoms into the open frameworks of zeolite structures has been to replace the typical silica alumina gel with gels containing other metal atoms. This concept has resulted in numerous unique molecular sieve compositions containing: aluminum and phosphorus[5]; silicon, aluminum and phosphorus (6); and with

NOTE: This chapter is part 6 in a series.

other metal atoms present in the framework with the aluminum and phosphorus as well (7).

The desire to synthesize molecular sieve compositions containing other than the typical silicon and aluminum atoms is evidenced by the large number of efforts, primarily in the primary synthesis area. The Secondary Synthesis process has now been extended to include substitution of both Fe^{3+} and Ti^{4+} into the frameworks of a number of zeolites. This paper will describe substitution of iron or titanium ions into the frameworks of zeolites Y, L, W, mordenite, ZSM-5 and LZ-202. Zeolites Y, L, W and mordenite were obtained from Union Carbide Corporation. Zeolon, a synthetic mordenite, was obtained from The Norton Company. ZSM-5 was synthesized according to the procedures described by Argauer et al., (8). LZ-202 is an omega type zeolite, synthesized without the organic template (9).

EXPERIMENTAL:

Typically, the ammonium or hydronium form of the zeolite is slurried in water and reacted with the requisite amount of the ammonium fluoride salt of either iron or titanium. Given the sparingly soluble nature of ammonium fluotitanate, the $(NH_4)_2TiF_6$ can be added to the zeolite slurry in slurry form, or directly as salt. Alternatively, the iron may be added to the zeolite slurry as a slurry of the ammonium fluoride salt crystals in water, or the FeF_3 crystals can be mixed with a water solution of ammonium fluoride or ammonium bifluoride, such that the composition of the treatment solution contains the stoichiometry of the ammonium iron fluoride salt, $(NH_4)_3FeF_6$. The $(NH_4)_3FeF_6$ crystals can also be added directly to the zeolite slurry. The amount of either metal ammonium fluoride salt added during the reaction is determined by the desired product composition and the anticipated completeness of the reaction.

Preferred conditions for the reaction of the zeolite with the metal ammonium fluoride are as follows. A zeolite-water slurry containing about 10-25 gm of zeolite per 100 cm^3 of water is preheated to 75-95°C. When substituting Ti, the titanium salt is added to the zeolite as a water slurry containing finely divided crystals, 10 gm of $(NH_4)_2TiF_6$ per 100 cm^3 of water. With iron substitution, the iron salt, when added as $(NH_4)_3FeF_6$, is added from a 10 wt.% solution of the salt in water. Alternatively, FeF_3 can be added to a solution of NH_4HF_2 or NH_4F such that the stoichiometry of fluorine (F_2) to Fe^{3+} is 3.0 and the total amount of salt in solution is about 10 wt.%. The addition rate of the metal ammonium fluoride salt to the zeolite slurry is about 0.005 moles of the metal ion per minute per mole of aluminum in the zeolite.

Following the metal ammonium fluoride salt addition, the reaction mixture is digested at 75-95°C for from 30 minutes to 48 hours.

The reaction conditions for the samples contained in this report are shown in Table 1. The washed products, together with the starting zeolites, were analyzed by X-ray powder diffraction and infrared spectroscopy; the chemical composition (SiO_2,

Table 1.   Experimental Conditions for the Substitution of Iron or Titanium for Aluminum in Selected Zeolites

Parameter	A	B	C	D	E	F
Sample Number	A	B	C	D	E	F
Zeolite Type	NH_4Y	NH_4 LZ-202	NH_4ZSM-5	ZSM-5	NH_4L	NH_4W
Product Designation	LZ-225	LZ-247	LZ-241	LZ-241	LZ-229	LZ-230
% Replacement of Al	50	50	50	100	100	50
Zeolite Slurry, wt.%	20	20	15	15	10	25
Addition Temp. Deg. C	75	95	95	95	95	95
Treatment Salt (s)	$(NH_4)_2TiF_6$	$(NH_4)_2TiF_6$	$(NH_4)_2TiF_6$	$(NH_4)_2TiF_6$	$(NH_4)_2TiF_6$	$(NH_4)_2TiF_6$
Wt.% salt in Solution	15	10	—	15	—	—
Addition Rate	—	—	instant	—	instant	instant
Mol. M/mol. Al/min.	0.005	0.010	—	0.010	—	—
Digestion Temp. Deg. C	95	95	100	100	100	100
Digestion Time, Hours	3 (Under N_2)	1	28	1.5	0.5	0.5

Parameter	G	H	I	J	K	L	M
Sample Number	G	H	I	J	K	L	M
Zeolite Type	NH_4Y	H_3O-Zeolon	H_3O-Mor.	H_3O-Mor.	H_3O-Mor.	H_3O-Mor.	NH_4L
Product Designation	LZ-224	LZ-226	LZ-226	LZ-226	LZ-226	LZ-226	LZ-228
% Replacement of Al	55	25	50	75	75	50	75
Zeolite Slurry, wt.%	10	5	15	15	15	15	10
Addition Temp. Deg. C	75	75	75	75	75	75	95
Treatment Salt (s)	$(NH_4)_3FeF_6$	$(NH_4)_3FeF_6$	FeF_3, NH_4HF_2	FeF_3, NH_4HF_2	FeF_3, NH_4HF_2	FeF_3, NH_4HF_2	$(NH_4)_3FeF_6$
Wt.% salt in Solution	—	—	10	10	10	10	10
Addition Rate	instant	instant	—	—	—	—	—
Mol. M/mol. Al/min.	—	—	0.005	0.005	0.005	0.005	0.005
Digestion Temp. Deg. C	75	100	75	75	75	75	100
Digestion Time, Hours	48 (Under N_2)	48 (Under N_2)	0.5	0.5	0.5	0.5	0.5 (Under N_2)

Al_2O_3, Fe_2O_3, TiO_2, M_2O) was determined by standard wet chemical methods. The relative X-ray crystallinity was obtained from the powder diffraction patterns by comparison of the peak areas of the treated zeolite with the starting zeolite in the region 6°-40°, 2θ, CuKd. The standard KBr wafer technique was used to measure the IR spectrum in the framework region, 200-1300 cm^{-1}. The method described previously (1) was used to measure the IR spectrum in the hydroxyl region. Adsorption capacity measurements were made on the various product samples and the starting materials by standard McBain-Bakr procedures: equilibrium oxygen capacity (wt.%) at 100 torr and 90K; equilibrium water capacity (wt.%) at 4.6 torr and 298K. A number of the samples were examined by standard Scanning Electron Microscopy techniques including EDAX, in order to determine whether any new phases were formed and deposited on the zeolite crystals and whether the substituting metal was evenly distributed throughout the zeolite crystals. The substituted zeolites were tested in n-butane cracking and their activity values (k_A) compared with those of the starting zeolites following procedures established by Rastelli et al. (10).

RESULTS AND DISCUSSION

Chemical analyses and physical property measurements made on the starting materials and the products of the ammonium fluotitanate reactions are shown in Table 2. The analytical data for the products of the iron ammonium fluoride reaction are shown in Table 3. Following treatment, the various zeolite products contained up to 16.1 wt.% TiO_2 in the zeolites treated with ammonium fluotitanate, and up to 16.9 wt.% Fe_2O_3 in the zeolites treated with ammonium iron fluoride. X-ray powder diffraction intensity is decreased in the substituted products, but retention of oxygen and water adsorption capacity indicates that pore volume has been retained. No extraneous peaks due to other crystalline phases were observed in the X-ray powder diffraction patterns of well washed products. There were no changes in the background of the patterns that would indicate the presence of amorphous material. The reduced intensity of the diffraction peaks can be explained by absorption of X-rays by the heavier and larger titanium or iron atoms. By way of comparison, lanthanum and silver exchanged Y show significant peak intensity and peak area losses proportional to the degree of lanthanum and silver ion exchange, due to X-ray absorption by the heavy exchange ion and unrelated to crystallographic degradation of the zeolite. Since the X-ray powder patterns showed all of the requisite reflections and no increase in the background attributable to amorphous material, the basic structure is maintained. Adsorption capacity for both oxygen and water are little changed showing retention of micropore volume. Retention of the basic structure and micropore volume are evidence that the loss in X-ray peak intensity is not due to crystal degradation. Since the cation equivalent (M^+/Al) is close to unity, except as will be noted later, it is logical to assume that all of the aluminum is in the framework.
Substitution of the smaller Si atom for Al in the zeolite

Table 2. Chemical Analyses and Physical Property Measurements of the Starting Zeolites and the Products of the Ammonium Titanium Fluoride Reaction

Zeolite Designation Sample	NH4-Y	Y LZ-225 A	LZ-202 NH4LZ-202	LZ-202 LZ-247 B	NH4 ZSM-5	ZSM-5 LZ-241 C	ZSM-5	ZSM-5 LZ-241 D	NH4L	L LZ-229 E	NH4 W	W LZ-230 F
$(NH_4)_2O$, wt.%	9.8	5.6	8.8	6.4	2.0	1.2	—	1.2	7.9	6.8	10.5	7.8
Al_2O_3, wt.%	21.9	14.9	18.7	13.3	5.1	2.6	3.4	2.6	19.8	15.7	30.8	16.7
TiO_2, wt.%	—	11.4	—	11.4	—	8.9	—	1.3	—	7.2	—	16.1
SiO_2, wt.%	65.7	66.6	73.0	69.0	93.1	88.3	95.5	94.7	67.8	68.3	67.3	58.9
Fluoride, wt.%	—	0.10	0	0.6	—	0.02	—	0.09	—	0.24	—	0.14
Na+K/Al	0.17	0.18	0.92	0	0.02	—	0.49	0.09	0.12	0.13	0.02	0.01
NH_4^+/Al	0.88	0.73	0.92	0.94	0.75	0.91	—	0.91	0.78	0.85	0.68	0.92
Cation Equivalent, M^+/Al	1.05	0.91		0.94	0.77	0.91	0.49	1.00	0.90	0.98	0.70	0.93
SiO_2/Al_2O_3	5.09	7.58	6.62	8.82	31.05	57.65	47.00	62.04	5.80	7.37	3.71	5.99
X-Ray Crystallinity, %I/Is. area	100	55	100	55	100	85	100	103	100	74	100	38
Framework Infrared: Asymmetric Stretch, cm^{-1}	1020	1032	1038	1042	1098	1103	1102	1103	1100	1104	1023	1035
Symmetric Stretch, cm^{-1}	786	795	815	811	794	797	798	800	770	774	783	784
Hydroxyl Region Infrared: Absolute Absorbance, 3710 cm^{-1}	0.038	0.114	0.114	0.210	0.191	0.143	0.243	0.108	0.058	0.167	0.053	0.269
Defect Structure, "z"	0.016	0.048	0.048	0.089	0.081	0.061	0.103	0.046	0.025	0.071	0.023	0.114
O_2 Adsorption Capacity 90K, 100 Torr (wt.%)	32.1	28.7	18.2	17.6	—	—	—	—	16.5	15.8	0	5.21
H_2O Adsorption Capacity 298K, 4.6 Torr (wt.%)	30.4	28.6	18.5	16.7	—	—	—	—	19.1	19.6	1.28	10.26
n-Butane Cracking, k_A	1.9 (a)	3.3 (a)	71 (b)	79 (b)	87 (c)	—	—	—	4.6 (b)	6.7 (b)	0.3 (c)	0.8 (c)

a) activated 1 hour, 798K, He.
b) activated 1 hour, 798K, Air.
c) activated 1 hour, 848K, Air.

Table 3. Chemical Analyses and Physical Property Measurements of the Starting Zeolites and the Products of the Ammonium Iron Fluoride Reaction

Zeolite Designation	NH_4Y	Y LZ-224	H_3O Zeolon	Zeolon LZ-226	H_3O Mor Synthetic Mordenite	Syn Mor LZ-226	Syn Mor LZ-226	Syn Mor LZ-226 Washed	Syn Mor LZ-226 Washed	NH_4L	L LZ-228
Sample		G		H		I	J	K	L		M
$(NH_4)_2O$, wt.%	9.5	5.7	—	2.9	—	2.9	3.2	3.6	3.5	7.9	5.2
Al_2O_3, wt.%	22.2	12.6	10.8	8.0	10.2	4.5	4.4	4.7	5.6	19.8	13.6
FeO_2, wt.%	—	16.9	—	4.1	—	3.8	7.6	3.8	3.1	—	13.5
SiO_2, wt.%	64.4	65.0	88.8	87.2	88.0	89.6	85.0	88.8	92.1	67.8	63.6
Fluoride, wt.%	—	0.20	0.03	0.40	0.08	0.05	0.34	0.03	0.0	—	0.93
Na+K/Al	0.19	0.21	—	—	—	—	—	—	—	0.12	0.15
NH_4^+/Al	0.84	0.89	0.03	0.72	0.08	1.29	1.43	1.48	1.23	0.78	0.74
Cation Equivalent, M^+/Al	1.03	1.10	—	0.72	—	1.29	1.43	1.48	1.23	0.90	0.89
Cation Equivalent, M^+/(Al + Fe)	—	0.60	—	0.54	—	0.84	0.68	0.97	0.92	—	0.55
SiO_2/Al_2O_3	4.93	8.86	14.00	18.39	14.69	33.97	33.13	31.98	27.61	5.80	7.91
$SiO_2/(Al_2O_3 + Fe_2O_3)$	—	4.47	—	13.90	—	22.12	15.67	21.11	20.56	—	4.85
Product Color	—	Brown	—	Brown	—	White	Beige	White	White	—	Beige
X-Ray Crystallinity, %I/Is	100	36	100	75	100	87	83	98	111	100	48
Framework Infrared: Asymmetric Stretch, cm^{-1}	1015	1028	1073	1072	1080	1076	1075	1079	1078	1100	1099
Symmetric Stretch, cm^{-1}	789	795	801	811	788	797	798	801	803	770	772
Hydroxyl Region Infrared: Absolute Absorbance, 3710 cm^{-1}	0.020	0.127	0.364	0.155	0.442	0.350	0.324	0.272	0.240	0.058	0.307
Defect Structure, "z"	0.009	0.054	0.154	0.066	0.188	0.148	0.137	0.115	0.102	0.025	0.130
O_2 Adsorption Capacity 90K, 100 Torr (wt.%)	35.2	29.4	19.1	19.0	19.0	18.7	18.6	18.8	18.1	16.5	16.8
H_2O Adsorption Capacity 298K, 4.6 Torr (wt.%)	32.1	29.7	16.2	13.4	14.8	12.3	13.0	13.0	13.6	19.1	20.3
n-Butane Cracking, k_A	1.9 (a)	6.4 (a)	—	—	90 (b)	12 (b)	13 (b)	15 (b)	26 (b)	4.6 (b)	6.7 (b)

a) activated 1 hour, 798K, He.
b) activated 1 hour, 798K, Air.

framework was expected to produce changes in the infrared spectrum of the zeolite in the region 200 cm^{-1}–1300 cm^{-1}, (11). The asymmetric stretch band in the region 950–1250 cm^{-1} is particularly sensitive to the SiO_2/Al_2O_3 ratio, increasing to higher wavenumbers with lower aluminum content. The symmetric stretch band in the region 750–835 cm^{-1} is more sensitive to the overall silicon content of the framework and does not shift significantly to higher wavenumbers unless there is substitution of silicon atoms into the dealuminated sites (1). Both Ti and Fe are larger than Al (4), and it might be expected that both asymmetric and symmetric stretch bands would shift to lower wave numbers. However, size of the substituting ion is only one of the factors contributing to the positions of these bands, making it difficult to predict the effect on band position. The position of the infrared band is related to bond strength, which is not necessarily a simple function of bond length, especially when changing rows within the periodic table. Some other factors influencing band position might be the number and structural position of the cations in the substituted product, or the structural position in the framework assumed by the substituting ion; some aluminum sites may react more readily than other sites.

The unpredictable effect of substituted iron or titanium on the framework infrared frequencies is supported by the data in both Tables 2 and 3. In the entire set of samples, the asymmetric stretch band shifts a maximum of 13 cm^{-1} for LZ–224 and 12 cm^{-1} for LZ–225. (LZ–224 is the product designation indicating iron substituted in the framework of zeolite Y. LZ–225 is the product designation used to indicate titanium substitution in the framework of zeolite Y. Product designations for all of the substituted zeolites contained in this report are shown in Table 1). A similar level of substitution by Si in zeolite Y results in a shift of 30 cm^{-1}. The effect on the symmetric stretch band is more variable, from –4 cm^{-1} for Ti substituted LZ–202 to +15 cm^{-1} for iron substituted mordenite. Several of the framework infrared spectra of the substituted products are compared with their respective starting materials and are shown in Figure 1. There are no remarkable effects of substitution on the overall shape of the spectra. No new absorption bands are detected, which is remarkable, since Taramasso et al. (12, 13) report a 950 cm^{-1} absorption band in their Ti containing ZSM-5 materials, which they attribute to titanium incorporated in the framework. Neither LZ–241 sample reported above shows any indication of an absorption band in this region. LZ–247, (spectrum 5 in Figure 1) containing 11.4 wt.% TiO_2 shows no indication of an absorption band in this region. The hydronium exchanged synthetic mordenite does have a band, as shown in spectrum 10 in Figure 1. The iron substituted mordenite samples (spectra 8 and 9) do not show the presence of the band; it was "removed" as a result of the substitution reaction. An absorption band at 950 cm^{-1} is normally attributed to an Si-OH stretch vibration (14, 15), and is typically observed in some acid or hydrothermally treated zeolites.

Formation of a broad absorption band in the hydroxyl region of the infrared spectrum due to formation of defect sites or "hydroxyl nests" in dealuminated sites was introduced previously (1).

The products discussed in this report are 22-68% aluminum depleted, relative to the respective starting materials, yet the hydroxyl region of the infrared spectrum shows that few hydrogen bonded OH groups were created as a result of the treatments (see the "z" values in the Tables). The value "z" is calculated from the measured absorbance at 3710 cm^{-1} in the hydroxyl region of the infrared spectrum, compared to that measured for a standard sample with a known number of defect sites (1). "z" numerically represents the mole fraction of defects in the framework of a zeolite as described below. The hydroxyl region infrared spectra of some of the treated products and their respective starting materials are shown in Figure 2, compared with that of a 48% Al-depleted NaY. Absolute absorbance measured at 3710 cm^{-1} for the aluminum depleted sample is 0.330 and is equivalent to a "z" value of 0.140. The treated products do not show the same broad absorption band. Some absorbance is measured, but the amount measured is substantially less than would be expected from the level of dealumination of the products. Since some starting materials, notably the H_3O-mordenite, already contain a high level of defects, the change in "z" value is a more accurate measure of the hydroxyl nests created as a result of the treatment.

An alternative method of describing the products of the metal ammonium fluoride process utilizes the calculated "z" values which were described above, together with the chemical analyses to express the products in terms of mole fractions of framework tetrahedra, i.e., the "TO_2" formula. The starting zeolite may be expressed as:

$$(Al_a Si_b []_z)O_2$$
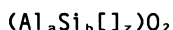
where "a" is the mole fraction of aluminum tetrahedra in the framework of the starting zeolite; "b" is the mole fraction of silicon tetrahedra in the framework of the starting zeolite; and "z" is the mole fraction of defect sites in the zeolite framework. "[]" is the symbol used to represent the defect sites. Numerically the sum of the values $a + b + z = 1$.

The products of the treatment are expressed in similar terms:

$$(Al_{(a-N)} Si_b E_c []_z)O_2$$

where "N" is the mole fraction of aluminum removed from the framework of the starting zeolite as a result of the treatment, "c" is the mole fraction of either titanium or iron tetrahedra inserted into the framework as a result of the treatment, and E is the symbol used to represent the substituting atom. Numerically the sum of the values for the treated zeolites, $(a-N) + b + c + z = 1$.

The calculated TO_2 formulas for the products contained in this report are as follows:

LZ-225 Ti-substituted NH$_4$Y.

NH$_4$Y:	$(Al_{0.278} Si_{0.706} \quad\quad []_{0.016})O_2$
LZ-225:	$(Al_{0.181} Si_{0.683} Ti_{0.088} []_{0.048})O_2$

A. TITANIUM SUBSTITUTED ZEOLITES   **B. IRON SUSTITUTED ZEOLITES**

1. Starting ZSM-5
2. LZ-241 Containing 1.3 wt.% TiO₂
3. LZ-241 Containing 8.9 wt.% TiO₂
4. Starting Omega type Zeolite, LZ-202
5. LZ-247, 11.4 wt.% TiO₂

6. LZ-224, 16.9 wt.% Fe₂O₃
7. Starting NH₄Y
8. LZ-226, 3.8 wt.% Fe₂O₃
9. LZ-226 Washed; 3.1 wt.% Fe₂O₃
10. Starting H₃O⁺ Mordenite
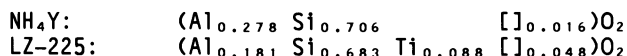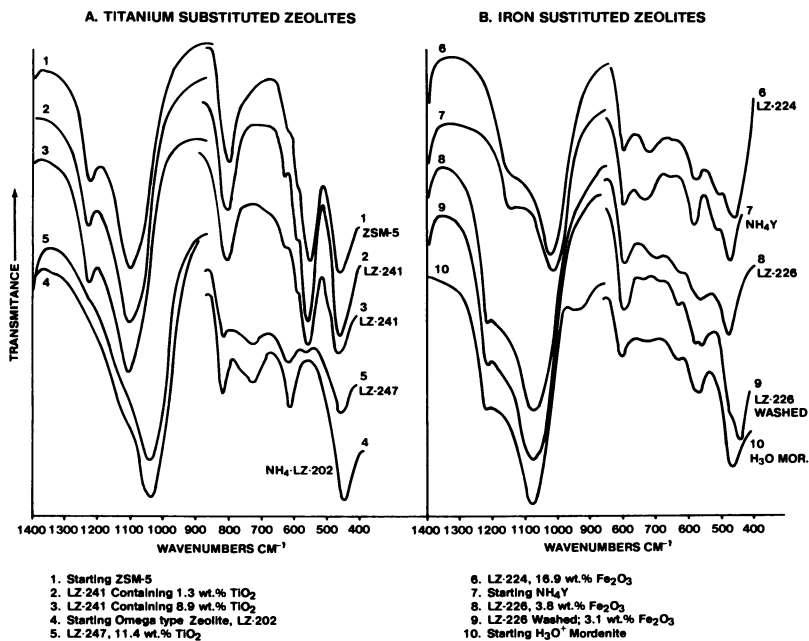
Figure 1.   Comparison of the Framework Region Infrared Spectra of Some Titanium or Iron Substituted Zeolites with the Untreated Starting Materials.
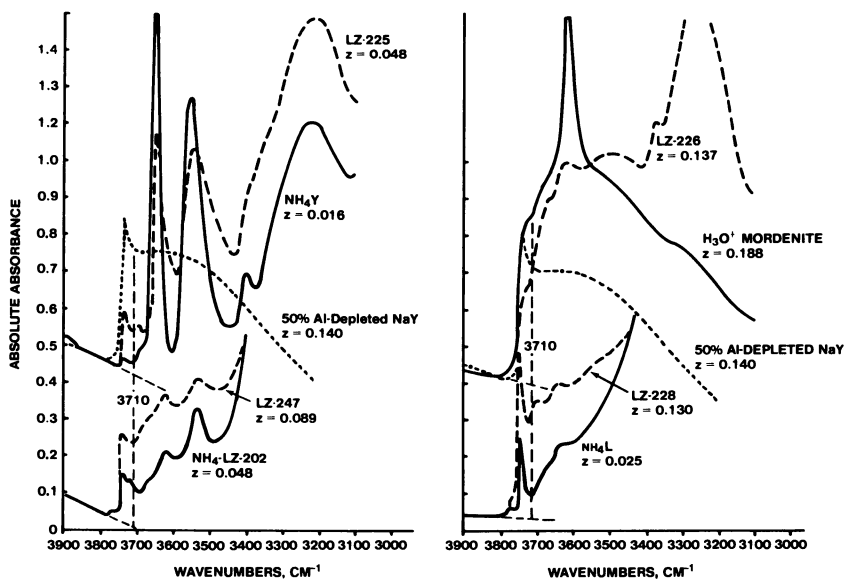
Figure 2.   Comparison of the Hydroxyl Region Infrared Spectra of Some Titanium or Iron Substituted Zeolites with Untreated Starting Zeolites a and 50% Al-Depleted NaY.

Sufficient $(NH_4)_2TiF_6$ was added to replace 50% of the framework Al with Ti. The LZ-225 product contained 11.4 wt.% TiO_2. Comparing the TO_2 formula of the starting NH_4Y with that of the LZ-225 product, certain properties of the LZ-225 can be calculated. The LZ-225 was 34% dealuminated (N/a X 100), with 95% of the dealuminated sites filled with Ti (c/N • 100). The change in defect structure was +0.032. There is a slight decrease in silicon content, a feature that was observed with all acid-sensitive zeolites.

LZ-247-Ti substituted Omega type zeolite.

$NH_4^+LZ-202$: $(Al_{0.221} Si_{0.731} \qquad\qquad []_{0.048})O_2$
LZ-247: $(Al_{0.153} Si_{0.675} Ti_{0.084} []_{0.089})O_2$
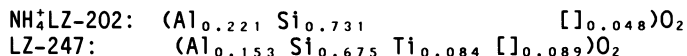
Sufficient $(NH_4)_2TiF_6$ was added to replace 50% of the framework aluminum in an Omega-type zeolite LZ-202 by titanium. The LZ-247 product contained 11.4 wt.% TiO_2. Comparison of the calculated TO_2 formulas shows that the LZ-247 was 31% dealuminated with all of the dealuminated sites filled with Ti. In this case some of the silicon was also removed during the treatment and some of the Si sites were apparently filled by Ti as well. The retained O_2 capacity suggests that the Ti in excess of the removed Al is also inserted into the framework since O_2 capacity has barely changed as a result of the treatment. The change in defect structure was +0.041.

LZ-229 Ti-substituted NH_4L.

NH_4L: $(Al_{0.250} Si_{0.725} \qquad\qquad []_{0.025})O_2$
LZ-229: $(Al_{0.187} Si_{0.688} Ti_{0.054} []_{0.071})O_2$
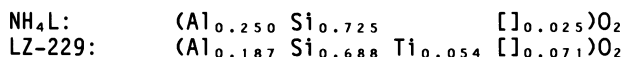
Sufficient ammonium fluotitanate was added to replace all of the framework aluminum in the NH_4L with titanium. The LZ-229 product contained 7.2 wt.% TiO_2. Perhaps because the sample was digested at reflux for only 30 minutes, only 25% of the aluminum was removed. However, 86% of the aluminum depleted sites were filled by Ti. A small amount of Si was also removed during the reaction. The change in defect structure was +0.046.

LZ-230 Ti-substituted NH_4W.

NH_4W: $(Al_{0.342} Si_{0.645} \qquad\qquad []_{0.023})O_2$
LZ-230: $(Al_{0.192} Si_{0.576} Ti_{0.118} []_{0.114})O_2$
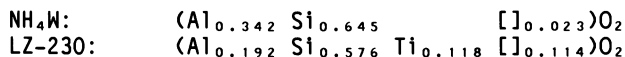
Sufficient ammonium fluotitanate was added to the NH_4W to replace 50% of the framework Al with Ti. The LZ-230 product contained 16.1 wt.% TiO_2. The actual amount of dealumination was 44%. Only 79% of the dealuminated sites were filled by Ti. Again, some Si was also removed during the treatment. There is a substantial change in the defect structure (+0.091). However, in view of the high level of TiO_2 in the sample, 0.091 is not excessive. Zeolite W is a small-pore zeolite (phillipsite structure), adsorbing very little O_2 or H_2O. Following substitution by Ti

for Al, oxygen capacity increased to 5 wt.% compared to none for
the NH_4W. Water capacity also increased from only about 1% for
the NH_4W to more than 10% for the LZ-230. This is one example
that demonstrates the increased pore diameter of the zeolite as a
result of substitution of the larger Ti ion [4].

LZ-241 Ti-substituted ZSM-5.

NH_4ZSM-5: $(Al_{0.056} Si_{0.863}   []_{0.081})O_2$
LZ-241: $(Al_{0.029} Si_{0.846} Ti_{0.064} []_{0.061})O_2$
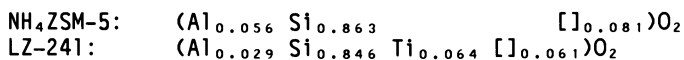
Sufficient $(NH_4)_2TiF_6$ was added to the ammonium exchanged
ZSM-5 to replace 50% of the framework Al with Ti. The LZ-241
product, Sample C, contained 8.9 wt.% TiO_2. The zeolite was 48%
dealuminated after reflux for 28 hours. All of the Ti was
incorporated into the zeolite. There was a small decrease in the
amount of defects, a feature observed with zeolites that are not
readily susceptible to acid attack and have a high silica content.
This has been attributed to "etching" of the surface of the zeolite
crystals by the combination of acid and fluoride, and transport of
the silicon atoms in solution to fill other defect sites in the
framework (1).

ZSM-5: $(Al_{0.037} Si_{0.860}   []_{0.103})O_2$
LZ-241: $(Al_{0.029} Si_{0.902} Ti_{0.010} []_{0.046})O_2$
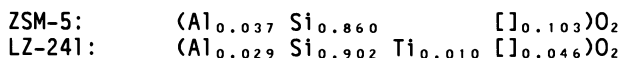
ZSM-5 with a higher SiO_2/Al_2O_3 ratio was treated with
$(NH_4)_2TiF_6$. The sample was calcined at 600°C to burn off
the organic template and used without ammonium exchange. Suffi-
cient salt was used to replace all of the framework Al with Ti.
The LZ-241 product, sample D, contained 1.3 wt.% TiO_2. However,
digestion was for only 1.5 hours. The shorter digestion time is
believed responsible for the low efficiency of the reaction. Only
22% of the aluminum was removed. Apparently, titanium readily
filled the dealuminated sites and a few of the previously vacant
sites, but compared to the amount of Ti added to the starting
ZSM-5, only 27% of the Ti was inserted into the zeolite framework.

LZ-224 Fe-substituted NH_4Y:

NH_4Y: $(Al_{0.286} Si_{0.705}   []_{0.009})O_2$
LZ-224: $(Al_{0.150} Si_{0.667} Fe_{0.129} []_{0.054})O_2$
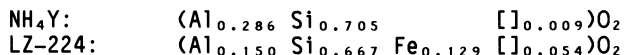
Sufficient ammonium iron fluoride salt was added to the
NH_4Y to replace 55% of the framework Al in the Y zeolite. The
LZ-224 product contained 16.9 wt.% Fe_2O_3. The product was
48% dealuminated with an apparent value of 95% substitution of Fe
into the dealuminated sites. This value is inflated due to the
fact that iron is also exchanged into the normal cation positions
as well. The color of the LZ-224 product was brown, indicating
the presence of the Fe cations. The normal cation equivalent,
M^+/Al, is greater than unity, indicating excess cation content
or that some of the cations are available to balance the negative
charge on the framework due to Fe^{3+} in the framework. However,

the cation equivalent of $M^+/Al+Fe$ (0.60), falls far short of the anticipated value of 1.0. The maintenance of O_2 and H_2O adsorption capacity support substitution of Fe in the framework.

LZ-226 Fe-substituted Synthetic Mordenite (Zeolon).

H_3O^+-Zeolon: $(Al_{0.106} Si_{0.740} []_{0.154})O_2$
LZ-226: $(Al_{0.080} Si_{0.816} Fe_{0.038} []_{0.066})O_2$
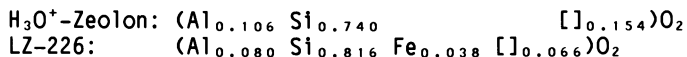
Sufficient $(NH_4)_3FeF_6$ was used to replace 25 % of the framework Al of the H_3O^+-Zeolon with Fe. The LZ-226 product contained 4.1 wt.% Fe_2O_3. The Zeolon was 25% dealuminated. Nearly all of the iron was incorporated into the zeolite. The product color was brown, again indicative of the presence of part of the Fe in cation positions. The cation equivalent was low, even the M+/Al being only 0.72. The adsorption capacity was fully maintained, suggesting that all of the iron is either substituted in the framework or exchanged in the zeolite as an extra framework cation.

LZ-226 Fe substituted synthetic mordenite (Mor).

H_3O^+-Mor: $(Al_{0.097} Si_{0.715} []_{0.188})O_2$
LZ-226: $(Al_{0.046} Si_{0.781} Fe_{0.025} []_{0.148})O_2$
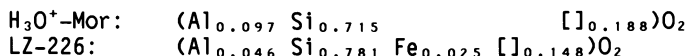
Iron was added to H_3O^+-mordenite from a mixture of FeF_3 and NH_4HF_2 in water, rather than as the $(NH_4)_3FeF_6$ salt solution. Sufficient iron salt was added to replace 50% of the framework aluminum atoms of the synthetic mordenite. The LZ-226 product, sample I, contained 3.8 wt.% Fe_2O_3 and was 53% Al-depleted, but only 49% of the Fe was incorporated into the product zeolite. The product was white and the cation equivalent, $M^+/Al+Fe$, was equal to 0.84. There are indications that etching occurred as well since there is an apparent increase in framework silicon and a reduction in the defect structure. An exact duplicate of this experiment, only with NH_4F as the fluoride salt, resulted in a brown sample containing a substantially lower cation equivalent. Concentration of the iron in solution and the more acidic nature of the bifluoride salt are believed responsible for maintenance of an iron species substituting in the framework, rather than exchanging as a cation.

LZ-226:(J) $(Al_{0.045} Si_{0.766} Fe_{0.052} []_{0.137})O_2$

The same starting mordenite used in the previous experiment was treated with sufficient FeF_3 and NH_4HF_2 solution to replace 75% of the framework Al with Fe. The LZ-226 product, sample J, contained 7.6 wt.% Fe_2O_3. Relative to the previous experiment, the only variable was the amount of iron added to the zeolite. The product was 54% depleted in Al, with the zeolite incorporating an equal amount of Fe. The product contained twice the amount of Fe as the previous experiment but was brown in color. The cation equivalent, M^+/Al, was substantially greater than 1.0 (1.42) but the $M^+/Al+Fe$ was only 0.68. The brown

color and the low cation content are evidence of cationic iron.
The iron concentration in solution and the pH of the system were
consistent with formation of a hydroxylated iron cation species
(16). By assuming that the cation species is $Fe(OH)_2^+$, and
that a cation equivalent of 1.0 must be achieved, the TO_2
formula can be recalculated as follows:

$$(Al_{0.047} \ Si_{0.779} \ Fe_{0.037} \ []_{0.137})O_2$$

The mordenite sample is still 51% Al-depleted, but only 70%
of the iron is present as framework Fe, about 5 wt.%.   The
remaining Fe is presumed to be the $Fe(OH)_2^+$ cation. Ammonium
oxalate has been shown to react with and exchange with cationic
iron (17). The sample was refluxed three times with 0.1 N
ammonium oxalate solution with the analytical results shown in
Table 3 used to calculate the following TO_2 formula for the
resulting white LZ-226 product:

$$(Al_{0.050} \ Si_{0.809} \ Fe_{0.026} \ []_{0.115})O_2$$

The LZ-226 product washed with ammonium oxalate contained
3.8 wt.% Fe_2O_3 (sample K in Table 3). The calculations
indicate 48% aluminum depletion with 44% replacement by Fe. The
cation equivalent, $M^+/Al+Fe$, is nearly unity. Oxygen and water
capacity have been maintained for both samples.
        A second sample of brown LZ-226 containing about 6 wt.%
Fe_2O_3 was washed with ammonium oxalate and characterized.
Following the ammonium oxalate wash, the product, sample L, con-
tained 3.1 wt.% Fe_2O_3. The calculated TO_2 formula is as
follows:

$$(Al_{0.059} \ Si_{0.818} \ Fe_{0.021} \ []_{0.102})O_2$$

The LZ-226 product was 39% dealuminated with Fe substituting
into 55% of the dealuminated sites in the framework. The product
was white and the cation equivalent, $M^+/Al+Fe$, was also near
unity.

LZ-228 Fe-substituted NH_4L.

NH$_4$L: $(Al_{0.250} \ Si_{0.725} \qquad \quad []_{0.025})O_2$
LZ-228: $(Al_{0.108} \ Si_{0.694} \ Fe_{0.068} \ []_{0.130})O_2$
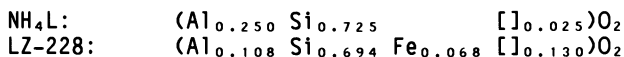
In this experiment sufficient iron salt as $(NH_4)_3FeF_6$
was added to replace 75% of the framework Al of the NH_4L. The
LZ-228 product contained 13.5 wt.% Fe_2O_3. The LZ-228 product
was 57% depleted in Al, with nearly 50% of the added iron incor-
porated into the zeolite, presumably in both framework and cation
positions. The sample was colored beige and the cation equiva-
lent, M^+/Al, was only 0.55. The oxygen and water capacities
were fully maintained, despite the presence of more than 13 wt.%
Fe_2O_3 in the product.
        Scanning electron microscopy and EDAX analysis evaluations
shown in Figure 3 are typical of the analyses obtained on all of
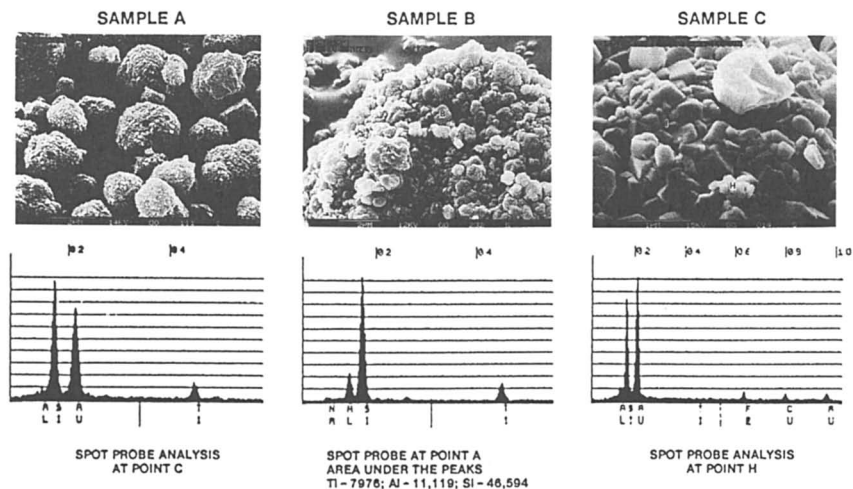
Figure 3. Scanning electron microscope and EDAX analysis of (A) LZ-241; Ti substituted ZSM-5; 1.3 wt.% TiO_2; (B) LZ-226; Ti substituted NH_4Y; 11.4 wt.% TiO_2; (C) LZ-226; Fe substituted H_3O mordenite; 3.8 wt.% Fe_2O_3.

the samples reported above. The SEM analysis showed that there was no change in the zeolite morphology resulting from any of the treatment. This is consistent with the interpretation that the crystal structure was maintained for all of the samples reported here. Sample A shows the typical morphology of ZSM-5 and is no different from the starting material in appearance. EDAX shows the presence of titanium in the sample of LZ-241. The amount of Ti is constant and an EDAX area scan does not differ from the individual spot probe analyses. Sample B is titanium-substituted NH_4Y, LZ-225. The accompanying EDAX spot probe analysis shows the presence of Ti in the sample. Measurement of the area under the respective peaks of Si, Al and Ti allows an estimation of the relative contents of these metals. The EDAX calculations of the Ti content at the point of the spot probe estimate that 11.5 wt.% TiO_2 is present, in agreement with the bulk chemical analysis which is reported as 11.4 wt.% TiO_2. An area scan of the surface is nearly identical to the spot probe analysis. Sample C shows that iron is present in the iron-substituted mordenite, LZ-226. As with previous samples, the area scan analysis does not differ from the individual spot probe analysis. None of the examined samples show the presence of other crystalline or amorphous phases. Small particles appear to have the same composition as the larger particles. The morphology of the substituted crystals is identical to that of the starting zeolites. The evidence is consistent with the even distribution of the substituting iron or titanium atoms throughout the zeolite crystals. It does not appear that there are any extraneous phases present in the zeolite. The results obtained are the expected results if iron or titanium had substituted into the frameworks of the respective zeolites.

The n-butane cracking values obtained with the titanium substituted zeolites all show an increase in k_A value over that obtained with the starting zeolite. This is notable in that the Ti is tetra-valent, and does not require a cation. With reduced cation content, the acidity should be reduced. However, the result obtained was the reverse. With iron-substituted products, the resulting k_A values varied with the zeolite. Although not discussed in detail in this paper, all Fe-containing products did show indications of metals activity; there was a dramatic increase in the amount of olefins produced.

CONCLUSIONS:

Teilen et al. (4) comment on the number of framework-substituted materials, particularly in the patent literature and conclude that in most of the cases, the alleged substituting element does not enter the framework of the zeolite. The only evidence given to support those claims of framework substitution are analytical data which show the presence of very small amounts of the "substituted" ion. Their criticism is valid, and the mere presence of some foreign material with the zeolite does not prove that the material is a part of the zeolite. In fact, the primary synthesis conditions used are generally very basic in nature; the pH is 13 or greater. A basic medium is more likely to cause pre-cipitation of the titanium or iron rather than a soluble species small enough to react to form the open frameworks of the zeolite (16). Perego et al. (13) also criticize the numerous reports of replacement of aluminum in the framework without a real proof of the occurrence of isomorphous replacement.

In the present work, iron or titanium have been incorporated into a number of zeolites. The loss of X-ray crystallinity is contrasted with the nearly full retention of both oxygen and water adsorption capacities, indicating that the substituted products retain their pore volume despite the presence of substantial amounts of the iron or titanium. The X-ray powder patterns show that no new crystalline phases are present and do not indicate the presence of amorphous materials. SEM and EDAX analysis do not show the presence of any new particulate material and support the presence of an even distribution of the iron or titanium throughout the zeolite crystals. The hydroxyl region infrared spectra do not show the presence of hydroxyl nests commensurate with the amount of aluminum removed during the reaction. The framework infrared spectra do not give a consistent picture of the effects of the incorporated ion on the frameworks of the zeolite. They do show that the respective shifts in the frame-work frequencies are not consistent with a picture of simple dealumination. In all, the evidence presented here is totally consistent with the conclusion that the Secondary Synthesis process has been successful in substituting iron and titanium into framework tetrahedral positions in a number of zeolites. Although not discussed in detail here, the data also show that some zeolites are more reactive than others and that time, temp-erature and particularly pH are important variables that control the substitution process.

REFERENCES:

1. Skeels, G.W; Breck, D.W. Proceedings of the Sixth
    International Zeolite Conference, Edited by D. Olson and
    A. Bisio, Butterworths Ltd, UK, (1984); pp. 87-96.
2. Breck, D.W. "Zeolite Molecular Sieves"; Wiley; New York,
    (1974); p. 320.
3. McNicol, B.D.; Pott, G.T. J. Catalysis, 25, 223, 1972.
4. Teilen, M.; Geelan. M.; Jacobs, P.A. "Proceedings of the
    International Symposium on Zeolite Catalysis"; Siofak,
    Hungary; Petofi Nyomda, Kecskemet, 1985, p.1-18.
5a. Wilson, S.T.; Lok, B.M.; Messina, B.M.; Cannan, T.R.;
    Flanigen, E.M. J. Amer. Chem. Soc., 1982, 104, 1146-1147.
5b. Wilson, S.T.; Lok, B.M.; Messina, B.M.; Cannan, T.R.;
    Flanigen, E.M. "Intrazeolite Chemistry"; The American
    Chemical Society: Washington, D.C., 1983, pp 79-106.
5c. Wilson, S.T.; Lok, B.M.; Messina, B.M.; Flanigen, E.M.
    "Proceedings of the Sixth International Zeolite Conference",
    Butterworths: Guilford, Surry, England, 1985; pp 97-109.
6a. Lok, B.M.; Messina, C.A.; Patton, R.L.; Gajek, R.T.;
    Cannan T.R.; Flanigen, E.M. U.S. Pat. 4,440,871, 1984.
6b. ibid., J. Amer. Chem. Soc., 1984, 106, 6092-6093.
7a. Wilson, S.T.; Flanigen, E.M. Eur. Pat. Appl. 0,132,708;
    Feb. 1985; Ibid., U.S. Pat. 4,567,029; 1986.
7b. Messina, C.A.; Lok, B.M.; Flanigen, E.M. Eur. Pat. Appl.,
    Jan. 1985; Ibid., U.S. Patent 4,544,143; 1985.
8. Argauer, R.J.; Landolt, G.R. U.S.Pat. 3,702,886.
9. Cannan, T.R. EURO-PCT Patent Application Publication Number
    0 230 452.
10. Rastelli Jr., H.; Lok, B.M.; Duisman, J.A.; Earls, D.E.;
    Mullhaupt, J.T. The Canadian Journal of Chemical
    Engineering; 60, 44-49; 1982.
11. Flanigen, E.M.; Khatami, H.; Szymanski, H.A. Molecular
    Sieve Zeolites, Advan. Chem. Ser. 101; American Chemical
    Society, Washington D.C.; 1971, p. 201.
12. Taramasso, M.; Perego, G.; Notari, B. U.S. Pat. 4,410,501.
13. Perego, G.; Bellussi, G.; Corno, C.; Taramasso, M.;
    Buonomo, F.; Esposito, A. Studies in Surface Science and
    Catalysis; 28, Edited by Y. Murakami, A. Iijima and J.W.
    Ward; Elsevier, Tokyo, Japan, 1986, pp 129-136.
14. Farmer, V.C. "The Infrared Spectra of Minerals";
    Mineralogical Society Monograph 4; The Mineralogical
    Society, London; 1974; pp. 368-369, 487-488.
15. Hino, M.; Sato, T. Bulletin of The Chemical Society of
    Japan, 44, 33-37, 1971.
16. Baes Jr., C.F; Mesmer, R.E. "The Hydrolysis of Cations";
    Wiley, New York; 1976; pp148-152, 226-237.
17. Szostak, R. private communication.

Chapter 30

High-Silica Faujasite by Direct Synthesis

Harry Robson

Department of Chemistry, Louisiana State University, Baton Rouge, LA 70803

The preparation of high-silica faujasite (LTY) by D. W. Breck certainly is one of the outstanding successes in zeolite synthesis because it established synthetic faujasite as a catalytic material. In the 30 years since, our efforts have only raised the product from Breck's 4.9 SiO_2/Al_2O_3 to about 6.0. But there are good indications that a still more silica-rich synthetic product would be a superior catalyst. For catalytic cracking, the optimum base-faujasite is about 10 SiO_2/Al_2O_3. In order to produce such a material, the synthesis batch should have a pH=11; but under these conditions, the rate becomes impossibly slow. Our experience in other zeolite synthesis systems indicates four approaches to increase the crystallization rate in these high-silica gels: 1) increased temperature, 2) amine additives, 3) non-aqueous solvents, and 4) improved seeding. Of these, the first three would impose a major cost increase on the faujasite product. Improved seeding could be compatible with existing equipment and processes.

We should remember that low temperature zeolite synthesis started with Milton's gel synthesis of A and X in the early 1950's(1). Large pore zeolites were substantially unavailable at that time. Natural faujasite was rare as it still is. Large port mordenite was still ten years in the future as were zeolites L and Omega. Zeolites were regarded as ion exchangers or as selective sorbents, not as catalysts.

Breck's preparation of type Y faujasite in the late 1950's still stands as the outstanding success in zeolite synthesis (2). Type X might have had some catalytic applications but I doubt the International Zeolite Association would exist without the interest and support generated by the catalytic applications of the Type Y materials. It didn't seem that critical at the time; after all Breck had reproduced a material which exists naturally. Synthetic counterparts of natural zeolites have been prepared dozens of times since (3). But the extra silica content, or perhaps the diminished alumina content, was enough to give high temperature stability in the acid form and to get zeolites into catalysts for petroleum processes (4).

In the thirty years since, we have increased the silica content of Breck's product by only about 4% in the composition of the total product (SiO_2/Al_2O_3: 4.9 → 6.0) as shown in Table I. This increase is not trivial, but it can't be said to have created new products or new processes. Perhaps the better way to consider it is the

number of tetrahedral positions in the faujasite unit cell which are occupied by Al^{3+}. For type X (2.7 SiO_2/Al_2O_3), 82 of the total 192 T-positions are Al^{3+}; for type Y, it is 56 Al^{3+} per unit cell. At 6.0 SiO_2/Al_2O_3, we have reduced this number only to 48.

Optimum Synthetic Faujasite. As a goal for synthesis research, we might seek a procedure which would yield any silica/alumina ratio up to pure SiO_2 in faujasite form. Although such a sample would be interesting from a research perspective, it would almost certainly be a disaster as a catalyst. (No alumina = no acidity). For catalytic cracking applications, the optimum zeolite component in the finished catalyst has been reported to be a SiO_2/Al_2O_3 of about 14 (24 Al^{3+}/U.C.) (5). Such a material when dispersed in a silica-alumina matrix and finished by current manufacturing procedures should have a unit cell size of about 24.29Å which is near optimum for catalytic cracking. The optimum zeolite component for a hydrocracking catalyst is not so narrowly defined but the evidence is such a material would be an improvement on current USY technology (6).

Table I. Synthetic Faujasites

Type	SiO_2/Al_2O_3	Cell Size	Al/UC
X	2.7	24.92Å	82
Y	4.9	24.72Å	56
Z	10	24.45Å	32

Ordered Al Distribution. But I believe we can be more explicit about our goal for the next generation of synthetic faujasite than simply more, i.e.higher SiO_2/Al_2O_3. There can be little doubt that the acid sites which are most effective in strong acid catalysis are the alumina tetrahedra isolated in the zeolite structure by at least two silica tetrahedra This was defined by Wachter (7) as zero next-nearest neighbors (0-NNN). We still do not have the technology to observe these alumina sites directly, but we can infer them from the ^{29}Si MAS-NMR spectra as the absence of $Si(OAl)_2$ and higher resonances.

To achieve a faujasite-type product with the maximum 0-NNN sites requires a 10 SiO_2/Al_2O_3 product with ordered distribution of Al^{3+} in the T-sites. This is the material I choose to designate type Z faujasite. In terms of the unit cell, this is $32Al^{3+}$/UC (32/(192-32)=0.2). It seems unlikely that stabilization or extraction treatments will yield such a product. The optimum zeolite reported by Pine, et. al. as $24Al^{3+}$/UC is at least 25% off the maximum possibly due to a significant concentration of $Si(OAl)_2$ in the parent zeolite.

Silica/alumina by Unit Cell Size. Unit cell size has proven to be a reliable indicator of the SiO_2/Al_2O_3 ratio of faujasite-type materials. Figure 1 plots unit cell size (Å) vs the number of Al^{3+} ions per unit cell. Conventional type Y materials are at the upper right (Al^{3+}/UC greater than 56). The anchor point at the lower left (Al^{3+}/UC=0) at 24.19Å is the consensus of many observations of the end product of repeated dealuminations. It is difficult to get reliable data in between. It is tempting to extrapolate the Dempsey, Kuhl, and Olson (8) curve to zero alumina with just enough curvature to terminate at 24.19 Å. Skeels and Breck data on USY-type materials (LZ-Y82 and LZ-Y20) probably show non-frame work alumina(9) The SiF_4-treated materials (LZ-210) reported by Skeels and Breck fall on the silica-rich side of the extrapolated curve. They may indicate non-framework silica; however, there could be a break in the curve at 56 Al^{3+}/UC. The dashed segment is linear over the range 24.64 to 24.19Å.
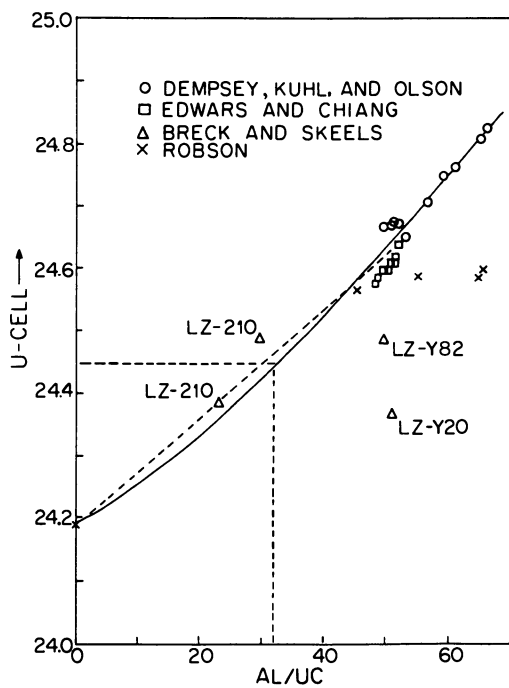
Figure 1. Change in faujasite unit cell(Å) with increasing Al^{3+} in T-positions (192 total Al^{3+} + Si^{4+} per unit cell).

Admittedly the case for type Z faujasite (10 SiO_2/Al_2O_3, 0-NNN) being a superior catalytic material is somewhat speculative at this point. Dealuminated type Y has given us materials with a higher SiO_2/Al_2O_3, but has not necessarily produced optimum alumina distribution (0-NNN). Until such materials are prepared and tested in catalytic applications we can only conjecture on their advantages. Type Y got us over the hump and into catalysis, but it was never the material we wanted. USY and LZ-210 are compromises to give us, at a considerable price, the materials we cannot prepare by crystallization.

High-Silica Faujasite by Means Other Than Synthesis

USY (ultra-stable type Y) is a good material which has served us well but which has probably been pushed to its limit (10). In simplified terms, as Al^{3+} is eliminated from the T-positions in the structure by thermal treatment in the presence of H_2O, they are replaced by Si^{4+} from some other portion of the crystal. Table II compares a typical USY (LZ-Y82) to the parent material, NaY. The SiO_2/Al_2O_3 ratio (5.77) probably understates the transformation because of non-framework alumina retained in the structure. Reduced crystallinity is evidence of structural damage; this same effect would be expected to reduce the zeolite character of its sorption properties. The reduction in cation content (0.38 Na/Al) renders it unsuitable for an alkaline application such as the ELF-Aquitaine aromatization catalyst.

Table II. Composition of High-Silica Faujasites

Sample	NaY	USY	LZ-210	Exp
SiO_2/Al_2O_3	4.92	5.77	9.31	5.99
Fluoride(%)	0	0.05	0	0
M^+/A	0.98	0.38	0.99	0.99
X-ray Cryst	100	73	106	87
U-Cell(Å)	24.69	24.52	24.49	24.57

LZ-210 (10) is a new material which doesn't seem to have attracted the attention its properties warrant. Unlike USY, Si^{4+} is supplied from external $(NH_4)_2SiF_6$ as Al^{3+} is eliminated. There is no loss in crystallinity at least for a moderate treatment (In this case, an apparent gain, 100→106). There is some retained flouride which might be a problem in a commercial cracking unit. Skeels and Breck indicate this residual flouride increases with more severe $(NH_4)_2SiF_6$ treatments. It also does not bode well for an alkaline catalyst application. The unit cell size (24.49Å) compares favorably with USY. But even with the proper SiO_2/Al_2O_3 ratio, there is a second requirement for type Z: 0-NNN. It would be fortuitous if the ammonium fluorosilicate extraction selectively removed Al (1-NNN) leaving Al (0-NNN). Since 0-NNN sites are the most acidic, they would be expected to react most rapidly with $(NH_4)_2SiF_6$.

The final column in Table II is a product of direct synthesis in my laboratory: I have labelled it "Exp" because it falls considerably short of the 10 SiO_2/Al_2O_3 which I believe is optimum for catalytic applications. At 5.99 SiO_2/Al_2O_3, it should have 48Al^{3+}/UC compared to 34 for LZ210 and 32 for the optimum type Z. Crystallinity is respectable (87%) but should be improved; additional work and study is needed in type Z synthesis. Na/Al = 0.99 indicates a good cation balance; the material has tested favorably in an alkaline application.

Is High-Silica Possible by Direct Synthesis?

For many years, the attitude has prevailed that we had reached the limit when the synthetic product duplicated natural faujasite (5.1 SiO_2/Al_2O_3). What nature has accomplished in 10,000 years we should not expect to exceed in hours or days in the laboratory. Fortunately our vision has not been so severely limited in the case of other zeolite phases. Table III compares natural materials to their high-silca synthetic counterparts for mordenite, ferrierite, and sodalite.

Table III. High-Silica Forms of Natural Zeolites

Phase	SiO_2/Al_2O_3	Means
Mordenite/HSM	11→28	Amine Additive
Ferrierite/ZSM-35	14→60	Amine Additive
Sodalite/Silica-sodalite	2→∞	Glycol Solvent
Faujasite/Type Z	5→10	?

High-silica mordenite (HSM) is the product of the Tonen group in Japan (11). It can be prepared with tetrapropylammonium hydroxide addition or by control of the time-temperature cycle in synthesis. At 28.5 SiO_2/Al_2O_3, it is comparable to the product of strong acid extraction. ZSM-35 is the counterpart of natural ferrierite; it was prepared by the Mobil group with pyrrolidyne, ethylenediamine, or butanediamine additives (12). Silica-sodalite was recently announced by Bibby and Dale (13). Natural sodalite has $SiO_2/Al_2O_3 = 2$; silica-sodalite exists in silica-rich forms up to pure SiO_2. This is the first example of a 4-6 ring structure which can be prepared in very high silica form. The principal change in their synthesis is substitution of glycol for water.

At this stage we would be happy to make type Z faujasite by any of these methods in order to have the material to prove its catalytic properties. But if it is to escape the laboratory and see service as a commercial catalyst it will have to be produced at a cost which can be justified by its advantages over other materials. The organic templates are expensive and sometimes toxic. No templated synthesis is yet a commercial process, with the possible exception of ZSM-5. Non-aqueous synthesis is not difficult in the laboratory; on commercial scale, it is a completely new undertaking. We will continue to test these techniques, but always with the hope that a better way will be found. It is unlikely that a single change in current synthesis procedure will open up the high-silica type Z region.

Commercial Synthetic Faujasite. At present commercially supplied type Y materials have increased from 4.6 to about 5.1 SiO_2/Al_2O_3 on the average. Laboratory syntheses now approach 6 SiO_2/Al_2O_3. In figure 2, a plot of synthesis experiments from the literature, I have chosen to plot composition of the synthesis batch as two ratios: Al/Si as abscissa and OH⁻/Si as ordinate. The point code shows a number of series where the investigator pushed toward a more silica-rich product (lower left). These plots show a sequence of experiments leading to the point where the batch failed to crystallize and the series ended, only to begin again at some other point or by another investigator.

My own experiments in this area are somewhat wider ranging but also are plagued by less than fully-crystalline products. Consistently I have observed that the initial faujasite crystals which form are more silica rich than the final product by a
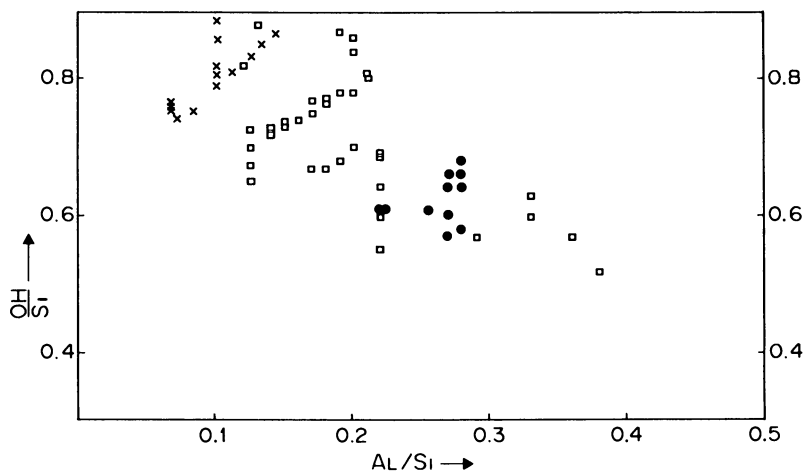
Figure 2. Overall batch composition of faujasite syntheses reported by several investigators (H_2O content not shown).

crystallization which continues to where faujasite is the major product. In some cases, the reaction ceased with less than 10% faujasite crystallinity but enough x-ray diffraction lines visible to calculate a cell size as low as 24.48 Å.

pH Controls Si/Al in the Zeolite Product.

For zeolite A and other alumina-rich phases, the synthesis is done in strongly alkaline systems which are not ordinarily described in pH terms. Further, measuring pH in alkaline systems at 100°C or above is not a trivial problem. But for silica rich systems, pH becomes a useful indicator of synthesis conditions. For most synthetic zeolites, pH is the primary control of Si/Al in the product.

This was nicely demonstrated by Donahoe and Liou (14) on phillipsite synthesis from (K, Na) alumino-silicate solutions. They tested a number of synthesis variables but concluded only pH was significant in determining product SiO_2/Al_2O_3. A plot of their data (Figure 3) shows a linear relationship, admittedly over a limited range. Our experience on other phases is similar although less precisely defined.

It is instructive to project this relationship to the silica/alumina range for type Z faujasite. Granting the uncertainty in extrapolation, the predicted value of pH = 11 for Si/Al = 5 (SiO_2/Al_2O_3 = 10) is entirely reasonable. Current laboratory type Y synthesis is near pH = 12.3; certainly reduction of the pH of the synthesis batch should produce a more silica-rich product. The size of the pH reduction required to produce 10 SiO_2/Al_2O_3 is in doubt, but the direction is unmistakable.

How Can We Promote Faujasite Crystallization at pH = 11?

The problem is the rate of crystallization which becomes impossibly slow using current technique if operating in this pH range. Table IV is a list of possible remedies and is definitely open-ended; new ideas are welcome.

Table IV. How Can We Promote Faujasite Crystallization at pH=11?

→Increase crystallization time or temperature

→Use amine additives (templating agents)

→Switch to non-aqueous solvents

→Improve nucleation

Longer crystallization treatments are not very promising experimentally. Figure 4 is from Kacerek & Lechert (15); it shows the rate of faujasite crystallization to be an exponential function of SiO_2/Al_2O_3 of the zeolite product. They indicate a break in the function to a markedly slower rate above 5.5 SiO_2/Al_2O_3. If we accept the lower rate which they predict, the synthesis of a 10 SiO_2/Al_2O_3 product requires nearly 10,000 years. Even if we extrapolate the low-silica data without the break (dashed line), our synthesis requires 200 days. In either case, the conclusion is the same: synthesis of type Z at 88°C is not a viable process.

Higher temperature treatments usually promote competing phases (gismondine /phillipsite or analcine) more than they promote faujasite. The 100 - 150°C region has not been adequately investigated in faujasite synthesis probably because autoclave experiments are more difficult than atmospheric pressure experiments and the more interesting results came at 100°C or less. Furthermore, faujasite is a metastable product and can easily degrade upon prolonged contact with the mother liquor, particularly at
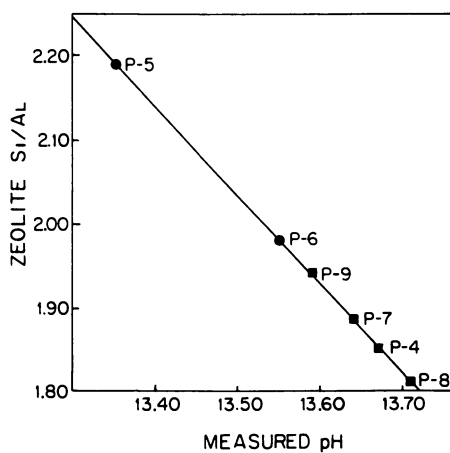
Figure 3. Framework Si/Al of phillipsite products vs. pH of the synthesis batch; ref (14).
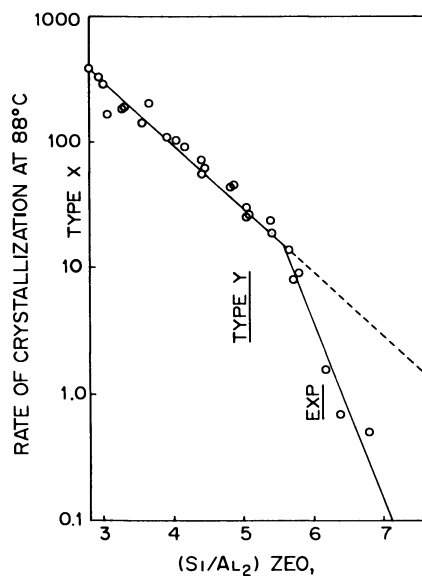
Figure 4. Rate of faujasite crystallization at 88 °C vs. SiO_2/Al_2O_3 of the framework; ref (15).

higher temperature. Table V shows loss of crystallinity and appearance of other phases in a preformed NaY faujasite after exposure to sodium silicate solutions. The degradation is rapid at 100°C in 10% Na_2SiO_3, but delayed for at least seven days in the less-alkaline water glass ($Na_2O \cdot 3.3\ SiO_2$). For 120°C or a more concentrated solution (20%), three days exposure is too much.

Table V. Recrystallization of NaY

(10g solution/g zeolite)

Treating Solution	pH	Days/°C	Product
10% Na_2SiO_3	13.2	3/100	FAU(s)+GIS
		7/100	
		GIS(m)+ANA	
10% $Na_2O\cdot3.3SiO_2$	11.4	7/100	FAU(100)
		12/100	FAU(95)
10% $Na_2O\cdot3.3SiO_2$	11.6	3/120	FAU(96)
20% $Na_2O\cdot3.3SiO_2$	11.4	3/100	FAU(82)

Amine Additives. It is precisely in this area, suppressing an undesired product in favor of the desired one, that additives can be most useful. High silica zeolites have been formed in the presence of amine additives. Vaughan (16) has prepared faujasite with 7.0 SiO_2/Al_2O_3 (24.52 A°) by addition of bis-(2-hydroxyethyl) dimethyl ammonium chloride in a slurry composition whose cation composition is 69% Na and 31% organic template (T). To scale this product up to commercial synthesis would require almost total recovery of the organic template. But its silica content makes it an interesting candidate for catalytic testing.

Perhaps we have concentrated too much on the quaternary amines as templating agents. Another approach is suggested by Verdijn in the synthesis of zeolite L(17). As showing in Table VI, by addition of only trace amounts of alkaline earth cations, especially strontium, the gel composition range which produced the desired zeolite L product was widened, the formation rate increased, smaller crystallites were obtained, and stirred synthesis became possible. The alkaline earths were very probably present when natural faujasite was formed. But their solubility in alkaline silicate liquors is low; 200 ppm Sr^{2+} is near saturation in the synthesis slurry.

Table VI. Synthesis of Zeolite L

The use of trace amounts of divalent cations significantly affects the synthesis aspects of zeolite L:

→ Gel composition range widened

→ Formation rate increased

→ Smaller crystallites obtained

→ Stirred synthesis possible

These observations suggest that the nucleation mechanism is greatly influenced.

The largest area of ignorance and therefore the most promising field for investigation lies in nucleation. Breck's synthesis required SiO_2 in the form of colloidal silica sol to make silica-rich type Y. We have since learned to seed the batch with a freshly prepared slurry (18), and use cheaper silica sources. But we are far from a chemical definition of the nucleating agent.

There is considerable data showing the synthesis can stall at low levels of crystallinity even though all the nutrients are present for continued growth. It has not been established that fresh addition of the "seed" slurry will reinitiate crystal growth, but growth of faujasite cryustals at 24.48Å, initiated but not sustained as noted in the previous section, indicates reinitiation should be possible. This "growth hormone" seems to be self generated in X and Y synthesis but lacking at conditions which would yield type Z.

Centrifugation of the Nucleation Slurry

Conventional wisdom ascribes nucleation to microcrystalline type X which in the presence of the proper nutrients grows into a full yield of type Y with no trace of its type X initiator. The "seed" composition is essentially sodium metasilicate solution with the addition of a small amount of sodium aluminate: $Na_2SiO_3 \cdot 0.16 \, NaAlO_2 \cdot 21 \, H_2O$. Comparatively little "seed" is necessary for a good Y synthesis; as little as 1% of the total Al_2O_3 may come from the seed.

But the actual nucleaant is probably a much smaller entity than the incipient faufasite crystal, even smaller than a sodalite cage which has been proposed as a secondary building unit It seems to; be a metastable unit which exists only temporarily in the depolymerization of the silica network and integration of Al^{3+} into a more stable structure. The nucleation slurries we have now are limited in shelf life and sensitive to the materials used in their preparation.

In my laboratory, I have attempted to concentrate the active component by centrifuging the nucleation slurry. As shown in Table VII, the solid cake removed by centrifrigation was almost inactive as a nucleating agent while the clear supernatant liquid was more active than the original slurry. Table VII indicates two synthesis batches of the same overall compostion (0.25 Al/Si, 0.51OH⁻/Si, 16H2O/Si) but prepared one with the total nucleation slurry, the other with the clear liquor. Whereas whole nucleation slurry gave a mixture of nearly equal amounts of faujasite and gismondine at this composition, the clear decantate gave full faujasite crystallinity with only a small amount of gismondine. By analysis, the clear decantate is richer in NaOH and leaner in $NaAlO_2$ than the whole slurry. Note that the initial faujasite crystals in poorly crystallized product appear to be more silia-rich than a fully crystalline product.

Table VII. Centrifugation Improves Nucleation Slurry

Seeding	Days/°C	Product	U-Cell
11%N.S.-whole	4/100	FAU(w)+LTA	24.58
	5/100	FAU(24)+GIS	24.57
10%N.S.-clear	4/100	FAU(96)+GIS	24.61
	4/90	FAU(100)+GIS	24.59

The ionic composition of dilute sodium silicate is a very complex problem involving Na_2O/SiO_2 ratio, water content, and even trace impurities. Equilibration seems to be very slow at ordinary temperatures. As shown in Figure 5, Harris, et.al, were able to identify a wide variety of structures in potassium silicate solutions which bear a striking resemblence to the secondary building units proposed for zeolite
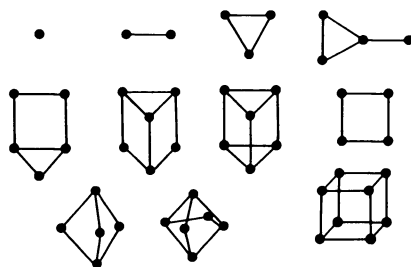
Figure 5. Structures of Silicate Ions in K-silicate Solution. (Reproduced from ref. 19. Copyright 1981 American Chemical Society.)

structures. For either sodium or potassium silicate, addition of alumina to the system should change the relative stability of these structures and create new ones.

In order to make type Z a reality, we need to continue to feed the nucleation component to the crystallizing batch. This could mean circulating the liquor from the crystallizer through an environment which recreates the essential ingredient. Figure 6 is a block diagram of what such a process might look like. There are many problems still to be solved beyond the compositon of the nucleation liquor, for example pH control in the crystallizer, but the product could be of great technological interest.
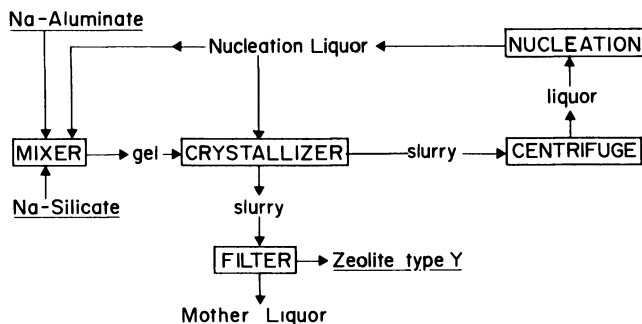
Figure 6. Flow diagram for a proposed modified batch synthesis process promoted by a nucleation agent

Literature Cited

1. Milton, R. M. U.S. Patents 2 882 243 & 2 882 244, 1959.
2. Breck, D.W. U.S. Patent 3 130 007, 1961
3. Robson, H. E. Chemtech 1978, 8, 176.
4. Rabo, J.A.; Poutsma, M. L. Molecular Sieves Zeolites-II, Advances in Chem. Series No. 102; American Chemical Society: Washington DC, 1971 p 284
5. Pine, L. A.; Maher, P. J.; Wachter, W.A. J. Catal. 1984, 85, 466
6. Ward, J. W.; Carlson, T. L. U.S. Patents 4 517 073, 1985 and 4 576 711, 1986.
7. Wachter, W. A. Proc. 6th Int. Zeolite Conf. 1983, p 141.
8. Dempsey, E.; Kuhl, G. H.; Olson, D. H. J. Phys. Chem. 1969, 73, 387
9. Skeels, G. W.; Breck, D. W. Proc. 6th Int. Zeolite Conf. 1983 p 87.
10. Lynch, J. et. al., Zeolites 1987, 7, 333.
11. Sakurada, S. et.al., European Patent 40 104, 1981.
12. Rollman, L.D. U.S. Patent 4 107 195, 1978.
13. Bibby, D. M.; Dale, M. P. Nature 1985, 317, 157
14. Donahoe, R. J.; Liou, J. G. Geochemica et Cosmochemica Acta 1985, p 34.
15. Kacirek, H.; Lechert, H. J. Phys. Chem. 1976, 80, 1291
16. Vaughan, D. E. W. U.S. Patent 4 714 601, 1987.
17. Verdijn, J. P. European Patent 142 355, 1984
18. McDaniel, C. V.; Duecker, H. C. U.S. Patent 3 574 538, 1971.
19. Harris, R. K.; Knight, C. T. G.; Hull, W. E. J. Am. Chem. Soc. 1981, 1577

Chapter 31

Secondary Synthesis of Faujasitic Catalysts

Halimaton Hamdan and Jacek Klinowski

Department of Chemistry, University of Cambridge, Lensfield Road, Cambridge CB2 1EW, England

Aluminium can be isomorphously substituted for silicon in the framework of zeolite Y by hydrothermal treatment of the dealuminated (ultrastabilised) zeolite with aqueous solutions of strong bases at elevated temperatures. The extent and efficiency of the reaction depend on the temperature, duration of treatment and especially on the kind and concentration of the basic solution. The degree of crystallinity and the thermal stability of the products are primarily controlled by the composition of the parent material. ^{29}Si and ^{27}Al magic-angle-spinning NMR (MAS NMR) indicates that the extent of realumination is determined by the number of available tetrahedral Si(0Al) sites. The distribution of aluminium and silicon atoms in the frameworks of the precursors and the products of the reaction is very different.

Properties of zeolites are intimately related to the type of occupancy of the tetrahedral sites. Modification of the composition of the framework by increasing the silicon content increases the thermal stability of the samples. The catalytically active centres in zeolites are the acidic (Brønsted) hydroxyl groups associated with tetrahedrally coordinated framework aluminium atoms. Catalytic activity is thus strongly dependent on the concentration and location of aluminium in the framework.

It is clearly desirable to be able to alter the Si/Al ratio of the framework, particularly in the case of zeolites X, Y and ZSM-5. This can be conveniently achieved by "secondary synthesis", i.e. by isomorphous substitution of Si or Al on the tetrahedral sites after the completion of the original zeolite crystallization (1-4). We shall demonstrate that:

1. Virtually all the extra-framework aluminium in dealuminated (ultrastabilized) zeolite Y can be re-substituted into the framework by treatment with an aqueous solution of KOH.
2. Under carefully controlled experimental conditions the crystallinity of the realuminated samples is retained.

3.   The realumination process strongly depends on parameters such as the residual sodium content of the parent material, duration of treatment, temperature, concentration of the realuminating solution and the kind of base.

4.   The distribution of Si and Al among the tetrahedral sites in the treated material is very different from that in as-prepared zeolite Y with the same Si/Al ratio.

Experimental

Sample Preparation. The parent sample for all experiments was zeolite Na-Y (Degussa) with Si/Al = 2.56. This has been ammonium exchanged by treatment with 2M aqueous solution of NH_4NO_3 at 80°C. 62% ammonium-exchanged zeolite (sample A) was prepared by a single contact, and samples B and C (with 82% and 90% ammonium content, respectively) by repeated contacts with the solution. Ammonium-exchanged samples were hydrothermally treated at 525°C for 18 hours in a horizontal tubular quartz furnace under deep-bed conditions while water was slowly injected into the tube by a peristaltic pump, keeping the partial pressure of H_2O above the zeolite bed at 1 atm. Ultrastable samples USYA, USYB and USYC were prepared by steaming samples A, B and C once, and sample USYD by steaming sample A at 525°C, ion exchanging and steaming again at 525°C for 18 hours.

Realumination was carried out at a constant preselected temperature by stirring the ultrastable material with an aqueous solution of a strong base. 50 ml of the basic solution per gram of zeolite was used in all experiments. The effect of contact time was studied by treating USYA with KOH solution for different lengths of time, the effect of temperature by treating USYA with KOH at 30, 60, 80 and 100°C (to yield samples USYA-1 to USYA-4, respectively) and the effect of concentration by subjecting USYA to 0.10, 0.25, 0.50, 1 and 2M KOH solutions (to give samples USYA-11 to USYA-15, respectively). Potassium (rather than sodium) hydroxide was deliberately used in the preliminary realumination of USYA in order to prevent the possibility that the increase in the framework aluminium content is due to recrystallization of the zeolite since it is known (5) that faujasites do not recrystallize from potassium-bearing solutions. Finally, the effect of the kind of base was studied by treating sample USY, prepared in the same way as sample USYA and with the framework Si/Al ratio of 5.08, with 0.25M solutions of KOH, NaOH, tetramethylammonium hydroxide (TMAOH) and NH_4OH at 80°C for 24 hours (yielding samples USYA-21 to USYA-24).

X-ray Diffraction. Powder x-ray diffraction (XRD) patterns were acquired on a Philips PW1710 vertical goniometer using Cu Kα radiation selected by a graphite monochromator in the diffracted beam. Unit cell parameters were calculated using silicon powder as an internal standard.

Magic-Angle-Spinning NMR (MAS NMR). ^{29}Si MAS NMR spectra were measured at 79.5 MHz using a Bruker MSL-400 multinuclear spectrometer. Samples were spun in Andrew-Beams rotors at 2.6 kHz using air as the spinning gas. Radiofrequency pulses of 4 μs duration were applied with 20 s recycle delay. 1000 transients were acquired for each spectrum. ^{29}Si chemical shifts are quoted in ppm from external tetramethylsilane (TMS).

^{27}Al MAS NMR spectra were measured at 104.26 MHz using powerful 0.6 μs radiofrequency pulses with a 0.2 s recycle delay. Samples were spun at 3.4 kHz in an aluminium-free probehead and Vespel rotors. Chemical shifts are quoted in ppm from external $Al(H_2O)_6^{3+}$. 10000 transients were acquired for each spectrum.

Infrared Spectra. IR absorption spectra in the zeolitic framework vibration region (1400-400 cm^{-1}) were recorded using a Nicolet MX-1 Fourier transform spectrometer and the conventional KBr disc technique.

Results and Discussion

^{29}Si MAS NMR spectra of dealuminated samples before treatment with KOH (Figure 1) are in complete agreement with earlier work (6-16) and consist of up to five signals in the chemical shift range of -85 to -105 ppm corresponding to Si(nAl) building blocks where n, which can be 0, 1, 2, 3 and 4, denotes the number of framework Al atoms linked, via bridging oxygens, to a given silicon. The spectra were deconvoluted using Gaussian peak shapes, and the so-obtained relative intensities (peak areas) of the individual Si(nAl) signals, I_n, are given Table I. The framework Si/Al ratios of the samples were calculated from the spectra using the formula (8,14):

$$(Si/Al)_{NMR} = \frac{I_4 + I_3 + I_2 + I_1 + I_o}{I_4 + 0.75\,I_3 + 0.5\,I_2 + 0.25\,I_1} \qquad (1)$$

The ^{29}Si MAS NMR spectra of samples treated with KOH (lower traces in Figure 1) are dramatically different form those of the starting materials. The intensities of the Si(0Al) signals are greatly reduced, and the intensities of the Si(1Al), Si(2Al), Si(3Al) and Si(4Al) signals correspondingly increased as listed in Table I, signifying that a considerable amount of aluminium has entered the zeolitic framework. This is consistent with the observed increase in the unit cell parameter. Using values of $(Si/Al)_{NMR}$ calculated from Equation 1 in conjunction with the values of the overall Si/Al ratio measured by atomic absorption (AA), the number of framework (subscript F) and non-framework (subscript NF) atoms per unit cell of 192 tetrahedral atoms can be calculated (8,15).

^{27}Al MAS NMR of the dealuminated and realuminated samples are given in Figure 2. It shows that the signal at ca. 60 ppm corresponding to tetrahedral framework aluminium decreases upon dealumination and increases again on reinsertion of Al into the framework. Any loss of
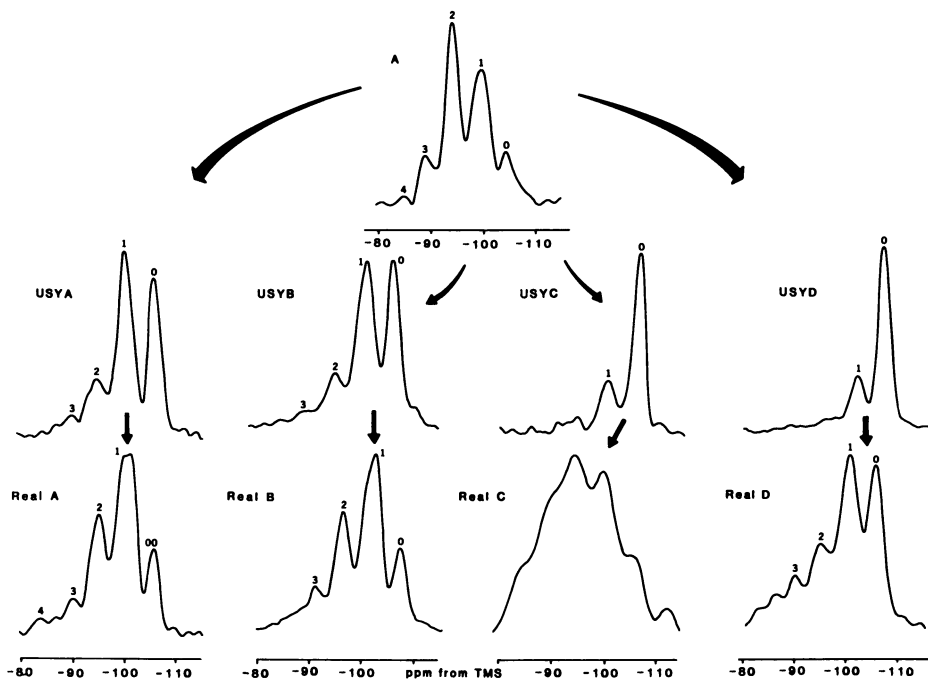
Figure 1. ^{29}Si MAS NMR spectra of the starting zeolite, the dealuminated (ultrastable) samples and the hydrothermally realuminated samples. Samples A, B, C and D (the spectra of which are identical) have been used to prepare dealuminated samples USYA, USYB, USYC and USYD, which upon treatment with KOH solution gave rise to samples Real A, Real B, Real C and Real D, respectively. Numbers above individual peaks give the n in Si(nAl).

TABLE I.   Relative populations of Si(nAl) tetrahedral building blocks in the samples (normalized to 100) calculated by Gaussian deconvolution of ^{29}Si MAS NMR spectra (see text)

Sample	Si(4Al)	Si(3Al)	Si(2Al)	Si(1Al)	Si(0Al)
A	1.2	12.3	37.2	40.0	9.3
USYA	0.0	1.4	14.3	48.6	35.8
Real A	2.7	8.4	30.0	47.2	11.7
B	1.4	11.4	41.3	36.5	8.4
USYB	0.0	3.8	12.4	44.7	39.1
Real B	0.0	4.8	25.4	51.3	18.5
C	1.7	11.9	40.2	35.9	10.3
USYC	0.0	0.0	0.0	28.1	71.9
Real C			amorphous		
USYD	0.0	0.0	2.1	21.2	76.8
Real D	4.1	5.5	21.1	38.6	30.6
USYA-1	0.5	3.0	22.1	56.8	17.8
USYA-2	2.3	5.7	24.7	56.1	11.2
USYA-3	2.7	8.4	30.0	47.2	11.7
USYA-4	0.0	4.8	19.1	50.2	25.9
USYA-11	0.0	1.2	29.0	47.0	22.9
USYA-12	2.6	9.9	23.9	49.9	13.6
USYA-13	3.1	10.0	31.7	45.0	10.2
USYA-14	7.9	17.5	36.5	32.1	6.0
USYA-15	24.5	25.6	35.4	14.4	0.0
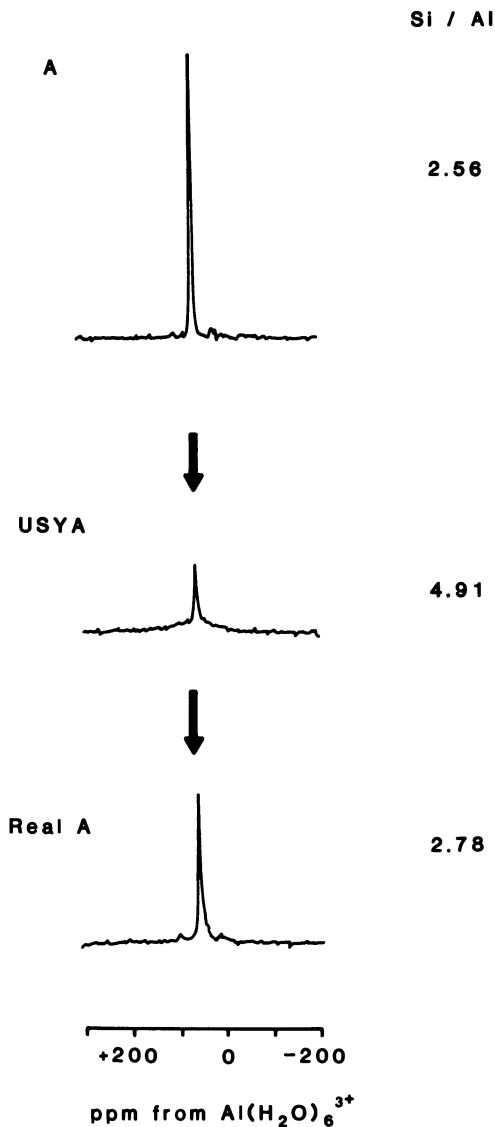
Figure 2. ^{27}Al MAS NMR spectra of hydrated samples A, USYA and Real A on the absolute intensity scale. 10,000 scans were acquired in each case using resonant rf pulses of 600 ns duration.

crystallinity of the treated sample (not observed in this case) is indicated by the formation of non-framework octahedral aluminium which resonates at about 0 ppm. Broadening of the tetrahedral linewidth upon realumination indicates that the distribution of the reinserted aluminium is less selective and different from that of the as-prepared material. A full discussion of the quantitative aspects of the ^{27}Al NMR spectra of dealuminated and re-aluminated zeolites is given in the accompanying paper ([3]).

Further support for the conclusion that extensive realumination has taken place comes from the increase in unit cell parameter and from IR spectra ([4]). The spectra of treated samples show shifts to lower frequencies in the framework vibration region with respect to the untreated samples, except for the T-O bending at ca. 450 cm^{-1} which is known ([17]) to be insensitive to framework composition. These changes are considerable and consistent with the increase in the framework aluminium content. The band at ca. 730 cm^{-1}, related to the symmetric Si-O-Al or to "isolated" AlO$_4$ tetrahedra, increases in intensity following the treatment. Furthermore, the band at ca. 812 cm^{-1} which is known to shift to lower frequencies and decrease in intensity with an increase in framework aluminium is clearly observed in the realuminated product.

Mechanism of Isomorphous Substitution. We suggest that the mechanism of realumination is as follows. Ultrastabilization removes framework Al at random ([12,13,18,19]). The extra-framework Al forms soluble (tetrahedral) aluminate anions upon contact with KOH. At the same time the zeolite undergoes partial dissolution in the base. Little is known about the solubility of zeolites in bases, and the only published work of which we are aware ([20]) deals with zeolites of low Si/Al ratio, but it is clear that the Si(0Al) building units are more soluble than the other four kinds in the same way in which silica is more soluble than aluminosilicates. The aluminate anions then enter the framework by elimination of Si(0Al) sites as described above. This was confirmed by the measurements of the composition of liquors after realumination. The liquor from sample USYA-13 contained 13.1% of the Si and 2.51% of the Al originally present in sample USYA from which it was prepared. This means that 10.01% of the sample was lost upon KOH treatment. In the case of sample USYA-15, prepared using 2M KOH solution, the total weight loss was ca. 13%. The weight loss depends very strongly on the concentration of the base: we have found ([4]) that only ca. 5% of a sample treated in 0.25M KOH (sample 9 in that reference) was dissolved in the course of treatment. The liquors always contained very little aluminium (Si/Al>5.5) and we believe that it is primarily the *amorphous* part of the ultrastable sample which is dissolved in the base.

Factors Controlling the Substitution

(1)   Residual sodium content. The degree of crystallinity of all samples was qualitatively determined from XRD pattern intensities with reference to the starting sample in the presence of an internal standard. The crystallinity of the realuminated products is higher than those of the siliceous samples from which they were produced. In fact, the crystallinity of the products is primarily governed by the characteristics of the parent dealuminated material. Highly siliceous samples USYA, USYB and USYC, prepared from samples A, B, and C respectively, have different degrees of crystallinity and Si/Al ratios as listed in Table II. Samples with low residual sodium content yield more siliceous products. Although the dealuminated samples are of comparable crystallinity to that of the starting NH_4,Na-Y, it is clear that the realuminated products are of very different quality. The aluminous zeolite derived from dealuminated sample Real A (with Si/Al=4.91) is highly crystalline while a partial collapse of structure is observed in sample Real B produced from ultrastable Y with a slightly higher Si/Al ratio. Sample Real C, derived from the precursor with Si/Al=14.2, is completely amorphous. Such loss of crystallinity must be attributed to the creation of a larger number of framework vacancies during steaming compounded by the dissolution of Si(4Si) sites in the course of treatment with the base. Dissolution is more rapid in more siliceous frameworks, the structure of which is destroyed before the vacancies can be reoccupied by the incoming aluminium atoms (4). Realuminated products of maximum crystallinity are prepared when the composition of the dealuminated material is carefully controlled. Our results show that dealuminated zeolite Y with Si/Al ratio as high as 15.75 (sample USYD) can be made more resistant to base treatment by ultrastabilization or repeated steaming, ammonium exchange and calcination. Such material remains crystalline upon realumination. This observation agrees with earlier work which established that repeated heat treatment and ion exchange "heal" the defects and thereby strengthen the framework structure (10-16,18,19). In conclusion, the most highly crystalline realuminated zeolites are prepared from medium-silica ultrastable materials, i.e. those which were made from parent samples high in residual sodium.

(2)   Contact Time. Table III shows that realumination initially proceeds very fast. 67% of the non-framework aluminium goes back into the framework during the first hour of contact with aqueous solution of KOH. In general, increasing the time of contact while other parameters are kept constant has little effect on the extent of realumination as indicated by the small decrease of the Si/Al ratio of the framework (from 2.80 to 2.72) after the length of treatment was increased from 4 to 24 hours.

(3)   Temperature. Table IV shows that realumination temperature plays an important role in the realumination process. Optimum Al reinsertion is achieved at 80±5°C (sample USYA-3), while lower and higher temperatures

TABLE II. The effect of residual sodium content on the products

Sample	Residual Na content	$(Si/Al)_{NMR}$	Crystallinity
A	38%	2.56	v. good
USYA		4.91	v. good
Real A		2.78	v. good
B	18%	2.52	v. good
USYB		4.95	good
Real B		2.44	good
C	10%	2.53	v. good
USYC		14.20	low
Real C		--	amorphous
A	38%	2.56	v. good
USYD		15.75	good
Real D		4.58	poor

TABLE III. The effect of contact time on sample USYA
treated with 0.25M KOH at 80°C

Time	$(Si/Al)_{NMR}$	Al_F	Al_{NF}	ΔAl_F	% realuminated
0.0	3.96	39	15	0	--
0.5	3.10	47	7	8	53
1.0	2.96	49	5	10	67
2.0	2.86	50	4	11	73
4.0	2.80	51	3	12	80
24.0	2.72	52	2	13	86

TABLE IV. The effect of temperature on realumination of sample
USYA with 0.25M KOH for 24 hours

Sample	Temp. (°C)	a_0 (Å)	$(Si/Al)_{NMR}$	Crystallinity
USYA-1	30	24.58	3.57	v. good
USYA-2	60	24.65	3.06	v. good
USYA-3	80	24.69	2.78	v. good
USYA-4	100	24.66	3.89	good

are less favourable. This is again caused by the competition between the dissolution of the framework in the base and the substitution of aluminium. At lower temperatures the dissolution is slow, and the substitution of aluminium less effective. When dissolution is much faster than the substitution, which is likely at elevated temperatures, the framework is rendered partially amorphous. This is confirmed by the ^{29}Si MAS NMR results in Figure 3. After treatment at 100°C (sample USYA-4), more Si(0Al) sites remain upon realumination because of the amorphous silica formed blocking the pores and preventing further incorporation of aluminium. XRD also shows a decrease in crystallinity of the product at high temperatures.

(4) Concentration of the realuminating solution. ^{29}Si and ^{27}Al MAS NMR spectra of samples realuminated with KOH solutions of different concentrations (0.1 to 2M) are given in Figure 4. The concentration of the basic solution clearly plays a controlling role in determining the outcome of the process. Table V indicates a large change in composition of the product as the concentration increases from 0.1 to 2M, accompanied by an increase in the unit cell parameter. The aluminous sample USYA-15 produced by exposing USYA to 2M KOH has an exceptionally low Si/Al ratio of 1.54 which is virtually that of zeolite X.

It is clear that substitution can occur only on Si(0Al), i.e. Si(4Si) sites. It is only on these that the central silicon atom can be isomorphously substituted by aluminium without violating the Loewenstein rule (22) which prohibits Al-O-Al linkages and which is obeyed in all hydrothermally synthesised zeolites. On the other hand, all four remaining kinds of Si(nAl) sites (with n= 1, 2, 3 and 4) can be generated in the course of Al substitution of Si(0Al) sites, as demonstrated by an increase in the intensity of the NMR signal at about -100 ppm and the accompanying decrease for the Si(0Al) signal at -105 ppm. It is therefore of interest to consider quantitatively the populations of the various types of site involved in the reaction.

All tetrahedral sites in the faujasite framework are crystallographically equivalent, and each has, by definition, four first-order tetrahedral neighbours. The number of second-order tetrahedral neighbours, which is structure-dependent and varies from zeolite to zeolite (23) is nine. It is important to note (4,24) that the number of Si(0Al) sites eliminated in the course of Si $\Rightarrow$ Al substitution is generally greater than the number of Al atoms inserted. In scheme 5 of Figure 5, for example, the central silicon has no second-order Al neighbours, and there is in effect a cluster of five Si(0Al) sites, which are marked with arrows. When the central silicon is substituted by Al, the remaining four Si(0Al) sites in the grouping are all converted into Si(1Al) sites, which means that they can no longer be substituted. As a result, one Al atom eliminates five Si(0Al) sites. In the other extreme (scheme 1 in Figure 5) one Al atom substituting the central silicon eliminates just one Si(0Al) site. In this case all four first-neighbour silicons are already linked to Al atoms in the second

coordination shell. In general, the number of Si(0Al) sites eliminated by one incoming Al is equal to the number of Si atoms in the first coordination shell which are not connected to aluminium atoms in the second coordination shell. Table I indicates that each incoming Al atom eliminates on the average two Si(0Al) sites, i.e. that these sites are mostly Type 2.

Three features of the spectra given in Figures 4 and 6 will be considered further. First, the Si(1Al) signal in some realuminated samples is distinctly broadened. Liu et al. (25) explained this effect. The faujasite structure contains only one kind of crystallographic tetrahedral site and, accordingly, the ^{29}Si spectrum of a purely siliceous analogue of faujasite consists of a single Si(0Al) signal. Because the aluminate tetrahedron is larger than the silicate tetrahedron, the introduction of aluminium into the framework results in distortion of the structure. The bond angles readjust themselves to accommodate the guest. As a result Si-O-Al angles are smaller than the original Si-O-Si angles, and the silicon atoms are deshielded. This distortion is reflected, to a lesser extent, in the chemical shifts of silicons more distant of the guest aluminium such as the second and further tetrahedral coordination shells. The introduction of the guest lifts the crystallographic and magnetic equivalence of the tetrahedral sites. Consequently, the Si(nT) building blocks with the same n no longer resonate at precisely the same NMR frequency and the lines are broadened. In the faujasite framework there are four nonequivalent kinds of oxygen. This means that each Si atom has four different Si-O-Si(Al) angles. It follows that these angles on the average give two kinds of Si(1T) structural groups (where T denotes Si or Al): those with the smaller [Si(1T^1)] and those with the larger [Si(1T^2)] Si-O-T angle. Si(1T^1) and Si(1T^2) groups resonate at different NMR frequencies, which gives rise to splitting in the spectrum. The Si(1Al^1) units resonate at ca. -100 ppm and the Si(1Al^2) units at ca. -101 ppm. For Si(0T) and Si(4T) there is only one kind of first-order environment, while for Si(3T) there are two and for Si(2T) three. As a result the corresponding NMR signals are broadened rather than split.

Examination of the spectra in Figure 4 clearly shows that, as the concentration of the base increases, aluminium is preferentially inserted in the Si(1Si^1) sites, which is to be expected since they offer more room to the incoming aluminate tetrahedra. The shoulder corresponding to the thus produced Si(1Al^1) units first appears in the spectrum of sample USYA-11, increases in intensity for sample USYA-12 (as more aluminium enters the framework), and becomes the dominant signal in the spectrum of sample USYA-13. The Si(1Si^2) site which initially accounts for most of the Si(1Si) signal becomes a shoulder in the spectrum of sample USYA-13 and completely disappears in sample USYA-14. Later, as the Si(1Si^1) sites are being filled, there is an increase in the Si(2Al) followed by the Si(3Al) and Si(4Al) sites indicated by a decrease in Si(1Al) in USYA-13, USYA-14 and USYA-15. Incorporation of aluminium into the framework is further demonstrated by ^{27}Al NMR spectra in Figure 4. Their relative absolute
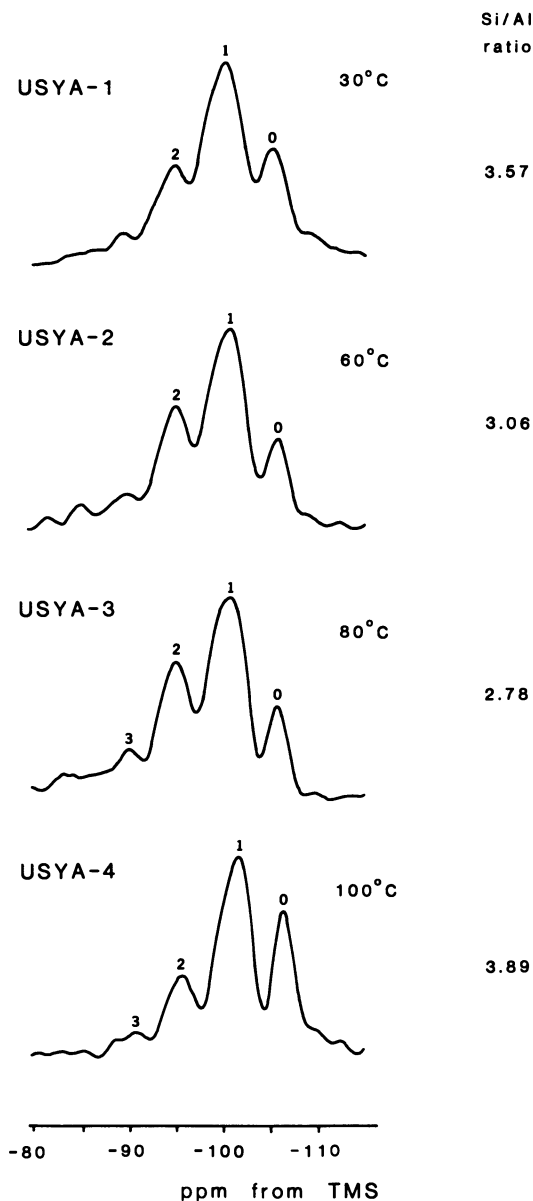
Figure 3. ^{29}Si MAS NMR spectra of samples derived from sample USYA by treatment with 0.25M KOH for 24 hours at different temperatures. The framework Si/Al ratios of the products are indicated in the right-hand column.
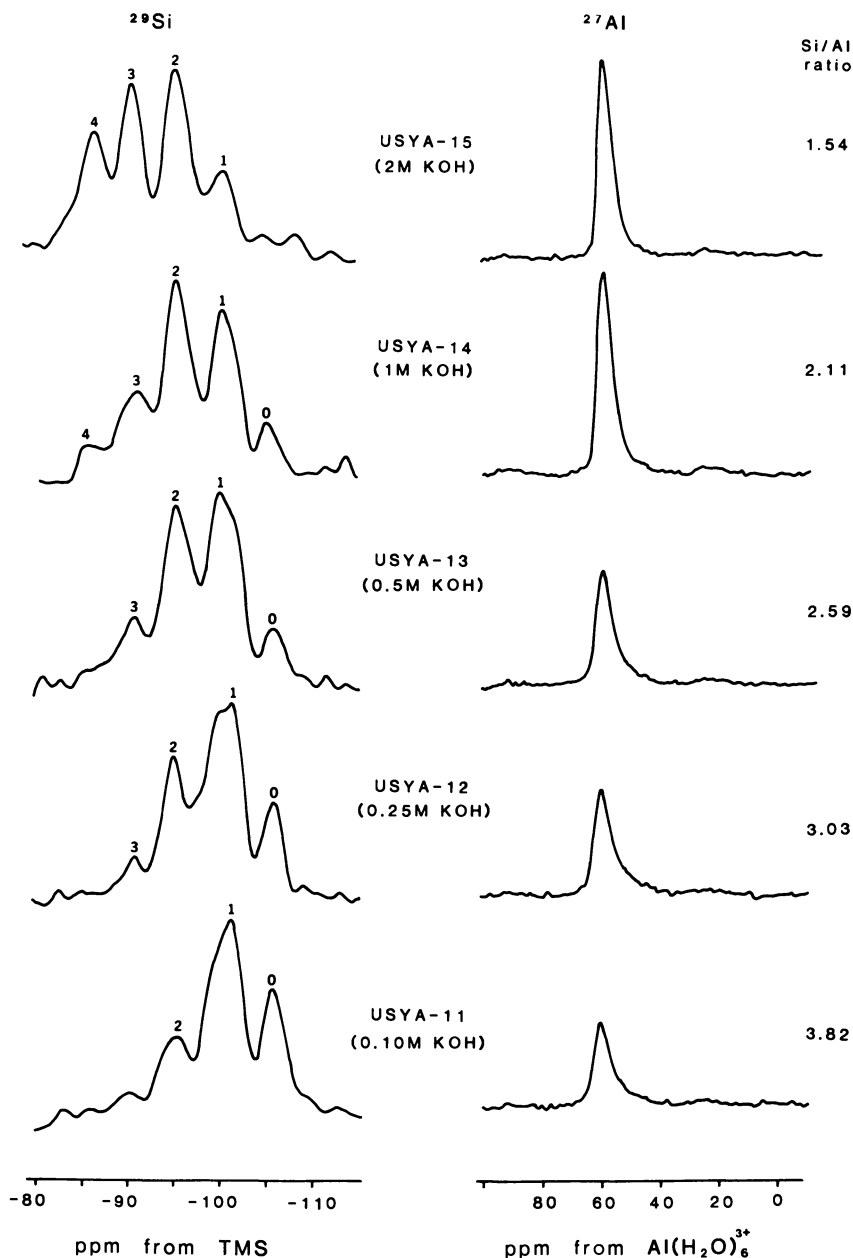
Figure 4. ^{29}Si and ^{27}Al MAS NMR spectra of samples derived from sample USYA by treatment with aqueous solutions of KOH of different concentrations for 24 hours. The framework Si/Al ratios of the products are indicated in the right-hand column.

TABLE V. The effect of concentration of KOH solution on sample
USYA treated at 80°C for 24 hours

Sample	Concentration (M)	$(Si/Al)_{NMR}$	$(Si/Al)_{XRD}$	a_0 (Å)
USYA-11	0.10	3.82	3.18	24.67
USYA-12	0.25	2.90	3.00	24.69
USYA-13	0.50	2.59	2.76	24.72
USYA-14	1.00	2.11	2.10	24.82
USYA-15	2.00	1.54	1.43	24.98
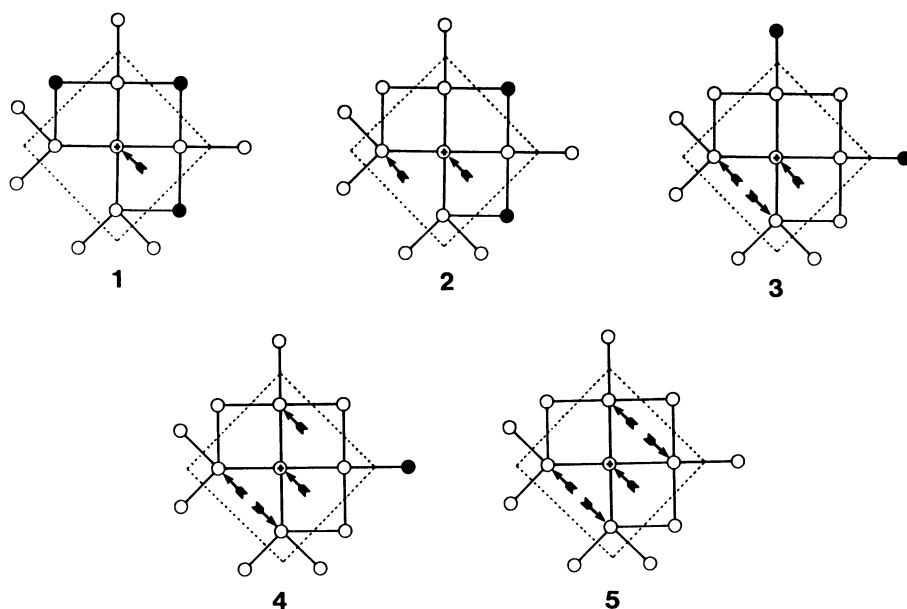
Figure 5. Possible tetrahedral environments of a silicon atom (marked with a cross) in the faujasite framework. First-order tetrahedral neighbours are separated from the second-order neighbours by the dotted line. Open circles denote silicon, closed circle aluminium; arrows indicate Si(0Al) sites. The number of such sites eliminated by substituting the central silicon by an aluminium is indicated under each diagram.
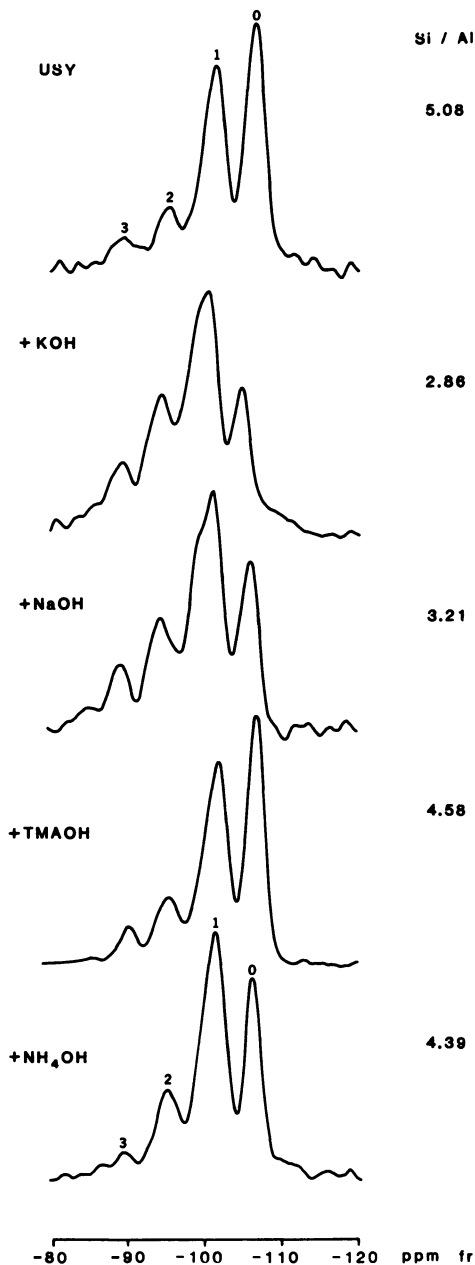
Figure 6. ^{29}Si MAS NMR spectra of samples derived from a dealuminated sample USY by treatment with 0.25M aqueous solutions of various bases for 24 hours. The framework Si/Al ratios of the products are indicated.

intensities are maximum in sample USYA-15. It is striking that the relative intensities of the Si(nAl) signals in the spectra of the products, and therefore the Si,Al distribution in the frameworks, are very different than in as-prepared samples of the same composition.

Second, there is a slight shift of all Si(nAl) signals to high field (more negative chemical shift) upon dealumination, and to low field (less negative chemical shift) upon realumination in comparison with the corresponding signals in the starting material (sample A). This is due (14) to the increase of the number of Al atoms in the second and further coordination shells of every Si, because of the dependence of the ^{29}Si chemical shift on the composition of the framework.

Third, the relative intensities of the Si(nAl) signals in realuminated samples are strikingly different from those in the as-prepared zeolites with the same framework composition, which means that the distribution of Si and Al in the treated zeolites is different. This is a consequence of the different site selectivities discussed above, but also of the fact that both the original Si(0Al) sites and the Si(0Al) sites *created during ultrastabilization* are available for Al substitution.

Realumination has also been carried out in different kinds of bases, and the results given in Figure 6 and Table VI prove that considerable amount of aluminium is reinserted into the framework in all kinds of basic solutions. The degree of realumination is related to the degree of solubility of the silica in the base, with the exception of TMAOH although it is more basic than NH_4OH. This must be due to the fact that TMA^+ cation is larger than NH_4^+.

Table VI.   The effect of the kind of base on the extent of realumination of sample USY. 0.25M aqueous solution was used at 80°C for 24 hours.

Sample	(Si/Al)$_{NMR}$	(Si/Al)$_{XRD}$	a_0(Å)
USY	5.08	5.62	24.51
+KOH	2.86	3.36	24.65
+NaOH	3.21	3.80	24.61
+TMAOH	4.58	4.82	24.55
+NH$_4$OH	4.39	4.49	24.56

Acknowledgment

Literature Cited

1.   Liu, X.; Klinowski, J.; Thomas, J. M. Chem. Phys. Lett. 1986, 127, 563.
2.   Man, P.P.; Klinowski, J. Chem. Phys. Lett., 1988, 147, 581.

3. Hamdan, H.; Klinowski, J. in this issue.
4. Hamdan, H.; Sulikowski, B.; Klinowski, J. J. Phys. Chem. 1989, 93, 350.
5. Barrer, R. M. In Hydrothermal Chemistry of Zeolites, Academic Press, London, 1982.
6. Klinowski, J. Progress in NMR Spectrosc. 1984, 16, 237 and references therein.
7. Lippmaa, E.; Mägi, M.; Samoson, A.; Engelhardt, G.; Grimmer, A.-R. J. Am. Chem. Soc. 1980, 102, 4889.
8. Engelhardt, G.; Lohse, U.; Lippmaa, E.; Tarmak, M.; Mägi, M. Z. Anorg. Allg. Chem. 1981, 482, 49.
9. Lippmaa, E.; Mägi, M.; Samoson, A.; Tarmak, M.; Engelhardt, G. J. Am. Chem. Soc. 1981, 103, 4992.
10. Klinowski, J.; Thomas, J. M.; Fyfe, C. A.; Gobbi, G. C. Nature (London) 1982, 296, 533.
11. Maxwell, I. E.; van Erp, W. A.; Hays, G. R.; Couperus, T.; Huis, R.; Clague, A. D. H. J. Chem. Soc., Chem. Comm.. 1982, 523.
12. Engelhardt, G.; Lohse, U.; Samoson, A.; Mägi, M.; Tarmak, M.; Lippmaa, E. Zeolites, 1982, 2, 59.
13. Engelhardt, G.; Lohse, U.; Patzelová, V.; Mägi, M.; Lippmaa, E. Zeolites 1983, 3, 233.
14. Klinowski, J.; Ramdas, S.; Thomas, J. M.; Fyfe, C. A.; Hartman, J. S. J. Chem.Soc., Faraday Trans. II 1982, 78, 1025.
15. Klinowski, J.; Fyfe, C. A.; Gobbi, G. C. J. Chem. Soc., Faraday Trans. I 1985, 81, 3003.
16. Engelhardt, G.; Michel, D. "High-resolution Solid-State NMR of Silicates and Zeolites, Wiley, Chichester (1987).
17. Flanigen, E. M.; Khatami, H.; Szymanski, H. A. In Molecular Sieve Zeolites-I; Flanigen, E. M.; Sand, L. B., Eds.; American Chemical Society, Washington, DC, 1971; ACS Adv. Chem. Ser. No. 101, p. 201.
18. Lohse, U.; Stach, H.; Thamm, H.; Schirmer, W.; Isirikjan, A. A.; Regent, N. I.; Dubinin, M. M. Z. Anorg. Allg. Chem. 1980, 460, 179.
19. Engelhardt, G.; Lohse, U.; Patzelová, V.; Mägi, M.; Lippmaa, E. Zeolites 1983, 3, 239.
20. Guth, J.-L.; Caullet, P.; Wey, R. Proc. 5th Intern. Zeolite Conf. Rees, L. V. C., Ed.; Hayden, London, 1980, p. 30.
21. Thomas, J.M.; Klinowski, J.; Ramdas, S.; Hunter, B.K.; Tennakoon, D.T.B. Chem.Phys. Lett. 1983, 102, 158.
22. Loewenstein, W. Am. Mineral. 1953, 39, 92.
23. Meier, W. M.; Moeck, H. J. J. Solid State Chem. 1979, 27, 349.
24. Liu, X. Ph. D. Thesis, University of Cambridge, 1986.
25. Liu, X.; Klinowski, J.; Thomas, J.M. Chem. Phys. Lett. 1986, 127, 563.

RECEIVED December 22, 1988

Chapter 32

Quadrupole Nutation NMR Studies of Second Generation Faujasitic Catalysts

Halimaton Hamdan and Jacek Klinowski

Department of Chemistry, University of Cambridge, Lensfield Road, Cambridge CB2 1EW, England

^{27}Al quadrupole nutation NMR reveals the presence of four kinds of aluminium in dealuminated zeolite Y: framework tetrahedral (F), non-framework tetrahedral (NFT), distorted framework tetrahedral (DFT) and non-framework octahedral (NFO). The DFT aluminium, which is reported for the first time here, is bonded to hydroxyl groups formed during de-alumination. In samples realuminated by hydrothermal isomorphous substitution in aqueous KOH at elevated temp-eratures both the NFO and NFT aluminium is reinserted into the framework and the intensity of the DFT signal is corresp-ondingly reduced. The NFT aluminium resonates at a lower frequency than the F aluminium, and is subject to stronger quadrupolar interactions. Quantification of the various NMR signals is essential for the determination of the distribution of aluminium in zeolites.

All NMR transitions of nuclei with I>1/2 are subject to first-order quad-rupole interactions with the exception of the central (1/2 ⇔ -1/2) transition which experiences only the second-order effects. Spectra of quadrupolar nuclei in polycrystalline samples give characteristic powder patterns for the central transition, whereas all other transitions are usually broadened beyond detection. While magic-angle spinning (MAS) reduces the line-width of the central transition by a factor of ca. 4 in comparison with a static spectrum, second-order quadrupole interactions cannot be averaged to zero by MAS. Approximately 85% of all nuclei have I>1/2, and many quadrupolar components of common solids, such as ^{23}Na and ^{39}K, have in addition narrow chemical shift ranges, which greatly complicates the interpretation of their spectra.

Quadrupole nutation NMR of nuclei with half-integer spin in pow-dered samples (1-8) can distinguish between nuclei subjected to different quadrupole interactions, the signals from which overlap in ordinary NMR spectra. The technique can be used for the determination of the local

environment of Al in zeolitic catalysts, which is essential for the under-
standing of their chemistry. One of the difficulties involved is that, as a
result of strong quadrupole interactions, the amounts of framework and
non-framework Al in thermally treated samples determined by the joint
application of ^{29}Si magic-angle-spinning (MAS) NMR (which monitors
framework Al) and of chemical analysis (which gives the *total* Al content)
are in striking disagreement with the results of ^{27}Al MAS NMR (9-11). The
latter underestimates the amount of Al, and indirect methods, such as
impregnation of the sample with ethanolic acetylacetone (12,13) prior to
measurement have been used to observe the "invisible" aluminium. We
have recently reported a series of advances towards quantitative determin-
ation of aluminium in zeolites by NMR (6-8), showing that all the Al can be
detected by NMR in the solid state provided certain experimental conditions
are met. We shall now demonstrate that:

1. During the course of hydrothermal dealumination (ultrastabilisation) of
    zeolite Y quadrupole nutation NMR detects *four* kinds of aluminium
    sites. In addition to signals from the framework (F), non-framework
    tetrahedral (NFT) and non-framework octahedral (NFO) aluminium
    there is a signal which we attribute to distorted framework (DFT)
    aluminium bonded to hydroxyl nests formed during dealumination.

2. When dealuminated zeolite Y is treated with an aqueous solution of a
    strong base such as KOH hydrothermal isomorphous substitution of
    silicon by aluminium takes place. Reinsertion of non-framework
    tetrahedral (NFT) and non-framework octahedral (NFO) aluminium
    reduces the distortion of the aluminate tetrahedra in the framework.

3. Realumination can only occur if there are sufficient suitable Si sites in
    the framework. Treatment of amorphous faujasites containing various
    kinds of aluminium leads to the formation of NFT aluminium with
    characteristic chemical shift and quadrupolar interactions.

A quadrupole nutation NMR experiment (see Figure 1) is performed
as follows. During the **preparation** period the spin system reaches thermo-
dynamic equilibrium. During the **evolution** period the sample is irradiated
with an rf field with a pulse of length t_1. The **detection** period corresponds
to the acquisition of the free induction decay (FID) over time period t_2. By
keeping t_2 constant and increasing t_1 by equal increments at regular
intervals, a series of FIDs is acquired. A double Fourier transformation in t_2
and t_1 gives a two-dimensional NMR spectrum with the axes F_2 (containing
the chemical shift and the second order quadrupolar shift) and F_1
(containing only the quadrupolar information). The projection of the
spectrum onto F_2 is equivalent to a normal powder spectrum showing the
combined effect of the chemical shift and quadrupolar interactions. The
projection onto F_1 gives the precession frequencies around the rf field in the
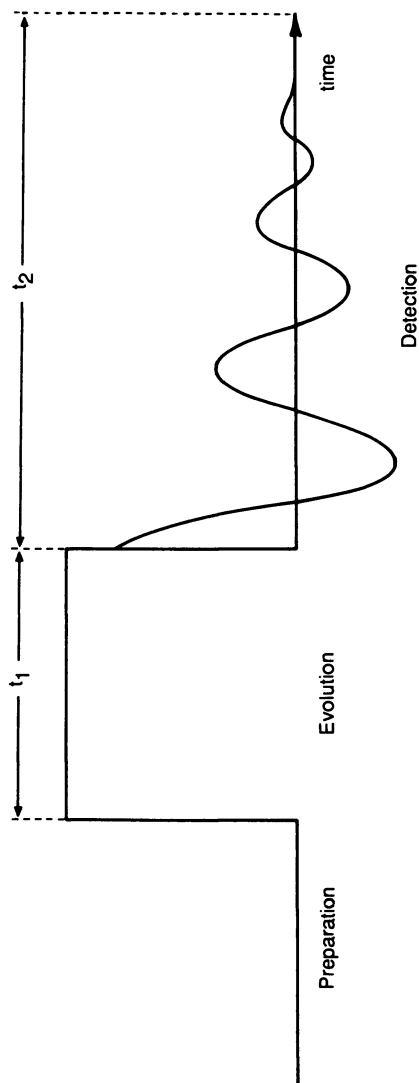
Figure 1. Schematic representation of the ^{27}Al quadrupole nutation experiment. The rf pulse of length t_1 is followed by the detection of the free induction decay in the absence of rf fields. Two-dimensional Fourier transformation of the series of FIDs gives the nutation spectrum.

rotating frame which depend on the ratio of the quadrupolar parameter ω_Q and the rf field strength ω_{rf}. When $\omega_Q << \omega_{rf}$ a strong peak appears at the nutation frequency $\omega_1 = \omega_{rf}$, while for $\omega_Q >> \omega_{rf}$ the peak is at $\omega_2 = (I+1/2) \omega_{rf}$. More complicated line shapes result for stationary samples in the intermediate cases (1, 5). The strength of the quadrupolar interaction, ω_Q, can be up to several MHz depending on the nucleus and the structure of the solid, while the strength of the rf pulse is normally insufficient to allow the quadrupolar interaction to be neglected during the irradiation of the spin system.

Experimental

The ^{27}Al nutation spectra were measured at 104.26 MHz using a Bruker MSL-400 multinuclear NMR spectrometer with a high-power static probe-head and a 5 mm diameter horizontal solenoidal coil. Using an aluminium nitrate solution the amplitude of the rf pulse ($\omega_{rf}/2\pi$) was adjusted and kept at a constant value of 70±5 kHz unless otherwise stated. Nutation experiments were performed on the same amount of each sample and the same number of transients was accumulated for samples in the same series. The rf pulse length was increased in 1 μs increments from 2 μs to 65 μs. The spectral width was 125 kHz, the recycle delay 0.2 s and the number of transients accumulated in each measurement was between 2000 to 4000. The FIDs were doubly Fourier transformed in the magnitude mode. A sine bell digitizer filter and zero filling were used in the F_1 dimension with no filter in the F_2 dimension.

Preparation of Samples. Dealuminated samples were prepared by hydro-thermal treatment of 62% ammonium-exchanged zeolite NH_4,Na-Y (sample 1). Samples D-1 and D-2 were made by steaming 20 g portions of sample 1 in a tubular quartz furnace (14) at 525°C with water being injected by a peristaltic pump with a flow rate of 12 ml/hour for 5 and 18 hours, respectively. The amorphous sample A-5 was prepared by repeated washing of sample 1 with 1M HNO_3 and steaming at 525°C. Another amorphous sample (A-6) was made by treating sample 1 with excess mixed aqueous solution of CH_3COONH_4 and $(NH_4)_2SiF_6$.

Realuminated samples R-3 and R-4 were prepared by hydrothermal isomorphous substitution (6,14) by stirring 1 g of sample D-2 in 50 ml of 0.5M and 2M KOH at 80°C for 24 hours. The treatment of amorphous alumino-silicates A-5 and A-6 in 0.5M KOH under the same conditions gave samples AR-7 and AR-8, respectively. The conditions of preparation of all samples are summarised in Table I.

TABLE I.   Conditions of preparation of samples. (S) denotes hydrothermal treatment (steaming); (R) denotes treatment with aqueous KOH; (Ch) denotes chemical treatment as described.

Sample no.	Prepared from sample no.	Treatment
1	parent Na-Y (Si/Al = 2.56)	62% NH_4-exchanged in 2M NH_4NO_3
D-1	1	(S) 525°C, 5 hr.
D-2	1	(S) 525°C, 18 hr.
R-3	D-2	(R) 0.5M KOH, 80°C, 24 hr.
R-4	D-2	(R) 2M KOH, 80°C, 24 hr.
A-5	1	(S) 525°C, 18 hr, 1M HNO_3 (twice)
A-6	1	(Ch) Aqueous CH_3COONH_4 + $(NH_4)_2SiF_6$, 80°C, 1hr.
AR-7	A-5	(R) 0.5M KOH, 80°C, 24 hr.
AR-8	A-6	(R) 0.5M KOH, 80°C, 24 hr.

Results and Discussion

All samples were characterized by x-ray diffraction (XRD) and by ^{29}Si and ^{27}Al MAS NMR. The unit cell parameters, framework Si/Al ratios and the numbers of framework Si and Al atoms per unit cell calculated from deconvolution using Gaussian peak shapes are given in Table II. All samples were fully hydrated over saturated NH_4Cl for 24 hours prior to NMR experiments.

XRD patterns of dealuminated samples D-1 and D-2 agree well with previous work (15). The samples are highly crystalline and the (cubic) unit cell parameter is reduced (Table II) by the dealumination of the framework. The Si/Al ratios of samples D-1 and D-2 were 3.10 and 4.91, respectively, which confirms that the degree of dealumination increases with the duration of hydrothermal treatment.

^{27}Al MAS NMR spectra of samples 1, D-2 and R-3 in the absolute intensity mode are given in Figure 2. As a result of dealumination, the intensity of the framework aluminium (F) signal at ca. 60 ppm in sample D-2 is much lower than in sample 1. The absence of spectral features at 0 ppm shows that aluminium extracted from the framework is in tetrahedral coordination, but the broadening of the ^{27}Al signal indicates that there is a wider range of quadrupole interactions than before thermal treatment.

The nutation spectrum of sample 1 (Figure 3) consists of two signals [at (60 ppm, 78 kHz) and (60 ppm, 195 kHz)], both with the same linewidth of 855 Hz and both corresponding to framework (F) aluminium. The presence of *two* signals is due to the fact that the quadrupole interaction characteristic of framework ^{27}Al is of the same order of magnitude as the strength of the rf pulse. Since the latter is insufficient to overcome the quadrupole interaction entirely, the excitation is not fully non-selective (8). We have confirmed this by examining the nutation spectrum (not shown) of the same sample irradiated with a stronger rf pulse (96 kHz, as compared to 70 kHz for the spectra shown in Figure 3). The spectrum still contained two signals, at (60, 101) and (60, 230), but the intensity of the first signal increased and that of the second decreased. This proves that both signals correspond to the same type of aluminium.

In general, dealumination of sample 1 for various periods leads to spectra composed of up to four signals:

1.	60 ppm, 78 kHz;	(F)
2.	-2 ppm, 78 kHz;	(NFO)
3.	56 ppm, 195 kHz;	(NFT)
4.	74 ppm, 195 kHz;	(DFT, see below).

Signals **1-3** have been assigned earlier (4,16). The highly crystalline dealuminated samples D-1 and D-2 apparently do not contain NFO aluminium (signal **3**) but do contain the three remaining types: the projection of

ppm from $Al(H_2O)_6{}^{3+}$
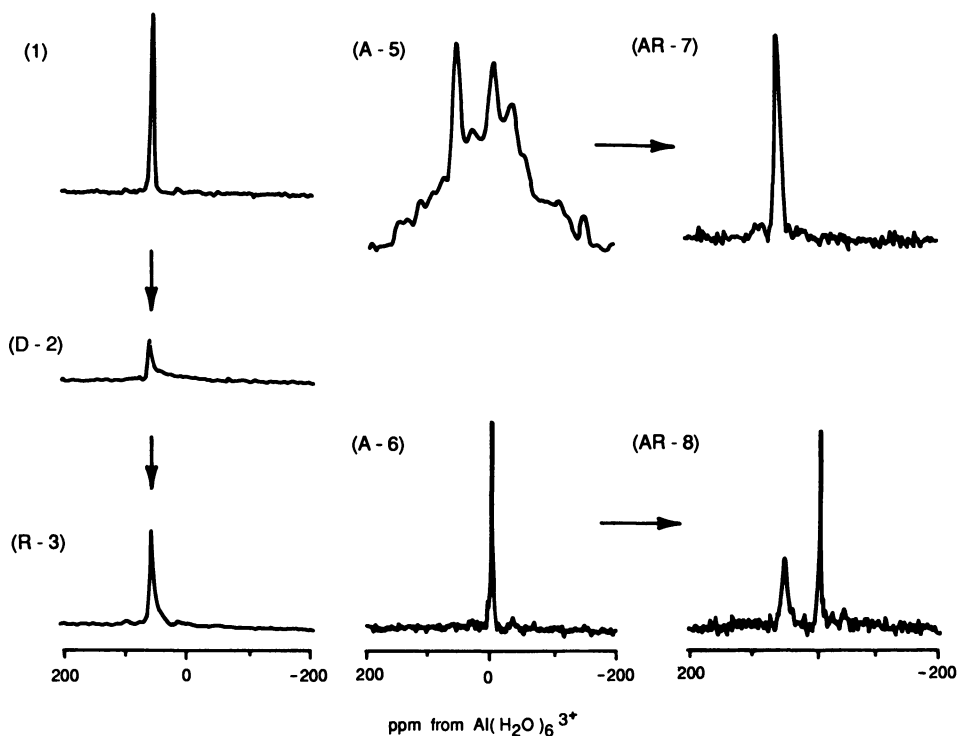
Figure 2. ^{27}Al MAS NMR spectra. The spectra of samples 1, D-2 and R-3, but not those of the remaining samples, are given in the absolute intensity mode.

TABLE II.   Unit cell parameters and the composition of the samples. Si_F and Al_F denote numbers of Si and Al atoms per unit cell of 192 tetrahedral atoms.

Sample	$a_0(\text{Å})$	$(Si/Al)_{NMR}$	Si_F	Al_F
1	24.69	2.56	138	54
D-1	24.58	3.10	145	47
D-2	24.52	4.91	160	33
R-3	24.72	2.59	139	54
R-4	24.98	1.54	116	76
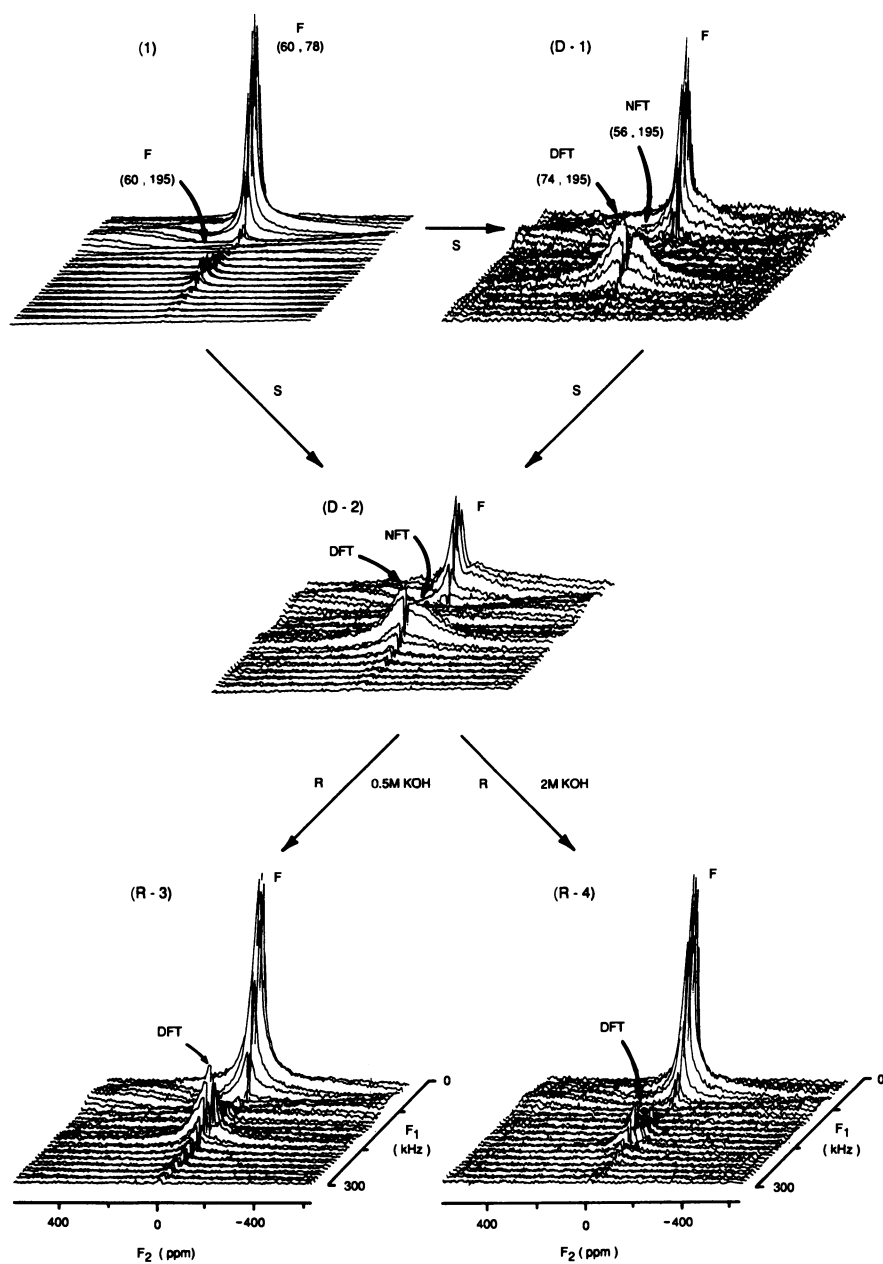
Figure 3. ^{27}Al quadrupole nutation spectra of crystalline samples.

the nutation spectra in Figure 3 onto F_2 gives a very broad signal at 60 ppm, while the projection onto F_1 clearly reveals three component signals (1,4,5). Signal **4** does not coincide with any of the previously assigned peaks. In order to assign it correctly, we must consider several arguments. Figure 3 shows that, as dealumination progresses, there is a change in relative intensities of the F and NFT signals and of the signal we wish to assign. The last two peaks first appear in sample D-1 and become more intense in comparison to the F signal in the more highly dealuminated sample D-2. Signal **4** cannot be part of either the F or the NFT peak since it occurs at a lower field: its projection onto F_2 is at 74 ppm and has a larger linewidth than signal F. The first step in the thermal treatment of zeolite NH_4,NaY is the formation of the H-form (17,18), which generates tetrahedral *framework* aluminium associated with the hydroxyl nests. These nests can be "healed" by the rearrangement of the framework during which the vacancies left by the expulsion of Al are reoccupied by Si from other regions of the sample. However, there is evidence that some hydroxyl nests do remain (19,20). The proton is more electronegative than silicon and deshields the ^{27}Al nucleus so that it resonates at lower field. The presence of the proton makes the environment of ^{27}Al asymmetric, i.e. increases quadrupole effects. A simple calculation based on the ^{29}Si MAS NMR spectra (see Table II) and the obvious fact that the *total* amount of Al in the sample remains constant upon heat treatment shows that 61% of the total aluminium (33 out of 54 atoms) in sample D-2 is part of the framework. Deconvolution of the ^{27}Al spectrum in Figure 2 based on the (incorrect) assumption that the linewidth of the ^{27}Al signal remains constant upon hydrothermal treatment, always gives much lower amounts of framework Al than calculated from ^{29}Si MAS NMR and XRD (9,10,18). Since it has been demonstrated that *hydrated* zeolites contain no "invisible" aluminium (6-8), one of the two signals at 195 kHz in F_1 in Figure 3 must represent *framework Al in sites distorted as a result of the hydrothermal treatment*. Signal **4** (at 74, 195) is therefore assigned to tetrahedral framework aluminium in a distorted environment (DFT). Since it occurs at a higher nutation frequency than the "ordinary" (F) aluminium, such Al is subject to stronger quadrupole effects. Earlier work (13) has shown that almost all non-framework aluminium dissolves in ethanolic acetylacetone but that no framework aluminium does so unless the treatment is continued for extended periods. The nutation spectrum of sample D-2 treated with acetylacetone indicates (not shown) that a considerable amount of NFT aluminium has been removed, but that the F and DFT signals remain virtually unaffected. This further confirms that framework aluminium is not complexed by acetylacetone, and that signal **4** comes from Al in the framework, but subjected to stronger quadrupole interactions than in untreated samples.

The intensity of the ^{27}Al MAS NMR spectrum of the realuminated sample R-3 (Figure 2) is greater than that of the dealuminated sample D-2. The F_2 projection indicates that aluminium in the latter sample is in the tetrahedral coordination. The nutation spectra (Figure 3) clearly show that

the aluminium does go back into the framework. As realumination progresses, the F signal at (60, 78) increases. By comparing nutation spectra of many realuminated samples containing different amounts of framework aluminium as a result of treatment with KOH solutions of different concentrations we have found that *both* the NFT and (whenever present in the ultrastable precursors) the NFO species are involved. Upon treatment with 0.5M KOH (sample R-3) the NFT signal disappears faster than the DFT signal, indicating that the initial stage of the reaction involves primarily a conversion of NFT aluminium into F aluminium. The intensity of the DFT signal falls significantly only after most NFT aluminium has gone back into the framework (as in sample R-4 which has been treated with a more concentrated base). Also, the F signal in the realuminated sample R-4 is much narrower than in sample D-2 from which it was prepared, which indicates that the distribution of F aluminium is more ordered and symmetrical. However, the effect is not sufficiently large for the chemical shifts and/or quadrupole interactions to be manifested as a change in the F_1 frequency. Aluminium reinsertion is evidently accompanied by a "relaxation" of the zeolitic framework. A treatment of the realuminated sample R-4 with acetylacetone does not remove aluminium from either the F or the remaining DFT sites.

Although there is ample proof by NMR in one and two dimensions that aluminium is indeed reinserted into the framework, it could be argued that part of the tetrahedral aluminium observed in hydrothermally treated samples is attributable to amorphous parts of the sample which cannot be distinguished from the crystalline part by ^{29}Si MAS NMR or the conventional ^{27}Al MAS NMR. Si(nAl) units in the amorphous phase generally give rise to very broad ^{29}Si NMR signals which overlap with signals from the crystalline regions of the sample ([19]). In order to demonstrate that our samples contain only *crystalline* aluminosilicate and therefore that this possibility may be dismissed, we have acquired nutation spectra of zeolite samples which have been deliberately made amorphous by chemical treatment (see Table I). We did not use thermal methods of amorphization so as to avoid recrystallization of compact aluminosilicates. The XRD patterns of the amorphous samples A-5 and A-6 are featureless with a broad hump at $2\theta = 22^0$. The ^{29}Si MAS NMR spectra of amorphous samples A-5 and A-6 (Figure 5) both feature a large broad peak at - 112 ppm, typical of amorphous silica ([18]). The ^{27}Al MAS NMR spectrum of sample A-5 (Figure 2) is broad and contains both octahedral and tetrahedral signals, indicating that many kinds of non-equivalent environments for aluminium are simultaneously present. This is further confirmed by the nutation spectrum of sample A-5 (Figure 4), composed of numerous weak features obscured by the noise. By contrast, the ^{27}Al MAS NMR spectrum of the amorphous sample A-6 features a narrow peak at -2 ppm (Figure 2) indicating that the aluminium is mobile and in octahedral coordination. There is an additional low intensity signal at 60 ppm indicating that a small amount of tetrahedral aluminium
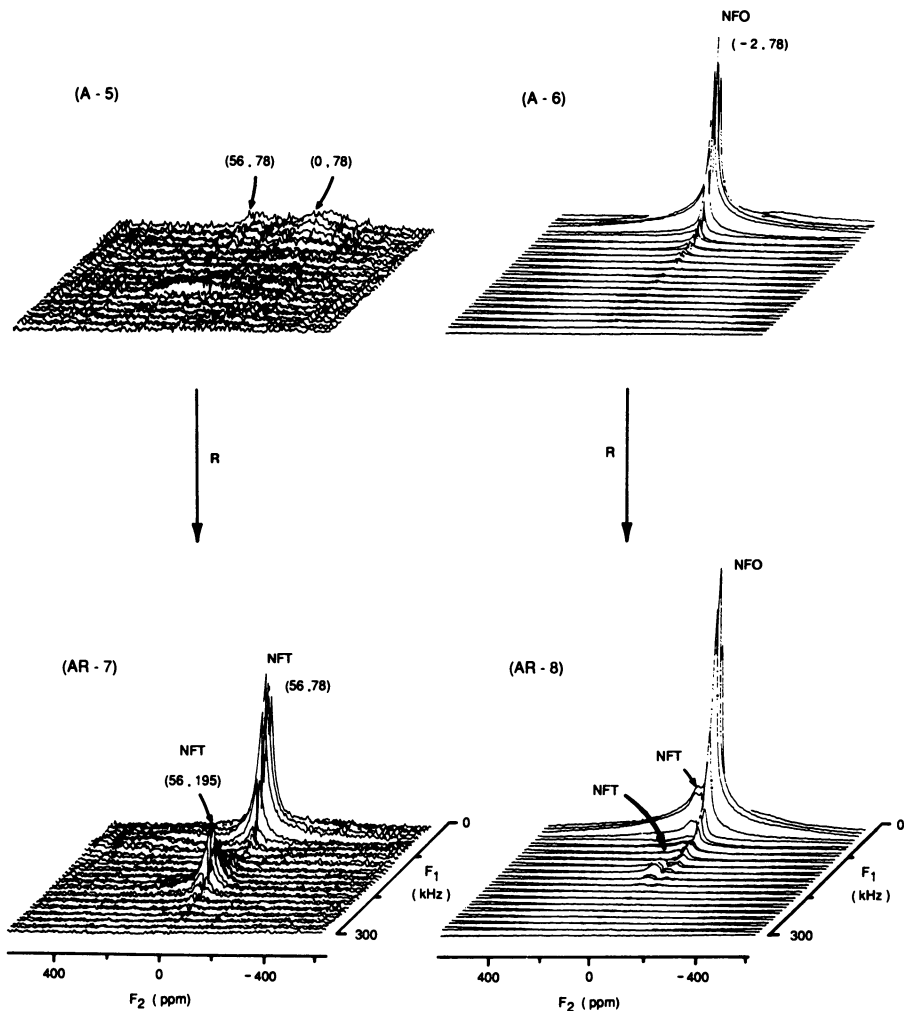
Figure 4. ^{27}Al quadrupole nutation spectra of amorphous samples.
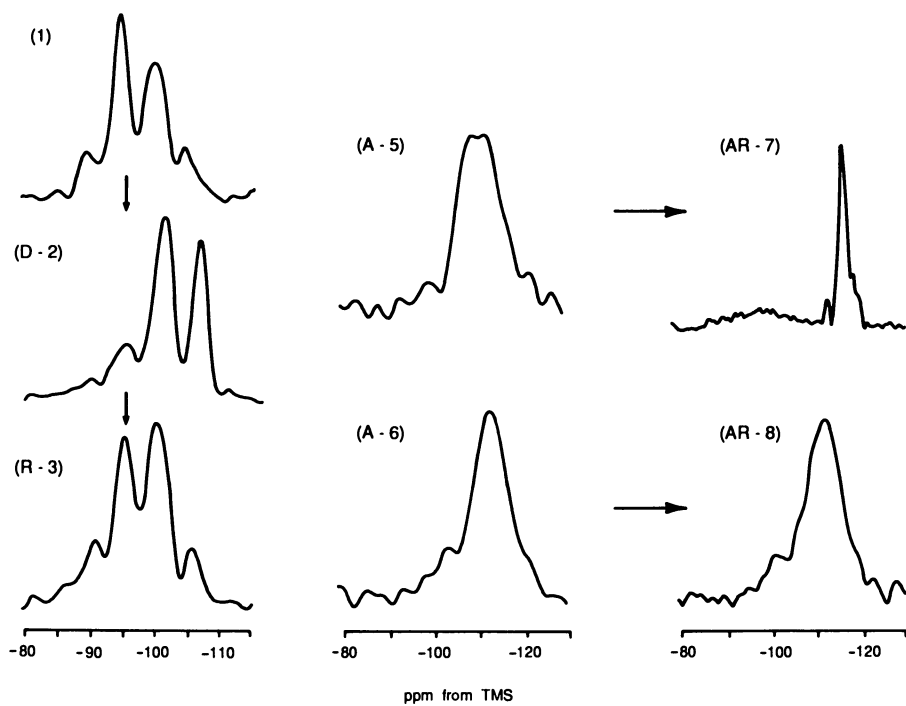
Figure 5. ^{29}Si MAS NMR spectra.

is also present. The nutation spectrum, however, shows only one signal, at (-2, 78), corresponding to NFO aluminium.

The treatment of samples A-5 and A-6 with aqueous KOH provides much information. The XRD pattern of sample AR-7 indicates that a new amorphous phase has been formed responsible for the appearance of the new broad hump at $2\theta=25^\circ$. The ^{29}Si MAS NMR spectrum features a large peak at -113 ppm and a shoulder at -115 ppm (Figure 5). Both are narrower than in the starting amorphous samples A-5 and A-6. The ^{27}Al MAS NMR spectrum of sample AR-7 (Figure 2) contains one narrow signal at 56 ppm, i.e. in the tetrahedral region. The nutation spectrum (Figure 4) gives two signals [at (56, 78) and (56, 195)], for instrumental reasons both corresponding to *the same kind* of Al (see above). The position of these peaks in F_2 and F_1 is as reported by Samoson et al. (4) and assigned to non-framework tetrahedral (NFT) aluminium. We agree with their conclusion, since the sample is completely amorphous and cannot contain tetrahedral framework (F) aluminium. The ^{27}Al MAS NMR spectrum of KOH-treated sample AR-8 (Figure 2) is composed of two signals (at -2 ppm and at 56 ppm), which indicates that some of the NFO aluminium has been converted to NFT aluminium. The nutation spectrum (Figure 4) shows three signals: (-2, 78), (56, 78) and (56, 195), which proves that all the forms of Al in the amorphous phase are converted to tetrahedral Al upon treatment with the base. However, the increased linewidth of the resulting NMR signals and the fact that they are located at higher field (56 ppm) along the F_2 axis compared with 60 ppm for the F signal indicates that they are due to NFT aluminium. Furthermore, large quadrupolar effects and low concentration of the latter species make the small difference in peak position unobservable by conventional ^{27}Al MAS NMR. It appears that the increase in ^{27}Al linewidth observed upon dealumination of zeolites is due to a superposition of the F and NFT signals.

Since the ^{29}Si MAS spectra of both base-treated amorphous samples (AR-7 and AR-8) contain peaks at more negative chemical shifts than in the crystalline materials (for example samples R-3 and R-4 in Figure 3) it is clear that NMR signals from the amorphous phase cannot interfere with the determination of Si/Al ratios in realuminated crystalline zeolites. Our assignment of signal 4 as due to DFT aluminium is therefore vindicated, and the reinsertion of Al into the zeolitic framework demonstrated quantitatively.

Acknowledgment

Literature Cited

1. Samoson, A.; Lippmaa, E. Phys. Rev., 1983, B28, 6567.
2. Samoson, A.; Lippmaa, E. Chem. Phys. Lett. 1983, 100, 205.
3. Samoson, A.; Lippmaa, E. J. Magn. Res., 1988, 79, 255.
4. Samoson, A.; Lippmaa, E.; Engelhardt, G.; Lohse, U.; Jerschkewitz, H.-G. Chem. Phys. Lett., 1987, 134, 589.
5. Kentgens, A.P.M.; Lemmens, J.J.M.; Geurts, F.M.M.; Veeman, W.S. J. Magn. Res., 1987, 71, 62.
6. Man, P.P.; Klinowski, J. Chem. Phys. Lett., 1988, 147, 581.
7. Man, P.P.; Klinowski, J. J. Chem. Soc., Chem. Comm. , 1988, 1291.
8. Man, P.P.; Klinowski, J.; Trokiner, A.; Zanni, H.; Papon, P. Chem. Phys. Lett., 1988, 151, 143.
9. Klinowski, J. Prog. Nucl. Magn. Reson. Spectrosc., 1984, 16, 237.
10. Klinowski, J.; Fyfe, C.A.; Gobbi, G.C. J. Chem. Soc., Faraday Trans. I, 1985, 81, 3003.
11. Sanz, J.; Serratosa, J.M. J. Am. Chem. Soc., 1984, 106, 4790.
12. Bosáček, V.; Freude, D.; Fröhlich, T.; Pfeifer, H.; Schmiedel, H. J. Colloid Interface Sci., 1982, 85, 502.
13. Grobet, P.J.; Geerts, H.; Martens, J.A.; Jacobs, P.A. J. Chem. Soc., Chem. Comm., 1987, 1688.
14. Hamdan, H.; Sulikowski, B.; Klinowski, J. J. Phys. Chem. 1989, 93 , 350.
15. Breck, D.W. "Zeolite Molecular Sieves: Structure, Chemistry and Use" Wiley, New York (1974).
16. Geurts, F.M.M.; Kentgens, A.P.M.; Veeman, W.S. Chem. Phys. Lett., 1985, 120, 206.
17. Kerr, G.T. J. Phys. Chem., 1967, 71, 4155.
18. Engelhardt, G.; Michel, D. "High-resolution Solid-State NMR of Silicates and Zeolites", Wiley, Chichester (1987).
19. Engelhardt, G.; Lohse, U.; Samoson, A.; Mägi, M.; Tarmak, M.; Lippmaa, E. Zeolites, 1982, 2, 59.
20. Engelhardt, G.; Lohse, U.; Patzelová, V.; Mägi, M.; Lippmaa, E. Zeolites, 1983, 3, 233.

Chapter 33

Mechanism of Rapid Zeolite Crystallizations and Its Applications to Catalyst Synthesis

Tomoyuki Inui

Department of Hydrocarbon Chemistry, Faculty of Engineering, Kyoto University, Sakyo-ku, Kyoto 606, Japan

Rapid syntheses of zeolites were accomplished. For the hydrogelatinous gel, after nucleation of the crystal growth, the precursor was treated by temperature-programmed heating, and the crystallization time was markedly reduced. The seed materials were also effective for this type of zeolite synthesis. On the other hand, for the precipitated gel, combined treatments of milling and temperature-programmed heating were highly effective for the synthesis of small and uniform zeolite materials within very short period of crystal growth. The zeolites prepared by the rapid crystallization method had better catalytic performance than that of catalysts prepared by conventional methods. Application of the method to the synthesis of a variety of zeolitic materials will be discussed.

In the last decade, shape selective zeolites such as ZSM-5 (1, 2) and ZSM-34 (3∿5) have been studied extensively. Particular interest has been paid to these new types of catalysts because of their excellent selectivity to gasoline or lower olefin synthesis from methanol. In general, however, these shape selective zeolites need a long crystallization period during their preparation. According to the patent literature, preparation of ZSM-34 requires between 25 and 196 days at 100°C, and that of ZSM-5 requires between 20 h and one week at a higher temperature for crystallization in hydrothermal conditions. Such a slow crystallization method would have the following disadvantages:
1) Extensive labor coupled with delay and expense.
2) Low reproducibility in the properties of crystals formed.
3) Production of large crystals. The effective diffusivity of these products would be low and unfavorable for their use in catalytic reactions.
4) Decrease in purity of crystal structure. Since large single crystals are easily obtained, the amount impurity in a crystal can be reduced. However, in the case of consecutive phase transformations (6), the possibility of coexisting crystal

structures increases, and, therefore, the purity of crystal
structure would be lowered. Also, large crystals formed by a
slow crystallization process give a concentration profile of
the crystal components, and this might be unfavorable for the
use of catalytic reactions.

Rapid crystallization would overcome the disadvantages of slow
crystallization and, more significantly, hetero elements could be
incorporated inside the crystals. Metal-incorporated zeolitic mate-
rials serve as bifunctional catalysts, exhibiting properties of both
metal catalysts and zeolite catalysts.

Experimental

ZSM-34 preparation. Preparation of ZSM-34 zeolite was based on the
patent literature (5). However choline was used instead of choline
chloride as the organic template, on the basis that zeolites pre-
pared by using choline have better performance for olefin synthesis
from methanol than zeolites prepared by using choline chloride (7).
    The reaction materials used were 30 wt% silica sol solution,
sodium aluminate, reagent grade sodium and potassium hydroxides, 50
wt% choline solution, and distilled water. Appropriate amounts of
sodium hydroxide, potassium hydroxide, and sodium aluminate were
dissolved in distilled water. After adding the choline solution, the
mixed aqueous solution was kept at 0°C. In another container, the
silica sol solution was also made at 0°C. The two solutions were
mixed quickly and stirred vigorously for 2 min using a Homo-Mixer
(Tokushuki Kako Kogyo Co.). An almost transparent, hydrogelatinous
mixture was obtained.
    The gel solution mixtures were packed in ampoules and crystal-
lized at 100°C for various periods from 0.25 to 131 days. The solid
products were washed with water to pH = 9 and dried overnight at
100°C, then calcined under passage of air at 540°C for 3.5 h. The
molar ratio of Si/Al, (Na + K)/Al, K/(Na + K), and choline/OH$^-$ were
fixed at 9.3, 7.3, 0.17, and 0.67, respectively. Based on the analy-
sis of the slow crystallization rate process, the hydrothermal
treatment was properly shortened by a temperature-programmed crysta-
llization. Furthermore, the effects of seed materials, type of
template, hydrothermal temperature, and Si/Al ratio of the gel
mixture on the crystallization were investigated.

ZSM-5 preparation. Preparation of ZSM-5 zeolite by Method 1 was
based on the method given in the patent literature (2), in order to
give us an authentic sample. However, the temperature condition for
crystallization was modified. A reaction mixture was prepared by
mixing the following three solutions A, B, and C. In case of Si/Al
atomic ratio 40, for example, solution A was composed of 2.70 g of
$Al_2(SO_4)_3 \cdot 16 \sim 18H_2O$, 6.20 g of H_2SO_4 (97.5%), 7.53 g of tetrapropy-
lammonium bromide (TPAB), and 60 g of distilled water. Solution B
was prepared by dissolving 69.0 g of No.3-brand water glass (28.93
wt% SiO_2, 9.28 wt% Na_2O, balance H_2O) in 45 g of distilled water.
Solution C was 130 g of 20 wt% NaCl aqueous solution. Solution A and
B were added dropwise to solution C in a Pyrex 300 ml beaker while
maintaining a pH of 9 $\sim$ 11 at room temperature and vigorously
stirring with an ultra-disperser. The reaction mixture was heated in

a one liter autoclave to 160°C with a heating rate of 1°C/min with-
out stirring and was kept at this temperature for 2 h. The tempera-
ture was then raised to 190°C with a heating rate of 0.33°C/min and
held at this temperature for 5 h. The product was washed with water
until no Cl ions were detected, dried at 120°C for 3 h, and then
calcined in an air stream at 540°C for 3.5 h. The material was then
converted into the ammonium form by repeated exchanges with 1M
NH_4NO_3 solution at 80°C for 1 h. The product was washed with water
at room temperature, dried overnight at 100°C and then heated in air
at 540°C for 3.5 h. The resulting powder was compressed in a tablet
machine, and this was crushed into 8 ∿ 15 mesh pieces to provide the
catalyst for the reaction.

In Method 2, the reacting mixture was crystallized by raising
the temperature from 160 to 210°C at a constant heating rate of
0.16°C/min while stirring at 60 rpm.

In Method 3, after centrifugal separation of the gel mixture
from the mother liquor, the gel was mechanically ground in a mortar
for 15 min. This procedure was repeated twice and the final mortar-
ing time was prolonged for another 15 min. The ground gel mixture
was returned to the mother liquor in an autoclave. The crystalliza-
tion conditions were the same as for Method 2.

In Method 4, the change in composition of the mother liquor
during the precipitation of $Na_2O-(TPA)_2O-Al_2O_3-SiO_2-H_2O$ synthesis-
gel mixture was minimized by modification of the procedure. To the
solution A, 11.95 g NaCl was added (solution A'), and to the solu-
tion C, 2.16 g TPAB, 14.32 g NaCl, 2.39 g NaOH, 1.80 g H_2SO_4 and 104
g H_2O were added (solution C'). The gel mixture was prepared as in
Method 1 with the solutions A', B, C'. After separation from the
mother liquor and grinding as in Method 3, the gel mixture was
returned to a different mother liquor which was separately formed by
Method 3. The crystallization condition were the same as for Method
2. When the crystals of different Si/Al were synthesized, only the
amount of Al was changed.

Various metallosilicates were prepared by Method 4, replacing
Al by other tradition metals at the stage of gel formation (8).

Characterization of catalyst. BET-surface areas of the sample were
measured by N_2 adsorption at liquid-nitrogen temperature. Thermo-
gravimetric analysis was carried out with a Shimadzu micro TG-DTA
30. X-ray diffraction (XRD) patterns of the zeolite calcined at
540°C were obtained with Cu Kα radiation using a Rigaku Denki
Gigerflex 2013 with a wide source. Morphology of the samples were
observed by a scanning electron microscope (SEM), Hitachi-Akashi MSM
102, with a resolution limit of 70 A. Bulk composition of the sam-
ples was analyzed by a Shimadzu atomic adsorption/flame emission
spectrophotometer (AA) AA-640-01 using appropriate hollow cathode
lamps for respective elements. Outer surface composition of the
crystals was analyzed by a X-raymicroanalyzer (EMAX), Horiba EMAX-
1800 attached to the scanning electron microscope. Temperature-
programmed desorption (TPD) of NH_3 was measured by a continuous flow
method with a Rigaku Denki micro TG-DSC. After adsorption of NH_3 at
80°C, elution by He was carried out at the same temperature; the
temperature was then raised to 750°C at heating rate of 20°C/min.
TPD profiles were obtained from differentials of the weight-loss
curves.

Catalytic reaction method. The methanol-conversion reaction was carried out in a ordinary flow reactor under atmospheric pressure. A 0.5 ml portion of the catalyst was packed into a Pyrex tubular reactor of 6 mm inner diameter. The reaction gas, composed of 20 ~ 100% MeOH balanced with N_2, was then allowed to flow through the catalyst bed at a temperature in the range 240 ~ 360°C and a space velocity (SV) in the range 400 ~ 4000 liter·liter^{-1}·h^{-1}. The olefin-conversion reaction was carried out in a flow reactor of 8 mm inner diameter. The reaction gas, composed of an olefin (C_2H_4, C_3H_6, or C_4H_8) and N_2 mixed at various ratios, was then allowed to flow through the catalyst bed at a temperature in the range 260 ~ 360°C and a space velocity in the range 900 ~ 4500 h^{-1}.

The paraffin-conversion reaction was carried out in a flow reactor of 8 mm inner diameter. The reaction gas composed of paraffin (C_1 ~ n-C_{20}) and N_2 mixed at various ratios was fed at a temperature range from 350 to 700°C and a space velocity of 1000 ~ 8000 h^{-1}.

Products were analyzed using TCD-FID, FID, and TCD type gas chromatographs equipped with integrators.

Results and Discussion

Rapid Crystallization from a Hydrogelatinous Precursor of Crystals.

Conventional preparation method. The mixed gel for crystallization of ZSM-34 was hydrogelatinous as noted in the experimental section. The change in crystal morphology and BET surface area as a function of the crystallization time at 100°C is shown in Fig.1 with the results of methanol conversion by these materials.

The gel mixture was converted into spherical particles within 3 days. The shape and size of spherical particles were maintained for about 3 months, but following that the particles became somewhat larger and irregular. The BET surface area decreased in the first 3 days. This period corresponds to the period of spherical particle formation from the gel mixture.

From the comparison of relative intensities of XRD patterns, the samples at 0.5 and 1 day showed very poor crystallinity; however, the sample at 3 days already showed the principal XRD lines of ZSM-34, although the relative intensities were still very weak. Of the materials prepared in the first 3 days, dimethyl ether (DME) was formed exclusively and increased sharply with an increase of the crystallization time. After 3 days of crystallization, the BET surface area increased sharply and then gradually approached its highest level. Considering this trend, hydrocarbon formation increased with decreasing DME formation. The XRD patterns of 16 days corresponded to the main crystal structures of ZSM-34 (5). This period corresponds to the period of intergrowth of the zeolite crystal in each individual particle. After a very long crystallization, such as 131 days, paraffin selectivity increased and olefin selectivity decreased. The most significant observation of these sequential experiments is that during the period of the first 3 days, all the gel mixture converted to spherical materials, precursors of the zeolite crystal with very little internal surface area. The crystallization occurs in each spherical particle, and the change in BET surface area with an increase in crystallization time, suggests that the rate of crystallization is rapid in the early stage, but slows down with increasing crystallinity.
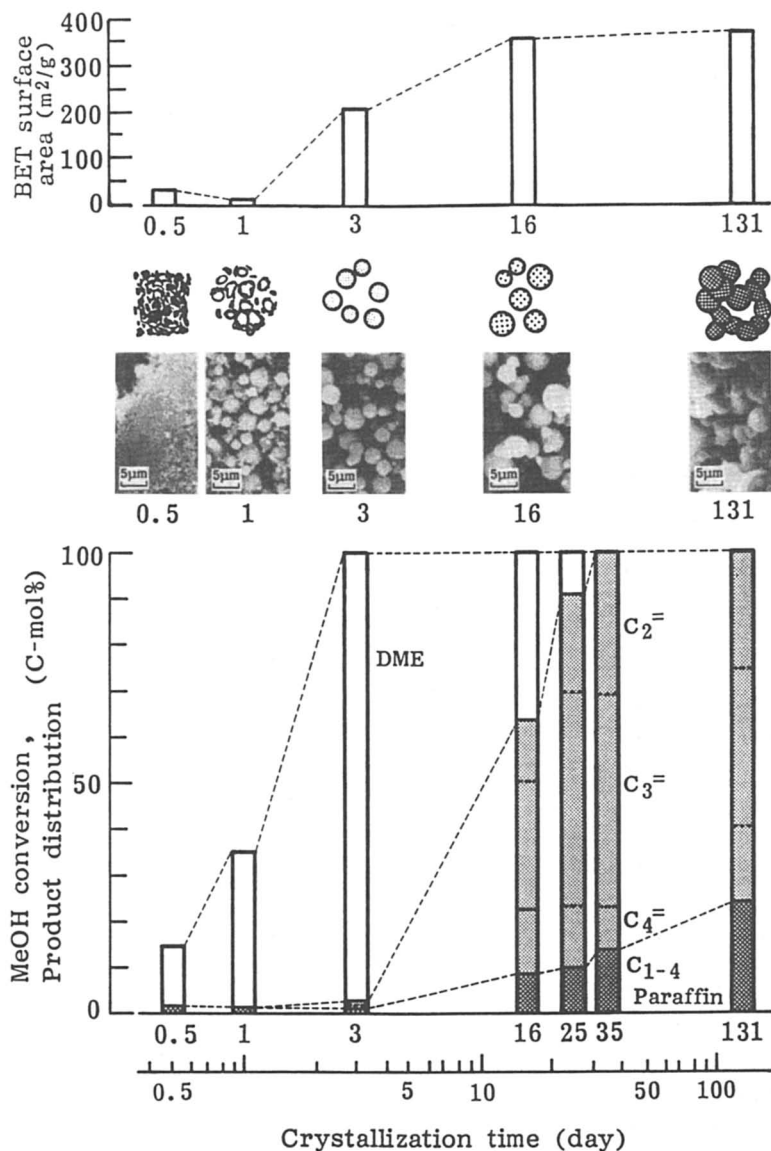
Figure 1. Change in properties of ZSM-34 zeolite with an increase of crystallization time.
Conditions of MeOH conversion, 12% MeOH, 88% N_2, 400°C, SV 930 h^{-1}.

Direct heating method. In order to confirm the change in crystallization process, the gel mixture was heated directly to 200°C with a constant heating rate of 2.8°C·min⁻¹, and then it was maintained for 2 h. The resulting product contained sodalite with ZSM-34, and the morphology was completely different from the crystals prepared by the conventional method.

As shown in Fig. 2, the catalytic activity of the zeolite prepared by the direct heating method for methanol conversion was higher than that of the zeolite crystallization for 25 days by the standard preparation method. However, deactivation of the catalyst by carbon deposit occurred early in the reaction, just as with the catalyst prepared by the standard method. Differences in crystallite morphology between those prepared by the standard method and the direct heating method would be attributed to the stage of the precursor formation. Therefore, after the precursor formation the rapid heating was adopted as described below.

Precursor heating method. The gel mixture was maintained at 100°C for 3 days for precursor formation. The precursor with the mother liquor was transferred to autoclaves, and the temperature was raised at a constant rate of 1.7°C·min⁻¹ to 130, 160, 190, and 220°C. The temperature was maintained at each level for 0.5 h. The synthesized materials were also treated in the same manner as the standard preparation method. XRD patterns showed that the zeolites prepared at 190 and 220°C were ZSM-34; however, the zeolite prepared at 220°C contained some sodalite structure. The zeolites crystallized at 130 and 160°C had insufficient XRD intensity of ZSM-34 patterns and showed an activity of only DME formation. When the crystallization temperature was raised to 190°C, DME decreased to ca. 1/10, and C_2-C_4 olefins increased dramatically. However, when the crystallization temperature was raised to 220°C, ethylene formation decreased markedly and DME increased.

As can be seen in Fig. 2, the catalytic activity of the zeolite prepared at 190°C for 0.5 h in the precursor heating method was the largest among those of the zeolites prepared by different methods. Furthermore, the selectivity to valuable ethylene and the catalyst life also increased markedly for the zeolite prepared by the precursor heating method.

Other factors enhancing crystallization rate. Kinds of organic template were changed for synthesis of ZSM-34 type zeolite, and it was found that tetramethylammonium hydroxide was the best template for the rapid crystallization (10). The crystallization was achieved in only 2 h at 187°C, corresponding to 1/1600 of the time in the standard method. In this case, the amount of necessary template was only 1/8 of choline hydroxide, producing the zeolite which had a rather better catalytic performance in methanol conversion (9). Seed crystals, prepared by grinding the preformed zeolite in an agate mortar, markedly reduced the crystallization time (10, 11). The comparative data for the zeolites with and without seed crystals are shown in Fig. 3. The size of zeolites formed was inversely related to the quantity of seed crystals added to the reagents of mixed gel formation. Zeolite crystals produced in the presence of 9 wt% seed crystals with all other conditions being identical, were about 1/70 the volume of zeolite crystals formed in the absence of seed crystals and were more uniform in shape. Whereas the change in BET
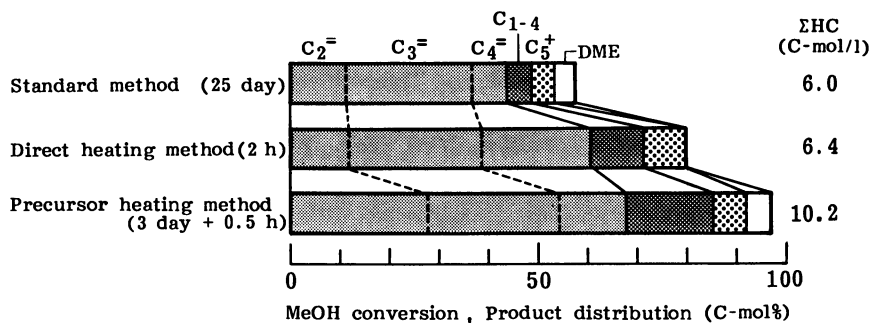
Figure 2. Comparison of methanol conversion on various ZSM-34 zeolites prepared by different methods.
Reaction conditions, 12% MeOH, 88% N_2, 400°C, SV 1000 h^{-1}.

Seed crystals added (wt%)	0	9.0
MeOH conv. (%)	100	100
Selectivity of C_2-C_4 olefines (C-mol%)	74.9	81.3
Integrated amount of hydrocarbon formed (C-mol)	25.9	56.4
Carbon in residual hydrocarbons (mol/l)	1.8	3.9
Catalyst life (h)	5.5	12.1
De (10^{-5} cm^2/sec)	3.06	6.17
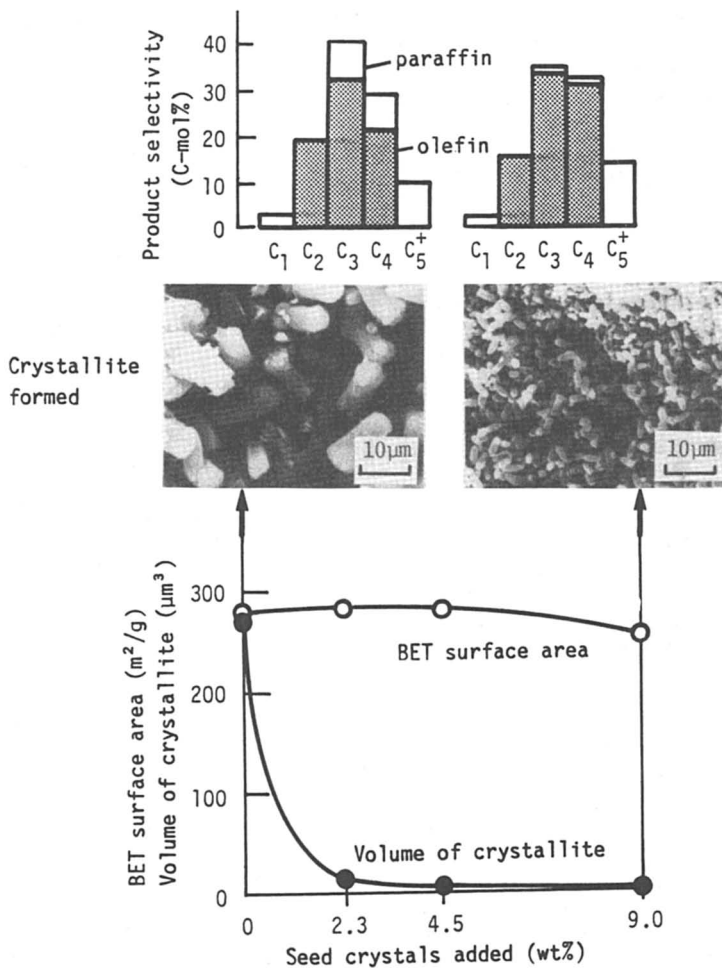
Figure 3. Effect of seed crystals on the crystallization and the catalytic performance of methanol conversion.

surface area was minor, the effective diffusivity of n-hexane increased in the zeolite with the seed crystals (11). The zeolite with the seed crystals converted methanol to light olefins with higher selectivity and longer catalyst life than the zeolite without seed crystal.

Metal incorporation into the zeolite using metal loaded seed materials. The combination of catalyst metal with zeolite catalyst is one of the most intriguing subjects for bifunctional catalysis. The achievement of prominent effect of the seed crystals on the crystallization of ZSM-34 type catalyst induced an idea that the seed material on which a catalyst metal had been supported previously would also be effective for rapid crystallization.

Instead of the seed zeolite crystals, a mixture of one part γ-alumina (0.2 µm) and three parts α-alumina (ca. 1 µm) was used as seed material. Fortunately, a similar effect on the crystallization was observed, although about 2 times the quantity of the seed materials was necessary (9). The metal pre-loaded γ and α-alumina mixture was then tried as the seed material and confirmed the same effect on crystallization. In the case of 0.4 wt% Ru (9) and 0.7 wt% Rh (12) in the catalyst product a longer catalyst life was obtained, i.e., 1.32 times and 1.65 times, respectively, without any significant change in the activity and selectivity compared with the non metal-loaded zeolite catalyst.

Carbon dioxide, which corresponded to ca 2% of converted methanol, was observed in the effluent gas from the reactor. This indicates that a part of deposited coke on the zeolite surface was burned with the oxygen derived from methanol by the action of the metal component. The metal component also acted as a combustion catalyst for coke during regeneration treatment with air. The effect of metal loading on the performance of methanol conversion was investigated. Of the four loading methods used [ion-exchange method, physical blending method, impregnation method and crystallization nuclei method (12)], the crystallization nuclei method exhibited the best performance. This new method allows the metal component to be highly dispersed upon each zeolite crystallite, maintaining the necessary properties of zeolite, because the dispersed metal particles are limited to the part of seed material located at one of the ends of the rice-shaped crystallites.

Rapid crystallization from a precipitated-gel precursor of crystals. In the course of pentasil zeolite ZSM-5 synthesis, the gel mixture obtained from starting aqueous solution is a low density precipitate, which is different from the hydrogelatinous state in ZSM-34 synthesis; it can be easily separated from the supernatant fluid by centrifuge.

Most of the silicon component feed has been already involved in this precipitate, and crystallizations occurs internally inside the solid phase of the precipitate. The precipitate itself is the precursor of the crystal. In fact, seed materials have no enhancement effect on the crystal growth as described above. Therefore, the following three hypotheses were considered and trials were made to substantiate them.

Uniform crystals could be synthesized by regulating the composition

of starting solutions. In the conventional method of ZSM-5 synthesis (Method 1), the composition of liquid phase markedly changes with an increase of precipitation. In such a case, the composition and the profile of components inside the crystals and their catalytic performances could be affected. Therefore, in order to synthesize crystals having a more uniform composition, compositions of the starting solutions should be regulated to minimize the composition change during the precipitation. Accordingly, the compositions of solution A and C were largely regulated as the solution A' and C' used for method 4. However, the mother liquor used during the hydrothermal treatment was the same as in the patent literature (Method 1), because the mother liquor was known to synthesize ZSM-5.

Uniform and small crystallites could be rapidly synthesized by milling of crystal precursor. The size and concentration profiles of precipitated particles affected not only the induction period and the rate of crystallization, but also the crystal structure and distribution of the acid sites. Accordingly, if the crystal precursor is as small and uniform as possible, the synthesis of a very small and uniform crystallites and very rapid crystallization would be expected. Such small particles would play the role of nuclei of the crystals. Therefore, in this study, the precipitated gel was milled by a motor driven mortar. The liquid phase separated from the gel by the progress of milling was removed twice by centrifuge (Method 3).

Temperature programmed crystallization considering the rate process could minimize the crystallization time. Most of the conventional hydrothermal syntheses are carried out at a constant temperature. As shown in Fig. 4, crystallization has an induction period and then rapid crystallization occurs at constant temperature. However, the rate of crystal growth then slows down and gradually decreases with an increase of crystallization time. Accordingly, much time is consumed in the latter stage of crystallization in which the rate has decreased. As zeolite crystals are a quasi-stable phase, those which have been formed in the early stage are kept in the hydrothermal condition for a long time, and a lack of uniformity could result from transformation into other unfavorable phases. Therefore, if the crystallization rate can be keep at a high level by changing the temperature of hydrothermal synthesis (Fig. 5), it is expected that the crystallization time will be reduced and the properties of crystals will be more uniform.

In this study, the crystallization temperature and the heating rate were varied using the milled precursor, and ZSM-5 crystals could be synthesized. For example, the temperature was elevated from 160 to 210°C with a constant heating rate of 0.2°C/min (Method 2). The crystals prepared by Methods 1 $\sim$ 4 had about same BET-surface area of 385 ± 11 m^2/g and the XRD patterns of ZSM-5. The average size of crystals reduced from 8 μm for Method 1 to 1 μm for Method 4. The concentration profiles of Si and Al from outside to inside the crystals became uniform with reducing size. The activity of methanol conversion, the yield of gasoline fraction, and the content of aromatics in the gasoline clearly increased for the product of Method 4 (Fig. 6).

Thus, it was confirmed that the three control conditions men-
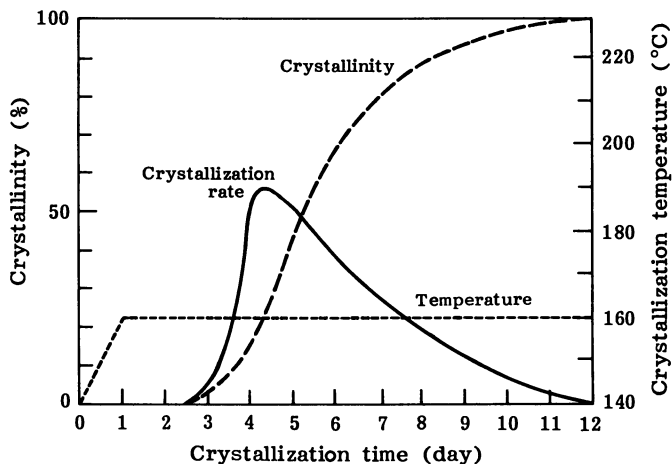
Figure 4. Conceptional illustration for the change of crystallization rate and crystallinity with time on hydrothermal treatment at a constant temperature in a conventional slow-crystallization method.
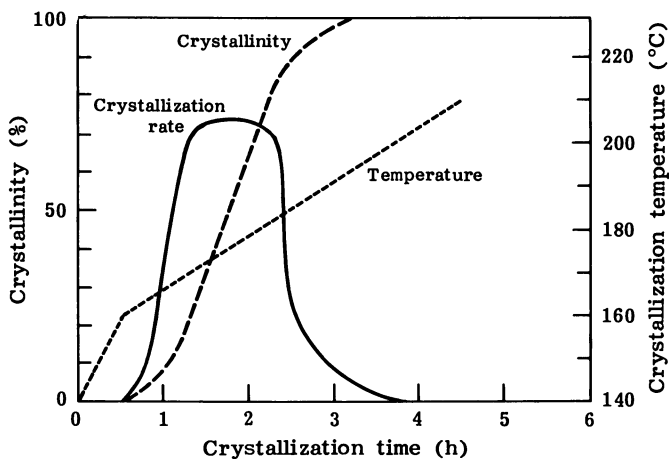
Figure 5. Conceptional illustration for the change of crystallization rate and crystallinity with time on hydrothermal treatment in the rapid-crystallization method with a programmed temperature rise.
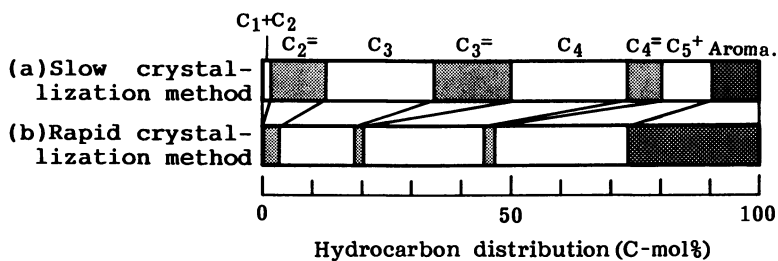
Figure 6.   Performance of methanol conversion on ZSM-5's pre-
pared by the slow and the rapid crystallization methods.
(a) H-ZSM-5(Si/Al=40) prepared by the conventional slow crys-
tallization method.
Reaction conditions, 30% MeOH-70% N_2, SV 1100 h^{-1}, 400°C, MeOH
conversion 100%
(b) H-ZSM-5(Si/Al=40) prepared by the rapid crystallization
method (Method 4).
Reaction conditions, 30% MeOH-70% N_2, SV 1100 h^{-1}, 300°C, MeOH
conversion 100%

tioned above were very effective in the rapid synthesis of crystals
and increasing the catalytic activity. This indicates that the Al is
more highly dispersed in the crystals and forms of acid sites more
effectively.

**Application of the rapid crystallization method to syntheses of
various metallosilicates.**
Various kinds of metallosilicate were synthesized by substituting
the Al ingredient of the pentasil zeolite ZSM-5 with other transi-
tion elements at the gel-formation stage in the rapid crystalliza-
tion method. As one of the extreme features of the metallosilicates,
H-Fe-silicates converted methanol exclusively to ethylene and pro-
pylene at a low temperature conditions around 300°C (13). This is
attributed to the properly weaker acidity than H-ZSM-5, and conse-
quent conversion is substantially eliminated. When the H-Fe-silicate
is used for conversion of light olefins, it yields a high octane-
number gasoline with an extraordinary high space-time yield and
selectivity (14). Another extreme was H-Ga-silicate (8, 15). This
catalyst gave a maximum selectivity to gasoline fraction from metha-
nol and yielded aromatics from paraffins with much higher selectivi-
ty than H-ZSM-5. A combination of Pt with H-Ga-silicate enhanced the
activity and markedly moderated the deactivation caused by coke
formation; Pt was effective for combustion of the deposited coke.
The marked effect on aromatization was also confirmed for H-Zn-
silicate (16).
     Metallosilicates incorporating catalytically active metal such
as V-silicate (17) and Cu-silicate (18) could also be prepared by
the rapid crystallization method. These novel catalytic materials
are expected as oxidation catalysts involving shape selective func-
tion.

Conclusion

In conclusion, the rapid crystallization method is very effective
not only for rapid synthesis, but also for synthesis of metal-
containing uniform zeolitic materials which show higher catalytic
activity and selectivity.

Literature cited
1. Meisel, S.L.; McCullough, J.P.; Lechthaler, C.H. Chemtech 1976,
    86.
2. Plank, C.J.; Rosinski, E.J.; Schwartz, A.B. Brit. Patent 1 402
    981, 1974.
3. Mobil Oil U.S. Patent 3 894 107, 1975.
4. Rubin, M.K.; Rosinski, E.J.; Plank, C.J. U.S. Patent 4 086 186,
    1978,
5. Mobil Oil Jpn. Patent. Application Disclosure 58 499, 1978.
6. Kostinko, J.A. Preprints of Symposia of Am. Chem. Soc. Las
    Vegas, 1982, 27, No.2, 487.
7. Inui, T.; Araki, E.; Sezume, T.; Ishihara, T.; Takegami, Y.
    React. Kinet. Catal. Lett. 1981,18,1.
8. Inui, T.; Yamase, O.; Fukuda, K.; Itoh, A.; Tarumoto, J.;
    Hagiwara, T.; Takegami, Y. Proc. 8th Intern Congr. Catal.,
    Berlin 1984, DECHEMA, Frankfurt am Main, Vol.III, p.569.

9.   Inui, T.; Ishihara, T.; Morinaga, N.; Takeuchi, G.; Araki, A.;
     Kanie, T.; Takegami, Y. Nippon Kagaku Kaishi 1982, 221.
10. Inui, T.; Morinaga, N.; Ishihara, T.; Kanie, T.; Takegami, Y. J.
     Catal. 1983, 79, 176.
11. Inui, T.; Ishihara, T., Morinaga, N.; Takeuchi, G.; Matsuda, H.;
     Takegami, Y. I&EC Res. Dev. 1983, 22, 26.
12. Inui, T.; Takeuchi, G.; Takegami, Y. Appl. Catal. 1982, 4, 211.
13. Inui, T.; Matsuda, H.; Yamase, O.; Nagata, H; Fukuda, K.; Ukawa,
     T.; Miyamoto, A. J. Catal. 1986, 98, 491.
14. Inui, T. React. Kinet. Catal. Lett. 1987, 35, 227.
15. Inui, T.; Makino, Y.; Okazumi, S.; Nagano, S.; Miyamoto, A. Ind.
     Eng. Chem. Res. 1987, 26, 647.
16. Inui, T.; Makino, Y.; Okazumi, F.; Miyamoto, A. Stud. Surf. Sci.
     Catal. 1987, 37, 487.
17. Inui, T.; Medhanavyn, D.; Praserthdam, P.; Fukuda, K.; Ukawa,
     T.; Sakamoto, A.; Miyamoto, A. Appl. Catal. 1985, 18, 311.
18. Inui, T.; Shibata, M; Okukawa, Y. Appl. Catal. to be submitted.

Chapter 34

Kinetics and Mechanism of Crystal Growth of Zeolite Omega

F. Fajula[1], S. Nicolas[1], F. Di Renzo[1], C. Gueguen[2], and F. Figuéras[1]

[1]Laboratoire de Chimie Organique Physique et Cinétique Chimique Appliquées, Unité Associée au Centre National de la Recherche Scientifique No. 418, Ecole Nationale Supérieure de Chimie de Montpellier, 8 Rue Ecole Normale, 34075 Montpellier Cedex, France
[2]Centre de Recherche ELF—France, BP 22, 69360 Saint Symphorien d'Ozon, France

The change in morphology of crystals of zeolite omega has been analyzed with respect to the evolution of the concentration of aluminium in the parent liquor. In agreement with the overlapping principle, crystal habit is determined by the faces with the lowest growing rate. As $[Al]$ decreases, morphology evolves from spheroidal to euhedral hexagonal passing through intermediate cylinder-shaped crystals. The growth rate of the (001) face presents an activation energy of 23 kcal/mol and is proportional to $[Al]^{0.8}$. For the growth of the (hk0), surface the activation energy is 30 kcal/mol and the rate is proportional to $[Al]^{1.6}$. These differences are attributed to the occurrence of different growth mechanisms on the two kinds of faces. The modeling of the crystal growth and the continuous feeding of the system by an aluminate solution allowed modification of the final <001> / <hk0> size ratio.

The application of the laws of crystal growth to the synthesis of zeolites is still a largely unfulfilled task. Most kinetic studies deal with the influence of the reaction variables (temperature, alkalinity, composition of the original medium) on the evolution of the crystallized component (1). Nucleation and crystal growth are generally not separated, but are described by a single kinetic equation. The yield versus time curves are indeed very useful for the modeling of zeolite synthesis (2). However, they do not contain quantitative information about the rates of crystal growth.

Experimental methods have not been conducive to consideration of the size of the crystals as the dependent variable in kinetics. In many media for example, it is not easy to part the growing crystals from the parent amorphous phase.

The first attempts to pass from dm/dt rate equations to dl/dt ones (where m is the mass of zeolite, l the size of the crystals and t is time) were based on the determination of average crystal sizes from the width of X-ray diffraction peaks (3). Microscope measurements of the increase of the size of the largest crystals

allowed Zhdanov and Samulevich (4) to establish size-versus-time
curves and to analyze nucleation and crystal growth separately in a
synthesis of zeolite Na-X. They interpreted these data by using an
equation of the type $Z=1-\exp(-kt^n)$, where Z is the degree of
conversion, k a constant, t time and n a value between 3 and 5.
Such a rate formulation was also proposed by Ciric (5) for zeolite
A crystallization. It is known as the Kholmogorov equation and
corresponds formally to that first proposed by Johnson and Mehl (6)
and Avrami (7,8) for solidification of metals.

The use of a law typical of the solid state to describe the
growth of zeolites was probably suggested by the presence of an
amorphous gel in the synthesis medium. The rearrangement of this
phase to form a zeolite network has been a favored theory until
researchers showed that zeolites can nucleate and grow directly
from solutions free of suspended solids (9).

The assumption that the crystallization of zeolites proceeds
through the incorporation of growth units present in the
surrounding solution allows elimination of time as independent
variable and adoption of kinetic equations of the type $r=kS^n$ (where
r is the rate and S represents the supersaturation), more rich in
predicting power.

At present the knowledge of the nature of the basic units taking
part in the growth process is only hypothetical, but kinetic
evidence is exactly what is needed to verify the self-consistency
of hypotheses about the mechanism of growth of zeolites. In
searching for such evidence, the synthesis of zeolite omega has
been studied in detail (10). This paper addresses the evolution of
the crystal habit during the synthesis and discusses it in relation
to the change of the aluminium concentration the reaction medium.

Experimental

Reactor and reagents. The crystallization of zeolite omega was
carried out in a 1 liter stainless steel autoclave equipped with a
thermocouple well, an anchor-shaped stirrer, an injection port and
a sampling outlet. The latter was designed to avoid accumulation of
material inside sampling pipe and valves in the course of the
reaction. The injection port was connected to a volumetric pump
(Gilson 302S), assuring a controlled flow of solution. The reactor
was heated by an electrical furnace which was regulated ($\pm 1^\circ$C)
through the thermocouple immersed in the reaction medium. In all
experiments the heating rate was 80°C/h and a stirring rate of 140
rpm was used.

The reagents were : sodium aluminate ($Al_2O_3 \cdot Na_2O$) from Carlo
Erba, sodium hydroxide pellets (Normapur from Prolabo),
tetramethylammonium hydroxide pentahydrate (TMA, Fluka purum
grade), non-porous silica (Zeosil 175 MP from Rhône Poulenc, pore
volume 0.08 ml/g, grain size 2-20 μm, H_2O 6.5 wt%), kaolinite des
Charentes (from Kaolins d'Arvor, surface area 24 m^2/g, grain size
4-15 μm, wt% Al 19.3, Si 21.3, Fe 0.29, Ca 0.1, Mg 0.13, K 0.5, Na
300 ppm), and deionized water.

Methods. The crystallization of silicoaluminate mixtures into zeolite omega in the temperature range 105-130°C was performed in the presence of a structure-directing mixture (SDM) (10,11). The method gives minimum overlap between the nucleation and growth steps as indicated by the very homogeneous distribution of size of the crystals in the final product. The use of kaolinite as the aluminium source presents two main advantages (10). First, the low solubility of the clay under the crystallization conditions prevents the formation of a gel. Second, under the low supersaturation levels achieved, secondary nucleation is hindered.

Syntheses. The structure-directing mixture had the composition $3.2Na_2O. 0.8TMA_2O. Al_2O_3. 8.2SiO_2. 160H_2O$. It was prepared by adding the sodium aluminate to the sodium-TMA hydroxide solution. After stirring for one hour, the silica was added. The final slurry was thoroughly mixed for 12 h and finally transferred into a sealed polypropylene bottle which was maintained in an oven at 50°C for 20 days in static conditions.

The crystallization mixture (500 ml) had the composition $3.2Na_2O. Al_2O_3. 8.6SiO_2. 160H_2O$ and was obtained by first preparing a suspension of kaolinite in the sodium hydroxide solution. The SiO_2/Al_2O_3 ratio was adjusted by addition of the appropriate amount of silica. After stirring for 5 h, 25 to 30 % in volume of aged SDM was added, at room temperature, to the freshly prepared hydrogel. The autoclave was sealed and heated under stirring to the desired temperature. Zero time corresponded to the time when the system reached the crystallization temperature.

Sampling and characterization. 10 ml samples, including liquid and solid phases, were withdrawn periodically from the autoclave during the crystallization. The slurries were collected in 70 ml of cold deionized water. The solid fraction was recovered by filtration and washed first with 250 ml of water. The clear solution, containing the diluted mother liquor, was preserved for chemical analysis. After additional washing (up to a pH of 9), the solid was dried at 70°C in air.

X-ray powder diffraction was used to identify the phases present. The only crystalline phase formed during the synthesis was zeolite omega. The degree of conversion of kaolinite into zeolite was estimated by calibrating the X-ray instrument (CGR Theta 60, CuKα monochromated radiation) with physical mixtures of the two components. Morphology and size of the crystals were determined by scanning electron microscopy on a Cambridge S100 instrument. Growth rates of different crystal faces were calculated from the relation $0.5 \delta l/\delta t$, where δl represents the increase of the size of the crystal in the direction normal to the face considered, in the time interval, δt, between two consecutive samplings. The synthesis procedure produced a narrow distribution of size : the precision in the determination of the sizes was ±0.05 µm. Identification of crystal orientations was ascertained from electron diffraction patterns recorded with a Jeol 200 CX microscope.

Chemical analyses were performed in the Service Central d'Analyses, CNRS, in Solaize, by flame photometry.

Results

Phenomenology of the crystallization. The conversion versus time curves obtained at three different temperatures are shown in Figure 1. With the synthesis procedure used, the sigmoid curves were characterized by shorter induction periods than the traditional method (11,12). As expected, temperature had a strong effect on the rate of crystallization. The overall crystallization rates may be approximated by the reciprocal of the times of half conversion. From these values an apparent activation energy of 22 ± 1 kcal/mol was obtained. With respect to literature data, this value exceeds that reported, for instance, for zeolite Na-X (1,4) but compares well with the 19.8 kcal/mol found for ZSM-11 (13).

A better picture of the crystallization phenomena was obtained from the microscope examination of the crystals at different stages of their development. The first crystals of zeolite omega appeared as spheres with diameters around 0.5-1 µm (Fig.2) . With the appearance of (001) faces, this form evolved into barrel-shaped particles (Fig.3). At a later stage of the syntheses, the habit evolved to euhedral hexagonal with the development of (100) faces (Fig.4).

The observed evolution in the morphology is consistent with the overlapping principle, i.e. the crystal habit is determined by the faces with the lowest growing rate (14). The apperance of low-index faces corresponded to the decrease of supersaturation related to the consumption of nutrient by the growing crystals.

In order to rationalize these evolutions, the composition of the solution surrounding the crystals has to be examined. The growth of zeolite omega is non-congruent in the sense that all elements of the parent gel are not incorporated quantitatively in the final crystalline product. Moreover the formed zeolite has a different composition than the liquid. Both features are comon to most zeolites (1,9). From our previous studies (10-12) on the zeolite omega synthesis it appears that the element with the higher yield of incorporation is aluminimun. Hence, we looked for correlations between growth rates and the concentration of aluminium in the liquid phase, as possible evidences for aluminium being the limiting element in the crystallization.

The change of $[\mathrm{Al}]$ as a function of time is shown in Figure 5 for an experiment carried out at 115°C. After about 10 hours, the concentration dropped rapidly as the zeolite formed.

When more experiments were considered, a good correlation could be established between the aluminium concentration and the variation of the crystal habit. Figure 6 reports data collected from seven crystallizations. Spherulites exhibiting high-index faces existed for the higher supersaturation levels. When the aluminium content became lower than 4-5 mmol/l, (001) faces appeared, while (100) faces formed only below 2-2.5 mmol/l.

The size of the crystals in the <001> and <hk0> directions are plotted as a function of time in Figure 7. It appears that the growth rates in the above directions do not follow parallel kinetics. In the <001> direction, crystal growth occurred during the whole crystallization process while the development of the crystals in the <hk0> directions rapidly decreased and stopped when (100) faces became exposed. Thus the growth kinetics of the (001)

and (hk0) faces have different dependences on the concentration of dissolved aluminium.

Dependence of the growth rates on the aluminium in solution. Figure 8 shows the influence of the concentration of aluminium (mmol/l) on the rate of growth (nm/h) for the (001) and (hh0) faces at 115°C (the aluminium concentration taken into account corresponds to the average value between two consecutive analyses). If the experimental data are represented in ln r versus ln [Al] plots, satisfactory linear correlations are found. Growth rates may then be represented as :

$$r_{001} = k [Al]^{0.8}$$ with k=5.5, 13 and 37.4 at 105°C, 115°C and 130°C respectively, E_a=23 kcal/mol, and

$$r_{hk0} = k [Al]^{1.6}$$ with k=0.94, 3.94 and 11.7 at 105°C, 115°C and 130°C respectively, E_a=30 kcal/mol.

Crystal habit modification. Several crystal habits have been reported in the open and patent literature for zeolite omega. Elongated hexagonal rods (15,16) or fibres (17) have been reported when the zeolite resulted from the recrystallization of another zeolite, Y (15) or S (17), or of clays (16). Moreover the natural counterpart of zeolite omega, mazzite, appears as bundles of needle-shaped particles (18). All these solids have been grown at low supersaturation levels, hence under conditions in which our results show that the growth in the direction <001> prevails on the growth normal to the c-axis (Fig.8).

This preferential growth may hinder many applications of the zeolite omega, whose unidimensional porosity, parallel to the c-axis, presents diffusional limitations which are functions of the elongation of the crystals. In the case of the syntheses we reported in Figure 7, the final ratio between <001> and < 100> size was 2.5 to 3.6. Knowledge of the growth kinetics of the different faces of the zeolite allowed us to attribute the main increase in < 001 > size to the long final period of growth at aluminium concentration lower than about 2 mmol/l (see Fig.5). Such a situation results from the need of complete conversion of a slightly soluble raw material as a clay.

Any possible way to modify the final <001> / <hk0> size ratio appeared to require that growth of crystals be conducted in an optimum range of supersaturation (corresponding to a concentration of aluminium between 2 and 4 mmol/l) without modification of the initial conditions, which determine the number of crystals nucleated. The practical way in which we realized this objective was the use of an initial synthesis medium containing only the aluminium present in the structure directing mixture. Once the nucleation occurred, an aluminate solution was injected in the autoclave in order to maintain the aluminium concentration at the desired level. The expected increase in growth surface was calculated using the above kinetic equations, and the flow rate of the injected solution was continuously adjusted in order to balance the incorporation of nutrient by the crystals.
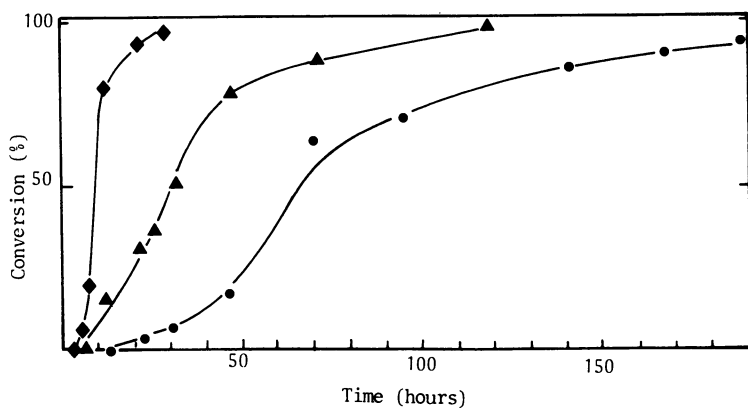
Figure 1. Crystallization curves for zeolite omega at ● 105°C,
▲ 115°C, ◆ 130°C.
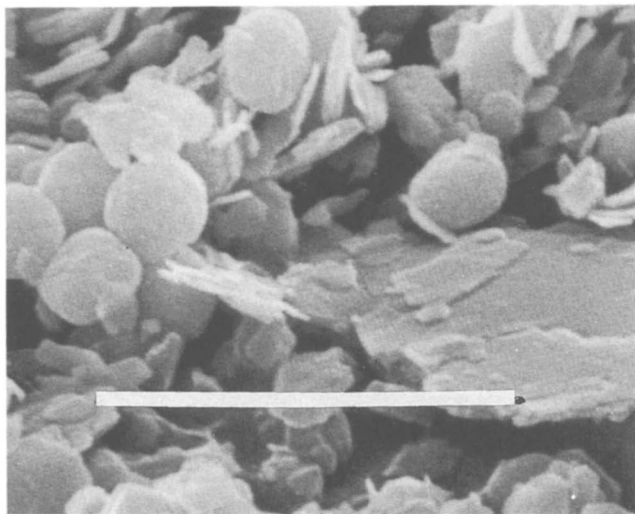
Figure 2. Mixture of unreacted kaolinite and of spheroids (high
index faces exposed) of zeolite omega obtained in the first
stages of the crystallization. Scale bar : 5 μm.
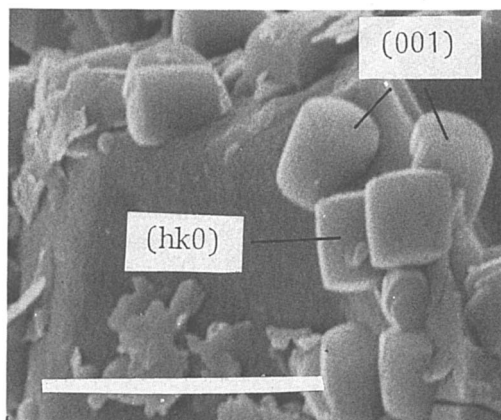
Figure 3. Kaolinite and barrel-shaped ((001) and (hk0) faces exposed) crystals of zeolite omega. (See text). Scale bar : 5 μm.
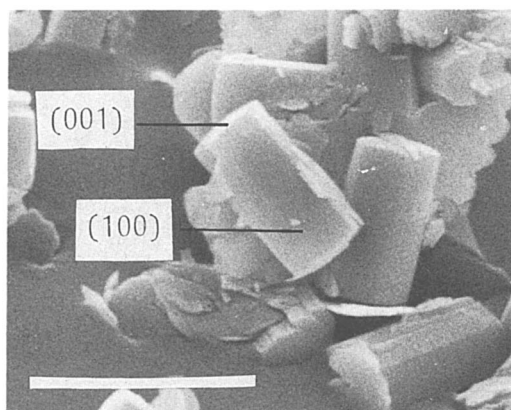
Figure 4. Hexagonal prisms ((001) and (100) faces exposed) of zeolite omega and kaolinite. (See Text). Scale bar : 5 μm.
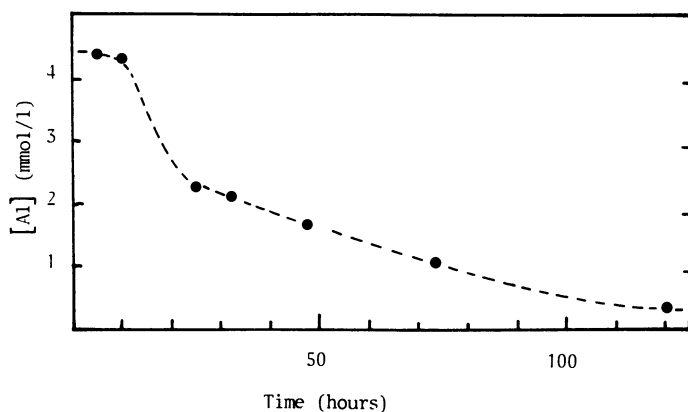
Figure 5. Variation of the concentration of aluminium in the crystallization solution at 115°C.
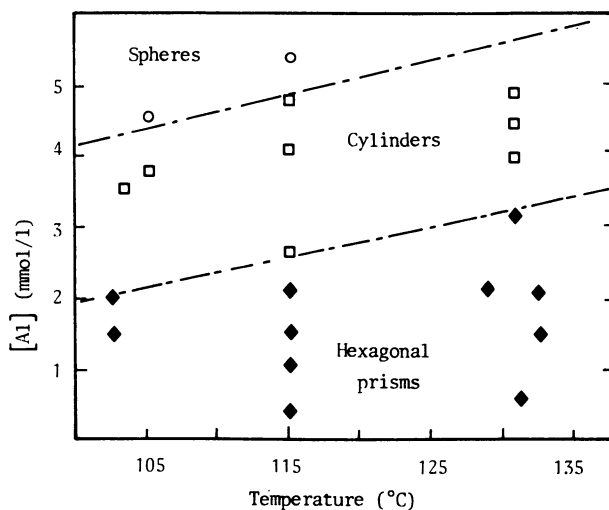
Figure 6. Crystal habit as a function of aluminium concentration and temperature.
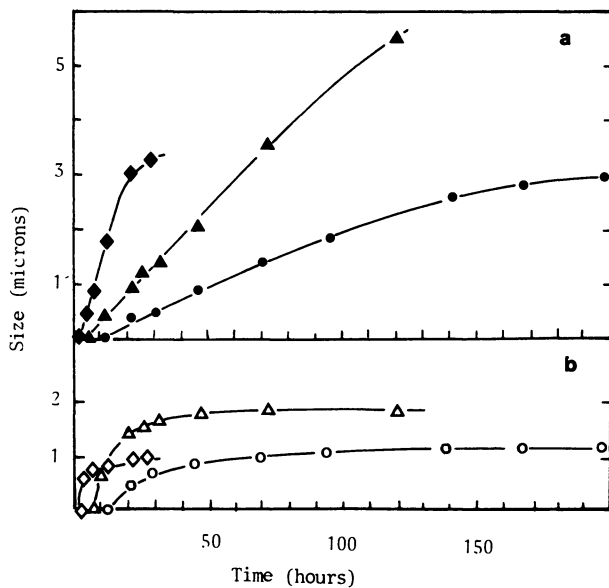
Figure 7. Variation with time of the crystal sizes: (a) < 001 > direction, (b) < hk0 > directions; O●105°C, △▲115°C, ◇◆130°C.
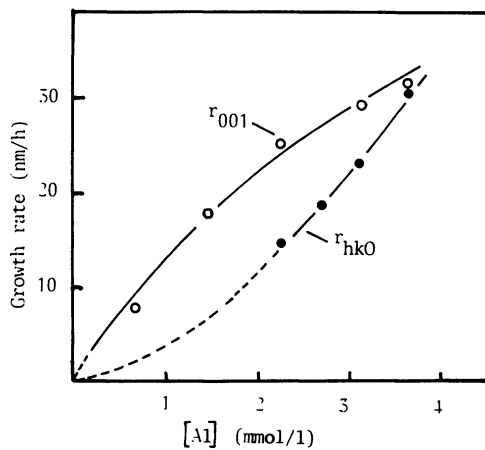
Figure 8. Growth rates of the (001) and (hk0) faces at 115°C as a function of aluminium concentration.

In such an experiment the initial mixture of silica, sodium hydroxide, water and structure directing mixture had a composition of $14(0.94Na. \ 0.06TMA)_2O. \ Al_2O_3. \ 39SiO_2. \ 890H_2O$. The mixture (470 ml) was heated at 115°C. The solution injected, prepared from sodium aluminate, sodium hydroxide and tetramethylammonium hydroxide, had the composition : [Al] 0.46 mol/l, [TMA] 0.06 mol/l, [Na] 1.70 mol/l. In Figure 9 the flow rate of the injected solution is reported, together with the variation of the aluminium concentration in the liquid phase of the synthesis medium. The simultaneous evolution of the <hk0> and <001> size of the crystals of zeolite omega is reported in Figure 10.

Considering the aluminium concentration plot in Figure 9, it can be observed that the first stages of the synthesis closely paralleded the pattern of the experiment reported in Figure 5. After 12 hours of synthesis a sharp rise of aluminium concentration was observed in correspondence with the beginning of the aluminate feeding. The subsequent decrease (15 hours) was related to an increasing consumption of aluminium (due to the increase of the growth surface) not totally balanced by the increase of the flow rate. As supersaturation decreased, the <hk0> growth slowed down. When [Al] reached the threshold of 2 mmol/l, the (100) faces formed and no further growth in the direction normal to the c-axis was observed (Fig.10). When the aluminium supply was continued for at least an hour after that the effective growth surface has been limited to the (001) surfaces, a subsequent concentration peak was observed (25 hours).

The final ratio between the <001> and the <hk0> size of the crystals was about 1.6, significantly lower than the value observed in crystals obtained by kaolinite conversion.

Discussion

The nature of the silicoaluminate units taking part in the zeolite growth is still unknown, despite the amount of experimental data collected about the species present in the solutions from which different zeolites are formed (19-22). Some of our results are particularly significant for this subject.

1) The rates of growth of zeolite omega correlate to the concentration of dissolved aluminium. The use of sources of aluminium as different as kaolinite, an aged silicoaluminate gel and a sodium aluminate solution does not affect the correlation. Thus as long as aluminium is concerned, no memory effect of the topology of the source can be observed. This argues for the formation of the growth units through reactions in solution.

2) For zeolite omega, aluminium appears to be the limiting element in the formation of the growth units. The incongruence of the synthesis and the excess of the elements other than aluminium could account for this result. In zeolitic systems not presenting these features, the occurence of such a strict relationship could be harder to establish.

3) The growth rates of the (001) face and of the lateral surface of the cylindrical crystals (here designed as (hk0) faces) present a different energy of activation and a different dependence on aluminium concentration. These results could support the hypothesis of different growth mechanisms on the different faces.
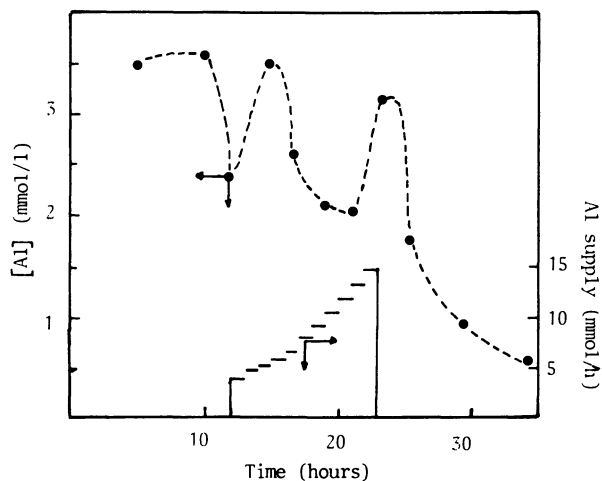
Figure 9. Synthesis of zeolite omega at 115°C with external supply of aluminium. Left scale: aluminium concentration in the autoclave solution. Right scale: rate of aluminium supply.
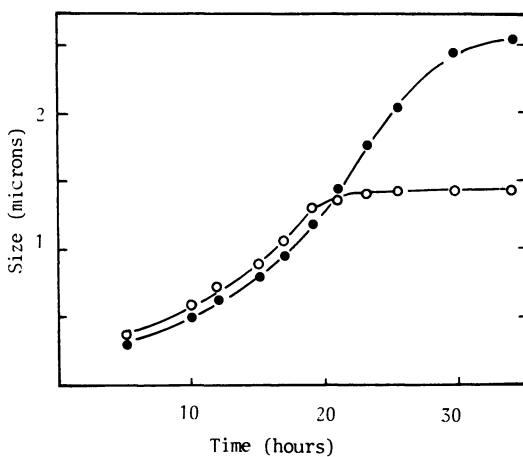
Figure 10. Synthesis of zeolite omega at 115°C with external supply of aluminium. Change of the crystal size in the <001> (●) and <hk0>(O) directions.

The growth rate of the face (001) presents an activation energy of 23 kcal/mol and is proportional to $[Al]^{0.8}$, a reaction order near unity. This behavior could be interpreted as the product of two near-to-linear dependences. On the one hand, there is a dependency between concentration of growth units and concentration of aluminium, and on the other hand, a dependency exists between rate of growth and supersaturation. Persistent growth at the lowest concentration levels analyzed suggests a very low value for the saturation concentration of aluminium in this experimental system. While fully arbitrary, it is tempting to hypothesize that some increase in viscosity with increasing aluminium concentration allows for the deviation from perfect linearity of the growth rate-versus-concentration plot, a phenomenon well known by researchers fond of crystal growth in gels (23).

Growth on the lateral surface of the cylinder-like crystals presents an activation energy of 30 kcal/mol and is proportional to $[Al]^{1.6}$. Thus a stepped surface (S-face, 24) with no defined crystallographic orientation like the (hk0) faces presents a reaction order nearly double than a formally flat face (F-face, 24) like (001). This result seems to be incompatible with the action of the same mechanism of growth on the two kinds of faces.

The dependency, higher than first-order, on aluminium for the growth rate in the <hk0> directions could be explained by the result of the product between two dependences : a first-order dependence of growth rate on supersaturation and a near-to-second-order dependence of the growth units concentration on the aluminium concentration. It would be speculative to attribute such a result to a need, for <hk0> growth, of silicoaluminate species dimer of the units responsible for growth on the (001) faces. Nevertheless, such an interpretation could find intuitive support in the topology of the zeolite omega framework (25). While the <001> growth can be easily visualized as the increase in length of pre-existing chains of five-members rings, the <hk0> growth must deal with the harder task of completing twelve-members rings probably not including any organic template (11,26).

This kind of difficulty could also account for the observed behavior of the (100) face, with growth so slow that no size increase normal to the c-axis could be detected in our experimental conditions once the hexagonal prism habit was attained.

Acknowledgments

Literature cited

1. For a review, see Barrer, R.M. Hydrothermal Chemistry of Zeolites, Academic: London, 1982; p 133.
2. Thompson,R.W.; Dyer,A. Zeolites 1985, 5, 202.
3. Kacirek, H.; Lechert, H. J. Phys. Chem 1975, 79, 1589.
4. Zhdanov, S.P.; Samulevich, N.N. Proc. 5th Int. Conf. on Zeolites; Rees, L.V.C., Ed.; Heyden: London, 1980, p 75.
5. Ciric, J. J. Colloid and Interface Sci. 1968, 28, 315.
6. Johnson, W.A.; Mehl, R.F. Trans. AIME, 1939, 135, 416.

7. Avrami, M. J. Chem. Phys. 1939, 7, 1103.
8. Avrami, M. J. Chem. Phys. 1940, 8, 212.
9. For a review, see Guth, J.L.; Gaullet, P. J. Chem. Phys. 1986, 83, 155.
10. Nicolas, S. Ph. D. Thesis, Université des Sciences et Techniques du Languedoc, Montpellier, 1987.

11. Nicolas, S.; Massiani, P.; Vera-Pacheco, M.; Fajula, F.; Figueras, F. Stud. Surf. Sci. and Catal. 1988, 37, 115.
12. Fajula, F.; Vera-Pacheco, M.; Figueras, F.Zeolites 1987, 7,203.
13. Hou, L.Y.; Sand, L.B. Proc. 6th Int. Conf. on Zeolites; Olson, D.; Bisio, A., Eds.; Butterworths: Guilford, 1984, p 887.
14. Strickland-Constable, R.F. Kinetics and Mechanism of Crystrallization, Academic : London, 1968, p.7.
15. Dwyer, F.G.; Chu, P.J. J. Catal. 1979, 59, 263.
16. Fajula, F.; Figueras, F.; Moudafi, L.; Vera-Pacheco, M.; Nicolas, S.; Dufresne, P.; Gueguen, C. French Pat. Appl. 8507772, 1985.
17. Araya, A.; Barber, T.J.; Lowe, B.M.; Sinclair, D.M.; Varma, A. Zeolites 1984, 4, 263.
18. Galli, E.; Passaglia, E.; Pongiluppi, D.; Rinaldi, R. Contrib. Mineral. Petrol. 1974, 45, 99.
19. Guth, J.L.; Caullet, P.; Jacques, P.; Wey, R. Bull. Soc. Chim. 1980, 3, 121.
20. Dent Glasser, L.S.; Harvey, G. Proc. 6th Int. Conf. on Zeolites; Olson, D.; Bisio, A., Eds.; Butterworth: Guilford, 1984, p 925.
21. Engelhardt, G.; Fahlke, B.; Mägi, M.; Lippmaa, E. Zeolites 1985, 5, 49.
22. Boxhoorn, G.; Sudmeijer, O.; Van Kasteren, P.H.G. J. Chem. Soc. Chem. Comm. 1983, 1416.
23. Henixh H.K. Crystals in Gels and Liesegang Rings; Cambridge University: Cambridge, 1988, p 50.
24. Hartman, P. Growth of Crystals, Sheftal, N-N., Ed., Consultant Bureau : New York, London, 1969, Vol.7, p.3.
25. Rinaldi, R.; Pluth, J.J.; Smith, J.V. Acta Cryst. 1975, 31, 1603.
26. Aiello, R.; Barrer, R.M. J. Chem. Soc.(A) 1970, 1470.

Chapter 35

Synthesis of the New Large-Pore Zeolite ECR-1

D. E. W. Vaughan and K. G. Strohmaier

Exxon Research and Engineering Company, Route 22 East, Annandale, NJ 08801

ECR-1 is a new 12-ring zeolite which crystallizes as a boundary phase between the crystallization fields of mazzite and mordenite when bis(2-hydroxyethyl) dimethyl- ammonium or bis(2-hydroxypropyl) dimethyl ammonium cations are present in the synthesis gels. Synthesis studies show that cocrystallization of these latter zeolites is rare and that nucleation parameters may dominate compositional stability.

Investigations of different alkylammonium template effects on faujasite (type Y) syntheses(1) have shown that when the template was bis(2-hydroxyethyl) dimethylammonium (DHEDM) or bis(2-hydroxy propyl) dimethylammonium (DHPDM), a new phase crystallized at the "phase" boundary between faujasite, mordenite and mazzite (Linde omega(2), ZSM-4(3)). This zeolite has been designated ECR-1(4) and seems to comprise a regular alternation of the structural sheets found in mazzite and mordenite(5). A detailed description of the structural charact-erization of ECR-1 is presented elsewhere at this meeting(6). Its proposed topology is illustrated in Figure 1, the main feature being a 12-ring channel parallel to the c-axis, similar to those in the parent structures. The previously unrecognised compatibility of the two structural components of ECR-1, and the manner in which they intergrow, revives the debate on the nature of zeolite petrogenesis and the size and configuration of the structural sub-units forming zeolite crystals. ECR-1 would seem to support a model based on templated sheet structures(7).
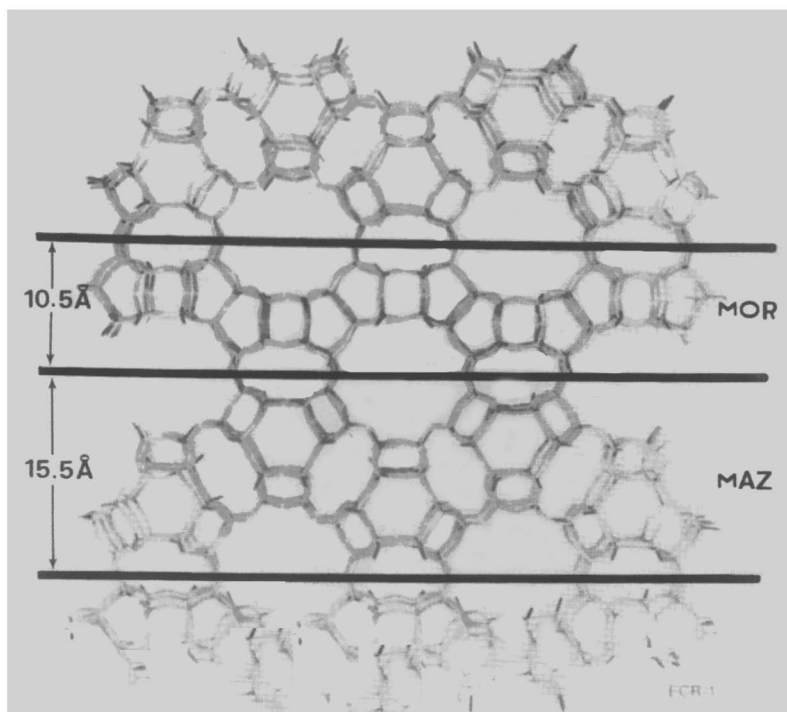
Figure 1. The proposed structural framework of ECR-1, showing alternate sheets of mazzite and mordenite, the 26.5Å repeat unit and the single 12-ring channel.

It is well known that in this sodium composition field with Si/Al in the range of 3 to 8, alkyl ammonium salts strongly influence the crystalline products. Mazzite analogues are the dominant phases promoted by the presence of TMA(2,3), choline, pyrrolidine(8) and DABCO(9). In the system described here, DHEDM is included in the mazzite structure when it forms (a material designated ECR-15), but the initial nucleation seems to require TMA at a low level. Syntheses of mazzite in near template-free syntheses have been described elsewhere (10,11), demonstrating that TMA is necessary only to nucleate this zeolite to promote complete crystallization. Mordenite has also been made in the presence of templates such as TEA(12) and neopentylamine(13), in addition to these DHEDM products. Recent general reviews of the influence of organic ammonium compounds and amines on zeolite syntheses in general have been published elsewhere(14,15).

EXPERIMENTAL

Synthesis Procedures
ECR-1 crystallizes in the presence of DHEDM and DHPDM from gels which would normally yield Y-faujasite in the absence of any organic template. The best products crystallized in the composition range with Si/Al between 3 and 6, at temperatures between 120°C and 160°C, using a 'seed' nucleant solution(16). Synthesis of DHEDM ECR-1 was made from a gel stoichiometry of:

$$0.6(DHEDM)_2O:1.35Na_2O:Al_2O_3:7.5SiO_2:110H_2O:(1.2NaCl)$$
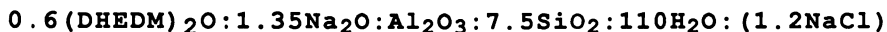
by first making a sodium aluminate solution by dissolving 8.23g NaOH and 14.6g alumina trihydrate in 20g water, then mixing it with 229g of waterglass solution(PQ Corp 'N' silicate) containing 8g of the seed solution(4,16) and 25g DHEDM chloride(Alfa Products) dissolved in 25g water. To this homogenised solution in a blender was slowly added a solution of 34.7g aluminum sulfate(17 hydrate) dissolved in 50g water, and the total gel weight was adjusted to 440g with water. This represents an approximately 0.1 molar preparation. The gel was then reacted in a Teflon lined Parr stainless steel reactor at 160°C for eight days (Spl-A). Chemical analysis by ICPAES gave an Si/Al ratio of 3.35, a value typical for most preparations of ECR-1, and almost identical to various synthetic mazzites synthesized over a wide range of compositions. The product of this reaction is shown in the scanning electron micrographs in Figure 2. An alternate method used the same stoichiometry but colloidal silica (Ludox HS-40, DuPont Co.) as the silica source and DHPDM iodide (RSA Corp.) as the template, yielding a similar Si/Al ratio product (Spl-B). A higher silica and base composition ($0.6DHEDM: 3.1Na_2O: Al_2O_3:$
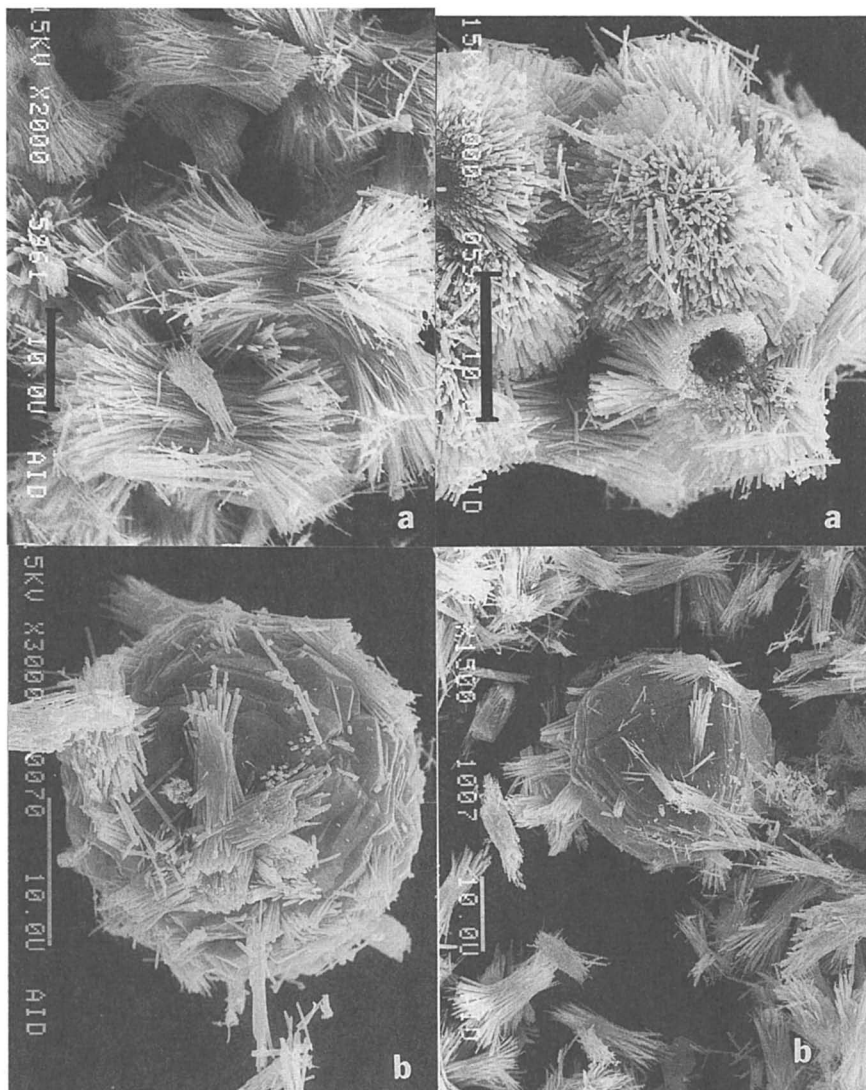
Figure 2. Scanning electron micrographs of various ECR-1 samples: (a) the DHEDM product described in the text. (b) Large analcime crystals with adhering ECR-1 crystals. Scale marks are 10μ.

$9SiO_2$: $130H_2O$) additionally seeded with ECR-1 product
produced a lower Si/Al ECR-1 (Spl-C). Essential product
properties are given in Table 1.

Extensive exploration of the ECR-1 crystallization
composition field is shown in Figure 3. At higher Si/Al
ratios mordenite is the major, and usually pure product,
and similarly mazzite at lower Si/Al ratios. ECR-1 is seen
only occasionally to cocrystallize with either of these
zeolites and it crystallizes rarely when the
template/sodium ratio is greater than 0.4.

TABLE 1
Selected Product Composition Details

Sample Spl	Template T	SiO_2/Al_2O_3	Unit Cell,Å a : b : c	nC_6H_{12} wt.%[1]	H_2O^{2}+ T[3] wt.%
A	HDEDM	6.70	18.15:26.31:7.31	1.6	10.8+1.4
B	HDPDM	6.88	18.13:26.18:7.31	2.3	11.5+2.5
C	HDEDM	6.54	18.15:26.09:7.31	2.0	9.4+1.0

1=1hr./45 torr/ 20°C;2= wt.loss < 400°C;3=wt.loss > 400°C.

Although high resolution electron microscopy studies have
identified mazzite overgrowths on ECR-1(5), similar
mordenite overgrowths have not yet been observed. In no
syntheses have mazzite and mordenite been observed to
cocrystallize.

Colloidal silicas, such as Ludox HS-40 and HS-30
(DuPont Co.), are equally effective silica sources, and
DHPDM may replace DHEDM. Alkyl ammonium hydroxides are as
effective as the halides, although their low aqueous
solution concentrations may increase the gel water levels
and extend the crystallization times. High template purity
seems to be an important variable in the synthesis of this
zeolite. ECR-1 products from various preparations are shown
in Figure 2. Wheatsheaf bundles of thick lath-like crystals
up to about 10μ in length are a characteristic morphology.
Analcite and P (gismondine) are usually the only impurity
phases in the middle of the ECR-1 crystallization field and
these are minimized by crystallizing the gels at lower
temperatures (120°C).

Analysis Methods
Products were analysed by x-ray diffraction using an
automated Siemens D500 diffractometer (CuKα radiation)
linked to a proprietary data base. The overlap of the
mazzite, mordenite and ECR-1 X-ray diffraction patterns
makes these materials difficult to differentiate,
particularly in mixtures, as shown in Figure 4. For
impurity reference purposes the analcite pattern is
included in this diagram. Indexed diffraction patterns of
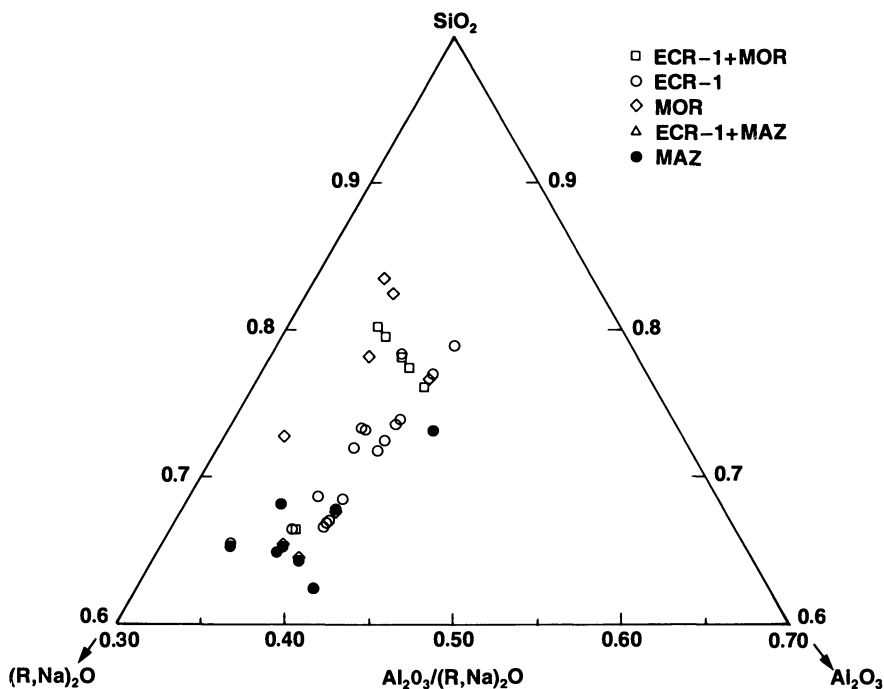
Figure 3. Composition crystallization diagram for experiments reported in this paper, showing crystallization fields of ECR-1(o), mazzite(●), mordenite (◊), ECR-1+ mazzite(Δ), and ECR-1+ mordenite (◻).
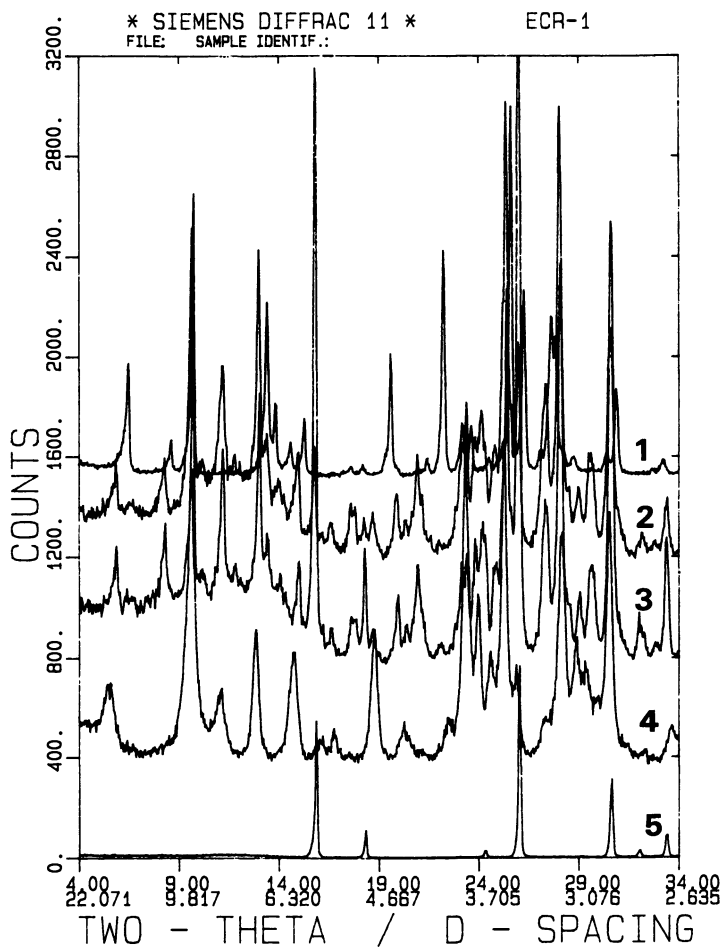
Figure 4. X-ray diffraction patterns (Cu K_α radiation) for DHEDM (3) and DHPDM (2) ECR-1, showing analcite impurity lines and an analcime reference pattern (5). Patterns for mazzite (4) and mordenite (1) crystallized from similar gels are shown for reference purposes.

the two different template forms of ECR-1 are given in Table 2. The symmetry is primitive orthorhombic with unit cell dimensions of about $\underline{a}$=7.31å, $\underline{b}$=18.15å and $\underline{c}$=26.31å. IR and SEM were important ancillary identification tools, as ECR-1 shows characteristic IR '5-ring' vibrations at 1210 and 1235 cm^{-1}, and the crystal morphology and agglomeration clusters are somewhat different from the similar typical characteristics of mazzite and mordenite (Figure 5). TGA was used as a useful guide to the template contents of the various zeolites formed, and n-hexane sorption capacities, after burnout of the organic template, were indicators of channel accessibilities. Details of the structural characterization of ECR-1 using several techniques is to be presented in a different symposium at this meeting(6).

DISCUSSION

ECR-1 crystallizes from gels in the presence of DHEDM and DHPDM which would normally yield Y-faujasite in the absence of an organic template. In the presence of TMA such gels crystallize pure synthetic mazzites as the stable zeolite, often after major development of faujasite in the early stages of crystallization. With increasing temperatures from 90°C to 160°C faujasite is eliminated as a component in the crystallization (or becomes such a short lived transitory phase that it is rarely observed). In the presence of the above two templates, faujasite is the stable phase below 100°C, and ECR-1 is the stable product above about 115°C. However, in the presence of even trace amounts of TMA in the template solutions, mazzite nucleates, and once nucleated it prevails as the stable product in the subsequent crystallization. Hydrothermal experiments with DHEDM and DHPDM in water and basic solutions at 160°C showed no breakdown of these templates that could be observed with ^{13}C-NMR, leading to the conclusion that template breakdown products were probably not responsible for the nucleation of mazzite types during the synthesis. Adequate monitoring of the template purity is necessary to ensure the exclusion of mazzite from the synthesis products in the primary crystallization field of ECR-1.

Analcite and P are the major impurity phase found in ECR-1 preparations, and at higher temperatures and longer crystallization times the former is often the major product. Initial ECR-1 syntheses invariably showed crystals of this zeolite growing on the outside of analcite crystals (Figure 2), indicating the possibility of the latter acting as a stabilising or nucleating surface. Several experiments with various analcite seeding modes negated this hypothesis.

N-hexane sorption experiments with numerous different samples showed major variations in sorption properties (capacities and rates, as shown in Table 1), some of which

TABLE 2

X-ray diffraction patterns of templated forms of ECR-1

			(PrOH)$_2$Me$_2$N		(EtOH)$_2$Me$_2$N	
h	k	l	d	I/Io	d	I/Io
1	1	0	14.9	11	14.8	20
1	2	0	10.6	18	10.6	15
2	0	0	9.10	63	9.10	44
1	3	0	7.87	36	7.85	8
1	0	1	6.77	40	6.76	45
1	1	1	6.56	9	6.57	10
2	3	0	6.31	15	6.29	19
3	1	0	5.91	22	5.89	16
2	4	0	5.31	9	5.32	9
3	3	0	4.99	14	4.97	14
1	4	1	4.73	16	4.73	6
3	4	0	4.44	17	4.44	18
1	6	0	4.22	22	4.23	35
3	3	1	4.11	3		
3	4	1	3.796	54	3.789	15
4	4	0	3.724	11	3.730	17
1	0	2	3.574	13	3.574	17
5	2	0	3.500	79	3.497	40
5	0	1	3.252	57	3.251	55
5	4	0	3.172	100	3.170	100
2	8	0	3.068	7	3.069	8
6	1	0	3.008	27	3.006	27
2	8	1	2.278	14	2.679	27
5	7	0	2.603	7	2.588	15
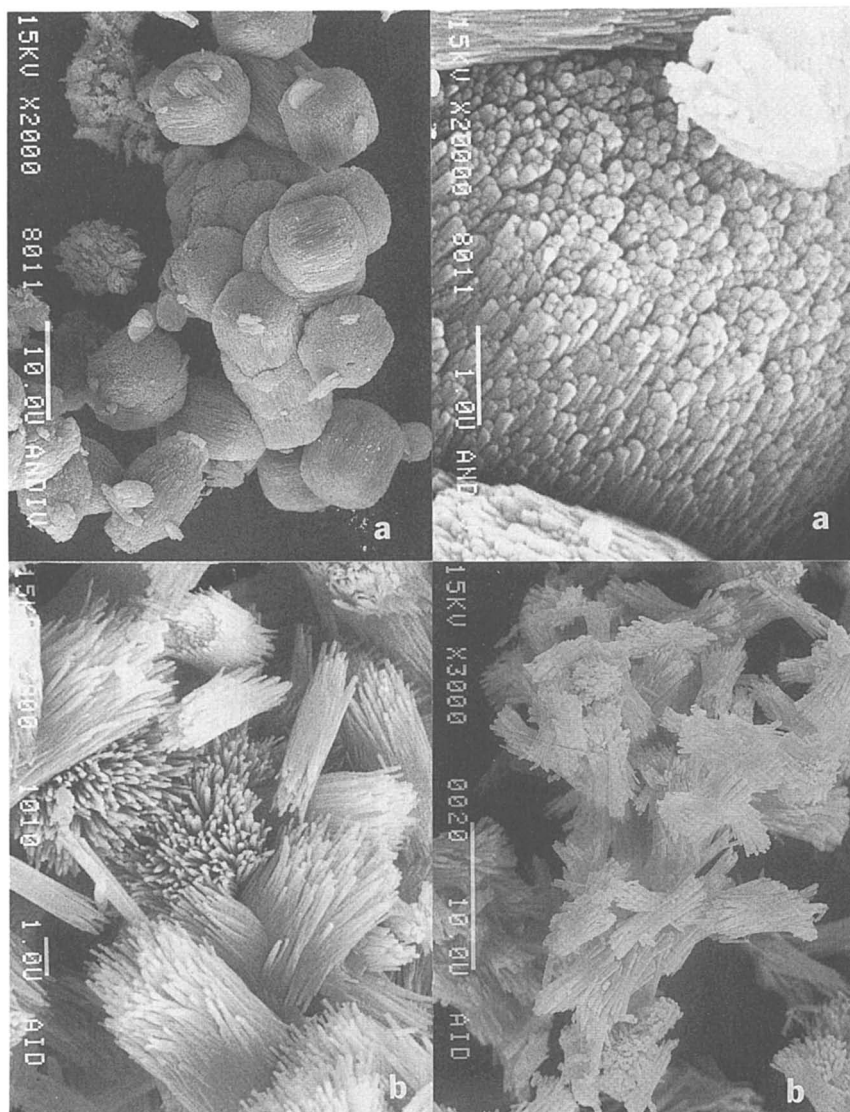
Figure 5. Scanning electron micrographs of zeolites cocrystallizing with ECR-1: (a) mordenite barrel like agglomerates; (b) pure samples of different mazzites showing similar morphology to ECR-1 but having a smaller aspect ratio and much shorter crystals. Scale markers are 1μ (LHS) and 10μ (RHS).

could be explained by the presence of analcite impurities. However, high resolution electron microscopy in the lattice imaging mode clearly shows the possibilities of twinning, intergrowths and overgrowths in this structure(5), and therefore the possibility of partly blocked structures. As mordenite sheets are a structural component in ECR-1, the possibility of small and large port varieties cannot be ignored. Long crystals of single channel zeolites are a complication because even minor pore blockages by detrital gel components or template degradation products can have major influences on sorption properties. The optimised preparations have n-hexane and cyclohexane sorption capacities comparable with Linde-L and large port mordenite (up to 8% wt.). Other sorption capacities are about 16% wt.for carbon dioxide and 13% wt.for water.

ECR-1 is a true boundary phase between two compatible structures - mazzite and mordenite - which normally crystallize with greatly disparate Si/Al ratios (3.4 and >5 respectively). Yet ECR-1 has an Si/Al ratio identical to mazzite, even though half of its component sheets are structurally characteristic of mordenite (in the structure proposal). This compositional incompatibility is further reflected in the almost complete lack of mixtures of mazzite with mordenite in the experiments so far completed. The ongoing search for ECR-1 with mordenite overgrowths is therefore an important objective in the understanding of crystallization mechanisms in this system, with particular interest in the possible compositional variation between all three component zeolites.

CONCLUSIONS

The compatibility of mazzite and mordenite structural units, and the existence of ECR-1 types of structures at the interface between the primary crystallization fields of the former, indicate that zeolite crystallization via templation of intermediate sheet structures is a plausible growth mechanism. Other zeolite groups showing similar possibilities include the pentasils, the ABC 6-ring structures and the cubic/hexagonal stacked faujasite sheets. The significance of the chemical dissimilarity between the constituent components of ECR-1 is of interest, but its elucidation requires more extensive crystallization studies combined with high resolution microprobe chemical analyses of crystal overgrowths.

ECR-1 has a complex crystallization and structural relation-ship with mazzite and mordenite, and this paper should be viewed as a progress report from an ongoing project. The problems are symptomatic of a number of recent studies of zeolites showing high degrees of structural complexity, such as ZSM-23(16), beta(17) and various FAU-BSS intergrown materials(18).

Literature Cited

1. Vaughan,D.E.W. and Strohmaier,K.G., <u>Proc. 7th. Intl. Zeolite Conf.</u>, Ed.Y.Murakami, A.Iijima and J.W.Ward, Kodansha/ Elsevier Press (**SSSC#28**), 1986, 207.
2. Flanigen,E.M and Kellberg,E.R., <u>U.S.Patent</u> 4,241,036, 1980.
3 Ciric,J., <u>U.S.Patent</u> 3,923,639, 1975.
4. Vaughan,D.E.W. and Strohmaier,K.G., <u>U.S.Patent</u> 4,657,748, 1987.
5. Leonowicz,M.E. and Vaughan,D.E.W., <u>Nature</u>, 1987, **329**, 819.
6. Vaughan,D.E.W.,Leonowicz,M.E.and Strohmaier,K.G., <u>Amer. Chem. Soc. Symp.Ser.</u>, Ed. S.A.Bradley et al, 1989, *in press*.
7. Vaughan,D.E.W., <u>Mater.Res.Soc. Symp.Vol.</u>**111**, Ed.M.M.J. Treacy, J.M.Thomas and J.M.White, 1988, 89.
8. Rubin,M.K., Plank,C.J. and Rozinski,E.J., <u>U.S. Patent</u> 4,021,447, (1977).
9. Rubin,M.K. and Rozinski,E.J., <u>U.S.Patent</u> 4,331,643, 1982.
10. Albers,E.W. and Vaughan,D.E.W., <u>U.S.Patent</u> 3,947,482, 1976.
11. Nicolas,S., Massiani,P., Vera Pacheco,M., Fajula,F. and Figueras,F., <u>Innovation in Zeolite Mater. Sc.</u>, Ed.P.J. Grobert et al, Elsevier Press (**SSSC#37**),1988, 115.
12. Chu,P., <u>U.S.Patent</u> 3,766,093, 1973.
13. Stewart,D.G. and Ball,W.J., Eur.Pat.Appl. 18,038, 1980.
14. Barrer,R.M., <u>"Hydrothermal Chemistry of Zeolites"</u>, Academic Press (London), 1982.
15. Lok,B.M., Cannan,T.R. and Messina,C.A., <u>Zeolites</u>, 1983,**3**,282.
16. Wright,P.A., Thomas,J.M., Millward,G.R., Ramdas,S. and Barri, A.I.,<u>J.Roy.Chem.Soc. Chem.Commun.</u>, 1985, 1117.
17. Treacy,M.M.J. and Newsam,J.M., <u>Nature</u>, 1988, **332**, 249.
18. Newsam,J.M., Treacy,M.M.J., Vaughan,D.E.W., Strohmaier, K.G. and Mortier,W.J., <u>J.Roy.Chem.Soc.Chem.Commun.</u>, 1989, *in press*.

Chapter 36

Directing Parameters in the Synthesis of Zeolites ZSM–20 and Beta

Zelimir Gabelica, Nicole Dewaele, Lutgarde Maistriau, Janos B. Nagy, and Eric G. Derouane

Facultés Universitaires Notre Dame de la Paix, Namur, Laboratoire de Catalyse, 61 Rue de Bruxelles, B–5000 Namur, Belgium

We describe a systematic investigation of various synthesis variables that usually affect the crystallization of faujasite-type structures from Si, Al, Na, tetraethylammonium (TEA) hydrogels. A careful control of parameters such as the composition of the precursor hydrogel, temperature and crystallization time is needed to selectively prepare and stabilize pure zeolite ZSM-20 in high yield.
Any slight deviation from optimized conditions (higher temperature, longer synthesis times, lower TEAOH contents...) invariably leads to the formation of the more stable zeolite Beta.
When Aerosil is used instead of tetraethylorthosilicate a novel faujasite polytype material having a different hexagonal packing is obtained. Zeolite ZSM-20 with a rather constant Si/Al ratio of 5 only crystallizes when the initial Al concentration is sufficient. TEA^+ together with the Na^+ ions directly act as counterions to neutralize the Al-framework negative charges and very few Si-O-R (R = Na or TEA) structural defects are generated. A higher initial Al concentration does not affect the final composition of the material but markedly increases the yield. A lower Al content definitely leads to the Si richer Beta phase, that incorporates TEA^+ counterions to Al negative charges and TEAOH ionic pairs, that occupy the maximum of the intracrystalline free volume, while Na^+ ions partly neutralize the $Si-O^-$ framework defect groups.

High silica zeolites with large pores and cavities are attractive materials for catalytic applications in a variety of industrial processes because of their high (hydro)thermal stability, enhanced hydrophobicity, strong acidity and particular good resistance to deactivation ([1]). Several patents report syntheses of silica variants of zeolite Y ([2,3]) but it appeared increasingly difficult to prepare faujasite-type materials of Si/Al ratio higher than about 3 ([4-6]). Among more siliceous materials with similar open pore systems and structurally related to faujasite, zeolites ZSM-3, CSZ-1 and CSZ-3 are prepared from wholly inorganic media, while ZSM-20 and SAPO-37 are the only FAU-like materials prepared in presence of specific structure-directing organic molecules "Table I".

Table I. Zeolites of Faujasite-type Structure.
Composition and structural Characteristics.

Zeolite	Framework cations	Framework Si/Al ratio	Structure (distances in Å)	Reference
X	Na^+	1-1.5	Cubic(a=24.94)	7
Y	Na^+	1.5-3	Cubic(a=24.73)	8
ZSM-3	Li^+, Na^+	1-3	Hexagonal(a=17.5;c=14.3)	9,10
ZSM-20	Na^+, TEA^+	3.5-5	Hexagonal(a=17.3;c=28.6)	11,13,34,37
FAU-POLYTYPE	Na^+, TEA^+	3.2	Hexagonal(a=17.46;c=28.48)	this work
CSZ-1	Cs^+, Na^+	2.8	Rhombohedral(a=17.37)	14
CSZ-3	$Cs^+,(Rb^+),Na^+$	2.5-3.5	Rhombohedral	15
SAPO-37	TMA^+, TPA^+	0.25-1	Cubic(a=24.61)	12, 16

From the topological point of view, with the truncated octahedra of faujasite, a large number of structures can be derived considering a close packing of hexagonal layers of sodalite cages (17).

Zeolite ZSM-20 is a member of this family. As a large pore material with open structure, when suitably modified, this zeolite proved to be a useful catalyst in some specific reactions, such as Diels-Alder cyclizations (18) or isomerizations of dichlorobenzenes (19). It crystallizes in presence of tetraethylammonium cations (TEA^+), a templating agent that also directs the formation of a variety of other zeolites "Table II". Data from Table II also clearly show that the nature of the zeolite directed by TEA^+ strongly depends on the gel chemistry and on other synthesis parameters or conditions and, indeed, for most of these materials, TEA^+ is not a specific template. By contrast, TEA^+ appears as an indispensible ingredient for ZSM-20 to crystallize, suggesting that these ions very specifically act as structure orienting agents in its nucleation and growth processes. Nevertheless, as again suggested by the various types of preparations proposed for ZSM-20 "Table II", the purity and crystallinity of this zeolite is probably also a function to some extent of the synthesis conditions.

Another zeolite that often (co)crystallizes in the presence of TEA^+, when the procedure leading to ZSM-20 is only slightly modified, is zeolite Beta. (11,30-32,34, 36, 37, 39), a true high silica zeolite with open pore system. Its crystallographic structure actually consists of a random intergrowth of two new zeolitic frameworks that, in common with the faujasite lattice, show fully three-dimensional pore system with 12 rings as the minimum constricting apertures (40). Stacking faults affect the net tortuosity along the c-axis but do not significantly alter the accessible pore volume.

The various parameters affecting the formation of zeolite Beta from alkali-TEA^+-containing aluminosilicate gels were recently thoroughly investigated (31), and a crystallization mechanism was proposed (30).In a preliminary paper, we have defined and optimized a series of synthesis parameters allowing the preparation in good yield of zeolite ZSM-20 from a hydrogel that usually yields the more stable zeolite Beta (32). However, the competitive and selective formation of both ZSM-20 and Beta from the same hydrogel compositions have not been systematically investigated.

The aim of the present paper is double. Firstly, we wish to question more precisely the role of TEA⁺ ions in competition with the Na⁺ cations and possibly in close relation with other synthesis parameters such as the silica source, or the alumina content, by comparing a series of other physicochemical characterizations(chemical composition, nature of the occluded organics, void volume...) of zeolites ZSM-20 and Beta. In a second step, we conduct a more in depth investigation of the whole synthesis conditions and their modification in order to propose selective preparation routes for both zeolites and to possibly define further favorable conditions for the formation of other potential open phases.

Table II. Zeolites synthesized in presence of TEA⁺ Ions under various Conditions (a non exhaustive List, adapted from Literature data)

Zeolite	Molar ratios in starting gel (for 1 Al$_2$O$_3$)				Synthesis conditions		Reference
	(TEA)$_2$O	Na$_2$O	SiO$_2$	H$_2$O	Cryst. T (°C)	Cryst.time (days)	
Mordenite	6.1(Br⁻)	24.1	50(w.glass)	497	180(static)	7	20
ZSM-12	8.3(OH⁻)	41.1	86.6(w.glass)	1109	180(static)	7	20
ZeolitePHI	9.3(OH⁻)	1.1	20(Si(OEt)$_4$)	58	100(static)	14	21
ZSM-25	5.7(Br⁻)	1.7	8.3(Aerosil)	279	135(-)	5	22
ZSM-8[a]	2.7(OH⁻)	1.1	50.1(Ludox)	663	180(-)	7	23
ZSM-8[a]	8.9(Br⁻)	28.8	96.5(w.glass)	1888	130(static)	8	24
ZSM-8[a]	9(Br⁻)	26	106(w.glass)	2400	140(static	5	25
ZSM-5	19.5(OH⁻)	366 ((NH$_4$)$_2$O)	319 (colloidal SiO$_2$)	4880	160(-)	3	26,27
Nu-2	7.5(OH⁻)	12.8	50(Aerosil)	500	95(static)	32	28
Beta	2.8(OH⁻	0.9.	27.1(Ludox)	166	150(-)	10	29
Beta	9.7(OH⁻)	1.6	30.8(Si(OEt)$_4$)	314	120(static)	14	11
Beta[b]	7.25(OH⁻)	1.5 (+ 0.5K$_2$O)	30 (Si(OEt)$_4$)	36	100(static)	±1	30,31
Beta[b]	6.25(OH⁻)	1.2	30.2 (Si(OEt)$_4$)	267	100(static)	10	32,thiswork
Faujasite	0.05-0.8(Br⁻)	13.3	12.5(w.glass)	270	100(agitated)	1-3	33
Faujasite	13.2(OH⁻)	1.25	30.2 (Si(OEt)$_4$)	598	100(static)	21-35	32,thiswork
Fau-polytype	12.5(OH⁻)	1.25	30.2(Aerosil)	243	100(static)	5	this work
ZSM-20[b]	13.2(OH⁻)	1.25	30.2 (Si(OAlk)$_4$)	243	100(static)	13	11,13,34-36
ZSM-20[b]	11.3(OH⁻)	1.25	11.1 (Si(OEt)$_4$)	267	100(static)	5-14	32,37, this work

(a) categorized as a ZSM-5-rich intergrowth (38)
(b) variable reactant ratios used; ratios given for optimal syntheses

Experimental

Syntheses

The original synthesis conditions as described by Valyocsik in the example 19 of his patent (34) were chosen as the starting procedure to which various modifications have been brought. After a preliminary series of optimization processes, a typical and reproducible preparation yielding pure, highly crystalline ZSM-20 in optimum yield could be proposed. The detailed conditions are described in a preceding paper (32). The following scheme depicts these conditions for a typical synthesis, chosen as starting point for the systematic study :

Si(OEt)$_4$	
+	
Na Aluminate, TEAOH, H$_2$O	

— mixing ——————→ GEL

1.25 Na$_2$O. Al$_2$O$_3$. 30 Si(OEt)$_4$. 26.4 TEAOH. 327 H$_2$O

Ester hydrolysis, then
evaporation (H$_2$O,
EtOH)
(95°C,12h)

FINAL GEL

1.25 Na$_2$O. Al$_2$O$_3$. 30 SiO$_2$. 26.4 TEAOH. 267 H$_2$O

Hydrothermal treatment
(PTFE containers, static
conditions, 100°C, 11
days)

100% CRYSTALLINE ZSM-20
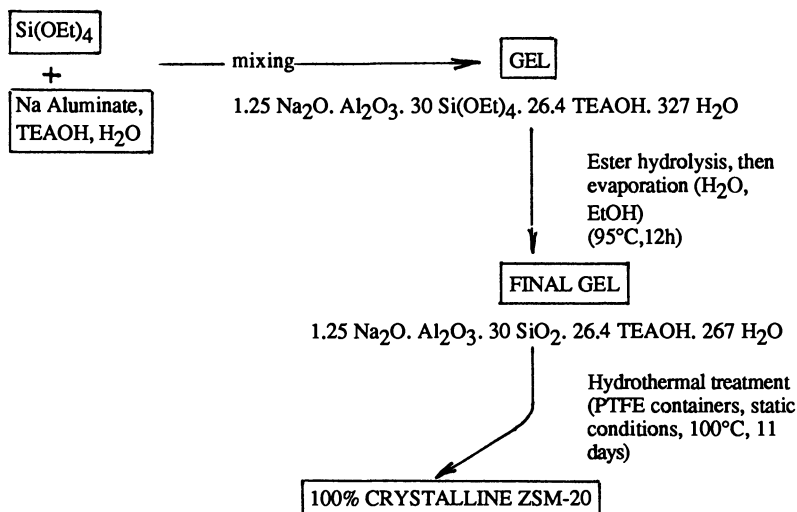
double unit cell (192 T atoms) :   Na$_{21.5}$ Al$_{36.7}$ Si$_{155.3}$ O$_{192}$ (TEA)$_{16.4}$ 95.5 H$_2$O
or, in terms of oxides, for 1 Al$_2$O$_3$:   0.59 Na$_2$O. Al$_2$O$_3$. 8.46 SiO$_2$.0.89TEAOH. 5.2 H$_2$O

Characterization techniques

The nature and crystallinity of the solid was determined by x-ray powder diffraction as detailed elsewhere (32). Isothermal (90°C) sorption measurements of n-hexane on a Stanton Redcroft STA 780 thermoanalyzer were either used to probe the intracrystalline pore volumes or to check the crystallinities (41). Si, Al and Na contents in the crystalline materials (compact pellets or individual crystallites) were determined by Energy Dispersive X-Ray Analysis (EDX) (42), while the water and organic contents were measured by thermal analysis (41). The structural arrangement of the silicic, aluminic and sodic species and the nature and structure of the organic compounds occluded in the zeolitic pores were elucidated using solid state high resolution MAS ^{29}Si-, ^{27}Al-, ^{23}Na- and ^{13}C-NMR respectively, following the recently redefined experimental conditions (43).

Results and Discussion

Primary critical variables in synthesis of ZSM-20

In order to define the important and critical variables affecting the synthesis of ZSM-20, a large series of modifications have been brought to the optimized synthesis procedure. Some preliminary trends (32), now completed by the present, more in depth study, can be summarized as follows :

As for most of the zeolites with very open structure, crystallization of ZSM-20 occurs in a rather low temperature range (90-120°C), in static conditions, and is complete after about 10-15 days heating. Longer crystallization times, higher temperatures or agitation ineluctably lead to the formation of other dense or amorphous phases, that also co-crystallize with zeolite Y (44,45) . More precisely, a rapid heating of the final gel above 100°C (130 or 170°C) resulted in the formation of zeolite Beta (see below). It was also observed that at these temperatures ZSM-20 initially formed at 100°C transforms into amorphous phase, probably also further precursor to Beta (32).

Another factor that necessitates a close control is the gel composition because a series of other structures like zeolites X, Y or Beta can easily crystallize from similar systems "Table II and Figure 1". The H_2O/SiO_2 ratio is also important to control. For higher initial water contents the crystallization rate of ZSM-20 considerably decreases. In very diluted systems, zeolite Y is more readily formed, although with a rather low rate due to the smaller Na^+ concentrations in such a system (33). Furthermore, the water content also affects the pH, the supersaturation conditions and the rate of hydrolysis of $Si(OEt)_4$ and hence the further condensation of the resulting $(Si(OH)_4)_n$ species(46).

Optimum ZSM-20 crystallization conditions were found to occur for H_2O/SiO_2 ratios of 8-10. More concentrated media favour the crystallization of zeolite Beta, in agreement with the overall gel composition proposed for its optimized formation (11, 31, 32, 34) : "Table II". Finally, as generally observed for a variety of other zeolites (47), in more diluted media, slightly larger ZSM-20 crystals can be prepared "Figure 2".

The presence of even traces of ethanol in the synthesis batch, stemming from an incomplete hydrolysis of $Si(OEt)_4$ during the ageing period results in a drastical reduction of the ZSM-20 crystallization rate ; zeolite Beta is then readily formed and achieves a fast growth at the expense of the ZSM-20 "Figure 3". This goes in line with the higher yields of Si-richer Beta observed when this zeolite is intentionally prepared in presence of ethanol (31). This was attributed to the lower solubility of silica in EtOH (31), but it is also probable that the whole system (nature and solubility of ZSM-20 aluminosilicate precursors and intermediates) is perturbed (32).

A modification of the order of mixing of the reactants may markedly affect the growth rate of ZSM-20 but pure crystals are always obtained, provided the composition of the final gel stays similar.

In agreement with the findings reported in another study (36), seeding proved efficient by considerably shortening the nucleation period of ZSM-20 "Figure 4". Moreover, the nucleation time is even more reduced when ZSM-20 seed crystallites (0.5 wt. % with respect to dry gel) were added after the complete evaporation of ethanol, thus confirming the inhibiting role of the latter in ZSM-20 crystallization.
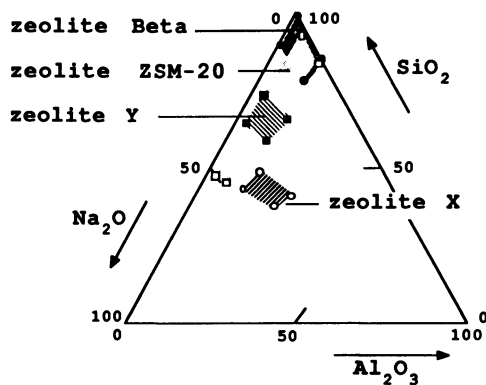
Fig 1   Ternary compositional diagram SiO_2-Al_2O_3-Na_2O defining specific crystallization domains for zeolites X (5), Y (5), Beta (29) and ZSM-20 (11).
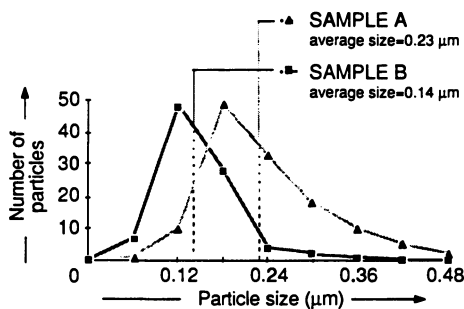
Fig 2   Comparison of the final crystal size distribution characterizing a ZSM-20 sample prepared in more diluted conditions (H_2O/SiO_2 = 8.9- sample B).
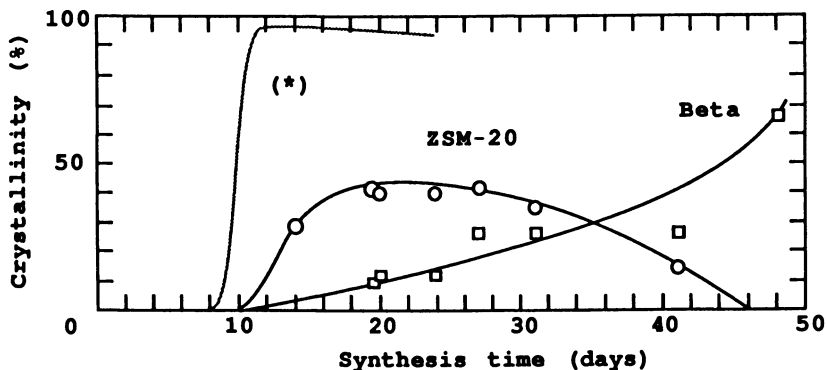
Fig 3   Crystallization kinetics of coexisting zeolites ZSM-20 (O) and Beta (O) formed in presence of ethanol (EtOH not completely eliminated) compared with that of pure ZSM-20 formed under the same conditions in complete absence of EtOH .
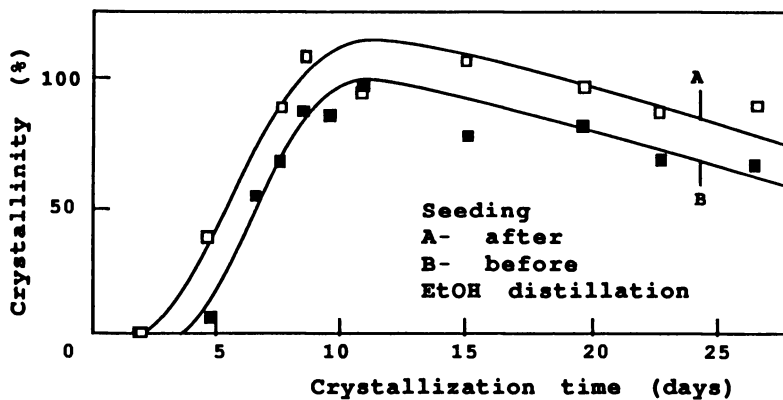
Fig 4   Influence of seeding on the crystallization kinetics of ZSM-20 .

Upon seeding, ZSM-20 appears better stabilized as no traces of zeolite Beta were found after 27 days heating. Our observation is in agreement with other recent works that showed the high efficiency of the addition of very small and freshly formed zeolite nuclei as seeds to batches giving zeolites TMA-Offretite (48) or TMA-Omega (49). Both materials were formed more rapidly and selectively, free from stable side phases like Analcime or Mordenite that usually co-crystallize in absence of seeds.

Seeding neither affects the final chemical composition of ZSM-20 nor the crystal size or morphology.In contrast to non-seeded systems, isolated individual crystallites of 0.45 μm diameter tend to form polycrystalline aggregates after long synthesis times (27 days).

In addition to our findings, it is to be noted that another study envisaged the importance of other variables. Ageing and use of other ingredients like Si(OMe)$_4$ or K$^+$ were among the parameters that also influenced in considerable extent the ZSM-20 preparation under these slightly different conditions (36).

Effect of Al concentration : rapid preparation of ZSM-20 in optimum yield

Al incorporation in a high silica zeolitic framework is a difficult and slow process so that these materials often crystallize with a low rate in Al-rich gels (50, 51). Indeed, such frameworks are often made from 5-1 SBU precursors that preferentially involve Si in the tetrahedral positions (52).
On the other hand, Al-rich zeolites are built up from SBU involving mainly rings containing an even number of T atoms, often 4 MR or 6 MR. Such rings are better stabilized by incorporating the maximum number of Al atoms on the available T sites and tend to reach the optimal Si/Al ratio of 1 (52).

If an Al-rich zeolite is prepared from a Si-rich gel, one can imagine two situations. Firstly the zeolite can be formed from the 4MR or 6MR that respectively contain less than 2 and 3 Al atoms and are thus less stable than the corresponding (2 Si, 2Al) and (3Si, 3Al) rings. Provided the amount of such species is sufficient, the resulting framework will be fairly enriched in Si.
The other situation supposes the formation of stable rings that contain the maximum number of Al atoms, from a Si-rich gel. This can be a slow process, kinetically limited by the slow Al incorporation stemming from Al poor gel phases. Such a system will yield a limited number of Al-rich zeolite nuclei with a fairly low rate. In such a case, a poor "synthesis efficiency", i.e. poor correlation between the Si/Al atomic ratio in the gel and that of the final zeolite, is observed (53) "Figure 5".
Any increase of the Al concentration in the gel will increase the rate of crystallization, as frequently observed for many low silica zeolites (54). Another consequence could be an overall increase of the zeolite yield resulting from an important consumption of Si species that will react with Al(OH)$_4$$^-$ species to form the appropriate (Si, Al) complexes.

At that stage, the actual mechanism that governs the nucleation and growth processes of the zeolite must obviously also play a determinant role in facilitating the Al incorporation. For example,under particular conditions, zeolite Y can grow through a structural rearrangement of the gel (55) and its composition then strongly depends on the dissolution-precipitation equilibria of the various aluminosilicate complexes that finally bring the desired amount of Al in the gel phase. In most of the cases, however, nuclei of zeolites with open structure such as zeolite Y (44, 45, 56-58) Beta, (30, 31) and ZSM-20 (32, 36), are formed in the liquid phase. The growth rate of the

crystallites so-formed will necessarily depend on the actual Al concentration in solution, and hence, on the solubility of the various oligomeric aluminosilicate precursor species stabilized under particular reaction conditions and present in solution along with residual Al $(OH)_4^-$ entities.

In the case of ZSM-20, the increase of the crystallization time with increasing Si/Al ratio in the gel was indeed observed and interpreted in terms of an increase of the viscosity of the gel (36). In parallel to what was already described in case of zeolite Beta (31), we can imagine the following, more precise picture. The fast reaction between hydrolyzed $(Si(OH)_4)_n$ species and $Al(OH)_4^-$ existing in strongly alkaline solution, rapidly yields sparingly soluble aluminosilicate species. The solution is nearly completely depleted in Al but still contains a major amount of Si species. Such a mechanism was proposed for ZSM-20 and confirmed by a complete kinetic study of its crystallization, as described in our previous paper (32). A rapid precipitation of aluminosilicate complex species readily formed upon mixing the ingredients, yielded a gel phase relatively rich in Al (Si/Al $\approx$ 1) while the solution contained mainly soluble silicate species.

Further on, the composition of both the solid and liquid phases did not change during the whole nucleation period (8 days). We have completed these observations by determining the evolution of the Si/Al ratio in the solid intermediate phases all along the synthesis course "Figure 6" and confirmed the composition of the liquid phase by using high resolution ^{29}Si NMR. The increase of the Si/Al ratio in the intermediate solid phases shows that the liquid phase starts to participate in the ZSM-20 formation as soon as its crystallization is induced (i.e. after about 8 days) and continues to participate all along the growth process for the next 3 days of reaction. At the end of the synthesis course, no Al could be detected in solution by ^{27}Al NMR, despite of the high intrinsic sensitivity of this nucleus. Two ^{29}Si NMR resonances observed between -90 and -100 ppm and belonging to the configurations $Q_2(0Al)$ and, in majority to $Q_3(0Al)$ (triangular prisms), confirm the absence of soluble Si,Al complexes, in contrast to what could be found in the final solution resulting from the crystallization of zeolite Y (58) "Figure 7". In this latter case, ^{29}Si NMR shows that faujasite Y essentially crystallizes in a medium involving more monomeric Si species present with a non-negligible number of Al bearing oligomeric soluble complexes. This marked difference between the two systems is mainly due to different synthesis (essentially pH) conditions.

Because the presence of aluminium appears necessary to crystallize ZSM-20 but also because its too low amount limits the overall yield of the process, an attempt was made to increase and maximize the Al concentration in the initial gel. To avoid any further modification of the gel composition, Na aluminate was replaced by hydrated $Al(OH)_3$ (Serva.A.R.). Table III compares the crystallinity and yield of ZSM-20 obtained with various initial Al concentrations.

On comparing samples A and D, it first appears that $Al(OH)_3$ is a more reactive Al source than Na aluminate , as nearly pure ZSM-20 is already formed after 9 days heating. Secondly, as expected from the mechanistic considerations, an increase of the initial amount of Al markedly accelerates the nucleation process of the ZSM-20 "Figure 8". Neither the crystallinity nor the Al content of the final zeolite are affected by the initial concentration. Analysis of the final liquid phases confirmed that in all cases all the aluminium was consumed during the growth process, which means that the overall yield in crystalline ZSM-20 has increased accordingly. Indeed this increase is confirmed experimentaly "Table III".
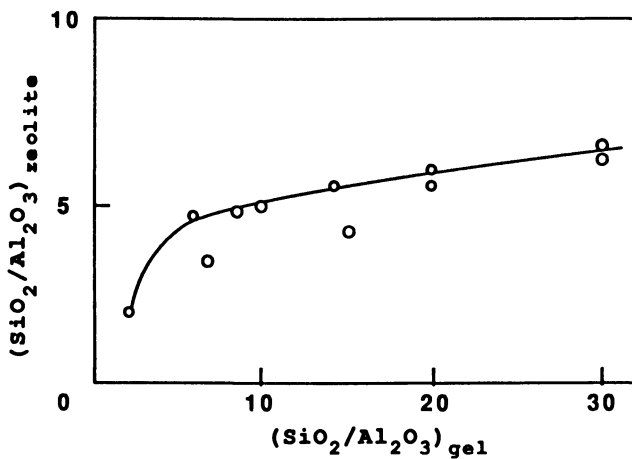
Fig 5   Relationship between Si/Al ratio in the gel and in a series of faujasite zeolite samples crystallized from it : example of poor synthesis efficiency (adapted from ref. 53).
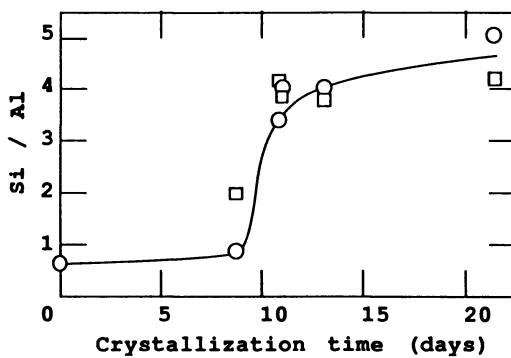
Fig 6   Variation of the Si/Al molar ratio characterizing the intermediate solid phases (ZSM-20 + gel isolated at various synthesis times : O = EDX values; O = ^{29}Si NMR values) .
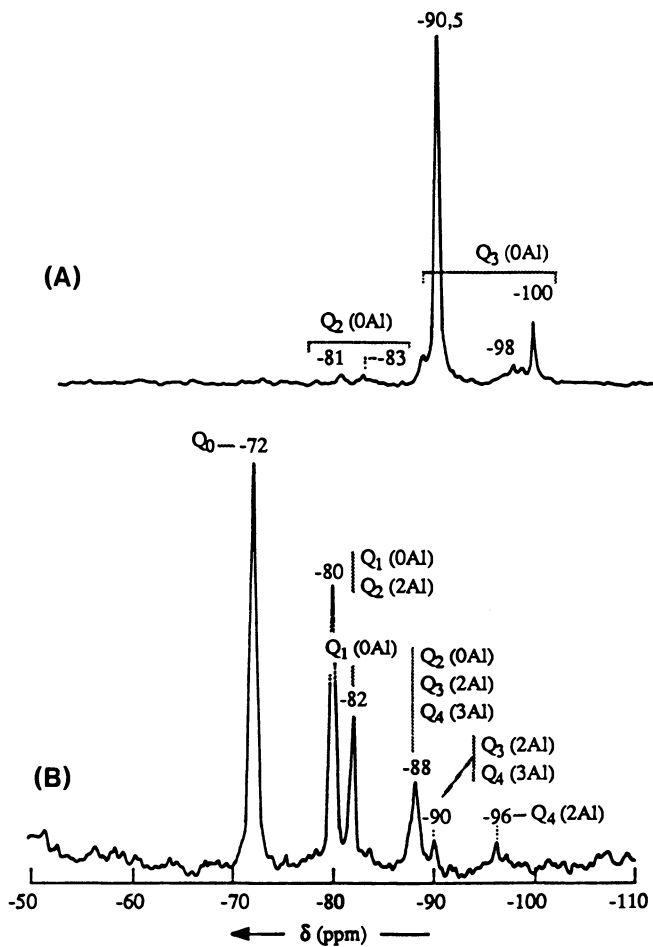
Fig 7 ^{29}Si NMR identification of the various (Si,Al) complexes present in the liquid phase after the complete crystallization of ZSM-20 (A) and of zeolite Y (B).
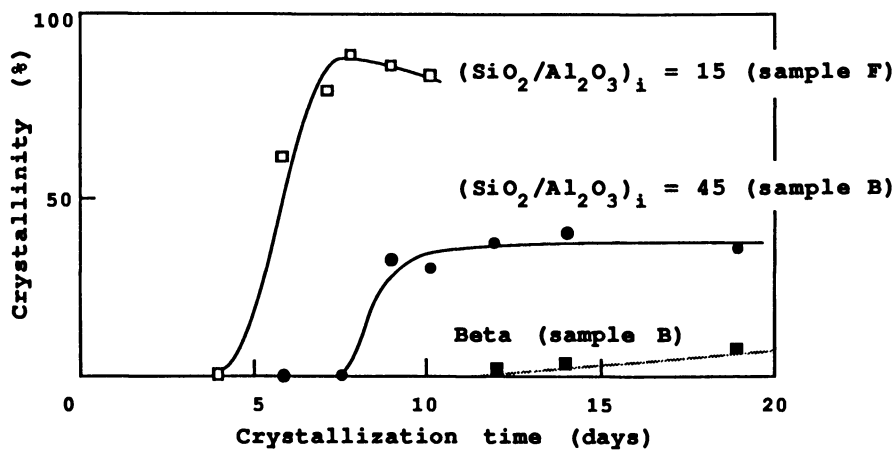
Fig 8   Influence of the initial Al concentration on the crystallization of zeolite ZSM-20.

The constant Si/Al ratio in the final zeolite phases indicates that more Si from the liquid phase is consumed to yield ZSM-20 and confirms that the initial Al content limits the yield in the reference conditions described in the patent recipes (34). Note that a too low initial Al content results in a preferential formation of zeolite Beta (sample B) that usually crystallizes from Si-rich gels "Table II".Finally, the overall ZSM-20 crystal size decreased as the initial Al content increases "Figure 9", indicating that a large number of nuclei, that ultimately yield numerous smaller ZSM-20 crystallites, are formed more rapidly when more Al is available in the gel phase. This confirms that in Al rich systems, the formation of the first nuclei involves Si,Al complexes or SBU that are numerous and that more readily achieve an appropriate Si/Al ratio.

Table III. Preparation of ZSM-20 from Hydogels of following molar Composition : 1.25 Na_2O x Al_2O_3 30.2 SiO_2 26.4 TEAOH   267 H_2O and involving variable Amounts of Aluminium

Sample	x	$(Si/Al)_{gel}$	Induction[a] period(days)	Synthesis time(days)	ZSM-20		
					% cryst.	Yield[b] %	Al/u.c.
A[c]	1	30	8	13	100	-	38.5
B	0.66	45	7.5	19	35	15 (+ traces of Beta)	-
C	0.86	35	6	10	86	19	39
D	1	30	5	9	87	25	40
E	1.2	25	6.5	10	82	27	40
F	2	15	4.5	10	84	34	44

(a) Time required for the first ZSM- 20 crystallites to be detected by XRD (see also figure 8)
(b) Calculated in terms of weight of SiO_2 in the zeolite with respect to that introduced in the gel
(c) Reference conditions involving Na aluminate

Effect of silica source : formation of a novel Faujasite-polytype phase

$(Si(OH)_4)_n$ low oligomeric species resulting from hydrolysis of Si-alkoxides are considered a priori more reactive towards aluminate species in basic media than those stemming from high surfacepowdered silicas like Aerosil. However, while the former are slowly and progressively released through hydrolysis, the latter are instantaneously available in large amounts to react readily with $Al(OH)_4^-$ species to yield the appropriate aluminosilicate polymeric zeolite precursors. The actual Si/Al ratio of the latter will then merely depend on the actual amount of the Si oligomers available at a time. It is therefore reasonable to suppose that slow hydrolysable $Si(OAlk)_4$ species will favour the formation of Al-richer zeolites, provided the alcohols so formed do not play any secondary perturbating role. Conversely, Aerosil should favour the nucleation of higher silica zeolites.
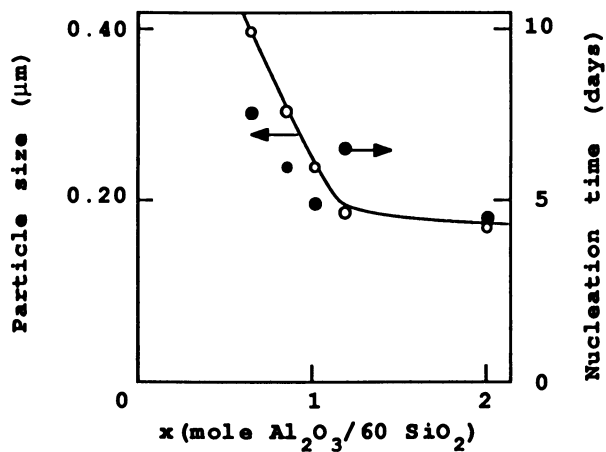
Fig 9   Correlation between nucleation time (days) and the average ZSM-20 particle size (µm), as a function of the initial Al content .

With these ideas in mind, we used Aerosil to prepare a silica-richer ZSM-20. Surprisingly, under our reference conditions, we observed the formation of another open structure, here called "FAU-polytype", that could not be identified by XRD to any of the known faujasite-type polymorphs."Figure 10". The doublet of the "Faujasite peak" at $2\theta=5.9°$ suggests a hexagonal symmetry, less regularly packed than in ZSM-20 and probably involving stacking of planes along the c-axis, as accounted for by the absence of a series of lines that characterize the ZSM-20 XRD pattern. A thorough structural determination of this material is in progress (59). It possibly belongs to one of the large number of structures theoretically predicted from a close packing of the hexagonal layers of the faujasite truncated octahedra (17).

The FAU-polytype is also readily obtained when the order of mixing of the reactants was changed in the reference synthesis, provided Aerosil is the Si source used and the crystallization temperature maintained at 100°C. This material systematically exhibits properties intermediate between ZSM-20 and zeolite Y "Table IV".

In particular, the Si/Al ratio of the FAU-polytype is higher than that characterizing zeolite Y but lower than that measured for the more siliceous ZSM-20. We conclude that under our temperature and compositional conditions, Aerosil provokes the formation of such a structure that accomodates the appropriate amount of Al to get stabilized. At 170°C, the same gel yields the thermodynamically more stable zeolite Beta. This observation again goes in line with the general idea that the development of nuclei of metastable zeolites is favoured by a low temperature aging /nucleation of gels (51).

Variation of TEAOH concentration and temperature: optimal formation of zeolite Beta

The general synthesis scheme of ZSM-20 clearly indicates that the amount of TEA in the precursor gel is in large excess with respect to the amount found incorporated in the final ZSM-20 unit cell. In order to reduce the global cost of the ZSM-20 synthesis, the use of lower TEAOH concentrations was systematically checked. The following typical TEA/Al_2O_3 molar ratios were chosen and compared to the value (26.5) that characterizes the reference system:

17.5 : as mean value falling within the preferential range, suggested in the patent literature (11,34)

12.5 : as the lower limit of that range, and

2.5 : value slightly lower than the ratio corresponding to the zeolite composition.
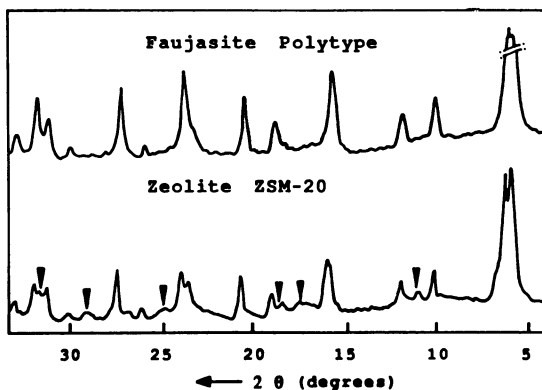
Fig 10   Comparison of XRD spectra of "Faujasite polytype" and ZSM-20; The marked peaks exclusively characterize ZSM-20.

Table IV. Physicochemical Characteristics of Zeolites crystallized from 1.25 Na_2O Al_2O_3 30.2 SiO_2 25 TEAOH [a] 243 H_2O Gel Batches[b], with various Si Sources and under different Conditions (For the Sake of comparison, all the Unit Cells are assumed to involve 192 T Atoms)

	FAUJASITE (45)	FAU-POLYTYPE	ZSM-20	Beta
Si source	Aerosil	Aerosil	$Si(OEt)_4$	Aerosil
T(°C)	100	100	100	170
Synth.time (days)	4.5	9	13	10
%crystallinity(XRD)	100	89[c]	100	100
(Si/Al)zeol.	2.4	3.0	4.0	10.3
Al/u.c.	55.6	48.0	38.4	17.0
Na/u.c.	55.6	40.0	20.7	15.3
H_2O/u.c.	245	123	90	16
TEA^+/u.c.	0	13.0	17.6	21.3
n-hexane (sorbed/u.c.)	27.8	28.1	30.3	21.4
u.c.volume(Å)^3	15,070	15,038	14,870	-

(a) except for Beta : 12.5 TEAOH
(b) for faujasite, the gel composition was different (45)
(c) compared to a 100 % crystalline faujasite used as standard

Results compiled in Table V show that a decrease of the initial TEAOH concentration automatically favours the crystallization of zeolite Beta, irrespectively to the source of silica used.

Table V. Crystalline Phases formed from the Reference Gel 1.25 Na_2O Al_2O_3 30.2 SiO_2 x TEAOH 243 H_2O involving different TEAOH Concentrations

Sample N°	TEA^+/Al_2O_3	Si source	Synthesis time (days)	Final product (% crystallinity)
1	26.0	Si $(OEt)_4$	11	ZSM-20 (100)
2	17.5	Si $(OEt)_4$	11	Beta
		Si $(OEt)_4$	15	Beta (85)
	2.5	Si $(OEt)_4$	13	Amorphous
		Si $(OEt)_4$	26	Amorphous
3	25	Aerosil	21	FAU-polytype (89)
4	17.5	Aerosil	12	Beta
		Aerosil	18	Beta (72)
5	12.5	Aerosil	4	Beta
		Aerosil	10	Beta (100)
	2.5	Aerosil	10	Amorphous
		Aerosil	26	Amorphous

Although all the TEA^+/Al_2O_3 ratios used do fall within the wide range recommanded by Wadlinger et al. (29) to prepare zeolite Beta, the most crystalline sample is obtained for TEA^+/Al_2O_3 = 12.5 and by using Aerosil as the silica source. The preparation conditions and some properties of the three most crystalline Beta samples synthesized at 100°C with different Si sources combined with optimum TEA^+/Al_2O_3 ratios are compared in Table VI.

Table VI. Synthesis Conditions and Properties of the three most crystalline Zeolite Beta Samples prepared at 100°C from Reference Hydrogels with optimized TEA^+/Al_2O_3 Ratios (sample N° as in Table V)

Sample N°	2	4	5
$(TEA^+/Al_2O_3)_{gel}$	17.5	17.5	12.5
Si source	$Si(OEt)_4$	Aerosil	Aerosil
Synth.time(days)	15	18	10[(a)]
% crystallinity(XRD)	85	72	100
(Si/Al)zeol.	9	9	10.3
Al/u.c.	19.2	19.2	17.0
Na/u.c.	17.2	21.1	15.3
$TEA^+/u.c.$[(a)]	20.4	17.9	15.8
TEAOH/u.c.[(a)]	1.6	4.0	5.5
$TEA^++TEAOH/u.c.$	22.0	21.9	21.3
$(TEA^++TEAOH/Al_2O_3)_{zeol.}$	2.3	2.3	2.5
$H_2O/u.c.$	17.6	16.9	15.7
n-hexane (sorbed/u.c.)	20.9	20.2	21.4

(a) a 100% crystalline Beta is already obtained after 5 days heating (see Figure 11)
(b)TEA^+ and TEAOH separately and quantitatively determined by thermal analysis (32)

Figure 11 shows the kinetics of crystallization of samples 2,4,and 5. Obviously the nucleation time for sample 5 is shorter than that characterizing samples 2 and 4 , prepared in presence of larger TEAOH concentrations after only 5 days heating at 100°C. It also appears that for a TEA^+/Al_2O_3 ratio of 17.5, the source of silica does not affect the nucleation time of samples 2 and 4. However, sample 2 $(Si(OEt)_4)$ achieves more rapidly a 100% crystallinity than sample 4 (Aerosil), suggesting a more efficient utilization of the $Si(OH)_4$ monomers stemming from a slow hydrolysis, to build up the final framework.

A series of preliminary results have suggested that synthesis temperatures higher than 100°C favour the formation of zeolite Beta with respect to ZSM-20 (32). We have therefore tried to further improve the synthesis conditions of zeolite Beta by heating the hydrogels that contained the optimized TEA/Al_2O_3 ratios (equivalent to samples 2,4 and 5, Table VI) at higher temperatures. A selected set of results are shown in Table VII and compared with the corresponding reference conditions that yielded ZSM-20, FAU-polytype and zeolite Beta at 100°C.
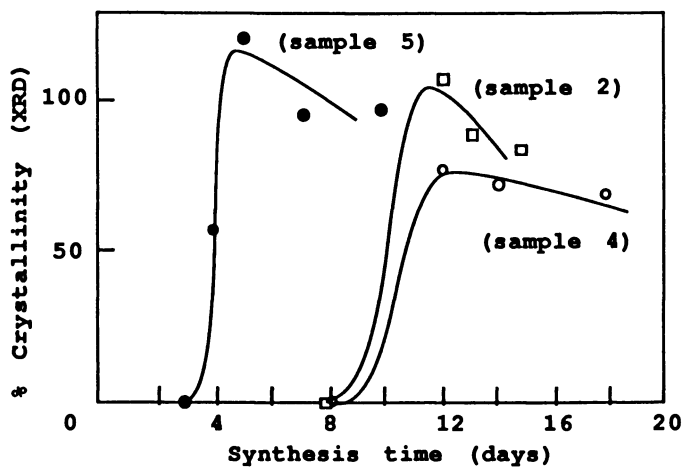
Fig 11 Crystallization kinetics of zeolite Beta , from reference hydrogels, at 100°C, using different silica sources and optimized TEA^+/Al_2O_3 ratios (samples 2,4,5 described in Tables V,VI,VII).

With Si(OEt)$_4$ as silica source, the reference gel (sample 1) that usually yields ZSM-20 at 100°C after 11 days heating starts to yield an admixture of zeolites ZSM-20 and Beta, after 15-20 days heating at 130°C,while Beta is the only crystalline phase detected after 31 days heating "TableVII".

Similar phenomena are observed when the gel is heated at 170°C but the whole process is markedly accelerated, so that nearly pure Beta is obtained after only 4 days heating. Note that the way to reach the high temperature (slow and progressive heating from 100°C to 170°C or direct introduction of the gel in an oven preheated at 170°C) does not affect the nature and composition of the final crystalline phases.

With Aerosil as silica source, the reference gel that already yields zeolite Beta at 100°C for TEA$^+$/Al$_2$O$_3$ ratios lower than 25, also logically yields the same zeolite more rapidly when heated at 130°C or 170°C (samples 4 and 5, Table VII). The apparent disadvantage to use a high temperature is the potential progressive dissolution of zeolite Beta to amorphous phase for longer synthesis times, as suggested by complete kinetic curves derived for samples 4a,4b, 5a, and 5b (61). (The crystallization times mentioned for these samples in Table VII are those for which the most crystalline phases are obtained.) Note also that these maximum crystallinities (60 to 80%) are obviously lower than that of the zeolite beta prepared for the same gel heated at 100°C for 11days . We therefore conclude that the conditions used to prepare sample 5 (TEA$^+$/Al$_2$O$_3$ = 12.5 and T = 100°C) are the optimum ones that yield 100% crystalline Beta. Alternatively, still fairly well crystalline Beta having similar composition (Table VII) can be prepared far more rapidly by conducting syntheses at higher temperatures, e.g. 170°C.

TableVII. Nature and physicochemical Characteristics of Zeolites crystallized from 1.25 Na$_2$O Al$_2$O$_3$ 30.2 SiO$_2$ x TEAOH 243 H$_2$O gel Batches, using various Si Sources and different Synthesis Conditions (TEAOH Concentration, Temperature...)

Sample N°	1	1a	1b	2	3	4	4a	4b	5	5a	5b
(TEA/Al$_2$O$_3$)$_{gel}$	26.4	26.4	26.4	17.5	25	17.5	17.5	17.5	12.5	12.5	12.5
Silica source		Si(OEt)$_4$					Aerosil				
T(°C)	100	130	170	100	100	100	130	170	100	130	170
Cryst.Time(days)	11	31	4	15	31	18	10	4	10	8	4
Zeolite formed	ZSM-20	Beta	Beta	Beta	FAU-polytype	Beta	Beta	Beta	Beta	Beta	Beta
% cryst.	100	80	84	85	89	72	80	61	100	64	78
(Si/Al).$_{zeol.}$	4	11.5	11.5	9	3.4	9	10.2	13.2	10.3	10.1	11.3
Al/u.c.	38.4	15.4	15.4	19.2	44	19.2	17.2	13.5	17.0	17.3	15.6
Na/u.c.	20.7	4.0	6.3	17.2	27.3	21.1	16.7	12.2	15.3	23.9	24.4
TEA$^+$/u.c.[a]	16.5	14.2	13.5	20.4	14.3	17.9	19.2	12.0	15.8	14.8	13.6
TEAOH/u.c.[a]	0	5.7	6.3	1.6	-	4.0	2.2	5.4	5.5	7.1	4.9
TEA$^+$+TEAOH/u.c.	16.5	19.9	19.8	22.0	14.3	21.9	21.4	17.4	21.3	21.9	18.5
H$_2$O/u.c.	67.9	12.4	14.9	17.6	57.3	16.9	16.4	14.3	15.7	24.7	15.1
n-hexane (sorbed/u.c.)	28.2	21.2	20.6	20.9	27.9	20.2	20.4	18.5	21.4	18.1	17.8

(a) See remark (b) Table VI

Competitive roles of Na⁺ and TEA⁺ ions in forming and stabilizing frameworks of zeolites ZSM-20 and Beta

Zeolites ZSM-20 and FAU-Polytype

A series of preliminary test syntheses of ZSM-20 from reference gel compositions using variable TEA^+/SiO_2 values (TEA^+ introduced as bromide as to keep the alkalinity constant) revealed that ZSM-20 is formed in optimal conditions for ratios close to 0.9, value which was recommended by Valyocsik (34). For values lower than 0.5, dense phases such as Analcime, zeolite P or compact Na silicates are formed. For higher TEA^+ concentrations (TEA^+/SiO_2 higher than 1.5), thermodynamically more stable Hydroxysodalite or zeolite Omega (ZSM-4) co-crystallize.

Pure, 100 % crystalline zeolite ZSM-20 synthesized under optimized reference conditions (sample listed in Table IV) exhibits two ^{13}C-NMR resonances at 6.5 ppm(terminal methyl group) and 52.5ppm (methylene group), values that well characterize free TEA^+ ions in solution. This demonstrates that the TEA^+ ions keep their integrity when occluded within the ZSM-20 framework. Narrow ^{13}C-NMR lines ($\Delta H \approx$ 30-50 Hz) suggest that the organic ions are located in cavities where they retain some degree of mobility, most probably in the supercages where the electric field gradient is reduced.

A ^{23}Na-NMR line at -10 ppm suggests the presence of hydrated Na⁺ ions in non negligible interactions with anionic aluminic sites.

Quantitative determination of Al, Na⁺ and TEA⁺ ions in a series of well crystalline ZSM-20 samples "Table VIII" confirms our earlier proposals (12,32) , indicating that the neutralization of the structural Al-bearing anionic sites is completely and exclusively achieved by both TEA⁺and Na⁺cations.

TableVIII Na⁺,TEA⁺ and Al contents of some highly crystalline ZSM-20 samples synthesized under various Conditions close to the Reference Preparation

Sample	% crystallinity	Amounts per unit cell				
		Na⁺	TEA⁺	(Na⁺+TEA⁺)	Al	(Na⁺+TEA⁺-Al)
I[a]	100	20.9	16.5	37.4	38.4	- 1
II	>90	20.7	17.6	38.3	38.4	- 0.1
III	>90	24.6	14.5	39.1	38.5	+0.6
IV	87	21.5	16.4	37.9	36.7	+1.2
V	94	22.3	15.3	37.6	38.4	- 0.8
VI	95	22.9	17.0	39.9	40.3	+0.4

(a) Reference sample (Table IV)

TG-DTA and ^{23}Na-NMR data have shown that the amount of TEA⁺ and Na⁺ ions progressively occluded in the ZSM-20 crystals, isolated at different stages of the synthesis ,were proportional to the amount of ZSM-20 crystallites formed (32). This suggests that the TEA⁺,Al and Na⁺ molar ratios probably stay fairly constant

within the growing crystallites or,in other words, that their framework is achieved in the same way all along the growth process. We therefore conclude that, besides their structure orienting role, TEA$^+$ions, along with Na$^+$, also stabilize the ZSM-20 framework by acting as counterions to the negative charges induced by the presence of Al, all along the crystallization course. This observation also suggests that very few Si-O-TEA or Si-O-Na defect groups are generated in the structure. Moreover, only one DTA peak characterizing the decomposition of the organic molecule under nitrogen flow was observed at 440°C and attributed to TEA$^+$ cationic species (61). Neutral TEAOH ionic pairs or Si-O-TEA defects could not be characterized by any typical DTA peak located at lower temperatures, as in zeolite Beta (see below) or as found for Si-O-TPA in ZSM-5 (62).

Quantitative TG data reveal that the average amount of TEA$^+$ ions occluded per unit cell of ZSM-20 is 16-17, i.e. about 2 TEA$^+$ per each of the 8 supercages of the structure (32), the remaining free volume being occupied by hydrated Na$^+$ cations. Sorption measurements on the calcined sample also show that about 2 n-hexane molecules are incorporated in the lattice in replacement of one TEA$^+$ ion. As n-hexane is not able to extend through the hexagonal prisms of the structure, 4 n-hexane molecules should then be exclusively located in the supercages that offer enough empty space after calcination.

Our results show that TEA$^+$ ions act as specific templates by favoring the formation of the ZSM-20 structure: they stabilize it by both filling its pore volume and neutralizing the negative framework charges during growth. This latter role is achieved in complement with the Na$^+$ ions. It is remarkable that, despite the very high TEA$^+$/Na$^+$ ratio in the gel (10.56), this ratio falls to the reproducible values of 0.7-0.8 in the crystalline zeolite. This suggests that the zeolite structure, exclusively directed by TEA$^+$ ions, achieves its stabilization by accomodating bulky TEA$^+$ and less voluminous Na(H$_2$O)$_y$$^+$ cations in such a specific ratio as to allow the framework to be completely neutralized. More precise estimations have shown that about 2/3 of the available Na$^+$ ions are located in the sodalite cages of the structure where they exclusively neutralize the Al negative charges, while the other 1/3 completes the neutralization and the filling of the supercages. In other words, the TEA$^+$/Na(H$_2$O)$_y$$^+$ molar ratio in the final zeolite is governed by the respective molar volumes of these ions required to fill up completely the void volume. The final stabilization of the Si/Al ratio to the reproducible value of about 4-5 is adjusted by taking from the gel the amount of Al necessary for the compensation of the positive charges of both stabilizers. This explains why Si-richer ZSM-20 framework can not be well stabilized.

Zeolite Omega and SAPO-37 are two other metastable structures that need the careful use of specific organic and/or inorganic stabilizers playing a dual complementary role. A careful adjustment of Na$^+$ and TMA$^+$ concentrations allows one to prepare the large pore unidirectional zeolite Omega (49). Lower TMA$^+$ concentrations lead to Analcime and Mordenite while higher amounts stabilize Sodalite. Similarly, SAPO-37, another Faujasite-like structure, crysallizes from TPA$^+$/TMA$^+$ ratios adjusted to about 40 in the gel precursor (12). Lower ratios yield SAPO-20, a Sodalite type structure involving mainly TMA$^+$ stabilized sodalite cages, while higher ratios result in the crystallization of SAPO-5.

Finally, the TEA$^+$ and Na$^+$ cations probably also play their complementary stabilizing role in the case of the FAU-polytype structure, as suggested by the chemical analysis (Table IV). The Al framework negative charges are also nearly completely co-neutralized by both Na$^+$ and TEA$^+$ ions. This is not surprising if one considers that the FAU-polytype structure only differs from that of ZSM-20 by the close packing of the Faujasite truncated octahedra, that probably necessitate similar stabilization by Na$^+$ and TEA$^+$.

Zeolite Beta

Thermal analysis is an appropriate technique to investigate the precise nature of the organic molecules occluded in zeolite frameworks (41). For a series of zeolite Beta samples synthesized under various conditions (Table VII) DTA provides evidence for presence of both TEA$^+$ ionic species (DTA sharp peak near 460°C) and TEAOH ionic pairs (weak broader DTA peak recorded near 345°C) (61). Similar conclusions were proposed by Perez-Pariente et al. (31) for a number of Beta samples prepared under slightly different conditions : TEA$^+$ ions undergo decomposition above 350°C while the neutral TEAOH species are released between 220 and 350°C . Our TG-DTA combined system allowed a quantitative determination of both species (Table VII).

The complete chemical analysis of these samples indicates that the total amount of cationic species per unit cell, Na$^+$+ TEA$^+$, is close to 30-35, thus in large excess to the number of 15-18 negative charges per unit cell, that are generated by the framework Al. This also definitely indicates that a non-negligible number of Si-O$^-$ defect groups are created in the structure and neutralized by either TEA$^+$ or Na$^+$ cations. For most of the samples , the TEA$^+$/Al ratio is close to 1, while Na$^+$/ Al values are more dispersed and always smaller than 1,especially for samples synthesized in presence of Si(OEt)$_4$. This suggests that the framework negative charges are preferentially neutralized by TEA$^+$ and that the defect groups should essentially be of the Si-O-Na type. This hypothesis is in agreement with the observation by Perez-Pariente et al., (31) who demonstrated that the actual TEA$^+$/TEAOH ratio varies with Si/Al, and that for Si/Al values close to those characterizing our Beta samples (about 10-11), TEA$^+$constitutes the largest fraction of the organics in the pores. TEA$^+$ and TEAOH actually filled about 70-75 % of the free pore volume of a zeolite Beta with Si/Al =11, the remaining void volume being occupied by hydrated Na$^+$ cations(30,31).In that case, 80 to 90 % of the negative lattice charges were neutralized by TEA$^+$. This suggests that in our zeolites, where TEA$^+$/Al is close to 1, TEA$^+$ are probably preferred as the counterion to the framework negative charges. Na$^+$ ions should partly complete the framework neutralization, if needed, and, in agreement with Perez-Pariente et al. (31), are probably located in positions not readily accessible to TEA$^+$. The remaining Na$^+$ ions essentially neutralize the Si-O$^-$ defect groups generated during synthesis. This assumption is also substantiated by the conclusions of Perez-Pariente et al. (30) who stated that Na$^+$, but not TEA$^+$, neutralize the Si-O$^-$ groups located on the surface of the aluminosilicate gel particles, prior to crystallization. TEA$^+$ ions, already counterions to the negatively charged aluminosilicate complexes, the zeolite precursors in the gel phase, are logically the only cations incorporated in the zeolitic lattice during crystallization. The amount of TEAOH species per unit cell is variable and inversely proportional to the total amount of Na$^+$ + TEA$^+$cationic species "Figure 12" . This
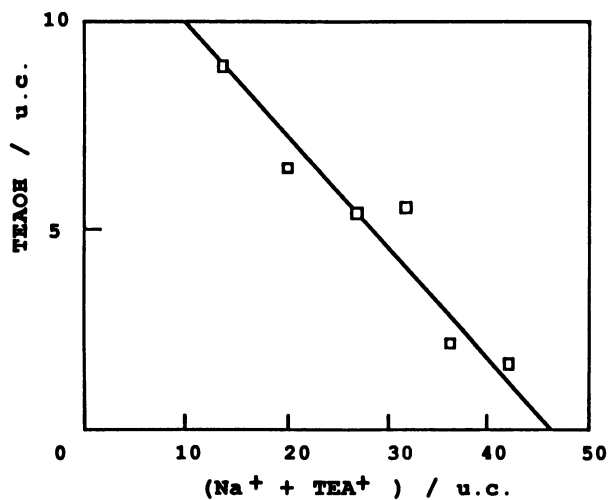
Fig 12 Correlation between the amount of (TEAOH) and cationic (TEA$^+$ + Na$^+$) species in a series of zeolites Beta synthesized under various conditions.

demonstrates that, in addition to the neutralizing TEA$^+$ cations, a further incorporation of TEAOH is needed to stabilize the framework by filling more completely the void volume not occupied by TEA$^+$ + Na$^+$ions. Indeed the total TEA$^+$+ TEAOH amount is fairly constant (20-21 per unit cell) and is always close to the amount of n-hexane molecules that could be sorbed on the calcined samples (Table VI). This also confirms that TEA$^+$ ions are definitely not neutralizing the Si-O$^-$ defect groups.

It is also remarkable that the total amount of Na$^+$is very low in samples synthesized from Si(OEt)$_4$, irrespective of the synthesis temperature (TableVII). Presumably the Si(OH)$_4$ species progressively released by hydrolysis have time to form the adequate TEA aluminosilicate precursors and few Si-O-Na defects are created, as indicated by ^{29}Si NMR (61). Conversely, a large amount of reactive silica species stemming from Aerosil are immediately available and are randomly neutralized either by TEA$^+$ or Na$^+$. A highly defected structure is therefore more easily generated.

Conclusions

ZSM-20 is a highly metastable zeolite. Its preparation necessitates the use of very specific and drastic conditions : low synthesis temperatures, adequate nucleation period and a careful selection of the ingredient nature and composition. A severe and simultaneous control of all the synthesis parameters is indispensible to obtain pure ZSM-20 in high yield and reproducible conditions.

The ZSM-20 framework is specifically and exclusively oriented by TEA$^+$ templates. The silica species must be progressively consumed in the formation of the first SBU, and low alkyl chain alkoxides revealed to be excellent precursors producing such reactive Si(OH)$_4$ species. Their further reaction and rearrangement with the other reactants is a slow and progressive process necessitating a long induction period and generally results in the building of a non-defected final framework. Its formation however also necessitates a maximal stabilization that is optimally provided by the complementary presence of TEA$^+$ and Na$^+$ ions, both acting as pore fillers and framework neutralizers. The complete filling of the void volume necessarily supposes the final incorporation of the Na$^+$ and TEA$^+$ ionic species in a very specific ratio that also governs the subsequent Al incorporation. This explains the fairly constant final Si/Al value of about 4-5 found in many ZSM-20 zeolites. Any further structural incorporation of Al in different amounts would be difficult and ineluctably result in the net stabilization of the framework. Nevertheless, the use of higher initial Al concentrations results in an advantageous consumption of more Si species from the liquid phase and in a noticeable increase of the ZSM-20 yield.

All other conditions fixed, the use of Aerosil results in the instantaneous formation of a large amount of low oligomeric silicate species in the reaction medium. A different final arrangement of the first building units is obtained, and a novel Faujasite-polytype structure having a different hexagonal packing could be stabilized. Any other slight deviation from the optimal conditions defined for ZSM-20, such as the use of higher reaction temperatures, longer synthesis times, non-complete elimination of EtOH from the system or the use of lower H$_2$O or TEAOH initial concentrations, results in the formation of the thermodynamically more stable higher silica zeolite Beta. Indeed, the formation of this three dimensional wide pore intergrowth type structure requires less critical experimental conditions. For example, the framework of zeolite Beta can be essentially stabilized by pore filling with TEA$^+$

and TEAOH. It also can accomodate Al in a wider compositional range and is not readily destabilized by the presence of Si-O-Na defect groups that are often generated during synthesis.

The thorough investigation of a whole set of experimental variables that affect the crystallization of zeolites ZSM-20, Beta and FAU-polytype, and their careful optimization enabled us to propose selected recipes to obtain pure materials rapidly in good yield.

Literature cited

1. Scherzer, J., in Catalytic Materials : Relationship between Structure and Reactivity ; Whyte T. E., Jr et al., Eds.; ACS Symposium Series 248, American Chemical Society : Whashington, DC,1984; p 154.
2. See e.g. Lechert, H. ,Stud.Surf.Sci.Catal.,1983, 18,107 and references therein.
3. Arika, J. ; Aimoto, M. ; Miyazaki, H. ; Eur.Patent 128 766, 1984.
4. Young, B. A. ; U.S.Patent 3 341 284, 1967.
5. Robson, H. E. ; U.S. Patent 3 343 913, 1967.
6. Whittam, T.V.; U.S.Patent 4 016 246, 1977.
7. Milton, R. M. ; U.S.Patent 2 979 381,1961.
8. Breck, D.W;U.S.Patent 3.130.007,1964.
9. Ciric, J. ; U.S.Patent 3 415 736, 1968.
10. Perez-Pariente, J. ; Formez, V. ; Martens, J. A. ; Jacobs, P.A; Stud.Surf.Sci. Catal., 1988, 37, 123.
11. Ciric, J. ; U.S.Patent 3 972 983, 1976.
12. Saldarriaga, L.S. ; Saldarraga, C. ; Davis, M. E. ; J.Amer.Chem.Soc., 1987, 109, 2686.
13. Ernst, S. ; Kokotailo, G. ; Weitkamp, J. ; Zeolites, 1987, 7, 18.
14. Treacy, M. M. J ; Newsam, J. M. ; Beyerlein, R. A. ; Leonowicz, M. E ; Vaughan, D. E. W. ; J.Chem.Soc.Chem.Commun, 1986, 1211.
15. Vaughan, D.E.W ; Barrett, M.G.; U.S.Patent, 4 333 859, 1982.
16. Lok, B. M. ; Messina, C. A.; Patton, R.L.;Gajek, R.T.; Cannan,T.R.; Flanigen, E. M. ; J.Amer.Chem.Soc., 1984, 106, 6092.
17. Kokotailo, G. T. ; Ciric, J. ; Adv Chem Ser, 1984, 102, 823.
18. Dessau, R. M. ; J.Chem.Soc.Chem.Commun, 1986, 1167.
19. Litterer, H. ; Ger.Patent 3 334 673, 1985.
20. Rosinski, E. J. ; Rubin, M. K. ; U.S.Patent 3 832 449, 1974.
21. Grose, W. R. ; Flanigen, E. M.; U.S. Patent 4 124 686, 1978.
22. Doherty, H. G. ; Rosinski, E. J. ; Plank, C. J. ; Eur.Patent 15 702, 1980.
23. Plank, C. J. ; Rosinski, E. J. ; Rubin, M. K. , Brit. Patent, 1 333 243, 1973.
24. Gabelica, Z. ; Derouane, E. G. ; Blom, N. ; Appl Catal., 1983, 5, 109.
25. Gabelica, Z. ; Cavez-Bierman, M. ; Bodart, P. ; Gourgue, A. ; B.Nagy, J. ; Stud.Surf.Sci.Catal, 1985, 24, 55.
26. Bibby, D. M. ; Milestone, N. B. ; Aldridge, L. P. ; Nature, 1980, 285, 30.
27. Parker, L. M.; Bibby, D. M. ; Patterson, J. E. ; Zeolites, 1984, 4, 169.
28. Whittam ,T. V., Eur. patent, 55 046, 1981.
29. Wadlinger, R. L. ; Kerr, G.T. ; Rosinski, E. J. ; U.S.Patent 3 308 064, 1975.
30. Perez-Pariente P.; Martens, J. A. ; Jacobs, P. A. ; Appl. Catal., 1987, 31, 35.
31. Perez-Pariente, P.; Martens, J.A.; Jacobs, P.A.; Zeolites, 1988, 8, 46.
32. Dewaele, N.; Maistriau, L. ; B.Nagy, J. ; Gabelica, Z. ; Derouane, E. G. ; Appl. Catal., 1988, 37, 273.
33. Vaughan, D. E. W. ; Strohmaier, K. G. ; Stud.Surf.Sci.Catal., 1986, 28, 207.

34. Valyocsik, E. W. , Eur. Patent 12 572, 1980.
35. Chester, A.W. ; Chu, Y. F. ; U.S. Patent 4 377 721, 1983.
36. Ernst, S. ; Kokotailo, G.T. ; Weitkamp, J. ; Stud.Surf.Sci.Catal., 1988, 37, 29.
37. Derouane, E. G. ; Dewaele, N. ; Gabelica, Z. ; B.Nagy, J. ; Appl.Catal., 1986, 28, 285.
38. Jacobs, P.A.; Martens. J. A. ; Synthesis of high Silica Aluminosilicate Zeolites, Elsevier, Amsterdam, 1987, p 191.
39. Ref 38, p 16.
40. Treacy, M. M. J.; Newsam, J. M. ; Nature, 1988, 322, 249.
41. Gabelica, Z.; B.Nagy, J. ; Derouane, E.G. ; Gilson, J. P .; Clay Minerals, 1984, 19, 803.
42. Gabelica, Z. ; Blom, N.; Derouane, E.G.; Appl.Catal., 1983, 5, 227.
43. B.Nagy, J. ; Bodart, P.; Collette, H.; El Hage-Al Asswad, J.; Gabelica, Z.; Aiello, R.; Nastro, A.; Pellegrino, C.; Zeolites, 1988, 8, 209.
44. Dewaele, N. ; Bodart.P. ; Gabelica, Z. ; B.Nagy, J.; Acta Chim. Hung, 1985, 119, 233.
45. Dewaele, N.; Bodart. P.; Gabelica, Z.; B.Nagy, J.; Stud. Surf. Sci. Catal., 1985, 24, 119.
46. Hoebbel, D.; Z.Anorg. Allgem. Chem., 1980, 485, 15.
47. Von Ballmoos, R. ; Gubser, R.; Meier, W. M. ,Proc. 6th Intern. Zeolite Conf., 1983, p 803.
48. Moudafi, L. ; Dutartre, R; Fajula, F. ; Figueiras, F.; Appl.Catal., 1986, 20, 189.
49. Nicolas, S. ; Massiani, P. ; Vera Pacheco, M. ;Fajula, F.; Figueiras,F. ; Stud. Surf.Sci. Catal., 1988, 37, 115.
50. Rollmann, L. D. In Zeolites, Science and Technology; Ribeiro, F. R.; et al., Eds; N.Nijhoff, Den Haag, 1984, p 109.
51. Gabelica, Z. ; Derouane, E. G.; Blom, N. in Catalytic Materials Relationship between Structure and Reactivity; White, T.E.; Jr. et al. ; Eds; ACS Symposium Series N 248; American Chemical Society; Whasington, D.C., 1984; p 219.
52. Guth, J. L ; Caullet, P. ; J.Chim. Phys. 1983, 83, 155.
53. Ref.38, p 344.
54. See e.g. Breck, D.W. : Zeolite molecular Sieves, Structure,Chemistry and Use,Wiley, New-York, 1974.
55. Fahlke, B. ; Starke, P.Seefeld, V.; Wieker, W. ; Wendlandt, K.P.; Zeolites, 1987, 7, 1209.
56. Kacirek, H. ; Lechert, H.; J Phys Chem, 1975, 79, 1589.
57. Kasahara, S. ; Itabashi, K. ; Igawa, K.; Stud.Surf.Sci.Catal., 1986, 28, 185.
58. Bodart, P.; B.Nagy, J. ;Gabelica, Z. ; Derouane, E. G. ; J.Chem.Phys., 1986, 83, 777.
59. Dewaele, N. ; B.Nagy, J. ; De Roover, B. ; Maistriau, L. ; Derouane, E. G. ; Gabelica, Z.; Guth, J. L. ; in preparation.
60. Barrer, R. M. Hydrothermal Chemistry of Zeolites, Academic press, London, 1982.
61. Dewaele, N., PhD Thesis, University of Namur, Belgium, 1988.
62. Gabelica, Z. ; B.Nagy, J.; Bodart, P.; Nastro, A. ; Thermochim. Acta, 1985, 93, 749.

RECEIVED March 6, 1989

Chapter 37

Synthesis and Characterization of Zeolite ZSM–20

D. E. W. Vaughan[1], M. M. J. Treacy[1], J. M. Newsam[1],
K. G. Strohmaier[1], and W. J. Mortier[2]

[1]Exxon Research and Engineering Company, Route 22 East,
Annandale, NJ 08801
[2]Exxon Chemical Holland, B.V., P. O. Box 7335,
3000 HH Rotterdam, Netherlands

Syntheses of zeolite ZSM-20 from various Na_2O-
TEA_2O-Al_2O_3-SiO_2-H_2O gel compositions under a
variety of crystallization conditions have been
investigated. In particular, the influence of K^+
cations, and the addition of seeds and nuclei
have been studied. Products were characterized
by chemical analyses, sorption measurements,
infra-red spectroscopy, powder X-ray diffraction
(PXD) and electron microscopy. Confirming
earlier work, materials similar to those
described in the original ZSM-20 patents are
formed only from a narrow range of gel
compositions. Structurally, however, such
products are not phase-pure, comprising crystals
of cubic and mixed cubic and hexagonal stackings
of faujasite sheets.

ZSM-20 (1) is a large pore zeolite that has recently
attracted interest because of its properties as a
cracking (2) and hydrocracking catalyst (3). It is one of a
series of materials related structurally to faujasite (FAU-
framework (4)) that have been described as having hexagonal
symmetry, including CSZ-1 (5), ZSM-2 (6), ZSM-3 (7), and
twinned zeolite Y (8). These various materials all have
high sorption capacities for substituted aromatic
molecules, a characteristic of pore systems with apertures
defined by 10 or more T-atoms (T = tetrahedral species, Si
or Al etc.). Zeolite CSZ-1 was originally described as
having a hexagonal unit cell with a= 17.4Å and c=
28.4Å (5, 9), corresponding to that described for the
hexagonal variant of faujasite (labelled here by framework
code *BSS*) by Breck and others (10-12). More recent work (13)
has, however, demonstrated that CSZ-1 adopts the FAU-

framework, but with a slight rhombohedral distortion (possibly induced by strain associated with twin faults near the center of the very thin crystallites (14)). Zeolite ZSM-3 has also been described as having hexagonal symmetry, but without a defined c-axis constant, reflecting that sheets of sodalite cages are connected along **c** in both hexagonal and cubic stackings in a highly disordered manner (15). No structure has yet been proposed for zeolite ZSM-2. Characterization of zeolite ZSM-20 using n-decane hydrocracking as a test method (16) is consistent with it possessing a 3-dimensional 12-ring pore system, and the PXD pattern has been indexed on the basis of a hexagonal unit cell with a = ~17.3Å and c = ~28.6Å (17), as expected for a material adopting the *BSS*-framework (10-12).

We describe here further studies of the crystallization of zeolite ZSM-20, focusing on minority factors that proved to be important in developing a successful synthesis. We outline X-ray powder diffraction and electron microscopy data which illustrate that, structurally, ZSM-20 comprises a faulted and intergrown mixture of blocks of both hexagonal (*BSS*) and cubic (FAU) stackings of sheets of sodalite cages (18). Mixed phase behavior in a zeolite synthesis system is often reflected in considerable variability in the PXD patterns (reflecting changes in the relative amounts of the two (or more) phases from one preparation to the next). The relative proportions of the cubic and hexagonal components in ZSM-20 samples, however, are found to fall within relatively narrow bounds in both the present materials and those described previously in the literature (1,16-22).

Experimental – Syntheses

Zeolite ZSM-20 is synthesized in the Na_2O-TEA_2O-Al_2O_3-SiO_2-H_2O composition system (TEA= tetraethylammonium cation), using tetramethylorthosilicate (TMOS) or tetraethylorthosilicate (TEOS) as the silica source (1). The latter is the preferred silica source in most recently published work (19-22). Syntheses based on a range of silica sources demonstrate that ZSM-20 formation is sensitive to the specific gel composition, preparation and crystallization conditions. Minor changes in these variables can totally inhibit the growth of crystalline products, or promote the crystallization of other zeolites such as beta or high silica chabazites (herschellite) (when residual TMOS is not completely hydrolyzed and evolved as methanol, and remains in the system during crystallization). Several groups have reported syntheses of ZSM-20 (19-22) and modifications of Example 19 of the Valyocsik U.S. Patent (20,22) are described as providing the most reliable results. Optimized syntheses produce highly crystalline ZSM-20 in as little as four days. Zeolite beta typically replaces ZSM-20 with increasing

reaction time. ZSM-20 is more aluminum deficient than zeolite Y, with Si:Al ratios of > 3.5, and typically 4.2, and is therefore appropriately compared with high silica FAU-framework materials such as CSZ-3 (23) and ECR-4 (24) prepared by direct synthesis from different cation containing systems. Hydrocarbon sorption capacities of ZSM-20 materials, in the range of 17 - 20 wt.%, are more similar to those of the latter high silica materials than that typical of zeolite Y.

Recently published reports of ZSM-20 syntheses include evaluations (20,21) of the patent examples of Ciric (1) and Valyocsik (19); investigations of the role of gel structure and composition (22); and studies of pressure and temperature effects (22). The procedures used by Ciric and Valyocsik are outlined in Figure 1, and illustrate the potential problems with reproducibility in the former case.
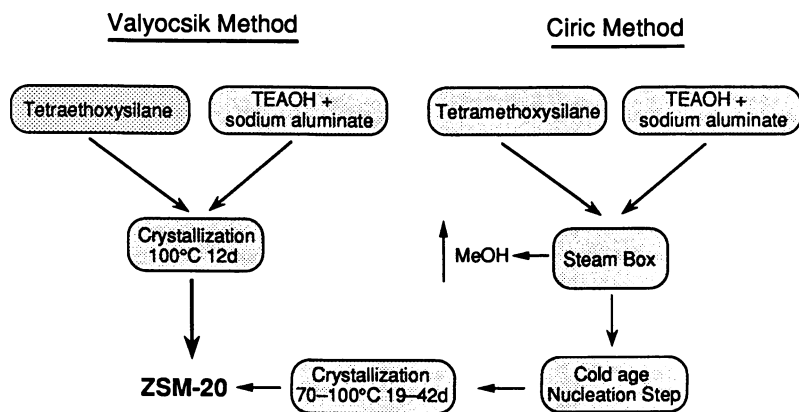
Figure 1. Schematic comparisons of the Ciric and Valyocsik methods for the synthesis of ZSM-20.

The intermediate stages of the gel aging may be viewed as nuclei incubation periods, and the presence of even small amounts of residual methanol may influence the final products. We have examined both the influences on the crystallization products of potassium cations(an undisclosed impurity in some commercial TEA products), and the variability in products derived from optimized ZSM-20 gel compositions seeded in a variety of ways. Although the original ZSM-20 patent describes successful syntheses based on TMOS as a silica source (1), we have been unsuccessful in duplicating the patent examples using presently

available TMOS. The ZSM-20 precursor gel structure appears to play an important role in bringing in the product, and minor variations in source TMOS may be a problem. The TEOS synthesis route is more reliable, reflecting the simplified gelation process (Figure 1), less sensitivity to variability in this particular reagent, or more consistent reagent quality. The differences between the use of tetramethyl- and tetraethylorthosilicate are partly illustrated in the experiments described below. All experiments were carried out in Teflon (DuPont Co.) bottles at 95° to 100°C in a steam bath (TMOS and TEOS preparations only) followed by crystallization in an air oven without stirring.

The effect of K^+ addition to the basic synthesis (using different silica sources) on the various products at high levels of crystallization at 100°C is illustrated in Figure 2 and Table 1. Sodium aluminate was the source of alumina. The base synthesis without K^+ yielded good ZSM-20 after 3 days at 100°C following a 3 day cold age at room temperature (22°C). When K^+ was present, high silica disordered chabazites, of the 'G' variety (25), and zeolite beta (26,27) were the major products, with a minor development of offretite (probably Linde T (29)). Scanning electron micrographs of these products are shown in Figure 2.

Crystallization of ZSM-20 appears to be suppressed by the presence of either K^+ or residual methanol in the gel, and products usually common at longer crystallization times then predominate. The use of an external nucleation solution (30) significantly increases the Na_2O content of the gel, and promotes the formation of beta, cha and gis.

TABLE 1

K^+ INFLUENCES ON ZSM-20 SYNTHESES

#	Gel Composition $R_2O:Na_2O:K_2O:SiO_2:H_2O$					Details* C/S/Si	Xtln time	Products
1	9.9	1.1	0	32	455	C, TEOS	3d	ZSM-20
2	9.9	1.1	1.1	32	455	C, TMOS	28d	cha
3	9.6	1.1	1.1	31	530	C, TMOS	38d	cha>>off
4	9.9	1.1	1.1	32	500	C, TEOS	28d	amorphous
5	10.0	1.1	1.1	31	425	C, HS40	17d	ß>cha
6	10.0	1.8	1.1	31	425	S, HS40	9d	ß
7	9.6	2.2	1.1	30	410	S, Cab	18d	ß>cha>gis

* Details: C=cold aged; S= seeded; Si= silica source

Zeolite beta characteristically replaces ZSM-20 at long age times in the standard synthesis (1)- represented by experiment #1 in Table 1. In most of these syntheses zeolite beta seems to be an unavoidable low level impurity. The experiments detailed in Table 2 examine the effects of various nucleation and seeding methods on ZSM-20
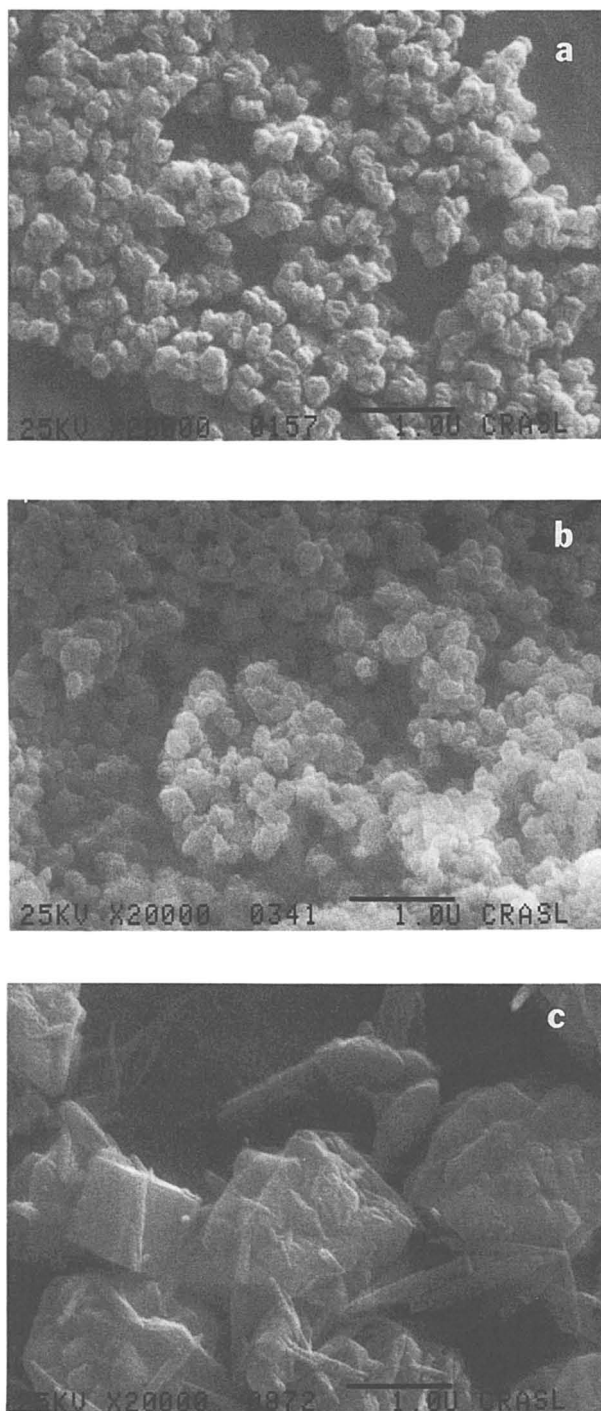
Figure 2. SEM of ZSM-20 (a) and co-crystallization products beta (b) and cha with off (c).

crystallizations. These were conducted in potassium free systems, where the TEA was first treated at room temperature with acid washed clinoptilolite to remove any residual traces of potassium cations.

TABLE 2

NUCLEATION INFLUENCES ON ZSM-20 SYNTHESES

Composition: $9.7(TEA)_2O: 1.14Na_2O: Al_2O_3: 24.2SiO_2: 370H_2O$.

Seeding mode	Crystallization Products			
	2d	3d	5d	8d
0.1g ZSM-20 Xtals	am	am	am	am
0.1g FAU-Y Xtals	am	am	ß>fau	ß>fau
1d age 23°C	ns	am	am	ß
2d age 23°C	am	ns	ZSM-20	ZSM-20>ß
5d age 23°C	am	ns	ß	ns
11d age 23°C	ns	ns	ß	ns

ns= no sample; am= amorphous products;

      Cold aging(1) is a competitive nuclei breeding step which clearly has an optimum time period for ZSM-20, after which promoters of zeolite beta predominate. Attempts to induce crystallization by addition of crystalline products of ZSM-20 or type-Y, without any cold aging step, failed to demonstrate any seeding effects. In these cases beta was the primary product. The ZSM-20 products characteristically show a morphology of twinned and intergrown "hexagonal" plates or squashed octahedra about 0.1µ in diameter (similar to those observed for a potassium "platelet faujasite"(31)), with the additional feature of having many crystals growing out from the plate surface. The plates have an aspect ratio of about 3, and are sometimes agglomerated into small spherules.

Experimental – Characterization of Synthesis Products

Chemical analysis and sorption data. Chemical analyses (ICP-AES) of highly crystalline and pure ZSM-20 materials give Si/Al ratios in the range of 3.7 (Table 2) to 4.7 (Table 1). Na/Al ratios of 0.7 are typical, as are (Na+TEA)/Al ratios of about 1.1. Single point n-hexane sorption capacities at 40 torr and 23°C, after burn off of the TEA at 550°C in air for 3 hours, are invariably in the range of 18% to 20% wt.- values typical for high silica directly synthesized faujasite type product(24).

Infra-red spectroscopy. I.R. spectra are frequently used to identify structural components in zeolites, and to compare identities. Figure 3 compares the I.R. spectra for

the ammonium exchanged forms of Y, ZSM-20 and ZSM-3. The first two are identical in all essential characteristics, except for minor peak broadening and a weak shoulder at ⌐920cm.$^{-1}$ in the ZSM-20 spectrum. These are in distinct contrast to the spectrum for ZSM-3, which, though having the essential features of the other two spectra, is highly degraded, probably reflecting a high level of disorder, even though morphologically it was similar to ZSM-20 in crystal size distribution.

Powder X-ray diffraction. Powder X-ray diffraction (PXD) data were measured on an automated Siemens D500 diffractometer using Cu Kα radiation from a fine-focus X-ray tube operating at 1200W, and with 1° incident beam divergence slits. Samples were generally measured after full equilibration with atmospheric moisture. Typical PXD patterns are shown in Figure 4, and like the scanning electron micrographs, they give the impression of a pure phase, even when cocrystallized with other zeolites, such as beta, shown in Figure 4b.

Comparison between the PXD pattern observed for a typical ZSM-20 material (Figure 4a) with that calculated on the basis of distance least squares optimized atomic coordinates for the *BSS* framework (Figure 5a) illustrates that the observed peak positions are in general reproduced by a hexagonal cell (1,17) with a = 17.37Å and c = 28.50Å. However, the distributions of reflection intensities are clearly different between the observed and simulated PXD patterns, with the presence of several broad peaks being a particular feature of the ZSM-20 pattern. The discrepancies cannot be explained on the basis of either slight deviations from the ideal framework geometry or the scattering contributions of the non-framework species. The observed pattern is, however, reproduced reasonably well when modelled as a simple sum of cubic(FAU) and hexagonal(*BSS*) components in the approximate ratio BSS:FAU = ⌐ 2 - 2.5 (18) (Figure 5c).

The first main feature in the PXD patterns contains contributions from the 0 1 0 ($2\theta_{calc}$ = 5.88°), 0 0 2 (6.20°) and 0 1 1 (6.64°) reflections from the hexagonal component (*BSS*), and from the 1 1 1 reflection of the cubic component (FAU) which occurs at (6.25°), effectively coincident with 0 0 2$_{hex}$ (Figure 5). The lower angle data are affected by spreading of the incident beam beyond the sample, and contain significant contributions from the non-framework components. Nevertheless, the relative intensities of the first three peaks provide a rough quantitative measure of the relative amounts of the cubic (FAU) and hexagonal (*BSS*) components. As illustrated in Figure 5c, optimal agreement between the observed and simulated patterns is obtained for a ratio *BSS*:FAU = ⌐ 2.5. Approximately this same distribution of intensities is
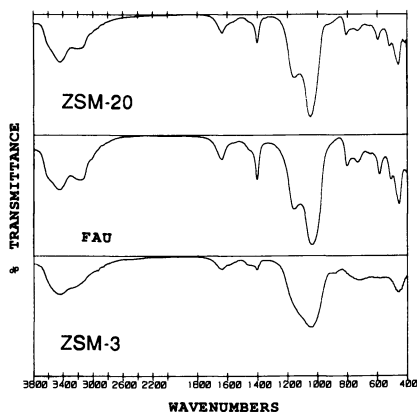
Figure 3. Comparative infra-red spectra for ammonium exchanged Y-FAU, ZSM-20 and ZSM-3.
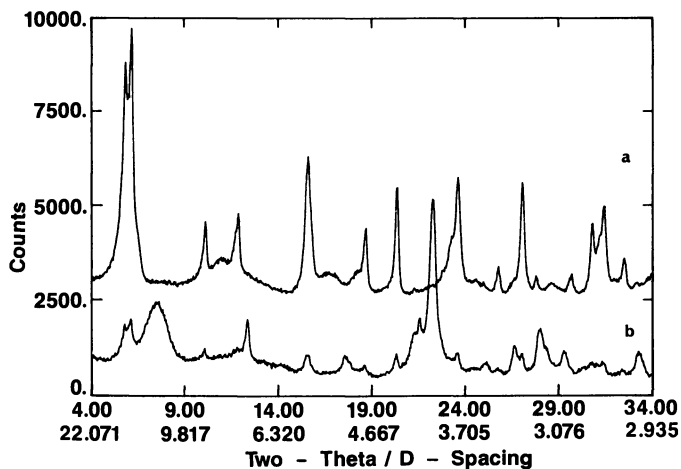
Figure 4. Observed powder X-ray diffraction patterns for a typical ZSM-20 material(a) and a beta contaminated product(b).

COUNTS
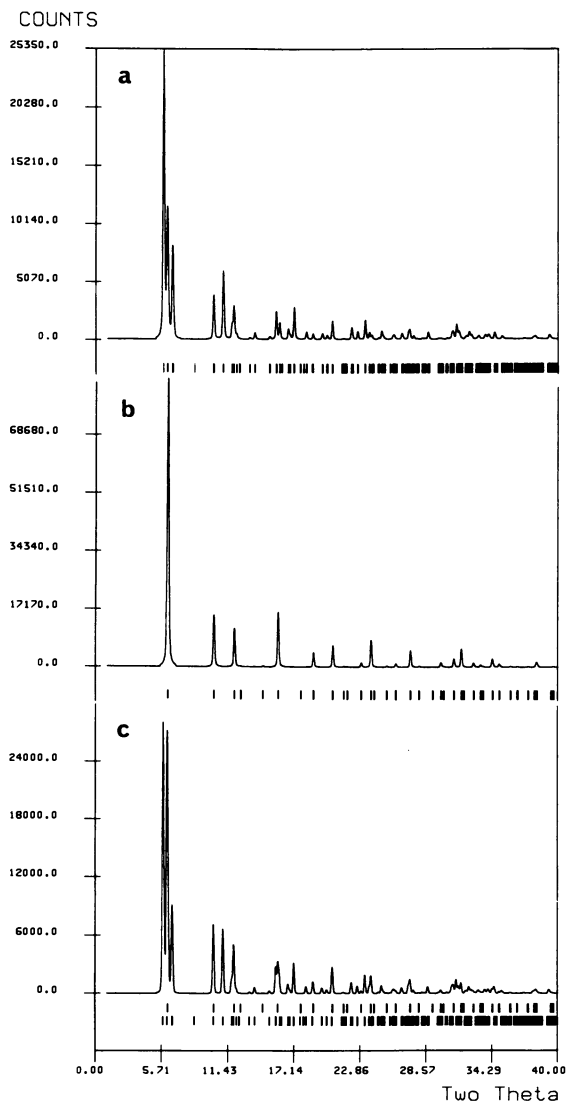
Figure 5. Calculated powder X-ray diffraction profiles
for the FAU (a) and BSS frameworks (b) and the sum of
these two components in the ratio BSS:FAU = 3.0 (c)
which approximates observed profiles for zeolite ZSM-20
materials (lower vertical bars- positions of allowed
reflections).

reported for all ZSM-20 preparations (1,14-20). Zeolite ZSM-20 thus comprises intergrown blocks of cubic and hexagonal stackings of faujasite sheets, but in relative amounts that fall within quite narrow bounds. This limited variability in the relative concentrations of the two components reflects partly the relatively narrow window of compositions and conditions under which ZSM-20 can be crystallized. In addition, we suspect that it also reflects the manner in which the cubic and hexagonal components intergrow in this system.

Although the cubic and hexagonal components separately form blocks extended over several unit cells, they are coherently intergrown. Symptomatic of this stacking behavior, the peak widths in the measured PXD patterns are index-dependant (Figure 4). The 1 0 3$_{hex}$ reflection at 11.0° is, for example, considerably broader than the adjacent 1 1 0$_{hex}$ reflection (Figure 4). The pattern of peak widths illustrated in Figure 4 is typical of all previously reported PXD profiles (17,20,22) and it is a second characteristic of ZSM-20 materials. A full treatment of the effects of coherent, clustered faulting on the simulated PXD data (28) reproduces quantitatively the pattern of peak widths and intensities observed for ZSM-20 materials, and corroborates their description as faulted mixtures of cubic and hexagonal stackings of faujasite sheets in typical relative concentrations BSS:FAU of 2 to 2.5:1. The result of such a calculation in the 2Ø range 4° to 19° is compared in Figure 6 with the experimental X-ray diffraction pattern of a seeded ZSM-20 product (Table 2). Using a value for α = ~0.7 (α = BSS /(BSS+FAU)), the experimental intensity relationships are closely matched.

<u>Electron Microscopy.</u> Several samples were examined by transmission electron microscopy (TEM) in a Philips 430T operating at 300 kV. Samples were prepared by ultra-sonically dispersing the calcined zeolite in ethanol, and collecting the dispersed zeolite crystallites on a standard 200 mesh 3mm Cu grid covered with a thin (~20 nm) amorphous carbon film.

High resolution electron microscopy shows directly that ZSM-20 is an intergrowth of the cubic and hexagonal modes of stacking of faujasite sheets (Figure 7). There are qualitative similarities with CSZ-1 and CSZ-3 materials (13,14). As for CSZ-1 and CSZ-3, ZSM-20 crystallites adopt a hexagonal tabular morphology with an aspect ratio, platelet width to thickness, of ~3:1, compared with ~8:1 for CSZ-1 and ~4:1 for CSZ-3. Unlike CSZ-1 and CSZ-3, however, the ZSM-20 platelets tend to intergrow, with platelet normals mutually inclined at ~70°.

There is a high density of twinning in most of the ZSM-20 platelets, with ~65% of the FAU (111) planes being twinned to produce a crystallite which is predominantly
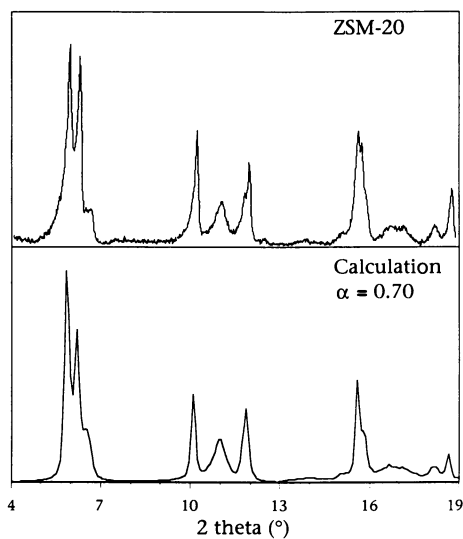
Figure 6. Experimental X-ray diffraction pattern of a
ZSM-20 material compared with a pattern calculated using
the coherent faulting model (28). The value α represents
the probability that successive (111) planes will
interconnect via a mirror operation rather than through
an inversion. Thus α=0 represents pure FAU, and α=1
represents pure *BSS*. ZSM-20 has α=0.7.
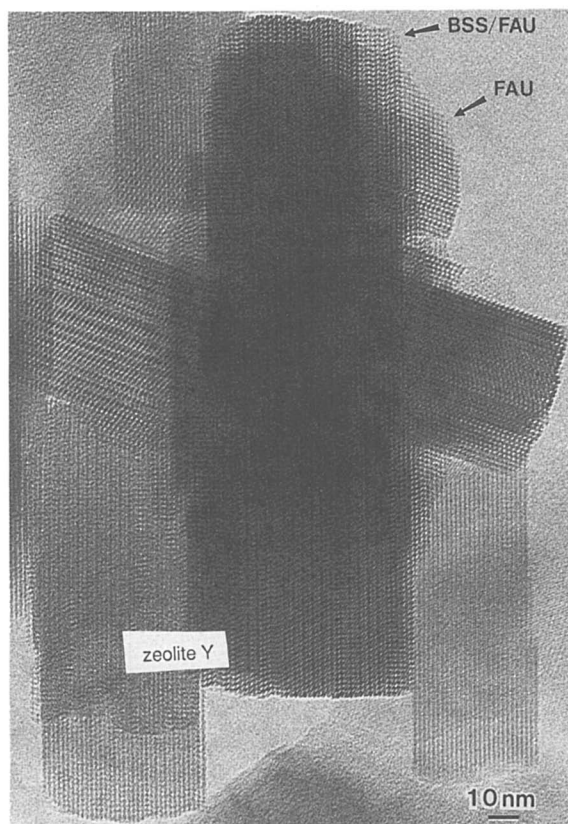
Figure 7. Electron micrograph of a typical ZSM-20 crystallite aggregate. Regions of both hexagonal ABAB... (BSS) and cubic ABCABC... (FAU) stacking are evident.

hexagonal (*BSS*) in stacking character. In CSZ-1, about 10% of the (111) planes are twinned (13,14). However, in ZSM-20, some of the interpenetrating crystallites tend to have a significantly lower twin density (see Figure 7). This arises because hexagonal stacking sequences cannot interpenetrate coherently when crystal axes are inclined. However, the unfaulted cubic FAU-stacking can interpenetrate coherently when crystallites are mutually rotated by ~70°. The interpenetrant growth may thus promote the occurrence of the cubic stacking, as suggested by the stacking in the crystallite that protrudes from the intergrown crystallite in Figure 7.

Discussion

As is discussed elsewhere (18), the cubic (FAU) and hexagonal (*BSS*) stackings of sheets of sodalite cages differ in the character of the symmetry operation that relates successive sheets along the $[111]_{cubic}$ or $[001]_{hex}$. Pairs of sodalite cages within the sheets are in both cases related (approximately) by inversion centers at the centers of the hexagonal prisms. In the cubic case, successive sheets along $[111]_{cubic}$ are also related by inversion centers at the centers of the hexagonal prisms. In the hexagonal(*BSS*) form (10-12), these inversion centers are replaced by mirror planes that bisect the hexagonal prisms along $[001]_{hex}$. A stereoview of the *BSS* framework based on distance least squares optimized atomic coordinates (which are given elsewhere) is shown in Figure 8. The geometries of the pore systems in the FAU and *BSS* frameworks differ significantly (Figure 8). In the former, supercages have four 12-ring apertures arranged tetrahedrally, interconnecting adjacent supercages in a face-centered cubic array. In contrast two types of supercages occur in *BSS*. The larger, which form straight channels along $[001]_{hex}$, have five 12-ring apertures (Figure 9). The smaller have three 12-ring apertures and provide lateral connections between channels. These differences in the supercage configurations are likely to be reflected in significant differences in sorption and catalytic properties. There is therefore a significant incentive for attempts to synthesize materials that have a larger proportion of the hexagonal stacking than is found in ZSM-20 materials.

The limited variation observed in the relative proportions of the cubic and hexagonal components in ZSM-20 zeolites must be related to crystallization conditions. Zeolite ZSM-20 can be made reproducibly provided that the recommended conditions are strictly followed. The syntheses are particularly sensitive to character of the reagents used, and to residual alcohol in the gel. This latter variable may be responsible for a degree of non-
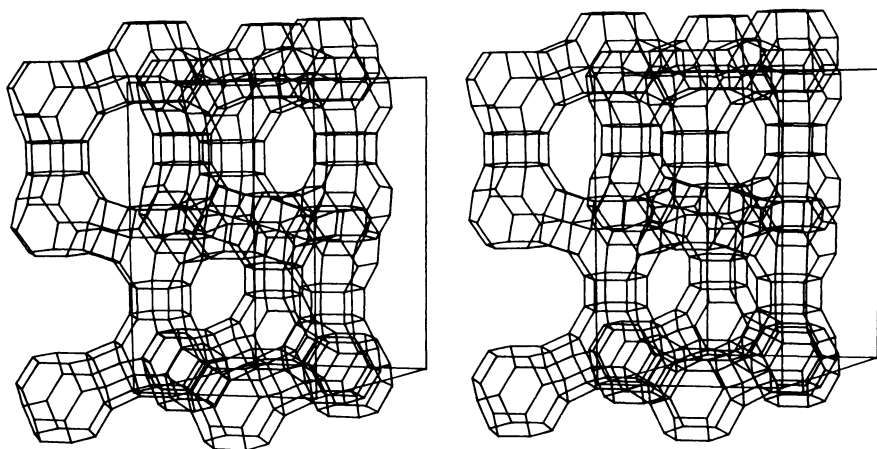
Figure 8. Stereoview of the BSS framework drawn as straight lines connecting adjacent tetrahedral vertices. Atomic co-ordinates are based on distance least squares optimized values.

A

B

C
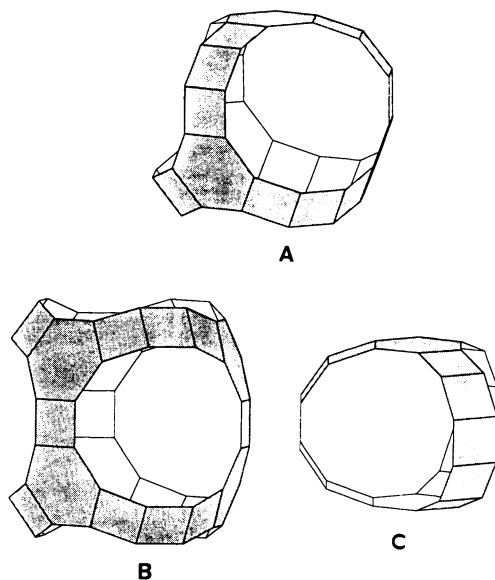
Figure 9. Outlines of the supercages in the FAU framework (A), and of the two different supercages in the BSS framework (B and C). The larger cages (B) are connected in a continuous fashion, forming straight channels along the crystallographic c direction.

reproducibility in crystallization rates in otherwise identical gels. Reaction times are apparently optimized when the cold age step is some 2 to 4 days. As illustrated here, the form and perfection of the layer stackings in ZSM-20 materials can be categorized by both powder X-ray diffraction and, more directly, by high resolution lattice imaging. Spatially resolved measurements of compositions and, perhaps, of framework or non-framework compositional zoning are also feasible. Details of the relationship between synthesis conditions and crystallized structure may yet guide attempts to make the pure hexagonal form (*BSS*).

Acknowledgments

Literature Cited

1. Ciric, J. <u>U.S. Patent</u> 3 972 983, 1976 (Mobil Oil Corp.).
2. Ciric, J. <u>U.S. Patent</u> 4 021 331, 1977 (Mobil Oil Corp.).
3. Weitkamp, J.; Ernst, S.; Cortes-Corberan, V.; Kokotailo, G. In <u>7th. Intl. Zeolite Conf. Posters</u>; Japan Assoc. Zeolites, Tokyo, 1986; 239.
4. Meier, W. M. and Olson, D. H., <u>Atlas of Zeolite Structure Types 2nd. Edn.</u>; Butterworths: Surrey UK, 1987.
5. Barrett, M. G.; Vaughan, D. E. W. <u>U.S. Patent</u> 4 309 313, 1982 (W. R. Grace Co.).
6. Ciric, J. <u>U.S. Patent</u> 3 411 874, 1968 (Mobil Oil Corp.).
7. Ciric, J. <u>U.S. Patent</u> 3 415 736, 1968 (Mobil Oil Corp.).
8. Audier, M.; Thomas, J. M.; Klinowski, J.; Jefferson, D. A.; Bursill, L. A. <u>J. Phys. Chem.</u> 1982, <u>86</u>, 581-584.
9. Millward, G. R.; Thomas, J. M.; Ramdas, S.; Barlow, M. T. In <u>Proc. Sixth Int. Zeolite Conf.</u>; Olson, D.; Bisio, A. Eds.; Butterworths: Surrey UK, 1984; pp. 793-802.
10. Breck, D. W. <u>Zeolite Molecular Sieves</u>; J.Wiley: New York, 1974 (reprinted R.E.Krieger: Malabar FL, 1982) pp. 56-58.
11. Moore, P. B.; Smith, J. V. <u>Mineralog. Mag.</u> 1964, <u>35</u>, 1008-1014.
12. Breck, D. W.; Flanigen, E. M. In <u>Molecular Sieves</u>; Barrer, R. M. Ed.; Soc.Chem.Ind.: London, 1968; pp.47-61.

13. Treacy, M. M. J.; Newsam, J. M.; Beyerlein, R. A.; Leonowicz, M. E.; Vaughan, D. E. W. J.Chem.Soc.Chem.Comm. 1986, 1211-1214.
14. Treacy, M. M. J.; Newsam, J. M.; Vaughan, D. E. W.; Beyerlein, R. A.; Rice, S. B.; DeGruyter, C. B. In Microstructure and Properties of Catalysts; Treacy, M. M. J.; Thomas, J. M.; White, J. M. Eds.; Mater. Res. Soc. Symp. Proc. No. 111; Materials Research Society: Pittsburgh, PA, 1988; pp. 177-190.
15. Kokotailo, G T.; Ciric, J. In Molecular Sieve Zeolites – 1; Flanigen, E. M.; Sand, L. B. Eds.; Amer. Chem. Soc. Adv. Chem. Ser. No. 101; American Chemical Society: Washington, DC, 1971; pp. 109-121.
16. Weitkamp, J.; Ernst, S.; Kumar, R. Appl. Catal.; 1986, 27, 207-210.
17. Derouane, E.; Dewaele, N.; Gabelica, Z.; Nagy, J. B. Appl. Catal.; 1986, 28, 285-293.
18. Newsam, J. M.; Treacy, M. M. J.; Vaughan, D. E. W.; Strohmaier, K. G.; Mortier, W. J. J.Chem.Soc. Chem.Comm.; 1989, in press.
19. Valyocsik, E. W. European Pat. Appl. 12 572, 1983 (Mobil Oil Corp.).
20. Ernst, S.; Kokotailo, G. T.; Weitkamp, J. Zeolites; 1987, 7, 180-182.
21. Ernst, S.; Kokotailo, G. T.; Weitkamp, J. In Innovation in Zeolite Materials Science; Grobet, P. J. et al. Eds.; Elsevier: Amsterdam, 1987; pp. 29-36.
22. Dewaele, N.; Maistriau, L.; Nagy, J. B.; Gabelica, Z.; Derouane, E. G. Appl. Catal.; 1988, 37, 273-290.
23. Vaughan, D. E. W.; Barrett, M. G. U.S. Patent 4 333 857, 1982(W. R. Grace Co.).
24. Vaughan, D E. W. U.S. Patent 4 714 601, 1987 (Exxon Research and Engineering Co.).
25. Barrer, R. M.; Baynham, J. W. J.Chem.Soc.(London); 1956, 2882.
26. Wadlinger, R. L.; Kerr, G. T. U.S. Patent 3 308 069, 1967 (Mobil Oil Corp.); (reissued No. Re.28 341, 1975).
27. Treacy, M. M. J.; Newsam, J. M. Nature; 1988, 332, 249-251.
28. Treacy, M. M. J.; Newsam, J. M.; Vaughan, D. E. W.; Deem, M. W. in preparation, 1988.
29. Gard, J. A.; Tait, J. M. In Molecular Sieve Zeolites – 1; Flanigen, E. M.; Sand, L. B. Eds.; Amer. Chem. Soc. Adv. Chem. Ser. No. 101; American Chemical Society: Washington, DC, 1971; pp. 230-236.
30. Vaughan, D. E. W; Edwards, G. C.; Barrett, M. G. U.S. Patent 4 340 573, 1982 (W.R.Grace Co.).
31. Edwards, G. C.; Vaughan, D. E. W.; Albers, E. W. U.S. Patent 4 175 059, 1979 (W.R.Grace Co.).

Chapter 38

Studies on the Kinetics of ZSM–23 Crystallization

S. Ernst[1], R. Kumar[1,3], and J. Weitkamp[2]

[1]Department of Chemistry, Chemical Technology, University of Oldenburg, Ammerlaender Heerstrasse 114–118, D–2900 Oldenburg, Federal Republic of Germany
[2]Institute of Chemical Technology I, University of Stuttgart, Pfaffenwaldring 55, D–7000 Stuttgart 80, Federal Republic of Germany

To optimize the synthesis conditions for zeolite ZSM-23 with respect to synthesis time and purity of the product, its crystallization kinetics was studied in detail by X-ray powder diffraction and scanning electron microscopy. The following reaction parameters were varied: Temperature, SiO_2/Al_2O_3, OH^-/SiO_2, H_2O/SiO_2, pyrrolidine/SiO_2. Pertinent results are: i) increasing temperature or decreasing Al-content of the gel leads to shorter induction periods and enhanced crystallization rates, ii) at SiO_2/Al_2O_3 = 70 to 150 pure ZSM-23 can be obtained; for lower or higher values other phases may form; iii) an optimum value for OH^-/SiO_2 seems to exist (ca. 0.1) below which the crystallization rate is slow and above which impurity phases (e.g., cristobalite) appear before complete crystallization is achieved and, iv) a minimum concentration of pyrrolidine is required for ZSM-23 to crystallize. Alternatively, the use of heptamethoniumbromide as template was studied. Its main advantage is the much wider range of SiO_2/Al_2O_3 ratios with which ZSM-23 can be synthesized.

ZSM-23 is a medium pore high silica zeolite with interesting catalytic and adsorptive properties (1 - 5). Recently, its framework topology was shown to have orthorhombic symmetry (Pmmn) with unit cell parameters of a = 0.501 nm, b = 2.152 nm and c = 1.113 nm. The pore structure of ZSM-23 consists of linear, non-interpenetrating channels with teardrop shaped openings of ca. 0.45 x 0.56 nm (6). It was proposed to denote this framework topology as MTT (Mobil-twenty-three) (6). Based on a comparison of X-ray powder data, it was suggested that two other zeolites, viz. KZ-1 (7) and ISI-4 (8) also possess the MTT framework (6).
The synthesis of ZSM-23 can be accomplished in the presence of organic templates, viz. pyrrolidine (1), heptamethoniumbromide (9, 10), octamethoniumbromide (10), certain imidazole derivatives (11)

---

[3]On leave from the Inorganic Chemistry Division, National Chemical Laboratory, Pune 411 008, India

and diisopropanolamine (12). Regarding the synthesis of ZSM-23 using pyrrolidine as the organic base, there are some contradictory reports in the literature: It is reported (6) that in a preferred synthesis of ZSM-23, sources of silica, alumina, caustic soda and pyrrolidine are reacted at 150°C to 160°C until the crystallization is complete. On the other hand, it has been frequently stated (10, 12, 13) that with pyrrolidine as template, the synthesis of pure ZSM-23 failed. Instead, ZSM-5 was the major phase formed.

Suzuki et al. (14) have shown that upon variation of the gel composition as many as five different zeolite structures (ZSM-5, ZSM-35, ZSM-39, ZSM-48 and KZ-1) can be synthesized in the presence of pyrrolidine (14). Hence, not only the nature of the organic template but also the gel chemistry and synthesis conditions have a marked influence on the structure of the crystalline product. In a recent systematic study it was pointed out that especially pH and Na^+-content have to be carefully adjusted in order to avoid the formation of phases other than ZSM-23 (4).

In an attempt to optimize the synthesis of ZSM-23 in the presence of pyrrolidine, the influence of the gel composition on the crystallization kinetics was studied in detail. For comparison, some experiments with heptamethoniumbromide as template are also included.

Experimental

All synthesis experiments were carried out in rotating stainless steel autoclaves with an approximate volume of 250 cm^3. After each experiment, the autoclaves were cleaned with 40 wt.-% HF to minimize seeding effects by residual crystallization products. The preparation of the synthesis mixture was as follows. Fumed silica with a surface area of ca. 200 m^2/g (CAB-O-SIL M-5) was mixed with about 90 % of the total amount of distilled water. To this mixture were added subsequently under stirring: NaOH pellets (Merck, p.a.), pyrrolidine (Fluka, p.a.) as structure directing agent, $Al(NO_3)_3 \cdot$ 9 H_2O (Merck, p.a.) dissolved in the remaining 10 % water and concentrated sulfuric acid (98 wt.-%, Merck, p.a.). When heptamethoniumbromide was used as template, a sodium waterglass solution (Merck, 28.5 wt.-% SiO_2, 8.8 wt.-% Na_2O, 62.7 wt.-% H_2O) and $Al_2(SO_4)_3 \cdot$ 16 H_2O were used as the silica and the alumina sources, respectively. Heptamethoniumbromide (N,N,N,N',N',N'-hexamethylheptamethylendiam-moniumdibromide; C_7-Diquat) was prepared from 1,7-dibromoheptane and trimethylamine according to (9). The composition of the reaction mixtures was calculated as described by Rollmann and Valyocsik (15). The mixtures were thoroughly homogenized, filled in the autoclaves and afterwards rotated in a furnace thermostated at the desired temperature. Periodically, autoclaves were withdrawn from the oven and quenched with cold water. The crystalline products were filtered, washed with distilled water, dried at 120°C in air and afterwards characterized by X-ray powder diffraction (CuK_α-radiation) and scanning electron microscopy. Percentage crystallinities of ZSM-23 were estimated from the height of the peak at 2Θ = 22.8°.

Results and Discussion

Based on preliminary experiments the following standard gel composition was selected for further systematic investigations: SiO_2/Al_2O_3 = 110, OH^-/SiO_2 = 0.1, H_2O/SiO_2 = 45, Na^+/SiO_2 = 0.41 and R/SiO_2 = 0.45 (R: pyrrolidine). To check the influence of crystallization temperature on the kinetics of ZSM-23 formation from this gel composition, the synthesis was conducted at 160°C, 170°C and 180°C. The results are shown in Figure 1. Increasing temperature results in a shorter induction period and enhanced crystallization rates. At 180°C, completely crystallized ZSM-23 can be obtained after about 1 day. The X-ray powder pattern of a sample synthesized in this manner is shown in Figure 2. The line positions and relative intensities agree very well with published data (1). No peaks due to other crystalline phases could be observed. The product crystallites typically possess a disc like morphology. The discs are almost always intergrown (cf. Figure 3).

In the synthesis of zeolites the alkalinity of the reaction mixture is one of the major factors which govern nucleation and crystal growth (16, 17). Therefore, OH^-/SiO_2 was varied in the range -0.25 to 0.19 by adjusting the amount of H_2O added to the gel. Negative values of OH^-/SiO_2 simply indicate that more moles of acid were added to the gel than of hydroxide. A possible contribution of the template to OH^- concentration is not taken into account. The results are depicted in Figure 4. Apparently, there exists a minimum value for OH^-/SiO_2 below which crystallization of ZSM-23 is very slow. Increasing the alkalinity (OH^-/SiO_2 up to 0.10) results in a drastic acceleration of crystallization. A further increase to OH^-/SiO_2 = 0.19 does not bring about a further enhancement. Rather, after about 20 hours the crystallinity of ZSM-23 is no longer improved, instead cristobalite starts to crystallize as impurity phase (not shown in Figure 4). For gels with OH^-/SiO_2 = 0.10 and 0.03 cristobalite is only observed for extended synthesis times after complete crystallization of ZSM-23. Both, the decrease in nucleation time and the enhanced rates of crystal growth with increasing OH^-/SiO_2 ratios can be attributed to an increased solubility of the reactants at higher alkalinities. This results in a higher supersaturation of the mother liquor (16). It is known from the synthesis of other high-silica zeolites (e.g., ZSM-5 (18) and ZSM-12 (19)) that the crystallite size increases with decreasing pH of the gel. The reason is the slower rate of nucleation which results in a smaller amount of crystals which are formed initially. Fewer crystals can grow to a bigger size before the reactants are completely consumed. It has now been found that this rule also holds for ZSM-23. Figure 5 shows a scanning electron micrograph of ZSM-23 produced from a reaction mixture with OH^-/SiO_2 = 0.03. The crystals possess the same morphology as those obtained at OH^-/SiO_2 = 0.10 (cf. Figure 3) but are about twice as large. From the variation of the OH^- concentration in the initial gel, the following main conclusions can be drawn: i) An optimum value for OH^-/SiO_2 seems to exist (ca. 0.1) below which the crystallization rate is slow and above which impurity phases (e.g., cristobalite) appear before complete crystallization is achieved and, ii) the crystal size of ZSM-23 can be increased upon lowering OH^-/SiO_2 however, the crystallization time will increase too.
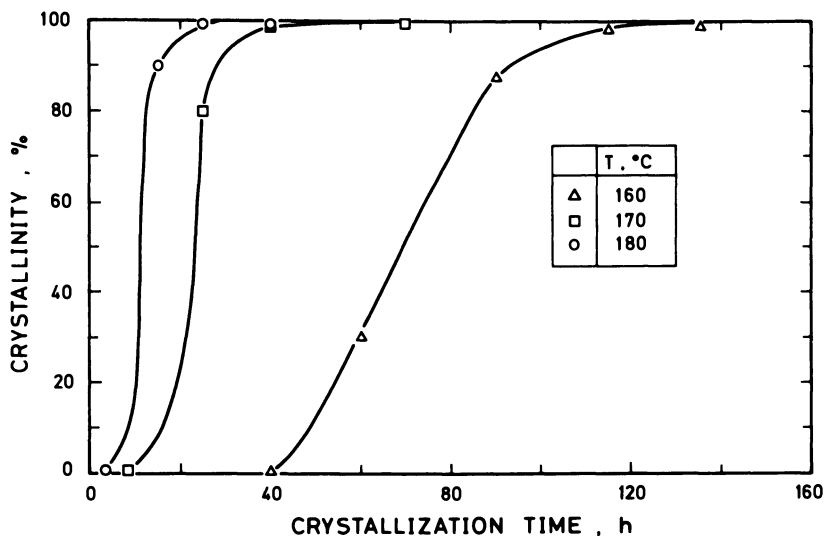
Figure 1.   Synthesis of ZSM-23 from the reaction mixture: $SiO_2/Al_2O_3 = 110$, $OH^-/SiO_2 = 0.1$, $H_2O/SiO_2 = 45$, $Na^+/SiO_2 = 0.41$, $R/SiO_2 = 0.45$: Influence of crystallization temperature.
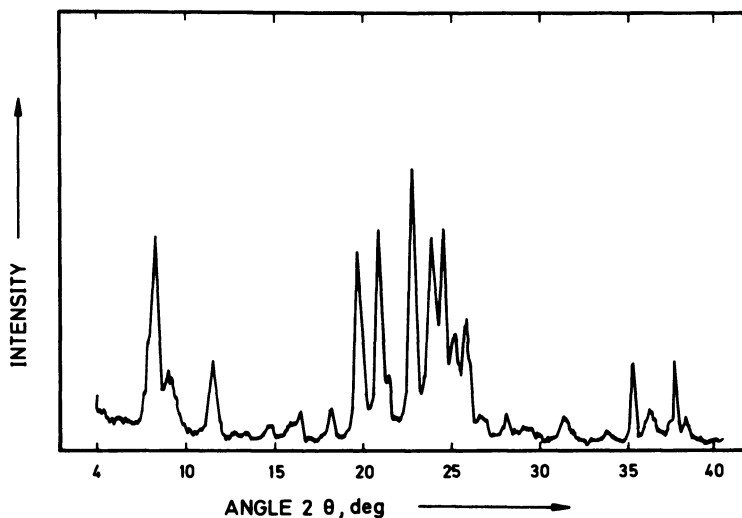
Figure 2.   X-ray powder pattern of ZSM-23 formed from the standard gel composition after ca. 1 day at 180°C.
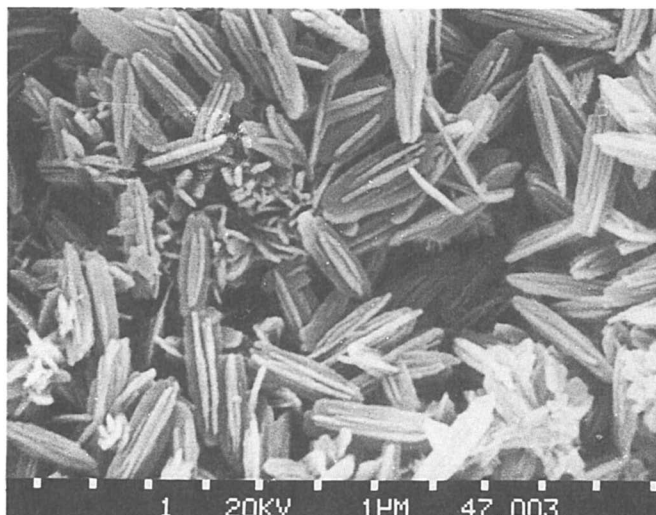
Figure 3. Typical crystallite morphology of ZSM-23. (The distance between two scale bars amounts to 1 μm).
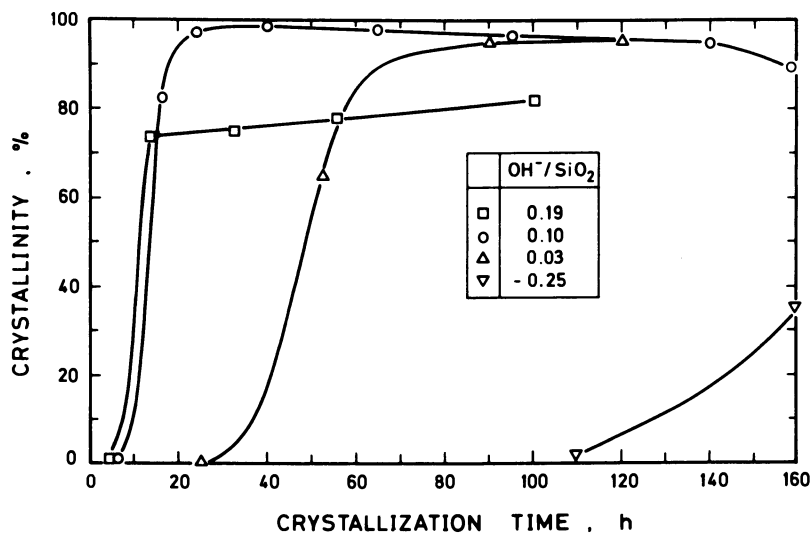
Figure 4. Influence of OH^-/SiO_2 on ZSM-23 crystallization (T = 180°C, SiO_2/Al_2O_3 = 110, H_2O/SiO_2 = 45, Na^+/SiO_2 = 0.41, R/SiO_2 = 0.45).
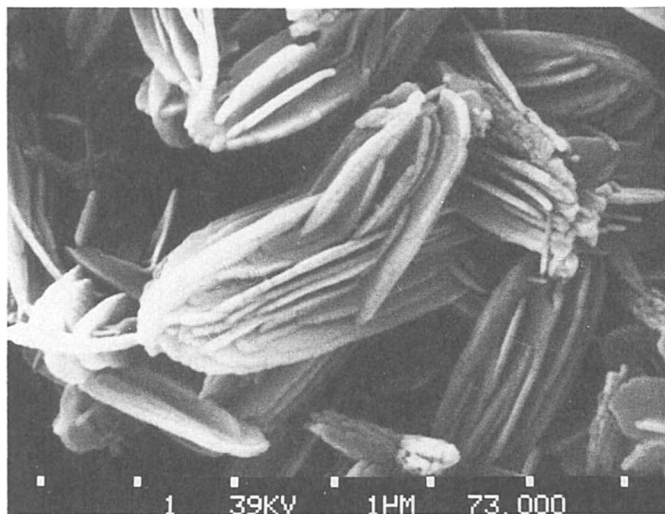
Figure 5. ZSM-23 crystallites grown from a gel with the composition $SiO_2/Al_2O_3 = 110$, $OH^-/SiO_2 = 0.03$, $H_2O/SiO_2 = 45$, $Na^+/SiO_2 = 0.41$, $R/SiO_2 = 0.45$ at $T = 180°C$.

The influence of the water content of the gel on the crystallization kinetics of ZSM-23 is shown in Figure 6. Obviously, crystallization is faster for the more concentrated systems. This observation can be easily rationalized if it is considered that with decreasing amount of water in the synthesis mixtures the concentration of the reactants and hence pH increases. This has the same effect as an increase in OH^-/SiO_2 ratio, viz. higher supersaturation of the mother liquor. The consequences have been discussed before.

In order to optimize the pyrrolidine concentration of the gel and to learn more about its role in the synthesis of the MTT framework, the molar ratio pyrrolidine/SiO_2 was varied by adding different amounts of the organic base to the reaction mixture. It can be seen from Figure 7 that the crystallization of ZSM-23 becomes faster if R/SiO_2 increases. However, at the highest value investigated in this study (R/SiO_2 = 0.67) cristobalite starts to form before ZSM-23 is completely crystallized. As a result, a value of ca. 0.45 for R/SiO_2 can be recommended to achieve both, fast crystallization and high purity. If no pyrrolidine is added to the synthesis mixture only cristobalite crystallizes, even after extended synthesis times (cf. Figure 7). This observation suggests that, at least for the gel composition used in this study, pyrrolidine is essential in the nucleation stage of ZSM-23. In additional experiments it was tried to synthesize ZSM-23 from pyrrolidine-free reaction mixtures using seeds. Either 1 or 2 wt.-% (based on SiO_2 in the gel) of uncalcined ZSM-23 seeds (obtained by crystallizing the standard reaction mixture) were added to a pyrrolidine-free gel of the composition: SiO_2/Al_2O_3 = 110, OH^-/SiO_2 = 0.1, H_2O/SiO_2 = 45, Na^+/SiO_2 = 0.41. After autoclaving at 180°C for several days, cristobalite was again the only crystalline product. These results suggest that pyrrolidine is not only important during the nucleation stage of ZSM-23 but also for its crystal growth. In this case its effect maybe that of a pore - filling agent. This suggestion is supported by the following rough estimation: According to the original patent (1), calcined ZSM-23 adsorbs about 5.5 wt.-% of n-hexane (at 25°C and $P_{n-hexane}$ ≈ 2.7 kPa). If this value is used and simply corrected for density differences, one would predict a sorption capacity for pyrrolidine of ca. 7.2 wt.-%. From the nitrogen content of most of the as-synthesized ZSM-23 samples in (1) a pyrrolidine content of ca. 6.6 wt.-% can be calculated. Hence, it is reasonable to assume complete or nearly complete porefilling of as-synthesized ZSM-23 with pyrrolidine. From these considerations it can be concluded that pyrrolidine helps not only in forming the ZSM-23 nuclei but acts also as pore-filling agent during crystal growth.

When the Na^+/SiO_2 ratio is varied between 0.17 and 0.25 keeping all other ratios constant, no significant changes in crystallization kinetics are observed. Since the covered range of Na^+/SiO_2 is only very restricted, no conclusions regarding the influence of sodium can be made at the present stage.

It is claimed (1) that ZSM-23 can be synthesized with pyrrolidine as template within a certain range of aluminium contents (SiO_2/Al_2O_3 = 40 - 250). However, upon increasing the aluminium content of the reaction mixture, crystallization rates decrease (cf. Figure 8). This observation was also made with other high silica zeolites,e.g.,
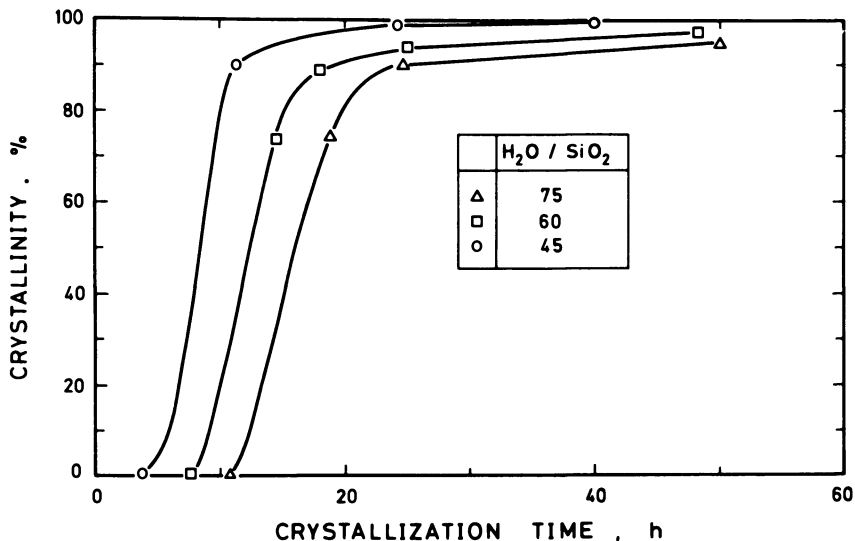
Figure 6. Influence of the water content on crystallization kinetics (T = 180°C, SiO_2/Al_2O_3 = 110, OH^-/SiO_2 = 0.1, Na^+/SiO_2 = 0.41, R/SiO_2 = 0.45).
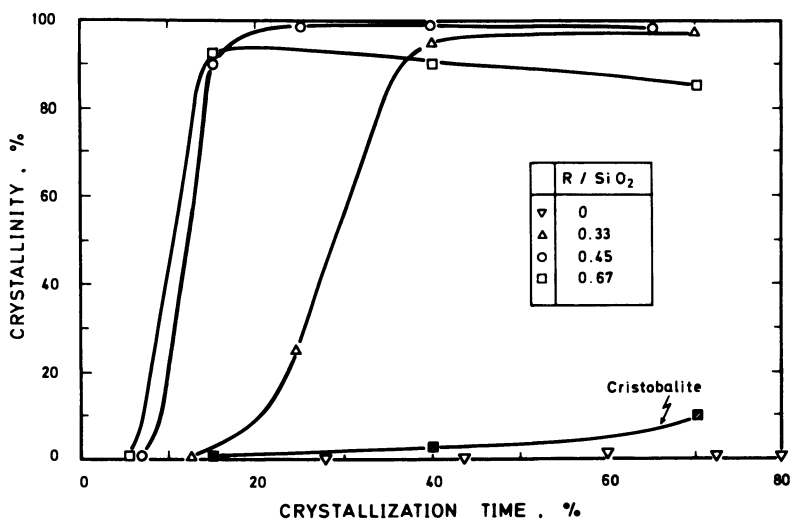
Figure 7. Influence of R/SiO_2 on the crystallization kinetics (T = 180°C, SiO_2/Al_2O_3 = 110, OH^-/SiO_2 = 0.1, H_2O/SiO_2 = 45, Na^+/SiO_2 = 0.41).
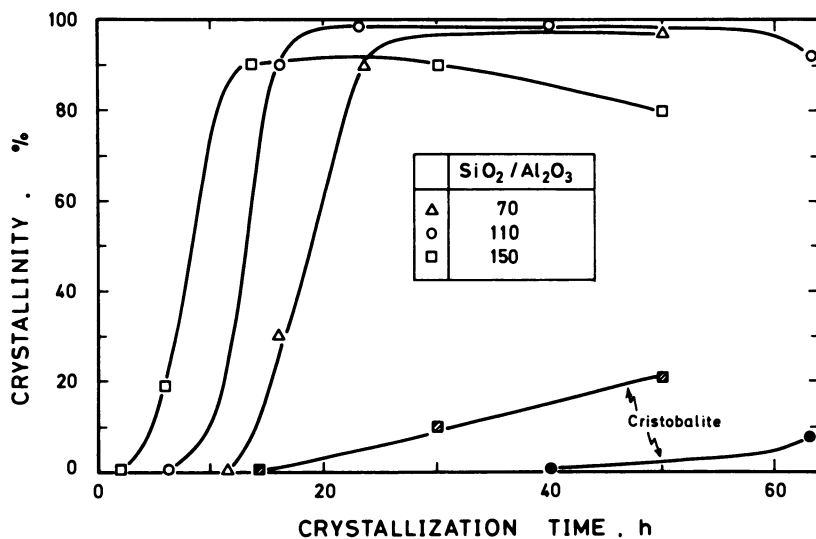
Figure 8.   Influence of aluminium content on the crystallization of ZSM-23 (T = 180°C, OH^-/SiO_2 = 0.1, H_2O/SiO_2 = 45, Na^+/SiO_2 = 0.41, R/SiO_2 = 0.45).

ZSM-5 (20 - 22) and ZSM-12 (19, 23). The reverse is known for the synthesis of low silica zeolites: Due to an increased silica content in the synthesis gel, the viscosity of the mixture is increased, which results in a decreased crystallization rate. As a possible explanation of these observations it is assumed that incorporation of aluminium into the framework of ZSM-23 is a difficult process, like it is for ZSM-5 (20). This is underlined by the decrease of the crystallite size of ZSM-23 with increasing aluminium content of the gel: For SiO_2/Al_2O_3 = 110, the crystallites are about 2 µm in length (cf. Figure 3) whereas it diminishes to less than 1 µm for SiO_2/Al_2O_3 = 70 (cf. Figure 9). These phenomena are in agreement with observations made earlier in the synthesis of ZSM-5 (20, 22, 24) and ZSM-12 (19) and seem to be of a more general validity in the synthesis of high-silica zeolites.

The results depicted in Figure 8 further indicate that, the more siliceous the synthesis mixtures are, the earlier cristobalite starts to form. Hence, if a ZSM-23 with relatively high SiO_2/Al_2O_3 ratio is to be synthesized, a careful optimization of crystallization time and, perhaps crystallization temperature should be made to obtain pure products. Increasing the aluminium content of the gel to SiO_2/Al_2O_3 ratios below ca. 50 also yields ZSM-23 but contaminated with ZSM-5 of a peculiar morphology (Figure 10).

It is claimed (9) that with C_7-diquat as template ZSM-23 can be synthesized in a much broader range of SiO_2/Al_2O_3 ratios than it is possible with pyrrolidine. Therefore, complementary synthesis experiments were conducted with C_7-diquat. In a gel with the composition OH^-/SiO_2 = 0.3, Na^+/SiO_2 = 0.59, R^+/SiO_2 = 0.15 the aluminium content was varied such as to obtain SiO_2/Al_2O_3 ratios between 60 and ∞. From all synthesis runs, pure and highly crystalline ZSM-23 was obtained after 1 to 4 days at 160°C under agitation. A typical X-ray powder pattern of a ZSM-23 sample synthesized in this way (SiO_2/Al_2O_3 = 140) is shown in Figure 11. The resolution of the pattern is considerably improved. Note, for example, that the first somewhat broad peak of ZSM-23 synthesized with pyrrolidine (cf. Figure 2) splits into two sharp lines (this difference also remains after calcination in air at 540°C). One could expect, that the sharper lines are due to a larger crystal size. However, as it can be seen from Figure 12, this is not the case. ZSM-23 produced from systems containing C_7-diquat has a plate-like habit with crystallite sizes around or below 1 µm. Hence, the reasons for the improved resolution of the XRD patterns are not clear at the moment. One could speculate that ZSM-23 obtained from pyrrolidine containing systems has some amorphous material occluded in the pores, resulting in a poorer crystallinity. This should result in different adsorptive and catalytic properties of ZSM-23 prepared with different templates.

Conclusions

Zeolite ZSM-23 can be readily synthesized with pyrrolidine as organic template and fumed silica as silica source. Pyrrolidine seems to intervene in the nucleation and crystal growth process, in the latter case most probably as pore-filling agent. By proper optimization of the gel composition and the synthesis conditions, ZSM-23 can be synthesized in less than one day. The synthesis of ZSM-23 has some
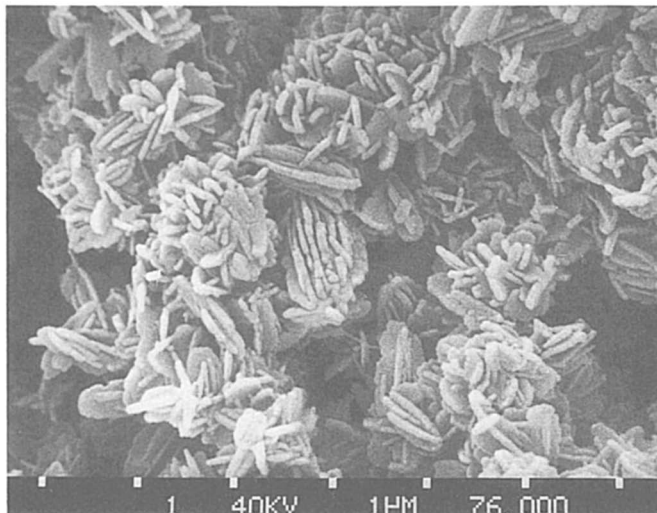
Figure 9. Crystallite morphology of ZSM-23 synthesized from a gel with $SiO_2/Al_2O_3 = 70$.
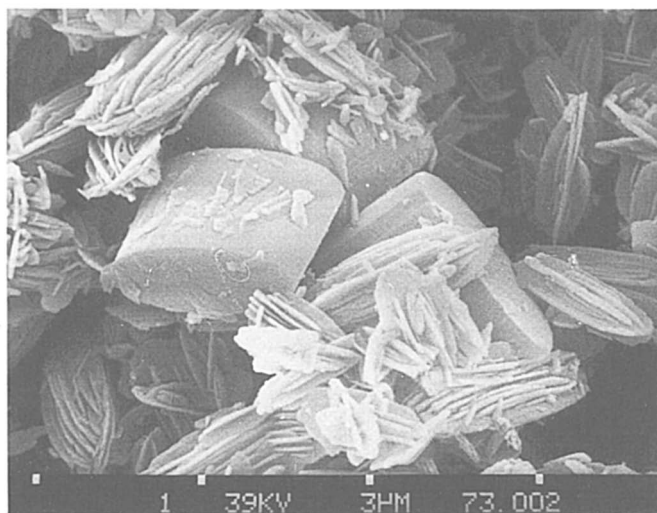
Figure 10. ZSM-5/ZSM-23 mixture obtained from a gel with $SiO_2/Al_2O_3 = 50$.
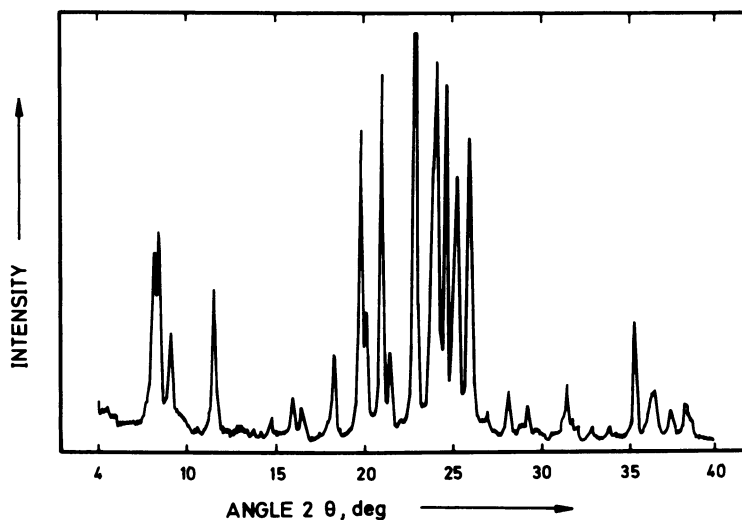
Figure 11. Typical X-ray powder pattern of ZSM-23 (SiO_2/Al_2O_3 = 140) obtained with C_7-diquat as template.
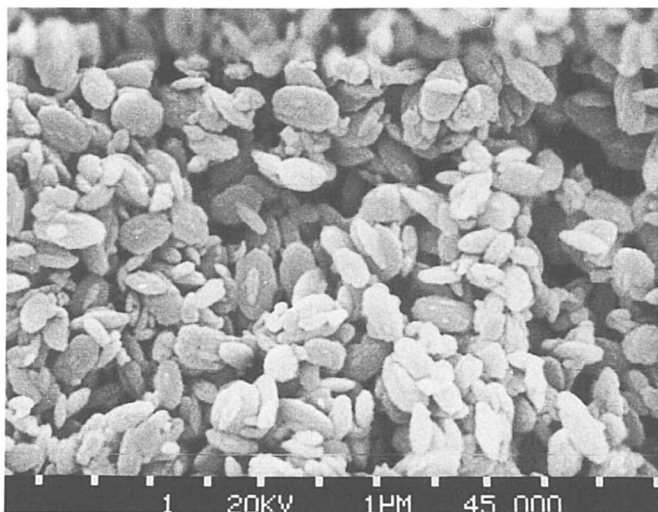
Figure 12. Typical crystallite morphology of ZSM-23 prepared from gels containing C_7-diquat as template.

features in common with the synthesis of ZSM-5 and ZSM-12: i) increasing the alkalinity of the gel reduces the crystallization time and the crystallite size of the product and ii) increasing the SiO_2/Al_2O_3 ratio in the gel enhances the rate of crystallization. Hence, these observations seem to be of a more general validity in the synthesis of high-silica zeolites. With C_7-diquat as template, ZSM-23 can be synthesized in a much broader range of SiO_2/Al_2O_3 ratios and with better resolved powder patterns. However, this template is not commercially available and its preparation requires costly reactants.

Acknowledgments

Literature Cited

1. Plank, C.J.; Rosinski, E.J.; Rubin, M.K. U.S. Patent 4 076 842, 1978.
2. Bendoraitis, J.G.; Chester, A.W.; Dwyer, F.G.; Garwood, W.E. Proc. 7th Intern. Zeolite Conf., 1986, p 669.
3. Wu, E.L.; Landolt, G.R.; Chester, A.W. Proc. 7th Intern. Zeolite Conf., 1986, p 547.
4. Ernst, S.; Kumar, R.; Weitkamp, J. Catalysis Today 1988, 3, 1 - 10.
5. Ernst, S.; Kokotailo, G.T.; Kumar, R.; Weitkamp, J. Proc. 9th Intern. Congr. Catalysis, 1988, p 388.
6. Rohrman, Jr., A.C.; LaPierre, R.B.; Schlenker, J.L.; Wood, J.D.; Valyocsik, E.W.; Rubin, M.K.; Higgins, J.B.; Rohrbaugh, W.J. Zeolites 1985, 5, 352 - 354.
7. Parker, L.M.; Bibby, D.M. Zeolites 1983, 3, 8 - 11.
8. Takatsu, K.; Kawata, N. Europ. Patent Appl. 102 497, 1984.
9. Valyocsik, E.W. U.S. Patent 4 490 342, 1984.
10. Casci, J.L. Proc. 7th Intern. Zeolite Conf., 1986, p 215.
11. Zones, S.I. U.S. Patent 4 483 835, 1984.
12. Barri, S.A.I. UK Patent Appl. GB 2 190 910 A, 1987.
13. Casci, J.L.; Lowe, B.M.; Whittam, T.V. U.S. Patent 4 528 171, 1985.
14. Suzuki, K.; Kiyozumi, Y.; Shin, S.; Fujisawa, K.; Watanabe, H.; Saito, K.; Noguchi, K. Zeolites 1986, 6, 290 - 298.
15. Rollmann, L.D.; Valyocsik, E.W. Inorganic Syntheses 1982, 22, 61 - 68.
16. Barrer, R.M. Zeolites 1981, 1, 130 - 140.
17. Jacobs, P.A.; Martens, J.A. Synthesis of High-Silica Aluminosilicate Zeolites; Elsevier Science Publishers: Amsterdam, Oxford, New York, Tokyo, 1987; p 70.
18. Ref. 17, p 74.
19. Ernst, S.; Jacobs, P.A.; Martens, J.A.; Weitkamp, J. Zeolites 1987, 7, 458 - 462.
20. Rollmann, L.D.; Valyocsik, E.W. Europ. Patent Appl. 21 675, 1981.

21. Chao, K.-J.; Tasi, T.C.; Chen, M.-S.; Wang, J.J. J. Chem. Soc., Faraday Trans I 1981, 77, 547.
22. Rommanikov, V.N.; Mastikhin, V.M.; Hočevar, S.; Držaj, B. Zeolites 1983, 3, 311.
23. Shou-He, X.; Hexuan, L. 7th Intern. Zeolite Conf., Preprints of Poster Papers 1986, 25.
24. Mostowicz, R.; Sand, L.B. Zeolites 1983, 3, 219.

Chapter 39

High-Resolution Electron Microscopic Studies of Zeolite ZSM–48

Angus I. Kirkland, G. Robert Millward, Stuart W. Carr,
Peter P. Edwards, and Jacek Klinowski

Department of Chemistry, University of Cambridge, Lensfield Road,
Cambridge CB2 1EW, England

We have prepared large spherulitic crystals of ZSM-48 from
silica-rich gels containing amines and structure-directing agents
(templates). Thermally treated (steamed) crystallites have been
studied by high-resolution electron microscopy (HREM) and
x-ray diffraction (XRD). At an interpretable point resolution of
ca. 3 Å in tandem with image simulations carried out according
to established procedures, HREM enabled us to establish the
imaging conditions under which the two previously proposed
topologies can be distinguished. The majority of crystallites of
ZSM-48 exhibit extensive (100) twinning.

Since the discovery of ZSM-48 as an impurity phase in ZSM-39 (1) and its
subsequent synthesis in an impurity-free form (2) the zeolite has been a
subject of structural studies by powder x-ray diffraction (3,4). These studies
have indicated a structure based on ferrierite sheets linked by oxygen atoms
located on mirror planes, and an orthorhombic lattice with pseudo I or
pseudo C centering. Schlenker et al. (5) reported that structures in which
the four independent T atoms in the ferrierite sheet are in the UUDD (U =
up, D = down) with Cmcm symmetry or in the UDUD with Imma sym-
metry show the best agreement between calculated Smith plots (6) and the
experimental x-ray powder patterns. Schlenker et al. (5) also report that a
structure based on random intergrowths of these two basic structures gives
rise to even better agreement. We have investigated the structure of ZSM-
48 by high resolution electron microscopy supported by image simulation
in order to test these conclusions and identified the optimum conditions
for imaging the zeolite.

Experimental

Zeolite ZSM-48 was synthesised according to ref. 7. A solution prepared by
mixing 0.56 g of sodium hydroxide, 0.43 cm^3 30% aqueous ammonia and

10 cm^3 of water was added with vigorous stirring to the thick slurry made by mixing 5 g fumed silica (Cab-O-Sil M5), 1.78 g hexamethonium bromide (HMBr$_2$) and 60 cm^3 water. This gave a free-flowing gel of composition 5 (HMBr$_2$) : 5 Na$_2$O : 5 (NH$_4$)$_2$O : 60 SiO$_2$: 3000 H$_2$O. The mixture was heated in a Teflon-lined autoclave at 200°C for 72 hrs. The spherical crystallites (yield 4.35 g) were collected, washed with water and dried at 80°C for 16 hrs. They were larger than reported in ref. 7 and had a different crystal habit from those studied in ref. 5.

The as-prepared ZSM-48 was calcined in air at 500°C for 48 hrs to give H,Na-ZSM-48. This was washed with 1.0 M HCl at 25°C for 3 hrs to give H-ZSM-48. The material was then heated at 450°C for 30 hrs in a tubular quartz furnace (Hamdan, H.; Sulikowski, B.; Klinowski, J. *J. Phys. Chem.,* in press) with water being injected at a rate of 12 ml per hour into the tube by a peristaltic pump so that the partial pressure of H$_2$O above the sample was 1 atmosphere. It was then exchanged with 1 M NH$_4$NO$_3$ and steamed at 650°C for a further 16 hrs. The ammonium exchange was repeated and the zeolite steamed at 650°C for 16 hrs and at 800°C for 8 hrs. XRD diffraction patterns (not shown) did not indicate any loss of crystall-inity upon thermal treatment.

High-resolution electron microscopic studies employed a modified JEOL-JEM200CX (8) operated at 200 kV with objective lens characteristics C$_s$ = 0.52 mm, C$_c$ = 1.05 mm leading to a theoretical point resolution as defined by the first zero in the phase contrast transfer function of 1.95 Å at the optimum or Scherzer (9) defocus position (400 Å underfocus).

Samples for electron microscopy were prepared by dispersing the as-synthesized zeolite in acetone and allowing one drop of the resultant suspension to dry onto an EM grid coated with a thin holey amorphous carbon film. Suitable crystallites were oriented along high symmetry zone axes in the selected area diffraction mode and subsequent high resolution images were recorded at electron optical magnifications of ca. 120,000x after correction of illumination system misalignments and residual object-ive lens astigmatism (10). In view of the established beam sensitivity of zeolites all images were recorded under conditions of low incident electron flux (11,12).

Simulated images were computed on an IBM 3084 mainframe computer using the multislice method (13) for [001], [010] and [100] project-ions, using programs written in this laboratory (14), and employing the atomic coordinates of Schlenker et al. (5) for both Cmcm and Imma space group symmetries. For all calculations electron optical parameters applic-able to our microscope were employed with images being calculated for crystal thicknesses of 20, 40, 60, 80 and 100 Å and for defoci of between -29 and -1029 Å in increments of 200 Å. No account was taken of focal spread or beam divergence envelopes. The calculations were performed for an aperture limited resolution of either 3.1 or 3.5 Å, which entailed using structure factors extending into reciprocal space to 0.7525 or 0.875 Å and evaluating the Fourier transform in the phase grating to 1.55 Å or 1.75 Å.

The choice of these artificial limits was felt to be appropriate since the theo-
retical point resolution limit of 1.95 Å at the optimum defocus is rarely
achieved for zeolitic specimens due to their sensitivity to the electron
beam. Typical total computation times were 120 s for each set of 25 images.

Results and Discussion

A scanning electron micrograph of as-prepared zeolite ZSM-48 (see
Figure 1) shows the typical size of the crystals and their habit. Figure 2
gives a representative low magnification high resolution micrograph of a
small crystallite of ZSM-48 oriented along the [001] direction with a thin
edge. From the micrograph and inset electron diffraction pattern it is
clearly evident that the crystal contains a number of twins on (100) planes
marked with arrows. These twin planes are found in almost all crystallites
but there appears to be no regular periodicity between them.
     Figure 3 shows an enlargement of approximately the marked area of
Figure 2 together with simulated images calculated for a crystal thickness of
100 Å and an objective lens defocus of -429 Å for both the UUDD (Cmcm)
and UDUD (Imma) structural models. From a comparison of experimental
and calculated images it is evident that simulations based on both struct-
ures of Schlenker et al. (5) give excellent agreement with those obtained
experimentally at this crystal thickness and objective lens defocus.
However, both Cmcm and Imma models would be expected to give rise to
very similar image contrasts for thin crystals in view of the similarity of
their projections along the [001] axis. Therefore, in the absence of addition-
al experimental images projected along alternative zone axes, exact differ-
entiation between the two structures is not possible at this resolution.
Hence, the proposal that the disorder present in this system may arise from
stacking faults involving a translation of c/2 cannot be confirmed.
     In parallel with these preliminary experimental imaging studies we
have also calculated additional simulated images for [001], [100] and [010]
incidence for both structural models at two different aperture limited
resolutions in order to establish the optimal conditions for high resolution
imaging. Figures 4-9 show the results of these calculations for [001], [100]
and [010] incidence, respectively, for both Cmcm and Imma topologies,
calculated in each instance for a resolution of 3.1 Å and objective lens
defoci of between -29 and -1029 Å and crystal thicknesses of 20-100 Å.
     For simulations calculated for the [001] projection both topologies
give rise to very similar image contrasts, at all the objective lens defoci and
crystal thicknesses considered for a resolution of 3.1 Å (see Figures 4 and 5).
Furthermore, it is evident that the image contrast is a true reflection of the
projected structure (with both the central 10-membered channel and the
satellite 5- and 6-membered channels visible) only for objective lens defoci
of between ca. -229 and -429 Å, and that this is true for all crystal thicknesses
considered. This is not surprising since it has been established (14-16) that
for values of objective lens defocus close to the optimum (-440 Å) that high
resolution image contrast should be directly interpretable in terms of the
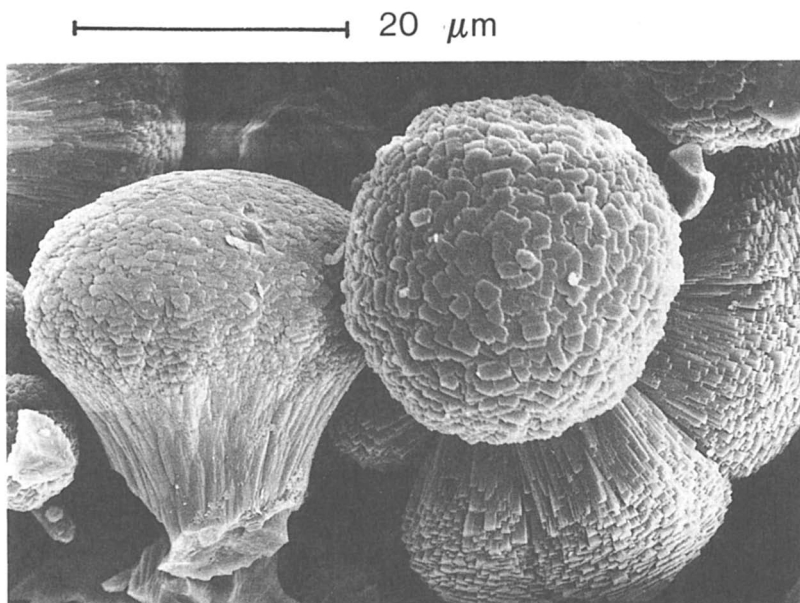
Figure 1.   Scanning electron micrograph of as-prepared zeolite ZSM-48.
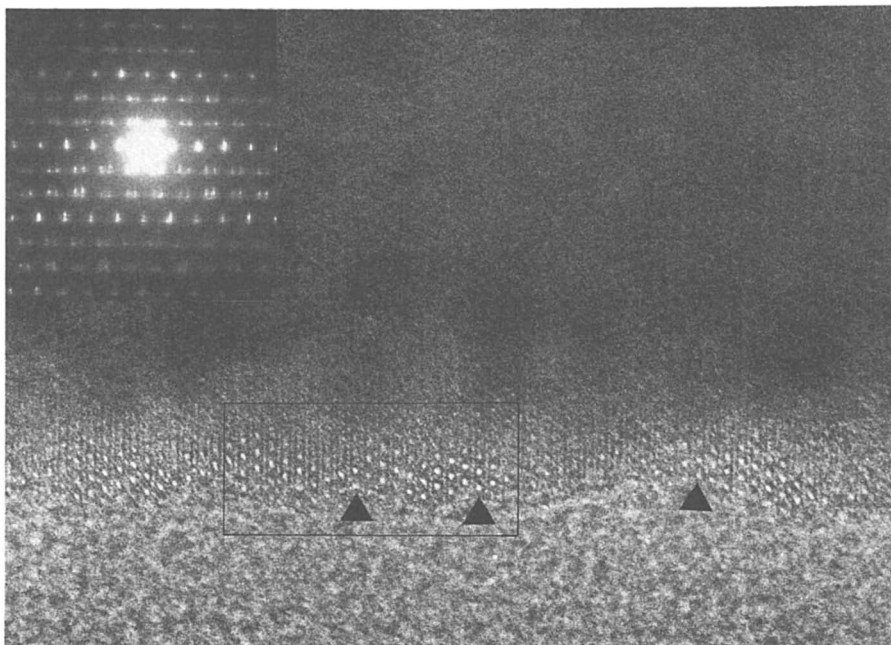
Figure 2.   A typical low magnification HREM image of ZSM-48 project-
ed along [001] with the corresponding electron diffraction pattern (inset).
Several twins on (100) planes are indicated.
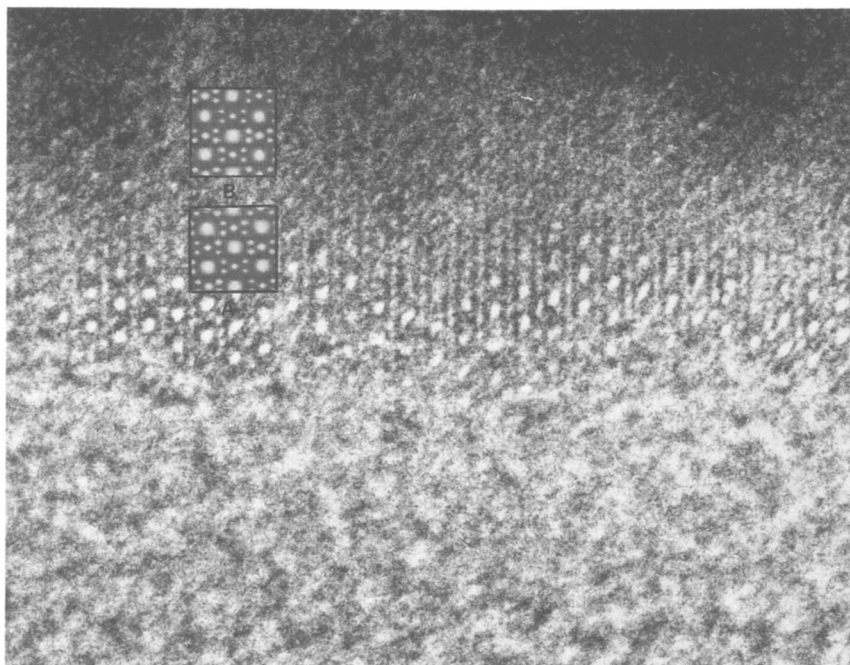
Figure 3.   An enlargement from approximately the marked area of Figure 2 together with calculated images (Δf = -429 Å, thickness 80 Å) based on (a) the UUDD and (b) UDUD models.
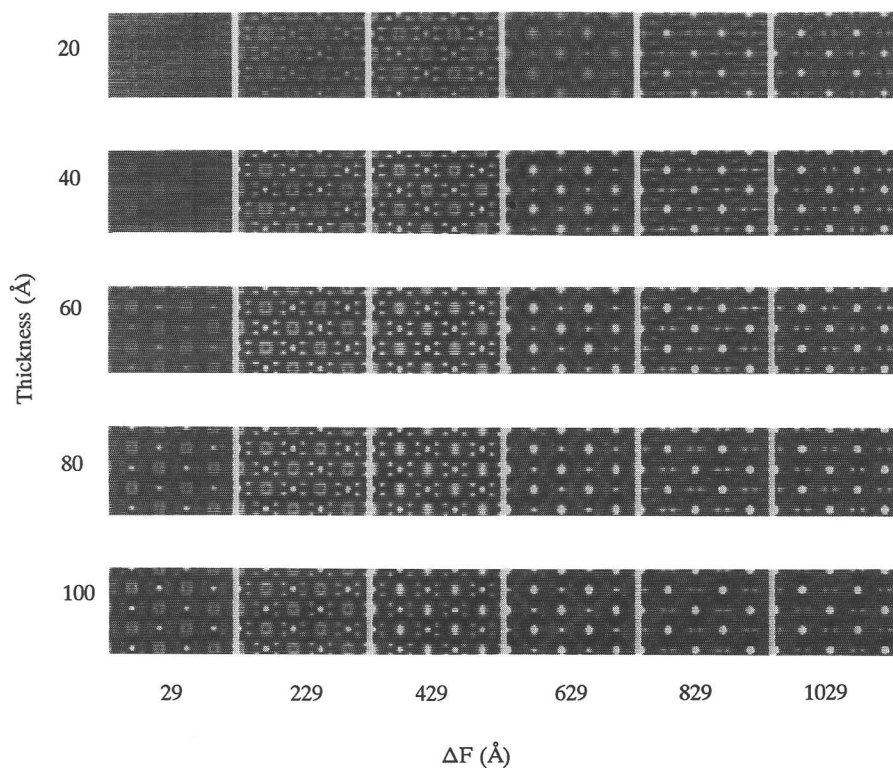
Figure 4. Calculated images for the Cmcm topology of zeolite ZSM-48 for [001] incidence (Δf =-29 to -1029 Å; thickness 20, 40, 60, 80 and 100 Å; resolution 3.1 Å).
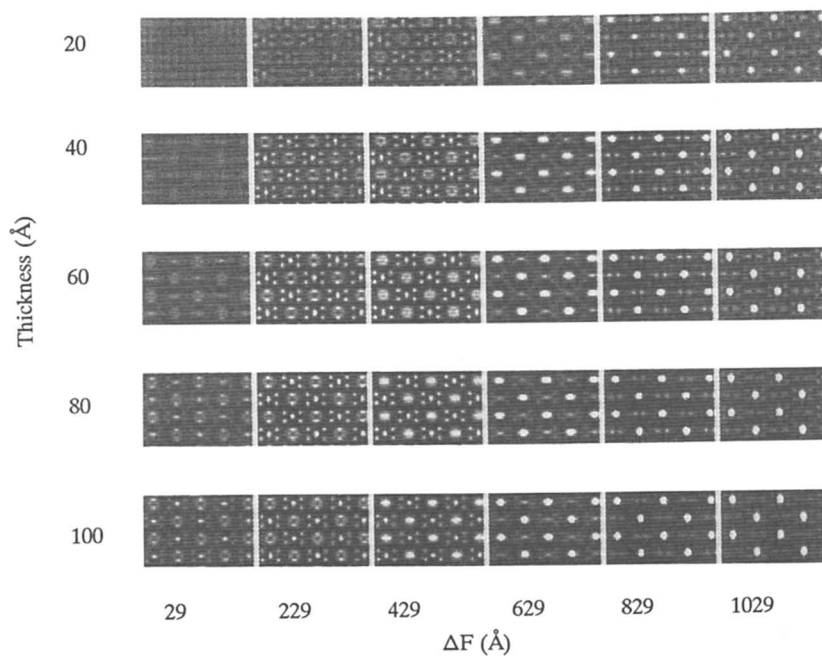
Figure 5.   As for Figure 4, but calculated for the Imma topology.
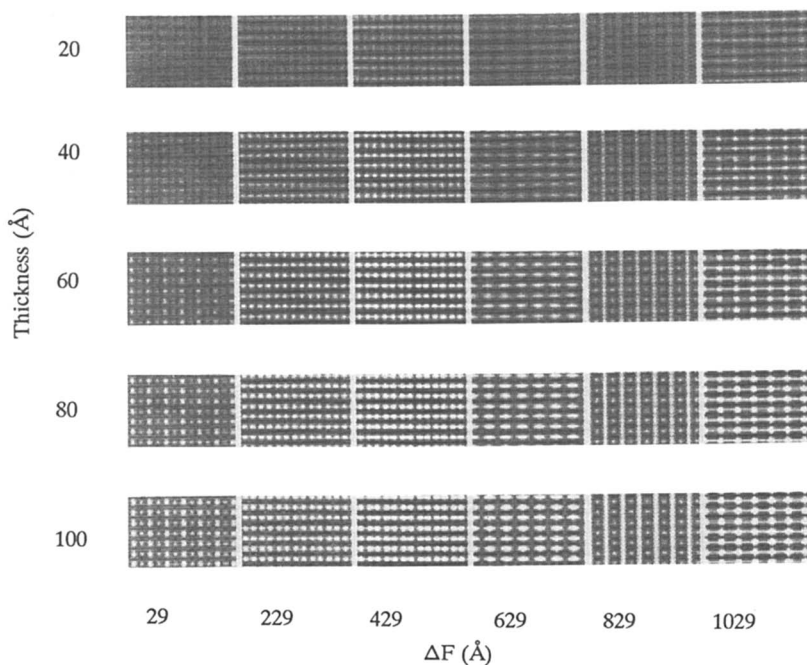
Figure 6.   As for Figure 4, but calculated for [010] incidence.
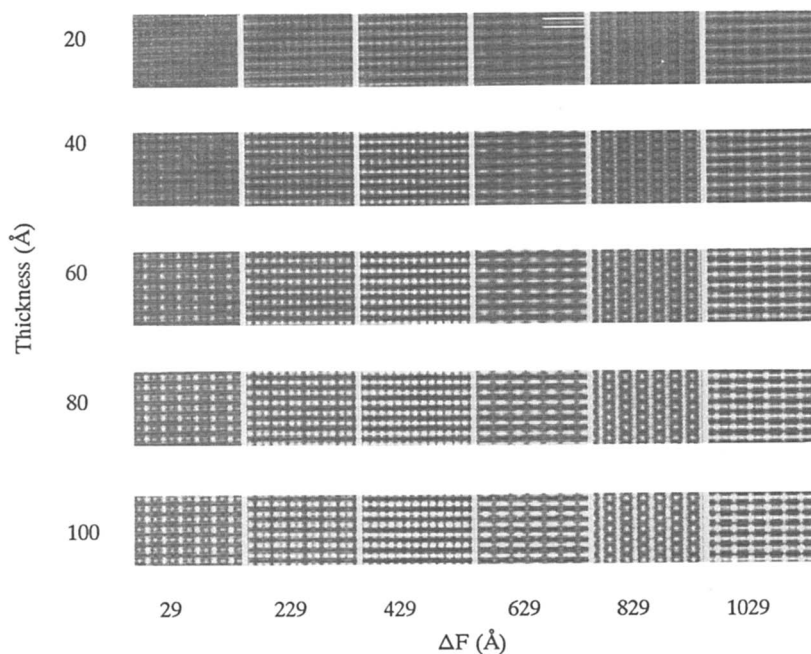
Figure 7. As for Figure 6, but calculated for the Imma topology.
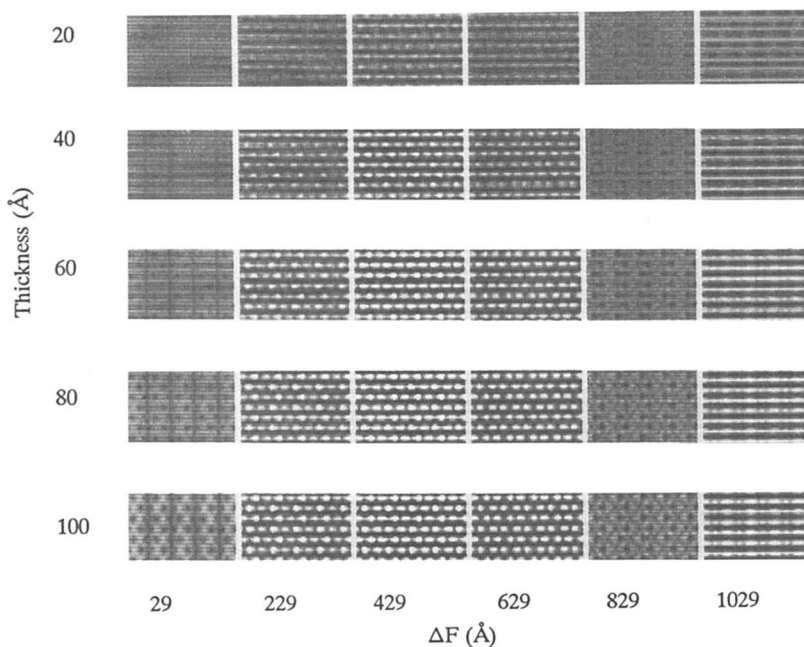
Figure 8. Calculated images for the Cmcm topology of zeolite ZSM-48 for [100] incidence (Δf =-29 to -1029 Å; thickness 20, 40, 60, 80 and 100 Å; resolution 3.1 Å).
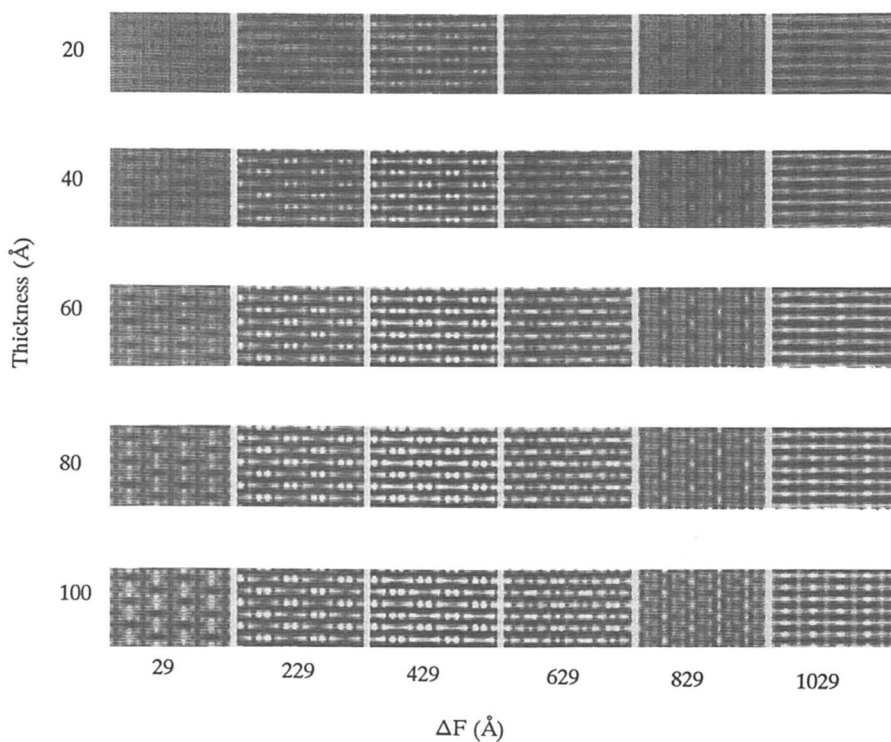
Figure 9.   As for Figure 8, but calculated for the Imma topology.

projected charge density of the structure for relatively weakly scattering specimens.

In an analogous fashion images projected along [010] of both structures are virtually indistinguishable at 3.1 Å resolution for all crystal thicknesses and objective lens defoci considered (Figures 6 and 7). Again, this is expected given the close similarity of the two projected charge densities and the above criterion. However, images calculated for [100] incidence for the two structures show notable differences in contrast at all crystal thicknesses and objective lens defoci, with the differences being most marked at defoci close to the optimum (Figures 8 and 9). Again, this difference may be rationalised in terms of the projected charge density of the structures which in this projection differ due to the arrangement of the four independent T atoms. For the case of the Imma topology all the 4-membered rings have the same size projected along the a axis but in the case of the Cmcm structure the 4-membered rings are alternately large or small. Simulations calculated at 3.1 Å resolution show that the [100] projection is the most suitable for differentiation of the two proposed topologies.

We have also calculated images for [001] incidence at 3.5 Å resolution in order to ascertain whether differences in the two structures may be identified at lower resolution as has previously been found for imaging silver clusters in zeolite Y (17), wherein differences invisible at high resolution became apparent when the resolution was decreased. Figures 10 and 11 show calculations performed for identical conditions to those of Figures 3 and 4 but with an aperture limited resolution of 3.5 Å as opposed to 3.1 Å. From these calculations it is apparent that at this resolution there are notable differences between images calculated for the two structures, with the satellite channels being clearly visible for the Cmcm topology but very much weaker for the Imma model. An examination of the diffracted beam amplitudes for the (00l) (l = 2, 4 or 6) beams reveals the reason for this difference.

Table I shows the calculated diffracted beam amplitudes for the (000), (002), (004) and (006) beams for both topologies, for a crystal 60 Å thick. The principal difference between the intensities for the two structures lies in the intensity of the (004) beam relative to (006). [Note that in both cases the intensity of the central (000) beam is approximately the same and hence the intensities are approximately normalised with respect to each other thus allowing direct comparison]. In the case of the Imma structure the (004) beam is weak with respect to the (006) and hence the (006) must be included to resolve the satellite channels clearly. At a limited resolution of 3.5 Å the (006) beam lies outside the objective aperture and hence the satellite channels are only very faint in the image. However, for the Cmcm model the relative intensities are reversed with the (004) beam stronger than the (006) and hence even if the (006) beam is excluded from the aperture the satellite channels will be clearly resolved.

In conclusion, we have shown that the [100] projection is the most suitable for distinguishing the two structure types at 3.1 Å resolution or
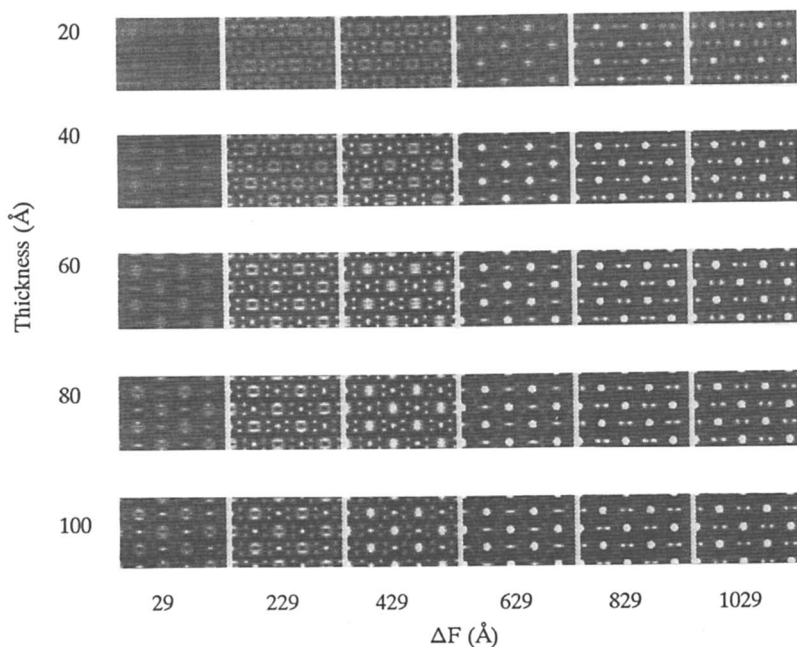
Figure 10.   Calculated images for the Cmcm topology of zeolite ZSM-48 for [001] incidence (Δf =-29 to -1029 Å; thickness 20, 40, 60, 80 and 100 Å; resolution 3.5 Å).
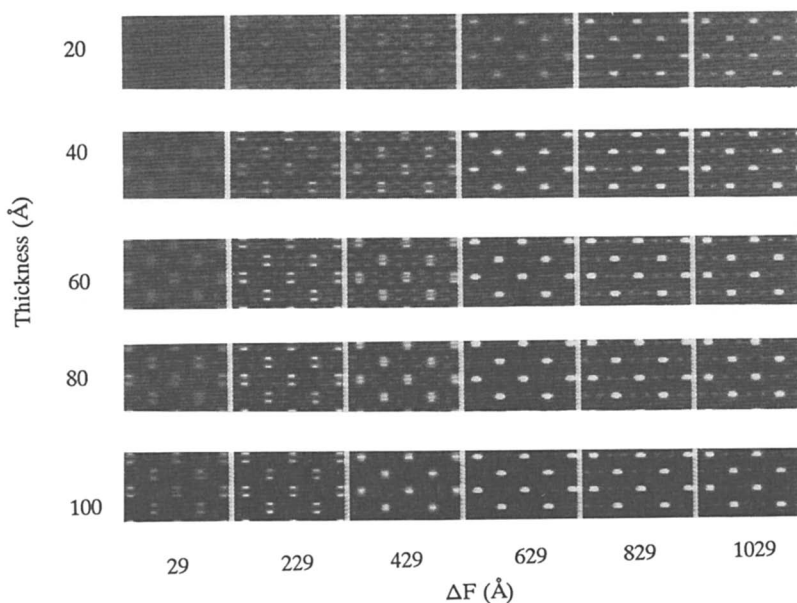
Figure 11.   As for Figure 10, but calculated for the Imma topology.

TABLE I.   Calculated diffracted beam intensities of the (00l) (l=2,4,6) beams for the two topologies of ZSM-48

Diffracted beam	Intensity (arbitrary units)		d (Å)
	Cmcm	Imma	
(006)	0.00096	0.0077	3.36
(004)	0.00144	0.000774	5.03
(002)	0.00668	0.00816	10.07
(000)	0.50	0.52	

greater but that at the lower resolution of 3.5 Å differences are also apparent for images recorded for the [001] projection. Therefore the proposal of Schlenker et al. of a disordered structure involving stacking faults of a translation of c/2 could be confirmed directly at high resolution for [100] incidence or at lower resolution for both [100] and [001] incidence. Further experimental studies are continuing to verify these proposals.

Literature Cited

1.   Schlenker, J.L.; Dwyer, F.G.; Jenkins, E.E.; Rohrbaugh, W.J., Kokotailo, G.T. Nature (London), 1981, 294, 340.
2.   Chu, P. US Patent 4,397,827, 1981.
3.   Rollman, C.D.; Valyocsik, E.W. US Patent 4,423,021, 1983.
4.   Chu, P. US Patent No. 4,448,675 (1984).
5.   Schlenker, J.L.; Rohrbaugh, W.J.; Chu., P.; Valyocsik, E.W.; Kokotailo, G.T. Zeolites, 1985, 5, 355.
6.   Smith, D.K. A Revised Program for Calculating X-ray Powder Diffraction Patterns, UCRL-502.64, Lawrence Radiation Laboratories, 1967.
7.   Dodwell, G.W.; Denkewicz, R.T.; Sand, L.B. Zeolites, 1985, 5, 153.
8.   Jefferson, D.A.; Millward, G.R.; Thomas, J.M.; Brydson, R.; Harriman, A.; Tsuno, K. Nature (London), 1986, 323, 428.
9.   Scherzer, C J. Appl. Phys., 1949, 20, 20.
10.   Smith, D.J.; Bursill, L.A.; Wood, G.J. Ultramicroscopy, 1985, 16, 19.
11.   Csencsits, R.; Gronsky, R. Ultramicroscopy, 1987, 23, 421.
12.   Treacey, M.M.J.; Newsam, J.M. Ultramicroscopy, 1987, 23, 411.
13.   Cowley, J.M.; Moodie, A.F. Acta Cryst., 1957, 10, 609; Goodman, P.; Moodie, A.F. Acta Cryst., 1976, A32, 823.
14.   Jefferson, D.A.; Millward, G.R.; Thomas, J.M. Acta Cryst., 1976, A32, 823.

15. Hirsch, P.B.; Howie, A.; Nicholson, R.B.; Pashley, D.W.; Whelan, M.J. Electron Microscopy of Thin Crystals, Butterworths, London, 1965, and references therein.
16. Cowley, J.M. Diffraction Physics, North Holland, 1975, and references therein.
17. Terasaki, O; Uppal, M.K.; Millward, G.R.; Thomas, J.M.; Watanabe, D. Proceedings of the 11th International Congress on Electron Microscopy, Kyoto, 1986, p. 1777.

Chapter 40

Competitive Role of Organic and Inorganic Cations in Directing One-Dimensional Zeolitic Structures

ZSM–48 and EU–1

Girolamo Giordano[1], Janos B. Nagy, Eric G. Derouane, Nicole Dewaele, and Zelimir Gabelica

Laboratory of Catalysis, Center for Advanced Materials Research, Facultés Universitaires Notre Dame de la Paix, Namur, 61 Rue de Bruxelles, B–5000 Namur, Belgium

The Bis-quaternary ammonium ions (e.g. hexamethonium, HM^{++}) favour the formation of two different one-dimensional zeolites, namely ZSM-48 and EU-1. The resulting structure essentially depends on the initial aluminium content in the starting hydrogel. The stability fields for both zeolites synthesized by using various reactant compositions have been established. Zeolite ZSM-48 is prepared from a silica hydrogel containing HM^{++} ions and alkali cations (Li, Na, and K), in presence or in absence of Al . For a higher initial Al content and increased crystallization time, zeolite EU-1 is obtained. The critical role of hexamethonium ions and inorganic cations on the crystallization rate of ZSM-48 was systematically studied. HM^{++} ions favor the ZSM-48 formation by interacting electrostatically with Al negative charges and stabilizing its structure by acting as pore fillers.

The synthesis of pure and highly crystalline zeolites from alluminosilicate hydrogels requires the study of the simultaneous effects of different parameters involved in the synthesis. Most of these zeolites are prepared in presence of organic directing

---

[1]Current address: Dipartimento di Chimica, Università della Calabria, Arcavacata di Rende, I–87030 Rende (CS), Italy

agents whose role can be drastically influenced by the actual composition of the hydrogel.

Recent work has pointed out the predominant templating role of bis-quaternary ammonium ions (e.g. hexamethonium ions) in directing one-dimensional zeolitic structures namely zeolites ZSM-48 and EU-1, the first representative member of the EUO family (1-4).

Zeolites having ZSM-48 topology also crystallize from hydrogels containing other linear organic structure directing agents, such as diamines (5) or various (poly)alkylamines (6).

Zeolite ZSM-50, another member of the EUO family possessing the topology of EU-1, also crystallizes in presence of dibenzyldimethylammonium ions (7).

The framework of ZSM-48 is composed of ferrierite-type sheets, connected in such a specific way as to generate linear 10-membered ring channels. The structure is a random intergrowth of the Imma-Cmcm frameworks and contains 48-T atoms per unit cell (8).

Recently Briscoe et al. (9) described the framework topology of zeolite EU-1. It consists of a unidimensional 10-membered ring channel system with side pockets formed at regular intervals off the channels. The unit cell contains 112-T atoms and the framework symmetry is Cmma.

The aim of this work is to evaluate the (competitive) role of other ingredients in stabilizing preferentially one or the other structure. The most interesting are the cationic species, namely the alkali and HM^{++} ions, potential neutralizing agents to AlO_2^- negatively charged framework centers. Indeed, alkali cations were shown to play an important role in the formation of many zeolites, either as structure directors in the nucleation process (10-12) or as stabilizing mineralizers during growth (11,12), thereby affecting the final size, morphology and composition of the crystallites.

Besides their obvious role as templates or structure directing agents (13) or as stabilizing pore fillers (3,14) the organic cations will also compete with alkali ions for the stabilization of the negatively charged framework (10,11,13).

The present approach consists in examining the structure and composition of selected crystalline zeolites obtained by heating under appropriate conditions hydrogels having the general composition:

$$x\ M_2O \quad y\ HMBr_2 \quad z\ Al_2O_3 \quad 60\ SiO_2 \quad 3000\ H_2O$$
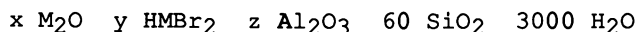
by systematically varying the initial cationic, organic and Al content to define the fundamental role of HM^{++} ions in each system, and to ultimately optimize the specific crystallization conditions for each zeolite.

Experimental

A series of hydrogels having the following molar composition:

$$x \; M_2O \quad y \; HMBr_2 \quad z \; Al_2O_3 \quad 60 \; SiO_2 \quad 3000 \; H_2O$$
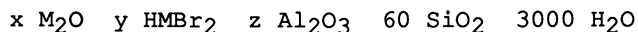
(where $HMBr_2$ stands for hexamethonium bromide; M= Li, Na or K; $0 \leq x \leq 12.5$; $0 \leq y \leq 25$ and $0 \leq z \leq 2$) was prepared by mixing the appropriate amounts of the following commercial ingredients: fumed silica (Aerosil Serva), aluminium hydroxyde (Serva), alkali hydroxyde (Janssen Chimica), hexamethonium bromide monohydrate (Janssen Chimica) and distilled water.

The reactants were carefully admixed in the following order: $Al(OH)_3$, MOH, $HMBr_2$, H_2O and SiO_2. The gel was transferred into a 60 ml Teflon-lined Morey-type autoclaves, and heated at 200 $\pm$ 2 °C, under autogeneous pressure, in static conditions. At predetermined times, the autoclaves were removed from the oven and quenched to room temperature in cold water. The reaction products were filtered, thoroughly washed with cold distilled water and dried overnight at 105 °C.

The identification of the solid phases and the determination of their crystallinities were carried out by X-ray powder diffraction (XRD), using a Philips PW 1349/30 X-ray diffractometer (Cu-Kα radiation). The crystallinity of each sample was evaluated by using as standard the most crystalline as-synthesized ZSM-48 from which the residual amorphous phase was further removed by ultrasonic treatment (15). Alkali and Al contents were determined by proton induced γ-ray emission (PIGE) (16) or atomic absorption, while the amount of organic and water molecules was evaluated by thermal analysis (Stanton Redcroft St 780 combined TG-DTA-DTG thermoanalyzer). The amount of defect groups in the structures was calculated from solid state MAS ^{29}Si-NMR (15).

Results and Discussion

Influence of the initial Al content

Preliminary adjustments of Na_2O and $HMBr_2$ concentrations defined gel compositions yielding each phase in reproducible conditions (see later). The values were:

$$Na_2O \quad 5 \; HMBr_2 \text{ for ZSM-48}$$
$$Na_2O \quad 10 \; HMBr_2 \text{ for EU-1.}$$

"Figure 1" shows the crystallinity variation for ZSM-48 and EU-1 zeolites, as a function of the initial
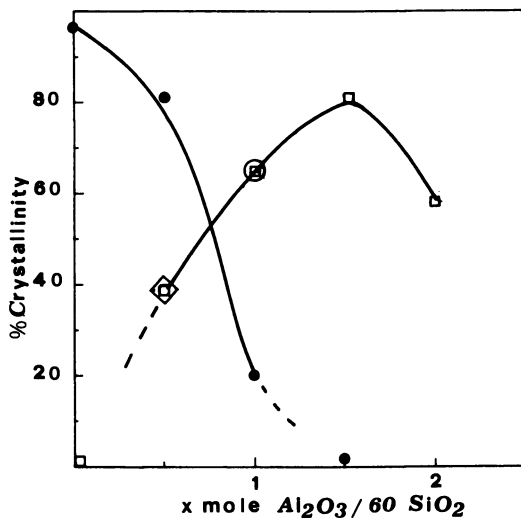
Figure 1. Variation of the percentage of crystallinity of zeolites ZSM-48 and EU-1 as a function of the Al_2O_3 content in the following precursor gel phases:

● = ZSM-48 $5Na_2O$ $5HMBr_2$ xAl_2O_3 $60SiO_2$ $3000H_2O$, (200°C, 66 h).

□ = EU-1 $10Na_2O$ $10HMBr_2$ xAl_2O_3 $60SiO_2$ $3000H_2O$, (200°C, 120 h).

◯ = EU-1 + ZSM-48 (30%)

◇ = EU-1 + ZSM-48 (40%) + α-quartz and cristobalite.

Al content (expressed in mole Al_2O_3 per 60 mole SiO_2), in each gel system. Nearly 100% crystalline ZSM-48 was obtained in Al-free gel systems. The crystallinity further markedly decreases until the upper limit of 1 Al_2O_3, above which no ZSM-48 crystals could be detected, even for longer reaction times. In the Al-free 10 Na_2O 10 $HMBr_2$ hydrogel, ZSM-48, cristobalite and α-quartz are the only crystalline phases detected, confirming that EU-1 can not be stabilized in such a system (2). For 0.5 Al_2O_3 about 40% crystalline EU-1 was detected along with ZSM-48 and smaller amount of cristobalite and α-quartz, and for 1 Al_2O_3 EU-1 and ZSM-48 are the only crystalline phases. EU-1 is the only phase present for 1.5 Al_2O_3, but over this value its crystallinity starts to decrease, in agreement with the well established inhibiting role of large amounts of Al in the crystallization rate of many zeolites (11).

Influence of $HMBr_2$

The amount of HM^{++} ions in the initial hydrogel drastically influences the nature of the zeolite formed and its crystallization kinetics. Pure and highly crystalline ZSM-48 is formed for a $HMBr_2$ molar concentration close to 2.5 ("Figure 2"). For higher $HMBr_2$ contents the crystallinity shows a slight decrease, probably due to a marked modification of the hydrogel composition and/or of the solubility of the various reactive species, induced by the excess of organic molecules. For HM^{++} concentrations lying between 1 and 2.5 mole, dense SiO_2 polymorphic phases co-crystallize with ZSM-48, while for lower HM^{++} concentrations, essentially below 0.5 mole, ZSM-5 was found to be predominant zeolitic phase. This latter observation confirms once more that Na^+ ions readily initiate the formation of 5-1 SBU in highly siliceous hydrogels (17,18).

Our investigations lead us to propose the following optimum composition to obtain 100% crystalline ZSM-48 after 48 h:

Na_2O 2.5 $HMBr_2$ 0-0.5 Al_2O_3 60 SiO_2 3000 H_2O
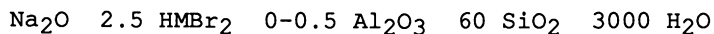
The optimum crystallinity of EU-1 was found in the 15-20 HM^{++} molar range and for 1.5 Al_2O_3 per 60 SiO_2 ("Figure 3").

Furthermore we could define more accurately the approximate gel composition in which pure EU-1 crystallizes with a relatively fast rate:

10 Na_2O 17.5 $HMBr_2$ 1.5 Al_2O_3 60 SiO_2 3000 H_2O
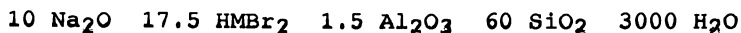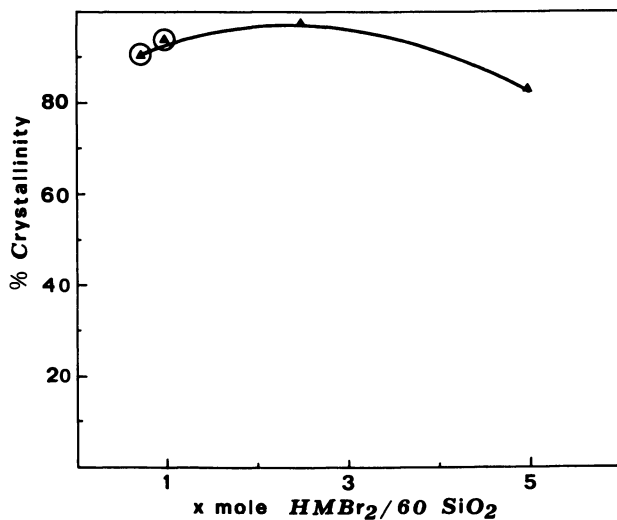
Figure 2. Variation of the percentage of crystallinity of zeolite
ZSM-48 synthesized from: $5Na_2O$ $xHMBr_2$ $0.5Al_2O_3$ $60SiO_2$ $3000H_2O$
gels (200 °C, 66 h), as a function of $HMBr_2$ content
○ = ZSM-48 + cristobalite.
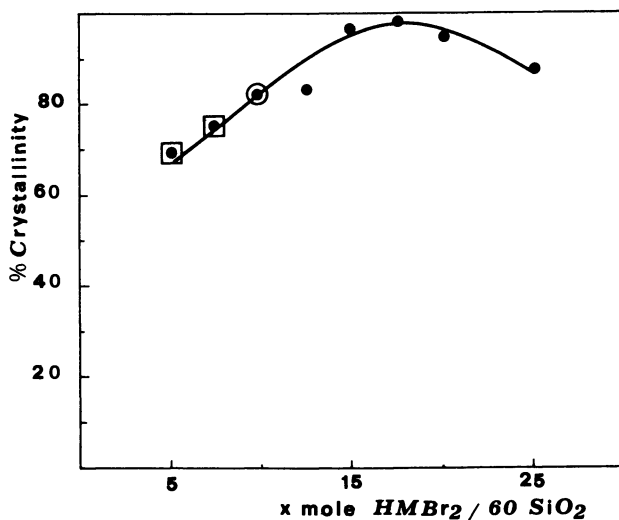
Figure 3. Variation of percentage of crystallinity of zeolite
EU-1 synthesized from: $10Na_2O$ $xHMBr_2$ $1.5Al_2O_3$ $60SiO_2$ $3000H_2O$
gels
(200 °C, 7 days), as a function of $HMBr_2$ content
● = EU-1
□ = EU-1 + α-quartz
○ = EU-1 + ZSM-48 (tracks).

crystallization of dense phases for low concentrations and general inhibition of crystallization for high HM^{++} contents. It is interesting to note that between 5 and 10 HM^{++}, ZSM-48 co-crystallizes with EU-1. A specific composition of both zeolites could not be measured but it seems reasonable to suppose that this ZSM-48 phase is not richer in Al than those crystallized from Si-richer gels, as most of the Al is probably utilized to build up the EU-1 framework.

Influence of NaOH concentration.
    The minimun Na_2O content (mole/60 mole SiO_2) to initiate the crystallization of ZSM-48 and EU-1 is respectively 2.5 and 7.5, while the highest crystallinity for each zeolite is observed for 5 and 10 mole Na_2O respectively ("Figure 4"). Because added as NaOH, a larger amount of Na^+ may also indirectly increase the crystallization through the more pronounced mobilizing effect of the OH^- ions (19), but also, more directly by stabilizing the first nuclei (10,11). The larger amount of Na^+ needed to accelerate the growth of an Al-richer material (here EU-1) suggests that, in both systems, Na^+ is at least as efficient as HM^{++} in the role of counterion to framework Al negative centers, in agreement to what is usually observed for zeolites synthesized in presence of both Na^+ and organic cations (12,15). Note that above these Na_2O optimum values, dense phases like α-quartz or cristobalite start to crystallize in both systems, as already observed in a previous study (2). Indeed as soon as the maximum amount of zeolite is formed the system is depleted in Al and merely behaves as usual Na-Si hydrogels.

Influence of the nature of alkali cations on the optimal synthesis procedure for ZSM-48.
    The different alkali cations affect nucleation and growth of zeolites in various ways, independently or in competition with the other organic cationic species. In particular, smaller hydrated structure-forming cations (towards water) like Li^+ or Na^+ readily favour, along the organic templates, the formation of regular structured aluminosilicate precursors or SBU, and essentially influence the nucleation process. Structure-breaking cations like K^+ induce less readily stable primitive building units, but can act as stabilizing mineralizers during growth (11,19).
    We have checked such a behaviour by replacing Na^+ ions by Li^+ and K^+, in the gels giving ZSM-48 in "optimum yield", namely

$$M_2O \quad 2.5\ HMBr_2 \quad x\ Al_2O_3 \quad 60\ SiO_2 \quad 3000\ H_2O$$
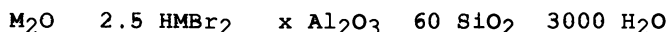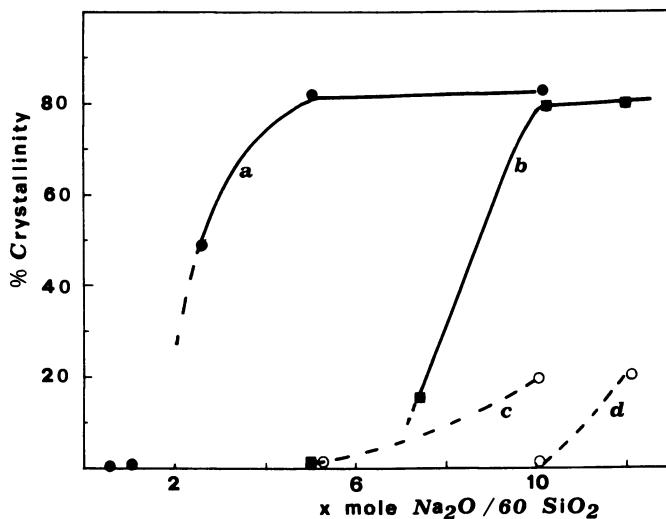
Figure 4. Percentage of crystallinity for zeolites ZSM-48 and
EU-1 as a function of Na_2O content in the gel.

Curve a: ZSM-48 synthesized from:
          xNa_2O $5HMBr_2$ $0.5Al_2O_3$ $60SiO_2$ $3000H_2O$;
curve b: EU-1 synthesized from:
          xNa_2O $10HMBr_2$ $1.5Al_2O_3$ $60SiO_2$ $3000H_2O$;
curve c: α-quartz and/or cristobalite co-crystallized with
          ZSM-48;
curve d: α-quartz co-crystallized with EU-1.

with two different Al contents (x= 0 or 0.5). The so obtained crystallization kinetic curves of ZSM-48 in absence ("Figure 5a") and in presence ("Figure 5b") of Al were compared for each cationic system. In all three cases, the crystallization was found faster in absence of Al, in agreement with what was generally observed for (M) ZSM-5 (20). In addition, the induction period varies in the following order:

$$Li \leq Na < K,$$

suggesting that the structure-forming Li^+ and Na^+ better favour the ZSM-48 nucleation process than K^+. The further growth rates for the three systems appear comparable ("Figure 5a").

Table I. Cation and Al contents of four ZSM-48 samples synthesized from 5 M_2O 2.5 $HMBr_2$ (0 or 0.5)Al_2O_3 60 SiO_2 3000 H_2O after 48 h

Sample	M^+/u.c. a	HM^{++}/u.c. b	Al/u.c. a
Na-ZSM-48	0.05	1.0	-
(Na+Al)ZSM-48	0.20	1.0	0.59
K-ZSM-48	0.22	1.1	-
(K+Al)ZSM-48	0.23	1.1	0.62

a: atomic absorption; b: TG-DTA

The amounts of incorporated alkali cations remain low (Table I) and these cations only neutralize the defect SiO^- negative charges for Al-free samples. Note that the HM^{++} content for each sample is similar, this strongly suggesting that the essential stabilization of the framework is achieved by the pore filling action, as in the similar system yielding Nu-10 (14). However, this filling is not completely achieved by the organics (about 85%), because, for structural reasons, about one HM^{++}/u.c. is the maximum possible amount that can be incorporated in the ZSM-48 framework (see below). Similar kinetics trends are observed in presence of aluminium ("Figure 5b") with the difference that Na^+ is also incorporeted during growth, in similar amount than K^+, both probably acting to a limited extent, as AlO_2^- counterions.
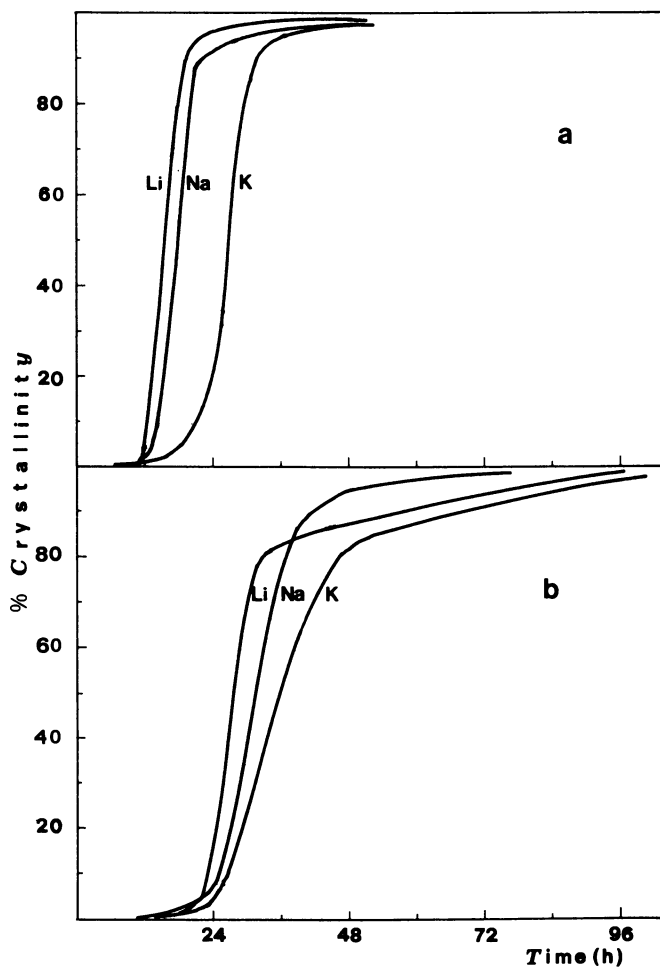
Figure 5.Crystallization kinetics of zeolite ZSM-48 in presence of Li^+, Na^+ and K^+ ions, without Al (a) and in presence of 0.5 mole Al_2O_3 in the gel (b): $5Na_2O$ $2.5HMBr_2$ (0 or 0.5)Al_2O_3 $60SiO_2$ $3000H_2O$.

Competitive role of Na+ and HM++ species

Unit cell composition of typical zeolites prepared from different Na^+ bearing hydrogels are reported in Table II.

The constant Na/Al ratios measured for two ZSM-48 samples crystallized from two different gel compositions at different synthesis times and from which the residual amorphous phase was removed by ultrasonic cleaning, confirms that Na^+ ions are continuously incorporated during growth. In neither case they can neutralize totally the Al bearing negative charges, suggesting that the HM^{++} ions also participate in this neutralization process. Nevertheless, the amount of organic ions was found to be remarkably constant, as in the case of the other alkali systems (Table I).

Similary, in sample 4, about one HM^{++} was again found occluded per unit cell of ZSM-48. However sample 4 contains a slightly larger amount of Na^+/u.c., and this may be due to the larger Na_2O content characterizing its hydrogel precursor (Table II). This suggests that Na^+ ions probably do not play their neutralizing role as counterions to Al. At least our observation confirms that, in our synthesis conditions, Na^+ do not bring Al to the structure.

Mechanism of HM++ action

All the ZSM-48 samples synthesized from the above envisaged gel systems, accomodate about one HM^{++} per unit cell, this corresponding to about 85% of the total pore filling. By contrast, the Al concentration can be different from one sample to another, as its incorporation is governed by the initial Al content in the gel, provided it is not too important. However, considering the framework charge balance, at least part of the HM^{++} ions must also act as Al counterions. We therefore propose the following model to explain the role of HM^{++} ions in directing syntheses of zeolites with linear channel systems such as ZSM-48 and EU-1.

During the first restructuration of the silicate or Si-rich aluminosilicate complexes prior to the zeolitic nucleation, the HM^{++} entities play a structure stabilizing role. By their particular linear shape, they favour the formation of channel systems. Simultaneously, they can also neutralize one AlO_2^- negative center of the aluminosilicate complex by its positive $-N^+(CH_3)_3$ ends. Note that this does not exclude the formation of a cell involving only one (or less) Al, that then interacts only with one positively charged end of the template. The other positive end will be solicitated only if enough Al is available in the gel, up to a **maximum of 2 Al per one HM^{++}, i.e. per unit cell.**

Table II. Nature crystallinity and chemical composition of various zeolites synthesized in presence of Na^+ and HM^{++} ions

Sample	Al_2O_3/SiO_2 (gel)	Synthesis time, (h)	Solid phase (%crystal.)	Composition per unit cell ^{a}					Pore filling (%)
				Al ^{b}	Na ^{b}	H_2O ^{c}	HM^{++} ^{d}	SiOR ^{e}	^{f}
1	0	48	ZSM-48 (97)	n.d.	n.d.	1.80	0.98	11.1	82
2	0.0083	66	ZSM-48 (81)	0.78	0.24	2.31	1.01	10.6	85
"	0.0083	90	ZSM-48 (75)	0.72	0.24	2.25	1.00	10.1	84
3	0.0083	48	ZSM-48 (93)	0.60	0.20	2.97	1.04	-	87
"	0.0083	66	ZSM-48 (97)	0.67	0.24	2.96	1.05	-	88
4	0.0083	48	ZSM-48 (83)	0.74	0.49	3.42	0.96	10.9	80
5	0.0250	120	EU-1 (80)	2.10	0.44	7.40	1.30	3.5	^{g}

Correspondence between sample number and gel composition:

1	5 Na_2O	5 $HMBr_2$		60 SiO_2	3000 H_2O
2	5 Na_2O	5 $HMBr_2$	0.5 Al_2O_3	60 SiO_2	3000 H_2O
3	5 Na_2O	2.5 $HMBr_2$	0.5 Al_2O_3	60 SiO_2	3000 H_2O
4	10 Na_2O	5 $HMBr_2$	0.5 Al_2O_3	60 SiO_2	3000 H_2O
5	10 Na_2O	10 $HMBr_2$	1.5 Al_2O_3	60 SiO_2	3000 H_2O

a   For sake of comparison, one unit cell of EU-1 is assumed to have 48 T atoms

b   Evaluated by PIGE

c   Evaluated by TG-DTA

d   Evaluated by TG-DTA and ammonia titration

e   Evaluated by 29Si-NMR

f   Percentage of filling as calculated by considering the length of one HM^{++} ion equal to 14.05 Å, and by considering the total channel length of one ZSM-48 unit cell equal to 16.8 Å.

g   The total length of the tortuous channel system of EU-1 is not known.

The Na and Al contents for sample 3 at (48 h) were evaluated by atomic absorption

The final structure so genereted is a Cmcm-Imma intergrowth (8) in which the Cmcm unit is only able to accomodate two Al at stable positions.

For larger Al gel concentrations rings involving an even number of T atoms (e.g. four membered rings) will be preferentially favoured and the final structure stabilized by the HM^{++} ions will be different in terms of geometry and concentration of stable T sites for aluminium (19). EU-1 is one example of such a structure, stabilized by HM^{++} ions under the particular conditions described.

For intermediate Al concentrations in the gel phases, one can suppose that both structures co-crystallize, each incorporating the appropiate amount of Al.

As a conclusion, HM^{++} ions are not exclusive templates for a given structure but will stabilize an aluminosilicate structure that is preliminarily favoured by other variables such as the Al content in the gel. They will act partly as counterions to the negative framework, partly as pore fillers. Obviously, they exclusively act as pore fillers in the Al free gels, in which alkali cations can be present (this work) or absent (2).

In ZSM-48 the presence of HM^{++} generates a marked number of structural Si—O—R defect groups (up to 11 SiOR/ u.c.) (R = H, M^+ or HM^{++}), as measured by ^{29}Si-NMR (Table II). In contrast, when a linear diaminoalkane is used as template a smaller amount of defect groups is measured (about 3.5 SiOR/u.c.) (21). The difference between these two values, about 8 SiOR/u.c., can be easily explained by considering the actual size of the bulky terminal trimethylammonium groups. Being larger (6.9 Å) than the average ZSM-48 channel diameter (about 5.3*5.6 Å), they are accomodated within the structure by creating 4 SiOR groups at each end of the channel that result from an empty T position ("Figure 6"). Such defect groups linked to empty T positions have also been detected in high silica ZSM-5 (15).By contrast few structural defects are detected in the EU-1 framework. This is easily explained by considering that the side pockets resulting from the high tortuosity of the structure (9) more easily accomodate the terminal trimethylammonium groups of the HM^{++} ion.

Conclusion

The framework of zeolite ZSM-48 can be oriented by hexamethonium (HM^{++}) templates in various gel systems having defined Al concentrations. The HM^{++} ions
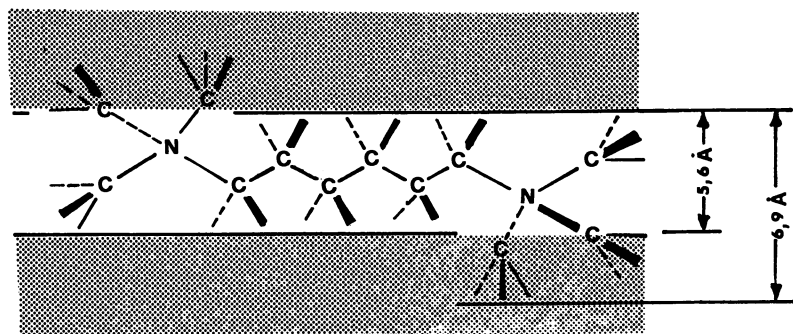
Figure 6.Schematic localization of hexamethonium ions in ZSM-48 channel structure, generating SiO⁻ defects near the terminal trimethylammonium groups of the template.

stabilize the zeolitic structure in formation and, by their particular linear shape, they favour the generation of the channel system. In addition, they also neutralize the negative charges of the structure, linked either to Si-O-Al$^-$ entities or to Si-O$^-$ defect groups. Because the complete filling by the HM^{++} ions represents one HM^{++} per unit cell, the maximum number of Al atoms that can be introduced into the framework, is therefore equal to two. Interestingly because of steric interactions, the HM^{++} ions introduce defect groups into the structure, the amount of which can be easily rationalized by supposing the presence of two missing T sites per unit cell. Note that if ZSM-48 is formed in presence of polymethylenediamines, much less defect groups are introduced in the structure. Alkali cations play a secondary role and probably neutralize the Si-O$^-$ defect groups.

A higher Al content in the hydrogel is a predominant variable that leads to a differently arranged Al-richer EU-1 framework. HM^{++} stabilize this framework as counterions along with the alkali cations and also as pore filling agents, but do not initiate its nucleation. The more open, tortuous pore structure that results, accomodates the HM^{++} ions easily, without much steric constraint, and the EU-1 structure contains a far smaller number of Si-O$^-$ defects than ZSM-48.

Literature cited

1. Casci, J.L.; Whittam, T.V.; Lowe, B.M. Proc. 6th Intern. Zeolite Conference, 1984, p 894.
2. Dodwell, G.W.; Denkewicz, R.P.; Sand, L.B. Zeolites 1985, 5, 153.
3. Dewaele, N.; Gabelica, Z.; Bodart, P.; B.Nagy, J.; Giordano, G.; Derouane E.G. Stud. Surf. Sci. Catal. 1988, 37, 65.
4. Casci, J.L. Stud. Surf. Sci. Catal. 1986, 28, 215.
5. Araya, A.; Lowe, B.M. J. Catal. 1984, 85, 135.
6. Chu, P. Eur. Patent 23 089, 1981 and U.S. Patent 4 397 827, 1983.
7. Kaeding, W.W. Eur. Patent 219 271, 1987.
8. Schlenker, J.L.; Rohrbaugh, W.J.; Chu, P.; Valyocsik, E.W.; Kokotailo, G.T. Zeolites 1985, 5, 355.
9. Briscoe, N.A.; Johnson, D.W.; Shannon, M.D.; Kokotailo, G.T.; McCusker, L.B. Zeolites 1988, 8, 74.
10. Gabelica, Z.; Blom, N.; Derouane, E.G. Appl. Catal. 1983, 5, 227 and references cited therein.
11. Gabelica, Z.; Derouane, E.G.; Blom, N. In Catalytic Materials: Relationship between Structure and Reactivity; White, T.E., Jr. et al., Eds.; ACS Symposium

Series No. 248; American Chemical Society: Washington, DC, 1984; p 219.

12. Nastro, A.; Gabelica, Z.; Bodart, P.; B.Nagy, J. <u>Stud. Surf. Sci. Catal</u>. 1984,<u>19</u>,131.

13. Lok, B.M.; Cannan, T.R., Messina, C.A. <u>Zeolites</u> 1983,<u>3</u>,252.

14. Pellegrino, C.; Aiello, R.; Gabelica, Z. In <u>ACS Symposium Series "Advances in Zeolite Synthesis"</u> (this book) and references cited therein.

15. B.Nagy, J.; Bodart, P.; Colette, H.; El Hage-Al Asswad, J.; Gabelica, Z.; Aiello, R.; Nastro, A.; Pellegrino, C. <u>Zeolites</u> 1988,<u>8</u>,209.

16. Debras, G.; Derouane, E.G.; Gilson, J.P.; Gabelica, Z.; Demortier, G. <u>Zeolites</u> 1983,<u>3</u>,37.

17. Nastro, A.; Colella, C.; Aiello, R. <u>Stud. Surf. Sci. Catal</u>. 1985,<u>24</u>,39.

18. Bellussi, G.; Perego, G.; Carati, A.; Cornaro, U.; Fattore, V. <u>Stud. Surf. Sci. Catal</u>.1988,<u>37</u>,37.

19. Guth, J.L.; Caullet, P. <u>J. Chim. Phys</u>. 1986,<u>83</u>,155.

20. Rollman, L.D. In <u>Zeolites, Science and Technology</u>; Ribeiro, F.R. et al., Eds.; M. Nijhoff, Den Haag, 1984, p 109.

21. Dewaele, N. Ph.D. Thesis, Namur University, Namur, 1988.

22. Van Santen, R.A.; Keijsper, J.; Ooms, J.; Kortbeek, A.G.T.G. <u>Stud. Surf. Sci. Catal</u>. 1986,<u>28</u>,169.

Chapter 41

Phase Identification of Hydrothermal Crystallization Products from $M_2O-SiO_2-SnO_2-H_2O$ Gels or Solutions

Edward W. Corcoran, Jr., J. M. Newsam, H. E. King, Jr., and D. E. W. Vaughan

Exxon Research and Engineering Company, Route 22 East, Annandale, NJ 08801

A number of phases have been produced by hydrothermal crystallizations from $M_2O-SiO_2-SnO_2-H_2O$ gels or solutions. The products of such syntheses are frequently multiphasic, complicating attempts at composition and structure definition. Preliminary microcrystal diffraction experiments using synchrotron X-rays and quantitative treatment of in-house powder X-ray diffraction data have enabled phase identification and facilitated the isolation of two largely phase-pure materials. Infrared spectroscopy and solid state ^{29}Si and ^{119}Sn nmr are consistent with the presence of octahedrally coordinated tin and tetrahedrally coordinated silicon in these phases.

The recent descriptions of the ALPO-n, SAPO-n and MeAPO-n families of microporous materials illustrate that hydrothermal syntheses can afford a wide and diverse range of four-coordinate framework structures based on near-regular tetrahedra [1,2]. As building blocks, octahedra and tetrahedra can also be combined, in various proportions, into a variety of structure types [3,4]. Reflecting the conditions used for conventional synthesis [3,4], most of these structures are condensed, with little accessible pore volume. There are, however, examples of both synthetic [5-7] and natural materials [8-11] that have microporous crystalline structures. Further, the formation chemistry of silicates and aluminosilicates [12,13] illustrates that the more open structures are generally produced under relatively mild conditions. Open octahedral-tetrahedral structures with large pore systems might therefore also be accessible under appropriate low temperature hydrothermal conditions.

As an exemplary system, we have been studying crystallizations from stannosilicate gels and solutions with various compositions in the system $M_2O-SiO_2-SnO_2-H_2O$ (M = Li, Na, K, Cs). Previous literature data (discussed below) suggest that there is scope for a range of structure types to be produced in this system, based both on possible variability in the relative proportions of octahedra and tetrahedra, and a possible diversity in the manners in which they can be interlinked. Broad scope in the possible product structures, however, implies that the simultaneous crystallization of more than one phase might be common. Initial scoping experiments are therefore likely to be complicated by problems associated with product multiphasic behavior.

In the present report we describe initial syntheses in the $M_2O-SiO_2-SnO_2-H_2O$ system. We illustrate how developments in characterization techniques can facilitate the identification of new phases in these types of systems. We mention use of synchrotron X-radiation in microcrystal diffraction experiments, full profile fitting of 'in-house' powder X-ray diffraction data, and infrared and solid state ^{129}Sn and ^{29}Si nmr spectroscopies.

Background on Crystalline Stannosilicates

Several minerals containing octahedrally-coordinated tin and tetrahedrally-coordinated silicon are known (Table 1). In addition to the naturally-occurring materials, hydrothermal crystallizations at higher temperatures (T>350°C) have been reported [14-18], including the syntheses of six sodium stannosilicates ($Na_2Sn_3Si_9O_{25}$, $Na_8Sn_7Si_{20}O_{58}$, $Na_4Sn_5Si_{10}O_{32}$, $Na_{10}Sn_2Si_9O_{27}$, $Na_{18}Sn_8Si_{12}O_{49}$, $Na_2Sn_2Si_6O_{17}$) [15-17], three calcium stannosilicates ($CaSnSiO_5$, $CaSnSi_3O_9$, $CaSnSi_3O_9 \cdot 2H_2O$) [14], and a potassium stannosilicate ($K_2SnSi_3O_9$) [18]. Presumably because of the severity of the reaction conditions employed, only one of these phases is reported to contain water [14].

Table 1. Stannosilicate Minerals*

Name	Approximate Composition	Reference
malayaite	$CaSnSiO_5$	19
brannockite	$(K,Na)Li_3Sn_2Si_{12}O_{30}$	20
sorensenite	$Na_4SnBe_2Si_6O_{18} \cdot 2H_2O$	21
eakerite	$Ca_2SnAl_2Si_6O_{16}(OH)_2 \cdot 2H_2O$	22
asbecasite	$Ca_3Ti_{0.8}Sn_{0.2}As_6Si_2Be_2O_{20}$	23
pabstite	$BaSn_{.77}Ti_{.23}Si_3O_{10}$	24
stokesite	$CaSnSi_3O_9 \cdot 2H_2O$	25
sverigeite	$NaMgMnBe_2SnSi_3O_{12}OH$	26

*Arandisite is reported to be a stannosilicate, but no structural or compositional data are available [27]. Other minerals which may contain tin have also been reported; examples include yftisite [28] and varlamoffite [29].

Some materials for which structural data are available are listed in Table 2. Incorporation of tin into tetrahedral frameworks has been reported [30], although details about the local tin coordination are still lacking.

Synthesis of Stannosilicates

The reactants tin(IV) chloride, alkali-metal base, and colloidal silica (Ludox-HS40) were thoroughly mixed at room temperature, according to the ratios 2-5M_2O:SnO_2:4-10SiO_2:80-100H_2O, for each synthesis [47]. Cabosil (fumed silica) and sodium stannate were also used as reactants. The resulting gels were heated (without cold-aging or agitation) in stainless steel autoclaves at temperatures of between 150°C and 225°C and at autogenous pressures for periods ranging from 3 days to 10 weeks. The reaction vessels were then cooled to room temperature and the product(s) removed and washed with water. Crystalline materials generally resulted but, as with zeolite syntheses, simultaneous crystallization of two or more phases is common. This is evident in Table 3 which lists major products from a range of starting compositions and conditions within the system.

When a gel with M = Na at a composition of 2Na_2O:SnO_2:4SiO_2:80H_2O is heated for three weeks at 200°C a stannosilicate phase, labelled A, results. The optimum reaction gel for producing this compound is obtained by mixing an aqueous sodium hydroxide solution with 40% colloidal silica (14.9g NaOH in 20g distilled H_2O; 27.4g Ludox-HS40) followed by addition of tin(IV) chloride in water (16.0g $SnCl_4 \cdot 5H_2O$ in 20g distilled H_2O). Chemical analyses of phase A materials indicate an approximate formula of $Na_8Sn_5Si_{12}O_{36} \cdot nH_2O$. Higher levels of both sodium and silica produced a different phase (designated L) at 200°C, though much longer synthesis times were necessary. Samples of this material typically contained an amorphous component which persisted even after crystallization periods of 6 weeks. Powder X-ray diffraction and scanning electron microscopy data on phase L materials suggest that it may have a layered structure.

When M = Na, Li (1:1) crystallization of a gel (with composition Li_2O:Na_2O:SnO_2:4SiO_2:80H_2O) for 3 weeks at 200°C yields another stannosilicate phase labelled B. The reaction gel for this material is created by combining aqueous base and silica with dissolved tin(IV) chloride (11.3g NaOH and 3.9g LiOH in 20g distilled H_2O with 27.9g Ludox-40; 16.3g $SnCl_4 \cdot 5H_2O$ in 20g distilled H_2O is added). Mixtures containing predominantly phase B were also recovered from M = Na gels when the silica source was varied. Phase B exhibited spherical aggregates of microcrystals in scanning electron micrographs. An approximate phase B formula of $Na_{16}Sn_8Si_{24}O_{72} \cdot nH_2O$ was indicated by chemical analysis.

Table 2. Some Stannosilicates, Stannogermanates and Related Materials
for which Structural Details are Known

Name	Formula	a (Å)	b (Å)	c (Å)	α (°)	β (°)	γ (°)	Ref.
Sorensenite	$Na_4 Sn Be_2 Si_6 O_{18} (H_2O)_2$	20.698(17)	7.442(5)	12.037(11)	90.	117.28(6)	90.	21,38
Malayaite	$Ca Sn Si O_5$	7.149	8.906	6.667	90.	113.4	90.	19,31
Benitoite-type	$Ba Sn Si_3 O_9$	6.728(5)	6.728(5)	9.838(5)	90.	90.	120.	32
Eakerite	$Ca_2 Sn Al_2 Si_6 O_{18} (OH)_2 (H_2O)_2$	15.892(7)	7.721(3)	7.438(3)	90.	101.34(3)	90.	22
Wadeite-type	$K_2 Sn Si_3 O_9$	6.860	6.860	10.120	90.	90.	120.	33
Wadeite-type	$Rb_2 Sn Si_3 O_9$	6.943	6.943	10.040	90.	90.	120.	33
Na,Sn-Silicate	$Na_4 Sn_2 Si_5 O_{16} H_2O$	20.883(2)	13.794(1)	5.231(1)	90.	90.	110.02(1)	34
Na,Sn-Silicate	$Na_8 Sn Si_6 O_{18}$	10.576(3)	10.183(2)	7.340(2)	90.	92.90(2)	90.	35
Na,Sn-Silicate	$Na_8 Sn Si_6 O_{18}$	7.344(1)	7.344(1)	7.344(1)	87.85(1)	87.85(1)	87.85(1)	36
Asbecasite	$Ca_3 Ti_{0.8} Sn_{0.2} As_6 Si_2 Be_2 O_{20}$	8.36(2)	8.36(2)	15.30(3)	90	90	120.	23
Varlamoffite	$Fe_6 Al_2 Sn_{26} Si_{1.5} O_{67} (H_2O)_{22.5}$	4.741	4.741	3.139	90	90	90	37
Stokesite	$Ca Sn Si_3 O_9 (H_2O)_2$	14.465	11.625	5.235	90	90	90	39
Nigerite – 24	$Al_{14.9} Sn_2 Fe_{2.8} Zn_{1.4} O_{30} (OH)_2$	18.826(10)	18.826(10)	18.826(10)	17.508(3)	17.508(3)	17.508(3)	40
Benitoite-type	$Ba Sn Ge_3 O_9$	6.894(5)	6.894(5)	10.233(5)	90.	90.	120.	32
Grenat-type	$Na_2 Ca Sn_2 Ge_3 O_{12}$	12.430	12.430	12.430	90.	90.	90.	42
Wadeite-type	$Cs_2 Sn Ge_3 O_9$	7.288	7.288	10.472	90.	90.	120.	33
Wadeite-type	$K_2 Sn Ge_3 O_9$	12.082	12.082	10.181	90.	90.	120.	33
Wadeite-type	$Rb_2 Sn Ge_3 O_9$	12.305	12.305	10.205	90.	90.	120.	33
Wadeite-type	$Tl_2 Sn Ge_3 O_9$	12.351	12.351	10.134	90.	90.	120.	33
Na,Sn-Germanate	$Na_4 Sn_2 Ge_4 O_{12} (OH)_4$	5.778	11.615	5.540	107.62	75.75	94.75	41
Na,Sn-Germanate	$Na_4 Sn_2 Ge_5 O_{16} (H_2O)$	6.951(1)	20.062(2)	5.370(1)	90.	90.	93.25(1)	43
Na,Sn-Germanate	$Na_6 Sn_4 Ge_5 O_{20} (OH)_2$	10.252(1)	15.504(2)	6.413(1)	96.89(1)	107.56(1)	91.63(1)	44
Na,Sn-Germanate	$Na_8 Sn_4 Ge_{10} O_{30} (OH)_4$	6.956	5.362	20.790	90.	106.21	90.	45
Na,Sn-Germanate	$Na_4 Sn_2 Si_3 O_{12}$	9.023(4)	9.023(4)	21.933(7)	90.	90.	120.	46

Table 3. Stannosilicate Reaction Components and Compositions

Gel Composition	Reactant Source	Time	Temp.	Product
$2Na_2O:SnO_2:4SiO_2:80H_2O$	colloidal silica, $SnCl_4 \cdot 5H_2O$	21d	200°C	A*
$5Na_2O:SnO_2:10SiO_2:80H_2O$	colloidal silica, $SnCl_4 \cdot 5H_2O$	60d	200°C	L*
$Li_2O:Na_2O:SnO_2:4SiO_2:80H_2O$	colloidal silica, $SnCl_4 \cdot 5H_2O$	21d	200°C	B*
$Cs_2O:Na_2O:SnO_2:4SiO_2:80H_2O$	colloidal silica, $SnCl_4 \cdot 5H_2O$	21d	200°C	K*
$2Na_2O:SnO_2:4SiO_2:80H_2O$	fumed silica, $SnCl_4 \cdot 5H_2O$	21d	200°C	B,A,L
$2Na_2O:SnO_2:4SiO_2:80H_2O$	colloidal silica, Na_2SnO_3	21d	200°C	A
$2Na_2O:SnO_2:4SiO_2:80H_2O$	sodium silicate, $SnCl_4 \cdot 5H_2O$	21d	200°C	A,L
$3Na_2O:SnO_2:6SiO_2:80H_2O$	sodium silicate, Na_2SnO_3	25d	200°C	L
$2Cs_2O:SnO_2:4SiO_2:95H_2O$	colloidal silica, $SnCl_4 \cdot 5H_2O$	30d	200°C	K
$K_2O:Na_2O:SnO_2:4SiO_2:80H_2O$	colloidal silica, $SnCl_4 \cdot 5H_2O$	7d	150°C	A
$K_2O:Na_2O:SnO_2:4SiO_2:80H_2O$	colloidal silica, $SnCl_4 \cdot 5H_2O$	7d	200°C	A,L

* Represents optimum preparation for phase purity

Crystallization of a reaction gel with a composition of $Cs_2O:Na_2O:SnO_2:4SiO_2:80H_2O$ yielded a product having a diffraction pattern similar to that of phase B, although with altered peak positions and intensities presumably reflecting cesium incorporation. The sole use of either LiOH or CsOH without NaOH in the reaction gel yielded stannosilicate phases other than A, B, or L.

Phase Identification

Sodium Stannosilicate Phase A

Examination of the first new phase encountered in the $Na_2O \cdot SiO_2 \cdot SnO_2 \cdot H_2O$ system (labelled A) yielded by chemical analysis a Si:Sn ratio of about 2.4. The powder X-ray diffraction pattern for the material is shown below in Figure 1. Thermogravimetric analysis data showed a reversible loss of 10% water, commencing at ~100°C. ^{29}Si nmr spectra measured from initial samples showed two peaks at chemical shifts of -88.5 ppm and -90.3 ppm from tetramethylsilane. ^{119}Sn nmr data showed a single, relatively sharp peak at -102 ppm from SnO_2, consistent with Sn(IV) octahedrally coordinated by oxygen, and without immediate Sn neighbors.

The main sharp features in the PXD pattern were indexed, with the aid of the VISSER program [48], on the basis of a monoclinic unit cell, with a = 6.509(8)Å, b = 11.615(4)Å, c = 6.524(4)Å, and β = 104.73(6)°. Several samples showed additional, broader lines with variable intensities relative to the phase A pattern that were not indexable on the basis of the monoclinic cell (Figure 2). These lines were ascribed to a second phase, an interpretation confirmed by experiments with acid washing. A treatment for 1h in 1M HCl, followed by water washing removed essentially all of these broader lines, leaving a largely intact phase A pattern (Figure 1). One phase A sample showed clearly defined splitting of the 110, 111 and 221 peaks (Figure 2). These 'splittings' were also not explicable on the basis of the monoclinic cell, suggesting initially that phase A might have a larger unit cell volume or symmetry lower than monoclinic (see below).

Scanning electron micrographs of typical phase A products showed well-defined plates, typically ~5μm thick and up to 15μm in length (Figure 3). Crystallites in this size range are amenable to study by microcrystal diffraction techniques using synchrotron X-rays [49-52] and, indeed, phase A samples were used in the process of developing these methods [52]. Diffraction data were collected (on beamline X10A at the National Synchrotron Light Source) from a phase A crystallite (5x10x10μm) selected from one of the early synthesis batches and mounted on a 50μm diameter solid glass fiber. A 120s

COUNTS
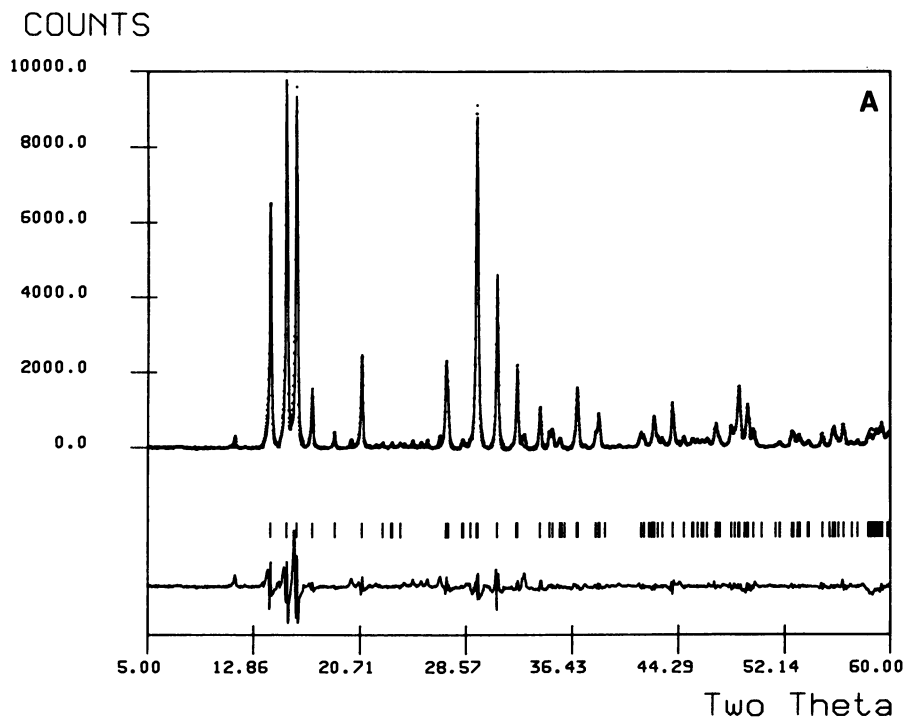
Figure 1. Results of full pattern fitting (after [53]) of the PXD pattern of an acid-treated phase A sample, based on an orthorhombic unit cell (refined lattice constants a = 7.940(3)Å, b = 10.338(4)Å, c = 11.591(5)Å). The low angle peaks are somewhat asymmetric and are hence not fitted well by the assumed symmetric pseudo-Voigt peak shape.

COUNTS
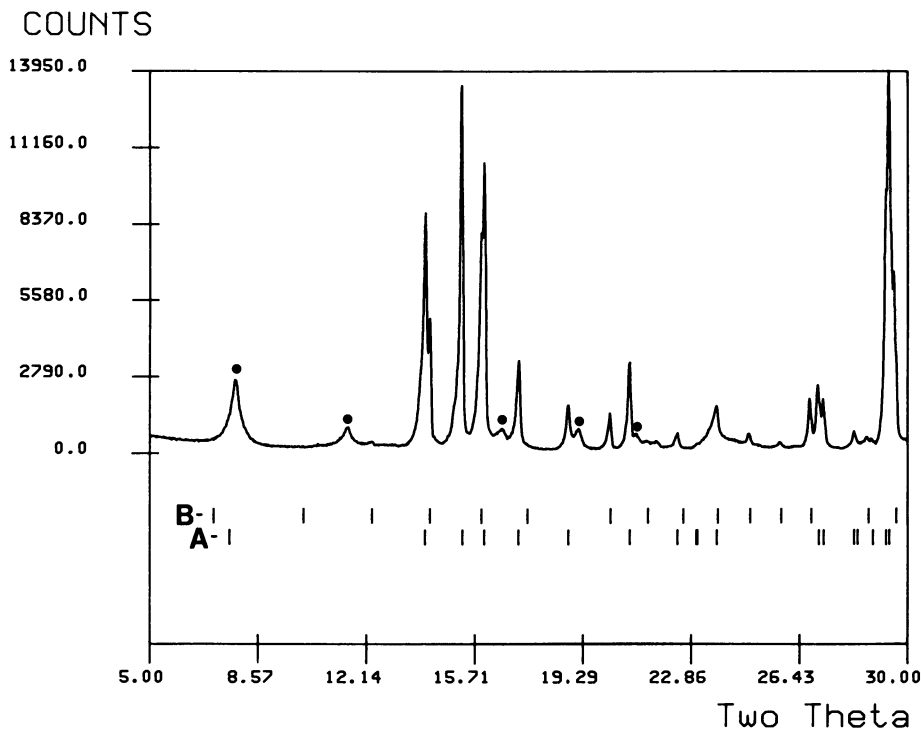
Figure 2. PXD data for a phase A preparation containing a significant phase B component. The sets of vertical bars indicate computed reflection positions based on a C-centered orthorhombic unit cell with a = 7.94Å, b = 10.34Å and c = 11.59Å (phase A – lower), and a primitive cubic unit cell with a = 12.44Å (phase B – upper). The positions of additional impurity peaks are indicated by ●.
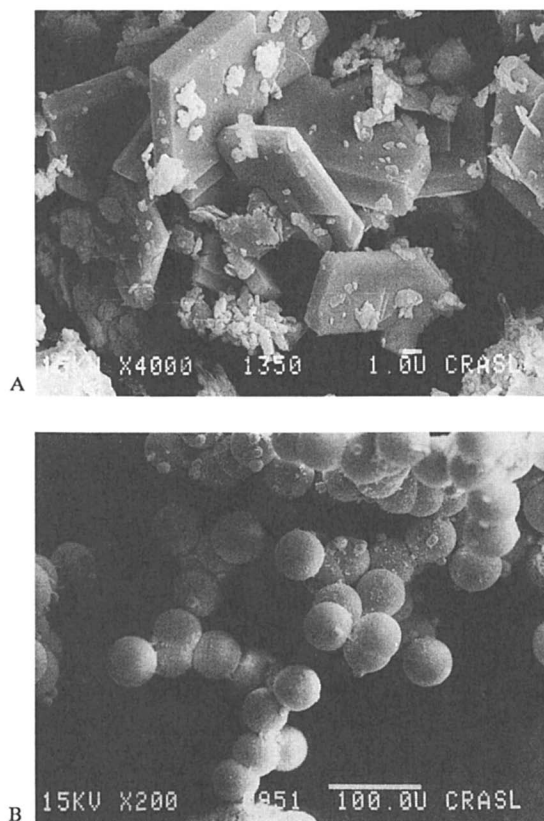
Figure 3. Scanning electron micrographs of typical phase A and phase B samples .

rotation photograph was used as the basis for initial peak location [52], and automatic indexing of the found peaks yielded a monoclinic cell of similar dimensions to that listed above. The near equality of the a and c axes and the resulting symmetry of the Niggli cell suggested that the true direct cell was C-centered orthorhombic. The unit cell constants then optimized based on the setting angles of 15 accurately centered reflections were a = 7.940(6)Å, b = 10.338(9)Å, c = 11.591(12)Å, α = 89.98(8)°, β = 89.94(7)° and γ = 89.98(7)°. The orthorhombic symmetry of the cell was confirmed by the similar intensities of each of several hkl, $\overline{h}$kl and hk$\overline{l}$ sets of reflections, typified by the reasonable merging residuals obtained for a limited set of intensity data collected from this same crystal. The PXD patterns of several phase A samples were subsequently indexed satisfactorily on the basis of similar C-centered orthorhombic unit cells. The results of a full pattern decomposition [53] based on this orthorhombic unit cell for an acid-treated phase A material (which contains additional low level peaks arising from degradation products) is shown in Figure 1. The microcrystal diffraction data indicated the space group to be C222$_1$ (No. 20) although the limited number of intensity data collected from the microcrystal (78 reflections, 24 unique) did not permit full structure solution.

These data, however, illustrate that the unit cell and phase information provided quite readily by microcrystal diffraction measurements using synchrotron X-rays can enable further analyses of powder or 'in-house' single-crystal diffraction data (the latter being well illustrated, for example, by the structural study of VOHPO$_4$·1/2H$_2$O [54]). Developments aimed at enabling accumulation of full, internally consistent and precise sets of intensity data from microcrystals in the 1-10μm size range are in progress [52].

Sodium Stannosilicate Phase B

Initial PXD patterns of phase B materials (encountered, as above, when fumed silica was used as the SiO$_2$ source, or when products were crystallized in the presence of LiOH [47]) were clearly multiphasic, but by cross comparing reflection appearances and intensities in data from three different samples, it proved possible to assign the main peaks in the PXD patterns to one of three phases, of which the predominant was labelled B. Attempts at indexing using the TREOR program [55] based on the positions of a number of the peaks ascribed to phase B yielded two possible unit cells, one tetragonal (with a = 8.812(1)Å and c = 12.460(2)Å) and the other monoclinic (with a = 6.950(3)Å, b = 12.467(5)Å, c = 4.911(1)Å and β = 116.24(2)°). A repeated synthesis of phase B yielded a much cleaner PXD pattern, that showed a well-defined (if weak) peak at 2θ ~12.3° which indicated the former cell to

be the better choice. The metrical relationship, c = √2a in this cell implied that the unit cell symmetry was in fact cubic, with a = ~12.4Å. Subsequent analyses have therefore been based on this description. The results of a typical full decomposition of the PXD pattern [53] of a later phase B synthesis is shown in Figure 4. Chemical analysis yielded a Si:Sn ratio of ~3 in phase B.

The fitting based on the cubic cell leaves unaccounted for peaks at, e.g., 2θ = 18.8°, 26.7°, and 38.5° (Figure 4). Comparison with interpretations of the multiphasic PXD patterns from earlier phase B syntheses enabled these peaks to be assigned to a second phase, identified from the JCPDS file as lithium metasilicate, $(Li_2SiO_3)_x$, (Figure 4). Peaks at these positions in phase B preparations are observed only when lithium hydroxide is a component in the synthesis mixture. The peak 'splittings' observed in one phase A product described above are now directly interpretable as deriving from the simultaneous presence of phase B (Figure 2).
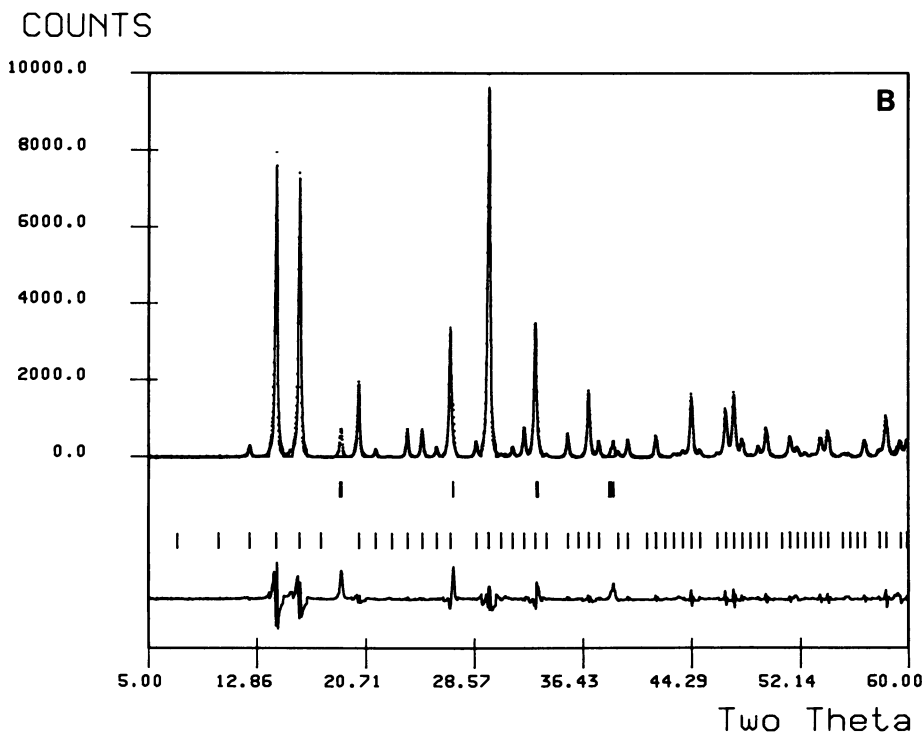
Figure 4. Results of full pattern fitting (after [53]) of the PXD pattern of a phase B sample, based on a cubic unit cell (refined lattice constant a = 12.437(1)Å). The upper reflection bars indicate the calculated positions of the most intense lines from the PXD pattern of lithium metasilicate.

Conclusion

The $M_2O-SiO_2-SnO_2-H_2O$ system clearly provides considerable scope for the synthesis of new octahedral-tetrahedral microporous solids. This account of the initial characterization of two of the phases accessible in this system illustrates that a variety of techniques can be helpful during the phase identification process. Descriptions of other stannosilicates and structural studies of these various phases are in progress.

Acknowledgment

We thank S. B. Rice for electron microprobe data, M. T. Melchior and C. F. Pictroski for solid state nmr measurements, A. J. Jacobson for helpful discussions, and L. B. McKusker for providing a version of and interfaces to G. S. Pawley's ALLHKL program [53].

Literature Cited

1. Smith, J. V. Chem. Rev. 1988, 88, 149-182.
2. Meier, W. M.; Olson, D. H. Atlas of Zeolite Structure Types; Butterworths: London, 1987.
3. Clearfield, A. Chem. Rev. 1988, 88, 125-148.
4. Raveau, B. Proc. Indian Acad. Sci. 1986, 96, 419-448.
5. Desmond, M. J.; Pesa, F.; Eshraghi, R. U.S. Patent 4 634 686, 1987.
6. Chang, C. D.; Chu, C. T-W. EP 237 212, 1987.
7. Corbin, D. R.; Whitney, J. F.; Fultz, W. C.; Stucky, G. D.; Eddy, M. M.; Cheetham, A. K. Inorg. Chem. 1986, 25, 2279-2280.
8. Mazzi, F.; Rossi, G. Zeit. Krist. 1965, 121, 243-257.
9. Moore, P. B.; Shen, J. Nature, 1983, 306, 356-358.
10. Ghose, S.; Gupta, P. K. S.; Campana, C. F. Amer. Miner. 1987, 72, 365-374.
11. Ghose, S.; Wan, C.; Chao, G. Y. Can. Miner. 1980, 18, 503-509.
12. Barrer, R. M. Hydrothermal Chemistry of Zeolites; Academic Press: New York, 1982.
13. Liebau, F. Structural Chemistry of Silicates; Springer-Verlag: New York, 1985.
14. Nekrasov, I. Y. Dokl. Akad. Nauk SSSR 1973, 212, 705-708.
15. Nekrasov, I. Y.; Dadze, T. P.; Boronikhin, V. A.; Rudnitskaya, E. S. Dokl. Akad. Nauk SSSR 1977, 232, 909-912.
16. Nekrasov, I. Y.; Dadze, T. P. Dokl. Akad. Nauk SSSR 1978, 243, 1286-1288.
17. Nekrasov, I. Y.; Dadze, T. P. Ocherki Fiz.-Khim. Petrol. 1978, 8, 193-212.

18. Nekrasov, I. Y.; Dadze, T. P.; Zayakina, N. V. Dokl. Akad. Nauk SSSR 1981, 261, 479-482.
19. Higgins, J. B.; Ribbe, P. H. Am. Miner. 1977, 62, 801-806.
20. Armbruster, T.; Oberhaensli, R. Am. Miner. 1988, 73, 595-600.
21. Metcalf-Johansen, J.; Groenbaek-Hazell, R. Acta Cryst., Sect. B 1976, 32, 2553-2556.
22. Kossiakoff, A. A.; Leavens, P. B. Amer. Miner. 1976, 61, 956-962.
23. Cannillo, E.; Giuseppetti, G.; Tadini, C. Atti Accad. Naz. Lincei, Cl. Sci. Fis., Mat. Natur., Rend. 1969, 46, 457-467.
24. Hawthorne, F. C. Neues Jahrb. Mineral. Monatsh. 1987, 1, 16-30.
25. Couper, A. G.; Clark, A. M. Mineral. Mag. 1977, 41, 411-414.
26. Dunn, P. J.; Peacor, D. R.; Simmons, W. B.; Gaines, R. V. Geol. Foeren. Stockholm Foerh. 1984, 106, 175-177.
27. Nekrasov, I. Y. Zakonomer. Raz. Polez. Iskop. 1973, 10, 183-197
28. Balko, V. P.; Bakakin, V. V. Zh. Strukt. Khim. 1975, 16, 837-842.
29. Amichba, T. M.; Chistyakova, N. I. Geokhimiya 1987, 11, 1647-1650).
30. Dwyer, F. G.; Jenkins, E. E. U.S. Patent 3 941 871, 1976.
31. Higgins, J. B.; Ross, F. K. Cryst. Struct. Comm. 1977, 6, 179-182.
32. Choisnet, J.; Deschanvres, A.; Raveau, B. J. Sol. State Chem. 1972, 4, 209-218.
33. Choisnet, J.; Deschanvres, A.; Raveau, B. J. Sol. State Chem. 1973, 7, 408-417.
34. Safronov, A. N.; Nevskii, N. N.; Ilyukhin, V. V.; Belov, N. V. Dokl. Akad. Nauk SSSR 1983, 269, 850-852.
35. Zayakina, N. V.; Rozhdestvenskaya, I. V.; Nekrasov, I. Y.; Dadze, T. P. Dokl. Akad. Nauk SSSR, 1980, 254, 353-356.
36. Safronov, A. N.; Nevskii, N. N.; Ilyukhin, V. V.; Belov, N. V. Dokl. Akad. Nauk SSSR, 1980, 255, 1114-1116.
37. Niggli, E. Leid. Geol. Med. 1953, 17, 207-213.
38. Maksimova, H. B. Dokl. Akad. Nauk SSSR 1973, 213, 91-93.
39. Vorma, A. Min. Mag., J. Min. Soc. 1963, 615-617.
40. Grey, I. E.; Gatehouse, B. M. Amer. Min. 1979, 64, 1255-1264.
41. Christensen, A. N. Acta Chem. Scan. 1970, 24, 1287-1293.
42. Durif, A.; Maupin, G. Acta Cryst. 1961, 14, 440-441.
43. Safronov, A. N.; Nevskii, N. N.; Ilyukhin, V. V.; Belov, N. V. Dokl. Akad. Nauk SSSR 1982, 267, 850-853.

44. Safronov, A. N.; Nevskii, N. N.; Ilyukhin, V. V.;
     Belov, N. V. <u>Dokl. Akad. Nauk SSSR</u> 1983, <u>268</u>, 360-
     363.
45. Larsen, F. K.; Christensen, A. N.; Rasmussen, S. E.
     <u>Acta Chem. Scand</u>. 1967, <u>21</u>, 1281-1292.
46. Rozhdestvenskaya, I. V.; Zayakina, N. V.; Nekrasov,
     I. Y. <u>Mineral. Zh</u>. 1985, <u>7</u>, 78-82.
47. Corcoran, E. W., Jr.; Vaughan, D. E. W. <u>Solid State
     Ionics</u>, 1988, in press.
48. Visser, J. W. <u>J. Appl. Cryst.</u>, 1969, <u>2</u>, 89-95.
49. Eisenberger, P.; Newsam, J. M.; Leonowicz, M. E.;
     Vaughan, D. E. W. <u>Nature</u>, 1984, <u>309</u>, 45-47.
50. Newsam, J. M.; Vaughan, D. E. W. in <u>ZEOLITES:
     Synthesis, Structure, Technology and Application</u>; B.
     Drzaj, S. Hocevar and S. Pejovnik eds.; Stud. Surf.
     Sci. Cat. <u>24</u>, Elsevier, Holland, 1985; pp 239-248.
51. Newsam, J. M.; King, H. E.; Liang, K. S. <u>Adv. X-ray
     Analysis</u> 1989, <u>32</u>, in press.
52. Newsam, J. M.; King, H. E.; Modrick, M. A. in
     preparation (1988).
53. Pawley, G. S. <u>J. Appl. Cryst</u>. 1981, <u>14</u>, 357-361.
54. Leonowicz, M. E.; Johnson, J. W.; Brody, J. F.;
     Shannon, H. F.; Newsam, J. M. <u>J. Sol. State Chem</u>.
     1985, <u>56</u>, 370-378.
55. Werner, P-E; Eriksson, L.; Westdahl, M. <u>J. Appl.
     Cryst</u>. 1981, <u>14</u>, 357-361.

Chapter 42

Computational Studies
of Zeolite Framework Stability

R. A. van Santen, G. Ooms, C. J. J. den Ouden, B. W. van Beest, and M. F. M. Post

Koninklijke/Shell-Laboratorium, Shell Research B. V., Badhuisweg 3, 1031 CM Amsterdam, Netherlands

For the purpose of determining the relative stabilities
of topologically different aluminum-free tetrahedral
networks, Hartree-Fock-level ab-initio calculations
have been done of the relative stability of three-,
four-, five- and six-unit $SiO(OH)_2$ rings. Very small
differences per T unit are found for the four-, five-
and six-rings; however, the energy per T unit is un-
favourable for the three-ring. Rigid ion lattice mini-
mization calculations have been performed on Al-free as
well as high-Al-content zeolite systems. The results
will be discussed for ZSM-5, mordenite and faujasite
structures. Very small energy differences, of the order
of ~ 20 kJ/mol, are again found for the Al-free net-
works. Open structures have less favourable energy than
dense structures due to decreased Madelung energy.
Large changes in relative energy are found upon variation
of the Al/Si ratio. Medium- and small-pore zeolites are
much more sensitive to an increase in aluminum content
than the wide-pore material. This should be ascribed to
stacking of the cations in the channels of the zeolite.
The implications of these results for zeolite synthesis
are discussed.

The theoretical work to be discussed here has been initiated with
the aim of providing support to fundamental studies of zeolite syn-
thesis. Central to our discussion is the question whether a synthe-
sis approach for new zeolites can be developed on the basis of
guidelines generated by computational design.
    For such an approach to be viable, certain fundamental physico-
chemical knowledge about zeolites and their behaviour is essential.
In particular, one needs to know:
- what zeolite structures are possible;
- what laws govern their synthesis.
    Many leads on new zeolite structures are available in the open
literature (1). We shall therefore concentrate on the second of the

two areas mentioned above, concerning the zeolite formation mechanism.

We are interested in the role of organic ions and organic molecules in zeolite synthesis. The use of organic molecules in zeolite synthesis mixtures in addition to inorganic bases is known to result in the medium-pore-size low-aluminum-content zeolites, such as ZSM-5, that revolutionized several processes of importance to the oil-refining and petrochemical industry.

Since, during synthesis, the organic molecules and ions become incorporated into the zeolite micropores in quantities much larger than required to neutralize the lattice framework, Flanigan (2) proposed that they act as a template around which the zeolite precursor molecules are formed. Barrer (3) proposed that adsorption of organic molecules during synthesis stabilizes the zeolite lattice. This second idea provided the starting point to our theoretical work. It can be understood on the basis of the following considerations.

The major characteristic of a zeolitic material that distinguishes it from a non-zeolitic one is its microporous structure, due to the presence of interconnected channels. This implies that, whereas the interfacial energy is a negligible quantity for large crystallites of non-porous materials, this is no longer more the case for a microporous system.

Consider, for instance, the interaction of the alumina-free silica framework of de-aluminated faujasite with water in the liquid phase. Per mol SiO_2, 1.3 mol H_2O can be occluded. The heat of evaporation of water is 36 kJ/mol and the heat of adsorption –30 kJ/mol, so per mol SiO_2 there is an energy cost of 20 kJ.

It is of interest to compare this figure with the heat of immersion of aluminum-rich faujasite. For a compound with composition $Na_{80}Al_{80}Si_{112}O_{384}$ one calculates –122.5 kJ/mol (4), which is mainly hydration energy of intra-channel sodium ions.

So in the crystallization of microporous systems there is a balance between the energy cost of micropore generation and the energy gain because of interfacial stabilization by occluded molecules. Clearly there is no gain for porous aluminum-free systems in water, so they will not be formed unless a trick is used.

These notions can be given a more exact expression by the use of the rule of Gibbs:

$$d\mu_i = R T / a \cdot [\Sigma_i \theta_i \cdot dln(p_i)] \tag{1}$$

In this expression μ_i is the interfacial chemical potential, a the average surface area, θ_i the fraction of the surface covered by the adsorbed molecule i, and p_i the corresponding partial pressure. Expression (1) can be partially integrated, assuming Langmuir adsorption for the adsorbed molecules, to give:

$$\mu_i = RT / f \cdot [ln(1-\Sigma_i\theta_i)] \tag{2}$$

In expression (2), f^{-1} is the fraction of cavities present in the structure per mol SiO_2. For instance, in silicalite f equals 24. Of course, crystallization of a microporous system completes with the formation of a dense system unless:

$$\mu_i < \mu^{dense} - \mu^{zeo.lat.} \tag{3}$$

In order to quantify this relation one needs information on the lattice energies of zeolites as a function of lattice topology and composition.

In the next sections calculations of the lattice energies of zeolites via several different computational approaches will be reported. Each approach is approximate; each has its own advantage(s).

To begin with, we shall discuss computations of the lattice energies of aluminum-free zeolites. We shall then go on to discuss the lattice energies of aluminum-containing zeolites. We shall conclude this paper with a discussion of the relevance of the results obtained to zeolite synthesis.

The Stability of Zeolitic Silica Lattices

Methods. Initial calculations were done using the semi-empirical Extended Huckel method (5). The purpose of these quantum chemical calculations was to explore the main electronic characteristics of chemical bonding in silica tetrahedral networks. The calculations showed that bonding can be considered covalent and can be considered to be due to localized SiOSi units.

Very small differences in bond strength between different silica polymorphs were found. Since the Extended Huckel Method is too approximate to calculate reliably the small diffferences in energy between low-density material, containing micropores, and high-density material without micropores, work was initiated to study the same problem but now with two rigorous techniques that are currently considered to be state of the art.

Hartree-Fock-level ab-initio calculations can provide reliable potential energy diagrams for small clusters. Such calculations can be applied to the zeolite lattice if the clusters are chosen carefully and use is made of the property that bonding is highly localized in these materials. Calculations were done using the GAMESS ab-initio package.

Since this approach does not account for long-range electrostatic potentials present in the extended material, the second approach chosen was the rigid-ion lattice energy minimization technique, widely used in solid-state chemistry. This method is based on the use of electrostatic potentials, as well as Born repulsion and bond-bending potentials parametrized such that computed atom-atom distances and angles and other material properties, such as, for instance, elastic constants, are well reproduced for related materials. In our case, parameters were chosen to fit α-quartz.

Results of Hartree-Fock Calculations. Using a STO3G basis set, calculations were performed on the open dimer (Figure 1) and 3-, 4-, 5- and 6-rings of C_{nv} symmetry (Figure 2), in which n stands for the number of $(SiO)(OH)_2$ units, the dangling bonds being saturated with H atoms. Figure 3 shows the equi-energy contours of the dimer as a function of bridging SiO length and SiOSi angle. The result fully concurs with results from similar work obtained by Gibbs et al.(6).

It can be seen that there is a steep increase in energy if the SiO distance starts to differ from its equilibrium value, but that the energy changes involved in angle variations are very small. The SiO bond strength is of the order of 450 kJ, whereas the change in energy with angle variation is only of the order of 20 kJ. The
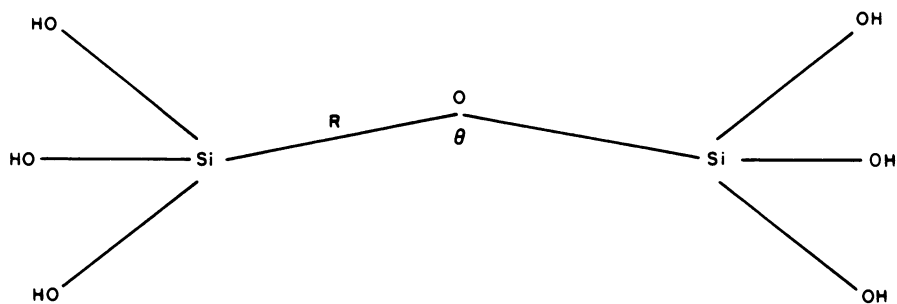
Figure 1. Dimer cluster; C_{2v} symmetry assumed.
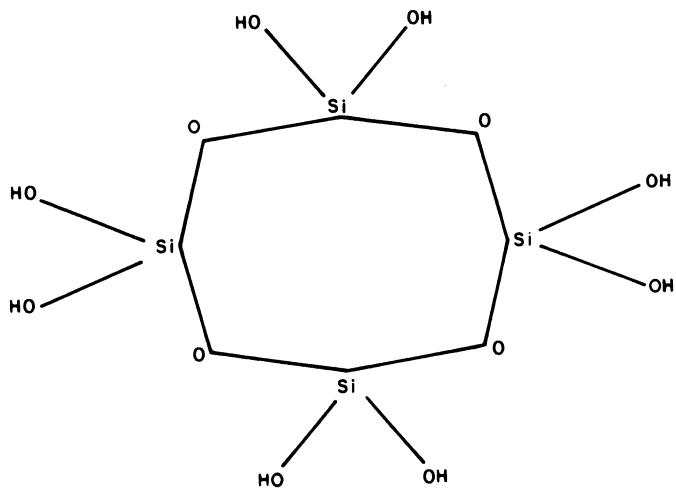
Figure 2. Ring structures; C_{nv} symmetry assumed (n=3, 4, 5, 6).
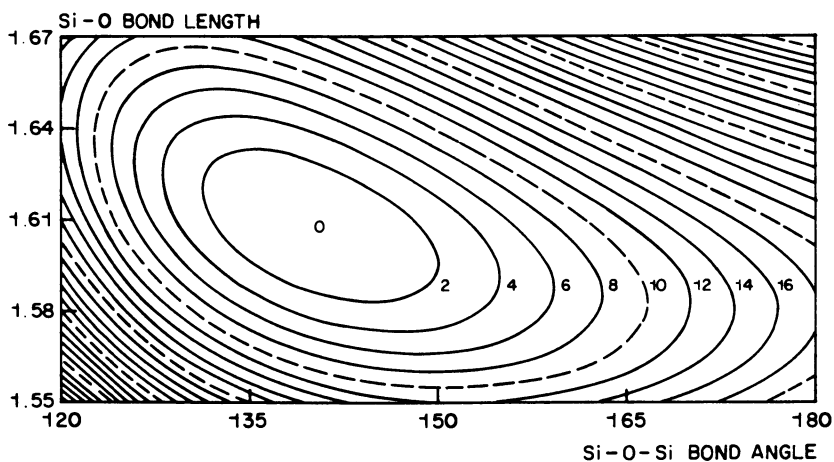
Figure 3. Total energy as a function of Si-O bond length and Si-O-Si bond angle. Contour lines in units of kJ/mol.

latter measurement agrees well with the very low rocking and torsional frequencies around the SiOSi bond measured by infrared experiments on zeolites (7). This implies that lattice deformation can take place at little energy cost as long as no SiO bonds are broken.

Tables I and II summarize the results found for the silicate ring clusters. Table I,A presents the computed total energies per $SiO(OH)_2$ unit. Bond lengths and bond angles in the rings were optimized within the constraint of C_{nv} symmetry. As can be seen in Table I,A the energy difference between the 3-ring and the other rings is considerable. However, the energy differences per unit $SiO(OH)_2$ of the 4-, 5- and 6-rings are computed to be within 1 kJ. Computed SiO distances and SiOSi angles are presented in Table II.

The reason for the instability of the 3-ring can be readily seen. Within the tetrahedra the OSiO angles differ from the optimum tetrahedral angles; in addition, the SiO distances appear enlarged. A clear trend in SiO distance as well as SiOSi angle is observed as a function of ring size: the SiO distance shortens, whereas the SiOSi angle increases. The relation between SiO distance and SiOSi angle is fully consistent with the potential energy diagram presented in Figure 1 and is due to changes in hybridization of the electrons on the O atom (5).

It is of interest to compare the extent to which geometry depends on ring size with the average bond lengths and angles observed in alumina-free zeolites with different numbers of rings. This comparison is given in Table III. A trend in angle and distance variation with increased amount of 5-rings compared to 4-rings similar to that observed in the calculations can be distinguished. The distances compare well; the average angle measured for mordenite and ZSM-5 appears somewhat large, though. This may be due to the difficulty in determining oxygen positions accurately.

Table I. Ring Structures

A. Total Energies

n (Ring Size)	e/n (a.u.)
3	−508.41206
4	−508.41547
5	−508.41578
6	−508.41580

B. Energy Differences in kJ/mol

n	3	4	5	6
3	0.000			
4	−8.944	0.000		
5	−9.765	−0.820	0.000	
6	−9.806	−0.861	−0.041	0.000

Table II. Optimized Geometries for Ring Structures

Distances in Ångstrom, angles in degrees

	3	4	5	6
Si-O	1.662	1.602	1.595	1.592
Si-Si	2.942	3.042	3.063	3.067
Si-O-Si	130.1	143.5	147.5	148.8
O-Si-O	105.7	108.3	108.4	108.1

Table III. Comparison of Average Distances (Ångstrom)
and Angles (Degrees) Calculated for a Few
Zeolites with Different Ratios of n-Rings (nR)

	4R(%)	5R(%)	6R(%)	Distance	Angle
Faujasite(26)	70	0	30	1.61	142
Mordenite(22)	5	95	0	1.58	157
ZSM-5(20)	5	85	10	1.59	156

The results of these calculations are consistent with our earlier conclusions. As long as no 3-rings are present in the alumina-free material, differences in covalent energy are very small. The ab-initio calculations indicate that these differences do not exceed 1 kJ/mol.

Rigid Ion Lattice Energy Minimization Calculations. Table IV presents lattice energies derived from fully converged rigid ion lattice energy minimization calculations. Again one notices the small difference in energy between dense and open structures. The dependence on density (8) is presented in Figure 4.

The lower energy of the more open structures relates to the decrease in Madelung energy. However, as Figure 2 shows, local topological effects also play a role. See, for instance, the difference in energy calculated between zeolite A and faujasite.

Table IV. Calculated Rigid Ion Lattice Energies
of Aluminum-Free Zeolite Lattices

Zeolite	Lattice Energy, kJ/mol
Faujasite	-11914
Mordenite	-11931
Zeolite A	-11931
Silicalite	-11945
Sodalite	-11949
α-Quartz	-11959

Discussion of Alumina-Free-Lattice Calculations. Two main conclusions emerge from the results presented so far. Firstly, the energy differences between tetrahedral networks with different ring systems are very small, except when the networks contain 3-rings not found in nature.

This is a very significant conclusion because it is widely believed (9) that, in order to synthesize systems with 5-rings, such as ZSM-5, the only requirement is to synthesize systems low in alumina. Both our quantum-chemical and our electrostatic lattice calculations contradict this theory. The calculations show, for example, that sodalite, which contains only 4- and 6-rings and no alumina, is more stable than ZSM-5, in which 5-rings predominate. This agrees with recent experimental work relating to the synthesis of high-silica sodalite (10).

Secondly, the decrease in lattice energy with increasing microporous volume reaches a maximum at 45 kJ/mol, the difference between α-quartz and faujasite, faujasite being the zeolite with the largest micropore volume.

Expressions 2 and 3 show that, in order to overcome this energy difference, the micropore cavities should be largely filled with adsorbed molecules. As mentioned earlier, in cases where low-alumina-content materials have been directly synthesized, high values for θ_i are invariably found. This confirms Barrer's postulation. The dominant interaction that governs narrow- and medium-pore zeolite synthesis is the strong interaction of the occluded organic molecule with the micropore wall.

Of interest with respect to this hypothesis is the significant difference in heat of paraffin adsorption between the medium-pore zeolite silicalite and large-pore, de-aluminated faujasite. The heat of paraffin adsorption is much smaller in the case of the de-aluminated faujasite, which has so far had to be prepared by an indirect route, than for silicalite, which can be synthesized direct in the presence of an organic molecule. The difference, which increases with chain length, is of the order of 5 kJ/mol per CH_2 unit, and may be ascribed to the optimum fit of hydrocarbon and channel in the case of the medium-pore zeolite (11, 12).

^{13}C solid-state NMR studies on occluded organic ions by ourselves (13) and others (14) have provided further evidence for the strong interactions between occluded organic molecule and micropore wall mentioned above. We have also reported lattice stabilization of silicalite (ZSM-5) by occlusion of tetrapropylammonium ions (15). It is therefore very unlikely that a synthesis procedure can be defined for the preparation of highly siliceous forms of large-pore (12-ring or larger) zeolites such as faujasite direct.

Variation of Zeolite Lattice Composition

The changes in heat of formation as a function of alumina content were studied via two different approaches.

One approach (4) is to calculate, for a certain zeolite structure, the Madelung and polarization energies for fixed lattice positions. The heat of formation due to ionic bonding is calculated both for the zeolitic aluminosilicate with varying amount of aluminum and

sodium ions and for the zeolitic silica, with the same framework distances as in the aluminum-containing material. The difference between the two heats of formation is assumed to represent the contribution of the total heat of formation due to ionic bonding stemming from the presence of aluminum ions and cations in a particular zeolite structure.

In these calculations averaged charges on the intra-tetrahedral lattice cation positions were used. The difference between the two heats of formation due to ionic bonding is added to the heat of formation due to covalent bonding resulting from the simple Extended Huckel Method for zeolitic silicas in order to arrive at the total heat of formation of the zeolite structure as a function of the amount of aluminum.

For the calculations we used the method and computer program described by Piken and Van Gool (16,17).

Adsorption of water into the pores of a zeolite structure may contribute considerably to the total heat of formation because of hydration of the cations present in the pores. Using empirical data on hydration with water we have estimated the magnitude of this effect (4).

The second approach involves the use of the rigid ion lattice energy minimization method discussed earlier. This technique proved especially useful for determining the stability of structures following calculation of their energy by the method discussed in the previous paragraph. The charges of aluminum and silicon were again averaged.

Results of Madelung and Potential Energy Calculations. Figure 5 gives the heat of formation due to ionic bonding for faujasite, mordenite and ZSM-5 in the presence and in the absence of Al^{3+} and Na^+ ions. Lattices with the same lattice constant are compared. SiO and AlO distances used are values extrapolated from low- and high-Al-content zeolite crystallographic data. The results for the total heat of formation computed in the way explained earlier are given in Figure 6. A decrease in the heat of formation with increasing aluminum content is observed. In the final step of the calculation the effect of hydration of the cations was taken into account. The results are presented in Figure 7.

Changing the aluminum content has a significant effect on the relative stability of zeolite structures with very different topology. While the heat of formation of the wide-pore zeolite is affected very little, the heats of formation of the medium-pore zeolites fall significantly.

Results of Lattice Energy Minimization Calculations. Relative lattice energies of faujasite, mordenite, silicalite and sodalite were compared. For the framework and cation positions of faujasite and sodalite the same data were used as before, from Hseu (18) and Olson (19), and Baerlocher (20) and Chao (21), respectively. For mordenite and sodalite the data of Meier (22) and Mortier (23) (on mordenite) and Baerlocher and Meier (24) (on sodalite) were used. The starting unit cells for faujasite and mordenite have the chemical composition $Na_x[Al_xSi_{48-x}O_{96}]$. For sodaite and ZSM-5 we used $Si_{12}O_{24}$ and $Na_x[Al_xSi_{96-x}O_{192}]$. The framework and cation positions were allowed to relax under constant pressure. Parameter values used and details of the calculation can be found in (25).

LATTICE ENERGY, kJ/mol x 10^3
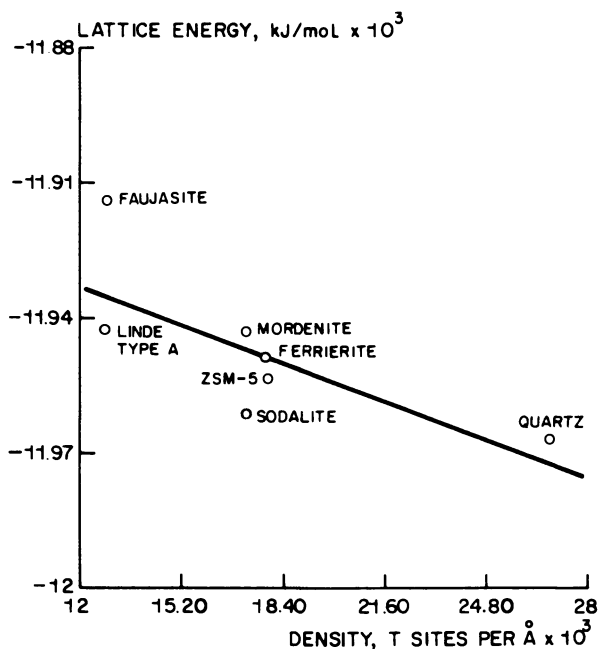
Figure 4. Lattice energy as a function of density.
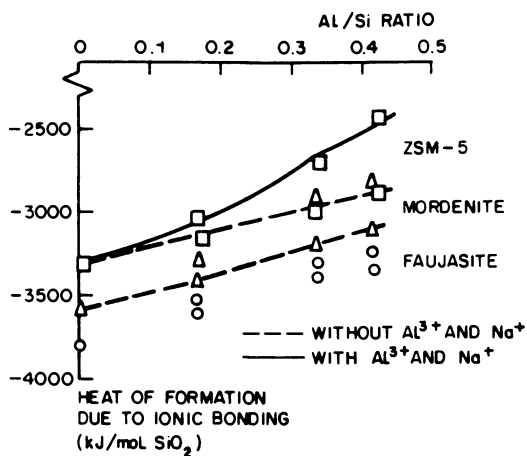
Figure 5. Influence of Al/Si ratio on heat of formation due to ionic bonding.
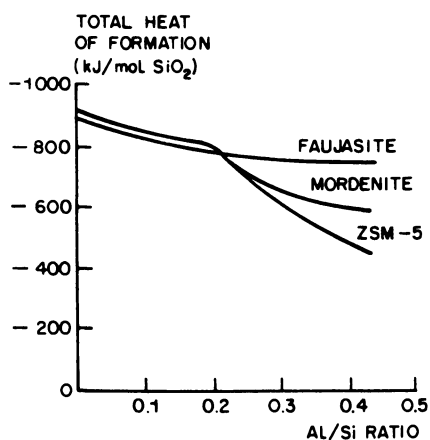
Figure 6. Total heat of formation as a function of Al/Si ratio without effect of hydration.
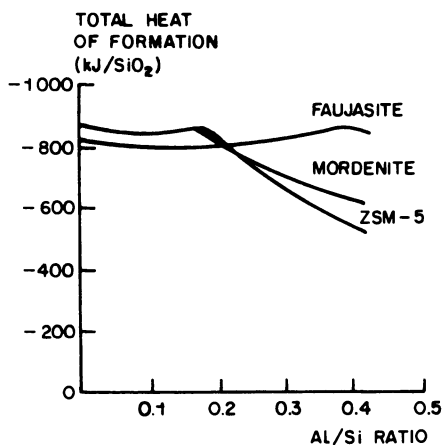
Figure 7. Total heat of formation as a function of Al/Si ratio with effect of hydration.

Figure 8A shows the computed lattice energies for faujasite and mordenite as a function of Al/Si ratio. These fully converged calculations agree very well with approximate calculations discussed earlier. At Al/Si ratios larger than 0.2 the lattice energy of mordenite starts to decrease compared to that of faujasite. Figure 8B shows computed lattice energies for ZSM-5 as a function of Al/Si ratio. Only the first two calculations are fully converged to an energy minimum. The calculations for Al/Si>0.05 correspond to calculations where no energy minimization is performed.

It appears that convergence of the calculations is only possible for a finite range of Al/Si ratios. This is shown in Figure 9. The maximum Al/Si ratio at which calculations converge is 0.05 for ZSM-5, 0.5 for mordenite and 0.8 for faujasite. Also indicated in the figure are the maximum Al/Si ratios which can be obtained by direct synthesis.

Discussion of the Calculated Al/Si Dependence. Both approaches show very clearly the great changes that occur in relative energy upon variation of the Al/Si ratio. Whereas the electrostatic contribution to the total energy is very small for the Al-free material, it becomes significant for Al-containing materials. The greater sensitivity of the medium-pore zeolites than the wide-pore material to the increase in aluminum content has to be ascribed to the stacking of the cations in the channels of the zeolite. For instance, it is shown in Figure 10B that a ZSM-5-type structure cannot accommodate sodium cations at a Si/Al ratio of 1.4, because the cations become so close that strong repulsive interactions take place. In addition, such low Si/Al ratios result in unfavourable channel positions having to be occupied. As can be seen in Figure 10A, for a Si/Al ratio of 11 the sodium cations are much less clustered together, so that repulsion is far less.

Impact on Zeolite Synthesis Strategies

We have presented evidence that the interaction of molecules or ions occluded in the micropores between themselves and with the zeolite wall plays a decisive role in the thermodynamics of zeolite formation.

It has been shown that the alumina-free zeolites are hydrophobic and hence interact unfavorably with water. This renders them thermodynamically unstable in aqueous solution with respect to dense phases. Only when organic molecules are occluded does water penetration decrease and the favourable interaction of occluded molecules with the zeolitic silica micropore wall become dominant. This is a means whereby the alumina-free zeolites may become thermodynamically stable.

We have also discussed the fact that a good fit between the organic molecule and zeolite wall is required for such a favorable interaction. This implies that synthesis techniques employing organic molecules may be expected to yield aluminum-free zeolites with pore dimensions of the order of the dimensions of the organics used.

It follows from the calculations on the lattice energy as a function of Al/Si ratio that synthesis of new wide-pore zeolites would require a different strategy. We have found that increasing
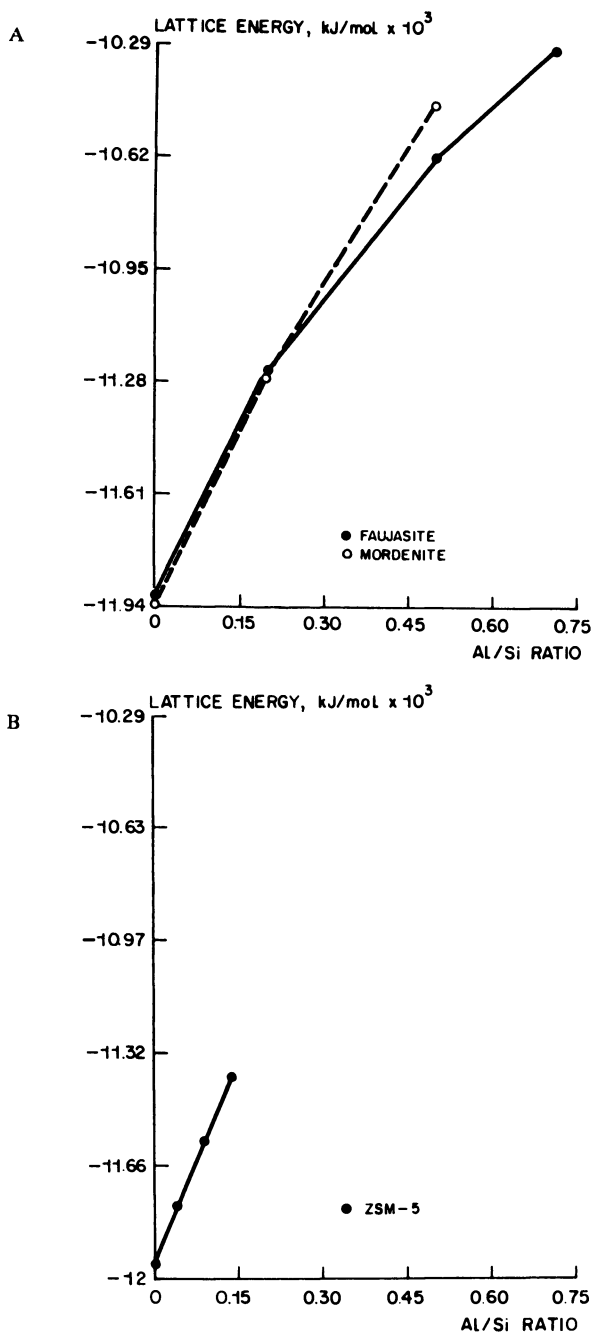
Figure 8. Lattice energy as a function of Al/Si.
        A: Faujasite and mordenite.
        B: ZSM-5.

MAXIMUM ALLOWABLE AL/Si RATIO
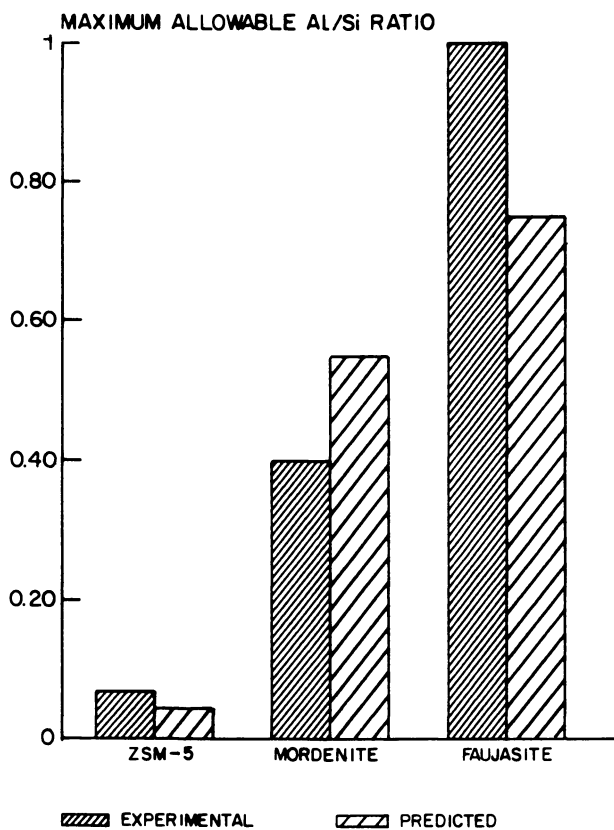
Figure 9. Experimental and predicted maximum allowable Al/Si ratios.
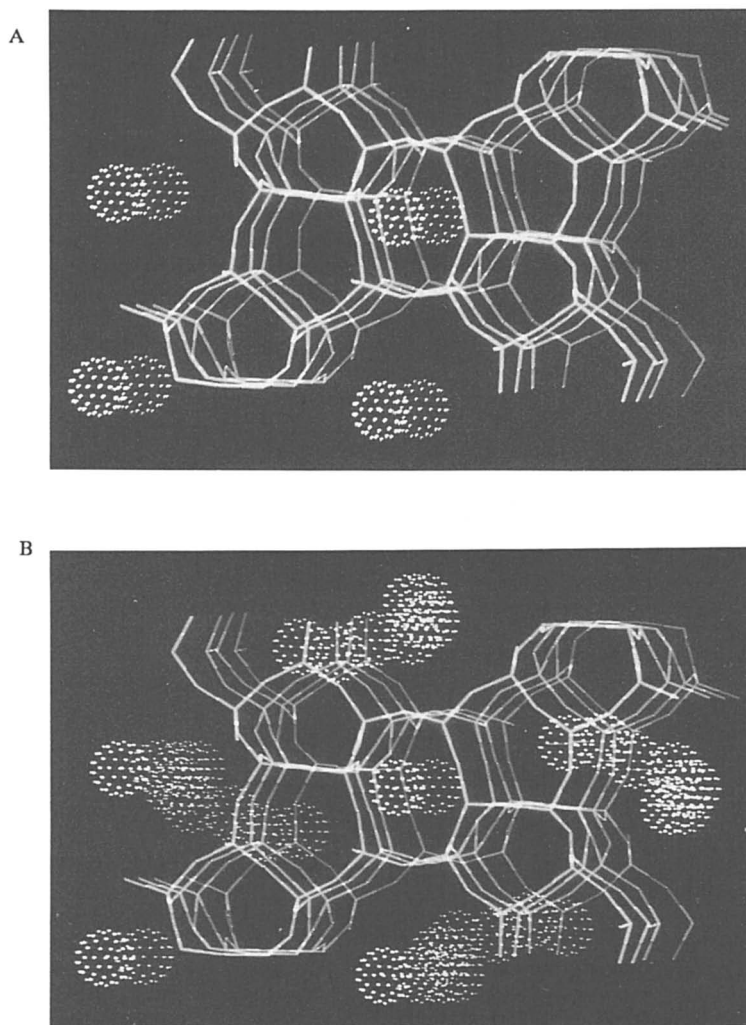
Figure 10. Sodium distribution in ZSM-5.

A: Si/Al = 11.

B: Si/Al = 1.4.

isomorphic substitution of cations of a lower valency for Si in the
tetrahedral zeolite framework causes large-ring structures to stabi-
lize with respect to dense structures. In small- to medium-pore zeo-
lites, the cations which will have to be introduced in the
micropore channels in order to compensate for the negative charge on
the zeolite lattice and to maintain charge neutrality will interact
with each unfavorably other if the concentration of low-valency
cations in the lattice is high. In wide-pore zeolites the repulsion
is less; moreover, more favorable channel positions may be available
than in the more dense zeolites.

In the search for wide-pore zeolite synthesis conditions,
therefore, efforts should be concentrated on the field where zeo-
lites are produced with a large amount of isomorphous substitution.

Lattice energy calculations can assist in assessment of which
cations are to be chosen in the zeolite lattice or channels in order
to stabilize the structure.

Literature Cited

1. See: a. Smith, J.V.; Bennet, J.M. Am. Miner. 1984, 69, 104.
        b. Meier, W.M. Proc. 7th Int. Zeolite Conf., Tokyo, 1983,
           p. 13.
2. Flanigan, E.M. Adv. Chem. Ser. 1973, 121, 119.
3. Barrer, R.M.
     a. Proc. Int. Symp. Zeolites, Portorosa, 1984.
     b. Zeolites 1985, 1.
     c. J. Phys. Chem. Solids 1960, 16, 84.
4. Ooms, G.; Van Santen, R.A.; Jackson, R.; Catlow, C.R.A.
     'On the Relative Stabilities of Zeolitic Aluminosilicates',
     Studies in Surf. Sci. and Catal. 1988, 37, 317.
5. Ooms, G.; Van Santen R.A. Rec. Trav. Chim. Pays Bas 1987, 106,
     69.
6. a. Gibbs, G.V. Am. Miner. 1982, 67, 421.
     b. Newton, M.D.; Gibbs, G.V. Phys. Chem. Minerals 1980, 6,
        305.
     c. O'Keeffe, M.; Domenges, B.; Gibbs, G.V. J. Phys. Chem. 1985,
        89, 2304.
7. Van Santen, R.A.; Vogel, L. Adv. Solid-State Chem. 2 (in
     press).
8. Meier, W.M.; Olson, D.H. Atlas of Zeolite Type Structures;
     Structure Commission of the International Zeolite Association
     (1978).
9. Mortier, W.J.; Geerlings, P.; Van Alsenoy, C.; Figeys, H.P.
     J. Phys. Chem. 1979, 83, 855.
10. Bibbey, D.M. Nature 1985, 317, 157.
11. Derouane, E.G. J. Catal. 1986, 100, 541.
12. Stack, H.; Lohse, U.; Thamen, H.; Schirmer, W. Zeolites 1986,
     6, 74.
13. Boxhoorn, G.; Van Santen, R.A.; Van Erp, W.A.; Hays, G.R.;
     Huis, R. Proc. 6th Int. Zeolite Conf. Reno (1983), Chem. Soc.
     Chem. Comm. 1984, 264.
14. Nagy, J.B.; Gobelica, Z.; Derouane, E.G. Zeolites 1983, 3, 43.
15. Van Santen, R.A.; Keijsper, J.J.; Ooms, G.; Kortbeek, A.G.T.G.
     Stud. Surf. Sci. Catal. 1986, 28, 169.

16. Piken, A.G.; Van Gool, W. Ford Motor Company, Scientific
    Laboratory, Technical Report SL 68010, 1968.
17. Van Gool, W.; Piken, A.G. J. Mat. Sci. 1969, 4, 95.
18. Hseu, T. PhD Thesis, University of Washington, 1972, University
    Microfilms, no. 73-13835, Ann Arbor.
19. Olson, J. J. Phys. Chem. 1981, 85, 2238.
20. Baerlocher, C. Proc. 6th Int. Zeolite Conf., Reno (1983),
    Chem. Soc. Chem. Comm. 1984, 264.
21. Chao, L. Zeolites 1986, 6, 35.
22. Meier, W.M. Z. Kristallograph. 1961, 115, 439.
23. Mortier, W.J.; Bosmans, H.J.; Uytterhoeven, J.B. J. Phys. Chem.
    1972, 76, 650.
24. Baerlocher, Ch.; Meier, W.M. Helv. Chim. Acta 1969, 52, 1853.
25. Ooms, G.; Van Santen, R.A.; Den Ouden, C.J.J.; Jackson, R.A.;
    Catlow, C.R.A. J. Phys. Chem., in press.
26. Bauer, W.H. Am. Miner. 1964, 49, 697.

Author Index

Affiliation Index

Subject Index

Affiliation Index

Subject Index

M

Madelung energy calculations, zeolite silica lattices, 625,626–627*f*
Magic angle spinning (MAS) NMR spectroscopy
  AlPO₄–H₃, 317,318*f*
  borosilicate zeolites, 396–400
  faujasitic catalysts, 450
  MCM–1, 314,316*f*,317
  method obtained, 307
MCM–1 zeolite
  anhydrous chemical composition, 306
  catalytic activity, 322,324*t*
  chemical composition, 317,320*t*
  effect on synthesis
    agitation, 320
    pH of gel, 319
    temperature, 319–320
  hydroxyl groups, 322,323*f*
  IR spectrum, 322,323*f*
  isomorphous substitution of Si, 320,321*f*,322,323*f*
  MAS NMR spectra, 320,321*f*
  pore filling, 324
  void structure, 324,325*t*,326
Metal aluminophosphate molecular sieves
  acronym, 329–330
  adsorption, 340,341*t*,342
  n-butane cracking values, 342*t*,343
  catalytic activity, 342*t*,343
  characterization, 339–343
  chemical analysis, 339,340*t*
  discovery, 329
  effect on synthesis
    di-*n*-propylamine, 338–339*t*
    quinuclidine, 336,337*t*
    tetraethylammonium, 333–334,335*f*,336
    tetramethylammonium, 333*t*
    tripropylamine, 329
  elemental composition of gel and product, 336,337–338*t*
  product distribution vs. gel Mg concentration, 334,335*f*,336
  structures, 330,331*t*
  synthesis conditions
    favoring structure formation, 338*t*
    for crystallization with di-*n*-propylamine, 338,339*t*
  synthesis procedure, 329
  thermal stability, 343
  X-ray crystallography, 340
  X-ray diffraction patterns, 330–331,332*f*
Metal incorporation, zeolites, 487
Metallosilicates, synthesis using rapid crystallization, 491
MFI zeolites, influence of organic molecules in synthesis, 221–222

MFI zeolites containing propylammonium cations
  calorimetric measurements, 224
  chemical formula per unit cell, 223*t*
  sample calorimetric cell, 224,225*f*
  standard enthalpy of formation, 228–229
  standard solution enthalpy, 228–229
  starting chemical molar composition, 222*t*
  synthesis, 222–223*t*,224
  thermochemical cycle, 224,226,227*f*
  thermochemical scheme for enthalpy of formation, 226*t*
MFT zeolites
  n-propyl alcohol adsorption, 188,192*f*,193
  synthesis, 180–185
Microporous crystals
  isotherms, 20,22*f*
  model for host–guest solutions, 20,22*f*,23*t*
  synthesis with host–guest solutions of zeolites, 18–19,20–21*t*
Microporous materials, hydrothermal syntheses, 603
Microporous silicoaluminophosphates
  AlPO₄–H₃ and MCM–1 zeolite characterization, 314–320
  conditions for synthesis, 319–320
  hydroxyl groups, 322,323*f*
  pore filling, 324
  catalytic activity, 322,324*t*
  influence of agitation and synthesis temperature of two-phase system, 307,308*t*,309,310–311*f*
  isomorphous substitution of Si, 320,321*f*,322,323*f*
  MCM materials, 305–306
  SAPO materials, 305–306
  scanning electron micrograph, 309,311*f*
  synthesis in emulsifying conditions with Pr₄N–OH, 309,312*t*,313*f*
  synthesis in nonemulsifying conditions with Pr₂N using increasing amounts of Si, 309,312*t*
  void structure of MCM–1 zeolite, 324,325*t*,326
  X-ray diffraction pattern, 308,310–311*f*
Mineralizers, role in zeolite synthesis, 18
M₂O–SiO₂–SnO₂–H₂O gels/solutions, phase identification of hydrothermal crystallization products, 603
Molecular sieve materials, interest in large crystals, 346–347
Molecular sieve zeolites
  catalysis, 5–6
  commercialization, 7
  crystal structure, 3
  hydrothermal synthesis, 2
  major contributors to discovery and commercialization, 8–9